

Synthesis and Evaluation of Novel Antivascular Agents for Two-Photon Activation

Natalie Barnes

School of Environment and Life Sciences

University of Salford, Salford, UK

Submitted in Partial Fulfilment of the Requirements of the Degree of Doctor of
Philosophy, May 2018

Contents

LIST OF FIGURES.....	V
LIST OF TABLES.....	XVI
LIST OF SCHEMES.....	XVIII
ACKNOWLEDGEMENTS.....	XX
DECLARATION.....	XXII
ABSTRACT.....	XXIII
ABBREVIATIONS.....	XXIV
1. INTRODUCTION.....	1
1.1 Cancer.....	1
1.1.1 What is cancer?.....	1
1.1.2 Cancer treatments.....	4
1.1.3 Anticancer drugs.....	6
1.1.4 Treatment of cancer with light – Photodynamic therapy.....	15
1.2 Combretastatins.....	19
1.2.1 Combretastatin A4 disodium phosphate in clinical trials.....	21
1.2.2 How do combretastatins act?.....	24
1.2.3 Synthesis of combretastatins.....	26
1.2.4 Recent developments in CA-4 based analogues.....	30
1.2.5 Structure-Activity Relationship of the combretastatins.....	34
1.2.6 Combretastatins investigated in the course of this work.....	35
1.3 Principles of photochemistry and photophysics.....	37
1.3.1 Absorption and fluorescence.....	37

1.3.2 The Stokes shift	38
1.3.3 Fluorescence lifetimes and quantum yields	39
1.3.4 Two-photon absorption	39
1.3.5 Photoisomerization of stilbenes	41
1.4 Fluorescence microscopy techniques	44
1.4.1 History of light microscopy	44
1.4.2 Fluorescence microscopy.....	44
1.4.3 Confocal Microscopy.....	45
1.4.4 Multiphoton fluorescence microscopy.....	46
1.4.5 Fluorescence lifetime imaging microscopy (FLIM)	47
1.4.6 Light sheet fluorescence microscopy (LSFM)	48
1.5 Aims of the project	50
2. MATERIALS & METHODS.....	51
2.1 Synthesis and purification of combretastatins	51
2.1.1 General procedures for compound purification and determination	51
2.1.2 Synthesis of combretastatins and related analogues.....	53
2.2 Experimental – bioactivity assays	85
2.2.1 Subculture and cell maintenance	85
2.2.2 Cell lines and composition of tissue culture media	86
2.2.3 MTT assay using adherent cell lines	88
2.2.4 Tubulin polymerisation assay	90
2.2.5 Cell cycle analysis.....	90
2.3 Experimental – Spectroscopy and microscopy	92
2.3.1 General.....	92
2.3.2 Spectroscopy and microscopy instrumentation	92
2.3.3 Extinction coefficients, spectral shifts and Lippert plots.....	93

2.3.4 Determination of fluorescence quantum yields Φ_F	94
2.3.5 Fluorescence lifetime measurements	95
2.3.6 Non-linear power dependence of combretastatins	95
2.3.7 2PA cross sections of combretastatins	96
2.3.8 Image analysis using Fiji	96
3. RESULTS & DISCUSSION - SYNTHESIS OF <i>E</i>- AND <i>Z</i>-COMBRETASTATINS	97
3.1 Synthesis of diarylalkynes using Sonogashira cross-coupling.....	97
3.2 Synthesis of <i>E</i> - and <i>Z</i> -combretastatins using the Wittig reaction	104
3.3 Synthesis of <i>Z</i> -combretastatins using Suzuki-Miyaura coupling	106
3.4 Synthesis of secondary alcohols from aldehydes	112
3.5 Iodine catalysed <i>Z</i> - to <i>E</i> - isomerisation.....	116
4. RESULTS & DISCUSSION – BIOLOGICAL EVALUATION OF COMBRETASTATINS.....	118
4.1 Cytotoxicity of <i>E</i> - and <i>Z</i> -combretastatins determined by MTT-assays.....	118
4.2 Tubulin polymerization activity of <i>Z</i> -combretastatin derivatives.....	129
4.3 Cell cycle analysis	139
5. RESULTS & DISCUSSION – SPECTROSCOPIC PROPERTIES OF COMBRETASTATINS	144
5.1 Extinction coefficients, spectral shifts and Lippert plots of <i>E</i> -combretastatins	145
5.2 Fluorescence quantum yields and lifetimes of <i>E</i> -combretastatins	151
5.2.1. Fluorescence quantum yield using the standard 9-chloroanthracene.....	151
5.2.2 Fluorescence lifetime and quantum yield of <i>E</i> -combretastatins.....	153
5.3 Nonlinear power dependence of <i>E</i> -combretastatins on two-photon excitation	156
5.4 Two-photon absorption (2PA) cross-sections of <i>E</i> -combretastatins.....	158
6. RESULTS & DISCUSSION – IMAGING OF COMBRETASTATINS IN LIVE MAMMALIAN CELLS..	160
6.1 Intracellular uptake and distribution of <i>E</i> -combretastatins in cell monolayers.....	160
6.2 Intracellular uptake and distribution of <i>E</i> -combretastatins in cell spheroids	172

6.3 Intracellular power dependence of <i>E</i> -combretastatins.....	186
7. CONCLUSIONS & FUTURE OUTLOOK.....	188
8. REFERENCES.....	190
9. APPENDIX.....	224
9.1 ¹ H- and ¹³ C- NMR spectra	224
9.2 FTIR spectra.....	258
9.3 Mass spectra	272
9.4 Absorbance and fluorescence spectra.....	277
9.4.1 (E)-4-(3',4',5'-Trimethoxystyryl)benzaldehyde (42)	277
9.4.2 (E)-2-Hydroxy-4-(3',4',5'-trimethoxystyryl)benzaldehyde (43)	278
9.4.3 (E)-4-(3',4',5'-Trimethoxystyryl)acetophenone (46).....	279

List of figures

Figure 1 Incidence Rate of the most common cancer types in the UK (based on figures from Cancer Research UK).....	1
Figure 2 A comparison of normal cell division and cancerous cell division (adapted from (Loeb, 2001)).....	3
Figure 3 Structures of adenine, cytosine and guanine	6
Figure 4 Structures of some alkylating agents.....	7
Figure 5 Structures of common anti-metabolite cancer drugs.	8
Figure 6 Structures of common DNA intercalating agents.	9
Figure 7 Structure of a microtubule in which the cross-section shows the 13 protofilaments (adapted from (Splettstoesser, 2015)).	10
Figure 8 Sketch of the mitotic spindle	11
Figure 9 Colchicine (left) and colchicine binding site on tubulin (right, (Techne, 2008)).....	12
Figure 10 Vinblastine (17) and Vincristine (18) (Noble, Beer & Cutts, 1958)	13
Figure 11 Taxol.....	14
Figure 12 Simplified Jablonski diagram showing energy levels and photochemical mechanisms of PDT (M. Scherer et al., 2017).....	17
Figure 13 Conversion of <i>E</i> -combretastatins to <i>Z</i> -combretastatins by photoisomerisation	18
Figure 14 Structure of combretastatin (Pettit <i>et al.</i> , 1982).....	19
Figure 15 Structures of <i>cis</i> -combretastatin A-4 (<i>Z</i> -CA-4) (left) and <i>cis</i> -combretastatin A4 disodium phosphate (<i>Z</i> -CA4P) (right)	20
Figure 16 <i>cis</i> -CA-4 (yellow) bound to the colchicine site of tubulin (Gaspari <i>et al.</i> , 2017)	24
Figure 17 Rounding of endothelial cells after treatment with <i>Z</i> -CA4 (Tozer et al., 2002)	25
Figure 18 CA-4 derivatives with heterocycles replacing the <i>cis</i> -olefinic bond	31
Figure 19 CA-4 derivatives with replacements and substitutions at <i>cis</i> -olefinic bond	32
Figure 20 CA-4 derivatives with modifications of <i>cis</i> -olefinic bond and B-ring	33
Figure 21 CA-4 derivatives with modification to the B-ring	34
Figure 22 Structure activity relationship of the combretastatins	34
Figure 23 Jablonski diagram adapted from Lakowicz, 2006	38
Figure 24 Jablonski diagram of two-photon absorption.	40

Figure 25 Nonlinear processes in the focal volume of a multiphoton microscope depending on the laser power	40
Figure 26 Commonly accepted energy surface for stilbene photoisomerization (adapted from Kovalenko <i>et al.</i> , 2010).....	42
Figure 27 Epi-fluorescence microscope (Abramowitz <i>et al.</i> , 2012).....	45
Figure 28 Comparison of confocal and multiphoton microscopy (Denk & Svoboda, 1997) ..	47
Figure 29 Siedentopf and Zsigmondy's lightsheet microscope with specimen holder mounted onto objective(a) and illuminating objective at 90° (b) for the collection of sunlight to observe gold particles (Siedentopf & Zsigmondy, 1902)	49
Figure 30 Basic light sheet fluorescence microscope (Adams <i>et al.</i> , 2015).....	49
Figure 31 labelling of olefinic CH	52
Figure 32 The reduction of MTT to MTT formazan.	88
Figure 33 Plot of drug concentration versus cell viability [%] of Z-CA4.	89
Figure 34 Example of plots acquired during cell-cycle analysis.....	91
Figure 35 Ketone isolated from secondary alcohol	114
Figure 36 Proposed structure of chromium complex.....	115
Figure 37 Structures of combretastatin derivatives	119
Figure 38 cis-CA-4 (yellow) bound to the colchicine site of tubulin (Gaspari <i>et al.</i> , 2017) ...	121
Figure 39 Combretastatin derivatives with varying <i>para</i> -substituents on the B-ring	122
Figure 40 Superimposition of the tubulin-cis-CA-4 (yellow) and tubulin-colchicine (grey) complex structures (Gaspari <i>et al.</i> , 2017).....	122
Figure 41 Effect of 53 on cell <i>viability</i> after 24, 48, 72 hours on HepG2, HeLa and HCT-116 cells	123
Figure 42 Effect of 42Z on cell <i>viability</i> after 24, 48, 72 hours on HepG2, HeLa and HCT-116 cells	123
Figure 43 Effect of 43Z on cell <i>viability</i> after 24, 48, 72 hours on HepG2, HeLa and HCT-116 cells	124
Figure 44 Structure of CA-4 and (Z)-1-(4-Methoxyphenyl)-2-(3,4,5-trimethoxyphenyl)-ethene	124
Figure 45 Effect of 46 on cell <i>viability</i> after 24, 48, 72 hours on HepG2, HeLa and HCT-116 cells	125
Figure 46 Binding of a) Z-CA-4 and b) E-CA-4 to tubulin (Gaspari <i>et al.</i> , 2017).....	127

Figure 47 Effect of 42E on cell <i>viability</i> after 24, 48, 72 hours on HepG2 cells.....	127
Figure 48 Effect of 43E on cell <i>viability</i> after 24, 48, 72 hours on HepG2 cells.....	128
Figure 49 Effect of 46E on cell <i>viability</i> after 24, 48, 72 hours on HepG2 cells.....	128
Figure 50 Polymerisation curve of control (blue), paclitaxel (orange) and CA-4 (grey).....	130
Figure 51 Polymerisation curve of control (blue), paclitaxel (orange), 42 (grey), 43 (yellow) 46 (light blue), 47 (green) and 53 (lilac).....	131
Figure 52 Polymerisation curve of control (blue), paclitaxel (orange), 45 (grey), 49 (yellow) and 50 (light blue).....	132
Figure 53 Polymerisation curve of control (blue), paclitaxel (orange), 44 (grey), 48 (yellow), 51 (light blue) and 52 (green)	133
Figure 54 Polymerisation curve of control (blue), paclitaxel (orange) compound 42E (grey), 43E (yellow) and 46E (light blue)	134
Figure 55 Polymerisation curve of control (blue), paclitaxel (orange) compound 42 (1 μ M, grey) (0.5 μ M, yellow) and (0.1 μ M, light blue).....	135
Figure 56 Polymerisation curve of control (blue), paclitaxel (orange), compound 43 (1 μ M, grey) (0.5 μ M, yellow) and (0.1 μ M, light blue).....	136
Figure 57 Polymerisation curve of control (blue), paclitaxel (orange) compound 46 (1 μ M, grey) (0.5 μ M, yellow) and (0.1 μ M, light blue).....	136
Figure 58 A plot of log concentration <i>versus</i> percentage tubulin inhibition to determine IC ₅₀	138
Figure 59 Schematic of the cell cycle	139
Figure 60 a) A dot plot of forwards scatter <i>versus</i> sideways scatter with gate applied to identify cell population; b) propidium iodide histogram with markers to identify stages of the cell cycle.....	141
Figure 61 The effect of compound 42 on cell cycle progression of HepG2 cells determined by flow cytometry.....	142
Figure 62 The effect of compound 43 on cell cycle progression of HepG2 cells determined by flow cytometry.....	143
Figure 63 The effect of compound 46 on cell cycle progression of HepG2 cells determined by flow cytometry.....	143
Figure 64 Lippert plot of E-combretastatins investigated. Inset: dipole moments of E- combretastatins	149

Figure 65 Normalised absorbance and emission spectra of <i>E</i> - and <i>Z</i> -CA4 (left) and compound 42 (right) in MeOH	150
Figure 66 Normalised absorbance and emission spectra of compound 43 (left) and compound 46 (right) in MeOH.....	150
Figure 67 Single exponential decay of 42E in DMSO. Fluorescence was excited at 680 nm (0.2 mW).....	151
Figure 68 Plot of fraction of light absorbed <i>versus</i> integrated fluorescence to determine gradient (relative slope) for the calculation of Φ_F of the fluorescence standard 9CLA in DCM (excited at 340 nm)	152
Figure 69 Normalized absorption and emission spectra of 9CLA in DCM (right)	152
Figure 70 Linear relationship between τ_F s and Φ_F s of compound 42 in different solvents (error bars indicate $\pm 10\%$ error)	154
Figure 71 A plot of excitation wavelength (nm) <i>versus</i> maximum fluorescence intensity in order to determine optimal excitation wavelength	156
Figure 72 Non-linear power dependences of E-combretastatins (5 μ M) in DCM at room temperature (fluorescence was excited at 730 nm for 43 and 760 nm for 42 and 46).....	157
Figure 73 Plot of fluorescence intensity (a.u.)/laser power (mW) versus laser power (mW) for of E-combretastatins (5 μ M) in DCM (fluorescence was excited at 730 nm for 43 and 760 nm for 43 and 46).	157
Figure 74 Two-photon absorption cross-sections (σ_2) of 42, 43 and 46 (1 μ M) in DCM (in GM units) measured at room temperature.....	159
Figure 75 Fluorescence imaging of Chinese hamster ovary (CHO) cells before and after addition of compound 42E at 25 °C Fluorescence at 400 nm was excited by two-photon absorption at 760 nm.....	161
Figure 76 A) intensity image of compound 42E in CHO cells; B) FLIM image of compound 42E in CHO cells; C) fluorescence lifetime distribution in ps.....	162
Figure 77 Uptake of compound 42E (1 μ M) by HEK293 cells over time at room temperature. 400 nm was excited by two-photon absorption at 760 nm	163
Figure 78 A) intensity image of compound 42E in HEK293 cells; B) FLIM image of compound 42E in HEK293 cells; C) fluorescence lifetime distribution in ps	164
Figure 79 Uptake of 43E (1 μ M) by CHO cells over time at room temperature. Fluorescence at 400 nm was excited by two-photon absorption at 720 nm	165

Figure 80 A) Intensity image of compound 43E in CHO cells; B) FLIM image of compound 43E in HEK293 cells; C) fluorescence lifetime distribution in ps	166
Figure 81 Uptake of 43E (1 μ M) by HEK293 cells over time at room temperature. Fluorescence at 400 nm was excited by two-photon absorption at 720 nm.....	167
Figure 82 A) Intensity image of compound 43E in HEK293 cells; B) FLIM image of compound 43E in HEK293 cells; C) fluorescence lifetime distribution in ps	167
Figure 83 Uptake of 46E (1 μ M) by CHO cells over time at room temperature. Fluorescence at 400 nm was excited by two-photon absorption at 760 nm	169
Figure 84 A) Intensity image of compound 46E in CHO cells; B) FLIM image of compound 46E in HEK293 cells; C) fluorescence lifetime distribution in ps	170
Figure 85 Uptake of 46E (1 μ M) by HEK293 cells over time at room temperature. Fluorescence at 400 nm was excited by two-photon absorption at 760 nm.....	171
Figure 86 A) Intensity image of compound 46E in HEK293 cells; B) FLIM image of compound 46E in HEK293 cells; C) fluorescence lifetime distribution in ps	172
Figure 87 A - 3D printed moulds B – spheroids mounted into agarose wells in MEM media.	173
Figure 88 Uptake of 42E (1 μ M) by HEK293 spheroids over time at room temperature.....	174
Figure 89 A) images showing different depths of the spheroid at time 0; B) images showing different depths of the spheroid at 120 s; C) images showing different depths of the spheroid at 300 s; D) images showing different depths of the spheroid at 600 s; E) plot of intensity <i>versus</i> time (s) of compound 42E at different depths of spheroid.....	176
Figure 90 uptake of compound 43E into HEK293 spheroid.....	178
Figure 91 A) images showing different depths of the spheroid at time 0; B) images showing different depths of the spheroid at 120 s; C) images showing different depths of the spheroid at 300 s; D) images showing different depths of the spheroid at 600 s; E) plot of intensity <i>versus</i> time (s) of compound 43E at different depths of spheroid.....	180
Figure 92 uptake of compound 46E into HEK293 spheroid.....	182
Figure 93 A) images showing different depths of the spheroid at time 0; B) images showing different depths of the spheroid at 120 s; C) images showing different depths of the spheroid at 300 s; D) images showing different depths of the spheroid at 600 s; E) plot of intensity <i>versus</i> time (s) of compound 46E at different depths of spheroid.....	184

Figure 94 Power dependence of compounds 42, 43 and 46 (5 μ M) fluorescence in CHO cells excited at 760 nm or 730 nm (cells were incubated for 30 min with compounds before fluorescence was excited).....	186
Figure 95 Power dependence of compounds 42, 43 and 46 (5 μ M) fluorescence in HEK293 cells excited at 760 nm or 730 nm (cells were incubated for 30 min with compounds before fluorescence was excited).....	187
Figure 96 $^1\text{H-NMR}$ of (Z)-4-(3',4',5'-trimethoxystyryl)benzaldehyde 42Z	224
Figure 97 $^{13}\text{C-NMR}$ of (Z)-4-(3',4',5'-trimethoxystyryl)benzaldehyde 42Z	224
Figure 98 $^1\text{H-NMR}$ of (E)-4-(3',4',5'-trimethoxystyryl)benzaldehyde 42E	225
Figure 99 $^{13}\text{C-NMR}$ of (E)-4-(3',4',5'-trimethoxystyryl)benzaldehyde 42E	225
Figure 100 $^1\text{H-NMR}$ of (Z)-2-hydroxy-4-(3',4',5'-trimethoxystyryl)benzaldehyde 43Z.....	226
Figure 101 $^{13}\text{C-NMR}$ of (Z)-2-hydroxy-4-(3',4',5'-trimethoxystyryl)benzaldehyde 43Z.....	226
Figure 102 $^1\text{H-NMR}$ spectra of (E)-2-hydroxy-4-(3',4',5'-trimethoxystyryl)benzaldehyde 43E	227
Figure 103 $^{13}\text{C-NMR}$ of spectra (E)-2-hydroxy-4-(3',4',5'-trimethoxystyryl)benzaldehyde 43E	227
Figure 104 $^1\text{H-NMR}$ spectra of (Z)-5-methoxy-2-(3',4',5'-trimethoxystyryl)benzaldehyde 44Z	228
Figure 105 $^{13}\text{C-NMR}$ spectra of (Z)-5-methoxy-2-(3',4',5'-trimethoxystyryl)benzaldehyde 44Z	228
Figure 106 $^1\text{H-NMR}$ spectra of (E)-5-methoxy-2-(3',4',5'-trimethoxystyryl)benzaldehyde 44E	229
Figure 107 $^{13}\text{C-NMR}$ spectra of (E)-5-methoxy-2-(3',4',5'-trimethoxystyryl)benzaldehyde 44E	229
Figure 108 $^1\text{H-NMR}$ spectra of (Z)-2-(3',4',5'-Trimethoxystyryl)benzaldehyde 45Z.....	230
Figure 109 $^{13}\text{C-NMR}$ spectra of (Z)-2-(3',4',5'-Trimethoxystyryl)benzaldehyde 45Z.....	230
Figure 110 $^1\text{H-NMR}$ spectra of (Z)-4-(3',4',5'-trimethoxystyryl)acetophenone 46Z.....	231
Figure 111 $^{13}\text{C-NMR}$ spectra of (Z)-4-(3',4',5'-trimethoxystyryl)acetophenone 46Z.....	231
Figure 112 $^1\text{H-NMR}$ spectra of (E)-4-(3',4',5'-trimethoxystyryl)acetophenone 46E	232
Figure 113 $^{13}\text{C-NMR}$ spectra of (E)-4-(3',4',5'-trimethoxystyryl)acetophenone 46E	232
Figure 114 $^1\text{H-NMR}$ spectra of (Z)-2-hydroxy-4-(3',4',5'-trimethoxystyryl)phenyl)acetophenone 47Z.....	233

Figure 115	¹³ C-NMR spectra of (Z)-2-hydroxy-4-(3',4',5'-trimethoxystyryl)phenyl)acetophenone 47Z.....	233
Figure 116	¹ H-NMR spectra of (E)-2-hydroxy-4-(3',4',5'-trimethoxystyryl)phenyl)acetophenone 47E.....	234
Figure 117	¹³ C-NMR spectra of (E)-2-hydroxy-4-(3',4',5'-trimethoxystyryl)phenyl)acetophenone 47E.....	234
Figure 118	¹ H-NMR spectra of (Z)-2-(3',4',5'-trimethoxystyryl)acetophenone 48Z.....	235
Figure 119	¹³ C-NMR spectra of (Z)-2-(3',4',5'-trimethoxystyryl)acetophenone 48Z.....	235
Figure 120	¹ H-NMR spectra of (Z)-4-(3',4',5'-trimethoxystyryl)benzotrile 50Z.....	236
Figure 121	¹³ C-NMR spectra of (Z)-4-(3',4',5'-trimethoxystyryl)benzotrile 50Z.....	236
Figure 122	¹ H-NMR spectra of (E)-4-(3',4',5'-trimethoxystyryl)benzotrile 50E.....	237
Figure 123	¹³ C-NMR spectra of (E)-4-(3',4',5'-trimethoxystyryl)benzotrile 50E	237
Figure 124	¹ H-NMR spectra of (Z)-2-hydroxy-4-(3',4',5'-trimethoxystyryl)benzotrile 51Z	238
Figure 125	¹³ C-NMR spectra of (Z)-2-hydroxy-4-(3',4',5'-trimethoxystyryl)benzotrile 51Z	238
Figure 126	¹ H-NMR spectra of (E)-2-hydroxy-4-(3',4',5'-trimethoxystyryl)benzotrile 51E	239
Figure 127	¹³ C-NMR spectra of (E)-2-Hydroxy-4-(3',4',5'-trimethoxystyryl)benzotrile 51E	239
Figure 128	¹ H-NMR spectra of (Z)-1-(4-(3',4',5'-trimethoxystyryl)phenyl)ethanol 52Z.....	240
Figure 129	¹³ C-NMR spectra of (Z)-1-(4-(3',4',5'-trimethoxystyryl)phenyl)ethanol 52Z.....	240
Figure 130	¹ H-NMR spectra of (E)-1-(4-(3',4',5'-trimethoxystyryl)phenyl)ethanol 52E.....	241
Figure 131	¹³ C-NMR spectra of (E)-1-(4-(3',4',5'-trimethoxystyryl)phenyl)ethanol 52E.....	241
Figure 132	¹ H-NMR spectra of (Z)-2-hydroxy-4-(3',4',5'-trimethoxystyryl)benzoicacid 53Z	242
Figure 133	¹³ C-NMR spectra of (Z)-2-hydroxy-4-(3',4',5'-trimethoxystyryl)benzoicacid 53Z	242
Figure 134	¹ H-NMR spectra of 5-iodo-1,2,3-trimethoxybenzene 55.....	243
Figure 135	¹ H-NMR spectra of trimethyl((3,4,5-trimethoxyphenyl)ethynyl)silane 56.....	243
Figure 136	¹ H-NMR spectra of 3,4,5-trimethoxyacetylene 57	244
Figure 137	¹ H-NMR spectra of 1-(4''-acetylphenyl)-2-(3',4',5'-trimethoxyphenyl)ethyne 58	244
Figure 138	¹ H-NMR spectra of 1-(4''- methoxyphenyl)-2-(3',4',5'-trimethoxyphenyl)ethyne 59	245

Figure 139 $^1\text{H-NMR}$ spectra of 1-(4''- formylphenyl)-2-(3',4',5'-trimethoxyphenyl)ethyne 60	245
Figure 140 $^{13}\text{C-NMR}$ spectra of 1-(4''- formylphenyl)-2-(3',4',5'-trimethoxyphenyl)ethyne 60	246
Figure 141 $^1\text{H-NMR}$ spectra of 1-(4''-cyanophenyl)-2-(3',4',5'-trimethoxyphenyl)ethyne 61	246
Figure 142 $^{13}\text{C-NMR}$ spectra of 1-(4''-cyanophenyl)-2-(3',4',5'-trimethoxyphenyl)ethyne 61	247
Figure 143 $^1\text{H-NMR}$ spectra of 1-(4''-acetyl-3''-hydroxyphenyl)-2-(3',4',5'-trimethoxyphenyl)ethyne 62	247
Figure 144 $^{13}\text{C-NMR}$ spectra of 1-(4''-acetyl-3''-hydroxyphenyl)-2-(3',4',5'-trimethoxyphenyl)ethyne 62	248
Figure 145 $^1\text{H-NMR}$ spectra of 1-(4''-formyl-3''-hydroxyphenyl)-2-(3',4',5'-trimethoxyphenyl)ethyne 63	248
Figure 146 $^{13}\text{C-NMR}$ spectra of 1-(4''-formyl-3''-hydroxyphenyl)-2-(3',4',5'-trimethoxyphenyl)ethyne 63	249
Figure 147 $^1\text{H-NMR}$ spectra of 1-(4''-cyano-3''-fluorophenyl)-2-(3',4',5'-trimethoxyphenyl)ethyne 64	249
Figure 148 $^{13}\text{C-NMR}$ spectra of 1-(4''-cyano-3''-fluorophenyl)-2-(3',4',5'-trimethoxyphenyl)ethyne 64	250
Figure 149 $^1\text{H-NMR}$ spectra of 3,4,5-trimethoxybenzyl bromide 66	250
Figure 150 $^1\text{H-NMR}$ spectra of 3,4,5-trimethoxy-benzyltriphenylphosphonium bromide 67	251
Figure 151 $^1\text{H-NMR}$ spectra of 5-(2,2-dibromovinyl)-1,2,3-trimethoxybenzene 69	251
Figure 152 $^1\text{H-NMR}$ spectra of 5-[(Z)-2-bromovinyl]-1,2,3-trimethoxybenzene 70	252
Figure 153 $^1\text{H-NMR}$ spectra of (Z)-2-(3',4',5'-trimethoxystyryl)benzotrile 71	252
Figure 154 $^{13}\text{C-NMR}$ spectra of (Z)-2-(3',4',5'-trimethoxystyryl)benzotrile 71	253
Figure 155 $^1\text{H-NMR}$ spectra of 2-hydroxy-4-(4,4,5,5-tetramethyl-1,3,2-dioxaborolan-2-yl)benzaldehyde 73	253
Figure 156 $^{13}\text{C-NMR}$ spectra of 2-hydroxy-4-(4,4,5,5-tetramethyl-1,3,2-dioxaborolan-2-yl)benzaldehyde 73	254

Figure 157 ¹ H-NMR spectra of 2-hydroxy-4-(4,4,5,5-tetramethyl-1,3,2-dioxaborolan-2-yl)acetophenone 75	254
Figure 158 ¹³ C-NMR spectra of 2-hydroxy-4-(4,4,5,5-tetramethyl-1,3,2-dioxaborolan-2-yl)acetophenone 75	255
Figure 159 ¹ H-NMR spectra of 2-Hydroxy-4-(4,4,5,5-tetramethyl-1,3,2-dioxaborolan-2-yl)benzoic acid 69.....	255
Figure 160 ¹ H-NMR spectra of (Z)-1-(5-methoxy-2-(3',4',5'-trimethoxystyryl)phenyl)ethanol 80	256
Figure 161 ¹³ C-NMR spectra of (Z)-1-(5-methoxy-2-(3',4',5'-trimethoxystyryl)phenyl)ethanol 80	256
Figure 162 ¹ H-NMR spectra of (Z)-1-(2-(3',4',5'-trimethoxystyryl)phenyl)ethanol 81	257
Figure 163 ¹³ C-NMR spectra of (Z)-1-(2-(3',4',5'-trimethoxystyryl)phenyl)ethanol 81.....	257
Figure 164 FTIR spectra of (Z)-4-(3',4',5'-trimethoxystyryl)benzaldehyde 42Z.....	258
Figure 165 FTIR spectra of (E)-4-(3',4',5'-trimethoxystyryl)benzaldehyde 42E.....	259
Figure 166 FTIR spectra of (Z)-2-hydroxy-4-(3',4',5'-trimethoxystyryl)benzaldehyde 43Z ...	259
Figure 167 FTIR spectra of (E)-2-hydroxy-4-(3',4',5'-trimethoxystyryl)benzaldehyde 43E ...	260
Figure 168 FTIR spectra of (Z)-5-methoxy-2-(3',4',5'-trimethoxystyryl)benzaldehyde 44Z ..	260
Figure 169 FTIR spectra of (E)-5-methoxy-2-(3',4',5'-trimethoxystyryl)benzaldehyde 44E ..	261
Figure 170 FTIR spectra of (Z)-2-(3',4',5'-trimethoxystyryl)benzaldehyde 45Z.....	261
Figure 171 FTIR spectra of (Z)-4-(3',4',5'-trimethoxystyryl)acetophenone 46Z.....	262
Figure 172 FTIR spectra of (E)-4-(3',4',5'-trimethoxystyryl)acetophenone 46E.....	262
Figure 173 FTIR spectra of (Z)-2-hydroxy-4-(3',4',5'-trimethoxystyryl)phenyl)acetophenone 47Z.....	263
Figure 174 FTIR spectra of (E)-2-hydroxy-4-(3',4',5'-trimethoxystyryl)phenyl)acetophenone 47E.....	263
Figure 175 FTIR spectra of (Z)-2-(3',4',5'-trimethoxystyryl)acetophenone 48Z.....	264
Figure 176 FTIR spectra of (E)-4-(3',4',5'-trimethoxystyryl)benzotrile 48E.....	264
Figure 177 FTIR spectra of (Z)-2-hydroxy-4-(3',4',5'-trimethoxystyryl)benzotrile 51Z	265
Figure 178 FTIR spectra of (E)-2-hydroxy-4-(3',4',5'-trimethoxystyryl)benzotrile 51E	265
Figure 179 FTIR spectra of (Z)-1-(4-(3',4',5'-trimethoxystyryl)phenyl)ethanol 52Z	266
Figure 180 FTIR spectra of (E)-1-(4-(3',4',5'-trimethoxystyryl)phenyl)ethanol 52E	266
Figure 181 FTIR spectra of (Z)-2-hydroxy-4-(3',4',5'-trimethoxystyryl)benzoic acid 53Z.....	267

Figure 182	FTIR spectra of 1-(4''-formylphenyl)-2-(3',4',5'-trimethoxyphenyl)ethyne 60	267
Figure 183	FTIR spectra of 1-(4''-acetyl-3''-hydroxyphenyl)-2-(3',4',5'-trimethoxyphenyl)ethyne 62	268
Figure 184	FTIR spectra of 1-(4''-formyl-3''-hydroxyphenyl)-2-(3',4',5'-trimethoxyphenyl)ethyne 63	268
Figure 185	FTIR spectra of 1-(4''-Cyano-3''-fluorophenyl)-2-(3',4',5'-trimethoxyphenyl)ethyne 64	269
Figure 186	FTIR spectra of (Z)-2-(3',4',5'-trimethoxystyryl)benzotrile 71	269
Figure 187	FTIR spectra of 2-hydroxy-4-(4,4,5,5-tetramethyl-1,3,2-dioxaborolan-2-yl)acetophenone 75	270
Figure 188	FTIR spectra of 2-hydroxy-4-(4,4,5,5-tetramethyl-1,3,2-dioxaborolan-2-yl)benzotrile 77	270
Figure 189	FTIR spectra of 2-Hydroxy-4-(4,4,5,5-tetramethyl-1,3,2-dioxaborolan-2-yl)benzoic acid 79	271
Figure 190	Mass spectra of (E/Z)-4-(3',4',5'-trimethoxystyryl)benzaldehyde (C ₁₈ H ₁₉ O ₄) 42	272
Figure 191	Mass spectra of (E/Z)-2-hydroxy-4-(3',4',5'-trimethoxystyryl)benzaldehyde 43	273
Figure 192	Mass spectra of (E/Z)-5-methoxy-2-(3',4',5'-trimethoxystyryl)benzaldehyde (C ₁₉ H ₂₁ O ₅) 44	273
Figure 193	Mass spectra of (Z)-2-(3',4',5'-trimethoxystyryl)benzaldehyde (C ₁₈ H ₁₈ O ₄ Na) 45	273
Figure 194	Mass spectra of (E/Z)-4-(3',4',5'-trimethoxystyryl)acetophenone (C ₁₉ H ₂₁ O ₄) 46	274
Figure 195	Mass spectra of (E/Z)-2-Hydroxy-4-(3',4',5'-trimethoxystyryl)phenyl)acetophenone (C ₁₉ H ₂₀ O ₅ Na) 47	274
Figure 196	Mass spectra of (Z)-2-(3',4',5'-trimethoxystyryl)acetophenone (C ₁₉ H ₁₉ O ₄) 48	275
Figure 197	Mass spectra of (E/Z)-2-hydroxy-4-(3',4',5'-trimethoxystyryl)benzotrile (C ₁₈ H ₁₈ NO ₄) 51	275
Figure 198	Mass spectra of (E/Z)-1-(4-(3',4',5'-trimethoxystyryl)phenyl)ethanol (C ₁₉ H ₂₃ O ₄)	276
Figure 199	Absorbance and fluorescence spectra of 42 in hexane (left) and MeCN (right)	277
Figure 200	Absorbance and fluorescence spectra of 42 in DCM (left) and EtOAc (right)	277
Figure 201	Absorbance and fluorescence spectra of 42 in DMSO	278
Figure 202	Absorbance and fluorescence spectra of 43 in hexane (left) and MeCN (right)	278
Figure 203	Absorbance and fluorescence spectra of 43 in DCM (left) and EtOAc (right)	279

Figure 204 Absorbance and fluorescence spectra of 46 in hexane (left) and MeCN (right) .279

Figure 205 Absorbance and fluorescence spectra of 46 in DCM (left) and EtOAc (right)280

List of tables

Table 1 Combretastatins extracted from <i>Combretum caffrum</i>	19
Table 2 Summary of Combretastatin A4 disodium phosphate clinical trials in various tumour types.....	22
Table 3 Names and structures of combretastatin drug candidates that were investigated..	35
Table 4 A comparison of microscopes used in the course of this work	48
Table 5: Alkynes synthesised following Sonogashira cross-coupling.	99
Table 6: <i>Z</i> - and <i>E</i> -stilbenes synthesised following the Wittig method	105
Table 7: <i>Z</i> -stilbenes synthesised following the Suzuki method	108
Table 8: Boronic ester synthesis	111
Table 9: <i>Z</i> -stilbenes synthesised following the Suzuki method	112
Table 10: <i>Z</i> -stilbenes with secondary alcohol functional group	113
Table 11 Ketones synthesised following oxidation with DMP.....	116
Table 12: <i>E</i> -stilbenes	117
Table 13: Half-Maximal Inhibitory Concentration of Synthesized Combretastatin Analogues in HEPg2, HeLa and HCT-116 cells	120
Table 14: Half-Maximal Inhibitory Concentration of Synthesized <i>E</i> -Combretastatin Analogues in HEPG2 cells.....	126
Table 15 Rate (<i>k</i>) and half-life ($t_{1/2}$) of tubulin polymerisation under varying conditions	133
Table 16 Polarities, dielectric constants (ϵ), refractive indices (η), viscosity (in centipoise (cP)) and the orientation polarizability (Δf) of the organic solvents used (Lide, 2002).....	144
Table 17 Stokes shifts (cm^{-1}) of <i>E</i> -combretastatins in different solvents	145
Table 18 Molar extinction coefficients (ϵ), absorption and emission peaks, and Stokes shifts of compound 42 (1 mM) in various solvents (estimated errors for $\epsilon(\lambda_{\text{max}})$ are $\pm 5\%$).....	146
Table 19 Molar extinction coefficients (ϵ), absorption and emission peaks, and Stokes shifts of compound 43 in various solvents (estimated errors for $\epsilon(\lambda_{\text{max}})$ are $\pm 5\%$)	147
Table 20 Molar extinction coefficients (ϵ), absorption and emission peaks, and Stokes shifts of compound 46 in various solvents (estimated errors for $\epsilon(\lambda_{\text{max}})$ are $\pm 5\%$)	147
Table 21 Fluorescence quantum yields (Φ_F) (standard error $\pm 5\%$) and fluorescence lifetimes (τ_F) (error $\pm 10\%$, single exponentials) of compound 42	153

Table 22 Fluorescence quantum yields (Φ_F) (standard error $\pm 5\%$) and fluorescence lifetimes (τ_F) (error $\pm 10\%$, single exponentials) of compound 43	155
Table 23 Fluorescence quantum yields (Φ_F) (standard error $\pm 5\%$) and fluorescence lifetimes (τ_F) (error $\pm 10\%$, single exponentials) of compound 46	155
Table 24 Rate of uptake (k) and half-life ($t_{1/2}$) of compound 42E in HEK293 spheroid at varying depths.....	177
Table 25 Rate of uptake (k) and half-life ($t_{1/2}$) of compound 43E in HEK293 spheroid at varying depths.....	181
Table 26 Rate of uptake (k) and half-life ($t_{1/2}$) of compound 46E in HEK293 spheroid at varying depths.....	185

List of schemes

Scheme 1 Generalised Wittig reaction	26
Scheme 2 Synthesis of Combretastatin A-4 utilizing the Wittig reaction (Pettit <i>et al.</i> , 1995a).	27
Scheme 3 Synthesis of Combretastatin A-4 prodrug (Bedford <i>et al.</i> , 1996)	27
Scheme 4 Synthesis of Combretastatin A-4 (Fürstner & Seidel, 1995)	28
Scheme 5: Synthesis of Combretastatin A-4 utilizing the Perkin reaction (Gaukroger <i>et al.</i> , 2001a)	28
Scheme 6: Synthesis of Combretastatin A-4 using Suzuki cross-coupling (Gaukroger <i>et al.</i> , 2001a)	29
Scheme 7: Synthesis of (E)-Combretastatin A-4 (Gaukroger <i>et al.</i> , 2001a).....	29
Scheme 8: Synthesis of Combretastatin A-4 using Suzuki cross-coupling (Molloy <i>et al.</i> , 2018)	30
Scheme 9: Sonogashira cross-coupling mechanism	98
Scheme 10: Copper catalytic cycle.....	98
Scheme 11: Synthesis of 3,4,5-trimethoxyphenylacetylene	99
Scheme 12: Mechanism of the formation of Pd ⁰ from Pd(OAc) ₂ and PPh ₃	100
Scheme 13: The rearrangement of a Pd ²⁺ intermediate to accelerate reductive elimination	101
Scheme 14: Catalytic hydrogenation mechanism	101
Scheme 15: Attempted semihydrogenation of alkynes with Lindlars catalyst	102
Scheme 16: Proposed mechanism for Pd(OAc) ₂ catalysed semihydrogenation of internal alkynes	103
Scheme 17: Attempted transfer hydrogenation with KOH/DMF	103
Scheme 18: Wittig mechanism	104
Scheme 19: Synthesis of 3,4,5-trimethoxybenzyltriphenylphosphonium bromide.....	105
Scheme 20: Suzuki coupling mechanism	107
Scheme 21: Two mechanisms considered for transmetalation of alkenylboranes with palladium complexes	107
Scheme 22: Synthesis of 5-[(Z)-2-Bromovinyl]-1,2,3-trimethoxybenzene	108
Scheme 23: Two routes to form boronic esters	109

Scheme 24: Miyaura borylation mechanism of action	110
Scheme 25: Grignard mechanisms	113
Scheme 26: Oxidation of secondary alcohols to ketones with PCC	114
Scheme 27: Oxidation of secondary alcohols to ketones with DMP	115
Scheme 28: Iodine catalysed <i>trans</i> isomerisation	117

Acknowledgements

Firstly, I would like to express my sincere gratitude to my supervisor Dr John Hadfield for the continuous support of my PhD research, for his patience and guidance. Besides my supervisor, I would like to thank Prof. Roger Bisby for his guidance and knowledge with the photochemistry part of my research and taking a break in his retirement to show me the ropes. My sincere thanks go to Prof. Stanley Botchway and Prof. Tony Parker who provided me with their knowledge and guidance during my visits to RAL.

Dr Steve Rossington and Dr Jim Wilkinson have been a huge help with their knowledge in organic chemistry. A huge thankyou to Kirit Amin for his patience (he needed it) and guidance with the NMR and Dr Alessia Candeo for all of her help at RAL, for working late with me and showing me round Oxford. All of the technicians at Salford do a great job, especially Dr Abby Ragazzon-Smith for her help with the LCMS, Dr Nanda Ayu Puspita for the help in cell culture and Mark Parlby and Andy Martin for letting me 'borrow' glassware.

I thank my fellow labmates Paddy and Andrew for their friendship, support and late night laughs in the lab and the pub, May for evening out the number of girls in the chemistry lab and being a great friend and Amjed for all of his chemistry knowledge - you're in charge now! I thank all of my friends in the office; Soran, Peter and Ryan for being great gym partners and great friends, Emyr for his constant supply of support and doughnuts, Arvind for being my agony aunt, Alice for being a great friend and everyone else for making the office a great place. I also thank everyone at RAL for being so welcoming and helpful.

A huge thankyou to Lisa for being the best flatmate I could ask for (shame about your cooking). Thanks for being so supportive and having a glass of prosecco and a scary movie ready when I'd had a bad day! Thankyou to the Natalie's who have been amazing friends since high school and always support me and Louise for all of your support and friendship over the years, I love you all!

Firozeh, you are like the big sister I never had, thankyou for being the best office neighbour and thankyou for being an amazing friend these past three years, I don't think I could have done this without you! Thankyou to Danielle for being like a sister to me and giving me the

two most beautiful godsons! Although you live at the other end of the country you've only ever been a phone call away (when you actually answer).

Last but not least I would like to thank my family - my brothers for being a constant reminder that I got both the brains and the beauty, Laura (hopefully Daniel puts a ring on it soon) and my Auntie Heather.

I love my parents for their continued support in everything I do; their belief in me keeps me going. You are the best parents I could ask for and I dedicate this to you.

Declaration

The work described in this thesis was carried out at the University of Salford and the Central Laser Facility between September 2014 and May 2018 by the author. No part of this thesis has previously been submitted for a degree or any other qualification within the University of Salford or any other institution.

Abstract

Cancer is one of the major causes of death worldwide, hence the development of novel effective treatments to combat this disease is important. Combretastatins are powerful anticancer drugs with some derivatives in advanced clinical trials for cancer therapy. Combretastatins are stilbenes isolated from the African shrub *Combretum caffrum*. These agents interact with tubulin in a similar way to colchicine, causing destruction of blood vessels within tumours by binding to tubulin dimers and inhibiting angiogenesis in developing tumours. *Cis*-combretastatins are effective chemotherapeutic agents showing potent activity, but their overall use has been limited due to associated toxicity in normal tissues; the corresponding *trans*-isomers are around 2 orders of magnitude less cytotoxic. Combretastatins undergo reversible photoisomerization upon irradiation with UV/visible light.

Previously, a novel form of two-photon phototherapy was proposed, in which the “inactive” *trans(E)*-combretastatins are used as pro-drugs that may be activated (converted to the *cis*-isomer) by localized irradiation with light at the tumour site. The use of near-infrared (NIR) light to trigger a nonlinear two-photon excited photoactivation process provides deeper light penetration into tissues.

This thesis describes the synthesis and characterisation of a range of combretastatin derivatives with improved two-photon cross sections as target compounds for two-photon excited anticancer phototherapy. The cytotoxicity and cell cycle analysis of the drug candidates were determined on live mammalian cell lines and candidates were screened for their inhibitory effects on tubulin polymerization; stilbenes with a B ring substitution of a *para*-carbonyl caused cell cycle arrest in the G₂M phase and were cytotoxic in the nanomolar range (MTT HepG2, HeLa, HCT 116 50 – 250 nM, tubulin polymerisation inhibition 280 – 390 nM). Photochemical properties such as fluorescence lifetimes, fluorescence quantum yields, and two-photon absorption characteristics of the combretastatin derivatives were investigated spectroscopically. Fluorescence-lifetime imaging microscopy (FLIM) and light sheet fluorescence microscopy (LSFM) were used to determine the real-time uptake of the inactive pro-drugs into live mammalian cell monolayers and spheroids and their intracellular distribution. In conclusion, the two-photon excited activation of *E*-combretastatins on live cells was demonstrated, making these *E*-combretastatins promising pro-drug candidates for two-photon excited anticancer phototherapy.

Abbreviations

^{13}C NMR	carbon nuclear resonance
^1H NMR	proton nuclear resonance
2APY	2-aminopyridine
2P	two-photon
2PA	two-photon absorption
2PE	two-photon excitation
ABS	absorbance
aq.	aqueous
Ar	argon
a.u.	arbitrary unit
BPin	<i>bis</i> (pinacolato)diboron
Brine	aqueous sodium chloride solution (saturated)
CA4P	combretastatin A-4 disodium phosphate salt
CDCl_3	deuterated chloroform
CHCl_3	chloroform
CHO	chinese hamster ovarian (cells)
CLSM	confocal laser scanning microscope
Cm^3	equivalent to ml
D	Debye
d	doublet
Da	Dalton

DCM	dichloromethane
dd	double boublet
DMF	dimethylformamide
DMSO	dimethylsulfoxide
<i>E</i>	from German "entgegen" = <i>trans</i> (lat. On the other side)
<i>E/Z</i> CA-4	<i>E/Z</i> -(3',4',5'-trimethoxyphenyl)-2-(4''-methoxy-3''hydroxyphenyl ethane (combretastatin A-4
EDTA	ethylenediaminetetraacetic acid
EG	ethylene glycol
eq.	equivalent(s)
esu	electrostatic unit
<i>et al.</i>	from Latin <i>Et alia</i> (and others)
Et ₂ O	Diethyl ether
EtOAc	ethyl acetate
EtOH	ethanol
FI	fluorescence intensity
FL	fluorescence
FLIM	fluorescence lifetime imaging microscopy
fPALM	fluorescence photoactivation localization microscopy
fs	femtosecond (10^{-15} s)
g	gram(s)
GC	gas chromatography

GM	Goeppert-Mayer, unit of σ_2
GTP	guanosine triphosphate
h	hour(s)
H ₂ SO ₄	sulphuric acid
HCl	hydrochloric acid
HeLa	immortal cervical cancer cells derived from Henrietta Lacks
HPLC	high performance liquid chromatography
HPV	human papillomavirus
HUVEC	human umbilical vein endothelial cells
Hz	Hertz
IC	internal conversion
IC50	half maximum inhibitory concentration
<i>in vacuo</i>	lat. "in empty space" (under a vacuum)
<i>in vitro</i>	lat. "in glass"
<i>in vivo</i>	lat. "within the living"
IR	infrared
<i>J</i>	coupling constant (Hz)
LE	locally excited state
Lit.	in the literature
logP	octanol-water partition coefficient
M	molar
m	multiplet

m.p.	melting point
MDR	multidrug resistance
MeCN	acetonitrile
MeOH	methanol
mg	milligram(s)
MgSO ₄	magnesium sulphate
MHz	megahertz
min	minute(s)
ml	millilitre(s)
mm	millimetre(s)
mM	millimolar
mol	mole(s)
MRI	magnetic resonance imaging
MTD	maximum tolerated dose
MTT	3-(4,5-Dimethylthiazol-2-yl)-2,5-diphenyltetrazolium bromide
mW	milliwatt(s)
NA	numerical aperture
NADH	nicotinamide adenine dinucleotide
NBS	N-bromosuccinimide
<i>N</i> -BuLi	<i>normal</i> -butyl lithium
NIR	near-infrared
nm	nanometer(s) (10 ⁻⁹ m)

nM	nanomolar (10^{-9} M)
NMR	nuclear magnetic resonance
ns	nanosecond (10^{-9} s)
OMe	methoxy group (-OCH ₃)
OPO	optical parametric oscillator
PALM	photoactivation localization microscopy
PBS	phosphate buffer solution
PDT	photodynamic therapy
PET	positron emission tomography
Pet.	Petroleum ether
Ph	phenyl
PMT	photomultiplier tube
ppm	parts per million
ps	picosecond (10^{-12} s)
R _f	retention factor (in TLC)
ROS	reactive oxygen species
rt	room temperature (approx.. 22 oC)
s	singlet
S ₀	singlet ground state
S ₁	electronic excited singlet state
sat.	saturated
SiO ₂	silica (silicon dioxide)

STED	stimulated emission depletion
STORM	stochastic optical reconstruction microscopy
<i>t</i> -	tertiary
t	triplet
T	triplet state
TBAF	tetra- <i>n</i> -butylammonium fluoride
TCSPC	time-correlated single photon counting
THF	tetrahydrofuran
TICT	twisted intramolecular charge transfer
TIRF	total internal reflectance microscopy
TLC	thin layer chromatography
TMS	tetramethyl silane
TRIR	time-resolved infrared
UV	ultraviolet
v/v	volume/volume ratio
VDA	vascular disrupting agent
VE	vascular endothelial
VR	vibrational relaxation
Z	from german "zusammen" = <i>cis</i> (lat. "on this side")
δ	chemical shift in NMR (usually given in ppm)
ΔF	orientation polarizability
ϵ	extinction coefficient or dielectric constant

η	refractive index
λ	wavelength (nm)
μl	microliter(s)
μm	micrometer(s)
μM	micromolar
μs	microsecond(s)
σ_2	two photon absorption cross section (in GM units)
τ_f	fluorescence lifetime
φ_F	fluorescence quantum yield
φ_{ISO}	photoisomerization quantum yield

1. Introduction

1.1 Cancer

1.1.1 What is cancer?

Statistical key facts

Cancer is a major public health problem worldwide; there are more than 360,000 new cases of cancer in the UK every year (with 51% being male) and an estimated 14 million worldwide. In the last decade, combined incidence rates for cancers has increased by 7% in the UK; this is expected to increase by a further 2% in the next 20 years and worldwide it is expected there will be 23.6 million new cases of cancer each year by 2030. To date there are more than 200 different types of cancer; the most common cancers in adults include breast, prostate, lung and bowel cancer which account for more than half (53%) of new cases in the UK (Figure 1) and around 40% in the world (Cancer Research UK, 2016).

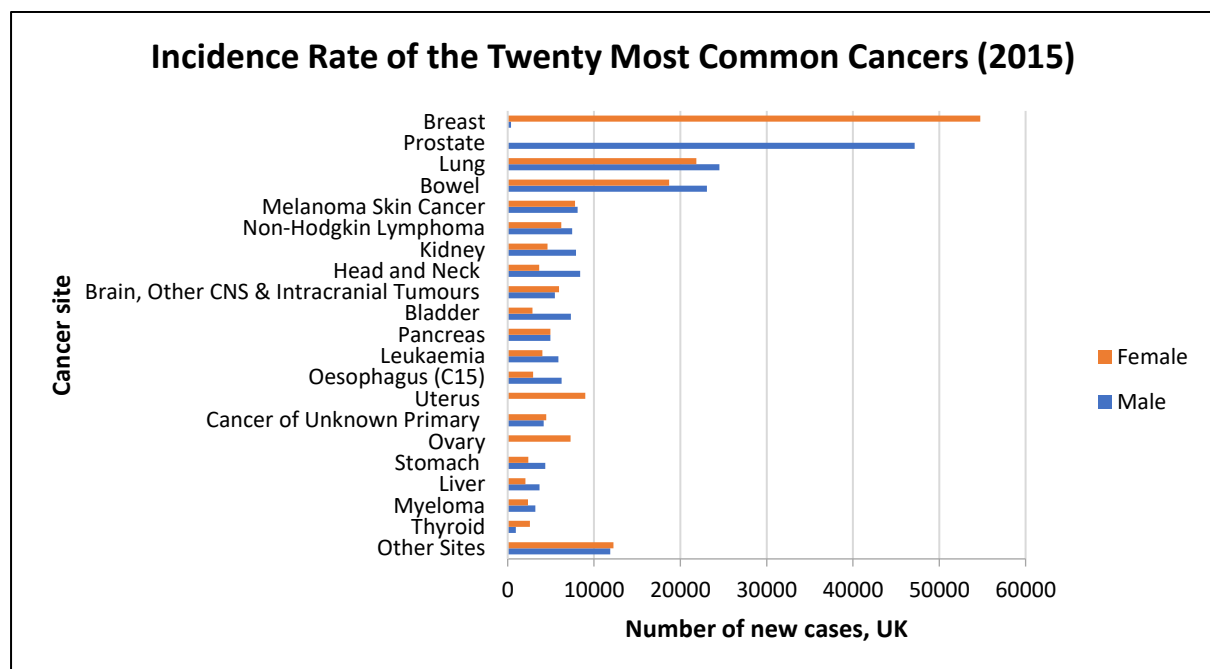


Figure 1 Incidence Rate of the most common cancer types in the UK (based on figures from Cancer Research UK)

Treatment for cancer is improving; cancer survival in the UK has doubled in the past 40 years and now 50% of people diagnosed with cancer, including the most commonly

diagnosed cancers, survive their disease for 10 years or more (Quaresma *et al.*, 2015) with survival rates being higher in women.

Each year in the UK there are around 164,000 (88,200 of which were male) cancer deaths and 8.2 million cancer deaths worldwide. Cancer accounts for more than a quarter of deaths in the UK with breast, prostate, lung and bowel cancer accounting for almost half of these deaths (Cancer Research UK, 2014). Cancer may arise in humans at any age but reported cases tend to rapidly escalate from the age of 55 (Bassily *et al.*, 2010) and more than a third of all cancer cases in the UK are diagnosed in people aged 75 and over; the natural aging process at the cellular level and a lifetime accumulation of mutations are the main causes of this increase.

Causes of cancer and cancer progression

Cancers originate from both environmental factors and genetics, meaning that there are multiple external factors combined with internal genetic changes that can lead to human cancers; 97% of cancers are caused by environmental factors such as tobacco, red meat, chemicals, and environmental pollutants; smoking is the largest cause of cancer in the UK (15%). Individuals with particular genetic predispositions are born with inherited mutations in genes involved in cancer making them more susceptible to cancer. For example, people with BRCA1, BRCA2 and p53 alterations are less able to suppress cancer growth (Vogelstein & Kinzler, 2004; Oliner *et al.*, 1992).

Tissues that are susceptible to malignancies can develop various forms of tumours; although each tumour has unique features, the basic mechanisms are similar. Healthy cells in the human body exist in a complex interdependent system that regulates their spread; healthy cells will only reproduce with the instruction of nearby cells, ensuring the maintenance of an appropriate tissue size and structure. Cancer cells however rapidly divide at an abnormal rate, affecting tissue structure and avoiding controls on growth with the potential to spread throughout the body (metastasis). The changes in a cell that lead to cancer occur due to extensive mutations in specific genes within the cell.

Eukaryotic cells contain genes; genes are specific sequences of DNA arranged as chromosomes located in the nucleus of the cell. Each gene codes for a specific protein, identifying the order in which amino acids must join together. Mutations in these genes can

cause changes in the activity or the quantity of the protein product. Two types of gene, proto-oncogenes and anti-oncogenes, can determine cancer; proto-oncogenes regulate cell growth and differentiation whilst anti-oncogenes suppress cell growth. Mutation of proto-oncogenes can lead to excessive multiplication causing either the formation of too much protein product or an overactive version of it, whilst mutation of an anti-oncogene deactivates its control over growth leading to deregulation of cellular proliferation (Alberts, 2008).

During the process of cell division, a collection of processes can occur by which a cell can identify and correct any damage to DNA. However, a cell that has accumulated a large amount of DNA damage, or one that no longer effectively repairs damage, can enter one of three possible states:

1. Senescence - the cell will become dormant
2. Apoptosis – programmed cell death
3. Tumour - Unregulated cell division

If a cell enters the third state i.e. becomes tumourous, the mutation will be passed on to the next cell during cell division (Figure 2) (Loeb, 2001).

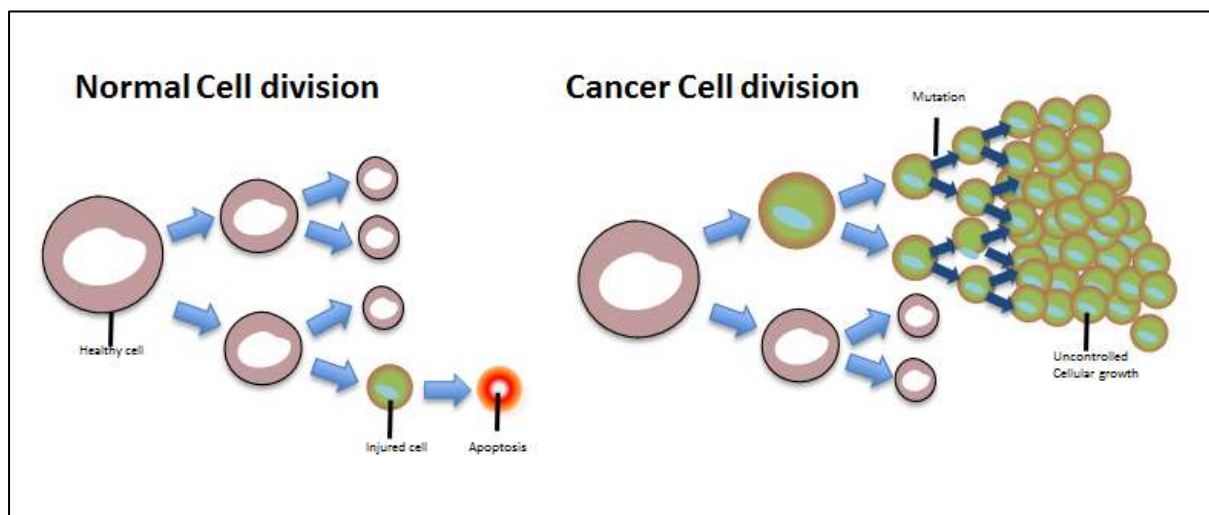


Figure 2 A comparison of normal cell division and cancerous cell division (adapted from (Loeb, 2001))

In the initial stages of cancer, molecular regulatory and biochemical mechanisms in cancer cells are very similar to those of “normal” cells and so aren’t recognised as being foreign by the body’s defence systems. The immune response is only partially triggered, and the

growth of the tumour becomes overwhelming. For this reason, early diagnosis and prompt treatment of cancer are important for the success of anticancer treatment and long-term survival of patient (Pantel *et al.*, 2008).

Tumours are classed as benign, pre-malignant or malignant. Benign tumours are not considered cancerous; they tend to grow at a slower rate and lack the ability to invade neighbouring tissues. Malignant tumours however are capable of invading other tissues and grow at an uncontrollable rate. Malignancy can be characterised by anaplasia (loss of structural differentiation), invasiveness and metastasis (Baba & Catoi, 2007). Metastasis occurs when cancerous cells break away from the primary tumour and invade other parts of the body; some cells are able to penetrate the circulatory or lymphatic system and circulate in the blood stream to other tissue. This process is known as hematogenous or lymphatic spread (Lorusso & Rüegg, 2012).

Types of cancer

There are numerous forms of cancer affecting cells all over the body. Types of cancer can be classified according to the type of cell or tissue that the cancer originates.

- Blastoma – Derived from embryonic tissue, thus most commonly found in children;
- Carcinoma – Derived from epithelial cells; this is the most common type of cancer, particularly in older people. Common forms are breast, lung, and colon;
- Germ line – Cancers derived from pluripotent cells i.e. testicle or ovary;
- Lymphoma / Leukaemia – These tumour classes come from hematopoietic cells. They tend to include cancer of the bone marrow, lymph and lymphatic system;
- Sarcoma – These are tumours of the connective tissue. All sarcoma originate from mesenchymal cells from bone marrow. Susceptible tissues include cartilage, bone, muscle and fat.

1.1.2 Cancer treatments

There are three traditional approaches to the treatment of cancer – surgery, radiotherapy and systemic therapy. These different modalities are well established and are often used in combination. Systemic therapies include hormonal therapy, targeted therapy, and chemotherapy; hormone therapy plays a significant role in the treatment of breast and

prostate cancer whilst targeted therapies are playing an increasingly important role in a number of tumour types (Caley & Jones, 2012). The sensitivity to treatment varies for different types of cancers and the drugs used (Foye *et al.*, 1995; Pratt, 1994; Rang *et al.*, 2003; Thurston, 2007). Novel approaches to the treatment of cancer are now evolving including the use of vaccination, immunotherapy, gene therapy, very specific small molecules (Knowles & Selby, 2005) and phototherapy (Thurston, 2007). The aim of cancer treatment is to stop uncontrolled growth, invasion and metastasis.

Surgery and radiotherapy dominated the field of cancer therapy into the 1960s. Surgery is most commonly used to remove small and well-defined tumours whilst radiotherapy involves irradiating the patient's cancer tissue with powerful x- or γ -rays causing genetic damage in the irradiated cells inducing apoptosis. Radiotherapy targets tumour cells so there is minimal damage to normal healthy cells surrounding the tumour, which makes it superior to surgery in many cases. However, some cancer cells are not completely eliminated, and this can lead to re-growth of the tumour. Both surgery and radiotherapy cannot be used to treat metastasised cancers and so chemotherapy is the treatment of choice if metastasis occurs (Foye *et al.*, 1995; Pratt, 1994; Thurston, 2007).

Chemotherapy is defined as the use of chemicals to treat disease; in this form of treatment the chemotherapeutic drugs are usually administered systemically and are distributed through the body *via* the blood stream. Chemotherapy may be used on its own or in combination with surgery and radiation therapy; chemotherapy is also often the final treatment if surgery and radiation therapy fail to eradicate all cancer cells. Chemotherapy agents disrupt the cell cycle by one or more processes resulting in cell death by apoptosis; either by directly interfering with DNA, or by targeting the key proteins required for cell division.

A chemotherapy cycle involves a cocktail of drugs being administered at repeated, regular intervals. The individual scheduling of chemotherapy cycles is determined by the ability of normal tissues to recover and should be the shortest time possible; the clinical uses for chemotherapy are determined by both the patient and tumour characteristics. Each cycle kills a constant fraction of cells with some repopulation between cycles. Tumours have less capacity for repair than normal tissues. Therefore, repeated cycles of chemotherapy

decrease the tumour population with time, but the interval between cycles allows normal cells to repopulate.

The side effects of chemotherapy vary according to the specific agent and dosage. The rapidly dividing cells of the bone marrow, gastrointestinal mucosa, hair follicles and gonads are among the most sensitive tissues in the body; thus common immediate adverse effects of chemotherapy include myelosuppression, nausea and vomiting, hair loss and reduced fertility (Caley & Jones, 2012). If only one malignant cell survives the anticancer therapy tumour re-growth might occur and as cancer is a proliferative disease the cancer cells continue uncontrolled growth (Foye *et al.*, 1995; Hepworth, 2000; Hirst, 2004; Thurston, 2007). The common drugs used in chemotherapy are described in the following sections.

1.1.3 Anticancer drugs

Cytotoxic drugs target rapidly dividing malignant cells and include alkylating agents, antimetabolites, DNA-intercalating agents and antimitotic drugs (microtubule disrupting agents) (Black & Livingston, 1990; Foye *et al.*, 1995).

Alkylating agents

Alkylating agents were one of the earliest classes of drugs used to treat cancer, dating back to the 1940s, and are still widely used today. These agents bind to DNA, RNA and some enzymes, hindering DNA replication; the most common targets are nucleophilic sites on DNA bases with main sites being nitrogen on adenine **1**, cytosine **2** and guanine **3** with guanine N7 (highlighted in red) being the most typical target (Figure 3) (Gates, 2009).

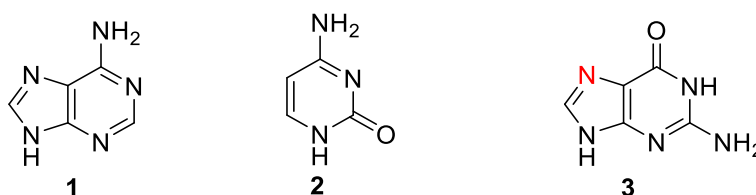


Figure 3 Structures of adenine, cytosine and guanine

Alkylating agents are used to treat many different cancers, including leukaemia, lymphoma, lung and breast cancer. Adverse effects of alkylating agents include bone marrow toxicity, immunosuppression, and in some cases they may even be carcinogenic and mutagenic (Atkins & Gershell, 2002; Foye *et al.*, 1995).

The biggest weakness of most cancer cells is that they are extremely sensitive to DNA damage; alkylating agents act by reacting with nucleotides on the DNA double helix, adding an alkyl group to some or all of them. Mono-alkylation (i.e. attachment at one site) prevents enzymes accessing the DNA and thus inhibit cell growth whilst dialkylating agents can attach either at two sites on the opposite strand (interstrand crosslinking) or on the same strand (intrastrand cross linking) so that DNA strands cannot be separated. All of these actions cause a block at the G₂ phase of the cell cycle and ultimately trigger apoptosis.

Interstrand crosslinkers prevent separation of strands and thus cell division. Examples include bischloroethylnitrosourea (BCNU) **4**, melphalan **5** and chlorambucil **6**. Intrastrand crosslinking is much less common and caused by compounds such as Cisplatin **7** (Fuertes *et al.*, 2003). Platinum based chemotherapeutics don't have an alkyl group so are termed "alkylating like" but act in a similar manner damaging DNA (Cruet-Hennequart *et al.*, 2008).

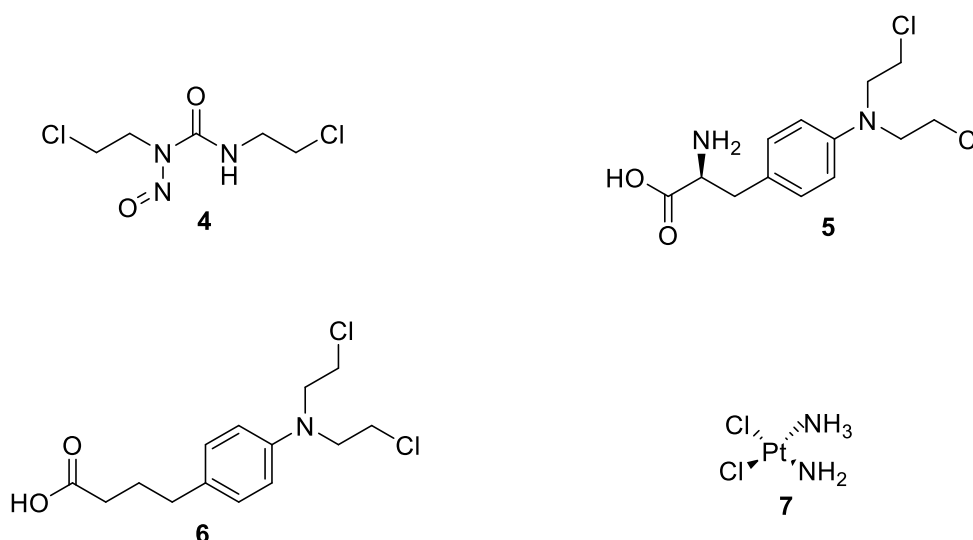


Figure 4 Structures of some alkylating agents.

Antimetabolites

Antimetabolites are drugs that bind to proteins and interfere with the enzymes that are necessary for DNA synthesis. They act as a substitute to the actual metabolites that would be used in the normal metabolism; they are characterised by low molecular weights with similar structures to naturally occurring molecules used in nucleic acid (DNA and RNA) synthesis. Generally, antimetabolites induce cell death during the S phase of cell growth when incorporated into RNA and DNA or inhibit enzymes needed for nucleic acid production (Takimoto & Calvo, 2008).

Five main groups of antimetabolites are actively used in cancer treatment; pyrimidine antagonists i.e. 5-fluorouracil **8** (Mader *et al.*, 1997) and purine antagonists i.e. fludarabine **9** can be grouped together as base analogues; sugar modified nucleoside analogues i.e. cytarabine **10** (Mehta *et al.*, 2011) and ribonucleotide reductase inhibitors i.e. triapine **11** (Sigmond *et al.*, 2007) can be grouped together as nucleoside analogues; and folate agonists i.e. methotrexate **12** (Obasaju *et al.*, 1993).

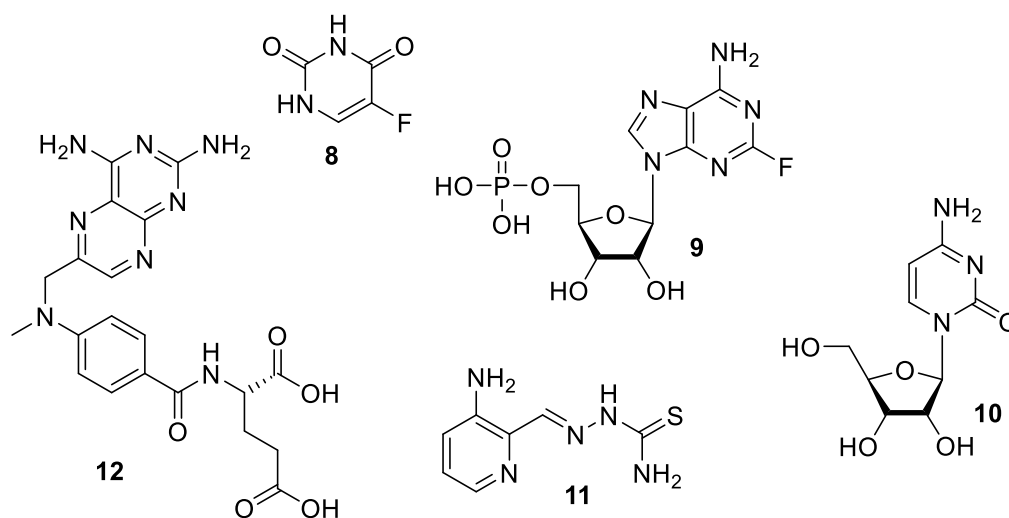


Figure 5 Structures of common anti-metabolite cancer drugs.

DNA-intercalating drugs

Intercalation is the insertion of molecules between the planar bases of DNA to form a DNA-drug interaction that causes cytotoxicity. Intercalation occurs when ligands of an appropriate size and chemical nature fit themselves in between base pairs of DNA; these ligands are typically polycyclic, aromatic, and planar. In order for an intercalator to fit between base pairs, the DNA must dynamically open a space between its base pairs by unwinding, inducing local structural changes to the DNA strand, such as lengthening of the DNA strand or twisting of the base pairs. These structural modifications can lead to functional changes, often to the inhibition of transcription and replication and DNA repair processes, which make intercalators potent mutagens.

DNA intercalators are often used in chemotherapeutic treatment to inhibit DNA replication in rapidly growing cancer cells. Examples include doxorubicin **13** and daunorubicin **14**, both of which are used in the clinical treatment of Hodgkin's lymphoma (Tulpule *et al.*, 2001).

These molecules act as topoisomerase inhibitors; topoisomerase catalyses the breaking of the phosphodiester backbone of DNA strands during the cell cycle (Freres, Jerusalem & Moonen, 2017). Dactinomycin **15** used for the treatment of children's cancers such as Ewing's Sarcoma (Balamuth & Womer, 2010) and Wilm's tumour (Ehrlich *et al.*, 2006).

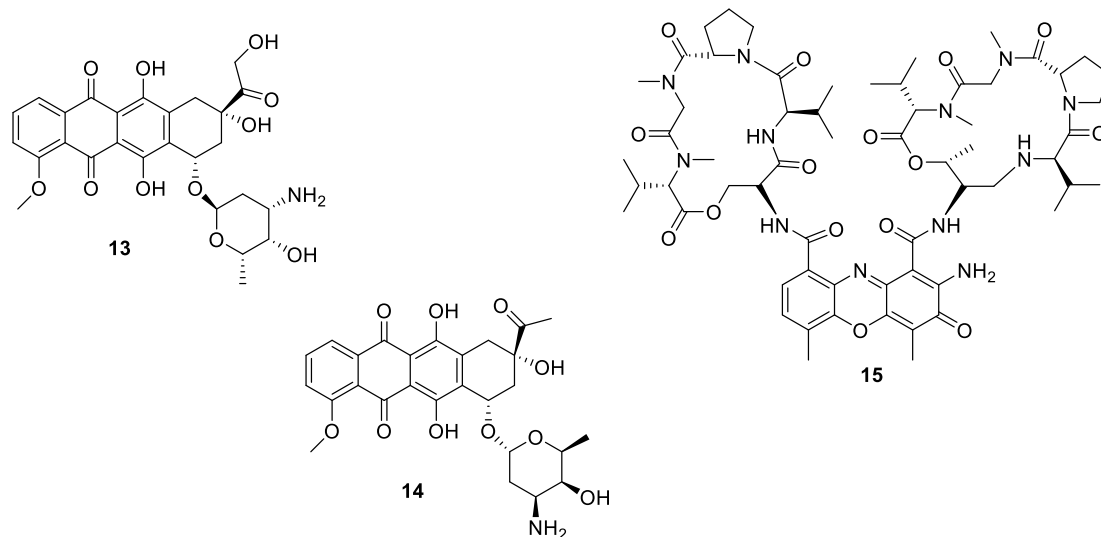


Figure 6 Structures of common DNA intercalating agents.

Antimitotic drugs

Antimitotic agents will be discussed in more detail as the combretastatin derivatives investigated in the course of this work belong to this group. Drugs that disrupt mitotic progression are used extensively for the treatment of cancer. Covered herein will be microtubule stabilizing agents and microtubule destabilizing agents. To understand the action of microtubule disrupting agents it is important to understand microtubules and their function in live mammalian cells and this will be discussed briefly.

Tubulin and Microtubules

Microtubules (Figure 7) are polar cellular structures involved in maintaining the structure of the cell, cell mobility, intracellular transport, cytoplasmic organelle distribution and chromosome segregation. These compounds are long tubular polymers essential for cell division in eukaryotic cells. Structurally microtubules are long hollow cylinders made up of 13 parallel linear protofilaments although microtubules composed of fewer (or more) protofilaments have been observed *in-vitro* (Chrétien *et al.*, 1992).

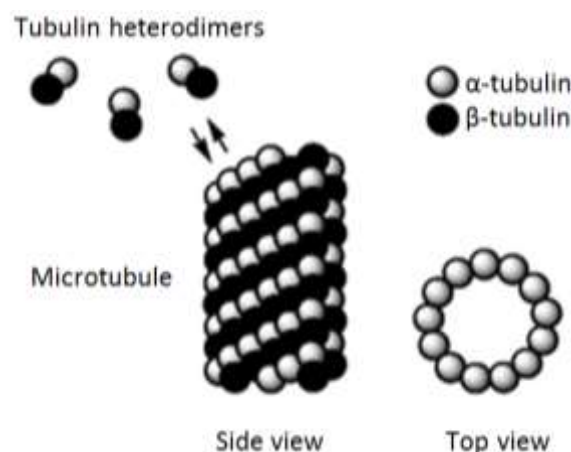


Figure 7 Structure of a microtubule in which the cross-section shows the 13 protofilaments (adapted from (Splettstoesser, 2015)).

Tubulin is a heterodimeric protein consisting of two globular subunits, α - and β -tubulin connected by non-covalent bonds. α - and β -subunits are 40 % identical at the amino acid level (Aylett *et al.*, 2011) with a mass of around 50,000 Daltons per dimer (Conde & Caceres, 2009). They can measure up to 50 μm in length and 24 nm in external diameter with the tubulin heterodimers maintained in equilibrium. α - and β -monomers have a binding site for one molecule of GTP; GTP binds very tightly to α -tubulin, whereas GTP is interchangeable with GDP when binding to β -tubulin.

Microtubules have a distinct polarity that is crucial for their biological function. Tubulin polymerises end to end, with the β -subunits of one tubulin dimer contacting the α -subunits of the next dimer. Therefore, in a protofilament, one end will have the α -subunits exposed while the other end will have the β -subunits exposed. These ends are designated the (-) and (+) ends, respectively. While microtubule elongation can occur at either end, it is significantly faster at the (+) end (Walker *et al.*, 1988). The cycle of tubulin

polymerisation/depolymerisation begins with the binding of GTP at the (+) end whilst in the GTP bound state (Heald & Nogales, 2002). When polymerised, GTP irreversibly hydrolyses to GDP through inter-dimer contacts. This microtubule depolymerisation occurs during the interphase of the cell cycle, the repolymerisation forms a labile structure called the mitotic spindle (Figure 8). This mitotic spindle is essential during mitosis.

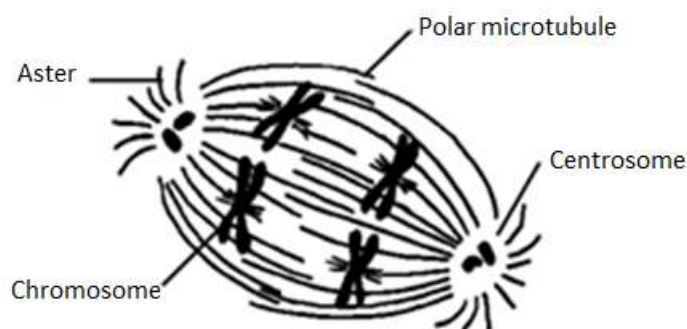


Figure 8 Sketch of the mitotic spindle

Mitosis is a key stage of cell division in which chromosomes are separated producing genetically identical daughter cells; the mitotic spindle is the cytoskeletal structure of cells that forms to separate these daughter cells. For this reason, tubulin is the target for many small molecules that act by interfering with microtubule polymerization or depolymerisation. Interference with microtubule formation hinders the formation of this mitotic spindle required for cell division leading to mitotic arrest and eventual apoptosis (cell death). Despite the mitotic spindle being an obvious target for anticancer drug development, it wasn't until the 1980s when research in this area became popular after taxanes were first reported as tubulin interactors. Most of the antimitotic agents in use today are plant derivatives (Hadfield *et al.*, 2003; Lin *et al.*, 1989; Patrick, 2009; Uppalapati *et al.*, 2011).

Microtubule destabilizing agents (inhibitors of tubulin polymerization)

Colchicine

In 1820 colchicine **16** was first isolated from the poisonous meadow saffron *Colchicum autumnale* by the French chemists Pelletier and Caventou (Pelletier & Caventou, 1820). Weisenberg first discovered that tubulin was the biological target for colchicine in the 1960s (Weisenberg *et al.*, 1968), but little progress was made in the research of the ligand-protein

structural relationship until a study was published by Bai over 30 years later (Bai *et al.*, 2000). The study used both molecular modelling and biochemical techniques in an attempt to identify the colchicine binding site of tubulin. The location of the site was finally validated by x-ray crystallography (Ravelli *et al.*, 2004).

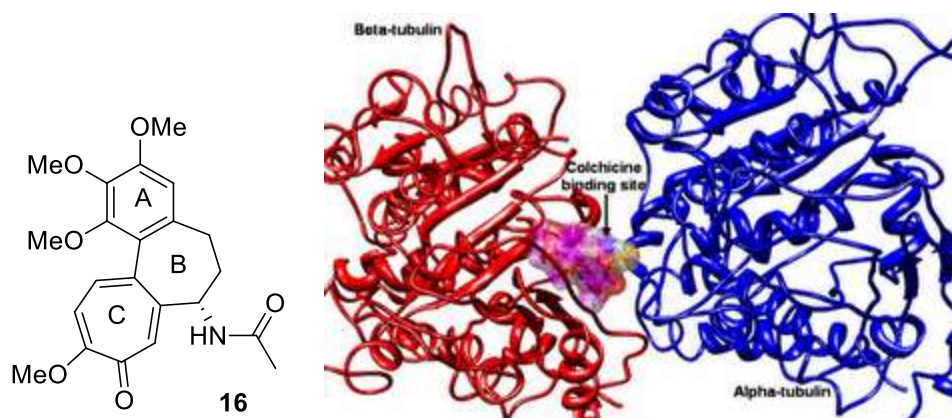


Figure 9 Colchicine (left) and colchicine binding site on tubulin (right, (Techne, 2008))

Colchicine binds to tubulin by first forming a weak, reversible complex thus causing a conformational change within the protein that leads to the formation of a stronger pseudo-irreversible complex, known as the allosteric effect (Skoufias & Wilson, 1992). In the tubulin binding site the colchicine A-ring sits in a hydrophobic pocket with the 3-position methoxy hydrogen bonded to a cysteine residue; the C ring interacts through van der Waals forces with 3 amino acid residues (two valines and one serine) whilst the carbonyl group acts as a H-bond acceptor. Upon binding to tubulin, microtubule assembly is prevented and the formation of the mitotic spindle is disrupted. Due to its antimitotic activity, colchicine was suggested for the treatment of cancer but associated side effects and high toxicity towards healthy cells hindered its progress in clinical trials (Bhattacharya *et al.*, 2016).

Vinca alkaloids

Vinca alkaloids are natural products that are well established in contemporary cancer treatment. The natural products vinblastine **17** and vincristine **18** were initially extracted from the Madagascar periwinkle *Catharanthus roseus* in the 1950s by Canadian scientists Noble and Beer (Noble *et al.*, 1958). Noble was investigating the purported anti-diabetic effects of the periwinkle extracts when experiments indicated the extracts destroyed the bone marrow. These findings led him to apply the extracts to blood cancers; since then vinblastine, vincristine and other vinca alkaloids have been crucial in cancer chemotherapy

worldwide. Vinca alkaloids are used in clinical practice to treat solid tumours, mainly of the lung, testicle and breast, Hodgkin's and non-Hodgkin's lymphomas and acute leukaemias. Side-effects that frequently occur include alopecia, mild myelosuppression, parasthesia and muscle weakness. Similar to colchicine, the vinca alkaloids bind to tubulin and inhibit the formation of microtubules causing mitotic arrest and subsequent apoptosis.

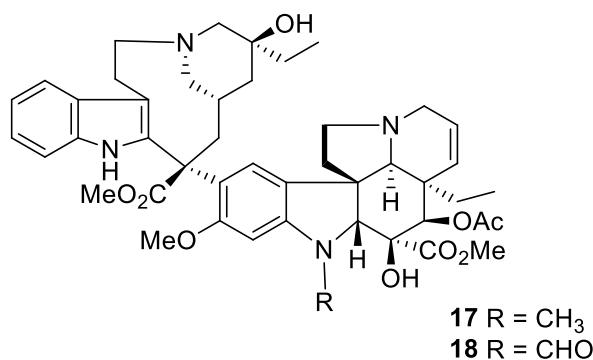


Figure 10 Vinblastine (17) and Vincristine (18) (Noble, Beer & Cutts, 1958)

Some evidence suggests that on top of their antimitotic activity vinca alkaloids have the ability to block the synthesis of nucleic acids with selectivity towards malignant cells (Foye *et al.*, 1995; Patrick, 2009; Pratt, 1994; Rang *et al.*, 2003; Thurston, 2007).

Microtubule stabilizing agents (inhibitors of tubulin depolymerization)

Taxoids

Taxoids bind to tubulin and stabilise microtubules by accelerating polymerisation; microtubule depolymerisation is inhibited resulting in a mitotic arrest, blocking cell division (Uppalapati *et al.*, 2011). Examples of taxoid agents currently in use as anticancer drugs are taxol (or paclitaxel) (Figure 11) and docetaxel (or Taxotere). Taxol **19** was first isolated from the bark of the Pacific yew tree *Taxus brevifolia* in the early 1960s by Wani and Wall, in 1971 the structure of taxol was published (Wani *et al.*, 1971). Taxol entered clinical trials in 1984 and was approved by the FDA for the treatment of ovarian cancer in 1992; taxol is now routinely used in the treatment of a number of cancers including ovarian, breast, lung and pancreatic cancer (Weaver, 2014). Side-effects induced by taxoid drugs include bone marrow suppression, neurotoxicity and hypersensitivity.

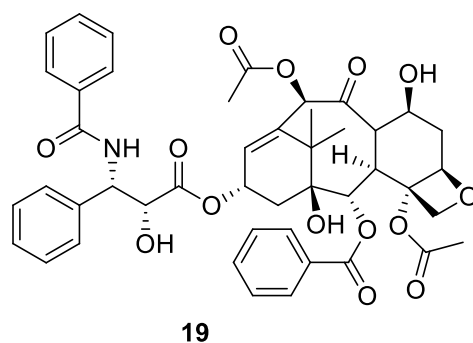


Figure 11 Taxol

Since the introduction of taxol to clinical use, a range of agents that interfere with microtubule depolymerisation have been developed including epithilones, discodermolide (Gunasekera *et al.*, 1990), laulimalide (Gapud *et al.*, 2004), cyclostreptin and taccalonolides.

Combretastatins are the compounds of interest in this work. They are classed as antimetabolites as they interact with tubulin in a similar way to colchicine. A pronounced selectivity towards endothelial cells of the tumour vasculature was observed with combretastatins and hence they may also be classified as vascular disrupting agents (VDAs) (Ley *et al.*, 2007; Ahmed *et al.*, 2003; Böhle *et al.*, 2000).

Targeting the tumour vasculature

One approach to control tumour growth proposed by Folkman (Folkman, 1971) was to target the vasculature that supplies essential nutrients, growth factors and oxygen. When a tumour grows to roughly 1-2 mm in diameter it requires its own independent vascular system; the supply of blood to cancer cells is essential for providing oxygen and nutrients and removing the cytotoxic waste produced to enable development. The tumour vasculature is formed by angiogenesis of existing blood vessels. Angiogenesis is stimulated by certain growth factors such as VEGF (vascular endothelial growth factor) and cytokines (Knowles & Selby, 2005; Patterson & Rustin, 2007; Rang *et al.*, 2003; Thurston, 2007).

In tumours, rapid growth of cells and overexpression of angiogenic factors leads to a disjointed network of blood vessels that differ drastically from healthy blood vessels; this vasculature is observed as a tangled, disorganised maze of immature vessels in which capillaries are unidentifiable (Konerding *et al.*, 2001). The corresponding lymphatic system is equally disordered, with fluid engorged vessels caused by dilation (Padera *et al.*, 2002). Tumour vessels are much more permeable than normal vasculature; they lack in smooth

muscle cells, resulting in an irregular basement membrane caused by gaps in the endothelial lining (Gee *et al.*, 2003). This permeability leads to accumulation of vascular contents causing a build-up in interstitial pressure (Vaupel *et al.*, 1987). Binding to the vasculature will cause rounding up of endothelial cells; the blocking of these microvessels will hinder the blood flow delivering essential nutrients, oxygen and growth factors to the tumour. In clinical trials some tumour cells in the tumour periphery survived treatment with antimitotic drugs, as they are fed by blood vessels of the normal healthy vasculature (Patrick, 2009b; Siemann, 2006).

There are two main groups that target the tumour vasculature; vascular targeting agents (VTAs) and vascular disrupting agents (VDAs). Whilst VDAs target the established tumour blood vessels, VTAs interfere with new vessel formation thus having a preventative action. Both approaches stop the blood flow to the tumour and hence the supply of nutrients and oxygen (Jain & Carmeliet, 2001; Patterson & Rustin, 2007; Siemann, 2006). Ligand-directed VDAs include antibodies, peptides or growth factors that display selective affinity towards endothelial cell receptors; upon binding to vasculature, cell death will be induced by coupling of an attached cytotoxic ligand (e.g. ricin).

The small molecule VDAs can be sub-divided into two groups; flavonoids and tubulin binding agents (inhibitors of microtubule polymerisation). Synthetic flavonoids such as flavone-8-acetic acid are VDAs that disrupt the actin cytoskeleton and cause DNA strand breaks that lead to apoptosis of endothelial cells (Cai, 2007) and tubulin-binding VDAs were described in detail in the previous section on antimitotic drugs. Combretastatin derivatives display strong potency against the tumour vasculature having direct cytotoxic effects.

1.1.4 Treatment of cancer with light – Photodynamic therapy

Photodynamic therapy (PDT) is a less invasive approach in the treatment of cancer. It is the use of inactive prodrugs that are activated by irradiation with light after administration to the patient generating a cytotoxic species. At present, PDT is mainly used in the treatment of wet age-related macular degeneration, for precancerous conditions of the skin (e.g. actinic keratosis) and in the palliative care of advanced cancers, for instance of the bladder or the oesophagus. It is also used for the treatment of other conditions such as macular

degeneration, bacterial infections and pathological myopia (Foye *et al.*, 1995; Gao *et al.*, 2006; Lane, 2003).

The use of light to treat diseases has been recognised for thousands of years; ancient Egyptian, Indian and Chinese cultures treated conditions such as vitiligo, rickets, psoriasis, psychosis, and even skin cancer with exposure to the sun. In 1903 Niels Finsen was awarded the Nobel Prize for his work on the use of an artificial red light source for the treatment of small pox and cutaneous tuberculosis (Hönigsmann, 2012). The first clinical trials of PDT took place in the late 1970s by Thomas Dougherty and co-workers on 113 patients (Dougherty *et al.*, 1978); the group obtained promising results treating cutaneous and subcutaneous malignant tumours using hematoporphyrin derivative (HpD) as the photosensitizer. Tumour regression was observed in 111 cases however skin photosensitization for up to 6 weeks after photosensitizer administration was observed (Beck *et al.*, 2007; Hönigsmann, 2012; Lane, 2003; Mitton & Ackroyd, 2008).

PDT is a two-stage procedure; an inactive photosensitiser is administered and after a delay to allow for optimal biodistribution, the treatment site is irradiated with visible or near-infrared light. Absorption of light by the photosensitiser initiates photochemical reactions that generate cytotoxic products resulting in the desired therapeutic effect. An ideal photosensitiser should show low toxicity in the dark, be soluble in water to ensure distribution throughout the body *via* the bloodstream, be selective to cancerous tissues and have a high absorption peak in the infrared region to ensure enough energy is provided to excite oxygen and demonstrate high penetration depths into tumours (Chang, 2000). Suitable agents should strongly absorb light in the visible or near infrared region, display high singlet oxygen quantum yields and fluorescence to allow monitoring of their uptake into tumours (Chang, 2000; Gao *et al.*, 2006; Wilson & Patterson, 2008).

Mechanisms of photodynamic therapy

There are two distinct approaches to PDT that define the chemical involvement of photosensitisers and cellular entities (Figure 12); indirect processes require the presence of oxygen (type I and II) and direct processes which directly activate photosensitisers to induce cell death (type III and IV).

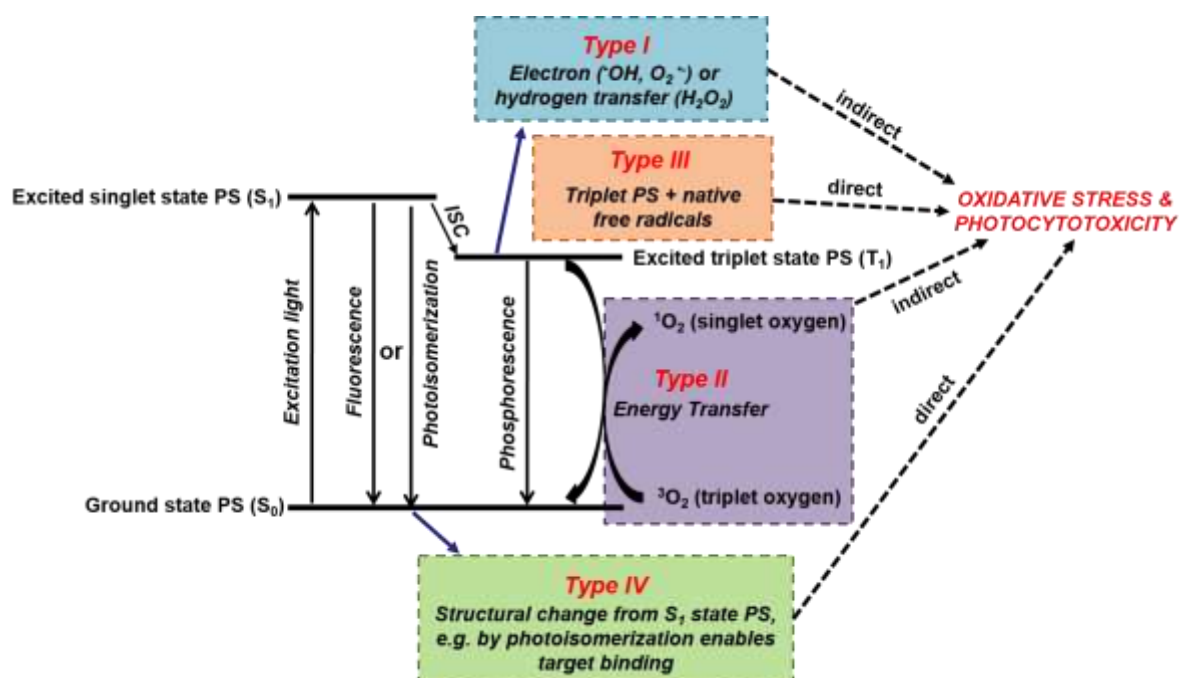


Figure 12 Simplified Jablonski diagram showing energy levels and photochemical mechanisms of PDT (M. Scherer et al., 2017)

In type I PDT electron transfer from an excited photosensitizer to oxygen forms a radical species (e.g. $O_2^{\cdot-}$), the radical species then oxidises intracellular biomolecules (nucleic acids, amino acids etc) eventually leading to cell death. In type II PDT, singlet oxygen (1O_2) is formed by energy transfer from an excited photosensitiser to molecular oxygen; singlet oxygen is generated when the photosensitizer transfers excess energy to oxygen; due to the short lifetime of singlet oxygen (10-320 ns), intracellular localisation of the photosensitizer is paramount. In type III reactions triplet state photosensitizers interact directly with intracellular structures without the need for oxygen (Chang, 2000; Foye *et al.*, 1995). The major limitation of PDT is the depth of tissue penetration at the excitation wavelength (Altshuler & Yaroslavsky, 2004; Lane, 2003a). It was found that wavelengths in the near infrared region (typically 600 – 800 nm) penetrate the farthest into biological tissues.

Scherer and co-workers have recently proposed Type IV PDT; in brief it involves a photosensitizer that binds to its molecular target upon photoisomerization when excited with light (Scherer *et al.*, 2017). Two-photon phototherapy (2PPDT) involves the use of two-photon excitation (2PE) in the NIR region (600-1000 nm) to excite photosensitisers; this longer wavelength allows for deeper penetration of the excitation light into tissue compared to UV/Vis light. The direct action of exciting the non-toxic prodrug *E*-

combretastatin to the highly cytotoxic Z-combretastatin by photoisomerisation (Figure 13) presents a new type of PDT the does not require oxygen or the interaction of photosensitizer with other molecules.

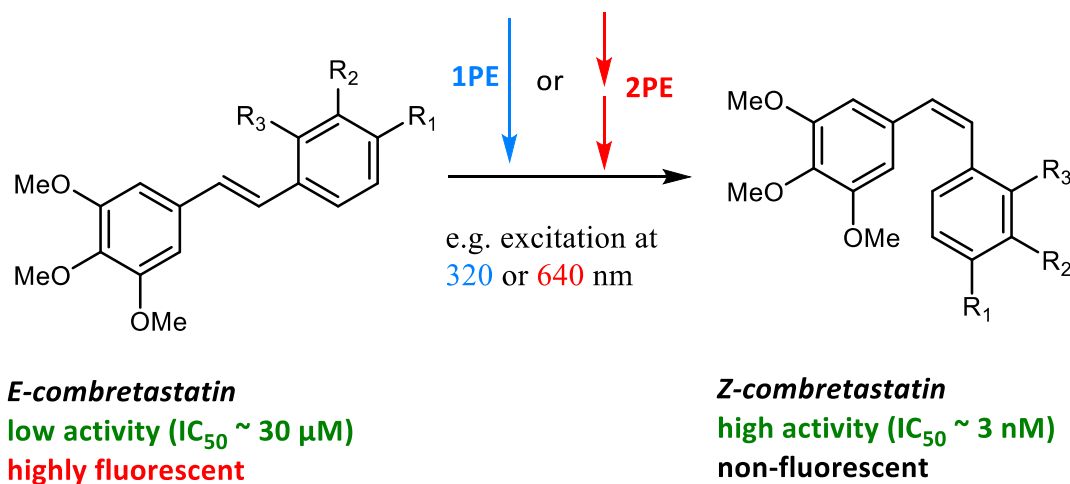


Figure 13 Conversion of *E*-combretastatins to *Z*-combretastatins by photoisomerisation

Even though PDT is successfully applied to treat certain cancers it also has some major drawbacks. The major limitation of traditional PDT is the depth of tissue penetration, which depends on the excitation wavelength. A further problem is posed by light-absorbing chromophores present in mammalian tissues, such as haemoglobin and melanin, which can inhibit the activation of a photosensitiser (Lane, 2003b; Wilson & Patterson, 2008b). Another disadvantage is photosensitisation of the skin; it is necessary that patients avoid exposure to light for some time after treatment (Patrick, 2009a; Yano *et al.*, 2011). Combretastatin A-4 has a half life of approximately 30 minutes and so photosensitisation is expected to be minimal after this time.

B-2	II	OH	OCH ₃	H	OCH ₃
B-3	II	OCH ₃	OCH ₃	H	OH
B-4	II	OCH ₃	H	H	OH

Structurally combretastatins are composed of two substituted benzene rings connected by a two-carbon bridge (stilbenes). Stilbenes exist in two distinct geometric conformations, *trans* and *cis* or *E* (German entgegen) and *Z* (German zusammen) respectively.

The most active derivative known to date *cis*-combretastatin A-4 (*Z*-CA-4) **21** was first described in 1989 (Hadfield *et al.*, 2003; Lin *et al.*, 1989; Pettit *et al.*, 1995a) with high toxicity against a range of cancer cell lines such as P388 lymphocytic leukaemia cells (Pettit *et al.*, 1995a), HUVEC (human umbilical vein endothelial cells) and K562 human leukaemia cells (Gaukroger *et al.*, 2003; Hadfield *et al.*, 2005). The insolubility of *Z*-CA-4 prevented clinical progression; solubility limitations were solved following the development of a series of CA-4 prodrugs, including ammonium, potassium, and sodium phosphate salt derivatives (Pettit *et al.*, 1995a). The water-soluble prodrug, combretastatin A4 disodium phosphate (*Z*-CA4P) **22** is converted into *Z*-CA4 by cellular phosphatases in the body.

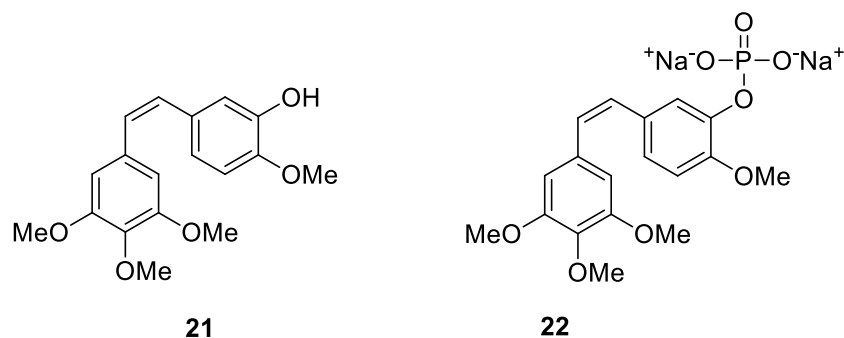


Figure 15 Structures of *cis*-combretastatin A-4 (*Z*-CA-4) (left) and *cis*-combretastatin A4 disodium phosphate (*Z*-CA4P) (right)

1.2.1 Combretastatin A4 disodium phosphate in clinical trials

Pre-clinical trials on mouse tumour models delivered promising results when it was observed that combretastatin A4 starved the blood supply to tumours and killed cancer cells. Rapid vascular shutdown was induced within 1 h of administration in mouse models with necrosis of the tumour cores noticeable 24 h after drug administration in oxygen-independent cancer cells with known chemotherapy resistance. Unfortunately, cells at the periphery of the tumour could feed off the vasculature of nearby healthy cells and so were resistant to treatment and showed signs of re-growth (Cancer Research UK, 2012b; Griggs *et al.*, 2001a; Griggs *et al.*, 2001b; Grosios, 1999; Patterson & Rustin, 2007). The uptake and de-phosphorylation of the watersoluble pro-drug Z-CA4P was faster in tumour vasculature than in smooth muscle cells indicating that it was a good candidate for clinical trials (Tozer *et al.*, 1999).

Clinical trials are classified into different phases; the earlier phases determine how safe a drug is and later phases test whether the new treatment is better than existing treatments. Phase I trials are usually small trials used to determine drug dosage tolerance of human patients and possible side effects; phase II trials aim to find out more about dosage and side-effects and determine which types of cancer the treatment works for. Phase III clinical trials usually involve more patients and compare new treatments with the best available treatment available. Phase IV trials are conducted after a drug has been given a licence to determine how well the drug works when used on a larger scale. The earliest clinical trials with combretastatins were carried out in patients with advanced cancers and investigated the effects of Z-CA4P on other vasculature dependent conditions such as age related macular degeneration and diabetic retinopathy (Griggs *et al.*, 2002).

To date, a number of clinical trials have been carried out on combretastatin A4 disodium phosphate to evaluate its anti-tumour activity (Table 2). Studies demonstrated that tumour blood flow returned to normal levels 24 h after a single injection of CA-4P (Horsman *et al.*, 2000); multiple dose scheduling at the maximum tolerated dose showed an improvement (Nabha *et al.*, 2001). Resistance to CA4-P at the tumour periphery was also observed in clinical trials (Tozer *et al.*, 2008); to overcome this combretastatins were investigated as a combination therapy to complement traditional anticancer approaches (Chaplin & Hill, 2002). Improved activity was observed when combretastatins were combined with

established chemotherapeutics (Grosios *et al.*; Siemann *et al.*, 2002; Morinaga *et al.*, 2003; Yeung *et al.*, 2007), hyperthermia (Horsman *et al.*, 2000; Eikesdal *et al.*, 2001; Horsman and Murata, 2002), and ionizing radiation (Landuyt *et al.*, 2001). It was found that when combretastatins were combined with other anticancer therapies the schedule of treatment determined the outcome, thus identifying a schedule dependence of combretastatin-mediated inhibition of tumour growth (Horsman & Siemann, 2006). Further to this, higher response rates were recorded in relapsed ovarian cancer patients treated with standard chemotherapy and combretastatin as compared with patients treated with chemotherapy alone (Zweifel *et al.*, 2011).

Table 2 Summary of Combretastatin A4 disodium phosphate clinical trials in various tumour types

Trial Phase	Drug candidate	Cancer Type	Dosage	Patient	Outcomes & side effects	Reference
I	Z-CA4P	Advanced solid tumours	Dose escalation study 18 – 90 mg/m ² intravenously for 10 min in the dark once every 3 weeks.	19	Starvation of tumours of blood supply, shrinkage of some solid tumours. Side effects include tumour pain, cardiopulmonary toxicity, faint flush, abdominal pain, nausea, vomiting, fever, light-headedness, headache, diarrhoea, hypo- or hypertension	(PSA-Rising, 2001)
I	Z-CA4P	Advanced solid tumours	Single-dose CA-4P 18–90 mg/m ² repeated 3-week interval	25	Starvation of tumours of blood supply. Side effects include tumour pain	(Dowlati <i>et al.</i> , 2002)
I	Z-CA4P	Advanced solid tumours	Dose escalation study 5 – 114 mg/m ² .	34	Rapid changes (30 min) in human tumour vasculature, but also changes in normal vasculature. Reversible changes, more slowly in tumours. Side effects include ataxia, faint flush, sensory neuropathy.	(Anderson <i>et al.</i> , 2003; Rustin <i>et al.</i> , 2003)
I	Z-CA4P	Advanced solid tumours	Dose escalation study 52 – 65 mg/m ² for 10 min intravenously on 5 consecutive days every 3 weeks.	37	Side effects include dose-limiting tumour pain and cardiopulmonary toxicity. Other side effects included ataxia, hypotension, nausea, dyspnoea, headache and sensory neuropathy.	(Stevenson <i>et al.</i> , 2003)
I	Z-CA4P	Advanced solid tumours	Dose escalation study 18 – 90 mg/m ² every 21 days.	25	QTc interval (electrical cycle of the heart) was prolonged as monitored by ECG. Side effects included acute coronary syndrome.	(Cooney <i>et al.</i> , 2004)
I	Z-CA4P + carboplatin	Advanced solid tumours	40 cycles of carboplatin 4 or 5 mg/m ² intravenously for 30 min; 60 min	16	Dose-limiting thrombocytopenia led to the early termination of this study.	(Bilenker <i>et al.</i> , 2005)

			later Z-CA4P 27 or 36 mg/m ² intravenously for 10 min on day 1 of 21 day cycle.			
I	Z-CA4P + bevacizumab	Advanced solid tumours	Bevacizumab (10 mg/kg) given 4 h after 2nd dose Z-CA4P 45–63 mg/m ²	16	Results were reproducible in a two-centre clinical trial setting	(Koh <i>et al.</i> , 2009)
I/II	Z-CA4P	Neovascular age-related macular degeneration	27, 36 or 45 mg/m ² intravenously once a week for 4 weeks.	8	Potential efficacy of CA4P in neovascular AMD. Side effects include elevated blood pressure and temperature, headache and nausea.	(Ibrahim <i>et al.</i> , 2013)
Ib	Z-CA4P + carboplatin and paclitaxel	Advanced solid tumours	Dose escalation study 36 – 54 mg/m ² . Intravenous for 10 min 20 h before carboplatin and paclitaxel were given.	46	Responses in 22 % of all patients in various tumour types such as ovarian, oesophageal, small cells lung cancer and melanoma. Side effects included, hypertension, tumour pain, drop of leukocyte and platelet numbers.	(Rustin <i>et al.</i> , 2010)
I	Z-CA4P + carboplatin and/or paclitaxel	Advanced solid tumours	Dose escalation study 36 – 54 mg/m ² .	41	Tumours responded to treatment. Side-effects included tiredness, sickness, headache and hypertension.	(Cancer Research UK, 2009a; Rustin <i>et al.</i> , 2010)
I	Z-CA4P	Advanced solid tumours	Dose escalation study 5 – 585 mg/m ² intravenously for 30 min.	25	Well tolerated. Side effects include Acute renal failure, ataxia.	(He <i>et al.</i> , 2011)
I	Z-CA4P + I-A5B7 (monoclonal antibody with radioactive iodine label)	Advanced bowel and pancreatic cancer	Unable to find best dosage for treatment.	12	Change of tumour perfusion. Side-effects included drop in blood cells, increased risk of infection, bleeding problems, tiredness, shortness of breath, mild allergic reactions, hypo- or hypertension.	(Cancer Research UK, 2012b)
I	Z-CA4P + bevacizumab	Advanced solid tumours	Z-CA4P at 45, 54 or 63 mg/m ² on day 1 and 8 then every 14 days. Bevacizumab 10 mg/kg 4 hours after Z-CA4P after day 8.	15	Profound vasculare change. CA4P in combination with bevacizumab appears safe and well tolerated.	(Nathan <i>et al.</i> , 2012)
I	Z-CA4P + radiotherapy	NSCLC prostate adenocarcinoma SCCHN	27–66 Gy in 6–33 fractions over 3–6 weeks, CA-4P 50–63 mg/m ² (2) 1, 3, or 6 doses. Patients with SCCHN also received cetuximab	39	Radiotherapy with CA4P appears well tolerated in most patients. Side effects include cardiac ischaemia and ataxia.	(Ng <i>et al.</i> , 2012)
I	Z-CA4P	Advanced solid tumours	20-85 mg/m ²	25	CA4P is generally well tolerated. Side effects include headaches, dizziness, vomiting, tumour pain,	(Liu <i>et al.</i> , 2014)

					vascular vagal excitation.	
II	Z-CA4P	Advanced metastatic anaplastic thyroid cancer	45 mg/m ² intravenously for 10 min on day 1, 8 and 15 of 28 day cycle in absence of disease progression.	26	Drug well tolerated. One third of patients survived more than 6 month. Side effects were not specified.	(Mooney <i>et al.</i> , 2009)
II	Z-CA4P + carboplatin and paclitaxel	Relapsed ovarian cancer	CA-4P 63 mg/m ² , 18 h later paclitaxel 175 mg/m(2) and carbopatin AUC 5 repeated every 3 weeks.	18	The addition of CA4P to paclitaxel and carboplatin is well tolerated and appears to produce a higher response rate. Side effects include neutropenia, thrombocytopenia, tumour pain, fatigue, and neuropathy.	(Zweifel <i>et al.</i> , 2011)
II	Z-CA4P + carboplatin and paclitaxel	Advanced ovarian cancer, primary peritoneal cancer and fallopian tube cancer in woman	n/a	44	11 cancers disappeared or shrank upon treatment with combination of 3 drugs. Side effects include drop of leukocyte and platelet numbers, tiredness, sickness, diarrhea, alopecia, peripheral neuropathy and balance problems (similar to normal carboplatin and paclitaxel side effects). Main Z-CA4P induced side effect was high blood pressure.	(Cancer Research UK, 2009a)
II/III	Z-CA4P + carboplatin and paclitaxel	Anaplastic thyroid cancer	60 mg/m ² intravenously on days 1, 8, 15 for 6 cycles.	80	Thyroidectomy followed by CA4P combination regimen showed a nonsignificant trend toward improvement in patient survival.	(Sosa <i>et al.</i> , 2012)

1.2.2 How do combretastatins act?

Combretastatins are antimitotic microtubule disrupting agents that act in a similar manner to colchicine; in their *cis*-form combretastatins bind strongly to the colchicine binding site in the β -tubulin subunit (Figure 16).

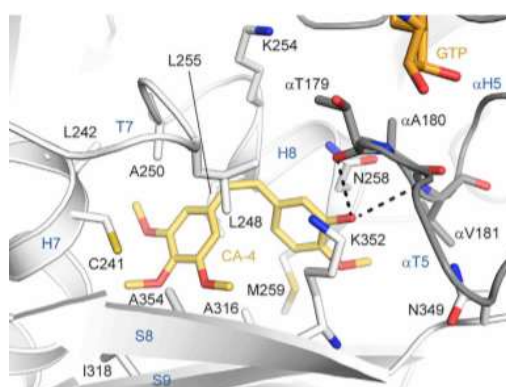


Figure 16 *cis*-CA-4 (yellow) bound to the colchicine site of tubulin (Gaspari *et al.*, 2017)

The similarity between the structures of combretastatin and colchicine prompted Hamel *et al.* to examine the interaction with tubulin before the most active derivative Z-combretastatin A4 was even discovered (Hamel & Lin, 1983; Tozer *et al.*, 2002). Binding to tubulin leads to a conformational change in the protein subunit thus preventing the formation of α,β -tubulin dimers, inhibiting *in vitro* tubulin polymerization, and eventually inducing apoptosis.

Induction of apoptosis and effects on tumour vasculature

Combretastatins effectively induce apoptosis in endothelial cells of tumour vasculature and are classified as vascular disrupting agents (VDAs) which were introduced in the section on antineoplastic drugs. Combretastatins preferentially target the immature endothelial cells of the tumour vasculature (Jain & Carmeliet, 2001; Tozer *et al.*, 2002). Clinical trial using Z-CA4P showed that upon binding to tubulin, endothelial cells became rounded as the cytoskeleton was no longer stable enough to maintain the normal cell shape; the rounding of cells blocks microvessels of the tumour thus hindering the blood flow and inducing apoptosis. Blocking microvessels essentially starved the tumour from its core outwards. Unfortunately animal models showed some peripheral cells survived the combretastatin treatment as they could 'feed' from nearby healthy cells (Hadfield *et al.*, 2007; Jain & Carmeliet, 2001; Thurston, 2007). The mechanisms involved in the shutdown of tumour vasculature by combretastatins are summarised in Figure 17.

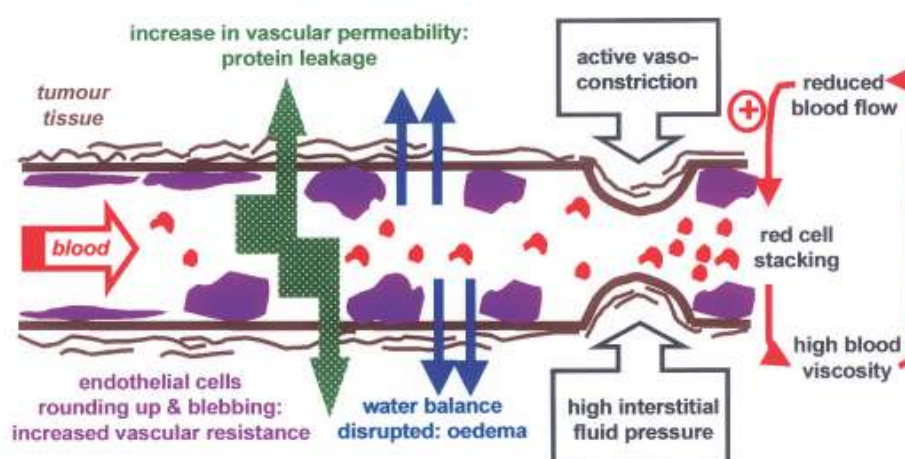
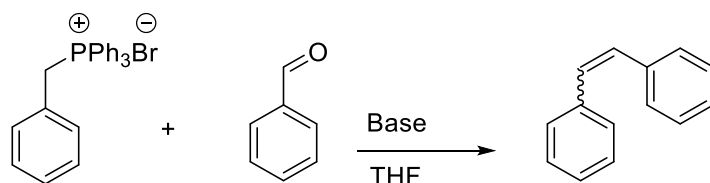


Figure 17 Rounding of endothelial cells after treatment with Z-CA4 (Tozer *et al.*, 2002)

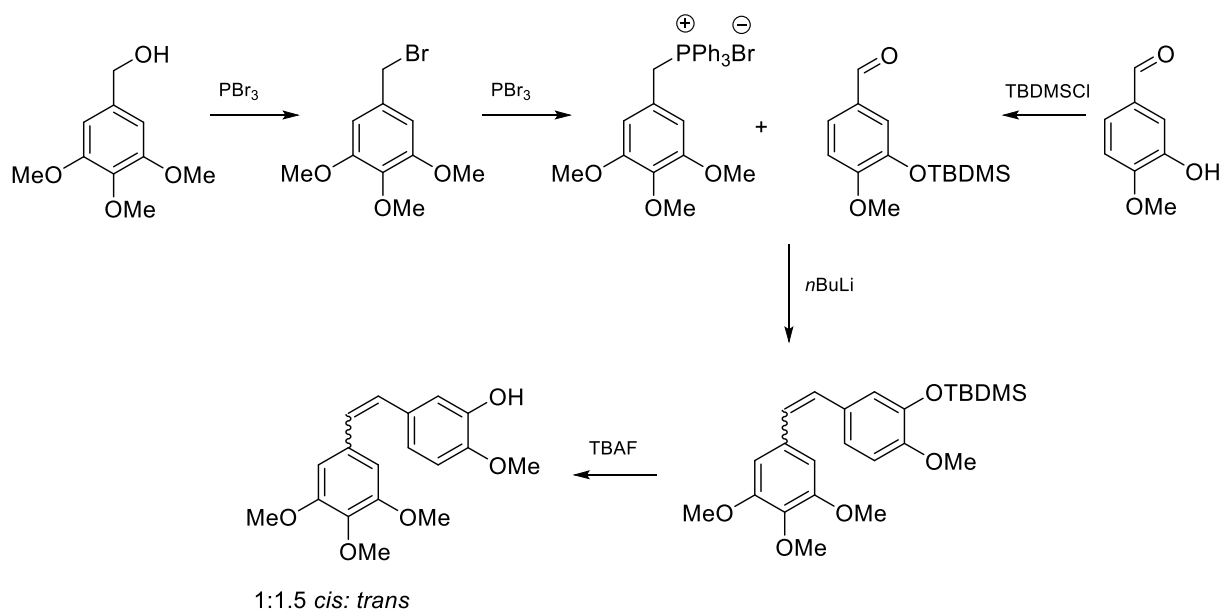
1.2.3 Synthesis of combretastatins

The complete synthesis of combretastatin A-4 was first published in 1995 and employed the Wittig pathway (Pettit *et al.*, 1995a). The reaction involves synthesising a benzyltriphenylphosphonium bromide; the 'Wittig reagent'; and reacting it with an appropriately substituted benzaldehyde in the presence of a base, usually *n*-butyllithium, to form the stilbene (Scheme 1). The reaction is non-selective and so gives both the *cis* and *trans* isomers that can be separated using column chromatography. The hydroxyl group requires protection before carrying out the Wittig reaction; this can be done using *t*-butyldimethylsilyl (TBDMS) chloride or chloromethyl methyl ether (CMME). Deprotection, using tetra-*n*-butylammomium fluoride (TBAF) or hydrochloric acid respectively, yields the phenol.



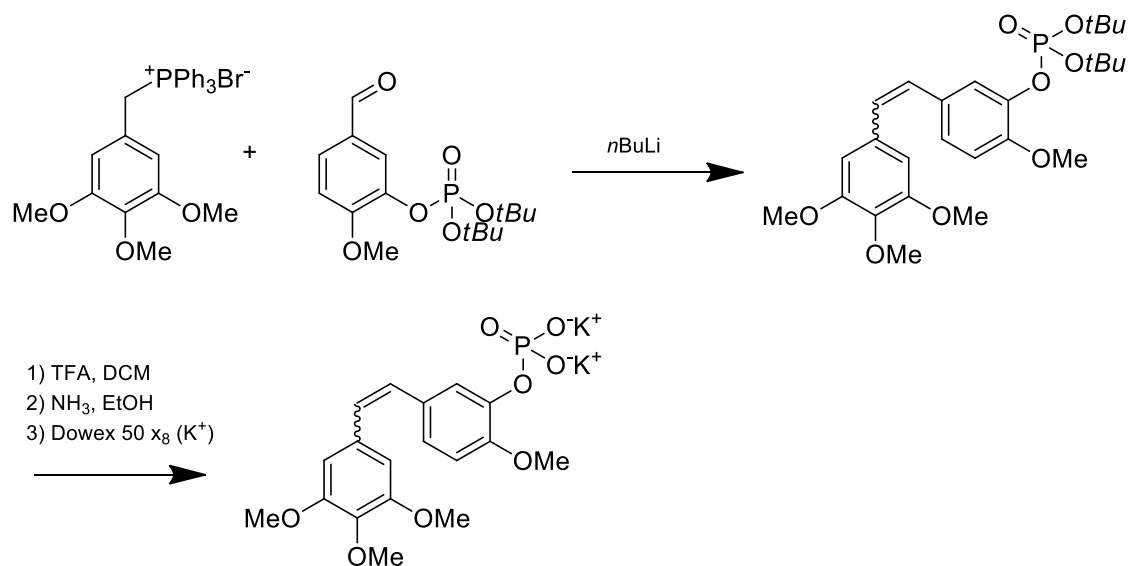
Scheme 1 Generalised Wittig reaction

Pettit and co-workers reported a five-step synthesis from 3,4,5-trimethoxybenzyltriphenylphosphonium bromide and isovanillin using *n*-butyllithium as the base (Pettit *et al.*, 1995a). Both *cis*- and *trans*- isomers of combretastatin A-4 were produced following this method in a ratio of 1:1.5 (*Z*:*E*); the overall yield of the *cis* isomer was 19 % (Scheme 2).



Scheme 2 Synthesis of Combretastatin A-4 utilizing the Wittig reaction (Pettit *et al.*, 1995a).

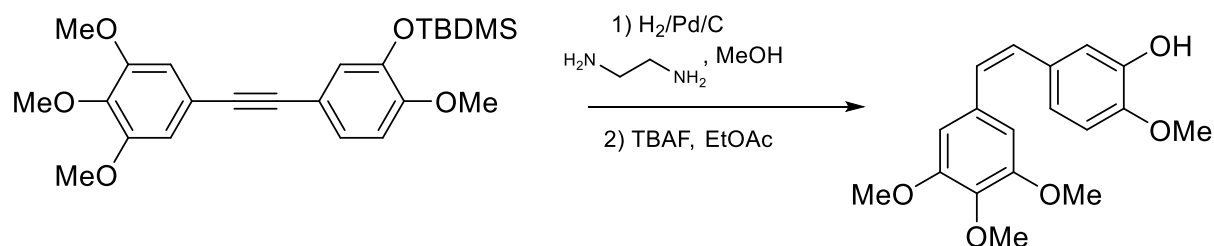
Bedford and co-workers produced the best selectivity using the Wittig route on the reaction of the benzyl bromide with the bis-*t*-butyl phosphate ester of isovanillin (Bedford *et al.*, 1996). The reaction afforded a 4:1 mixture of *Z*:*E* stereoisomers of the water soluble prodrug of combretastatin A-4 (55%) (Scheme 3).



Scheme 3 Synthesis of Combretastatin A-4 prodrug (Bedford *et al.*, 1996)

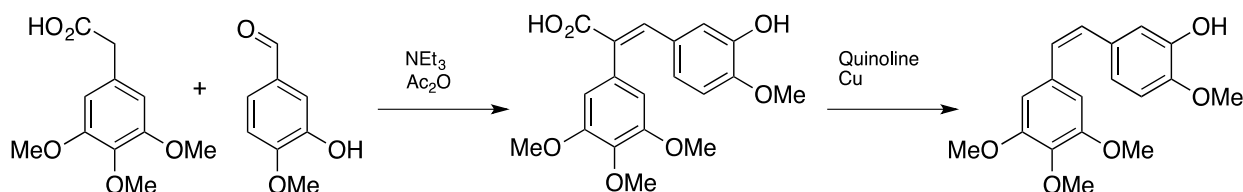
Although the Wittig method is one of the most utilized methods in the synthesis of combretastatins, it is problematic in that it is not stereoselective and so the yield of the desired *Z* isomer is vastly reduced. Isomers are difficult to separate quantitatively.

In an attempt to overcome this lack of selectivity, Furstner *et al.* developed a stereoselective route to combretastatins based on the Lindlar type semi-hydrogenation of an alkyne precursor (Furstner & Seidel, 1995). The synthesis of combretastatin A-4 (Scheme 4) was *Z* stereoselective but a small amount of the corresponding alkane was also isolated due to over-hydrogenation (86:14 respectively) (Furstner & Nikolakis, 1996); the alkane is difficult to separate, requiring HPLC and so this method is not ideal for large scale application.



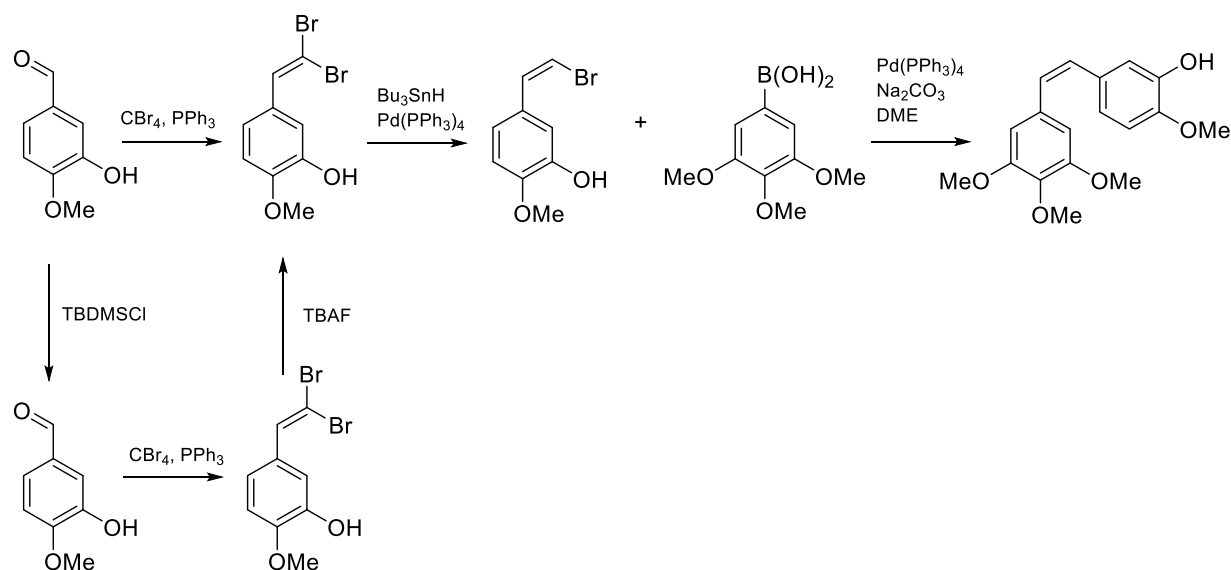
Scheme 4 Synthesis of Combretastatin A-4 (Furstner & Seidel, 1995)

An alternative synthetic route proposed by Gaukroger and co-workers for the stereoselective synthesis of *cis*-combretastatin A-4 (*Z*-CA4) is based on the Perkin condensation (Letcher, 1973) followed by decarboxylation with a copper catalyst. The reaction involved refluxing 3,4,5-trimethoxyphenylacetic acid and 3-hydroxy-4-methoxybenzaldehyde in the presence of triethylamine and acetic acid. Esterification, reduction and decarboxylation with powdered copper and quinoline affords combretastatin A-4 upon recrystallization (72%) (Scheme 5).



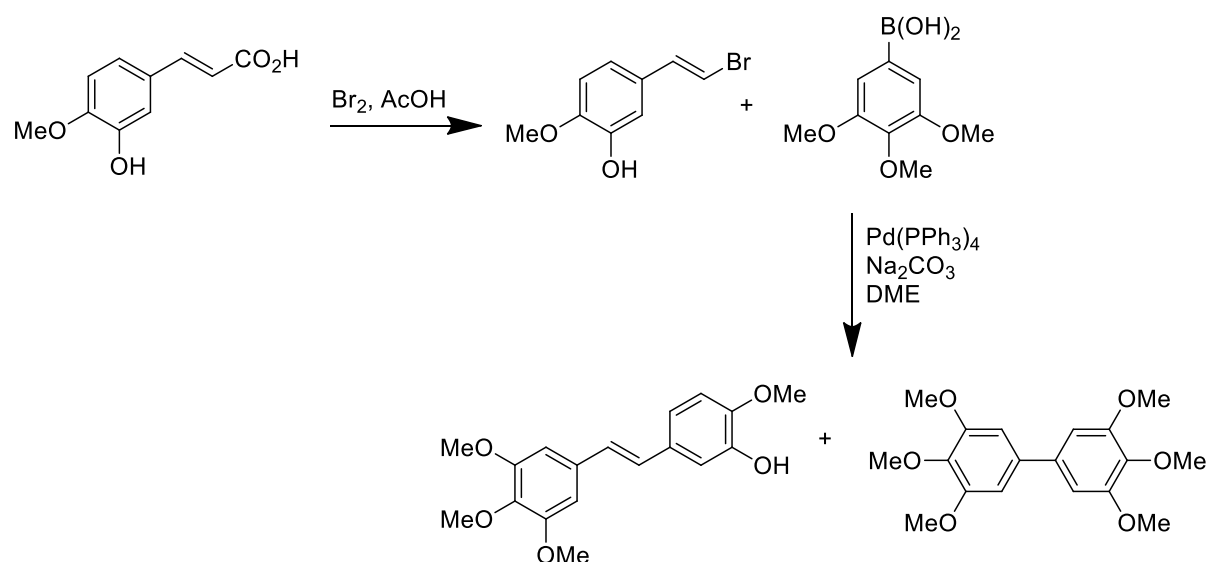
Scheme 5: Synthesis of Combretastatin A-4 utilizing the Perkin reaction (Gaukroger *et al.*, 2001a)

Substituted stilbenes can be synthesised selectively using the Suzuki cross-coupling of an ethenyl halide and aryl boronic acid. Gaukroger and co-workers synthesised combretastatin A-4 in a 6-step synthesis from (*Z*)-5-(2'-bromoethenyl)-2-methoxyphenol and 3,4,5-trimethoxybenzene boronic acid as shown in Scheme 6 (Gaukroger *et al.*, 2001a). Column chromatography and recrystallization afforded combretastatin A-4 in a good yield (70%), GC analysis indicated that the *Z*:*E* ratio was 99:1.



Scheme 6: Synthesis of Combretastatin A-4 using Suzuki cross-coupling (Gaukroger et al., 2001a)

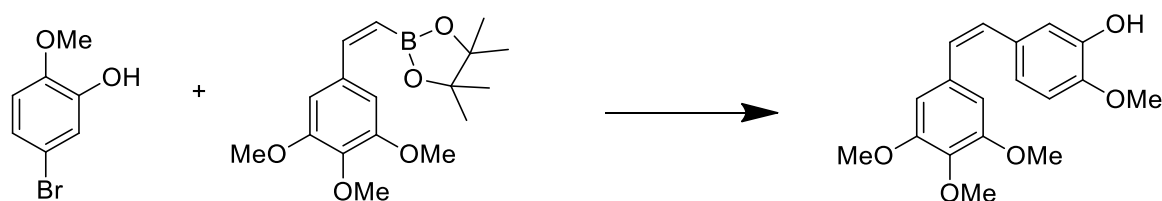
The synthesis of (*E*)-combretastatin A-4 by the same method was also reported by the group (Gaukroger *et al.*, 2001a). Bromination of 3-hydroxy-4-methoxy cinnamic acid afforded the (*E*)-vinyl bromide which was then reacted with 3,4,5-trimethoxybenzene boronic acid as above to form (*E*)-combretastatin A-4 (40%) and 3,3',4,4',5,5'-hexamethoxybiphenyl (6%) as a side product (Scheme 7).



Scheme 7: Synthesis of (*E*)-Combretastatin A-4 (Gaukroger et al., 2001a)

Recently Molloy and co-workers reported the Suzuki cross-coupling of a *cis*-styrene B-Pin; the *trans*-styrene B-Pin was first synthesised then photocatalysed ($\text{Ir}(\text{ppy})_3$, 450 nm) to the

corresponding *cis* isomer.; coupling with 5-bromo-2-methoxy phenol yielded CA-4 (84 %) (Molloy *et al.*, 2018).



Scheme 8: Synthesis of Combretastatin A-4 using Suzuki cross-coupling (Molloy *et al.*, 2018)

1.2.4 Recent developments in CA-4 based analogues

Modifications of combretastatins have mostly kept the more cytotoxic *cis*-conformation which included restriction of the *cis*- configuration by a heterocyclic moiety or changing the olefinic bond. Modifications to the B-ring were also investigated to try and improve activity and solubility.

Modifications at the olefinic bond

Replacement with a heterocycle

In order to retain the *cis*-configuration, the olefinic bond has been replaced with a heterocycle by a number of research groups; in most cases a five membered heterocycle such as pyrroles, imidazoles, thiazoles, thiophenes and azetidinones have been incorporated. Guan and coworkers reported the replacement of the olefinic bond with 1,2,5-selenadiazole; analogue **23** showed nanomolar activity across three cell lines (Guan *et al.*, 2014). Romagnoli and coworkers reported the replacement of the olefinic bond with an imidazole ring. Analogue **24** with a chloro and ethoxy group on the B-ring was most active with IC₅₀ values in the nanomolar range (0.4-3.8 nM) across 7 cell lines and inhibited tubulin polymerisation (IC₅₀ 0.87 μM) (Romagnoli *et al.*, 2016). CA-4 derivatives based on a pyrazole moiety (**25**) were synthesized through cycloaddition reactions of syndones in a regioselective manner by Brown and coworkers. Excellent cytotoxicity (7 nM) was observed against HUVEC cells (Brown *et al.*, 2016). Recently, triazoles have been identified as an important element in drug design; Madadi and coworkers synthesised a number of 4,5-disubstituted 2H-1,2,3-triazoles and evaluated their cytotoxicity across 60 cancer cell lines;

analogue **26** had IC₅₀ values <10 nM against almost all of the cell lines (Madadi *et al.*, 2015). Based on the rigidity of the thiophene moiety, Wang and coworkers synthesised a number of CA-4 derivatives with 2,3- diarylthiophenes; analogue **27** exhibited good IC₅₀ values (0.52-2.21 μM) and it was determined that these thiophene derivatives acted *via* the inhibition of tubulin polymerisation (Wang *et al.*, 2015). The Malebari group found that β-lactam analogues (**28**) were effective in chemoresistant HT-29 colon cancer cells; IC₅₀ values were reported in the nM range triggering G₂M cell cycle arrest by disrupting microtubular assembly (Malebari *et al.*, 2017).

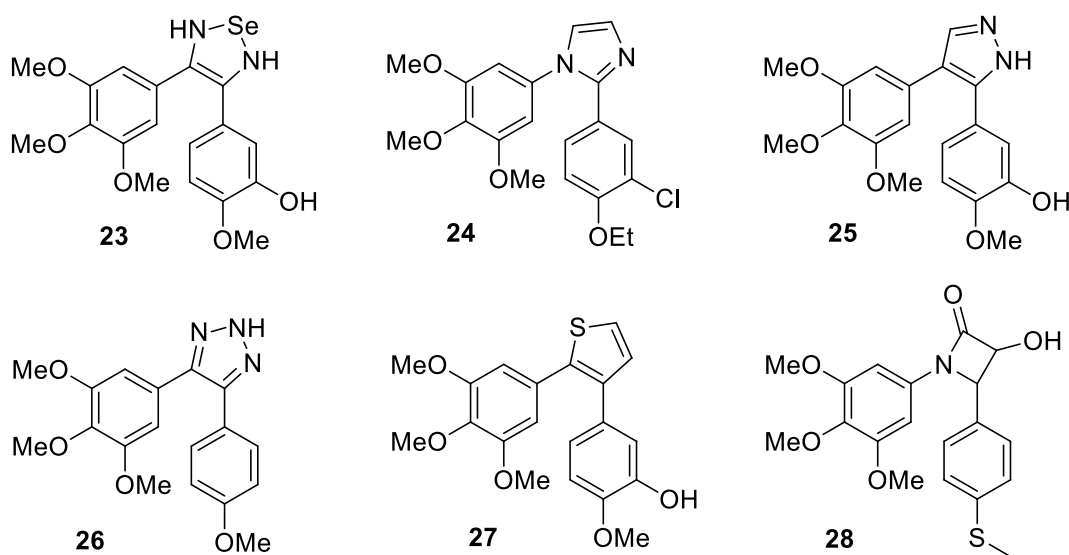


Figure 18 CA-4 derivatives with heterocycles replacing the *cis*-olefinic bond

Other replacements and substitutions

Amaral and coworkers reported N-acylhydrazone derivatives as antiproliferative agents with IC₅₀ values ranging from 4 nM to 18 μM; compound **29** can inhibit tubulin polymerisation and showed selectivity similar to that of CA-4 (Do-Amaral *et al.*, 2014). Engdahl's work on photoisomerisable azo-compounds were of particular interest to this work; irradiation at 400 nm of the *trans* isomer resulted in ca. 90% isomerisation to the *cis* isomer (**30**). The effect of *trans*-azo-CA4 on tubulin polymerization was little; upon irradiation at 400 nm good inhibition of tubulin polymerization was observed. They reported similar observations on the evaluation of cytotoxicity against HeLa cancer cells in the presence or absence of isomerizing light with a 200-fold increase in bioactivity compared to its *trans* counterpart (Engdahl *et al.*, 2015). An independent report by Borowiak and coworkers reported 250 times more activity of the *cis* form which is formed by isomerization of the *trans* form under

an appropriate light source (Borowiak *et al.*, 2015). Reddy and coworkers synthesised CA-4 derivatives with a benzoxazoles linked to the olefinic bond (**31**); IC₅₀ values of <0.1 μM were observed (Reddy *et al.*, 2016)

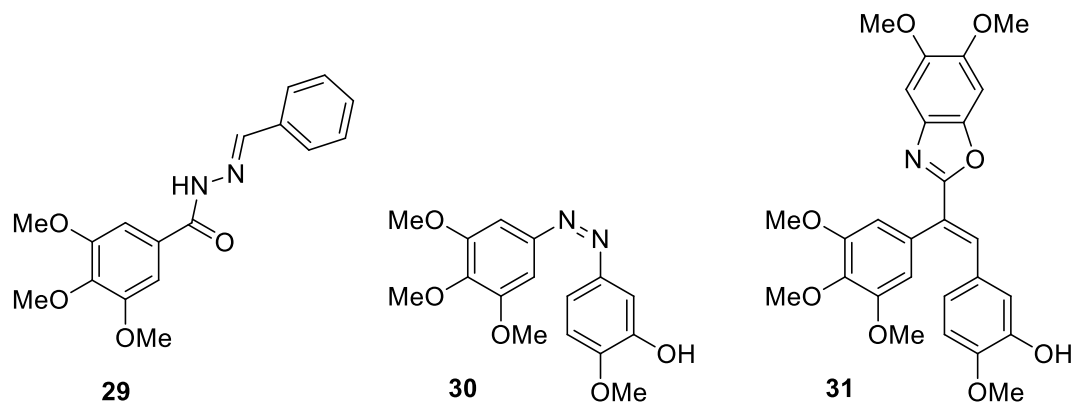


Figure 19 CA-4 derivatives with replacements and substitutions at *cis*-olefinic bond

Modifications of the olefinic bond and aromatic rings

There are a number of studies involving both modification on the olefinic bond and aromatic rings of CA-4. Kamal and Ashraf's group replaced the *cis*-olefinic bond with a pyridine ring and replaced the B-ring with a benzimidazole (**32**) or benzothiazole (**33**). IC₅₀ values from 31.1 μM to 40 nM were observed for this library of compounds (Ashraf *et al.*, 2016). Encouraged by these results they widened their scope to triazole and tetrazole derivatives; **34** was the most potent with a benzothiazole in place of the B-ring (Kamal *et al.*, 2015). The effect of replacing the *cis*-olefinic bond and B-ring with imidazole and indole rings respectively was investigated by Mahal's group; **35** was more active than CA-4 against drug resistant cell lines (10-31 nM) but did not significantly disrupt tubulin polymerisation (Mahal *et al.*, 2016).

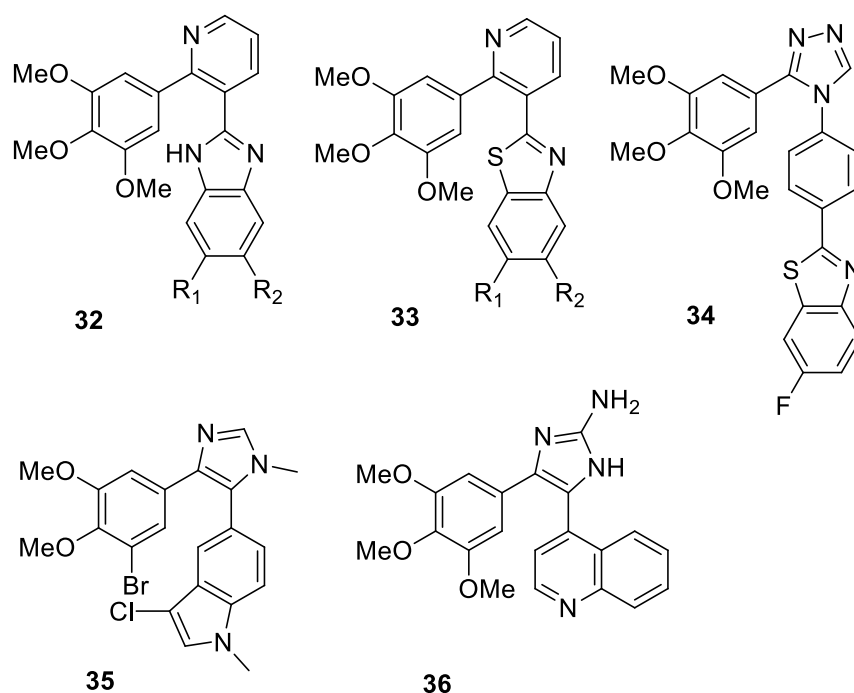


Figure 20 Ca-4 derivatives with modifications of *cis*-olefinic bond and B-ring

Modifications of the A- and B-rings

Simoni and co-workers developed a library of combretastatin derivatives with replacement of the A- and B-rings with benzofuran or benzothiophene; heterocombretastatins **37** and **38** inhibited tubulin polymerisation and bound to tubulin almost five times stronger than CA-4 (Simoni *et al.*, 2008). Kamal and co-workers used click chemistry to synthesise aminocombretastatins as tubulin polymerization inhibitors; compounds **39** and **40** exhibited excellent cytotoxicity with IC₅₀ values of 53 and 44 nM respectively; good tubulin inhibition was also observed with IC₅₀ values around 1 μM (Kamal *et al.*, 2014). Gerova and co-workers replaced the B-ring with a benzoxalone and synthesised a library of twenty-eight *cis*- and *trans*-isomers; of these synthesised derivatives, **41** showed cytotoxicity against the combretastatin resistant cell line HT-29 with an IC₅₀ value of 0.25 μM (Gerova *et al.*, 2016a).

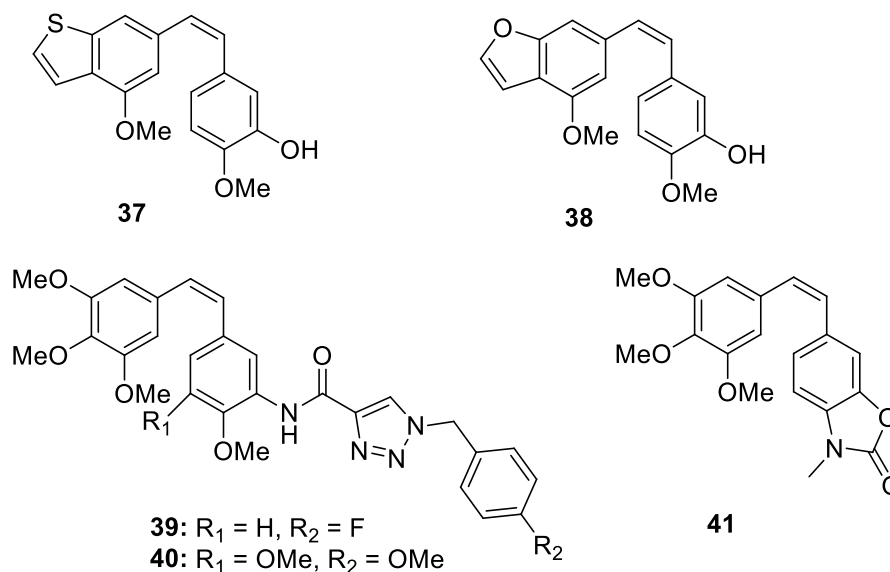


Figure 21 CA-4 derivatives with modification to the B-ring

1.2.5 Structure-Activity Relationship of the combretastatins

Based on the development of these new combretastatin analogues a structure-activity relationship of combretastatins can be determined:

1. The *cis*-configuration of the double bond is fundamental to achieve high cytotoxicity and antitubulin activity;
2. The trimethoxybenzene is considered essential to obtain optimal binding to tubulin;
3. B-ring structural modifications tolerated.

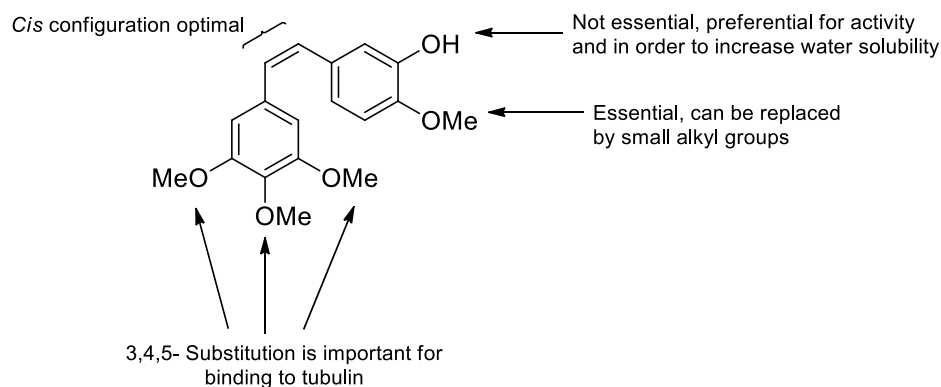
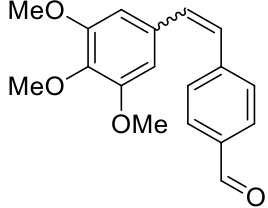
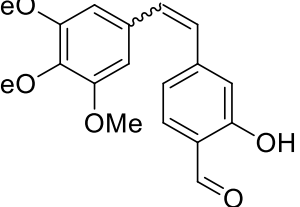
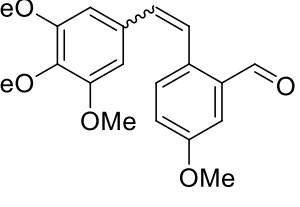
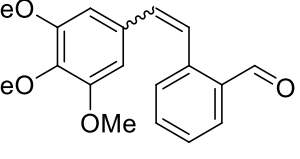
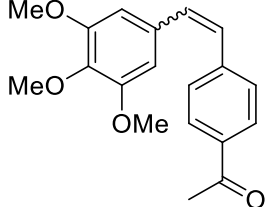


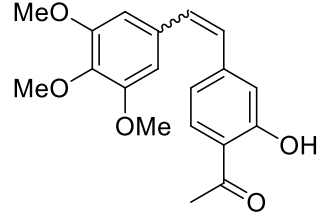
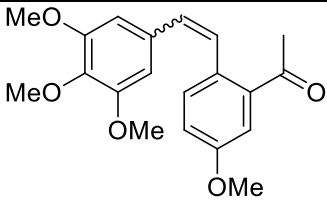
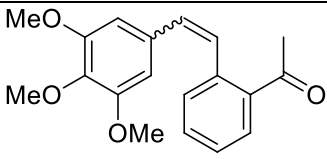
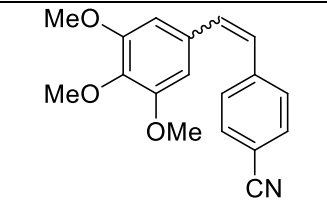
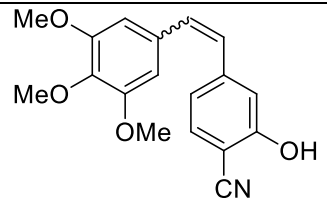
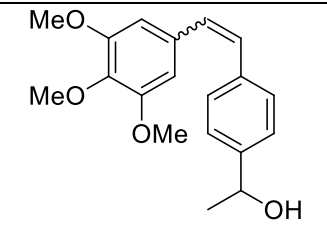
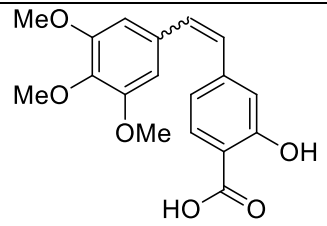
Figure 22 Structure activity relationship of the combretastatins

1.2.6 Combretastatins investigated in the course of this work

A number of combretastatin derivatives were studied in the course of this work (Table 3). Both *cis*- and *trans*-isomers were prepared; *cis*-isomers were assessed for their biological activity and the *trans*-isomers were used for the photochemical analysis and imaging.

Table 3 Names and structures of combretastatin drug candidates that were investigated

No.	IUPAC name	Structure
42	<i>(E/Z)</i> -4-(3',4',5'-trimethoxystyryl)benzaldehyde	
43	<i>(E/Z)</i> -2-hydroxy-4-(3',4',5'-trimethoxystyryl)benzaldehyde	
44	<i>(E/Z)</i> -5-methoxy-2-(3',4',5'-trimethoxystyryl)benzaldehyde	
45	<i>(E/Z)</i> -2-(3',4',5'-trimethoxystyryl)benzaldehyde	
46	<i>(E/Z)</i> -4-(3',4',5'-trimethoxystyryl)acetophenone	

47	(<i>E/Z</i>)-2-hydroxy-4-(3',4',5'-trimethoxystyryl)phenyl)acetophenone	
48	(<i>E/Z</i>)-5-methoxy-2-(3',4',5'-trimethoxystyryl)acetophenone	
49	(<i>E/Z</i>)-2-(3',4',5'-trimethoxystyryl)acetophenone	
50	(<i>E/Z</i>)-4-(3',4',5'-trimethoxystyryl)benzotrile	
51	(<i>E/Z</i>)-2-hydroxy-4-(3',4',5'-trimethoxystyryl)benzotrile	
52	(<i>E/Z</i>)-1-(4-(3',4',5'-trimethoxystyryl)phenyl)ethanol	
53	(<i>E/Z</i>)-2-hydroxy-4-(3',4',5'-trimethoxystyryl)benzoic acid	

1.3 Principles of photochemistry and photophysics

In this work *E*-combretastatins were investigated as potential prodrugs for type IV PDT; it is important to understand some of the fundamental principles of photochemistry and photophysics. Characteristics that were of particular interest in this work included the determination of fluorescence quantum yields, fluorescence lifetimes and two-photon absorption cross-sections.

1.3.1 Absorption and fluorescence

Spectroscopic methods rely on electronic transitions where a molecule is taken from its ground state to an electronically excited state. The energy difference (ΔE) between the two electronic states can be described by the following equation:

$$\Delta E = h\nu$$

Equation 1

where h is the Planck's constant ($6.626068 \times 10^{-34} \text{ m}^2 \text{ kg/s}$) and ν is the frequency of the light absorbed. In spectroscopy, the multiplicity of an energy level can be defined as $(2S + 1)$ where S is the total spin; the Pauli principle states that two paired electrons occupying an orbital have opposite (anti-parallel) spins giving a total spin of 0 thus the ground state has a multiplicity of one i.e. singlet. Upon excitation, one of the electrons is lifted to a higher energy level without changing its spin, it is still paired with the electron in the lower orbital and so the overall spin is 0 thus this excited state has a multiplicity of one; the excited single state. It is possible that the promoted electron spin flips to give an unpaired electron (parallel spins) and so $(2S + 1) = 3$; the triplet state. Triplet states usually arise from the excited singlet state as direct transitions from the ground state to the triplet state are "forbidden"; the spin of an electron cannot change during a transition involving the absorption of light. Upon absorption of light, an excited electronic state is generated; possible deactivation processes to return the molecule to its ground state are summarised by the Jablonski diagram (Figure 23).

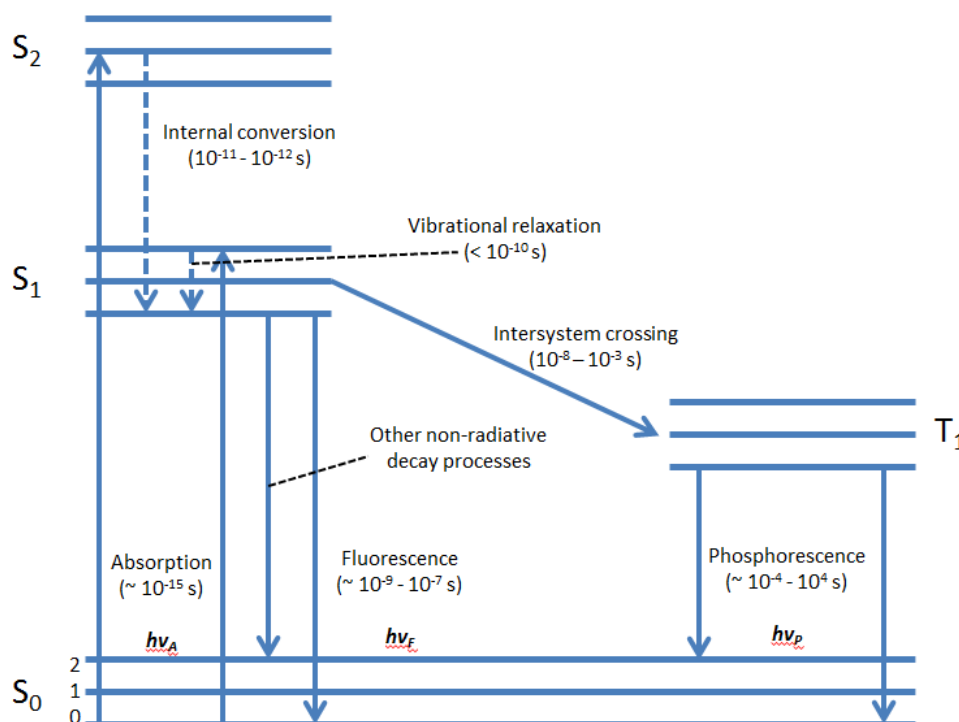


Figure 23 Jablonski diagram adapted from Lakowicz, 2006

Molecules usually exist in their singlet ground state (S_0); irradiation of the molecule with light leads to the formation of an electronically excited single state S_1 (S_2 , S_3 , also possible). Once in the excited state there are several decay pathways possible including radiative (emission of light) processes, non-radiative processes and energy redistribution (Figure 23). Other possible deactivation processes are resonance energy transfer to other molecules and electron transfer (Becker, 1969; Chang, 2000; Denney & Sinclair, 1991; Herman, 1998; Lakowicz, 2006; Lichtman & Conchello, 2005; Rendell, 1987).

1.3.2 The Stokes shift

The Stokes shift is an important characteristic of fluorescence spectroscopy named after its namesake George Stokes. The Stokes shift is the difference between the band maxima of the absorption and emission spectra with the emission spectra being red shifted. A system gains energy and enters an excited state upon absorption of a photon, vibrational relaxation occurs faster than the decay back down to the ground state by emission of fluorescence and energy is transferred from the excited state to the surrounding solvent molecules. This difference in energy is the Stokes shift. The extent of the Stokes shift generally increases with solvent polarity (Herman, 1998; Lakowicz, 2006; Parson, 2007; Rendell, 1987; Suppan, 1994).

1.3.3 Fluorescence lifetimes and quantum yields

Fluorescence lifetime is a measure of the average time a molecule resides in the electronically excited state before it decays back to the ground state by emission of a photon. Fluorescence lifetimes can vary from picoseconds to hundreds of nanoseconds depending on the fluorophore. Decay is usually exponential over time and can be described as $I = I_0 e^{-t/\tau}$ where I_0 is the intensity at time zero, I is the intensity at time (t) and the lifetime is a constant τ . Lifetimes are dependent on both internal factors such as competing deactivation processes and external factors such as collision quenching (by interaction with solvent or other molecules). In a uniform solvent the fluorescence decay is usually a single exponential; whilst fluorescence decay in heterogeneous environments is usually multi-exponential. Non-exponential decays may be observed when fluorophores are quenched by energy transfer or solvent relaxation.

The quantum yield is a measurable property of fluorescence that may correlate linearly with fluorescence lifetimes. The fluorescence quantum yield (Φ_F) is defined as the ratio of photons emitted to the number of photons previously absorbed by a molecule; values between 0 and 1 are possible. In this work fluorescence lifetimes and quantum yields were determined in a range of solvents and live cells to gain insight into the effects of environments on these photochemical properties.

1.3.4 Two-photon absorption

Maria Göppert-Mayer theoretically described the nonlinear simultaneous absorption of two photons by the same molecule in her doctoral dissertation in the 1930s (Göppert-Mayer, 1931); the first experimental evidence of this came 30 years later when Kaiser and Garrett demonstrated two-photon excitation in a $\text{CaF}_2:\text{Eu}^{2+}$ crystal (Kaiser & Garrett, 1961). In contrast to the linear one photon process, two photon absorption (2PA) is the simultaneous absorption of two photons, of half the energy (or twice the wavelength) of the corresponding one photon process (Figure 24). The first exciting photon promotes an electron to a virtual state; the second photon subsequently interacts with the virtual state electron and lifts it to a higher electronic excited state. Based on the assumption that each fluorophore is exposed to the same laser cross section, photons must arrive within 10^{-18} seconds of each other. The time scale of this overlap period is consistent with the lifetime

10^{-17} seconds of the intermediate virtual state, which is why it is referred to as simultaneous absorption, although it is not actually simultaneous (Mathai *et al.*, 2007).

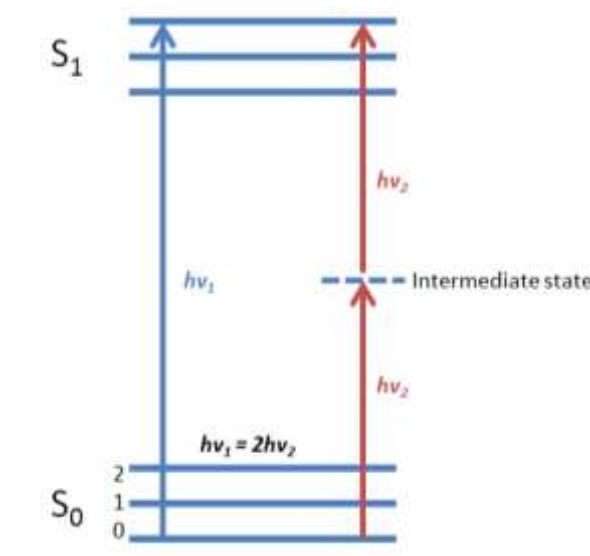


Figure 24 Jablonski diagram of two-photon absorption.

Current applications of non-linear processes include multiphoton fluorescence, photodynamic therapy, 3D optical data storage, optical power limiting and optogenetics (Gu *et al.*, 2016). The non-linear excitation processes utilised in this study for multiphoton microscopy are illustrated below; processes are excited in an extremely small focal volume using fs lasers (Figure 25).

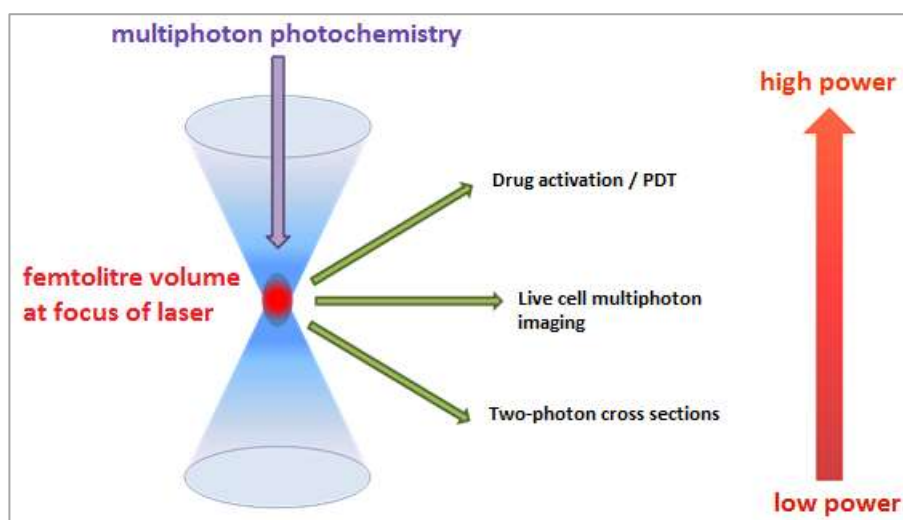


Figure 25 Nonlinear processes in the focal volume of a multiphoton microscope depending on the laser power

Amongst these processes, the multiphoton microscope may be used to measure 2PA cross sections (σ_2); the likelihood of 2PA increases relative to the square of light intensity and is represented by the two-photon cross section (σ_2) of the molecule. The low probability of 2PA, compared with the one-photon process, is reflected in small σ_2 values; high photon density is required to observe 2PA such as the density achieved with femtosecond laser pulses. Simple chromophores exhibit σ_2 values in the region of 1 Göeppert-Mayer (GM) unit (1 GM = 10^{-50} cm⁴ s photon⁻¹) however values of $\sigma_2 \geq 100$ GM are required in order to provide adequate light absorption at skin-safe laser intensities i.e. NIR light (Pawlicki *et al.*, 2009).

The measurement of 2PA cross-sections is rather complicated due to many potential instrumental problems and especially if one wants to determine the cross-sections of a compound for a broad range of wavelengths. When measuring cross sections, it is advised to use a well-characterised reference compound as standard to normalize the investigated compound such as 9-chloroanthracene (9CLA). Furthermore, the fluorescence spectrum of the reference and the tested compound should overlap, to enable detection within the same wavelengths range (Makarov, Drobizhev & Rebane, 2008a). The two major techniques used to characterise 2PA properties of a molecule are the Z-scan experiment or two-photon induced fluorescence (TPIF) (Mathai *et al.*, 2007).

1.3.5 Photoisomerization of stilbenes

The *trans*↔*cis* photoisomerization of stilbenes is a well-known process in photochemistry that was first described in 1931 (Olson, 1931); in 1940 Lewis and co-workers proposed that a molecule that exists in two stereoisomeric forms (such as stilbene) can be converted between each isomer *via* a common electronically excited state upon absorption of light. They found that the *cis*-isomer was only marginally fluorescent whilst the *trans*-isomers was much brighter; this was explained by the fact that stilbenes are planar in the *trans*-conformation whilst the *cis*-conformation is twisted out-of-plane. This out-of-plane twist makes the *cis*-conformer less stable and thus has a lower energy barrier and shorter lifetime of the electronically excited state. More than 20 years later Schulte-Frohlinde and co-workers and Malkin and Fischer determined *cis*→*trans* isomerization quantum yields of substituted stilbenes under varying conditions (*i.e.* solvents, temperature, concentration

and excitation wavelength). One of their major findings was that isomerization quantum yields strongly varied with solvent, concentration, temperature and substituents in *trans*→*cis* isomerisation whilst the effects were less prominent in *cis*→*trans* isomerisation (Schulte-Frohlinde *et al.*, 1962; Malkin & Fischer, 1962). The process of photoisomerization is a complex unimolecular reaction that may be influenced by solvent properties such as polarity and viscosity, concentration, temperature and excitation wavelength. Substituents on stilbenes can massively influence the rate of photoisomerization such as bulky side groups that induce steric hindrance or electron donors/acceptor groups that induce twisted intramolecular charge transfer (TICT). The potential energy surface scheme for stilbene photoisomerization from the excited singlet state that is presently accepted was proposed in 1968 (Figure 26) (Görner & Kuhn, 1995; Saltiel, 1968; Saltiel *et al.*, 1968).

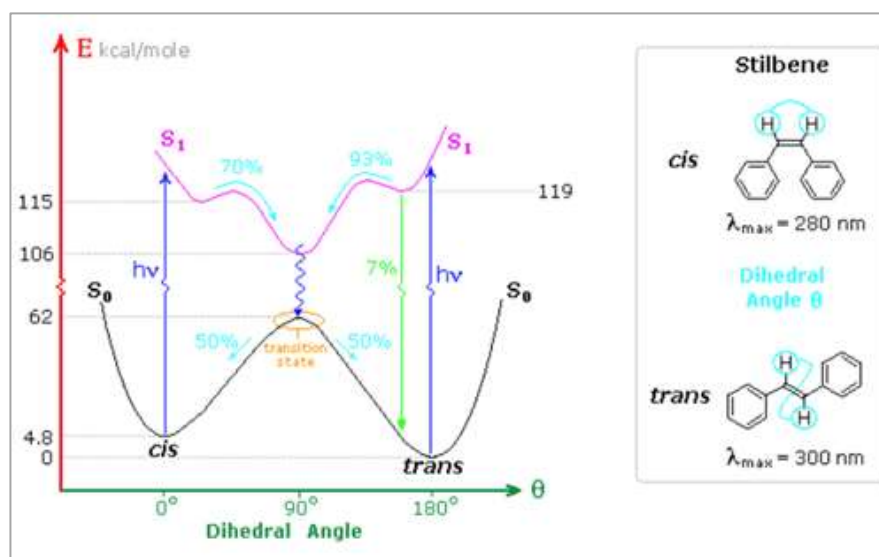


Figure 26 Commonly accepted energy surface for stilbene photoisomerization (adapted from Kovalenko *et al.*, 2010)

Figure 26 shows that a large potential energy barrier of the transition state (~ 62 kcal mol $^{-1}$) separates the *cis*- and *trans*-isomers. Upon excitation, the potential energy barrier is smaller than that of the ground state (9 kcal mol $^{-1}$ for *cis*- and 13 kcal mol $^{-1}$ for *trans*). Stilbene may return to the ground state by two competing deactivating pathways; fluorescence or isomerisation. Due to the difference in energy of the excited state of *cis*- and *trans*-isomers the isomerisation process is relatively slow ($\tau \sim 100$ ps) from the excited *trans*-isomer and much faster from the excited *cis*-isomer ($\tau \sim 1$ ps). The transition state is a common intermediate state of the *cis*- and *trans*-isomers with a dihedral angle twist of 90° , this state

has a very short sub-ps lifetime and hence is difficult to detect; as one of the isomers arrives at the transition state it rapidly decays back to the ground state by internal conversion. When reaching the ground state, the stilbenes diverge to either the *trans*- or *cis*-conformation (Waldeck, 1991; Weigel & Ernsting, 2010; Charlton & Saltiel, 1977; Saltiel & Megarity, 1972; Kovalenko *et al.*, 2010; Görner & Kuhn, 1995).

The photoisomerization of stilbenes is a reversible process and the photostationary state after irradiation is strongly dependent on the excitation wavelength; the *cis*-isomer frequently dominates the photostationary state because of the higher extinction coefficient of the *trans*-isomer in the long wavelength absorption band. As mentioned previously, the solvent influences photoisomerization quantum yields; the rate of photoisomerization is generally slower in solvents that are more viscous. For donor/acceptor-substituted stilbenes, as used in the course of this work, more polar solvents allow for faster photoisomerization. One-photon excited isomerization of combretastatins by irradiation with UV light and the use of *trans*-combretastatins as inactive pro-drugs was first suggested in 2000 (Hepworth, 2000); although one-photon isomerisation in the UV or visible wavelength range works well in solution, most of the excitation light is absorbed by chromophores in live tissues. Further to this UV/Vis light does not penetrate deep into tissues; two-photon excitation using femtosecond lasers in the NIR wavelength range allows deeper light penetration into tissue.

1.4 Fluorescence microscopy techniques

In the previous section, the fundamentals of photophysical and photochemical processes of stilbene derivatives were discussed. The fluorescence microscopy techniques employed in this work will be compared to other available techniques in the following section.

1.4.1 History of light microscopy

The first assembled microscopes were developed around 1590 by father and son Hans and Zacharias Janssen; other sources name Antoni van Leeuwenhoek (1632 – 1723) as the inventor of the microscope, owing to his discovery that magnification of a lens increases its curvature with his lenses allowing magnification up to 270 times. Until 1873 microscopes were manufactured using trial and error; at this time Ernst Abbe determined the fundamental laws of physics necessary to build effective microscopes and recognised the Abbe limit of resolution. The maximum resolving capacity of a conventional light microscope is restricted to ~ 200 nm (Gray, 2009). Nowadays a wide range of advanced optical microscopy techniques such as dark field, phase contrast, interference contrast exist as well as bright field microscopy. The microscopy techniques used in the course of this work include multiphoton fluorescence, fluorescence lifetime imaging microscopy (FLIM) and light sheet fluorescence microscopy (LSFM).

1.4.2 Fluorescence microscopy

Köhler, Reichert and Lehmann invented the first fluorescence microscope at the beginning of the twentieth century. Fluorescence microscopy allows monitoring of physiological processes within tissues with high sensitivity; fluorescence microscopy allows single molecule imaging and a wide range of fluorescent dyes allows for selective labelling of cellular structures. The most fundamental principle of fluorescence imaging is that following excitation of a fluorophore, fluorescence is emitted at a longer wavelength of lower energy that can be detected. Due to its simplicity, epi-fluorescence is still the most commonly used fluorescence microscopy in life sciences. In conventional epi-fluorescence, fluorescence is excited by mercury or xenon lamps (50 – 200 W), excitation wavelength can be selected using a filter. A dichroic mirror separates the emitted light from the excitation light by reflecting the excitation light onto the sample and the emitted light to a detector. A filter is also placed between the dichroic mirror and detector to help block any unwanted excitation

light. A typical fluorescent microscope is shown in Figure 27. Fluorescence detection is limited by the background fluorescence. The darker the background the better the image contrast (Abramowitz & Davidson, 2012; Davidson & Abramowitz, 1999; Herman, 1998; Lichtman & Conchello, 2005; Spring & Davidson, 2012).

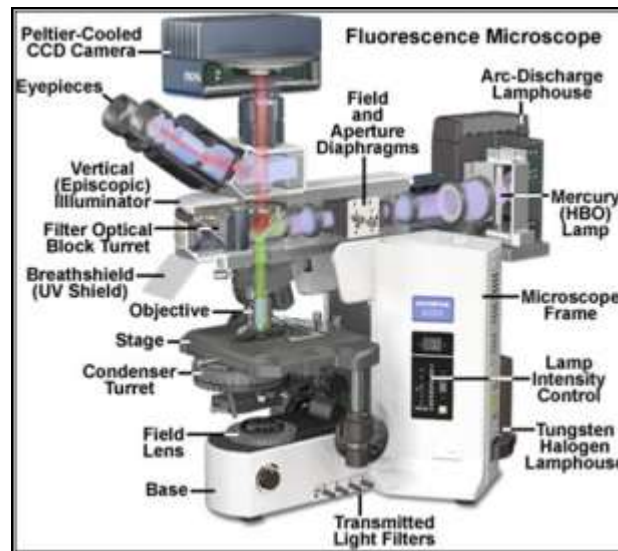


Figure 27 Epi-fluorescence microscope (Abramowitz *et al.*, 2012)

Epi-illumination (or wide-field) means the entire sample region is illuminated; image acquisition is faster compared to the laser scanning techniques discussed in the next section. Wide-field illumination allows for the observation of many fluorescent molecules at a time but may result in interference from other fluorophores or unwanted autofluorescence (Abramowitz & Davidson, 2012; Chang *et al.*, 2007).

1.4.3 Confocal Microscopy

The fundamental principles of confocal microscopy were patented in 1957 by Marvin Minsky (Minsky, 1957) but didn't become a standard technique in optical microscopy for another 30 years when the laser was developed. Confocal microscopy records images by scanning over a specimen with a laser as opposed to the wide-field approach in conventional epi-fluorescence microscopy. In confocal laser scanning microscopes (CLSM) an excitation light beam from a laser is focussed through an objective onto the sample. A pinhole located in the beam path between the dichroic mirror and the detector is used to reject out-of-focus fluorescence (blur), improving the signal-to-noise ratio and thus image resolution; only a small confocal spot of the sample is excited at a time rather than the

whole field of view as in conventional fluorescence microscopy. Confocal microscopy has the capability of non-invasive optical sectioning of biological specimens (with a thickness of $\sim 0.5 \mu\text{m}$) allowing the acquisition of 3D images. The major disadvantage of confocal compared with epi-fluorescence imaging is the prolonged image acquisition time due to exciting only a small confocal spot of the sample at a time and scanning over the field of view. Common laser light sources used in confocal microscopy are argon-ion (488 nm) or helium-neon lasers (543 nm) with high intensities (Chang *et al.*, 2007; Cox, 2002; Fellers & Davidson, 2012; Herman, 1998; Sheppard & Shotton, 1997; Spring & Davidson, 2012; Webb, 1996).

1.4.4 Multiphoton fluorescence microscopy

Multiphoton microscopy (also non-linear microscopy) is an advanced fluorescence technique compared to those previously discussed. Watt Webb and co-workers first applied multiphoton microscopy in 1990 (Denk *et al.*, 1990; König, 1999; Potter, 1996; So, 2002; So *et al.*, 2000). The main differences of multiphoton microscopy and confocal microscopy are the excitation light source and signal detection pathway. In multiphoton microscopy, two photons are absorbed simultaneously in a single quantum event leading to excitation of a fluorophore; for this to occur the wavelength must be double that used in one-photon microscopy technique. Compared to confocal microscopy, where a light cone is created in the sample, in multiphoton microscopy the excitation light in the focal plane is defined to a very small femtolitre volume; optical sectioning is facilitated as light reaches the focal plane more than in confocal microscopy. Less scattering is observed and so there is no need for a pinhole. Photobleaching and photodamage are also restricted since only fluorophores in the femtolitre volume are excited. Further to this the use of NIR light for fluorescence allows for deeper penetration into tissues.

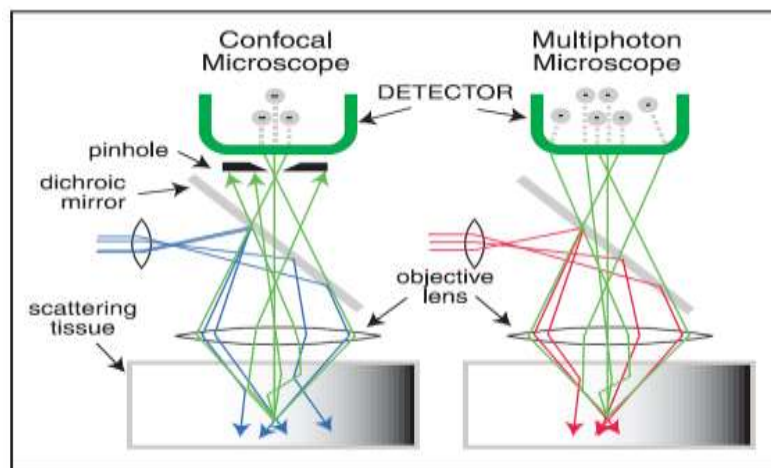


Figure 28 Comparison of confocal and multiphoton microscopy (Denk & Svoboda, 1997)

The light sources used for multiphoton microscopy are usually mode-locked pulsed lasers with high peak powers and relatively low average powers; high peak powers are required to achieve multiphoton excitation yet low average powers are necessary to prevent photo damage at the sample. For this reason the lasers required for multiphoton microscopy are often expensive.

1.4.5 Fluorescence lifetime imaging microscopy (FLIM)

Confocal and multiphoton scanning microscopy of live cells in three dimensions is an important tool in the life sciences; they are extremely sensitive and can deliver information about biochemical interactions on the molecular scale (Becker, 2012). The combination of confocal or multiphoton microscopes with fluorescence lifetime imaging systems allows the acquisition of fluorescence images with information on fluorescence lifetimes of fluorophores in heterogeneous environments. It relies on the fact that the fluorescence lifetime of a fluorophore depends on its environment as opposed to its concentrations; FLIM can discriminate different fractions of the same fluorophore in different states of interaction with its environment (Lakowicz, 2006). Further to this, FLIM is a sensitive fluorescence technique that can be used to distinguish between fluorophores with overlapping emission spectra, map intracellular dynamic processes and parameters such as pH or ion concentrations by fluorescence quenching (Becker *et al.*, 2004; Herman, 1998). Fluorescence lifetime change of a fluorophore can be determined upon binding to a biological target; comparison of these lifetimes to controls in different environments can give an idea as to the biological environment. Typical instrument response functions of FLIM

imaging systems are below 100 ps depending on the detection system in use, good single-exponential decays can be obtained by collecting a few hundred photons per pixel in a field of view. In the course of this work, FLIM was applied to explore intracellular uptake and distribution of combretastatin derivatives in live cells.

1.4.6 Light sheet fluorescence microscopy (LSFM)

Optical sectioning is the primary purpose of confocal techniques however, traditional scanning confocal microscopes are slow to acquire data and repeated exposure of the sample to excitation light may cause photobleaching. Light sheet fluorescence microscopy (LSFM) uses a plane of light to optically section and view tissues with subcellular resolution; compared with confocal and two-photon microscopy, LSFM is able to image thicker tissues (>1 cm) and because tissues are only exposed to a thin plane of light LSFM is less invasive. Specimen photobleaching and phototoxicity are minimized compared to wide-field fluorescence, confocal, or multiphoton microscopy previously discussed (Santi, 2011). Furthermore, the entire focal plane is illuminated simultaneously allowed for a faster acquisition of the entire field of view at high resolution with a shorter exposure time (Table 4).

Table 4 A comparison of microscopes used in the course of this work

Microscope	Resolution	Specimen (stack) size	Acquisition of stack	Photobleaching	Reference
Confocal	<micron	μm	msec	yes	(Marvin, 1961)
Two-photon	<micron	mm	msec	yes	(Denk <i>et al.</i> , 1991)
Light sheet	Micron	>cm	msec	minimal	(Voie <i>et al.</i> , 1993)

The first published account of orthogonal light sheet microscopy by Siedentopf and Zsigmondy dates back to 1902 (Siedentopf & Zsigmondy, 1902) in which sunlight was projected through a slit to observe gold particles (Figure 29). It was almost a century later that the first use of light sheet microscopy was reported for fluorescent imaging; Voie and co-workers employed light sheet microscopy to image the ear of a guinea pig using orthogonal plane fluorescence optical sectioning (OPFOS) (Voie *et al.*, 1993). OPFOS featured

all of the elements that are present in current LSFM devices - laser, beam expander, cylindrical lens, specimen chamber and orthogonal illumination of the specimen.

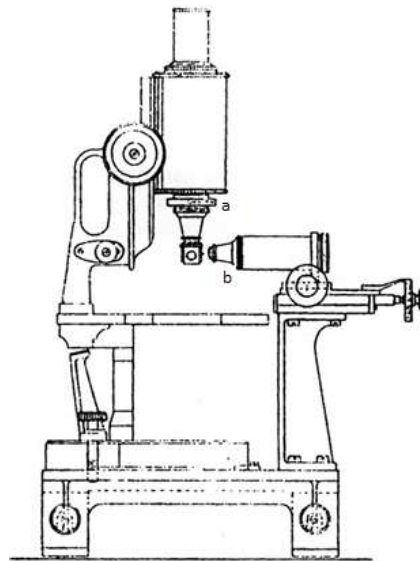


Figure 29 Siedentopf and Zsigmondy's lightsheet microscope with specimen holder mounted onto objective(a) and illuminating objective at 90° (b) for the collection of sunlight to observe gold particles (Siedentopf & Zsigmondy, 1902)

In a basic LSFM system an excitation laser is collimated and passed through an iris and focussed into a sheet of light through a cylindrical lens. The excitation light passes through the sample and emission is collected orthogonally by an imaging objective and imaged through a tube lens onto the detector (usually a sCMOS camera) (Adams *et al.*, 2015).

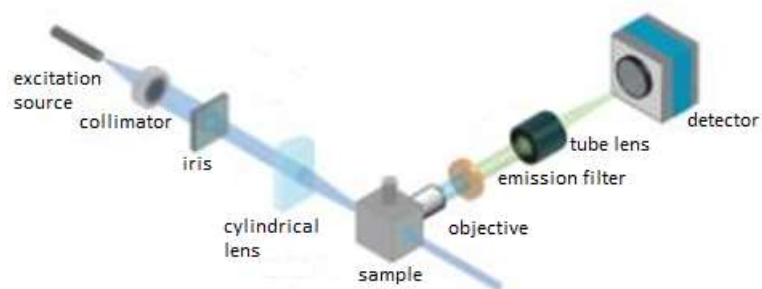


Figure 30 Basic light sheet fluorescence microscope (Adams *et al.*, 2015)

1.5 Aims of the project

The aim of this work is to develop combretastatin derivatives for type IV photodynamic therapy. This new form of photodynamic therapy does not require the generation of a reactive oxygen species as combretastatins are directly being activated by photoisomerization (Scherer *et al.*, 2017). Low tissue penetration from conventional light sources in the UV/Vis region is a major drawback of traditional 1 photon PDT; the application of multiphoton fluorescence microscopy will use NIR light (700 – 1000 nm) for the multiphoton excitation of the compounds of interest. Localized two-photon activation of the inactive *trans*-combretastatins at the tumour site would make this cancer treatment more selective than the direct administration of the highly active *cis*-derivatives.

To accomplish this a range of *cis*(*Z*)- and *trans*(*E*)-combretastatin derivatives have been designed to improve the 2PA cross sections whilst retaining the activity towards cancer cells in the *cis*-form. Modifications were made to the stilbene structure to provide charge transfer across the molecule (Pawlicki *et al.*, 2009); π -conjugated molecules with large changes of quadrupole moment exhibited larger σ_2 values (Albota *et al.*, 1998). This was achieved by adding EWG to the *ortho*- and *para*-positions on the B-ring to complement the electron-donating methoxy groups on the A-ring. Cytotoxicity and tubulin polymerisation inhibition of the *cis*(*Z*)-combretastatins were determined and the *trans*(*E*)-combretastatin derivatives were evaluated for their photochemical properties such as fluorescence quantum yields, fluorescence lifetimes and two-photon absorption cross-sections. The intracellular uptake and distribution of *E*-combretastatins into live cell monolayers was studied by confocal and two-photon fluorescence lifetime imaging microscopy and the uptake of *E*-combretastatins into spheroids was studied using light sheet fluorescence microscopy.

2. Materials & Methods

2.1 Synthesis and purification of combretastatins

2.1.1 General procedures for compound purification and determination

All combretastatins described were synthesised in the chemistry laboratories at the University of Salford. Compound analysis and structural determination were carried out by TLC (thin layer chromatography), ^1H - and ^{13}C -NMR (nuclear magnetic resonance spectroscopy), infrared spectroscopy, mass spectrometry and melting point measurements.

Solvents and Reagents

Anhydrous solvents for reactions were obtained as follows. Dry THF was obtained by distillation over sodium and benzophenone under argon as required. Dry toluene and acetonitrile were obtained by drying over activated 3 Å molecular sieves for 24 h. Any other solvents and reagents were used as provided by the supplier (Alfa Aesar).

Chromatography

Flash column chromatography was carried out on silica gel 60 Å pore size and a particle size of 40-63 µm from Fluorochem. Solvents were chosen according to TLC. TLCs were carried out on pre-coated aluminium backed silica plates (0.2 mm, 60 F254). The development of the products on the plates was visualised using UV254. R_fs were recorded to the nearest 0.01 decimal place. When mixed solvent systems were applied they are given in v/v (volumetric ratio).

^1H - and ^{13}C -NMR

^1H -NMR spectra were obtained using a Bruker AC-400 instrument in chloroform-d (unless stated otherwise). ^{13}C -NMR spectra were recorded at 100 MHz. Chemical shifts (δ) are given in parts per million (ppm) relative to tetramethylsilane (TMS). The coupling constants (J) are stated in Hertz (Hz) and reported to one decimal place. Spectra were analyzed using Bruker TopSpin software using data tables from the literature (Silverstein 1916-, 1998). Solvent peaks were determined from tables giving typical solvent shifts in NMR spectroscopy available in the literature (Gottlieb, Kotlyar & Nudelman, 1997).

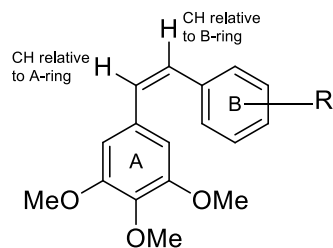


Figure 31 labelling of olefinic CH

Infra-Red

These spectra were obtained on a Bruker vector 22. Absorbance peaks of the compounds are reported as wave numbers (cm^{-1}).

Melting point

Melting points (MP) were recorded using a Gallenkamp melting point apparatus.

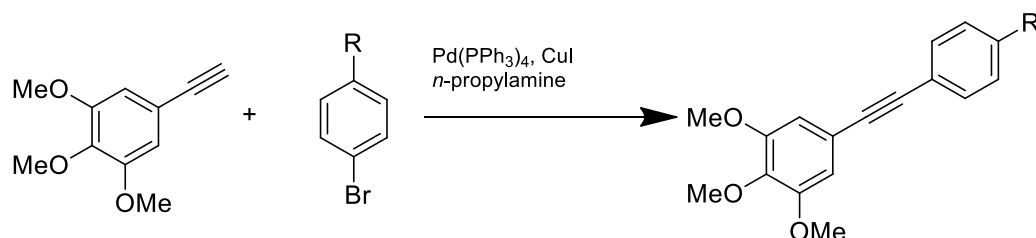
Mass Spectrometry

High resolution mass spectra were obtained from the EPSRC UK National Mass Spectrometry Facility (NMSF) at Swansea University.

2.1.2 Synthesis of combretastatins and related analogues

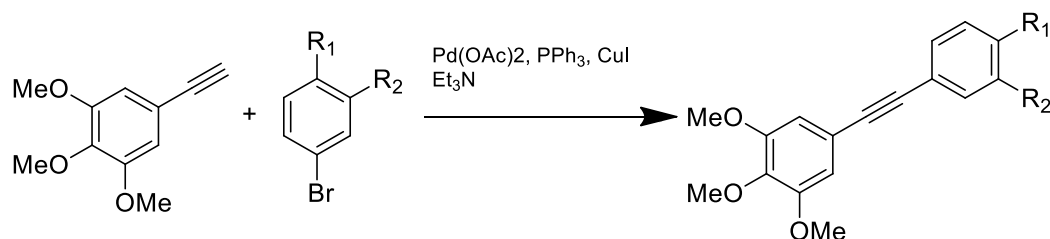
General procedures

Procedure A

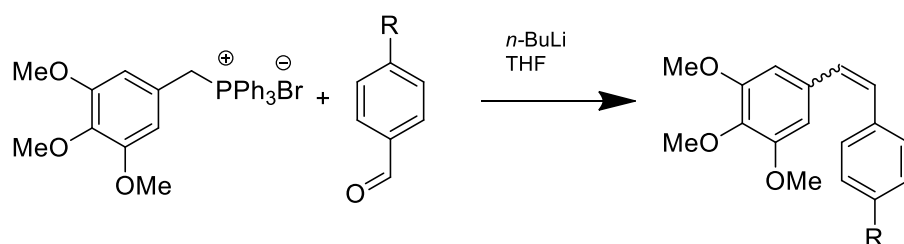


To a stirred solution of an aryl halide (0.52 mmol, 1 eq) in dry *n*-propylamine (30 mL) was added 3,4,5-trimethoxyphenylethyne (0.100 g, 0.52 mmol, 1 eq), tetrakis(triphenylphosphine)palladium (0) (0.120 g, 10.4 μmol, 2 mol %) and copper(I) iodide (0.005 g, 0.03 mmol, 6 mol %). The mixture was heated to reflux overnight, and upon completion filtered through a plug of celite and concentrated *in vacuo*. The residue was purified by flash column chromatography on silica gel and/or recrystallization (Hadfield & McGown, 1998).

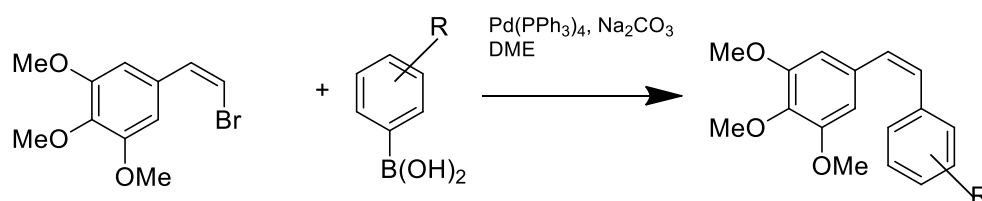
Procedure B



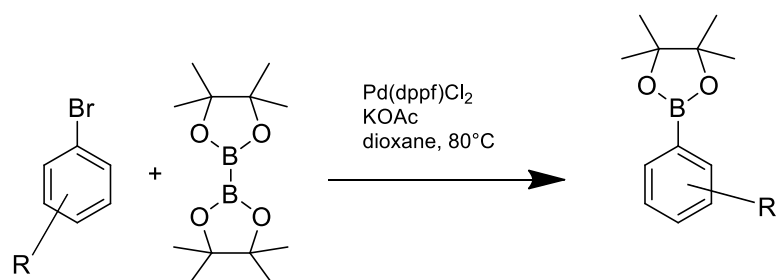
To a stirred solution of an aryl halide (0.46 mmol, 1 eq) in triethylamine (30 mL) was added palladium(II) acetate (0.006 g, 0.03 mmol, 7 mol %), copper(I) iodide (0.009 g, 0.05 mmol, 11 mol %) and triphenylphosphine (0.010 g, 0.04 mmol, 9 mol %). A stream of argon was bubbled through the mixture for 5 min and 3,4,5-trimethoxyphenylethyne (0.125 g, 0.65 mmol, 1.4 eq) was added. The reaction mixture was stirred at reflux overnight. On completion, the solution was filtered through a plug of celite and concentrated *in vacuo*. The residue was purified by flash column chromatography on silica gel and/or recrystallization.

Procedure C

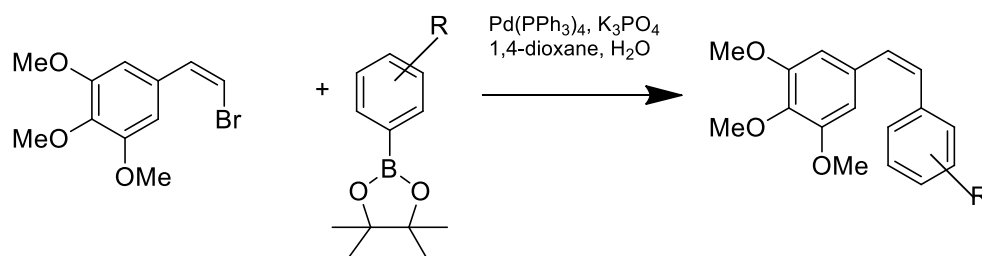
3,4,5-Trimethoxy-benzyltriphenylphosphonium bromide (0.784 g, 1.50 mmol, 1 eq) in dry THF (20 mL) was treated under argon with *n*-butyllithium (0.94 ml, 1.6 M, 1.50 mmol, 1 eq) at $-15\text{ }^\circ\text{C}$ for 20 min. Appropriately substituted aldehyde (1.50 mmol, 1 eq) was added and the reaction was allowed to reach room temperature whilst stirring. Upon completion, saturated NH_4Cl (20 mL) then H_2O (20 mL) was added and the product extracted into ethyl acetate (20 mL). The organic layer was washed with brine, water and dried (MgSO_4) and concentrated *in vacuo* and purified by flash column chromatography on silica gel and/or recrystallization (Pettit *et al.*, 1995a).

Procedure D

5-[(Z)-2-Bromovinyl]-1,2,3-trimethoxybenzene (0.187 g, 0.68 mmol, 1 eq) and *tetrakis* (triphenylphosphine) palladium(0) (0.119 g, 0.10 mmol, 15 mol %) were stirred in 1,2-dimethoxyethane (50 mL) under argon for 20 min. Aryl boronic acid (1.5 eq) and aqueous sodium carbonate (2 M, 3 eq) were added and the mixture heated at reflux for 20 h. The reaction mixture was allowed to cool to room temperature and passed through a plug of celite. The DME was removed *in vacuo* and DCM (20 mL) was added. The organic layer was washed with brine then water, dried (MgSO_4), and concentrated *in vacuo*. The residue was purified by flash column chromatography on silica gel and/or recrystallization (Strachan *et al.*, 1998).

Procedure E

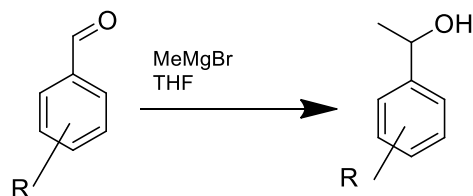
Into a thick-walled screw top flask containing a solution of appropriately substituted aryl halide (2.49 mmol, 1 eq) in dry 1,4-dioxane (10 mL) were added *bis*(pinacolato)diboron (0.632 g, 2.49 mmol, 1 eq) [1,1'-*Bis*(diphenylphosphino)ferrocene]palladium(II) dichloride (0.054 g, 0.07 mmol, 0.03 eq) and potassium acetate (0.732 g, 7.47 mmol, 3 eq). The flask was cooled to 0 °C under argon for 30 min. The reaction mixture was gradually warmed to room temperature, and stirred at 80 °C for 16 h. After cooling to room temperature, the solvent was evaporated to dryness under reduced pressure. The residue was dissolved in *n*-hexane (20 mL), and the solution was washed with H₂O (20 mL), brine (20 mL) and dried (MgSO₄), further purification was by recrystallization if stated (Mamiya *et al.*, 2015b).

Procedure F

Into a thick-walled screw top flask containing a solution of aryl boronic ester (2.00 mmol, 1.5 eq) and 5-[(*Z*)-2-bromovinyl]-1,2,3-trimethoxybenzene (0.366 g, 1.33 mmol) in dry 1,4-dioxane (5 mL) were added Pd(PPh₃)₄ (0.077 g, 5 mol %) and K₃PO₄ (0.848 g, 4.00 mmol, 3 eq). The flask was cooled to 0 °C and subjected to three evacuation/argon fill cycles. The reaction mixture was gradually warmed to room temperature, and stirred at 80 °C for 8 h. After cooling to room temperature, the solvent was evaporated to dryness under reduced pressure, the residue dissolved in CHCl₃ (10 mL) and washed with brine (10 mL) then water (10 mL), dried (MgSO₄), and concentrated *in vacuo*. The residue was purified by flash

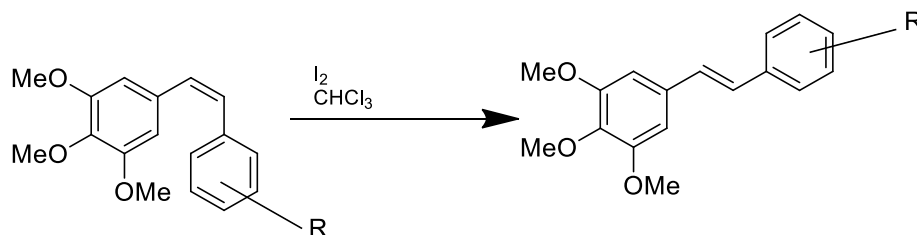
column chromatography on silica gel and/or recrystallization (adapted from Mamiya *et al.*, 2015a).

Procedure G



Aldehyde (0.34 mmol, 1 eq.) in dry THF (10 mL) was treated under argon with methylmagnesium bromide (0.22 ml, 3 M in THF, 2 eq.) at 0 °C for 1 hour. Upon completion the mixture was allowed to reach room temperature and was treated with aqueous ammonium chloride (5 mL). The product was extracted into ethyl acetate (10 mL), washed with water (10 mL) and brine (10 mL), dried (MgSO₄) and concentrated *in vacuo*. The residue was purified by flash column chromatography on silica gel and/or recrystallization.

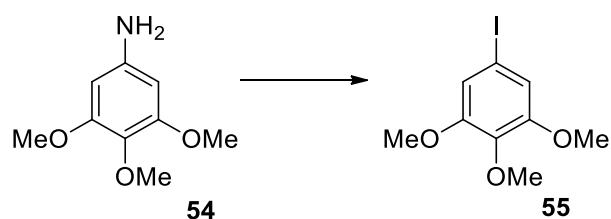
Procedure H



To a solution Z-stilbene (0.32 mmol) in chloroform (10 mL) was added iodine (0.008 g, 0.03 mmol, 10 mol %). The resulting solution was stirred at room for 2 h, after which the solution was washed thoroughly with saturated thiosulphate (10 mL) then water (10 mL), dried (MgSO₄) and concentrated *in vacuo* to afford the E-stilbene. The residue was purified by flash column chromatography on silica gel and/or recrystallization (Gaukroger *et al.*, 2001a).

Synthesis of diarylalkynes using Sonogashira cross coupling

5-Iodo-1,2,3-trimethoxybenzene (Cardolaccia, Li & Schanze, 2008)

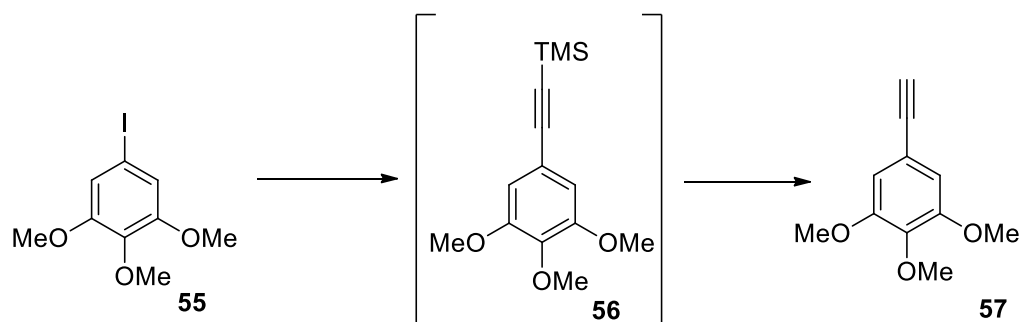


To a mixture of water (60 mL) and sulfuric acid (4 mL) was added 3,4,5-trimethoxyaniline (5.00 g, 27.30 mmol, 1eq.) and cooled to 0 °C. To this mixture was added a solution of sodium nitrite (18.85 g, 282.00 mmol, 10.3 eq.) in water (30 mL) drop-wise with stirring. The resulting diazonium salt was poured onto a 15 mL aqueous solution of potassium iodide (7.00 g, 42.20 mmol, 1.5 eq.) at 50 °C and stirred for 30 min. The solution was cooled to room temperature and an aqueous saturated solution of sodium sulfite was added to neutralize excess iodine until no further colour change was observed. The resulting aqueous solution was extracted with ether (3 x 50 mL), the organic phase was dried (MgSO₄) and concentrated *in vacuo* to give desired product (55) as a yellow-orange solid (6.63 g, 22.60 mmol, 83 %).

MP: 85-87 °C (lit. 86 °C) **Rf:** 0.46 (SiO₂ PE/EtOAc 3:1);

¹H δ ppm: 3.84 (3 H, s, OCH₃), 3.86 (6 H, s, 2 x OCH₃), 6.91 (2 H, s, Ar H).

3,4,5-Trimethoxyacetylene



To a solution of 5-iodo-1,2,3-trimethoxybenzene (5.00 g, 17.00 mmol, 1 eq.) in dry THF (30 mL), PdCl₂(PPh₃)₂ (119.30 mg, 0.17 mmol, 0.01 eq.), CuI (32.40 mg, 0.17 mmol, 0.01 eq.) and dry HN*i*Pr₂ (7.2 mL, 51.00 mmol, 3 eq.) were added. The reaction flask was packed in aluminium foil and ice-chilled trimethylsilylacetylene (2.6 mL, 18.70 mmol, 1.05 eq.) was

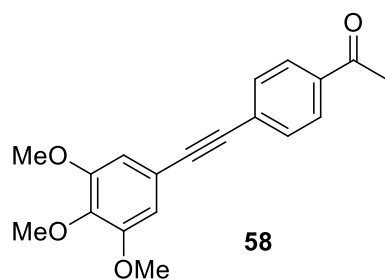
added by syringe. After stirring for 1 h at room temperature the reaction mixture was quenched by the addition of 5%-aqueous disodium EDTA solution (40 mL) and ether (40 mL). The aqueous phase was extracted with ether (2 x 40 mL), filtered through a plug of celite and the combined organic layers washed with brine (40 mL), dried (MgSO_4) and concentrated *in vacuo* to give the crude trimethyl((3,4,5-trimethoxyphenyl)ethynyl)silane (4.05 g, 90 %).

A solution of this silane (4.05 g, 0.02 mmol, 1 eq.) in MeOH (50 ml) was treated with K_2CO_3 (7.62 g, 0.06 mmol, 3 eq.) and the reaction mixture stirred for 3 h at room temperature. Water (40 mL) was added and the reaction was stirred for a further 10 min. After dilution of the mixture with ether (40 mL) the aqueous phase was separated and extracted with ether (3 x 40 mL). The combined organic layers were washed with brine (40 mL), dried (MgSO_4) and concentrated *in vacuo*. Flash column chromatography (PE/EtOAc, 10:1) yielded the desired product 57 as a pale yellow solid (1.8g, 9.4 mmol, 56 %).

MP: 68-70 °C (lit. 68-70 °C); **Rf:** 0.52 (SiO_2 PE/EtOAc 3:1);

^1H δ ppm: 2.95 (1H, s, CCH), 3.73 (3H, s, OCH_3) 3.75 (6H, s, 2 x OCH_3), 6.64 (2 H, s, Ar H).

1-(4''-Acetylphenyl)-2-(3',4',5'-trimethoxyphenyl)ethyne (Hadfield & McGown, 1998)

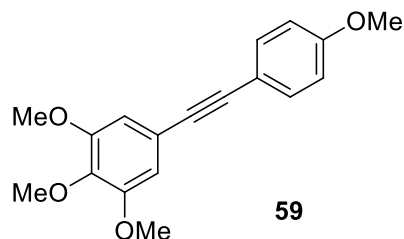


The above titled compound was prepared from 4-bromoacetophenone (0.102g, 0.52 mmol, 1 eq) and 3,4,5-trimethoxyphenylacetylene (0.100 g, 0.52 mmol, 1 eq) as in **procedure A**. Following flash column chromatography (SiO_2 , PE:EtOAc 10:1) and recrystallization from methanol, the above titled compound (58) was obtained as yellow needles (0.089 g, 0.29 mmol, 62 %).

MP: 125-128 °C (lit. 127 °C (Hadfield & McGown, 1998)); **Rf:** 0.76 (SiO_2 PE:EtOAc 3:1);

^1H δ ppm: 2.63 (3 H, s, CH₃), 3.90 (3 H, s, OCH₃) 3.91 (6 H, s, 2 x OCH₃), 6.81 (2 H, s, Ar *ortho* to OMe), 7.62 (2 H, d, $J = 8.2$, *meta* to COCH₃), 7.96 (2 H, d, $J = 8.4$, *ortho* to COCH₃).

1-(4''- Methoxyphenyl)-2-(3',4',5'-trimethoxyphenyl)ethyne (Hadfield & McGown, 1998)

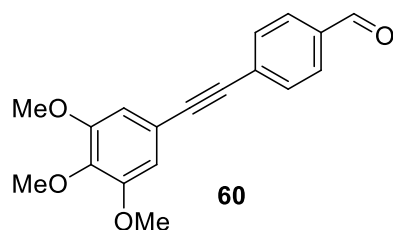


The above titled compound was prepared from 4-bromoanisole (0.122 g, 0.52 mmol) and 3,4,5-trimethoxyphenylacetylene (0.100 g, 0.52 mmol) as in **procedure A**. Following flash column chromatography (SiO₂, PE:EtOAc 10:1) and recrystallization from methanol, diarylalkyne 59 was isolated as white crystals (0.262 g, 0.88 mmol, 85 %).

MP: 118-121 °C (lit. 118-120°C); **Rf:** 0.64 (SiO₂ PE:EtOAc 3:1);

^1H δ ppm: 3.64 (3 H, s, 4'-OCH₃), 3.68 (3 H, s, OCH₃) 3.69 (6 H, s, 2 x OCH₃), 6.56 (2 H, s, *ortho* to -OCH₃), 6.69 (2 H, d, $J = 8.7$, *ortho* to 4''-OCH₃), 7.27 (2 H, d, $J = 8.7$, *meta* to 4''-OCH₃).

1-(4''- Formylphenyl)-2-(3',4',5'-trimethoxyphenyl)ethyne



The above titled compound was prepared from 4-bromobenzaldehyde (0.096 g, 0.52 mmol) and 3,4,5-trimethoxyphenylacetylene (0.100 g, 0.52 mmol) as in **procedure A**. Following flash column chromatography (SiO₂, PE:EtOAc 10:1) and recrystallization from methanol, diarylalkyne 60 was isolated as white crystals (0.096 g, 0.32 mmol, 71 %).

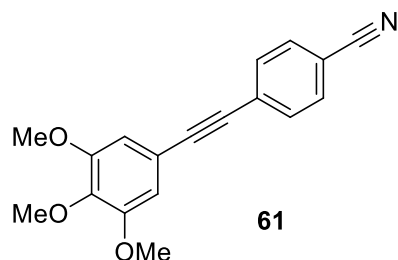
MP: 119-123 °C; **Rf:** 0.68 (SiO₂ PE:EtOAc 3:1);

^1H δ ppm: 3.81 (3 H, s, OCH₃) 3.82 (6 H, s, 2 x OCH₃), 6.72 (2 H, s, *ortho* to -OCH₃), 7.59 (2 H, d, $J = 8.1$, *meta* to CHO), 7.79 (2 H, d, $J = 8.1$, *ortho* to CHO), 9.95 (1 H, s, CHO);

^{13}C δ ppm: 56.2 (2 C, OCH₃), 61.0 (OCH₃), 87.7 (C) 93.6 (C), 109.0 (2 C, Ar C), 117.4 (Ar C), 129.5 (Ar C), 129.6 (2 C, Ar C), 132.0 (2 C, Ar C), 135.4 (Ar C), 139.4 (Ar C), 153.2 (2 C, Ar C), 191.4 (CHO);

V_{\max} cm^{-1} : 2929 (sp² C-H), 2850 (C-H aldehyde) 2208 (C≡C), 1741 (C=O aldehyde), 1574 – 1410 (sp² C-C), 1124 (C-O methoxy).

1-(4''-Cyanophenyl)-2-(3',4',5'-trimethoxyphenyl)ethyne



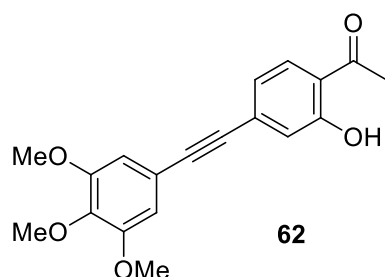
The above titled compound was prepared from 4-bromobenzonitrile (0.095 g, 0.52 mmol) and 3,4,5-trimethoxyphenylacetylene (0.100 g, 0.52 mmol) as in **procedure A**. Following flash column chromatography (SiO₂, PE:EtOAc 10:1) and recrystallization from methanol, the diarylalkyne **61** was isolated as white needles (0.097 g, 0.33 mmol, 64 %).

MP: 124-126 °C; **Rf:** 0.68 (SiO₂ PE:EtOAc 3:1);

^1H δ ppm: 3.90 (3 H, s, OCH₃) 3.91 (6 H, s, 2 x OCH₃), 6.80 (2 H, s, *ortho* to -OCH₃), 7.62 (2 H, d, $J = 8.2$, *meta* to CN), 7.66 (2 H, d, $J = 8.4$, *ortho* to CN);

^{13}C δ ppm: 56.2 (2 C, OCH₃), 60.4 (OCH₃), 86.7 (C), 93.9 (C), 109.0 (2 C, Ar C), 111.5 (2 C, Ar C), 117.5 (Ar C), 118.5 (CN), 128.2 (2 C, Ar C), 132.0 (Ar C) 132.1 (2 C, Ar C) 153.2 (Ar C);

V_{\max} cm^{-1} : 3008 (sp² C-H), 2227 (C≡C), 2212 (C≡N), 1575 – 1406 (sp² C-C), 1118 (C-O methoxy).

1-(4''-Acetyl-3''-hydroxyphenyl)-2-(3',4',5'-trimethoxyphenyl)ethyne

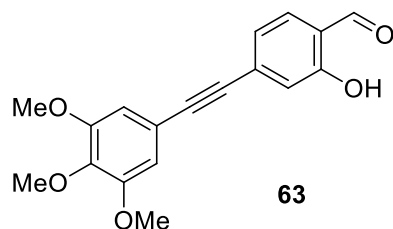
The above titled compound (62) was prepared from 4-bromo-2-hydroxyacetophenone (0.100 g, 0.46 mmol) and 3,4,5-trimethoxyphenylacetylene (0.125 g, 0.65 mmol,) as in **procedure B**. Following flash column chromatography (SiO₂, PE:EtOAc 6:1) and recrystallization from methanol, the diarylalkyne was isolated as pale yellow crystals (0.227g, 0.70 mmol, 76 %).

MP: 126-128 °C; **Rf:** 0.75 (SiO₂ PE:EtOAc 3:1);

¹H δ ppm: 2.52 (3 H, s, CH₃), 3.77 (3 H, s, OCH₃) 3.78 (6 H, s, 2 x OCH₃), 6.72 (2 H, s, *ortho* to -OCH₃), 6.92 (1 H, dd, *J* = 8.1, 1.5, *para* to OH), 7.01 (1 H, d, *J* = 1.5, *ortho* to OH), 7.59 (1 H, d, *J* = 8.1, *meta* to OH), 12.2 (1 H, s, OH);

¹³C δ ppm: 26.7 (CH₃), 56.2 (2 C, OCH₃), 61.0 (OCH₃), 87.6 (C), 93.3 (C), 109.1 (2 C, Ar C), 117.4 (Ar C), 119.2 (Ar C), 121.0 (Ar C), 122.0 (Ar C), 130.6 (Ar C), 131.2 (Ar C), 139.5 (Ar C), 153.2 (2 C, Ar C), 162.1 (Ar C), 203.9 (carbonyl C);

***V*_{max} cm⁻¹:** 3353 (O-H phenol) 2954 (sp² C-H), 2211 (C≡C), 1601 (C=O ketone), 1572 – 1410 (sp² C-C), 1236 (C-O phenol), 1124 (C-O methoxy).

1-(4''-Formyl-3''-hydroxyphenyl)-2-(3',4',5'-trimethoxyphenyl)ethyne

The above titled compound (63) was prepared from 4-bromo-2-hydroxybenzaldehyde (0.092 g, 0.46 mmol) and 3,4,5-trimethoxyphenylacetylene (0.125 g, 0.65 mmol,) as in **procedure B**. Following flash column chromatography (SiO₂, PE:EtOAc 6:1) and

recrystallization from methanol, the diarylalkyne was isolated as a pale yellow solid (0.102 g, 0.33 mmol, 71 %).

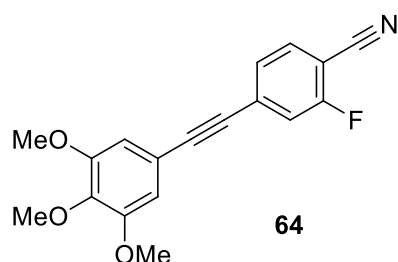
MP: 120-123 °C; **Rf:** 0.54 (SiO₂ PE:EtOAc 3:1);

¹H δ ppm: 3.81 (3 H, s, OCH₃), 3.82 (6 H, s, 2 x OCH₃), 6.72 (2 H, s, *ortho* to -OCH₃), 7.01 (1 H, dd, *J* = 8.0, 2.4, *para* to OH), 7.13 (1 H, d, *J*=2.4, *ortho* to OH) 7.46 (1 H, d, *J* = 8.0, *meta* to OH), 9.81 (1 H, s, CHO), 10.99 (1 H, s, OH);

¹³C δ ppm: 56.2 (2 C, OCH₃), 61.0 (OCH₃), 87.5 (C), 94.1 (C), 109.1 (2 C, Ar C), 117.2 (Ar C), 120.0 (Ar C), 120.2 (Ar C), 122.9 (Ar C), 128.2 (Ar C), 131.9 (Ar C), 139.6 (Ar C), 153.2 (2 C, Ar C), 161.4 (Ar C), 195.8 (CHO);

***V*_{max} cm⁻¹:** 3301 (O-H phenol), 2954 (C-H sp²), 2211 (C≡C), 1723 (C=O aldehyde), 1573 – 1411 (C-C sp²), 1124 (C-O methoxy), 1214 (C-O phenol).

1-(4''-Cyano-3''-fluorophenyl)-2-(3',4',5'-trimethoxyphenyl)ethyne



The above titled compound was prepared from 4-bromo-2-fluorobenzonitrile (0.092 g, 0.46 mmol) and 3,4,5-trimethoxyphenylacetylene (0.125 g, 0.65 mmol,) as in **procedure B**. Following flash column chromatography (SiO₂, PE:EtOAc 6:1) and recrystallization from methanol, the diarylalkyne 64 was isolated as a pale orange solid (0.086 g, 0.28mmol, 60 %).

MP:103-107 °C; **Rf:** 0.84 (SiO₂ PE:EtOAc 3:1);

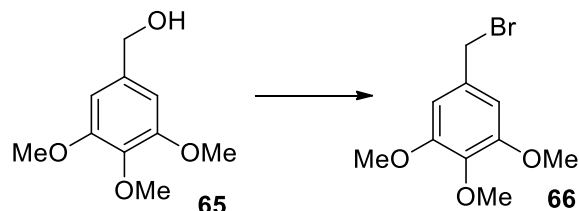
¹H δ ppm: 3.81 (9 H, s, OCH₃) 6.70 (2 H, s, *ortho* to OCH₃), 7.00 (1 H, dd, *J* = 7.8, 1.1, *para* to F), 7.04 (1 H, d, *J* = 1.1, *ortho* to F), 7.43 (1 H, d, *J* = 7.8, *meta* to F);

¹³C δ ppm: 56.2 (2 C, OCH₃), 61.0 (OCH₃), 91.5 (C), 94.5 (C), 109.0 (2 C, Ar C), 113.2 (Ar C), 116.9 (Ar C), 119.4 (Ar C), 121.2 (CN), 128.4 (Ar C), 128.8 (Ar C), 132.6 (Ar C), 139.4 (Ar C), 150.0 (2 C, Ar C), 153.2 (Ar C);

V_{max} cm^{-1} : 2953 (C-H sp^2), 2210 (C≡C), 2207 (C≡N), 1570 – 1412 (C-C sp^2), 1125 (C-O methoxy), 1080 (C-F).

Synthesis of E- and Z- combretastatins using Wittig chemistry

3,4,5-Trimethoxybenzyl bromide (Gaukroger, 2001)

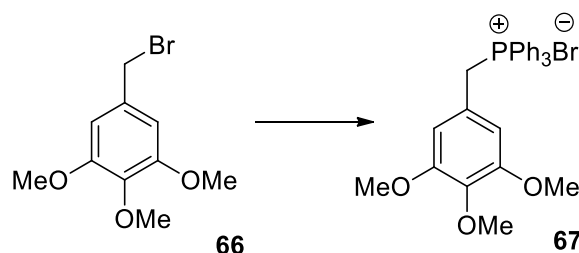


PBr₃ (0.7 ml, 7.0 mmol, 0.6 eq.) was added to a solution of 3,4,5-trimethoxybenzyl alcohol **65** (2.16 g, 11.0 mmol, 1 eq.) in dichloromethane (10 mL) at 0 °C in two equivalents 1 hour apart. Upon completion (approximately 1 h after second addition) H₂O (5 mL) was added followed by saturated aqueous NaHCO₃ (5 mL). The organic layer was washed in H₂O (2 x 10 mL), dried (MgSO₄) and solvent removed *in vacuo* yielding 3,4,5-trimethoxybenzyl bromide **66** as a white solid (2.23 g, 8.54 mmol, 78 %).

MP: 71 – 72 °C (lit. 71 – 72 °C (Gaukroger, 2001)); **Rf**: 0.56 (SiO₂ petrol:EtOAc 3:1);

¹H δ ppm: 3.86 (3 H, s, OCH₃), 3.88 (6 H, s, 2 x OCH₃), 4.48 (2 H, s, CH₂), 6.63 (2 H, s, *ortho* to OCH₃).

3,4,5-Trimethoxy-benzyltriphenylphosphonium bromide (Pettit et al., 1987)

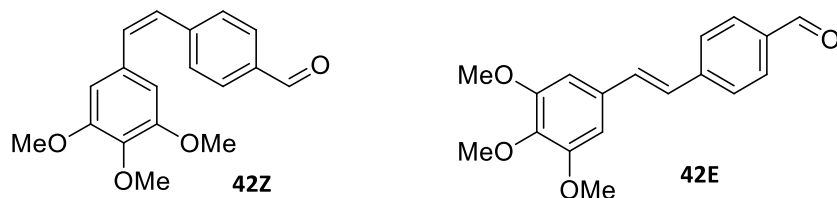


A solution of triphenylphosphine (2.79 g, 10.65 mmol, 1.2 eq) in toluene (5 mL) was added to a stirred solution of 3,4,5-trimethoxybenzyl bromide **66** (2.23g, 9.00 mmol, 1 eq.) in toluene (5 mL). Stirring was continued for 24 h after which time the phosphonium salt **67** precipitated out and was collected by vacuum filtration (4.32 g, 8.25 mmol, 88 %).

MP: 223-226 °C (lit 223-224 °C), **Rf**: 0.52;

^1H δ ppm: 3.70 (3 H, s, OCH₃), 3.72 (6 H, s, 2 x OCH₃), 5.28 (2 H, s, CH₂), 6.41 (2 H, s, *ortho* to OCH₃), 7.52 - 7.72 (15 H, m, 3 x Ph).

(E/Z)-4-(3',4',5'-Trimethoxystyryl)benzaldehyde



Stilbenes were prepared from 3,4,5-trimethoxy-benzyltriphenylphosphonium bromide **67** (0.784 g, 1.50 mmol, 1 eq) and 4-(diethoxymethyl)benzaldehyde (0.312 g, 1.50 mmol) as in **procedure C**. To the crude mixture was added dilute HCl (1 M, 10 mL) and the reaction mixture stirred for 30 mins in order to remove the protecting group to afford the aldehyde. Following flash column chromatography (SiO₂, Petrol:EtOAc 100:1) *cis* alkene **42Z** was isolated as a bright yellow solid (0.183 g, 0.61 mmol, 41%).

Mp: 98-100 °C; **Rf**: 0.45 (SiO₂ petrol:EtOAc 3:1);

^1H δ ppm: 3.57 (3 H, s, OCH₃), 3.76 (6 H, s, 2 x OCH₃), 6.37 (2 H, s, *ortho* to OCH₃), 6.51 (1 H, d, $J = 12.3$, CH relative to A-ring), 6.58 (1 H, d, $J = 12.3$, CH relative to B-ring), 7.37 (2 H, d, $J = 8.2$, *meta* to CHO), 7.69 (2 H, d, $J = 8.2$, *ortho* to CHO), 9.08 (1 H, s, CHO);

^{13}C δ ppm: 55.9 (OCH₃), 60.9 (OCH₃), 106.1 (2 C, Ar C), 125.5 (2 C, Ar C), 128.6 (olefinic C), 129.6 (olefinic C), 130.1 (2 C, Ar C), 131.8 (Ar C), 135.0 (Ar C), 137.7 (Ar C), 140.0 (Ar C), 153.0 (2 C, Ar C), 191.5 (CHO);

ν_{max} cm^{-1} : 3000 (C-H sp²), 2970 (C-H ald), 2940 (C-H ar), 1687 (C=O), 1600 (C=C ar), 1564-1413 (C-C sp²), 1163 (OMe), 795 (*p*-sub), 736 (*cis*-alkene).

m/z: [M+H] calcd for C₁₈H₁₉O₄ 299.1278, found 299.1278.

Further elution afforded *trans* stilbene **42E** as a bright yellow solid (0.192 g, 0.64 mmol, 43%). **Mp**: 162 °C; **Rf**: 0.42 (SiO₂ petrol:EtOAc 3:1);

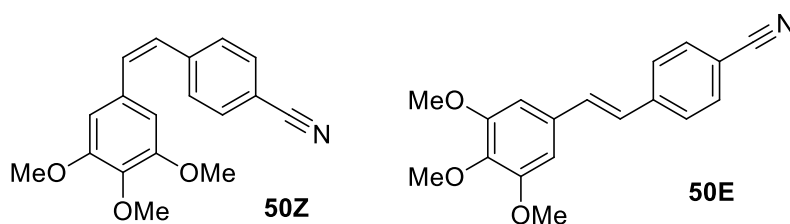
^1H δ ppm: 3.88 (3 H, s, OCH₃), 3.98 (6 H, s, 2 x OCH₃), 6.75 (2 H, s, *ortho* to OCH₃), 7.03 (1 H, d, $J = 16.2$, CH relative to A-ring), 7.18 (1 H, d, $J = 16.2$, CH relative to B-ring), 7.63 (2 H, d, $J = 8.1$, *meta* to CHO), 7.86 (2 H, d, $J = 8.1$, *ortho* to CHO), 9.97 (1 H, s, CHO);

^{13}C δ ppm: 56.0 (2 C, OCH₃), 61.0 (OCH₃), 104.3 (2 C, Ar C), 126.8 (2 C, Ar C), 129.6 (olefinic C), 130.2 (olefinic C), 132.1 (2 C, Ar C), 132.3 (Ar C), 135.2 (Ar C) 138.7 (Ar C), 143.4 (Ar C), 153.5 (2 C, Ar C), 191.6 (CHO);

V_{\max} cm^{-1} : 2967 (C-H sp²), 2822 (C-H ar), 2724 (C-H ald), 1689 (C=O), 1597 (C=C alkene), 1565-1419 (C-C sp²), 1164 (OMe), 976 (*trans*-alkene), 781 (*p*-sub).

m/z : [M+H] calcd for C₁₈H₁₉O₄ 299.1278, found 299.1278.

(*E/Z*)-4-(3',4',5'-trimethoxystyryl)benzonitrile



Stilbenes were prepared from 3,4,5-trimethoxy-benzyltriphenylphosphonium bromide **67** (0.784 g, 1.50 mmol, 1 eq) and 4-cyanobenzaldehyde (0.196 g, 1.50 mmol) as in **procedure C**. Following flash column chromatography (SiO₂, Petrol:EtOAc 100:1) *cis* alkene **50Z** was isolated as a light brown solid (0.172 g, 0.58 mmol, 39%).

Mp: 91 °C (lit.90-92 °C (Scherer, 2012)); **Rf**: 0.43 (SiO₂ petrol:EtOAc 3:1);

^1H δ ppm: 3.60 (6 H, s, 2 x OCH₃), 3.78 (3 H, s, OCH₃), 6.33 (2 H, s, *ortho* to OCH₃), 6.47 (1 H, d, J = 12.2, CH relative to A-ring), 6.60 (1 H, d, J = 12.2, CH relative to B-ring), 7.31 (2 H, d, J = 8.4, *meta* to CN) 7.47 (2 H, d, J = 8.4, *ortho* to CN);

^{13}C δ ppm: 56.0 (2 C, OCH₃), 61.0 (OCH₃), 104.1 (2 C, Ar C), 110.5 (Ar C), 118.9 (CN) 126.28 (2 C, Ar C), 132.0 (olefinic C), 132.4 (olefinic C), 132.5 (2 C, Ar C), 133.5 (Ar C), 138.8 (Ar C), 141.8.4 (Ar C), 153.5 (2 C, Ar C);

V_{\max} cm^{-1} : 2930 (C-H sp²), 2240 (C≡N), 1560-1410 (C-C sp²), 1170 (OMe), 781 (*p*-sub), 644 (*cis*-alkene).

Further elution afforded *trans* stilbene **50E** as a golden yellow solid (0.185 g, 0.63 mmol, 42%). **Mp**: 153-156 °C (lit. 159 – 162 °C (Osterod *et al.*, 2001)); **Rf**: 0.39 (SiO₂ petrol:EtOAc 3:1);

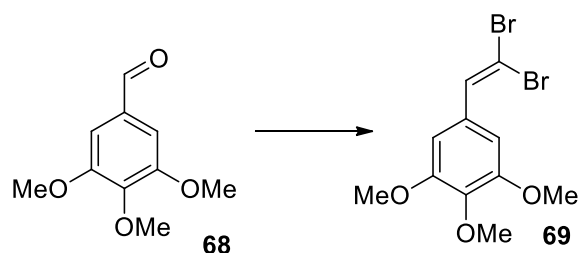
^1H δ ppm: 3.91 (6 H, s, 2 x OCH₃), 3.95 (3 H, s, OCH₃), 6.78 (2 H, s, *ortho* to OCH₃), 7.01 (1 H, d, $J = 16.2$, CH relative to A-ring), 7.17 (1 H, d, $J = 16.2$, CH relative to B-ring), 7.59 (2 H, d, $J = 8.1$, *meta* to CN), 7.66 (2 H, d, $J = 8.1$, *ortho* to CN);

^{13}C δ ppm: 56.2 (2 C, OCH₃), 61.0 (OCH₃), 104.1 (2 C, Ar C), 110.5 (Ar C), 119.0 (Ar C) 126.8 (2 C, Ar C), 131.5 (olefinic C), 132.9 (olefinic C), 132.6 (2 C, Ar C), 133.1 (Ar C), 137.9 (Ar C), 142.3 (Ar C), 153.5 (2 C, Ar C);

V_{max} cm^{-1} : 2936 (C-H sp^2), 2221 (C \equiv N), 1581-1420 (C-C sp^2), 1174 (OMe), 968 (*trans*-alkene), 825 (*p*-sub).

Synthesis of Z-combretastatins using Suzuki cross coupling with boronic acids

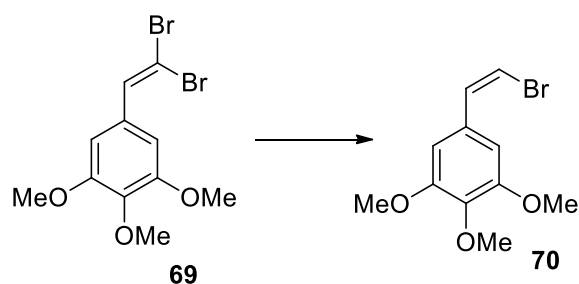
5-(2,2-Dibromovinyl)-1,2,3-trimethoxybenzene (Gaukroger et al., 2003)



To a well stirred solution of CBr_4 (6.34 g, 19.05 mmol, 1.5 eq.) in DCM (30 mL) at 0 °C were added triphenylphosphine (10.02 g, 38.1 mmol, 3 eq.) and 3,4,5-trimethoxybenzaldehyde **68** (2.5 g, 12.7 mmol, 1 eq.). Stirring was continued at 0 °C for 20 min and water (10 mL) was added. The aqueous layer was separated and extracted with chloroform (20 mL). Combined organic layers washed with water (20 mL) and brine (20 mL), dried (MgSO_4) and concentrated *in vacuo*. Flash chromatography (silica gel, Petrol: Ethyl acetate 1:1) gave the title compound **69** as a pale yellow solid (3.70 g, 10.5 mmol, 83 %).

MP: 93-95 °C (lit 95°C); **Rf:** 0.46 (SiO_2 petrol:EtOAc 3:1);

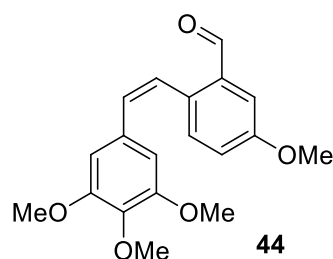
^1H δ ppm: 3.79 (3 H, s, OCH₃), 3.80 (6 H, s, 2 x OCH₃), 6.72 (2 H, s, Ar H), 7.33 (1 H, s, alkene).

5-[(Z)-2-Bromovinyl]-1,2,3-trimethoxybenzene (Gaukroger et al. 2003)

To a stirred solution of 5-(2,2-dibromovinyl)-1,2,3-trimethoxybenzene **69** (3.50 g, 10.00 mmol, 1 eq.) in dry toluene (20 mL) was added *tetrakis*(triphenylphosphonium)Pd(0) (0.46 g, 0.03 mmol, 0.04 eq.), tri *n*-butyltin hydride (2.91 g, 10 mmol, 1 eq.) and pyridine (1-2 drops) with stirring under argon. The resulting mixture was stirred overnight and solvent removed *in vacuo*. Flash chromatography (silica gel, chloroform) followed by recrystallisation from 30 % ethanol afforded the title compound **70** as pale yellow crystals (1.98 g, 7.25 mmol, 73 %).

MP: 63-66 °C (lit. 65°C); **Rf:** 0.62 (SiO₂ petrol:EtOAc 3:1);

¹H δ ppm: 3.80 (3 H, s, OCH₃), 3.81 (6 H, s, 2xOCH₃), 6.73 (2 H, s, *ortho* to OCH₃), 6.89 (1 H, d, *J* = 8.2, alkene-bromine) 7.32 (1 H, d, *J* = 8.2, alkene-bromine).

(Z)-5-Methoxy-2-(3',4',5'-trimethoxystyryl)benzaldehyde

Z-Stilbene was prepared from 5-[(Z)-2-bromovinyl]-1,2,3-trimethoxybenzene **70** (0.187 g, 0.68 mmol, 1 eq) and (2-formyl-4-methoxyphenyl)boronic acid (0.185 g, 1.03 mmol) as in **general procedure E**. Following flash column chromatography (SiO₂, Petrol:EtOAc 10:1) *cis* alkene **44** was isolated as a pale yellow solid (0.177 g, 0.54 mmol, 79%).

Mp: 89 °C; **Rf** 0.45 (SiO₂ petrol:EtOAc 3:1);

¹H δ ppm: 3.60 (3 H, s, OCH₃) 3.82 (6 H, s, 2 x OCH₃), 3.88 (3 H, s, OCH₃), 6.31 (2 H, s, *ortho* to OCH₃), 6.72 (1 H, d, *J* = 12.20, CH relative to A-ring), 6.88 (1 H, d, *J* = 12.20, CH relative to

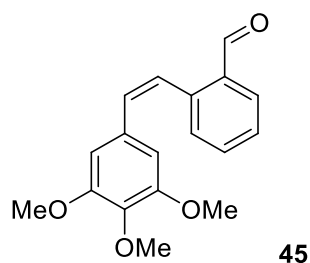
B-ring), 7.13 (dd, $J=2.87, 8.60$, 1 H, *para* to CHO) 7.28 (d, $J= 8.60$, 1 H, *meta* to CHO), 7.43 (d, $J= 2.87$, 1H, *ortho* to CHO), 10.25 (s, 1 H, CHO);

^{13}C δ ppm: 55.6 (OCH₃), 55.8 (2 C, OCH₃), 60.9 (OCH₃), 106.4 (2 C, Ar C), 110.9 (Ar C), 114.6 (Ar C), 121.7 (Ar C), 125.2 (olefinic C), 131.3 (olefinic C), 131.9 (Ar C), 133.3 (Ar C), 134.2 (Ar C), 134.4 (Ar C), 152.9 (Ar C), 159.1 (2 C, Ar C), 191.7 (CHO);

ν_{max} cm^{-1} : 2943 (C-H alkene), 2843 (C-H sp^2), 2746 (CHO), 1685 (C=O), 1574-1417 (C-C sp^2), 1166 (OCH₃), 829 (*p*-sub), 749 (*o*-sub), 704 (*cis*-alkene).

m/z : [M+H] calcd for C₁₉H₂₁O₅ 329.1384, found 329.1385.

(Z)-2-(3',4',5'-Trimethoxystyryl)benzaldehyde



Z-Stilbene was prepared from 5-[(Z)-2-bromovinyl]-1,2,3-trimethoxybenzene **70** (0.187 g, 0.68 mmol, 1 eq) and 2-formylphenylboronic acid (0.154 g, 1.03 mmol) as in **general procedure D**. Following flash column chromatography (SiO₂, Petrol:EtOAc 10:1) *cis* alkene **45Z** was isolated as a bright yellow solid (0.171 g, 0.58 mmol, 84%).

Mp: 91-93 °C; **Rf**: 0.41 (SiO₂ petrol:EtOAc 3:1);

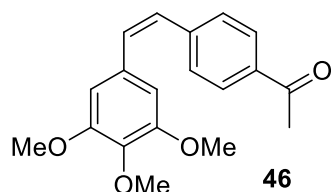
^1H δ ppm: 3.48 (3 H, s, OCH₃), 3.71 (6 H, s, 2 x OCH₃), 6.15 (2 H, s, *ortho* to OCH₃), 6.66 (1 H, d, $J = 12.5$, CH relative to A-ring), 6.86 (1 H, d, $J = 12.5$, CH relative to B-ring), 7.27 (1 H, d, $J = 7.5$, Ar H), 7.34 (1H, t, $J= 7.5$, Ar H), 7.47 (1H, m, Ar H), 7.85 (1 H, d, $J = 7.5$, Ar H);

^{13}C δ ppm: 56.2 (2 C, OCH₃), 60.9 (OCH₃), 104.1 (2 C, Ar C), 125.8 (olefinic C), 127.2 (Ar C), 127.7 (Ar C), 128.9 (olefinic C), 130.6 (Ar C), 131.1 (Ar C), 133.3 (Ar C) 134.0 (Ar C), 137.6 (Ar C), 141.5 (Ar C), 153.5 (2 C, Ar C), 192.0 (CHO);

ν_{max} cm^{-1} : 2960 (C-H sp^2), 1681 (C=O), 1580-1420 (C-C sp^2), 1127 (OMe), 730 (*o*-sub), 702 (*cis*-alkene).

m/z: [M+H] calcd for C₁₈H₁₉O₄ 299.1278, found 299.1278

(Z)-4-(3',4',5'-Trimethoxystyryl)acetophenone



Z-Stilbene was prepared from 5-[(Z)-2-bromovinyl]-1,2,3-trimethoxybenzene **70** (0.187 g, 0.68 mmol, 1 eq) and 4-acetylphenylboronic acid (0.169 g, 1.03 mmol) as in **general procedure D**. Following flash column chromatography (SiO₂, Petrol:EtOAc 10:1) *cis* alkene **46** was isolated as a light yellow solid (0.162 g, 0.52 mmol, 76%).

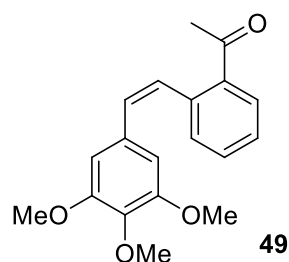
Mp: 79-81 °C; **Rf**: 0.52 (SiO₂ petrol:EtOAc 3:1);

¹H δ ppm: 2.51 (3 H, s, CH₃), 3.59 (6 H, s, 2 x OCH₃), 3.77 (3 H, s, OCH₃), 6.38 (2 H, s, *ortho* to OCH₃), 6.51 (1 H, d, *J* = 12.2, CH relative to A-ring), 6.57 (1 H, d, *J* = 12.2, CH relative to B-ring), 7.31 (2 H, d, *J* = 8.1, *meta* to COCH₃), 7.78 (2 H, d, *J* = 8.1, *ortho* to COCH₃);

¹³C δ ppm: 26.4 (CH₃), 55.9 (2 C, OCH₃), 61.0 (OCH₃), 106.1 (2 C, Ar C), 128.3 (2 C, Ar C), 128.4 (2 C, Ar C), 128.8 (olefinic C), 129.1 (olefinic C), 132.3 (Ar C), 137.4 (Ar C), 139.5 (Ar C), 143.5 (Ar C), 153.0 (2 C, Ar C), 193.5 (carbonyl C);

***V*_{max} cm⁻¹**: 2927 (C-H sp²), 1670 (C=O), 1577-1419 (C-C sp²), 1362 (CH₃), 1185 (OMe), 838 (*p*-sub), 758 (*cis*-alkene).

m/z: [M+H] calcd for C₁₉H₂₁O₄ 313.1431, found 313.1434.

(Z)-2-(3',4',5'-Trimethoxystyryl)acetophenone

Z-Stilbene was prepared from 5-[(Z)-2-Bromovinyl]-1,2,3-trimethoxybenzene **70** (0.187 g, 0.68 mmol, 1 eq) and 2-acetylphenylboronic acid (0.169 g, 1.03 mmol) as in **general procedure D**. Following flash column chromatography (SiO₂, Petrol:EtOAc 10:1) *cis* alkene **49Z** was isolated as a yellow solid (0.182 g, 0.58 mmol, 85%).

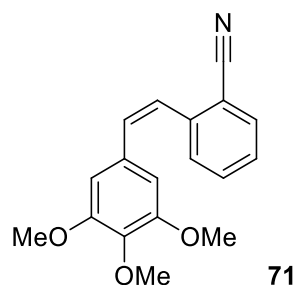
Mp: 74-77 °C; **Rf:** 0.54 (SiO₂ petrol:EtOAc 3:1);

¹H δ ppm: 2.56 (3 H, s, CH₃), 3.60 (6 H, s, 2 x OCH₃), 3.82 (3 H, s, OCH₃), 6.28 (2 H, s, *ortho* to OCH₃), 6.56 (1 H, d, *J* = 12.3, CH relative to A-ring), 6.92 (1 H, d, *J* = 12.3, CH relative to B-ring), 7.33 (2 H, d, *J* = 7.4, Ar H) 7.36 (t, *J* = 4.58, 1 H, Ar H), 7.79 (d, *J* = 7.4, 1 H, Ar H);

¹³C δ ppm: 29.5 (CH₃), 55.7 (2 C, OCH₃), 60.9 (OCH₃), 106.4 (olefinic C), 126.7 (Ar C), 127.7 (Ar C), 129.1 (olefinic C), 129.9 (olefinic C), 130.0 (Ar C), 131.2 (Ar C), 131.6 (Ar C), 132.0 (Ar C), 137.2 (Ar C), 138.0 (Ar C). 152.7 (olefinic C), 200.7 (carbonyl C);

***V*_{max} cm⁻¹:** 2956 (C-H sp²), 1682 (C=O), 1580-1417 (C-C sp²), 1354 (CH₃), 1180 (OMe), 755 (*o*-sub), 727 (*cis*-alkene).

***m/z*:** [M+H] calcd for C₁₉H₂₁O₄ 313.1431, found 313.1434

(Z)-2-(3',4',5'-Trimethoxystyryl)benzotrile

Z-Stilbene was prepared from 5-[(Z)-2-bromovinyl]-1,2,3-trimethoxybenzene **70** (0.187 g, 0.68 mmol, 1 eq) and 2-benzotrileboronic acid (0.151 g, 1.03 mmol) as in **general**

procedure D. Following flash column chromatography (SiO₂, Petrol:EtOAc 10:1) *cis* alkene **71Z** was isolated as a pale yellow solid (0.145 g, 0.49 mmol, 72%).

Mp: 85-89 °C; **Rf:** 0.43 (SiO₂ petrol:EtOAc 3:1);

¹H δ ppm: 3.57 (6 H, s, 2 x OCH₃), 3.76 (3 H, s, OCH₃), 6.28 (2 H, s, *ortho* to OCH₃), 6.67 (1 H, d, *J* = 12.3, CH relative to A-ring), 6.71 (1 H, d, *J* = 12.3, CH relative to B-ring), 7.25 (d, *J*=8.10, 1 H, Ar H) 7.35 (m, 2 H, Ar H), 7.60 (d, *J*=8.10, 1 H, Ar H);

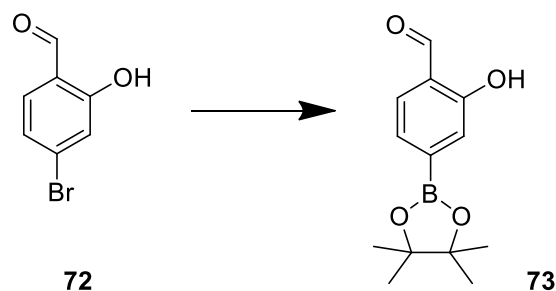
¹³C δ ppm: 55.8 (2 C, OCH₃), 60.9 (OCH₃), 106.2 (2 C, Ar C), 112.4 (Ar C), 117.8 (CN), 125.3 (olefinic C), 127.5 (Ar C), 130.0 (olefinic C), 131.2 (Ar C), 132.2 (Ar C), 132.8 (Ar C), 133.5 (Ar C), 134.2 (Ar C), 141.5 (Ar C), 141.5 (2 C, Ar C);

*V*_{max} cm⁻¹: 2930 (C-H sp²), 2240 (C≡N), 1560-1410 (C-C sp²), 1170 (OMe), 731 (*o*-sub), 644 (*cis*-alkene).

m/z: [M+Na] calcd for C₁₈H₁₇NO₃Na 318.12, found 318.00

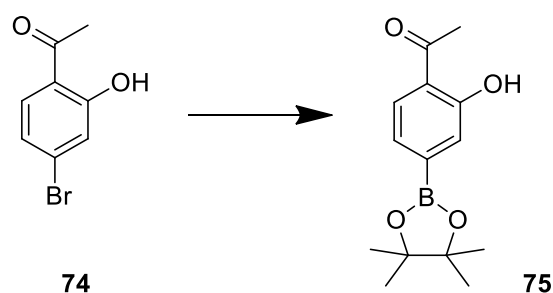
Boronic ester synthesis

2-Hydroxy-4-(4,4,5,5-tetramethyl-1,3,2-dioxaborolan-2-yl)benzaldehyde (Mamiya, Ousaka & Yashima, 2015a)



The above titled boronic ester was synthesised from *bis*(pinacolato)diboron (0.632 g, 2.49 mmol, 1 eq) and 4-bromosalicylaldehyde **72** (0.500 g, 2.49 mmol, 1 eq) as in **general procedure E**. Following recrystallization from hexane, boronic ester **73** was isolated as a white solid (0.482 g, 1.94 mmol, 78%).

¹H δ ppm: 1.28 (12 H, s, 4 x CH₃), 7.35 (2 H, m, Ar H), 7.48 (1 H, d, *J* = 8.16, *meta* to OH), 9.86 (1 H, s, CHO), 10.76 (1 H, s, OH);

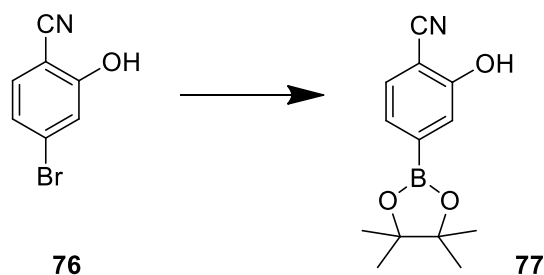
2-Hydroxy-4-(4,4,5,5-tetramethyl-1,3,2-dioxaborolan-2-yl)acetophenone

The above titled boronic ester was synthesised from *bis*(pinacolato)diboron (0.632 g, 2.49 mmol, 1 eq) and 1-(4-bromo-2-hydroxyphenyl)ethanone **74** (0.535 g, 2.49 mmol, 1 eq) as in **general procedure E**. Following recrystallization from hexane, boronic ester **75** was isolated as a white solid (0.451 g, 1.72 mmol, 69%).

$^1\text{H } \delta$ ppm: 1.28 (12 H, s, 4 x CH₃), 2.58 (3 H, s, CH₃), 7.22 (1 H, dd, $J = 7.87, 0.97$, *para* to OH), 7.35 (1 H, d, $J = 0.97$, *ortho* to OH), 7.64 (1 H, d, $J = 7.87$, *meta* to OH), 11.99 (1 H, s, OH);

$^{13}\text{C } \delta$ ppm: 24.9 (4 C, CH₃), 26.9 (1 C, CH₃), 84.3 (2 C, C-O), 114.5 (1 C, C-COCH₃), 119.9 (1 C, Ar C), 124.6 (1 C, Ar C), 124.8 (1 C, C-B), 129.6 (1 C, Ar C), 158.8 (1 C, C-OH), 201.2 (1 C, C=O);

ν_{max} cm⁻¹: 2967 (CH₃), 1640 (C=O), 1500-1410 (C-C sp²), 886 (1,2,4-trisubstituted ring), 820 (*p*-sub), 734 (*o*-sub).

2-Hydroxy-4-(4,4,5,5-tetramethyl-1,3,2-dioxaborolan-2-yl)benzotrile

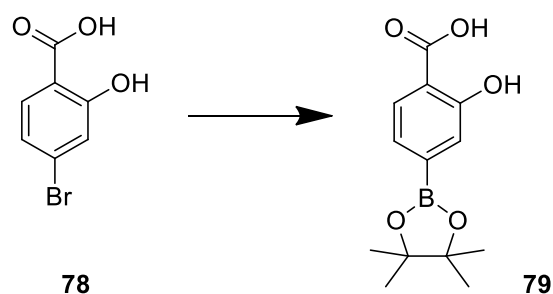
The above titled boronic ester was synthesised from *bis*(pinacolato)diboron (0.632 g, 2.49 mmol, 1 eq) and 4-bromo-2-hydroxybenzotrile **76** (0.493 g, 2.49 mmol, 1 eq) as in **general procedure E**. Following recrystallization from hexane, boronic ester **77** was isolated as a white solid (0.464 g, 1.89 mmol, 76%).

$^1\text{H } \delta$ ppm: 1.27 (12 H, s, 4 x CH₃), 7.14 (1 H, dd, $J = 7.71, 1.28$, *para* to OH), 7.35 (1 H, d, $J = 1.28$, *ortho* to OH), 7.36 (1 H, d, $J = 7.71$, *meta* to OH), 10.49 (1 H, s, OH);

^{13}C δ ppm: 24.9 (4 C, CH_3), 84.5 (2 C, C-O), 94.6 (1 C, C-CN), 105.2 (1 C, C-B), 116.4 (1 C, CN), 120.1 (1 C Ar C), 127.9 (1 C, Ar C), 132.8 (1 C, Ar C), 158.2 (1 C, Ar C-OH).

V_{max} cm^{-1} : 3245 (OH), 2982 (CH_3), 2242 (CN), 1570-1410 (C-C sp^2), 881 (1,2,4-trisubstituted ring), 830 (*p*-sub), 742 (*o*-sub).

2-Hydroxy-4-(4,4,5,5-tetramethyl-1,3,2-dioxaborolan-2-yl)benzoic acid



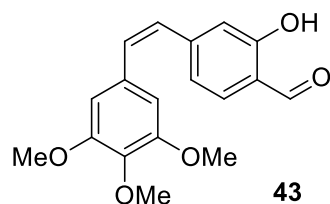
The above titled boronic ester was synthesised from bis(pinacolato)diboron (0.632 g, 2.49 mmol, 1 eq) and 4-bromo-2-hydroxybenzoic acid **78** (0.540 g, 2.49 mmol, 1 eq) as in **general procedure E**. Following recrystallization from hexane, boronic ester **73** was isolated as a white solid (0.375 g, 1.42 mmol, 57%).

^1H δ ppm: 1.34 (12 H, s, 4 x CH_3), 7.31 (1 H, dd, $J = 8.02, 1.21$, *para* to OH), 7.44 (1 H, d, $J = 1.21$, *ortho* to OH), 7.44 (1 H, d, $J = 8.02$, *meta* to OH), 12.07 (1 H, s, COOH);

^{13}C δ ppm: 24.9 (4 C, CH_3), 84.4 (2 C, C-O), 123.9 (1 C, Ar C), 125.5 (1 C, Ar C), 132.6 (1 C, Ar C), 144.9 (1 C, Ar C-B), 166.5 (1 C, Ar C-OH), 176.8 (1 C, COOH).

Synthesis of Z-combretastatins using Suzuki cross coupling with boronic esters

(Z)-2-Hydroxy-4-(3',4',5'-trimethoxystyryl)benzaldehyde



Z-Stilbene was prepared from 5-[(Z)-2-bromovinyl]-1,2,3-trimethoxybenzene **70** (0.366 g, 1.33 mmol) and 2-hydroxy-4-(4,4,5,5-tetramethyl-1,3,2-dioxaborolan-2-yl)benzaldehyde **73** (0.496 g, 2.00 mmol) as in **general procedure F**. Following flash column chromatography

(SiO₂, Petrol:EtOAc 10:1) *cis* alkene **43Z** was isolated as a pale yellow solid (0.226 g, 0.72 mmol, 54%).

Mp: 85-89 °C; **Rf:** 0.46 (SiO₂ petrol:EtOAc 3:1);

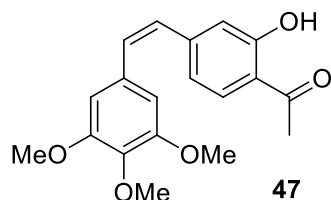
¹H δ ppm: 3.71 (3 H, s, OCH₃), 3.87 (6 H, s, 2 x OCH₃), 6.50 (2 H, s, *ortho* to OCH₃), 6.51 (1 H, d, *J* = 12.3, CH relative to A-ring), 6.53 (1 H, d, *J* = 12.3, CH relative to B-ring), 6.68 (1 H, dd, *J* = 7.7, 1.8, *para* to OH), 6.69 (1 H, d, *J* = 1.8, *ortho* to OH), 7.43 (1 H, d, *J* = 7.7, *meta* to OH), 9.83 (1 H, s, CHO), 11.06 (1 H, s, OH).

¹³C δ ppm: 56.2 (2 C, 2 x OCH₃), 61.0 (1 C, OCH₃), 104.2 (1 C, *o*-OH), 106.2 (2 C, *o*-C-OCH₃), 114.8 (1 C, C-CHO), 126.6 (1 C, *o*-CHO), 128.3 (1 C, *p*-OH) 131.6 (1 C, ArC), 132.0 (2 C, CH), 138.9 (1 C, C-O CH₃), 153.0 (2 C, C-O CH₃), 153.5 (1 C, C-OH), 195.7 (1 C, C=O).

*V*_{max} cm⁻¹: 3100 (OH), 3050 (C-H sp²), 2940 (C-H ald), 1643 (C=O), 1619 (*cis*-alkene stretch), 1564-1413 (C-C sp²), 1419 (C-H bend, CHO), 1288 (OH bend), 1183 (OCH₃), 827 (1,2,4-trisubstituted ring), 721 (*cis*-alkene bend).

m/z: [M+H] calcd for C₁₈H₁₉O₅ 315.1230, found 315.1227

(Z)-2-Hydroxy-4-(3',4',5'-trimethoxystyryl)phenyl)acetophenone



Z-Stilbene was prepared from 5-[(*Z*)-2-bromovinyl]-1,2,3-trimethoxybenzene **70** (0.366 g, 1.33 mmol) and 2-hydroxy-4-(4,4,5,5-tetramethyl-1,3,2-dioxaborolan-2-yl)acetophenone **75** (0.524 g, 2.00 mmol) as in **general procedure F**. Following flash column chromatography (SiO₂, Petrol:EtOAc 10:1) *cis* alkene **47Z** was isolated as a pale yellow solid (0.244 g, 0.74 mmol, 56%).

Mp: 71-75 °C; **Rf:** 0.53 (SiO₂ petrol:EtOAc 3:1);

¹H δ ppm: 2.62 (3 H, CH₃), 3.72 (6 H, s, 2 x OCH₃), 3.87 (3 H, s, OCH₃), 6.51 (2 H, s, *ortho* to OCH₃), 6.52 (1 H, d, *J* = 12.5, CH relative to A-ring), 6.66 (1 H, d, *J* = 12.5, CH relative to B-

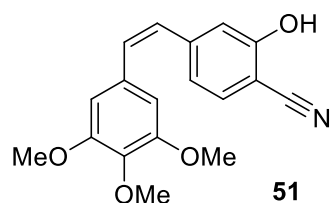
ring), 6.83 (1 H, dd, $J = 8.2, 1.6$, *para* to OH), 6.97 (1 H, d, $J = 1.6$, *ortho* to OH), 7.60 (1 H, d, $J = 8.2$, *meta* to OH), 12.27 (1 H, s, OH).

^{13}C δ ppm: 26.6 (1 C, CH₃), 56.0 (2 C, 2 x OCH₃), 61.0 (1 C, OCH₃), 106.2 (2 C, o-C-OCH₃), 118.3 (C-COCH₃), 128.5 (1 C, o-COCH₃), 130.3 (1 C, p-OH), 131.8 (1 C, ArC), 132.9 (1 C, Ar C), 146.0 (1 C, C-OCH₃), 153.0 (2 C, C-O CH₃), 162.4 (1 C, C-OH), 203.8(1 C, C=O).

V_{max} cm^{-1} : 3100 (OH), 3000 (C-H sp^2), 2940 (C-H), 1671 (C=O), 1620 (*cis*-alkene stretch), 1557-1419 (C-C sp^2), 1328 (OH bend), 1182 (OCH₃), 880 (1,2,4-trisubstituted ring), 736 (*cis*-alkene bend).

m/z : [M+H] calcd for C₁₉H₂₁O₅ 329.1384, found 329.1386.

(Z)-2-Hydroxy-4-(3',4',5'-trimethoxystyryl)benzonitrile



Z-Stilbene was prepared from 5-[(Z)-2-bromovinyl]-1,2,3-trimethoxybenzene **70** (0.366 g, 1.33 mmol) and 2-hydroxy-4-(4,4,5,5-tetramethyl-1,3,2-dioxaborolan-2-yl)benzonitrile **77** (0.490 g, 2.00 mmol) as in **general procedure F**. Following flash column chromatography (SiO₂, Petrol:EtOAc 10:1) *cis* alkene **51Z** was isolated as a dark yellow solid (0.199 g, 0.64 mmol, 48%).

Mp: 95 °C; **Rf**: 0.46 (SiO₂ petrol:EtOAc 3:1);

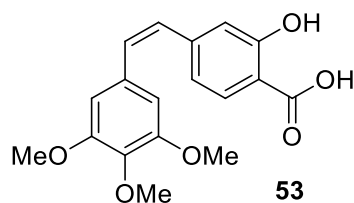
^1H δ ppm: 3.70 (6 H, s, 2 x OCH₃), 3.85 (3 H, s, OCH₃), 6.45 (2 H, s, *ortho* to OCH₃), 6.48 (1 H, d, $J = 12.2$, CH relative to A-ring), 6.63 (1 H, d, $J = 12.2$, CH relative to B-ring), 6.88 (1 H, dd, $J = 9.0, 1.2$, *para* to OH), 6.98 (1 H, d, $J = 1.2$, *ortho* to OH), 7.39 (1 H, d, $J = 9.0$, *meta* to OH).

^{13}C δ ppm: 55.9 (2 C, 2 x OCH₃), 61.2 (1 C, OCH₃), 99.8 (1 C, C-CN), 106.0 (2 C, o-C-OCH₃), 121.4 (CN), 128.1 (1 C, o-COCH₃), 1331.5 (1 C, p-OH), 132.8 (1 C, ArC), 132.9 (1 C, Ar C), 143.9 (1 C, C-OCH₃), 153.1 (2 C, C-O CH₃), 159.4 (1 C, C-OH).

$V_{max} \text{ cm}^{-1}$: 3232 (OH), 2925 (C-H sp^2), 2221 (CN stretch), 1605 (*cis*-alkene stretch), 1580-1411 (C-C sp^2), 1396 (OH bend), 11853 (OCH_3), 829 (1,2,4-trisubstituted ring), 738 (*cis*-alkene bend).

m/z : [M+H] calcd for $\text{C}_{18}\text{H}_{18}\text{NO}_4$ 312.1230, found 312.1234.

(Z)-2-Hydroxy-4-(3',4',5'-trimethoxystyryl)benzoic acid



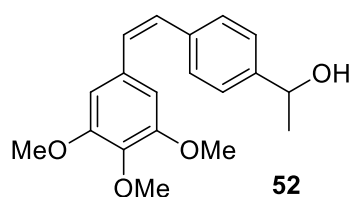
Z-Stilbene was prepared from 5-[(Z)-2-bromovinyl]-1,2,3-trimethoxybenzene (0.366 g, 1.33 mmol) and 2-hydroxy-4-(4,4,5,5-tetramethyl-1,3,2-dioxaborolan-2-yl)benzoic acid (0.528 g, 2.00 mmol) as in **general procedure F**. Following flash column chromatography (SiO_2 , Petrol:EtOAc 10:1) *cis* alkene **53Z** was isolated as a white solid (0.184 g, 0.56 mmol, 43%).

Mp: 85-87 °C; **Rf**: 0.57 (SiO_2 petrol:EtOAc 3:1);

$^1\text{H } \delta$ ppm: 3.70 (6 H, s, 2 x OCH_3), 3.85 (3 H, s, OCH_3), 6.45 (2 H, s, *ortho* to OCH_3), 6.48 (1 H, d, $J = 12.2$, CH relative to A-ring), 6.63 (1 H, d, $J = 12.2$, CH relative to B-ring), 6.88 (1 H, dd, $J = 9.0, 1.2$, *para* to OH), 6.98 (1 H, d, $J = 1.2$, *ortho* to OH), 7.39 (1 H, d, $J = 9.0$, *meta* to OH).

Synthesis of secondary alcohols from aldehydes

(Z)-1-(4-(3',4',5'-Trimethoxystyryl)phenyl)ethanol



Z stilbene was prepared from (Z)-4-(3',4',5'-trimethoxystyryl)benzaldehyde **42Z** (0.105 g, 0.34 mmol) as in **general procedure G**. *Cis* alkene **52Z** was isolated as a bright yellow oil (0.094 g, 0.30 mmol, 90%).

Rf: 0.43 (SiO_2 petrol:EtOAc 3:1);

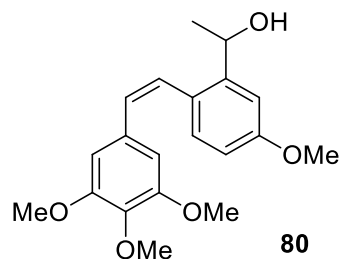
^1H δ ppm: 1.39 (3 H, d, $J = 6.50$, CH_3), 3.58 (6 H, s, 2 x OCH_3), 3.76 (3 H, s, OCH_3), 4.81 (q, $J = 6.48$, 19.39, 1 H, CH), 6.39 (s, 2 H, *ortho* to OCH_3), 6.50 (d, $J = 12.20$, 1 H, CH relative to A-ring), 6.51 (d, $J = 12.20$, 1 H, CH relative to B-ring), 7.19-7.20 (d, $J=8.18$, 4 H, Ar H).

^{13}C δ ppm: 25.3 (CH_3), 55.8 (2 C, OCH_3), 60.9 (OCH_3), 70.2 (CH), 106.0 (2 C, Ar C), 125.2 (2 C, Ar C), 129.1 (2 C, Ar C), 129.7 (olefinic C), 130.2 (olefinic C), 132.6 (Ar C), 136.7 (Ar C), 137.2 (Ar C), 144.8 (Ar C), 152.9 (2 C, Ar C).

ν_{max} cm^{-1} : 3200 (OH stretch), 2920 (C-H alkene), 2849 (C-H sp^2), 1581-1420 (C-C sp^2), 1420 (CH_3), 1235 (OH *in plane*), 1173 (OMe), 1034 (C-O), 825 (*p*-sub), 732 (OH *out of plane*), 703 (*cis*-alkene).

m/z : [M+H calcd for $\text{C}_{19}\text{H}_{23}\text{O}_4$ 315.1591, found 315.1592

(Z)-1-(5-Methoxy-2-(3',4',5'-trimethoxystyryl)phenyl)ethanol

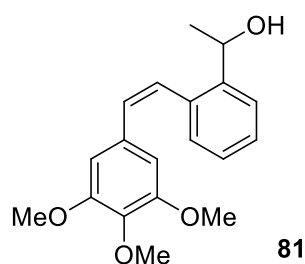


Z stilbene was prepared from (Z)-5-methoxy-2-(3',4',5'-trimethoxystyryl)benzaldehyde **44Z** (0.111 g, 0.34 mmol) as in **general procedure G**. *Cis* alkene **80Z** was isolated as a pale yellow oil (0.081 g, 0.23 mmol, 69%).

Rf: 0.38 (SiO_2 petrol:EtOAc 3:1);

^1H δ ppm: 1.34 (d, $J = 6.40$, 3 H, CH_3), 3.51 (s, 6 H, 2 x OCH_3), 3.72 (s, 3 H, OCH_3), 3.75 (s, 3 H, OCH_3), 5.04 (q, $J = 6.44$, 19.23, 1 H, CH), 6.24 (s, 2 H, *ortho* to OCH_3), 6.43 (d, $J = 12.12$, 1 H, CH relative to A-ring), 6.58 (d, $J = 12.12$, 1 H, CH relative to B-ring), 6.68 (dd, $J = 2.72$, 11.18, 1 H, *para* to $\text{C}(\text{OH})\text{CH}_3$), 7.03 (d, $J=11.18$, 1 H, *meta* to $\text{C}(\text{OH})\text{CH}_3$), 7.09 (d, $J=2.72$, 1 H, *ortho* to $\text{C}(\text{OH})\text{CH}_3$).

^{13}C δ ppm: 24.2 (CH_3), 55.4 (OCH_3), 55.7 (2 C, OCH_3), 60.9 (OCH_3), 67.4(CH), 106.2 (2 C, Ar C), 110.2 (Ar C), 113.2 (Ar C), 127.6 (Ar C), 127.7 (olefinic C), 130.7 (olefinic C), 130.9 (Ar C), 132.1 (Ar C), 137.2 (Ar C), 145.3 (Ar C), 152.7 (Ar C), 159.5 (2 C, Ar C).

(Z)-1-(2-(3',4',5'-Trimethoxystyryl)phenyl)ethanol

Z-Stilbene was prepared from (Z)-2-(3',4',5'-trimethoxystyryl)benzaldehyde **45Z** (0.105 g, 0.34 mmol) as in **general procedure G**. *Cis* alkene **81Z** was isolated as a bright yellow oil (0.088 g, 0.28 mmol, 82%).

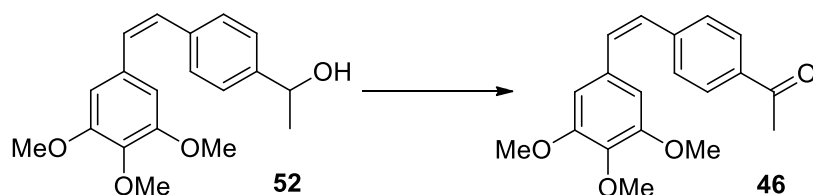
Rf: 0.47 (SiO₂ petrol:EtOAc 3:1);

¹H δ ppm: 1.34 (d, *J* = 6.232, 3 H, CH₃), 3.47 (s, 6 H, 2 x OCH₃) 3.71 (s, 3 H, OCH₃), 5.06 (q, *J* = 6.24, 19.13, 1 H, CH), 6.20 (s, 2 H, *ortho* to OCH₃), 6.47 (d, *J* = 12.26, 1 H, CH relative to A-ring), 6.66 (d, *J* = 12.18, 1 H, CH relative to B-ring), 7.14 (m, *J*=26.69, 2 H, Ar H) 7.12-7.40 (m), 7.53 (d, *J*= 7.45, 1 H, Ar H);

¹³C δ ppm: 24.2 (CH₃), 65.2 (2 C, OCH₃), 60.8 (OCH₃), 68.0 (CH), 106.2 (2 C, Ar C), 126.3 (Ar C), 127.5 (olefinic C), 127.6 (Ar C), 128.1 (Ar C), 129.3 (olefinic C), 131.2 (Ar C), 131.8 (Ar C), 135.0 (Ar C), 135.6 (Ar C), 142.9 (Ar C), 153.4 (2 C, Ar C);

***V*_{max} cm⁻¹:** 2938 (C-H alkene), 1600 (C=C ar), 1579-1420 (C-C ar), 1419 (CH₃), 1237 (OH *in plane*), 1187 (OMe) 1003 (C-O), 770 (*o*-sub), 702 (*cis*-alkene).

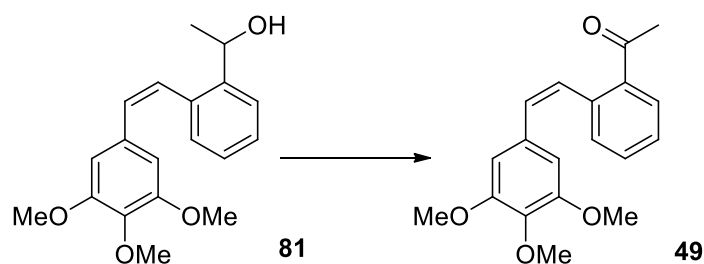
***m/z*:** [M+H calcd for C₁₉H₂₃O₄ 315.1591, found 315.1592.

Oxidation of secondary alcohol to ketone**(Z)-4-(3',4',5'-Trimethoxystyryl)acetophenone**

To a stirred solution of (Z)-1-(4-(3',4',5'-trimethoxystyryl)phenyl)ethanol **52** (0.100 g, 3.2 mmol, 1 eq.) in DCM (10 mL) was added pyridinium chlorochromate (0.103 g, 4.8 mmol, 1.5

eq.) and an equal mass of silica gel (0.103 g, 60 Å 40-63 µm). Stirring was continued for 2 h and the resulting mixture was passed through a plug of celite. Water (10 mL) was added to the filtrate and the aqueous layer was separated and extracted with chloroform (20 mL). Combined organic layers washed with water (20 mL) and brine (20 mL), dried (MgSO₄) and concentrated *in vacuo*. Flash chromatography (silica gel, Petrol: Ethyl acetate 5:1) gave the title compound **46** as a light yellow solid (0.065 g, 2.08 mmol, 65%).

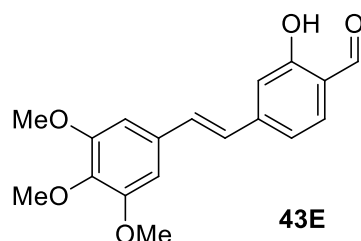
(Z)-2-(3',4',5'-Trimethoxystyryl)acetophenone



To a solution of Dess-Martin periodinane (in DCM (5 mL) was added a solution of of (Z)-1-(2-(3',4',5'-trimethoxystyryl)phenyl)ethanol **81** (0.100 g, 3.2 mmol, 1 eq.) in DCM (5 mL). The resulting mixture was stirred for 1 h then diluted with diethyl ether (10 mL) and added to NaOH (1.3M, 5 mL). The mixture was stirred for a further 10 min, organic layer extracted, washed with NaOH ((1.3M, 10 mL), water (10 mL), dried (MgSO₄) and concentrated *in vacuo*. Flash chromatography (silica gel, Petrol: Ethyl acetate 5:1) gave the title compound **49** as a yellow solid (0.064 g, 2.04 mmol, 64%).

Cis → trans isomerization using iodine

(E)-2-Hydroxy-4-(3',4',5'-trimethoxystyryl)benzaldehyde



E-stilbene was prepared from (Z)-2-hydroxy-4-(3',4',5'-trimethoxystyryl)benzaldehyde **43Z** (0.100 g, 0.32 mmol) as in **general procedure H**. *Trans* alkene **43E** was isolated as a bright yellow solid (0.095 g, 0.30 mmol, 95%).

Mp: 153-159 °C; **Rf:** 0.43 (SiO₂ petrol:EtOAc 3:1);

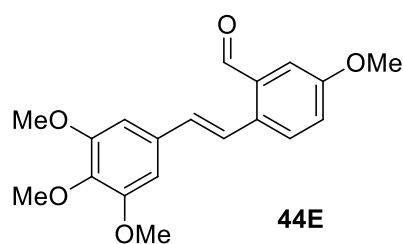
^1H δ ppm: 3.91 (3 H, s, OCH₃), 3.95 (6 H, s, 2 x OCH₃), 6.79 (2 H, s, *ortho* to OCH₃), 6.98 (1 H, d, $J = 16.2$, CH relative to A-ring), 7.11 (1 H, dd, $J = 8.2, 1.3$, *para* to OH), 7.15 (1 H d, 1.28, *ortho* to CHO), 7.21 (1 H, d, $J = 16.2$, CH relative to B-ring), 7.55 (1 H, d, $J = 8.2$, *meta* to CHO), 9.88 (1 H, s, CHO), 11.13 (1 H, s, OH).

^{13}C δ ppm: 56.2 (2 C, 2 x OCH₃), 61.0 (1 C, OCH₃), 104.2 (1 C, o-OH), 106.2 (2 C, o-C-OCH₃), 114.8 (1 C, C-CHO), 126.6 (1 C, o-CHO), 131.2 (1 C, p-OH) 133.2 (1 C, ArC), 134.0 (2 C, CH), 138.9 (1 C, C-O CH₃), 153.0 (2 C, C-OCH₃), 162.0 (1 C, C-OH), 195.5 (1 C, C=O).

V_{max} cm^{-1} : 3100 (OH), 3050 (C-H sp^2), 2940 (C-H ald), 1643 (C=O), 1670 (*trans*-alkene stretch), 1564-1413 (C-C sp^2), 1419 (C-H bend, CHO), 1288 (OH bend), 1183 (OCH₃), 827 (1,2,4-trisubstituted ring), 998 (*trans*-alkene bend).

m/z : [M+H] calcd for C₁₈H₁₉O₅ 315.1230, found 315.1227.

(*E*)-5-Methoxy-2-(3',4',5'-trimethoxystyryl)benzaldehyde



E-Stilbene was prepared from *Z*-1-(3,4,5-trimethoxyphenyl)-2-(2'-formyl-4'-methoxyphenyl)ethene **44Z** (0.105 g, 0.32 mmol) as in **general procedure H**. *Trans* alkene **44E** was isolated as a bright yellow solid (0.093 g, 0.28 mmol, 89%).

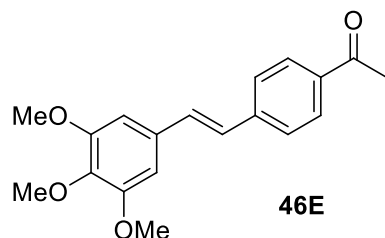
Mp: 151-153 °C; **Rf:** 0.42 (SiO₂ petrol:EtOAc 3:1);

^1H δ ppm: 3.90 (3 H, s, OCH₃), 3.92 (6 H, s, 2 x OCH₃), 3.95 (3 H, s, OCH₃), 6.78 (2 H, s, *ortho* to OCH₃), 6.89 (1 H, d, $J = 16.14$, CH relative to A-ring), 7.18 (1 H, dd, $J = 2.81, 8.75$, *para* to CHO) 7.38 (1 H d, $J = 2.81$, *ortho* to CHO), 7.64 (1 H d, $J = 8.75$, *meta* to CHO), 7.81 (1 H d, $J = 16.14$, CH relative to B-ring), 10.38 (1 H, s, CHO);

^{13}C δ ppm: 55.6 (OCH₃), 56.2 (2 C, OCH₃), 61.0 (OCH₃), 103.9 (2 C, Ar C), 110.0 (Ar C), 114.0 (Ar C), 121.2 (Ar C), 123.4 (olefinic C), 128.8 (Ar C), 129.5 (olefinic C), 131.3 (Ar C), 132.8 (Ar C), 135.1 (Ar C), 139.8 (Ar C), 153.5 (2 C, Ar C), 159.2 (Ar C), 192.0 (CHO);

$V_{max} \text{ cm}^{-1}$: 2935 (C-H sp^2), 2836 (C-H ald), 1679 (C=O), -1415 (C-C sp^2), 1168 (OMe), 972 (*trans*-alkene), 832 (*p*-sub), 750 (*o*-sub).

(E)-4-(3',4',5'-Trimethoxystyryl)acetophenone



E-stilbene was prepared from (*Z*)-4-(3',4',5'-trimethoxystyryl)acetophenone **46Z** (0.100 g, 0.32 mmol) as in **general procedure H**. *Trans* alkene **46E** was isolated as a light brown solid (0.098 g, 0.31 mmol, 98%).

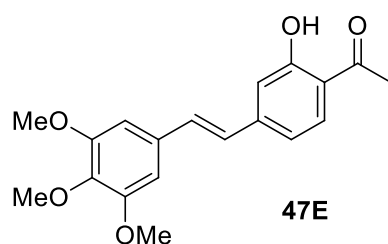
Mp: 150-155 °C; **Rf**: 0.49 (SiO₂ petrol:EtOAc 3:1);

¹H δ ppm: 2.64 (3 H, s, CH₃), 3.90 (6 H, s, 2 x OCH₃), 3.95 (3 H, s, OCH₃), 6.79 (2 H, s, *ortho* to OCH₃), 7.06 (1 H, d, *J* = 16.4, CH relative to A-ring), 7.18 (1 H, d, *J* = 16.4, CH relative to B-ring), 7.61 (2 H, d, *J* = 8.4, *meta* to COCH₃), 7.98 (2 H, d, *J* = 8.4, *ortho* to COCH₃);

¹³C δ ppm: 26.6 (CH₃), 56.2 (2 C, OCH₃), 61.0 (OCH₃), 103.4 (2 C, Ar C), 126.4 (2 C, Ar C), 126.9 (2 C, Ar C), 128.9 (olefinic C), 129.1 (olefinic C), 131.4 (Ar C), 137.4 (Ar C), 139.5 (Ar C), 1439.7 (Ar C), 153.5 (2 C, Ar C), 197.8 (carbonyl C);

$V_{max} \text{ cm}^{-1}$: 2930 (C-H sp^2), 1669 (C=O), 1578-1420 (C-C sp^2), 1360 (CH₃), 1151 (OMe), 980 (*trans*-alkene), 837 (*p*-sub).

m/z: [M+H] calcd for C₁₉H₂₁O₄ 313.1431, found 313.1434.

(E)-2-hydroxy-4-(3',4',5'-trimethoxystyryl)phenyl)acetophenone

E-stilbene was prepared from (*Z*)-2-hydroxy-4-(3',4',5'-trimethoxystyryl)phenyl)acetophenone **47Z** (0.105 g, 0.32 mmol) as in **general procedure H**. *Trans* alkene **47E** was isolated as a bright yellow solid (0.099 g, 0.30 mmol, 94%).

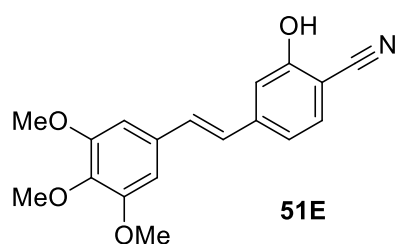
Mp: 148-150 °C; **Rf:** 0.51 (SiO₂ petrol:EtOAc 3:1);

¹H δ ppm: 2.64 (3 H, CH₃), 3.91 (3 H, s, OCH₃), 3.95 (6 H, s, 2 x OCH₃), 6.79 (2 H, s, *ortho* to OCH₃), 6.97 (1 H, d, *J* = 16.4, CH relative to A-ring), 7.08 (1 H, dd, *J* = 7.6, 1.3, *para* to OH), 7.11 (1 H, d, *J* = 1.3, *ortho* to OH), 7.18 (1 H, d, *J* = 16.4, CH relative to A-ring), 7.73 (1 H, d, *J* = 7.6, *meta* to OH), 12.40 (1 H, s, OH).

¹³C δ ppm: 26.6 (1 C, CH₃), 56.0 (2 C, 2 x OCH₃), 61.0 (1 C, OCH₃), 106.2 (2 C, *o*-C-OCH₃), 115.5 (C-COCH₃), 118.5 (1 C, *o*-COCH₃), 120.4 (1 C, *p*-OH), 130.5 (1 C, ArC), 133.2 (1 C, Ar C), 145.5 (1 C, C-OCH₃), 153.0 (2 C, C-O CH₃), 162.7 (1 C, C-OH), 203.6 (1 C, C=O).

***V*_{max} cm⁻¹:** 3100 (OH), 3000 (C-H sp²), 2940 (C-H), 1671 (C=O), 1645 (*trans*-alkene stretch), 1557-1419 (C-C sp²), 1328 (OH bend), 1182 (OCH₃), 975 (*trans*-alkene bend), 880 (1,2,4-trisubstituted ring).

***m/z*:** [M+H] calcd for C₁₉H₂₁O₅ 329.1384, found 329.1385.

(E)-4-(3',4',5'-Trimethoxystyryl)benzonitrile

E-stilbene was prepared from (*Z*)-4-(3',4',5'-trimethoxystyryl)benzonitrile **51Z** (0.099 g, 0.32 mmol) as in **general procedure H**. *Trans* alkene **51E** was isolated as a bright yellow solid (0.093 g, 0.29 mmol, 93%).

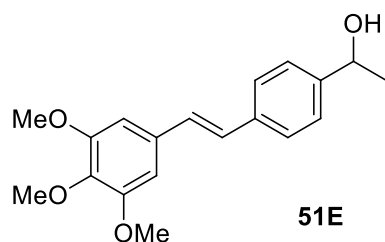
Mp: 153-156 °C; **Rf:** 0.43 (SiO₂ petrol:EtOAc 3:1);

¹H δ ppm: 3.63 (3 H, s, OCH₃), 3.79 (6 H, s, 2 x OCH₃), 5.89 (1 H, br s, OH), 6.37 (2 H, s, *ortho* to OCH₃), 6.97 (1 H, d, *J* = 16.4, CH relative to A-ring), 7.08 (1 H, dd, *J* = 7.6, 1.3, *para* to OH), 7.11 (1 H, d, *J* = 1.3, *ortho* to OH), 7.18 (1 H, d, *J* = 16.4, CH relative to B-ring), 7.73 (1 H, d, *J* = 7.6, *meta* to OH), 12.40 (1 H, s, OH).

¹³C δ ppm: 55.9 (2 C, 2 x OCH₃), 61.2 (1 C, OCH₃), 99.8 (1 C, C-CN), 106.0 (2 C, *o*-C-OCH₃), 121.4 (CN), 128.1 (1 C, *o*-COCH₃), 1331.5 (1 C, *p*-OH), 132.8 (1 C, ArC), 132.9 (1 C, Ar C), 143.9 (1 C, C-OCH₃), 153.1 (2 C, C-O CH₃), 159.4 (1 C, C-OH).

***V*_{max} cm⁻¹:** 3230 (O-H), 3000 (C-H sp²), 2220 (CN), 1671 (C=O), 1650 (*trans*-alkene stretch), 1580-1424 (C-C sp²), 1340 (OH bend), 1186 (OCH₃), 979 (*trans*-alkene bend), 892 (1,2,4-trisubstituted ring).

***m/z*:** [M+H] calcd for C₁₈H₁₈NO₄ 312.1230, found 312.1234.

(E)-1-(4-(3',4',5'-Trimethoxystyryl)phenyl)ethanol

E-stilbene was prepared from (*Z*)-1-(4-(3',4',5'-trimethoxystyryl)phenyl)ethanol **51Z** (0.100 g, 0.32 mmol) as in **general procedure H**. The *trans* alkene **51E** was isolated as a yellow oil (0.083 g, 0.27 mmol, 83%).

R_f: 0.42 (SiO₂ petrol:EtOAc 3:1);

¹H δ ppm: 1.44 (3 H, d, *J* = 6.58, 3 CH₃), 3.79 (3 H, s, OCH₃), 3.85 (6 H, s, 2 x OCH₃), 4.83 (1 H, q, *J* = 6.37, 19.21, CH), 6.67 (2 H, s, *ortho* to OCH₃), 6.92 (1 H, d, *J* = 16.36, CH relative to A-ring), 6.97 (1 H, d, *J* = 16.36, CH relative to B-ring), 7.30 (2 H, d, *J* = 8.18, Ar H), 7.42 (2 H, d, *J* = 8.18, Ar H);

¹³C δ ppm: 25.1 (CH₃), 56.1 (2 C, OCH₃), 61.0 (OCH₃), 70.2 (CH), 103.6 (2 C, Ar C), 125.6 (2 C, Ar C), 126.6 (2 C, Ar C), 127.8 (olefinic C), 128.6 (olefinic C), 133.1 (Ar C), 136.5 (Ar C), 138.0 (Ar C), 145.2 (Ar C), 153.4 (2 C, Ar C);

***V*_{max} cm⁻¹**: 2935 (C-H alkene), 2836 (C-H ar), 1601 (C=C ar), 1581-1416 (C-C ar), 1226 (OH *in plane*), 1168 (OMe), 1033 (C-O), 972 (*trans*-alkene), 832 (*p*-sub), 730 (OH *out of plane*).

m/z: [M+H calcd for C₁₉H₂₃O₄ 315.1591, found 315.1592.

2.2 Experimental – bioactivity assays

2.2.1 Subculture and cell maintenance

Thawing of adherent cells

When thawing cells two T25 flasks were prepared per *vial* of frozen cells. A cryovial containing 1 ml of the frozen cell stocks was taken from the liquid nitrogen and allowed to thaw in a 37 °C water bath (5 min). Then 0.5 mL of the cell suspension was transferred into each of two sterile T25 tissue culture flasks and re-suspended in 4.5 mL complete tissue culture medium. After 24 h the cells had attached to the tissue culture flask, the medium was removed and replaced with 5 mL fresh culture medium to remove excess DMSO.

General subculture of adherent cells

Adherent cells in culture were subcultured by first removing the old medium from the tissue culture flask (T25 or T75, B.D. Falcon, VWR International Ltd.) and the adhered cells were then washed with sterile phosphate buffer saline (1x PBS, VWR) (2 x 5 mL for T25 and 2 x 10 mL for T75) and trypsin (0.5 mL for T25 or 2 mL for T75; trypsin-EDTA in PBS with phenol red) was added. The flask was incubated for 5 min at 37 °C until cells had detached from the flask as observed with a light microscope and cells resuspended in complete cell culture medium (1.5 mL for T25 or 6 mL for T75). This cell suspension was split into T25 (1 mL each) or T75 (4 mL each) tissue culture flasks and diluted in complete medium (4 mL for T25 and 11 mL for T75 flasks). Cells were left to adhere and proliferate in a humidified incubator (37 °C 5% CO₂). Subculture was routinely carried out every two to three days depending on cell confluence.

Freezing of adherent cell stock

Cell stocks in liquid nitrogen were prepared for each cell line from three confluent T25 tissue culture flask. Cells were detached as per subculture and complete medium (4.5 mL) was added into the first T25 flask and cells resuspended. This cell suspension was transferred to the second T25 flask and the new suspension was transferred to the third flask. The concentrated cell suspension was transferred to a centrifuge tube and cells were centrifuged at 1500 rpm for 5 min, supernatant discarded and cell pellet resuspended in foetal calf serum (FCS) (10 mL) containing 10% dimethylsulfoxide (DMSO, Alfa Aesar).

Aliquots (1 mL) in cryovials were prepared and transferred into an isopropanol freezing container and allowed to freeze in a -80 °C freezer overnight before being transferred to liquid nitrogen at -196 °C for long term storage.

Spheroid growth and maintenance

Spheroids were grown on agarose in 96-well U-bottom plates. Agarose (0.3 g) was dissolved in deionised water (20 mL) to make a 15 % solution and autoclaved for 80 min. In a sterile cell culture hood agarose (100 µL) was added into each well of a 96-well U-bottomed plate and allowed to set for 1 h. HEK293 cells were re-suspended in complete media (10 mL) as per sub culture to obtain a homogenous suspension. Cells in 10 µL complete tissue culture medium were counted on a disposable C-Chip haemocytometer slide (Neubauer improved grid) and diluted to the desired concentration (1×10^5 cells mL⁻¹) in a final volume of 10 mL. 100 µL of the diluted cell suspension was added into the middle wells of the agarose-lined 96-well plate being careful not to pierce the agarose. PBS (200 µL) was added to the outer wells and plates stored in the incubator (37 °C, 5 % CO₂). Media was added as required and spheroids typically grew within 3 days.

2.2.2 Cell lines and composition of tissue culture media

HepG2

HepG2 cells were obtained from the biobank at the University of Salford. HepG2 is a cell line derived from the liver tissue of a 15-year-old Caucasian American. The HepG2 cell line was originally established in 1979 by Barbara Knowles and colleagues, and reported as a hepatocellular carcinoma (Aden *et al.*, 1979). HepG2 cells contain 55 chromosome pairs and secrete a number of major plasma proteins such as albumin and transferrin. They are an adherent cell line; the epithelial-like cells grow as monolayers and in small aggregates with a doubling time of 48 hours. Typically HepG2 cells were subcultured every two to three days. Cells were grown in DMEM medium (Gibco) supplemented with FBS (10 %), penicillin (100 units/mL), streptomycin (100 µg/mL) and L-glutamine (2 mM).

HeLa cells

HeLa cells were obtained from the European Collection of Cell Cultures. This cell strain was first extracted from an epidermoid carcinoma of the cervix from a patient called Henrietta Lacks by George O. Gey in 1951 (Scherer & Syverton, 1952). This immortal cell line was the

first strain to be grown successfully in cell culture laboratories and is most commonly used to date due to its durable and prolific properties. The doubling time of cultured HeLa cells is around 24 hours. Typically HeLa cells were subcultured every two days. The endothelial cell monolayers were routinely grown in DMEM (Gibco) containing FBS (10 %), penicillin (100 units/mL), streptomycin (100 µg/mL) and L-glutamine (2 mM).

HCT 116 cells

HCT 116 cells are one of three colorectal carcinoma subpopulations from a single male human. HCT 116 is a human colon cancer cell line that is commonly used to study cancer biology as it is a growth factor independent cell line with a doubling time of approximately 21 h. The recommended medium for HCT-116 cells is McCoy's 5A medium but various publications suggest HCT cells can grow efficiently in DMEM (ref). HCT-116 cells were grown in DMEM (Gibco) containing FBS (10 %), penicillin (100 units/mL), streptomycin (100 µg/mL) and L-glutamine (2 mM).

CHO cells

Chinese hamster ovary (CHO) cells were obtained from the European Collection of Cell Cultures. CHO cells are a good model for tissue and culture radiation studies due to their low chromosome number; these adherent cells possess only 22 chromosomes. It is a very stable, fast growing cell line with a doubling time of 14-17 hours (Tjio & Puck, 1958; Puck, Cieciora & Robinson, 1958). CHO cells display a slightly elongated shape and tend to form tightly packed rafts of cells (Romano *et al.*, 2009; Puck, Cieciora & Robinson, 1958). CHO cell monolayers were grown in phenol-red free DMEM medium (Gibco) supplemented with FCS (10 %), penicillin (100 units/mL), streptomycin (100 µg/mL) and L-glutamine (2 mM).

Hek293 cells

Human embryonic kidney cells are a cell line grown in tissue culture. HEK 293 cells are popular for their ease of growth. The type of kidney cell that the HEK293 cell line came arose from is unknown but most kidney cells are endothelial, epithelial or fibroblast cells. Hek cells were grown in phenol-red free MEM medium (Gibco) supplemented with FBS (10%), penicillin (100 units/mL), streptomycin (100 µg/mL) and L-glutamine (2 mM).

Although Hek293 are a non-cancerous cell line, they are a stable cell line suitable for imaging and so were used to optimise the imaging process.

2.2.3 MTT assay using adherent cell lines

Colourimetric assays using the tetrazolium salt thiazolyl blue (MTT) are widely used for numerous studies in cell biology such as cytotoxicity and cell viability (Stockert *et al.*, 2012). The MTT assay is a well-established live cell bioassay allowing the determination of the IC₅₀ (half-maximum inhibitory concentration) of a variety of small organic compounds on various live cell lines. MTT gives a yellow aqueous solution, which on reduction by the mitochondrial enzyme succinate dehydrogenase found in living cells gives purple formazan crystals (Figure 32). These formazan crystals can be dissolved in DMSO to give purple solutions with different intensities; it is widely accepted that the amount of MTT formazan is proportional to the number of living cells (Uphoff & Drexler, 2011) as the more living cells producing mitochondrial reductase, the more MTT is reduced to MTT formazan. The optical density in the wells was measured at 540 and 690 nm using a UV/visible platereader.

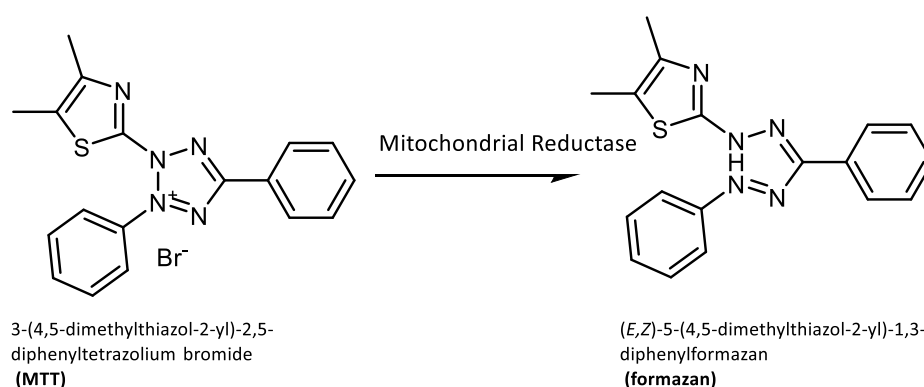


Figure 32 The reduction of MTT to MTT formazan.

As the degree of cell growth inhibition was determined at a range of increasing concentrations for each drug candidate, it was possible to obtain a plot showing the percentage growth inhibition *versus* drug concentration. The intensity measured for the no drug control represents 100% growth, or no cell inhibition, so any treated cells can be compared against this to establish cell growth inhibition.

MTT assays were carried out on HepG2, HeLa and HCT-116 cells that were grown as described previously. Cells were detached as per subculture (section 2.2.1). All cells were resuspended in complete cell culture media (4.5 mL) to obtain a homogeneous cell suspension. Cells in 10 μ L complete tissue culture medium were counted on a disposable C-Chip haemocytometer slide (Neubauer improved grid) and diluted to the desired

concentration (ca. 10 mL total volume were needed per 96-well plate) in a sterile pipetting trough. Using a multichannel pipette 100 μ L of the diluted cell suspension was added into each well of a flat-bottomed treated 96-well MTT plate. MTT plates were then stored in the incubator (37 $^{\circ}$ C, 5 % CO₂) for 24 h to allow for cells to adhere. Drug candidates were prepared as concentration stocks in DMSO (usually 10 mM). A serial dilution series of each of the concentrated drug samples was prepared by diluting stocks into cell culture medium. 100 μ L of the drug solutions were added onto the cells in the 96-well plates in triplicate on duplicate plates; drug solutions were added in increasing concentration down the plate. Following incubation of the plates for the specified time, MTT solution (50 μ L; 3 mg/mL in PBS) was added to each well. Following incubation for another 3 h the wells were aspirated to remove all liquid taking care not to disrupt any of the purple formazan crystals that had formed. The crystals were dissolved in DMSO (100 μ L) and optical densities of the wells were read on a spectrophotometer platereader (Multiskan Ascent, Thermo Labsystems) at 540 nm with 690 nm as a background reading. Graphs displaying the dose response *versus* change in optical density were obtained from the calculation of the mean absorption of the samples per concentration. The absorbance measured for the control sample, which was not treated with a drug candidate, was normalised to 100 % cell growth (no inhibition of cell growth). The graphs allowed the determination of the IC₅₀s (where 50 % of the cell growth was inhibited) for each of the drug candidates that were tested. An example for a typical plot is shown below (Figure 33).

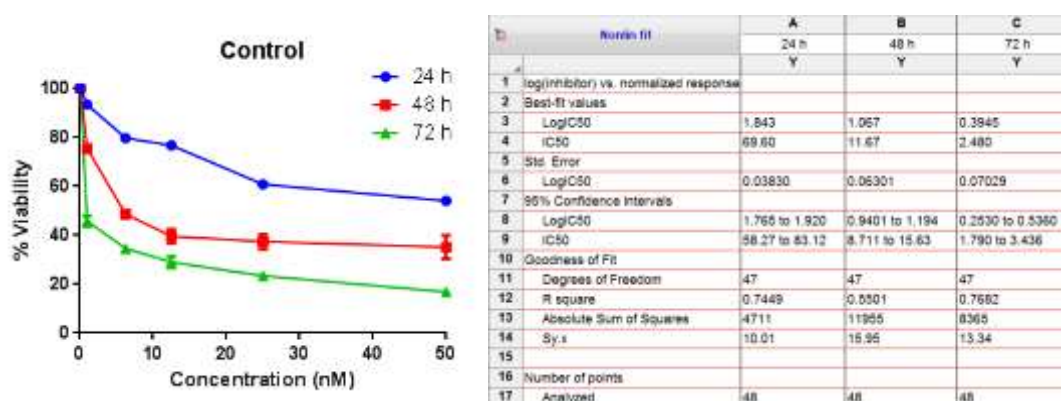


Figure 33 Plot of drug concentration versus cell viability [%] of Z-CA4.

2.2.4 Tubulin polymerisation assay

A fluorescence-based tubulin polymerization assay was performed according to the manufacturer's protocol (cat # BK011P, Cytoskeleton, Inc.). The fluorescence based tubulin polymerisation assay was chosen as it is more sensitive and precise; variation between duplicates is less than that of the absorbance based tubulin polymerisation assay (BK006P, Cytoskeleton, Inc.). Prior to beginning the assay, a number of components needed to be reconstituted and stored at -70 °C. Buffer (1,4-piperazinediethanesulfonic fluorescent reporter acid, ethylene glycol tetraacetic acid, MgCl₂ and fluorescent reporter) was reconstituted in Milli-Q water (10 mL) and aliquoted and guanosine triphosphate (GTP) was reconstituted in ice cold sterile water (300 µL) to give 100 mM. GTP (100 nM, 15 µL) was added to ice cold buffer (1.5 mL); tubulin powder (10 mg, >99 % pure) was completely resuspended in supplemented buffer (1.1 mL) to give a concentration of 10 mg mL⁻¹; tubulin mix was aliquoted and drop frozen in liquid nitrogen. To a pre warmed (37 °C) black flat-bottomed 96 well plate was added test compounds (final concentration 1 µM, 5 µL) or buffer (5 µL). Tubulin reaction mixture was prepared on ice consisting of buffer (243 µL), glycerol buffer (112 µL), GTP (100 mM, 4.4 µL) and tubulin stock (10 mg mL⁻¹). Tubulin reaction mixture (50 µL) was added into each well and tubulin polymerization was followed by a time-dependent increase in the fluorescence due to the incorporation of a fluorescence reporter into the microtubules as the polymerization proceeded. The fluorescence emission at 405 nm (excitation at 355 nm) was measured using a Spectramax M2 microplate reader. CA-4 was used as a control and Paclitaxel was used as a positive control in each assay.

2.2.5 Cell cycle analysis

Cell cycle analysis using flow cytometry was performed on HepG2. Cells were detached as per subculture (section 2.2.1) and counted as previously described and a 24-well plate was seeded at 50,000 cells per well and allowed to adhere for 24 h in the incubator (37 °C, 5 % CO₂). Drug candidates were prepared in complete medium at concentrations of the IC₅₀ from the 10 mM stocks and added to wells (1 mL). Cells were incubated for the drug exposure time required (24, 48, 72 h). The adherent cells were detached as per sub-culture and resuspended in the old media and transferred to a universal tube and centrifuged at 1500 rpm for 5 min. The supernatant was removed and PBS (2 mL) added, and transferred to an Eppendorf tube and again centrifuged at 1500 rpm for 5 min. The PBS was removed

and cells were resuspended in ice-cold ethanol (70 %, 500 μ L), cells were vortexed for 10 seconds and stored in the fridge at 4 °C for 30 min. The cell pellet was washed twice with PBS (2 mL) and a solution of ribonuclease A was added (50 μ L; 100 μ g/mL in PBS) and allowed to stand at rt for 15 min. In the dark a solution of propidium iodide was added (300 μ L; 50 μ g/mL in PBS) and left for 15 minutes at rt. The DNA content of cells was measured by flow cytometry (BD FACSVerser flow cytometer) and the cell cycle profiles were analysed on the basis of the DNA content histograms.

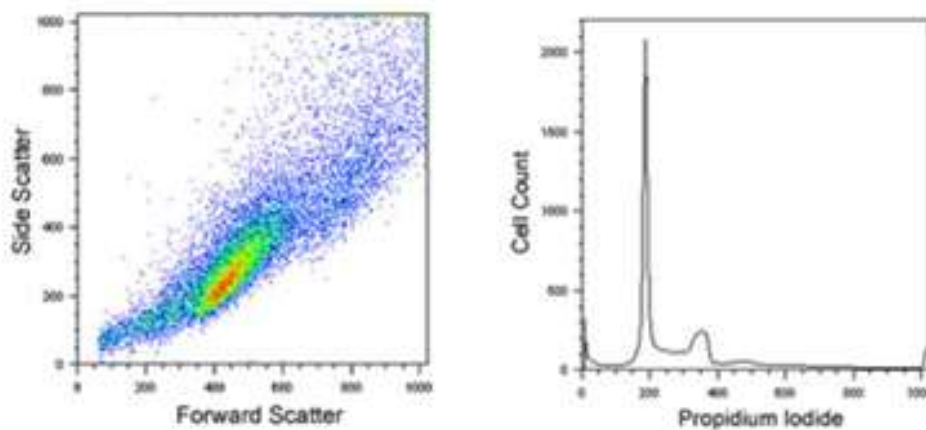


Figure 34 Example of plots acquired during cell-cycle analysis.

2.3 Experimental – Spectroscopy and microscopy

2.3.1 General

Spectroscopic grade solvents for the measurement of absorption and fluorescence spectra were purchased from commercial sources such as Sigma Aldrich, Alfa Aesar and used as supplied. Solvents were spectrophotometrically tested for impurities and background fluorescence. Fluorescence standards, dyes and reagents were also purchased from commercial sources and used as supplied. Fluorescence quantum yield standards used in the course of this work were 2-aminopyridine (2APY), anthracene and 9-chloroanthracene (9CLA).

2.3.2 Spectroscopy and microscopy instrumentation

Measurement of absorption and emission spectra

Absorption spectra were measured using a PerkinElmer Lambda 25 (190 to 1100 nm, 1 nm bandwidth). The UV/vis spectrophotometer was blanked using pure solvent before measuring sample absorptions. Steady state fluorescence emission measurements were carried out on a Jobin Yvon Horiba fluoromax-3. Fluorescence spectra of each solvent were recorded and the spectra were corrected by subtracting the fluorescence background.

Confocal and multiphoton fluorescence lifetime imaging (FLIM) microscopy

Two-photon excited fluorescence lifetimes, FLIM images, and two-photon spectra were recorded using the combined laser scanning confocal multiphoton FLIM and spectral detection setup at CLF. The system consists of a titanium-sapphire (Ti:sapphire) laser (Mira, Coherent Ltd.) tunable from 700 to 1000 nm and an optical parametric oscillator (OPO, Coherent Ltd.) pumped by a second Ti:sapphire laser for multiphoton excitation. Samples were irradiated on the stage of a Nikon TE2000-U inverted fluorescence microscope using a x60 water immersion objective (numerical aperture (NA) 1.2). Sample fluorescence was transmitted through a dichroic filter to an Acton spectrograph (Acton 275) connected to a CCD camera (Andor iDUS) allowing for the measurement of two-photon excited emission spectra and fluorescence intensities. Fluorescence lifetime measurements in liquid samples as well as fluorescence lifetime imaging (FLIM) in cells were collected when emitted light was directed to a Hamamatsu microchannel plate photomultiplier (PMT) R3809U linked to a

time-correlated single photon counting (TCSPC) system (Becker & Hickl SPC-830 and SPCimage software).

Light sheet fluorescence microscopy

Uptake measurements of the spheroids were recorded using the Leica TCS SP8 DLS system at RAL. The excitation source used for imaging was a laser diode emitting at 405 nm through a Leica HC PL Fluotar 2.5x/0.07 objective for the illumination onto the sample. A Leica HC APO L 10x/0.3 W water dipping objective was used for the detection with a notch filter to filter the emission. For each image, the field of view was 735.76 μm x 735.76 μm with 2048x2048 pixels; each pixel corresponded to 0.359 μm x 0.359 μm with an exposure time for each plane of 150 ms. Unless otherwise stated, 48 planes were collected with a spacing of 2.5 μm .

2.3.3 Extinction coefficients, spectral shifts and Lippert plots

Molar extinction coefficients were calculated from the measured absorption spectra applying the Beer-Lambert law:

$$A_{\lambda} = \epsilon_{\lambda} c \ell$$

Equation 2

where A is the absorbance at wavelength λ , ϵ is the extinction coefficient at wavelength λ , c is the sample concentration and ℓ is the path length of the sample cuvette. Molar extinction coefficients are given in units of $\text{M}^{-1} \text{cm}^{-1}$. Absorption and fluorescence spectra of *E*-combretastatins were recorded in a range of organic solvents and the Stokes shift between absorption and emission was determined for each compound. The solvent Stokes shift can be calculated from the Lippert-Mataga equation:

$$\nu_{\text{A}} - \nu_{\text{F}} = \frac{2}{hc} \left(\frac{\epsilon - 1}{2\epsilon + 1} - \frac{\eta^2 - 1}{2\eta^2 + 1} \right) \frac{(\mu_{\text{G}} - \mu_{\text{E}})^2}{a^3} + \text{constant}$$

Equation 3

Where h ($6.62 \times 10^{-34} \text{ m}^2 \text{kg/s}$) is the Planck's constant, c ($3 \times 10^{10} \text{ cm s}^{-1}$) is the speed of light, a (8 Å) is the Onsager radius, ν_{A} and ν_{F} describe the absorption and emission wavenumbers (cm^{-1}) respectively. The dielectric constant (ϵ) and refractive index (η) are solvent properties and the electric dipole moments in the ground state and excited state are given in Debye

(D). The first part of this equation mathematically describes the spectral shifts caused by electron redistribution in the solvent molecules and reorientation of solvent redistribution. The second part refers to the redistribution of electrons. Calculating the difference of the two will give the spectral shift that is caused by orientation of solvent molecules.

Lippert plots for the determination of the spectral sensitivity of absorption and emission of *E*-combretastatins in a range of solvents were prepared from a plot of $(V_A - V_F) \cdot 10^{-3}$ versus the orientation polarizability (ΔF).

$$\Delta F = \left(\frac{\epsilon - 1}{2\epsilon + 1} - \frac{\eta^2 - 1}{2\eta^2 + 1} \right)$$

Equation 4

The slope of the Lippert plot was used to determine the change in dipole moment ($\mu^* - \mu$) of the *E*-combretastatins from the following equation:

$$(\mu^* - \mu)^2 = \frac{\text{slope}}{2} * hca^3$$

Equation 5

Where h is the Planck's constant ($6.62 \times 10^{-34} \text{ m}^2\text{kg/s}$), c ($3 \times 10^{10} \text{ cm s}^{-1}$) is the speed of light, a (4.2 \AA) is the Onsager radius based on volume. The units of $(\mu^* - \mu)$ from this equation are electrostatic unit (esu) cm, since $1 \text{ Debye (D)} = 1 \times 10^{-18} \text{ esu cm}$ the change in dipole moment can be calculated in Debye.

2.3.4 Determination of fluorescence quantum yields Φ_F

One-photon excited fluorescence quantum yields at room temperature were determined using the fluorescence standards anthracene in EtOH ($\Phi_F = 0.28$) or 9-chloroanthracene (9CLA) in DCM ($\Phi_F = 0.90$; determined relative to anthracene in EtOH). The standards were diluted to obtain a range of solutions with optical densities ≤ 0.1 . Absorption and corrected fluorescence spectra were recorded in standard 10 mm quartz cuvettes. The standards of the Φ_F calculations were excited at 349 nm. Combretastatins were excited at the wavelengths specified with a narrow slit width to reduce photoisomerization and photobleaching of samples during irradiation. Integrated fluorescent intensities vs. $1 - 10^{-\text{ABS}}$ at excitation wavelengths were plotted using Microsoft excel to give a straight line passing

through 0 intercept. The slope obtained from this graph is proportional to the quantum yield of samples and can be used in the following equation:

$$\Phi_s = \Phi_r * \left(\frac{\text{Grad } s}{\text{Grad } r} \right) * \left(\frac{\eta^2 s}{\eta^2 r} \right)$$

Equation 6

Where subscripts s and r refer to sample and reference respectively, Φ is the fluorescence quantum yield, grad is the gradient and η is the refractive index of the solvent (applied to correct for differing solvents).

2.3.5 Fluorescence lifetime measurements

Solutions of combretastatins in different solvents and of concentrations less than 0.5 mM (to avoid self quenching) were prepared and placed in a custom-made dish with cover slip to avoid solvent evaporation. Fluorescence lifetimes were measured using the FLIM system and data processed using the TPSPC software package by Becker & Hickl. Unless otherwise stated lifetimes were recorded to 10^3 - 10^4 counts in peak channel and good fits were obtained for single exponential decay.

2.3.6 Non-linear power dependence of combretastatins

Power dependences of the *E*-combretastatin derivatives in solution and cells were measured using the multiphoton microscope to determine if the absorptions were a two photon process. All samples were excited using the multiphoton FLIM system as described above. For experiments in solution, 9CLA (5 mM) in DCM and *E*-CA4F (5 mM) in DCM was used as an absorption reference standard. Demonstrating the two-photon absorption of 9CLA at the excitation wavelengths of *E*-combretastatins was important as it was also used as the standard for the two photon absorption (2PA) cross sections. Solutions of 9CLA were excited at 720 and 760 nm at increasing laser powers (mW). Solutions of *E*-combretastatins were excited at wavelengths specified and excited at increasing laser powers on the multiphoton FLIM microscope stage. Plots of fluorescence intensity vs. laser power (mW) were prepared using Microsoft excel.

2.3.7 2PA cross sections of combretastatins

Solutions of *E*-combretastatins in DCM of an approximate concentration of 0.5 mM were prepared and placed in a custom made dish with cover slip to avoid solvent evaporation. A solution of 9CLA (1 mM) in DCM was prepared as a reference sample for the 2PA measurements. 2PA spectra were recorded by tuning the laser to excitation wavelengths in a range from 680-760 nm. Fluorescence spectra were acquired using the Leica LAS X software on the lightsheet microscope system. Sample 2PA cross-sections at each wavelength were calculated from the intensity data using a corrected version of the equation by Mathai (Mathai *et al.*, 2007).

$$\sigma_{2s} = \frac{c_r}{c_s} * \frac{I_{\lambda s}}{I_{\lambda r}} * \frac{\left(\frac{FI_{\lambda r}}{\Sigma FI_r}\right)}{\left(\frac{FI_{\lambda s}}{\Sigma FI_s}\right)} * \frac{\Phi_r}{\Phi_s} * \sigma_{2r}$$

Equation 7

The subscripts s and r refer to the sample of interest and reference respectively, σ_2 describes the two-photon absorption cross-section, c is the concentration, I_λ is the two-photon induced fluorescence intensity at the wavelength λ , FI_λ is the one-photon induced fluorescence intensity at the wavelength λ , ΣFI is the integrated intensity of one-photon induced fluorescence spectra and Φ the one-photon fluorescence quantum yield.

2.3.8 Image analysis using Fiji

Fiji is an image processing package which was used to analyse the uptake of combretastatins (Schindelin *et al.*, 2012). Images were converted to .tif and imported into the software. The smallest units from which an image is composed are its pixel; the pixels are measurements of the light being emitted by a sample. Fiji allows for the analysis of individual pixel to determine a value for the fluorescence of the overall image.

3. Results & discussion - Synthesis of *E*- and *Z*-

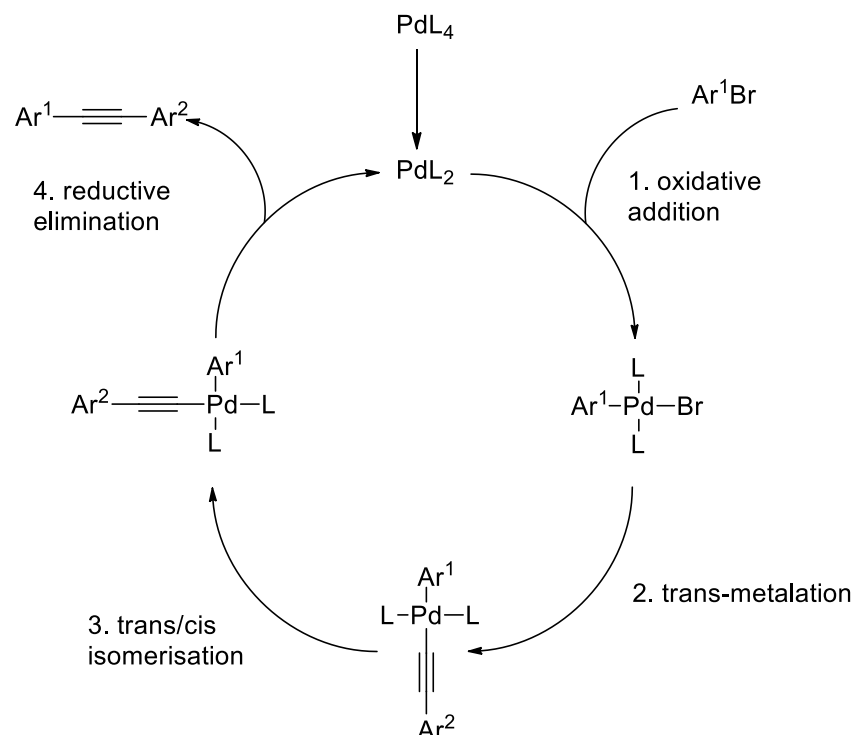
Combretastatins

A range of combretastatin derivatives in the *cis(Z)*- and *trans(E)*- conformation have been successfully synthesised using either the Wittig reaction (Wittig and Schöllkopf, 1954) or the Suzuki cross-coupling reaction (Miyaura *et al.*, 1979) followed by iodine catalysed *cis* to *trans* isomerisation (Dickinson & Lotzkar, 1937; Gaukroger *et al.*, 2001b). Secondary alcohols were synthesised from the corresponding aldehydes using a Grignard reaction (Grignard, 1900) and then oxidised to the corresponding ketone. Another method investigated was the synthesis of diarylalkynes using the Sonogashira coupling method followed by hydrogenation to the corresponding alkene.

3.1 Synthesis of diarylalkynes using Sonogashira cross-coupling

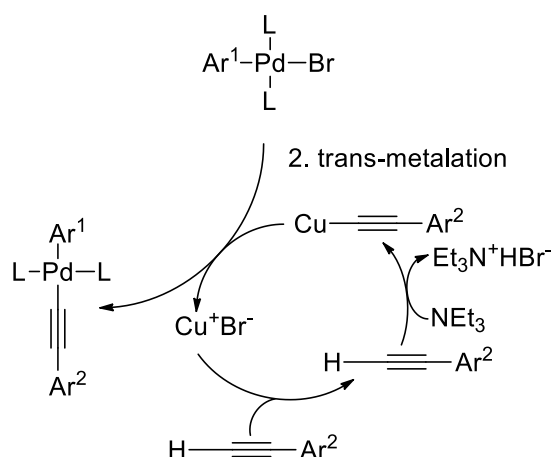
Sonogashira cross-coupling, first reported in 1975 by Kenkichi Sonogashira (Sonogashira *et al.*, 1975), is the coupling of a terminal sp hybridised carbon of an alkyne with a sp^2 carbon of an aryl or vinyl halide. The reaction can be carried out under mild conditions, such as at room temperature, using a palladium source as catalyst, a copper co-catalyst in a basic solvent. Although the addition of copper was beneficial in increasing the reactivity, it was necessary to avoid the presence of oxygen in order to avoid alkene homocoupling through a copper-mediated Hay/Glaser reaction (Evano *et al.*, 2008) and so reactions were carried out in an inert atmosphere.

The Sonogashira cross-coupling reaction can be employed in the synthesis of complex molecules. The general reaction scheme can be found in Scheme 9. The palladium-cycle is a typical C-C cross-coupling formation; the addition of the aryl or vinyl halide and subsequent oxidation of Pd^0 to Pd^{2+} is thought to be the rate-limiting step. It is presumed to proceed by an end-on ligation of the halogen to the palladium and so could be regarded as electron donating (Chinchilla & Nájera, 2011). The terminal alkyne and copper catalyst form a copper acetylide in the copper catalytic cycle. Transmetalation of palladium with the copper acetylide reagent forms a Pd-C bond and regenerates the copper halide catalyst. Isomerisation brings the two groups closer together and the reductive elimination of Pd^{2+} to Pd^0 is the driving force for the formation of a new C-C bond.



Scheme 9: Sonogashira cross-coupling mechanism

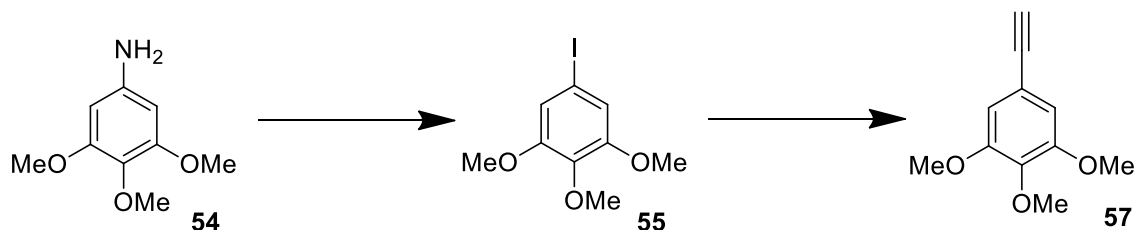
The trans-metalation step features a second catalytic cycle of copper which is still poorly understood. It is suggested that the presence of base results in the formation of a π -alkyne complex which makes the terminal proton on the alkyne more acidic, leading to the formation of the copper acetylide, which continues to react with the oxidative addition product, with regeneration of the copper halide (Scheme 10).



Scheme 10: Copper catalytic cycle

5-Iodo-1,2,3-trimethoxybenzene **55** was prepared, as described by Cardolaccia and co-workers from the corresponding aniline **54** (Cardolaccia *et al.*, 2008). The aniline was reacted with sodium nitrite to form a diazonium salt which was then iodinated to give the

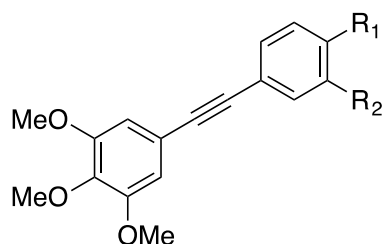
iodo-benzene **55** in excellent yield (83%). 5-Ethynyl-1,2,3-trimethoxybenzene **57** was prepared in fair yield (56%) by the coupling of iodo-benzene with trimethylsilylacetylene followed by deprotection with potassium carbonate (Scheme 11).



Scheme 11: Synthesis of 3,4,5-trimethoxyphenylacetylene

5-Ethynyl-1,2,3-trimethoxybenzene and *tetrakis*(triphenylphosphine)palladium(0) in dry *n*-propylamine (method A) or palladium(II) acetate and triphenylphosphine in dry triethylamine (method B) was added to appropriately substituted aryl halides and heated to reflux, to afford diarylalkynes (Table 5).

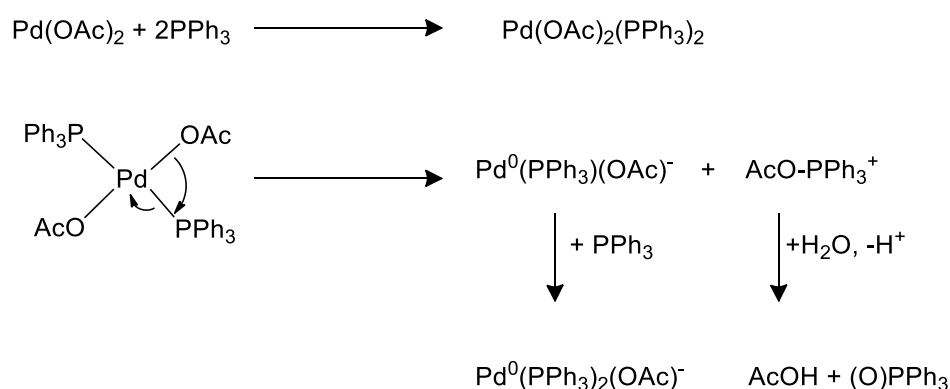
Table 5: Alkynes synthesised following Sonogashira cross-coupling.



Compound	R ₁	R ₂	Method	Yield (%)
58	COCH ₃	H	A	62
59	OCH ₃	H	A	78
60	CHO	H	A	62
61	CN	H	A	64
62	COCH ₃	OH	B	76
63	CHO	OH	B	71
64	CN	F	B	60

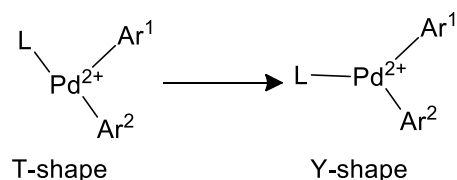
Diarylalkynes in which the second ring were para substituted were synthesised in good yields (~65%) following method A whilst diarylalkynes that were para/meta substituted on the second ring did not couple under these reaction conditions but coupled well following method B.

Several studies have focused on the influence of steric and electronic effects of ligands on individual steps of the catalytic cycle. In the oxidative addition step, electron-withdrawing ligands can stabilise palladium complexes whilst electron-donating ligands generate an electron-rich complex which reacts faster (Christmann & Vilar, 2005) explaining for the higher yield observed when the R group was electron donating. A second method, in which a stronger base was used with Pd(OAc)₂ and PPh₃ generating the 16-electron anion [Pd(PPh₃)(OAc)]⁻ *in situ* (Scheme 12) to undergo oxidative addition, gave diarylalkynes in good yields.



Scheme 12: Mechanism of the formation of Pd⁰ from Pd(OAc)₂ and PPh₃

For reactions with a slow trans-metalation step, it has been reported that the formation of a T-shaped 14-electron intermediate can enhance the step and further rearrangement to a Y-shaped species accelerates reductive elimination (Scheme 13) (Espinet & Echavarren, 2004). It may have been the case that the more substituted aryl ring slowed the trans-metalation step; the 14-electron palladium complex formed in the oxidative addition of Pd⁰(PPh₃)₂(OAc)⁻ appeared to overcome this.

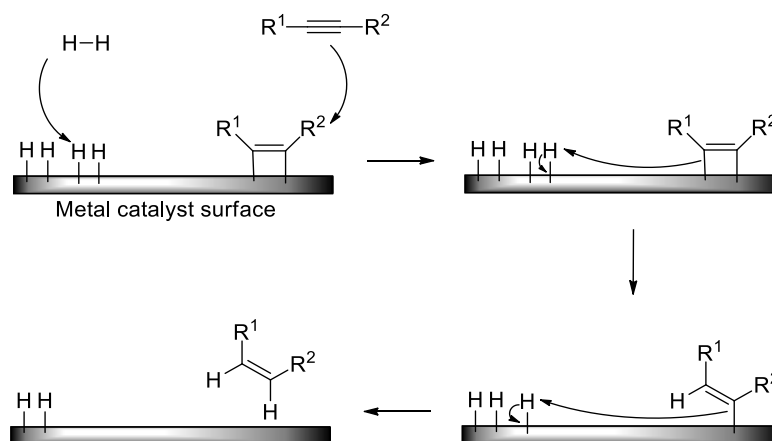


Scheme 13: The rearrangement of a Pd²⁺ intermediate to accelerate reductive elimination

3.1.1 Semihydrogenation of alkynes

Alkynes contain two carbon-carbon π -bonds which can be reduced to form alkanes, reducing just one of these π -bonds forms an alkene. The selective hydrogenation of internal alkynes to *cis*-alkenes can be achieved by hydrogenation with molecular hydrogen in the presence of Lindlar's catalyst and transfer hydrogenation with hydrogen donors. Catalysts can cause either *anti*- or *syn*-addition of hydrogens across the triple bond and thus determine the geometry of the product. There is a lot of literature describing the hydrogenation of alkynes using nanocatalysts which were not possible to explore at Salford. Examples include catalysts such as nanoporous gold (Wagh & Asao, 2015), single crystal nanoparticles (Attard *et al.*, 2013), iron nanoparticles (Phua *et al.*, 2009) and silica supported copper nanoparticles (Fedorov *et al.*, 2016).

The general catalytic hydrogenation mechanism on metal catalysts of alkynes is comparable to that of alkenes. With the presence of a metal catalyst, the H-H bond in gaseous H₂ cleaves and each hydrogen attaches to the metal surface as does the alkyne or alkene. A hydrogen atom is transferred, forming a C-H bond followed by a second hydrogen forming the second C-H bond. Due to the physical arrangement of the alkyne or alkene on the metal surface, the two hydrogens add to the same face of the double bond i.e. *syn* addition (Scheme 14).

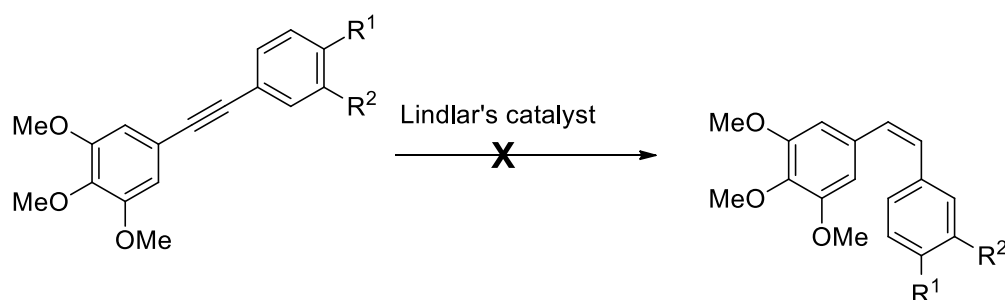


Scheme 14: Catalytic hydrogenation mechanism

Lindlar's Catalyst

Hydrogenation is an interruptible process and so can be stopped using modified catalysts at the transitional alkene stage. The Lindlar hydrogenation (Lindlar, 1952) is a stereoselective reduction of alkynes to *cis*-alkenes in the presence of palladium supported on calcium carbonate and "poisoned" with lead acetate and quinoline to reduce the activity. However, *cis/trans* isomerization and over-reduction of alkenes to the corresponding alkanes due to the difficulty of the control of a stoichiometric amount of H₂ may occur. Further, the use of lead and highly flammable H₂ gas is undesirable (Richmond & Moran, 2015).

Appropriately substituted alkynes were dissolved in hexane and treated with hydrogen gas *via* balloon, Lindlar's catalyst was added and the mixture stirred but upon analysis the alkyne had not hydrogenated. The reaction was repeated in an autoclave in which the pressure was increased to two atmospheres but still no hydrogenation was observed.



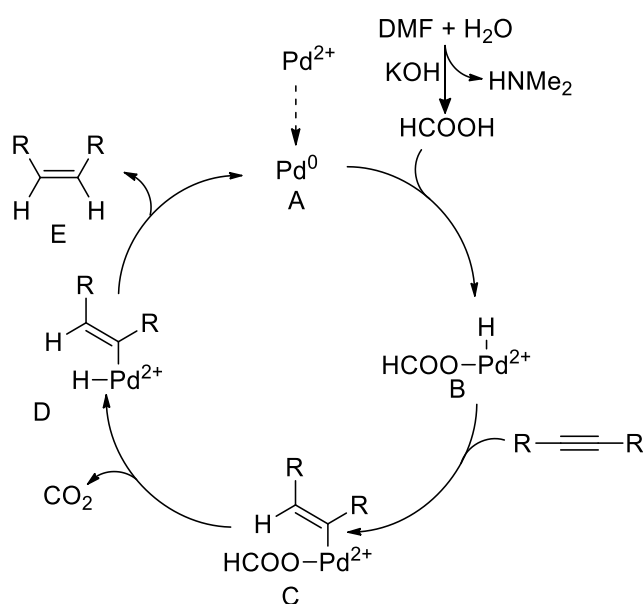
Scheme 15: Attempted semihydrogenation of alkynes with Lindlar's catalyst

Lindlar's catalyst purchased commercially is known for its variability between batches (Richmond & Moran, 2015). Further, due to the electron donating nature of the methoxy groups on one ring and the electron withdrawing groups on the other ring the alkyne bond has a low electron density. It has been reported that for alkyne hydrogenation, high electron density is preferable as a low electron density increases the energy barrier of the reaction (Rajaram *et al.*, 1983).

Transfer hydrogenation

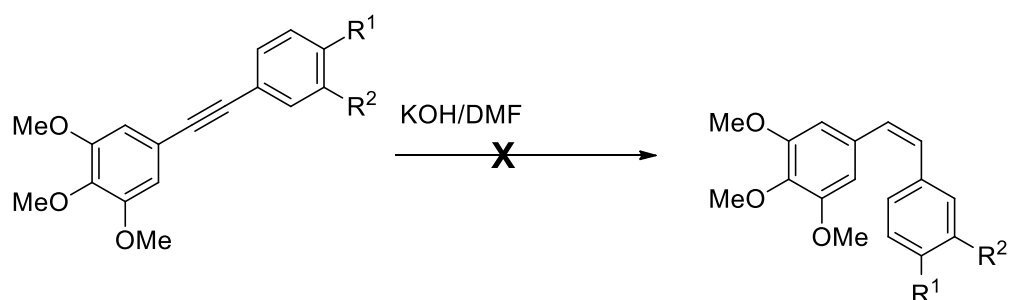
Transfer hydrogenation is the addition of hydrogen to a molecule from a source other than gaseous H₂, avoiding the use of highly flammable H₂ gas. The use of hydrogen donors also allows for better control over chemoselectivity. Transfer hydrogenation agents include silanes (Trost & Braslau, 1989; Semba *et al.*, 2012) and formic acid (Tani *et al.*, 1993).

Li and co-workers reported the semihydrogenation of various internal alkynes in which formic acid was generated *in situ* from KOH and DMF as a hydrogen source to give *cis*-alkenes (Li *et al.*, 2010). They proposed a mechanism for the Pd(OAc)₂ catalysed semihydrogenation. Formic acid is formed from DMF and water in the presence of potassium hydroxide; the oxidative addition of formic acid to Pd⁰ gave intermediate B followed by insertion of alkyne into Pd-H bond to give intermediate C. Decarboxylation and reductive elimination of the C-C bond afforded *cis* alkenes E, regenerating the Pd⁰ (A, Scheme 16).



Scheme 16: Proposed mechanism for Pd(OAc)₂ catalysed semihydrogenation of internal alkynes

Alkyne, KOH and catalytic Pd(OAc)₂ in DMF were added to a sealed vial under an argon atmosphere and heated to 145 °C with stirring for 6 h. Upon analysis the alkyne remained. The reaction time was increased and the reaction was also repeated in the microwave but no reduction was observed.

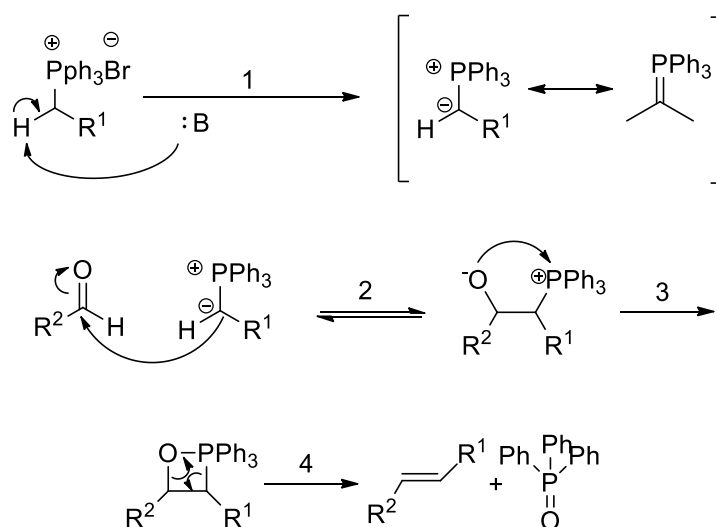


Scheme 17: Attempted transfer hydrogenation with KOH/DMF

Again, the issue of hydrogenation may have arisen from the substituents on the second ring causing an electron-deficient alkyne bond that is less favourable to bond to the palladium. Upon introduction to the palladium cycle the alkyne is reduced, the electron-deficient alkynes are again not favourable for this reaction. Due to time constraints, other methods were explored to synthesise combretastatins.

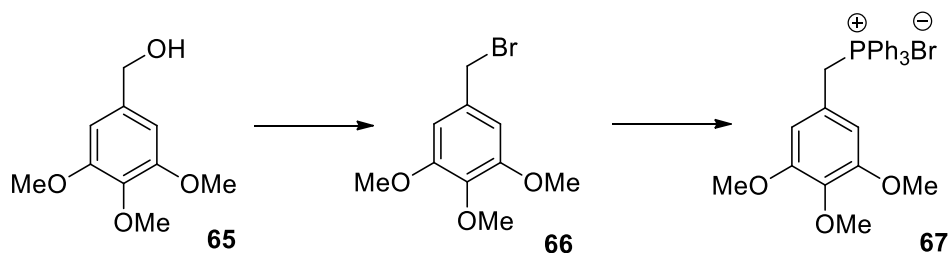
3.2 Synthesis of *E*- and *Z*-combretastatins using the Wittig reaction

The Wittig reaction is one of the most commonly used methods in the synthesis of alkenes owing to quite mild reaction conditions and easily obtainable starting materials; ylides are formed *in situ* upon deprotonation of the corresponding phosphonium salt. The Wittig reaction is one of the most commonly used procedures for the preparation of combretastatin derivatives (Pettit *et al.*, 1995; Pinney *et al.*, 2000) with the complete synthesis of CA4 first being published in 1995 utilising this method (Pettit *et al.*, 1995a). In short, the Wittig reaction occurs between a carbonyl compound (most commonly aldehyde or ketone) and a phosphonium ylide to give an alkene with phosphine oxide as the by-product (Wittig & Schöllkopf, 1954) as shown in Scheme 18. In the presence of a base, the phosphonium salt forms an ylide; the ylide can be represented in the fully ionic ylide form or the ylene form (Scheme 18, step 1). Addition of the ylide to a carbonyl leads to a zwitterionic intermediate (step 2) which then closes to form a four-membered ring (step 3). The driving force for the final step is the formation of a very stable phosphine oxide (step 4).



Scheme 18: Wittig mechanism

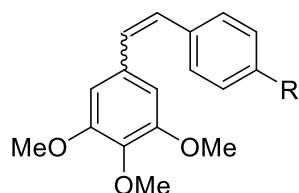
3,4,5-Trimethoxybenzyltriphenylphosphonium bromide **67** was prepared as described (Gaukroger *et al.*, 2001) from the corresponding benzyl alcohol **65**. The benzyl alcohol **65** was reacted with phosphorous tribromide to give bromide **66** in excellent yield (78%). The corresponding phosphonium salt **67** was prepared in excellent yield (88%) by the reaction of triphenylphosphine with the benzyl bromide **66** (Scheme 19).



Scheme 19: Synthesis of 3,4,5-trimethoxybenzyltriphenylphosphonium bromide

The ylide, formed by reaction of the 3,4,5-trimethoxy-benzyltriphenylphosphonium bromide **67** with *n*-butyllithium in THF at -15 °C, was treated with appropriately substituted benzaldehydes to afford a mixture of *E*- and *Z*-stilbenes, Table 6.

Table 6: *Z*- and *E*-stilbenes synthesised following the Wittig method



Compound	R	Configuration	Yield (%)
42Z	CHO	<i>Z</i>	41
42E	CHO	<i>E</i>	43
50Z	CN	<i>Z</i>	39
50E	CN	<i>E</i>	42

The Wittig reaction provided a mixture of *cis*- and *trans*-combretastatins. Experimental conditions such as the presence of lithium salts or the nature of the solvent noticeably influence the selectivity of the reaction (Schlosser, 1970) and the type of ylide has a high level of geometrical control (Vedejs & Peterson, 1994). Phosphorus ylides can be classified according to their reactivity; stabilised ylides with strongly conjugating substituents tend to

favour *E*-alkenes whilst non-stabilised ylides favour *Z*-alkenes. 'Semi-stabilised' ylides with moderate conjugation do not give preference to either isomer as observed in the synthesis of combretastatin derivatives (Maryanoff, 1989). The ylide formed in this reaction was semi-stabilised and so gave a 1:1 mixture of *E*:*Z* alkenes.

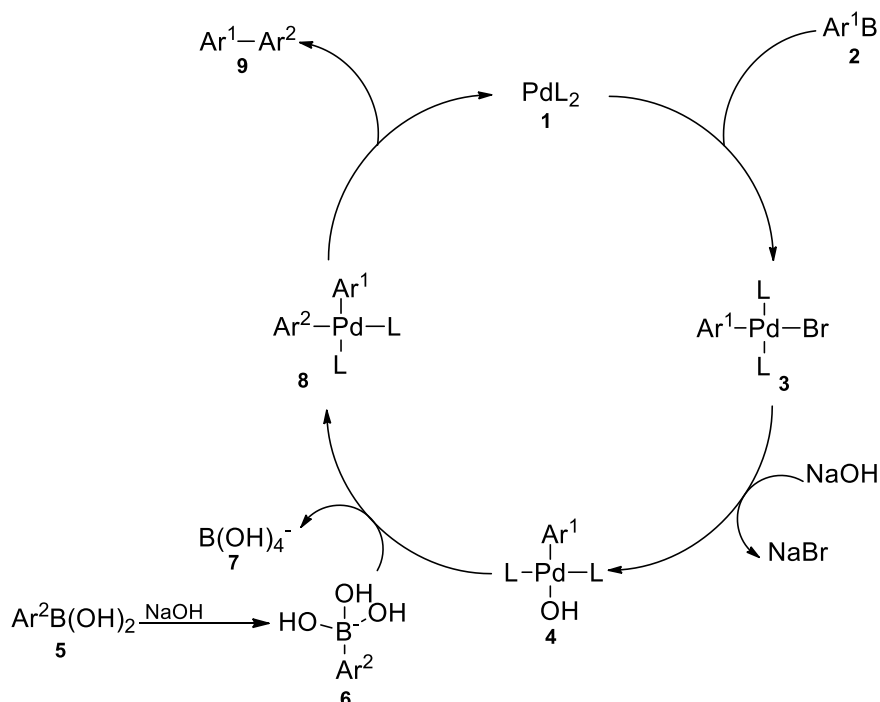
The *cis*- and *trans*- isomers were separated using column chromatography and in all cases the *cis*-isomers were the first to elute. Separation was extremely difficult and time consuming as the *R_f* values of the *cis* and *trans* isomers were very close; the difficulty of separation of combretastatin isomers by flash column chromatography has been reported (Hadfield *et al.*, 2006).

The Wittig reaction in the synthesis of combretastatins was non-stereoselective owing to the semi-stabilised ylide generated *in situ* from the alkyl phosphonium salt creating isomers difficult to separate. For this reason, a reaction with increased *cis* selectivity was desirable and so the Suzuki method was utilised to stereoselectively synthesise *cis* stilbenes.

3.3 Synthesis of *Z*-combretastatins using Suzuki-Miyaura coupling

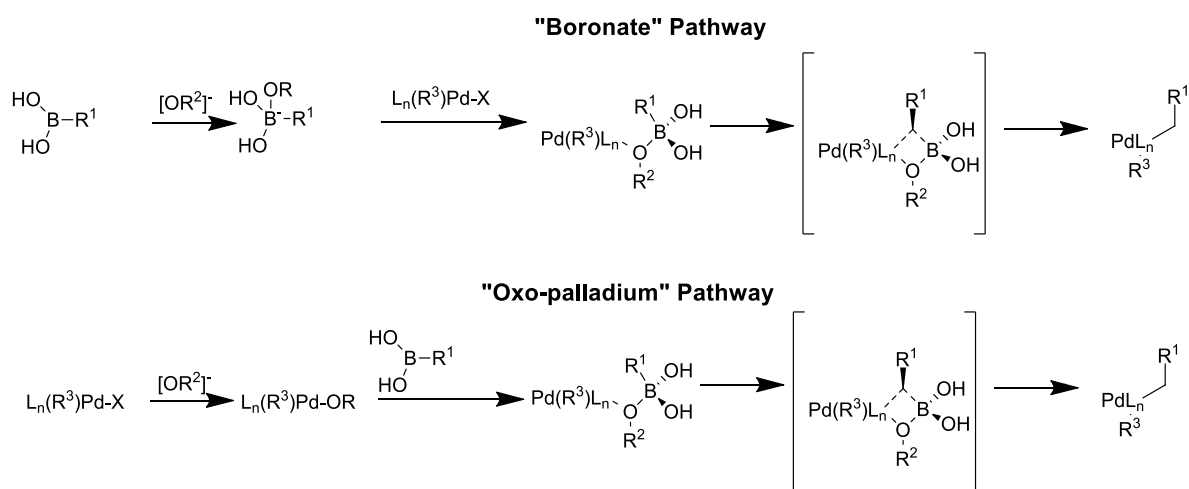
Suzuki-Miyaura cross-coupling, first published in 1979 by Akira Suzuki, is perhaps the most widely-applied carbon-carbon bond forming reaction between aryl or vinyl halides with aryl or vinyl organoboron reagents catalysed by a transition metal (Miyaura *et al.*, 1979; Miyaura & Suzuki, 1979). The Suzuki-Miyaura reaction is an attractive approach to cross-coupling and has a broad application in the formation of carbon-carbon bonds owing to the mild reaction conditions and broad functional group toleration (Ishiyama *et al.*, 1995). Organoboron reagents are typically environmentally benign and commercially available and readily react with palladium complexes.

The simplest mechanism for the Suzuki reaction used for the formation of a carbon-carbon bond is shown in Scheme 20. The first step is oxidative addition of palladium (1) to the alkyl / aryl halide (2); palladium is further oxidised upon donation of electrons to form a Pd-C bond (3). Addition of base gives intermediate (4) and transmetalation with nucleophilic organic groups transferred from boron (6) to palladium forms a second Pd-C bond (8). Reductive elimination drives the formation of a single carbon-carbon bond (9).



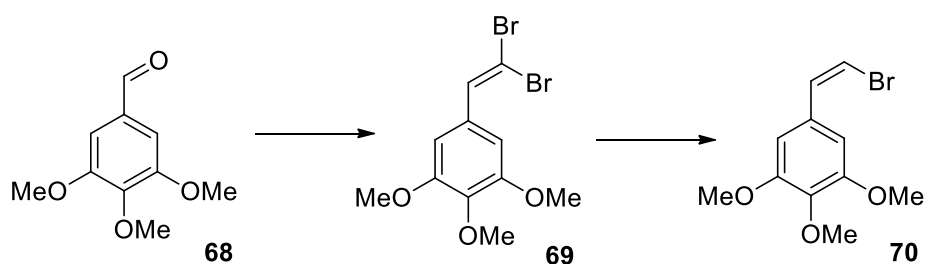
Scheme 20: Suzuki coupling mechanism

Suzuki and Miyaura conducted a study to determine the role of base in the reaction (Miyaura *et al.*, 1985). They considered whether the role of the base was to react with the borane to make it more nucleophilic (boronate pathway) or whether it reacted with the palladium to make a more reactive species (oxo-palladium pathway). Further stoichiometric studies gave evidence in favour of the oxo-palladium pathway (Miyaura *et al.*, 1985; Suzuki, 1999).



Scheme 21: Two mechanisms considered for transmetalation of alkenylboranes with palladium complexes

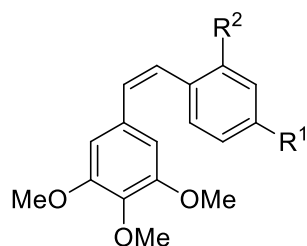
5-(2,2-Dibromovinyl)-1,2,3-trimethoxybenzene **69** was prepared from 3,4,5-trimethoxybenzaldehyde **68** (Gaukroger *et al.*, 2001a). The benzaldehyde was reacted with carbon tetrabromide and triphenylphosphine following the Corey-Fuchs reaction; a one-carbon homologation of an aldehyde comparable to a Wittig reaction to give the dibromovinyl **69** in excellent yield (83%). Stereoselective debromination with tri *n*-butyltin hydride in dry toluene afforded 5-[(*Z*)-2-bromovinyl]-1,2,3-trimethoxybenzene **70** in excellent yield (73%, Scheme 22).



Scheme 22: Synthesis of 5-[(*Z*)-2-Bromovinyl]-1,2,3-trimethoxybenzene

5-[(*Z*)-2-Bromovinyl]-1,2,3-trimethoxybenzene and *tetrakis*(triphenylphosphine) palladium(0) in dry DME were deoxygenated and treated with appropriately substituted boronic acids and Na₂CO₃ at 80 °C as per **procedure D** to afford *Z*-stilbenes Table 7.

Table 7: *Z*-stilbenes synthesised following the Suzuki method

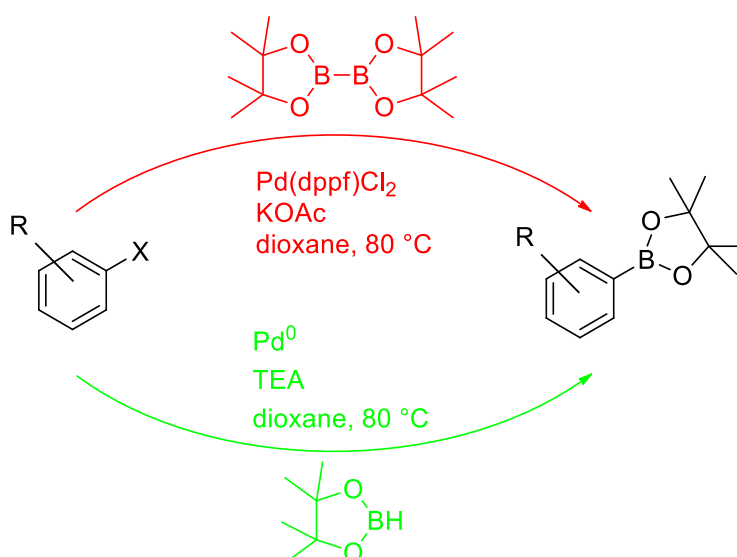


Compound	R ¹	R ²	Yield (%)
44	OMe	CHO	79
45	H	CHO	84
46	COCH ₃	H	76
49	H	COCH ₃	85
71	H	CN	71

The *cis*- isomer was separated from the de-borylated starting material following column chromatography. Separation was much easier than that observed in Wittig chemistry and in all cases the de-borylated starting material eluted first. The Suzuki method preserved alkene geometry from starting material to product affording selectively *cis*- stilbenes in each case, allowing for much higher yields (70-80%). Varying the functional groups of the aryl boronic acid didn't cause much variation in yield, due to the broad functional group toleration of this cross-coupling method.

Not all required boronic acids were commercially available and required synthesis. Although boronic acids are more reactive, the synthesis of the corresponding boronic pinacol esters was favoured due to their stability towards column chromatography making them easy to isolate and purify. Furthermore, boronic esters dissolve readily in apolar solvents and unlike boronic acids, are not hydrogen bond donors or able to oligomerise making them more stable reagents (Lennox & Lloyd-Jones, 2014).

Boronic esters can be synthesised by Miyaura borylation (Ishiyama *et al.*, 1995), a palladium catalysed reaction with bis(pinacolato)diboron (B_2pin_2) and Musada borylation (Murata *et al.*, 1997) that uses pinacol borane directly (Scheme 23).

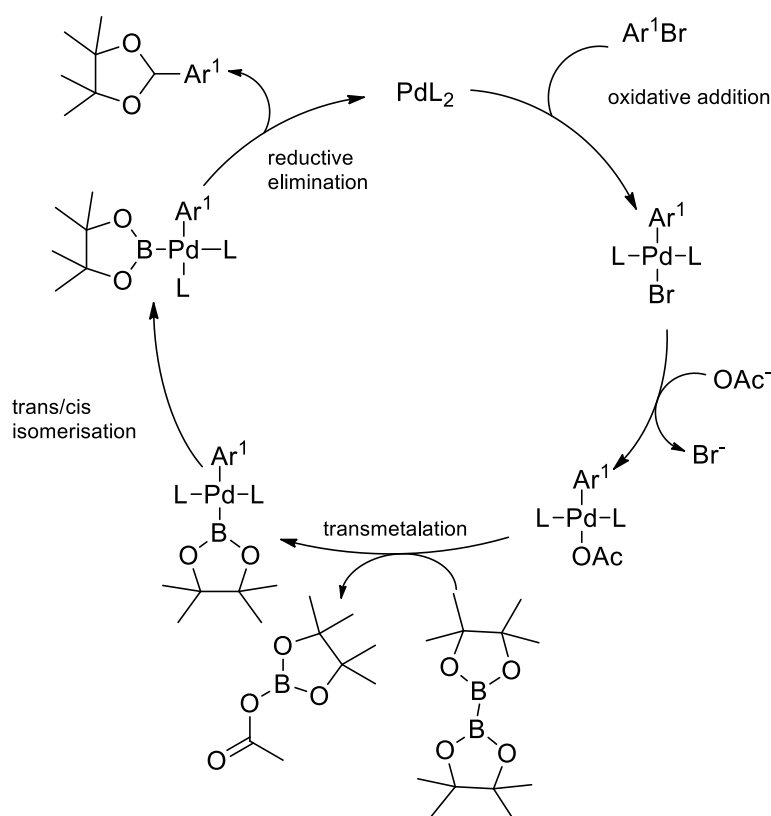


Scheme 23: Two routes to form boronic esters

Boronic esters were synthesised following the Miyaura borylation transformation; this route is highly functional group tolerant and uses commercially available starting materials, allowing access to a wide variety of substrates (Lennox & Lloyd-Jones, 2014).

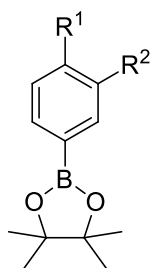
3.3.1 Miyaura borylation

The Miyaura borylation (Scheme 24) is mechanistically similar to the Suzuki-coupling in that it proceeds through Pd⁰/Pd²⁺ oxidation. Oxidative addition of an aryl halide increases the oxidation state of Pd⁰ to Pd²⁺ forming a Pd-O bond. Although B₂Pin₂ is a poor Lewis acid, the formation of Pd²⁺ through a Pd-O bond drives the transmetalation step. The driving force for the final step is the formation of a stable boronate and the reductive elimination of Pd²⁺ to Pd⁰.



Scheme 24: Miyaura borylation mechanism of action

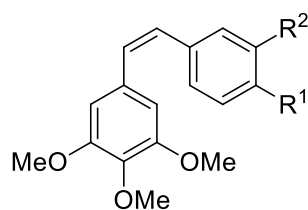
Appropriately substituted aryl halide, Pd(dppf)₂Cl₂, KOAc and *bis*(pinacolato)diboron in dry 1,4-dioxane were stirred under argon at 0 °C then heated to 120 °C in a sealed vial as per **procedure E** to afford boronates **73-79** (Table 8).

Table 8: Boronic ester synthesis

Compound	R ¹	R ²	Yield (%)
73	CHO	OH	78
75	COCH ₃	OH	69
77	CN	OH	76
79	COOH	OH	57

The reaction required longer than the 5 h reported in the literature (Mamiya *et al.*, 2015a) but upon heating overnight and recrystallizing from hexane, boronates were obtained in good yields (~70%). Competitive Suzuki–Miyaura coupling between the resulting boronic ester and organohalide could be problematic and so the choice of base was crucial to suppress Suzuki–Miyaura coupling; a hard Lewis-base such as KOAc (Takagi *et al.*, 2002) gave the greatest selectivity, avoiding competitive coupling.

Coupling of 5-[(*Z*)-2-bromovinyl]-1,2,3-trimethoxybenzene **70** and appropriately substituted boronic pinacol esters in dry 1,4-dioxane and water in the presence of K₃PO₄ and *tetrakis*(triphenylphosphine) palladium(0), as per **procedure F**, afforded a number of *Z*-stilbenes (Table 9).

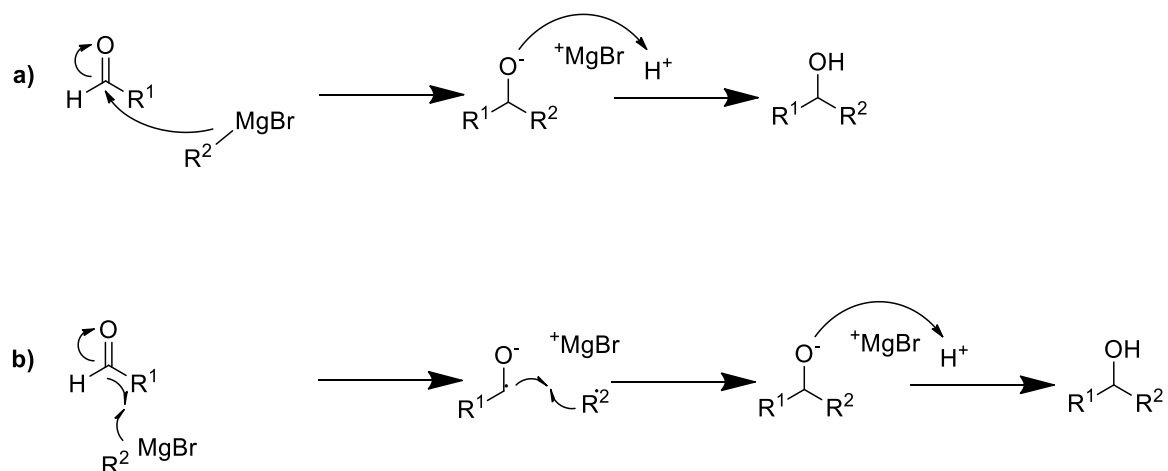
Table 9: Z-stilbenes synthesised following the Suzuki method

Compound	R ₁	R ₂	Yield (%)
43	CHO	OH	54
47	COCH ₃	OH	56
51	CN	OH	48
53	COOH	OH	43

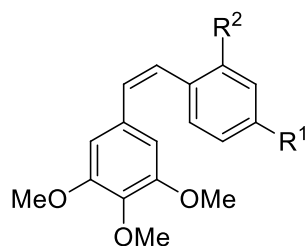
Yields were much lower following the coupling of 5-[(*Z*)-2-bromovinyl]-1,2,3-trimethoxybenzene **70** with boronic esters than observed in the coupling with boronic acids owing to the σ -donating ability of carbon, allowing the lone pairs of oxygen in boronic esters to be more readily conjugated into the electron deficient boron centre (Lennox & Lloyd-Jones, 2014).

3.4 Synthesis of secondary alcohols from aldehydes

The Grignard reaction, named after its namesake Victor Grignard and for which he was awarded the Nobel Prize, is the addition of an organomagnesium halide (Grignard reagent) to an aldehyde or ketone to form a secondary or tertiary alcohol respectively (Grignard, 1900). Grignard reagents are strong nucleophiles; the electronegativity of carbon (2.5) and magnesium (1.31) make the bond polarized towards the carbon making it more electron rich, allowing the carbon to act as a nucleophile. The nucleophilic carbon attacks the electrophilic carbonyl, performing a 1,2-addition to give an alkoxide. Addition of acid gives the alcohol (Scheme 25a). More hindered reagents are thought to proceed through a single-electron transfer mechanism (Scheme 25b).

**Scheme 25: Grignard mechanisms**

Combretastatin derivatives with an aldehyde substituent were treated with an excess of methyl magnesium bromide in THF at 0 °C to afford secondary alcohol as per **procedure G** (table 6).

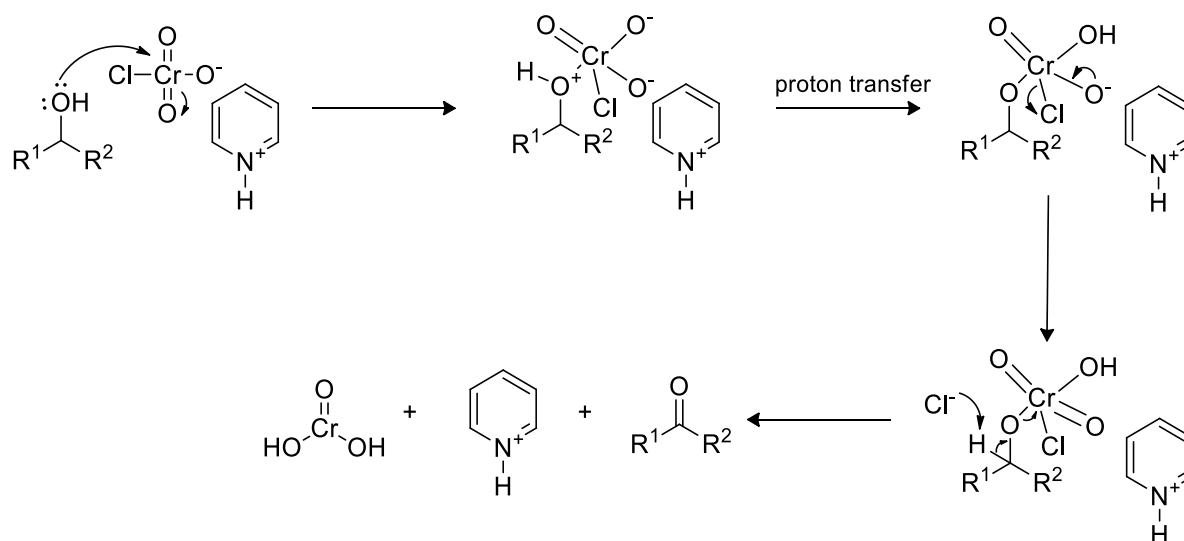
Table 10: Z-stilbenes with secondary alcohol functional group

Compound	R ¹	R ²	Yield (%)
52		H	90
80	OMe		69
81	H		82

The secondary alcohol were isolated upon addition of saturated ammonium chloride to quench the excess Grignard reagent. The reaction reached completion after approximately 1 h in good yields.

3.1.4.1 Oxidation to corresponding ketones

Pyridinium chlorochromate (PCC) oxidises primary alcohols to aldehydes and secondary alcohols to ketones in an elimination type reaction. A lone pair of electrons on the oxygen can attack chromium forming a Cr-O bond followed by proton transfer of the hydrogen on the positively charged oxygen to an oxygen on the chromium. The chlorine is displaced which removes the proton on the carbon adjacent to the oxygen in a 1,2-elimination type reaction.



Scheme 26: Oxidation of secondary alcohols to ketones with PCC

Secondary alcohols were treated with excess PCC and an equal mass of silica in DCM at room temperature for 2 hours. Ketone **46** was isolated in good yield (46%, Figure 35).

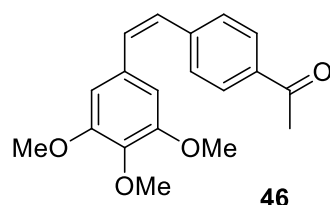


Figure 35 Ketone isolated from secondary alcohol

However combretastatins with the secondary alcohol in the *ortho*-position appeared to have decomposed upon analysis. It is possible that due to the close proximity of the alcohol to the alkene bond, the chromium formed a complex (Figure 36) with the alkene and cleaved the double bond. This is supported in the ¹H-NMR spectra which appeared to be

that of 3,4,5-trimethoxybenzaldehyde. The reaction appears to have proceeded in an oxidative cleavage reaction in which the C-C bond is cleaved, forming a C=O bond.

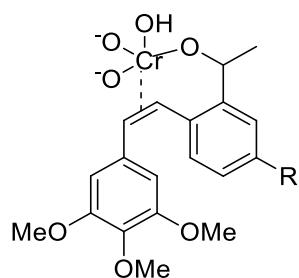
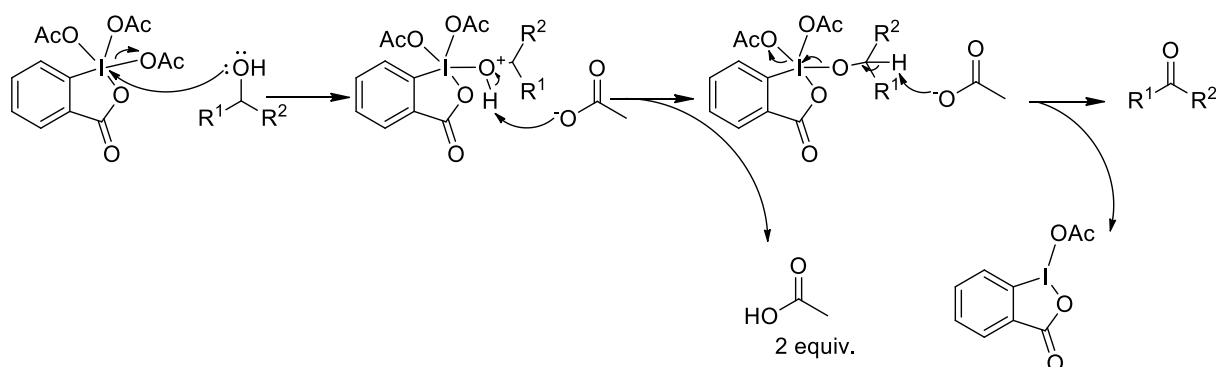


Figure 36 Proposed structure of chromium complex

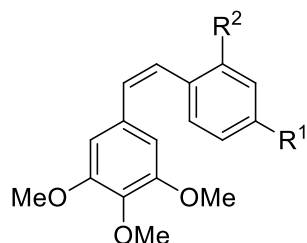
Dess-Martin periodinane (DMP) is one of the mildest reagents for oxidation of alcohols (Meyer & Schreiber, 1994). It is reactive and mild enough to be used for sterically hindered alcohols (Stevenson *et al.*, 1997). A lone pair of electrons on the oxygen can attack iodine forming an I-O bond, the acetoxy deprotonates the proton on the carbon adjacent to the oxygen forming acetic acid, thus generating the C-O double bond in a 1,2-elimination type reaction (Scheme 27).



Scheme 27: Oxidation of secondary alcohols to ketones with DMP

DMP is a highly functional group tolerant reagent and appeared to overcome the issue of oxidative cleavage of the double bond. Secondary alcohols in DCM were added to DMP in DCM and stirred at room temperature for 1 hour and treated with NaOH. (Table 11).

Table 11 Ketones synthesised following oxidation with DMP



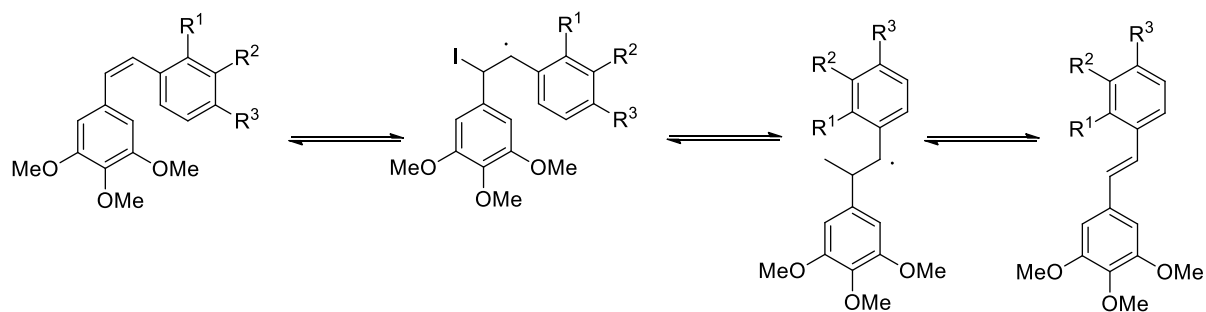
Compound	R ₁	R ₃	Yield (%)
48	OMe	COCH ₃	57
49	H	COCH ₃	64

Combretastatins with the secondary alcohol in the *ortho*-position were oxidised to the corresponding ketones in fair yields.

3.5 Iodine catalysed *Z*- to *E*- isomerisation

Cis and *trans* isomers often have different physical properties arising from the difference in shape; *trans* isomers tend to be more stable than *cis* isomers due to steric interactions of substituents in the *cis*-isomer. This difference in stability makes isomerisation from *cis* to *trans* easy to achieve.

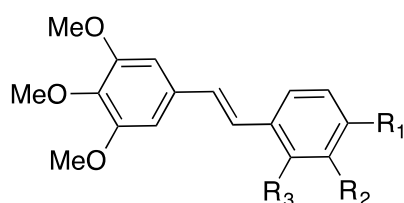
The ability of iodine to speed the equilibration of alkenes has been known since the 19th century (Liebermann, 1890). The assumed mechanism of *cis/trans* isomerisation of alkenes based on kinetic studies (Dickinson & Lotzkar, 1937) is through a 3-step process; the addition of iodine to a *cis*-alkene to give a *syn*-alkane, internal rotation to the *anti*- product and finally detachment of the iodine to give the *trans*-alkene (Scheme 28).



Scheme 28: Iodine catalysed *trans* isomerisation

The appropriate *cis*-stilbenes were treated with a catalytic amount of iodine in DCM and stirred at room temperature for two hours to afford the *trans*-stilbene.

Table 12: *E*-stilbenes



Compound	R ₁	R ₂	R ₃	Yield (%)
43E	CHO	OH	H	95
44E	OMe	H	CHO	89
46E	COCH ₃	H	H	98
47E	COCH ₃	OH	H	94
51E	CN	OH	H	93
52E		H	H	83

Trans isomers were isolated upon washing with sodium thiosulphate affording *trans*-stilbenes in good yields. Due to the increased stability of the *trans* stilbene the equilibrium of isomerisation favours the *trans*-configuration allowing for quick selective isomerisation in the presence of iodine. Varying the R groups on the B-ring did not seem to affect yields as all had electron withdrawing effects. It was reported that stilbenes with electron donating substituents isomerise quicker because of the electrophile character of the iodine (Muizebelt & Nivard, 1968).

4. Results & Discussion – Biological Evaluation of Combretastatins

The *in vitro* biological activity of combretastatin derivatives was assessed using the MTT assay in order to determine growth inhibition of cells. Combretastatin A-4 was used as a standard so that the data obtained for new compounds could be compared with that of an existing antivasular compound in the literature. A tubulin polymerization assay was used to screen the compounds for their effects on tubulin polymerization activity. Paclitaxel was used as a standard to observe increased tubulin polymerisation and colchicine and combretastatin A-4 were used as standards in the inhibition of tubulin polymerisation. Compounds of interest were further evaluated using flow cytometry to confirm the stage of the cell cycle these compounds are the most active.

4.1 Cytotoxicity of *E*- and *Z*-combretastatins determined by MTT-assays

The library of synthesised target compounds were first screened using the MTT assay; the anticancer activity of both *E*- and *Z*-combretastatin derivatives of interest were tested on adherent *in vitro* cancer cell lines using the MTT-assay. In short, the MTT assay can be used to determine the half maximal inhibitory concentration (IC_{50}) i.e. the required concentration to inhibit the growth of cells by 50 % of a variety of small organic compounds on live cell lines.

4.1.1 Cytotoxicity of *Z*-combretastatins

Combretastatins were screened in HepG2 (liver cancer), HeLa (cervical cancer) and HCT116 (colon cancer) cells using the MTT assay (Table 13). CA-4 was used as a control to compare the potency of the new combretastatin derivatives and values were comparable to those in the literature (Gerova *et al.*, 2016a; Zheng *et al.*, 2014; Tarade *et al.*, 2017), the IC_{50} for ZCA-4 on HepG2 differed from that in the literature (Gerova *et al.*, 2016a) due to the number of cells seeded per well. The IC_{50} for *Z*-combretastatins tested against HepG2, HeLa and HCT116 cells are shown in Table 13. Of the tested compounds, compounds **42**, **43**, **46** and **53** were found to potently inhibit the growth of HepG2, HeLa and HCT116 cells (Figure 37).

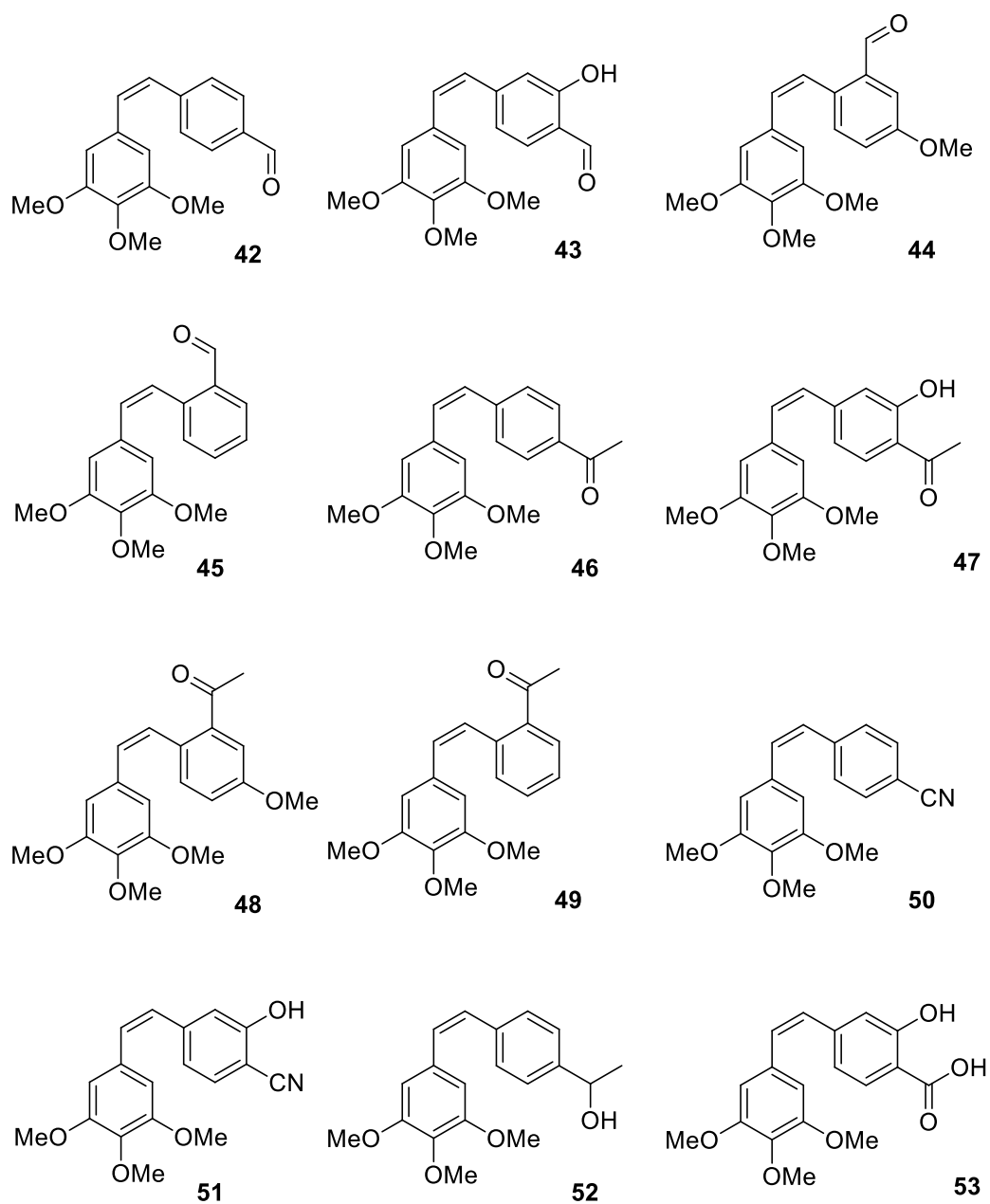


Figure 37 Structures of combretastatin derivatives

Table 13: Half-Maximal Inhibitory Concentration of Synthesized Combretastatin Analogues in HEPg2, HeLa and HCT-116 cells

Compound	IC ₅₀ a [μM]								
	HepG2			HeLa			HCT-116		
	24 h	48 h	72 h	24 h	48 h	72 h	24 h	48 h	72 h
42	1.86 ± 1.31	0.64 ± 0.10	0.25 ± 0.05	1.42 ± 0.66	0.35 ± 0.10	0.28 ± 0.06	1.15 ± 0.57	0.68 ± 0.31	0.27 ± 0.15
43	2.43 ± 1.41	0.64 ± 0.26	0.23 ± 0.05	1.21 ± 0.60	0.29 ± 0.11	0.07 ± 0.01	1.74 ± 1.47	0.58 ± 0.27	0.09 ± 0.03
44	6.01 ± 4.1	0.54 ± 0.26	0.14 ± 0.03	1.53 ± 0.59	0.39 ± 0.12	0.15 ± 0.03	2.02 ± 1.32	0.19 ± 0.07	0.14 ± 0.09
45	33.76 ± 9.32	10.08 ± 4.98	1.06 ± 0.38	24.30 ± 8.75	9.86 ± 5.71	1.21 ± 0.31	29.94 ± 10.12	9.12 ± 7.01	2.61 ± 1.51
46	1.09 ± 0.57	0.70 ± 0.36	0.06 ± 0.03	0.83 ± 0.19	0.37 ± 0.13	0.14 ± 0.02	1.45 ± 0.59	0.52 ± 0.12	0.25 ± 0.12
47	1.54 ± 0.94	0.76 ± 0.48	0.37 ± 0.09	1.30 ± 0.56	0.49 ± 0.2	0.34 ± 0.10	1.37 ± 0.74	0.85 ± 0.65	0.35 ± 0.23
48	8.00 ± 5.18	1.14 ± 0.57	0.46 ± 0.12	1.61 ± 0.45	0.74 ± 0.12	0.14 ± 0.08	2.34 ± 0.70	0.93 ± 0.56	0.45 ± 0.12
49	> 50	27.78 ± 11.44	24.16 ± 12.3	30.86 ± 10.56	17.22 ± 5.75	14.92 ± 7.83	49.76 ± 4.87	23.61 ± 10.20	13.10 ± 5.42
50	20.16 ± 4.90	1.26 ± 0.85	0.96 ± 0.35	12.38 ± 4.48	4.35 ± 1.40	0.46 ± 0.10	20.84 ± 8.31	1.87 ± 0.76	1.42 ± 0.40
51	1.07 ± 0.65	0.56 ± 0.28	0.53 ± 0.24	2.14 ± 0.97	0.95 ± 0.34	0.58 ± 0.13	1.03 ± 0.22	0.83 ± 0.48	0.79 ± 0.21
52	1.52 ± 0.96	0.66 ± 0.35	0.2 ± 0.11	2.90 ± 0.84	1.02 ± 0.15	0.65 ± 0.16	1.46 ± 0.73	0.96 ± 0.17	0.56 ± 0.20
53	1.36 ± 0.87	0.35 ± 0.29	0.04 ± 0.01	0.94 ± 0.13	0.26 ± 0.12	0.04 ± 0.01	0.79 ± 0.39	0.19 ± 0.05	0.12 ± 0.04
bCA-4	0.75 ± 0.45	0.037 ± 0.02	0.006 ± 0.001	0.014 ± 0.004	0.013 ± 0.004	0.007 ± 0.002	0.135 ± 0.03	0.026 ± 0.005	0.010 ± 0.003

^aIC₅₀ values were determined at 24 48 and 72 hour time points. The IC₅₀ values were determined using non-linear regression software on GraphPad. Values are expressed as mean ± SD of 6 values; values were obtained in triplicate in two separate experiments. ^bCA-4 IC₅₀ values are comparable to those in the literature; HepG2, HeLa (Zheng *et al.*, 2014), and HCT-116 (Tarade *et al.*, 2017).

A structure-activity relationship was established based on the variation of the B-ring of compounds tested; the potency of combretastatins relies on the interactions of the compound with the colchicine binding site of tubulin, which is shaped by residues of strands βS8 and βS9, loop βT7, helices βH7 and βH8 of β-tubulin, and loop αT5 of α-tubulin (Gaspari *et al.*, 2017).

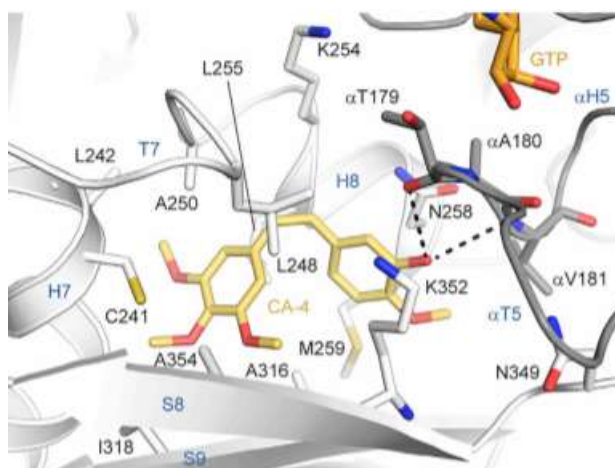


Figure 38 cis-CA-4 (yellow) bound to the colchicine site of tubulin (Gaspari *et al.*, 2017)

The presence of substituents in the 4-position provided good growth inhibition, based on the binding determined for CA-4 (Gaspari *et al.*, 2017). It can be presumed this is due to hydrophobic interactions with β Met259, β Ala316, and β Asn349 located below the combretastatins; a linear group in the 4 position (compounds **50** and **51**) showed poorer activity suggesting the substituent required a group of a similar size or orientation to that of the 4-methoxy of CA-4 to form these interactions. Gossiau *et al.* identified that 4-Br substitution gave lower IC_{50} values than compounds with 4-OMe substitution (Gossiau *et al.*, 2008); and Cushman *et al.* identified 4-Cl, 4-Br and 4- NO_2 (Figure 39) substitution of the B-ring vastly decreased cytotoxicity (Cushman *et al.*, 1991) suggesting groups similar to the 4-methoxy are required for activity. Further to this, compounds with no substituents in the 4-position showed particularly poor activity; after 72 hours the activity is decreased 10 fold for compounds lacking para-substitution. Cushman *et al.* also saw a drastic decrease in activity when the 4-substitution was removed (Cushman *et al.*, 1991) suggesting substitution in this position is required for potency. More recent literature also suggested a lack of 4-substitution resulted in lower IC_{50} values in the μM range (Stefański *et al.*, 2018). The observed cytotoxicity may be due to the disruption of cell signalling pathways involved in regulating and maintaining the cytoskeleton of endothelial cells in the tumour vasculature (Nasir *et al.*, 2017).

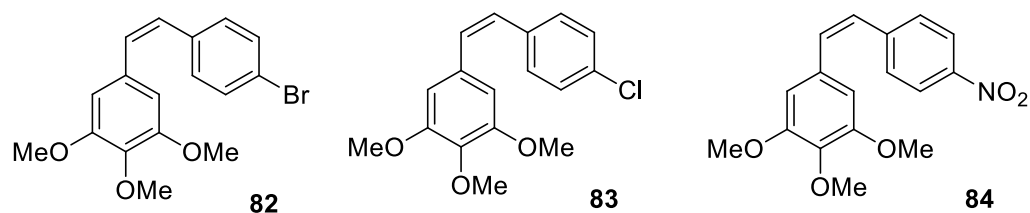


Figure 39 Combretastatin derivatives with varying *para*-substituents on the B-ring

Compounds with 3,4-substitution showed an increased activity compared to the corresponding mono substituted compounds with only a substituent in the 4-position. It was determined that the hydrogen of the 3-OH group of CA-4 bound to α T179 of tubulin; this OH group is not present in colchicine and so this interaction is not present in the colchicine-tubulin binding mode (Gaspari *et al.*, 2017, Figure 40). Compounds with a 3-OH group were capable of forming this hydrogen bond thus making them more potent across all cell lines.

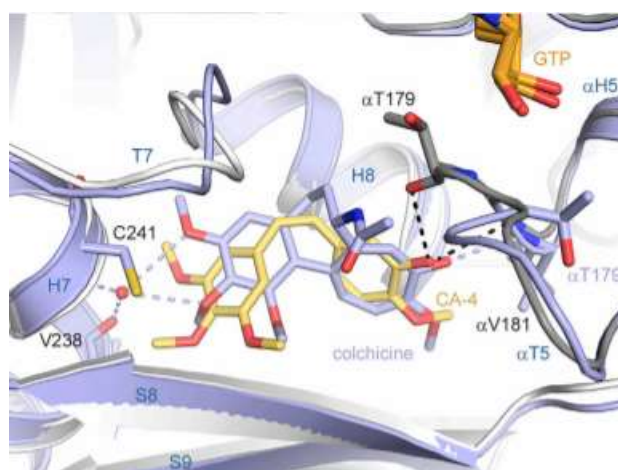


Figure 40 Superimposition of the tubulin-cis-CA-4 (yellow) and tubulin-colchicine (grey) complex structures (Gaspari *et al.*, 2017).

Compound **53Z** was shown to be the most active of all drug candidates tested across all cell lines. The compound is structurally similar to that of CA-4; the B-ring is 3,4-substituted with a carboxylic acid in the 4-position and a 3-hydroxy group capable of forming hydrophobic interactions with β -tubulin residues. Graphs showing the concentration of drug versus cell viability at different time points across the cell lines can be seen in Figure 41. It can be noted that the error bars for HCT-116, especially after 24 h were much larger than those observed for the other cells. The cells had not grown much and so differences in cell density per well was more evident.

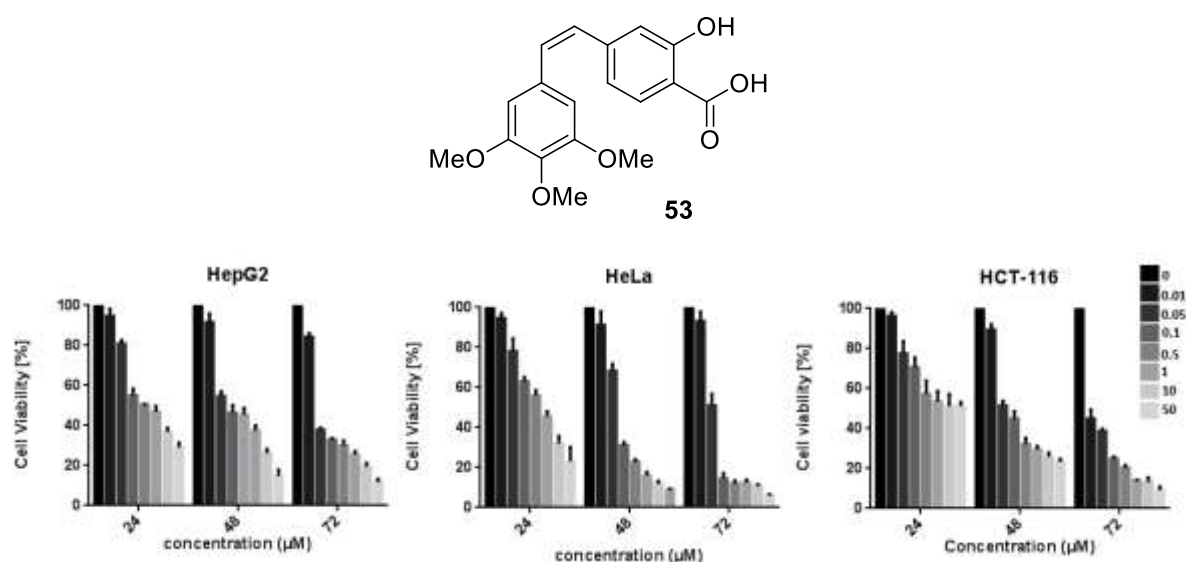


Figure 41 Effect of **53** on cell viability after 24, 48, 72 hours on HepG2, HeLa and HCT-116 cells

Graphs showing the concentration *versus* cell viability for compound **42Z** at different time points across the cell lines can be seen in Figure 42. Again, an increase in cytotoxicity with time was observed across all cell lines.

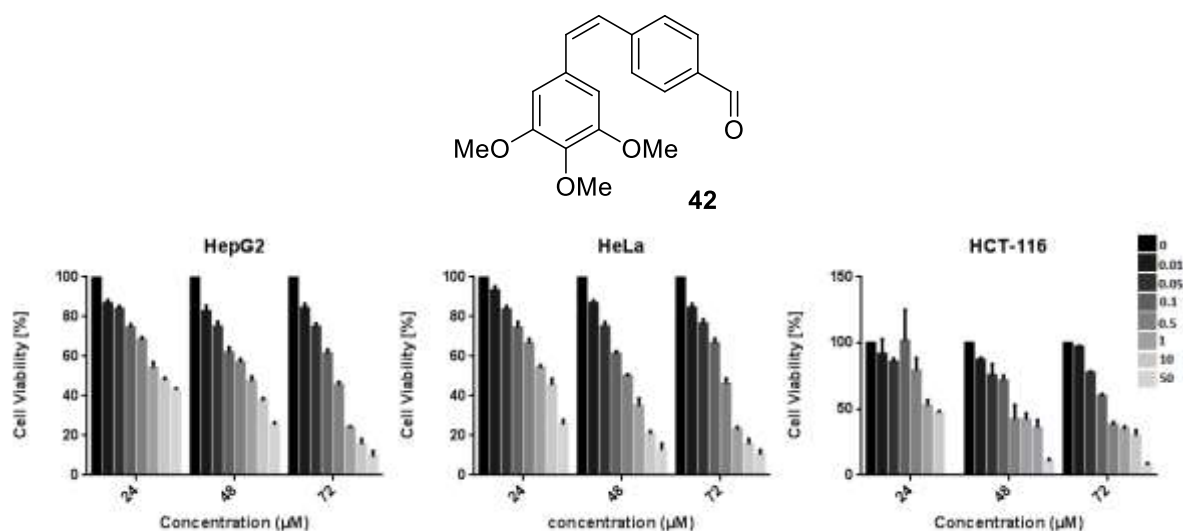


Figure 42 Effect of **42Z** on cell viability after 24, 48, 72 hours on HepG2, HeLa and HCT-116 cells

Comparing compound **43Z** to **42Z**, a higher degree of activity was observed (Figure 43); although not essential for cytotoxicity, the 3-OH group on compound **43Z** increased activity. This may be due to interactions such as H-bonding with the αT179 (Gaspari *et al.*, 2017), thus making a more stable complex.

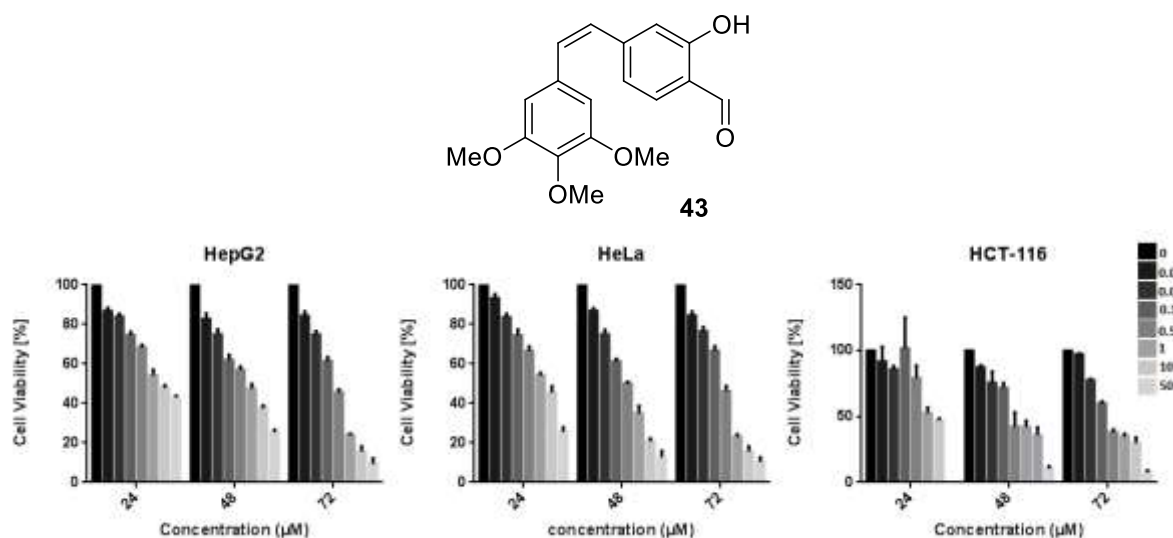


Figure 43 Effect of 43Z on cell viability after 24, 48, 72 hours on HepG2, HeLa and HCT-116 cells

These results are similar to Cushman and co-workers findings; the IC_{50} values of CA-4 and its 4-methoxy equivalent (Figure 44) were also similar with CA-4 being slightly more cytotoxic. The 4-methoxy substituted stilbene **85** had a similar IC_{50} to CA-4 **21** across a number of cell lines further suggesting that the 3-OH is not required for activity but increases it (Cushman *et al.*, 1991).

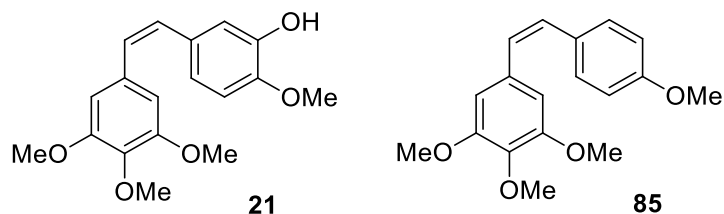


Figure 44 Structure of CA-4 and (Z)-1-(4-Methoxyphenyl)-2-(3,4,5-trimethoxyphenyl)-ethene

Compound 46 showed excellent activity across all cell lines (Figure 45), however it was not as cytotoxic as CA-4. Comparing aldehyde **42** and ketone **46**, the structures are similar with a carbonyl in the 4-position, however the formyl group of compound **42** only has one hydrogen capable of interacting with β -tubulin through van der Waals interactions (Mustafa *et al.*, 2017) compared to the three hydrogens of the 4-methoxy group of CA-4 and the 4-acetyl of compound **46**, which may explain the higher activity of compound **46** relative to compound **42** across the cell lines. Cushman *et al.* identified that 4-NMe₂ gave increased activity compared to compounds with other substituents in the 4-position (Cushman *et al.*,

1991). A comparison of the structures shows that the methyl groups lie in a similar position thus likely to form van der Waals interactions with the β -tubulin subunit of the binding site.

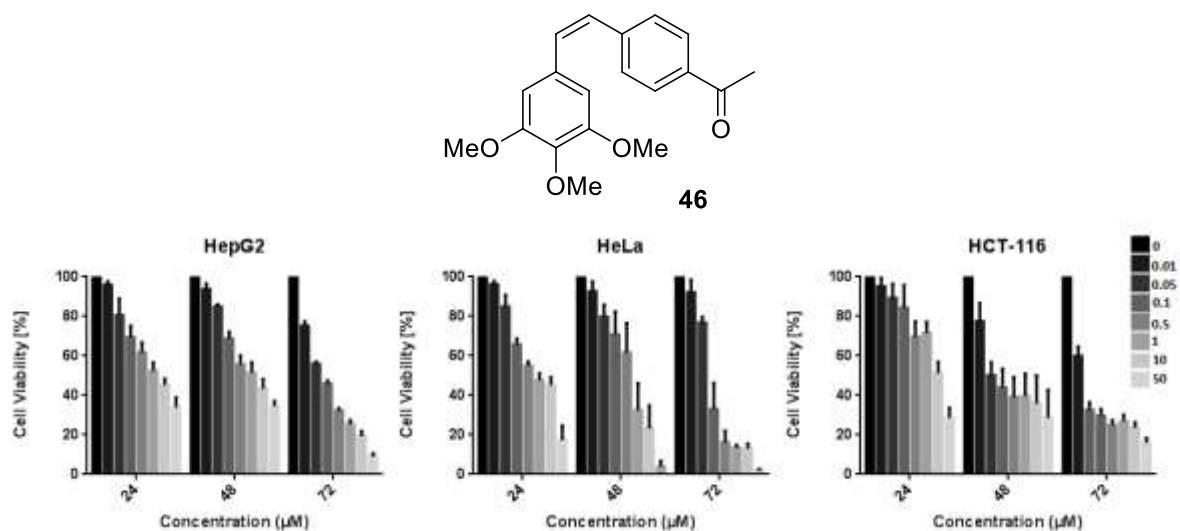


Figure 45 Effect of 46 on cell viability after 24, 48, 72 hours on HepG2, HeLa and HCT-116 cells

4.1.2 Cytotoxicity of E-combretastatins

The cytotoxicity of *E*-combretastatins was determined to ensure the drug was less active than the corresponding *Z*-combretastatin. It was essential that the *E*-combretastatins were completely pure as even small impurities of the *Z*-isomers were shown to have a large effect on MTT-assay results; the IC₅₀ value of pure 100 % *E*-CA4 is reported as 30 μ M on K562 cells (Hepworth, 2000). Using a 95:5 *E*:*Z* mixture of CA4 the IC₅₀ value was about three orders of magnitude lower (0.03 μ M on K562 cells).

E-Combretastatins were screened in HepG2 cells using the MTT assay (Table 14) to confirm lower potency compared to the corresponding *Z*-combretastatins. HepG2 cells were used for further studies as the cell line is widely accepted as a standardized experimental model with biological properties of human liver carcinoma cells. CA-4 was again used as a control and values were comparable to those in the literature (Gerova *et al.*, 2016a) with the number of cells seeded per well take into consideration. The IC₅₀ for *E*-combretastatins tested against HepG2 cells are shown in Table 14.

Table 14: Half-Maximal Inhibitory Concentration of Synthesized *E*-Combretastatin Analogues in HEPG2 cells

Compound	IC ₅₀ ^a [uM]			
	HepG2			
	24 h	48 h	72 h	72 h (Z)
42E	16.36 ± 10.05	5.21 ± 2.25	1.51 ± 0.24	0.25 ± 0.05
43E	22.21 ± 9.03	7.70 ± 4.35	1.20 ± 0.57	0.23 ± 0.05
44E	#	#	0.23 ± 0.00	0.14 ± 0.03
45E	#	#	14.62 ± 3.36	1.06 ± 0.38
46E	29.18 ± 7.32	10.36 ± 5.86	0.29 ± 0.11	0.06 ± 0.03
47E	#	#	#	0.37 ± 0.09
48E	#	#	>50	#
49E	#	#	30.60 ± 8.55	24.16 ± 12.3
50E	#	#	26.50 ± 7.68	0.96 ± 0.35
51E	#	#	30.92 ± 9.87	0.53 ± 0.24
52E	#	#	1.45 ± 0.21	0.2 ± 0.11
53E	#	#	0.24 ± 0.11	0.04 ± 0.05
Z-CA-4	0.75 ± 0.45	0.037 ± 0.019	0.006 ± 0.001	0.006 ± 0.001

^aIC₅₀ values were determined at 24 48 and 72 hour time points. The IC₅₀ values were determined using non-linear regression software on GraphPad. Values are expressed as mean ± SD of 6 values; values were obtained in triplicate in two separate experiments.

In all cases the *E*-combretastatins were at least 1 order of magnitude less cytotoxic than the corresponding *Z*-combretastatins, although the difference is not as evident as with CA-4 where there is a significant difference in cytotoxicity.

Gaspari and co-workers conducted a study to determine the difference in binding of Z-CA-4 and *E*-CA-4 to the colchicine-binding site of tubulin to explain the difference in cytotoxicity (Gaspari *et al.*, 2017). Structural distortions of the bound *trans*-CA-4 molecule in the colchicine binding site of tubulin is the likely cause of its reduced activity in comparison with that of its *cis*-isomer; the αT5-loop residue αThr179 is flipped towards the binding site, stabilising the bound *cis*-CA-4 conformation.

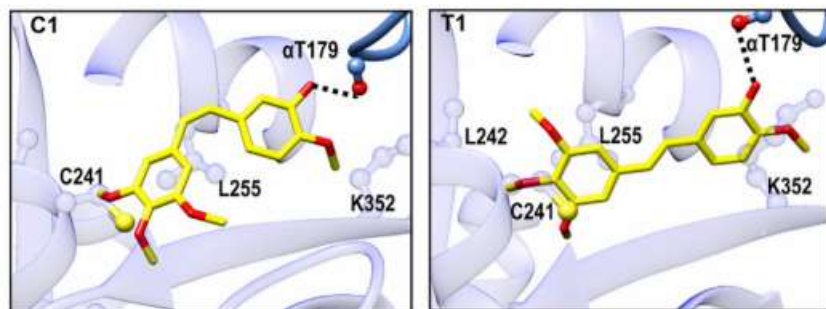


Figure 46 Binding of a) Z-CA-4 and b) E-CA-4 to tubulin (Gaspari *et al.*, 2017).

The IC_{50} values of compounds of interest at 24, 48 and 72 hours were calculated in order to identify if cytotoxicity was time dependant as observed in the Z-combretastatins. Figure 47 shows a plot of concentration *versus* cell viability for compound 42e after 24, 48 and 72 hours. As with the corresponding Z-combretastatin, cytotoxicity appeared to be time dependent; a decrease in IC_{50} values with time of exposure to the drug showed a similar trend to that of Z-combretastatins with the IC_{50} being around one order of magnitude lower with increasing time.

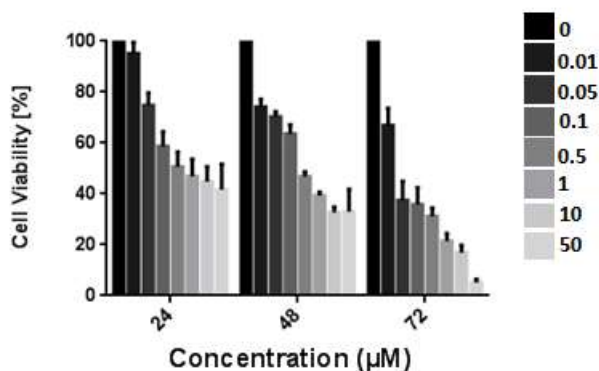


Figure 47 Effect of 42E on cell viability after 24, 48, 72 hours on HepG2 cells

Comparing compound **43E** to **42E**, a higher degree of activity was observed (Figure 48); although not essential for cytotoxicity, the 3-OH group on compound **43E** again appeared to increase activity, as observed with the corresponding Z-combretastatins. Again, at each time point cytotoxicity was increased by around one order of magnitude compared to that of the corresponding Z-combretastatin.

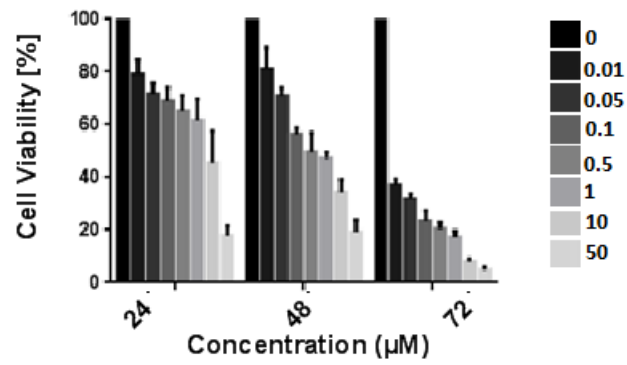


Figure 48 Effect of 43E on cell viability after 24, 48, 72 hours on HepG2 cells

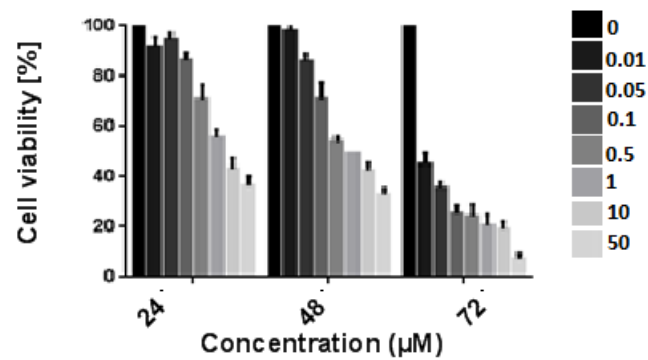


Figure 49 Effect of 46E on cell viability after 24, 48, 72 hours on HepG2 cells

4.2 Tubulin polymerization activity of Z-combretastatin derivatives

Microtubule-targeting agents can be classified into two main groups, stabilisers and destabilisers, based on their mechanisms of action. Both stabilisers and destabilisers affect microtubule dynamics and arrest cells in mitosis (Kanthou *et al.*, 2004); paclitaxel is a microtubule-stabilising agent that inhibits depolymerisation thus enhancing microtubule polymerization and Z-combretastatins are microtubule-depolymerizing agents, inhibiting microtubule polymerization. CA-4 is a microtubule-destabilising agent that binds with tubulin at the same site as that of colchicine (Pettit *et al.*, 1989, 1995b). CA-4 induces microtubule disassembly resulting in cytotoxic effects across various human cancer cell lines (Simoni *et al.*, 2006).

A tubulin polymerization assay kit (cat # BK011P, Cytoskeleton, Inc.) was used to assess the effect of compounds on tubulin polymerisation. The kit is an adaptation of an assay originally described by Bonne *et al.* The basic principle is that the increase in number of microtubules gives higher fluorescence due to the incorporation of a fluorescent reporter into microtubules (Bonne *et al.*, 1985). The experiment was carried out based on the product protocol as described in version 4.0 of the tubulin polymerization assay kit manual; a reaction mixture of porcine brain tubulin (>99% pure, 2 mg/mL) and GTP (1 mM) in a buffer solution was added to the test compounds (1 μ M unless otherwise stated) and incubated at 37 °C with fluorescence monitored (excitation = 355 nm and emission = 405 nm) every 30 s for 3 h to generate a polymerization curve (Figure 50). The optimal excitation range for the assay was 340-360 nm \pm 20 nm and emission was 410-460 nm \pm 20 nm; emission at 405 nm was used in order to decrease the background fluorescence of combretastatins.

The control polymerisation curve showed the three phases of microtubule polymerisation; nucleation (phase I in Figure 50), growth (phase II in Figure 50), and steady state equilibrium (phase III in Figure 50). The anti-mitotic paclitaxel was used as a second control to confirm the assay was working; paclitaxel (3 μ M) eliminated the nucleation phase of polymerisation, thus enhancing the V_{max} of the growth phase (Kampan *et al.*, 2015). CA-4 (1 μ M) showed a drastic decrease in the V_{max} due to its destabilising effect (Sriram *et al.*, 2008; Wu *et al.*, 2007).

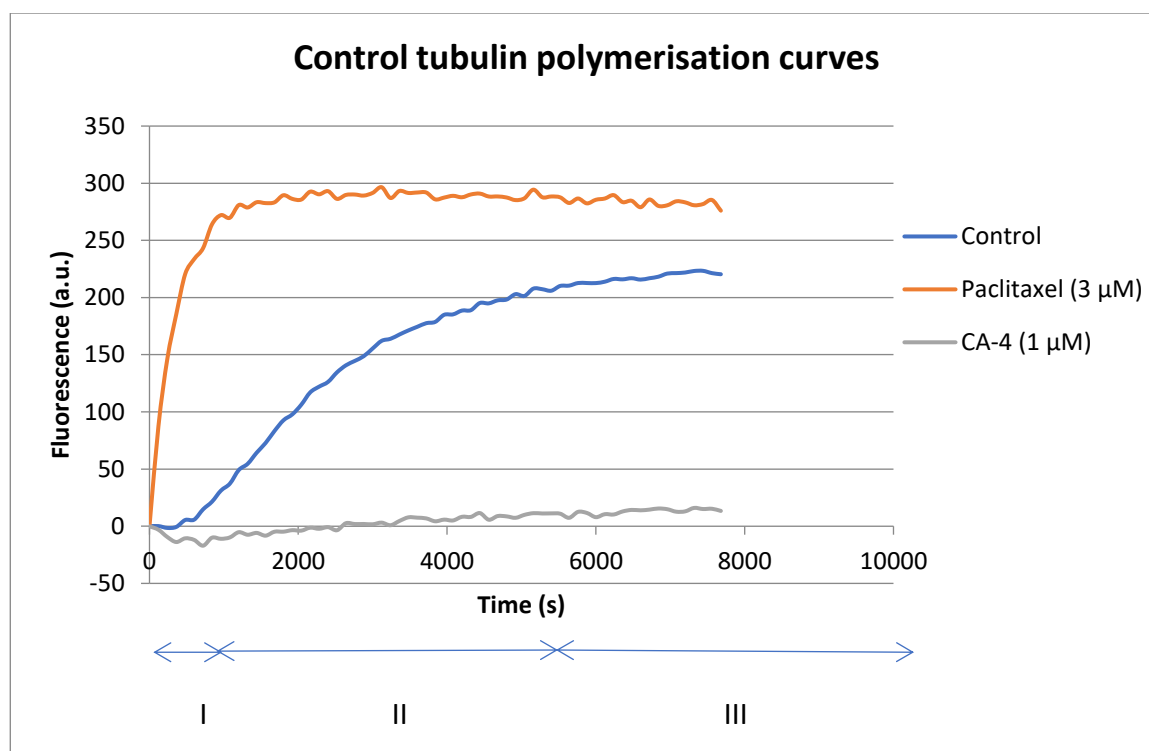


Figure 50 Polymerisation curve of control (blue), paclitaxel (orange) and CA-4 (grey)

The experiment was repeated in duplicate with a no drug control and paclitaxel (3 μM) with each batch of tubulin; in each case the untreated tubulin showed a typical polymerisation curve and paclitaxel eliminated the nucleation phase, enhancing the polymerisation (Kampan *et al.*, 2015). Duplicates were averaged and corrected for background fluorescence. The inhibition of tubulin polymerisation was preliminarily determined at 1 μM for all *Z*-combretastatin derivatives then further validated at 0.1 μM and 0.5 μM for compounds of interest (42, 43 and 46).

The tubulin polymerisation curves for all *Z*-combretastatins identified in Table 14 had a V_{max} between the control and CA-4 as expected for compounds that effectively disrupt tubulin polymerisation (Mangiatordi *et al.*, 2017). The most cytotoxic compounds inhibited tubulin polymerisation most efficiently with inhibition comparable to that of CA-4 (Sriram *et al.*, 2008; Wu *et al.*, 2007). A plot of time *versus* fluorescence for compounds **42**, **43**, **46**, **47** and **53** showed a huge decrease in the V_{max} values due to their destabilising effect (Figure 51). These results confirmed the intracellular target of these combretastatin derivatives is the inhibition of tubulin polymerisation dynamics as each were potent inhibitors of polymerisation with a V_{max} quantitatively similar to that of CA-4 (Wu *et al.*, 2007). Binding of combretastatin derivatives to tubulin appeared to be rapid; it was reported that pre-

incubation did not enhance the inhibitory effects of CA-4 on tubulin polymerization (Nam, 2003).

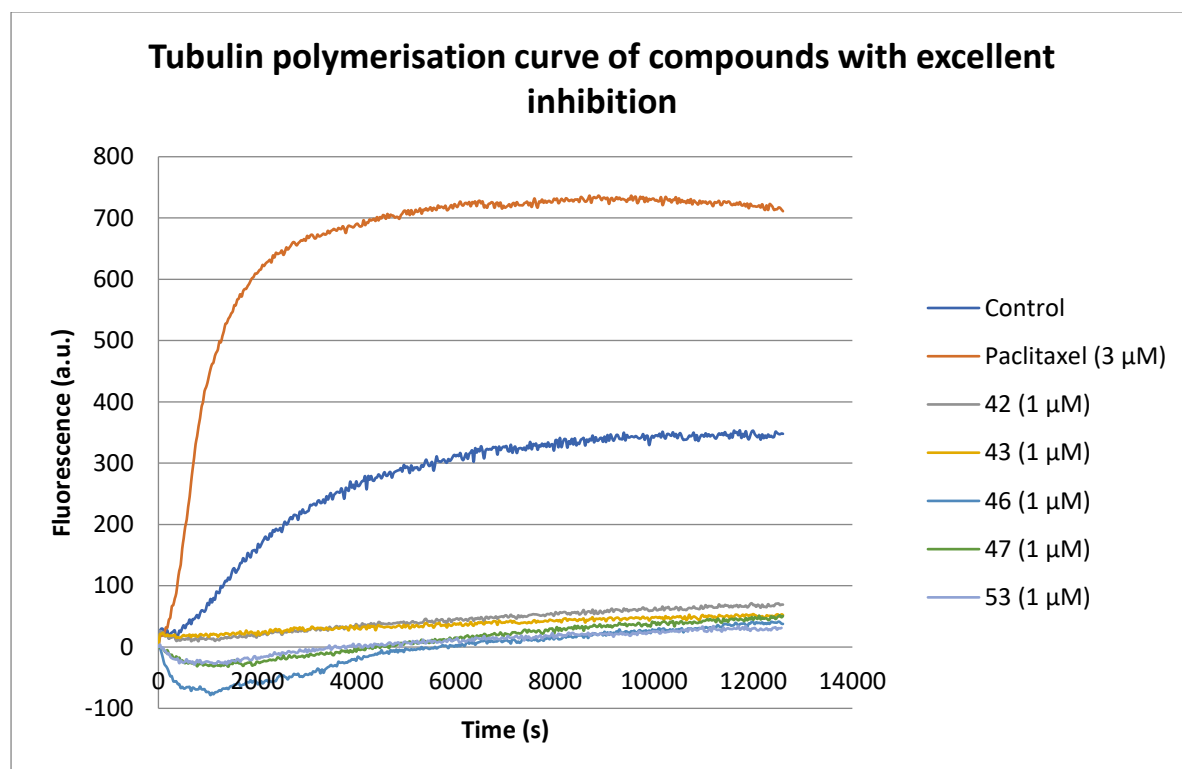


Figure 51 Polymerisation curve of control (blue), paclitaxel (orange), 42 (grey), 43 (yellow) 46 (light blue), 47 (green) and 53 (lilac)

The least cytotoxic compounds in Table 14 also showed the least inhibitory effects on tubulin growth (Figure 52). The growth curves for compounds **45**, **49** and **50** were comparable to that of the control tubulin growth curve with clear nucleation, growth and steady state phases suggesting these compounds did not affect the final proportion of tubulin polymerised at a concentration of 1 μM ; the V_{max} for compounds **45** (330), **49** (454) and **50** (303) were similar to that of the normal curve (345). Removal of the *para*-substituent on the B-ring resulted in compounds **45** and **49** that were minimally active as both inhibitors of tubulin assembly and in regards to the cytotoxicity towards the cancer cell lines; alterations to the B-ring also affected both the cytotoxicity and tubulin inhibition in the literature (Sriram *et al.*, 2008). Final tubulin growth upon treatment with these compounds appeared to be comparable to that of untreated tubulin. The observed intracellular cytotoxicity may be caused by the disruption of cell signalling pathways involved in regulating and maintaining the cytoskeleton of endothelial cells in the tumour vasculature upon slowing the rate of polymerisation (Nasir *et al.*, 2017). This may be due to

the weaker binding of these compounds in the tubulin site due to a lack of B-ring binding (Gaspari *et al.*, 2017).

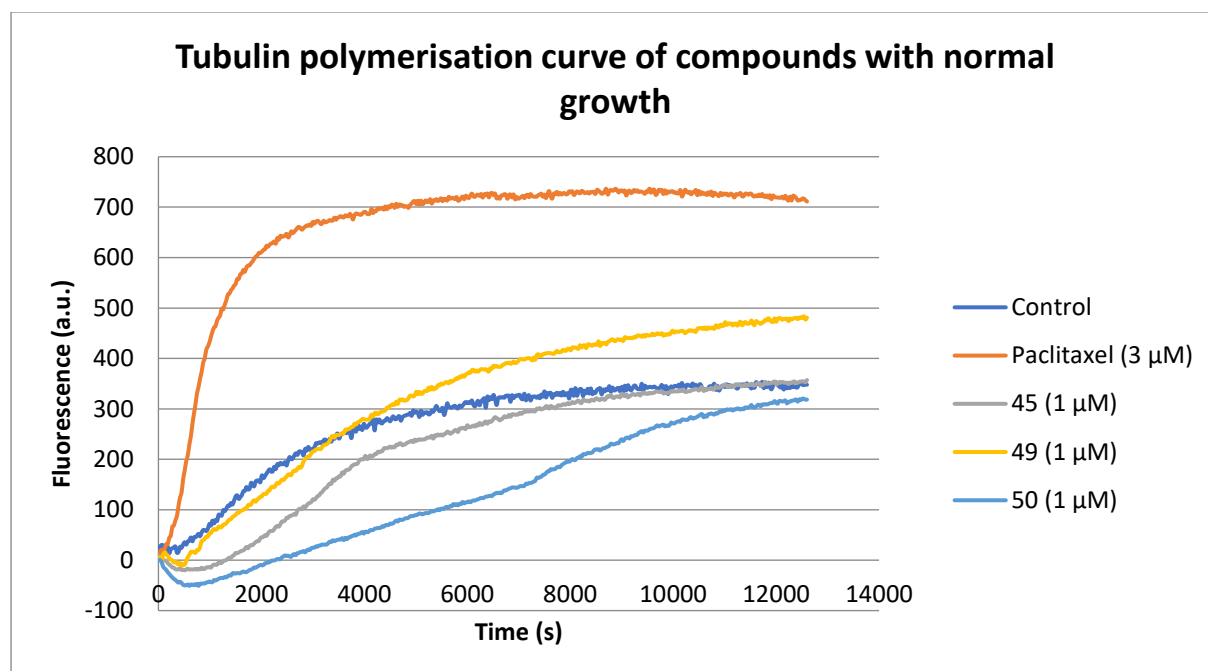


Figure 52 Polymerisation curve of control (blue), paclitaxel (orange), 45 (grey), 49 (yellow) and 50 (light blue)

The slope of the growth phase could be related to the rate of tubulin polymerisation for these compounds by fitting the data to pseudo-first order association curve (Table 15). The rate (k) of microtubule formation under normal conditions was $3.46 \times 10^{-4} \text{ s}^{-1}$ with a half-life of 2005 s i.e. the time taken for half of the microtubule formation. Incubation with compounds **45** and **49** decreased the rate of microtubule formation with k values of $1.94 \times 10^{-4} \text{ s}^{-1}$, $2.05 \times 10^{-4} \text{ s}^{-1}$ respectively. Values for compound **46** were not determined as the one-phase association was ambiguous. The half-life of tubulin formation also increased upon treatment with compounds **45** and **49** suggesting that although the final volume of microtubules was not inhibited, these compounds slowed down the rate of tubulin polymerisation and thus still disrupted the cell signalling pathways (Nasir *et al.*, 2017) causing some cytotoxicity in cells.

Table 15 Rate (k) and half-life (t_{1/2}) of tubulin polymerisation under varying conditions

Conditions	k (s ⁻¹)	t _{1/2} (s)
No drug control	3.46 x10 ⁻⁴	2005
Paclitaxol (3 μM)	9.52 x10 ⁻⁴	728
Compound 45 (1 μM)	1.94 x10 ⁻⁴	3568
Compound 49 (1 μM)	2.05 x10 ⁻⁴	3378

The tubulin polymerisation curves for the other Z-combretastatins synthesised had a V_{max} between the control and CA-4 as expected for compounds that effectively disrupt tubulin polymerisation (Mangiatoridi *et al.*, 2017). Synthesised compounds were found to possess moderate to good activity in tubulin assembly inhibition as shown in the plot of time *versus* fluorescence (Figure 53). The inhibition of tubulin polymerisation correlated with the cytotoxicity towards cancer cell lines thus confirming the main mode of action of synthesised combretastatin derivatives is the inhibition of tubulin polymerisation (Mangiatoridi *et al.*, 2017; Wu *et al.*, 2007; Sriram *et al.*, 2008; Mikstacka *et al.*, 2013).

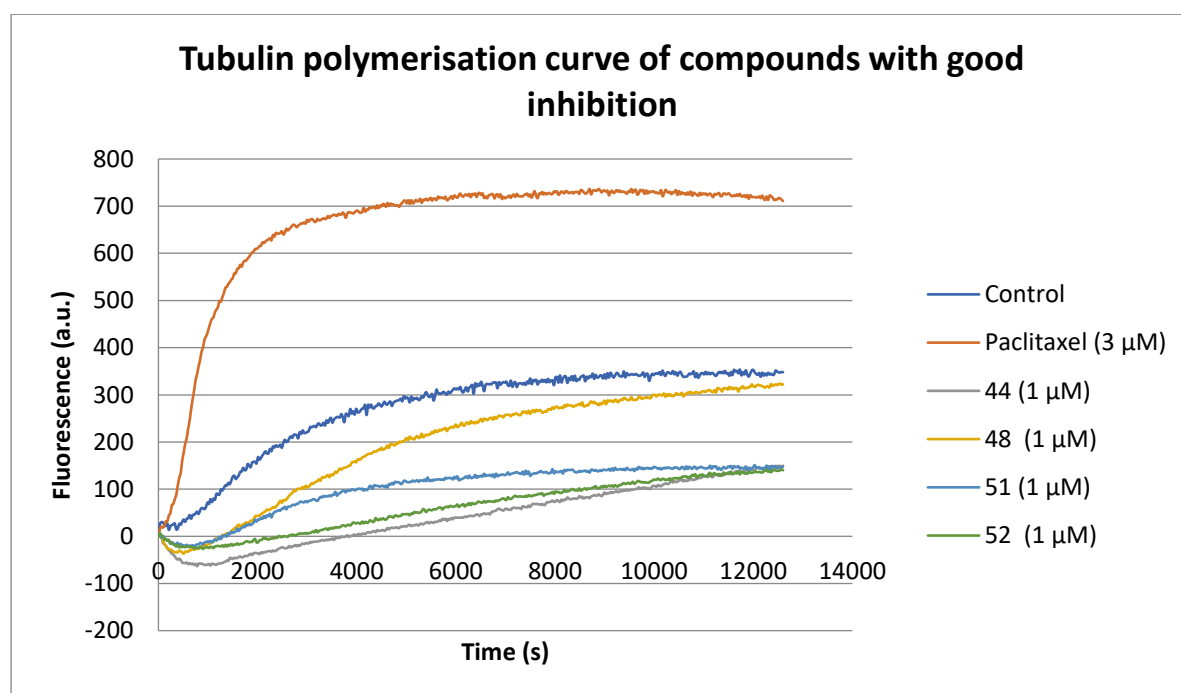


Figure 53 Polymerisation curve of control (blue), paclitaxel (orange), 44 (grey), 48 (yellow), 51 (light blue) and 52 (green)

The effect of *E*-combretastatins on tubulin polymerisation was also determined for compounds **42**, **43** and **46**. Due to the price of the kit and the number of assays possible, only the *E*-isomers of combretastatins of interest were assessed. Compounds of interest were determined based on their cytotoxicity, tubulin inhibition and photochemical properties (chapter 5).

E-combretastatins appeared to have little to no effect on the growth of the tubulin (Figure 54); the growth curves were comparable to that of the control tubulin growth curve with clear polymerisation phases. The binding of *E*-combretastatins to the colchicine site of tubulin is known to be weaker than that of *Z*-combretastatins (Gaspari *et al.*, 2017). Studies in the literature also found that upon treatment with *E*-combretastatin derivatives, tubulin growth appeared to be normal whilst the corresponding *Z*-combretastatins inhibited tubulin polymerisation (Engdahl *et al.*, 2015).

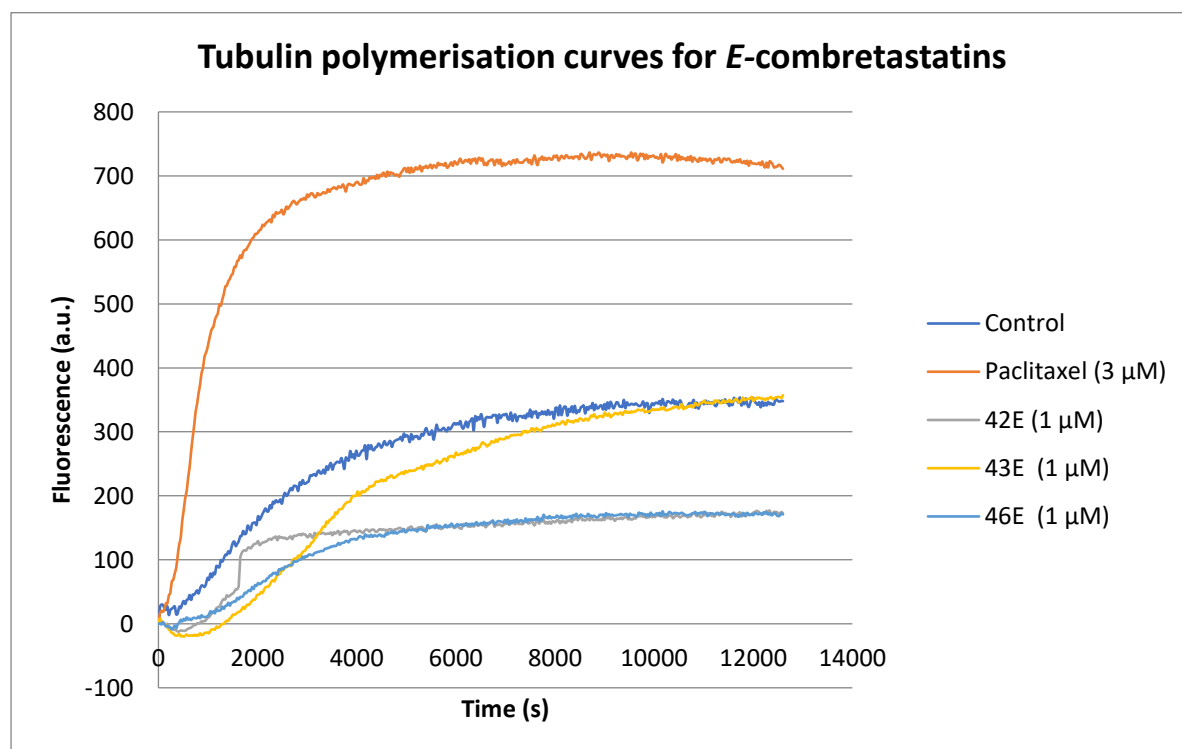


Figure 54 Polymerisation curve of control (blue), paclitaxel (orange) compound **42E** (grey), **43E** (yellow) and **46E** (light blue)

The inhibition of tubulin polymerisation is described in the literature as being dose dependent (Borowiak *et al.*, 2015; Mangiatordi *et al.*, 2017); the rate of inhibition of polymerisation decreased with concentration of compounds **42** (Figure 55), **43** (Figure 56) and **46** (Figure 57). A concentration dependent effect can be appreciated by looking at the

shift of the compound profiles at different concentrations. In each instance a concentration of 0.1 μM appeared to have little effect on the tubulin growth. The growth curves were comparable to that of the control curve with clear nucleation, growth and steady state equilibrium phases. An increase of concentration to 0.5 μM showed an increase in inhibition of tubulin polymerisation with a clear decrease in the V_{max} of fluorescence. Treatment with 1 μM of compounds **42**, **43** and **46** almost completely inhibited the polymerisation and was comparable to that of CA-4, one of the most potent tubulin polymerization inhibitors (Wang *et al.*, 2017; Lu *et al.*, 2012).

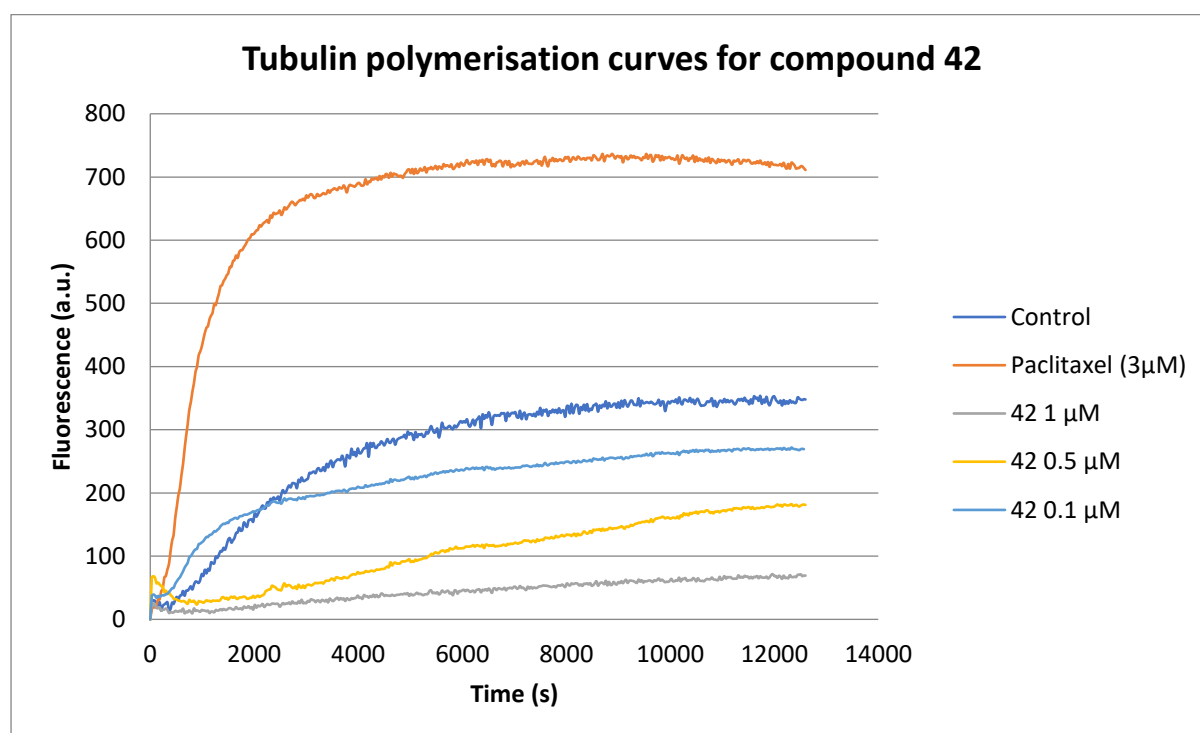


Figure 55 Polymerisation curve of control (blue), paclitaxel (orange) compound 42 (1 μM , grey) (0.5 μM , yellow) and (0.1 μM , light blue)

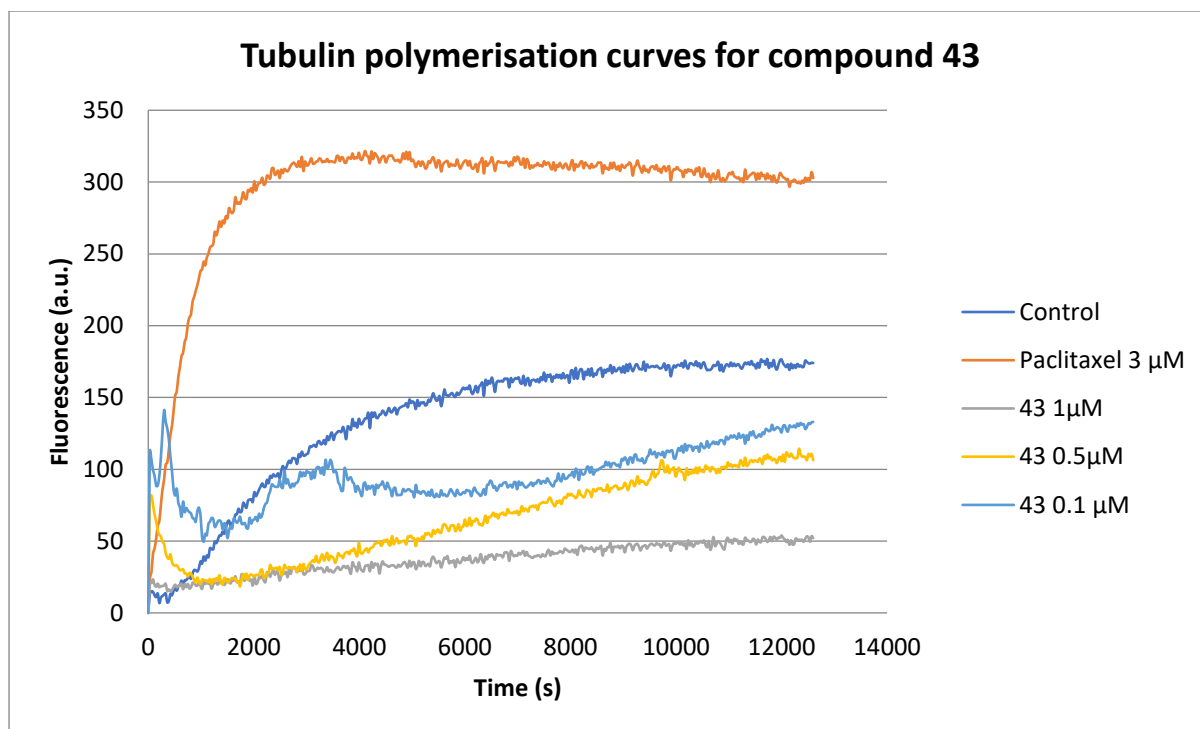


Figure 56 Polymerisation curve of control (blue), paclitaxel (orange), compound 43 (1 μM , grey) (0.5 μM , yellow) and (0.1 μM , light blue)

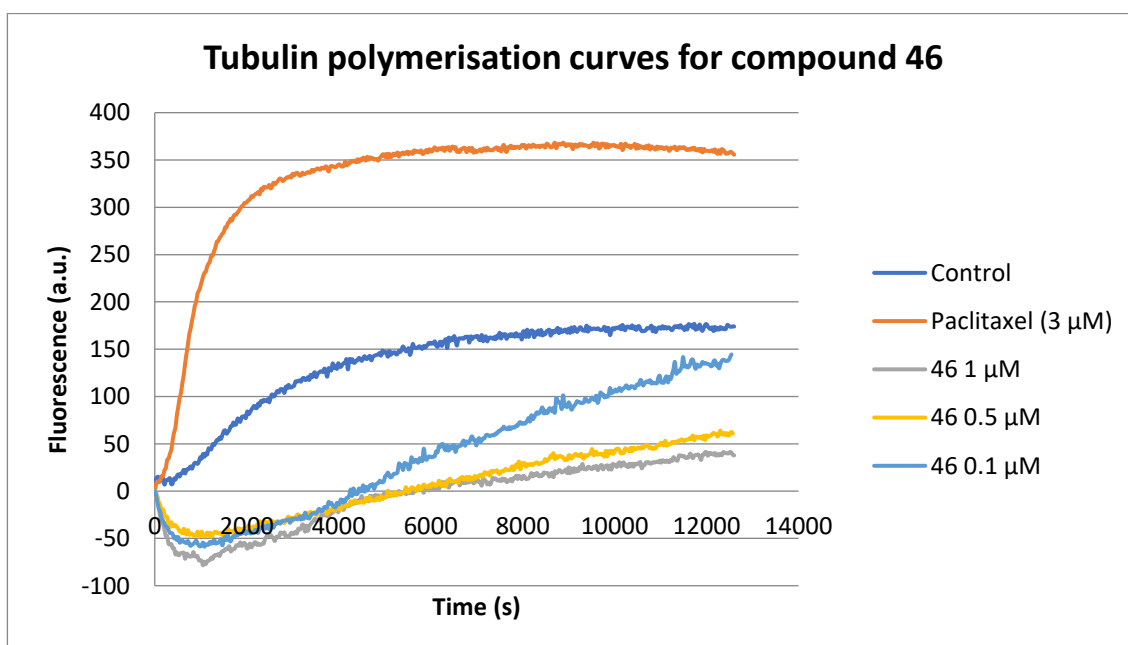


Figure 57 Polymerisation curve of control (blue), paclitaxel (orange) compound 46 (1 μM , grey) (0.5 μM , yellow) and (0.1 μM , light blue)

Upon treating tubulin with varying concentrations of the combretastatins, an IC_{50} (concentration that inhibits tubulin polymerization to 50%) could be determined. CA-4 is one of the best-known inhibitors of tubulin polymerization *in vitro* with IC_{50} values reported to range from 0.53 to 2.4 μM (Sriram *et al.*, 2008; Wu *et al.*, 2007). The tubulin polymerisation IC_{50} of colchicine is reported as 2.68 μM (Lu *et al.*, 2012). A plot of \log_{10} concentration versus percent of control V_{max} was plotted to determine the IC_{50} of compounds **42**, **43** and **46** (Figure 58). The V_{max} of the control polymerisation curve was used to quantify 100% tubulin growth. The growth of tubulin upon treatment with varying concentrations of Z-combretastatins could then be quantified as a percentage. The compounds showed IC_{50} values of around 0.3 μM , showing a 10-fold inhibition of tubulin polymerisation than that of colchicine 2.68 μM (Lu *et al.*, 2012). Combretastatin A-4 (CA-4) is reported as one of the most potent tubulin polymerization inhibitors (Wang *et al.*, 2017; Lu *et al.*, 2012). Compounds **42**, **43** and **46** showed an improved tubulin polymerisation IC_{50} value over CA-4 suggesting these compounds were effective in the inhibition of tubulin and thus disrupted the cell signalling pathways involved in regulating and maintaining the cytoskeleton of endothelial cells in the tumour vasculature. Tubulin is a labile protein; polymerisation occurs readily at 37 °C with a loss of 5% polymer per degree reduction in temperature and significant protein denaturation will occur after more than one freeze / thaw cycle. Further to this, higher concentrations of tubulin are more useful for detecting inhibition; the differing IC_{50} values for CA-4 may be a result of a change in these conditions.

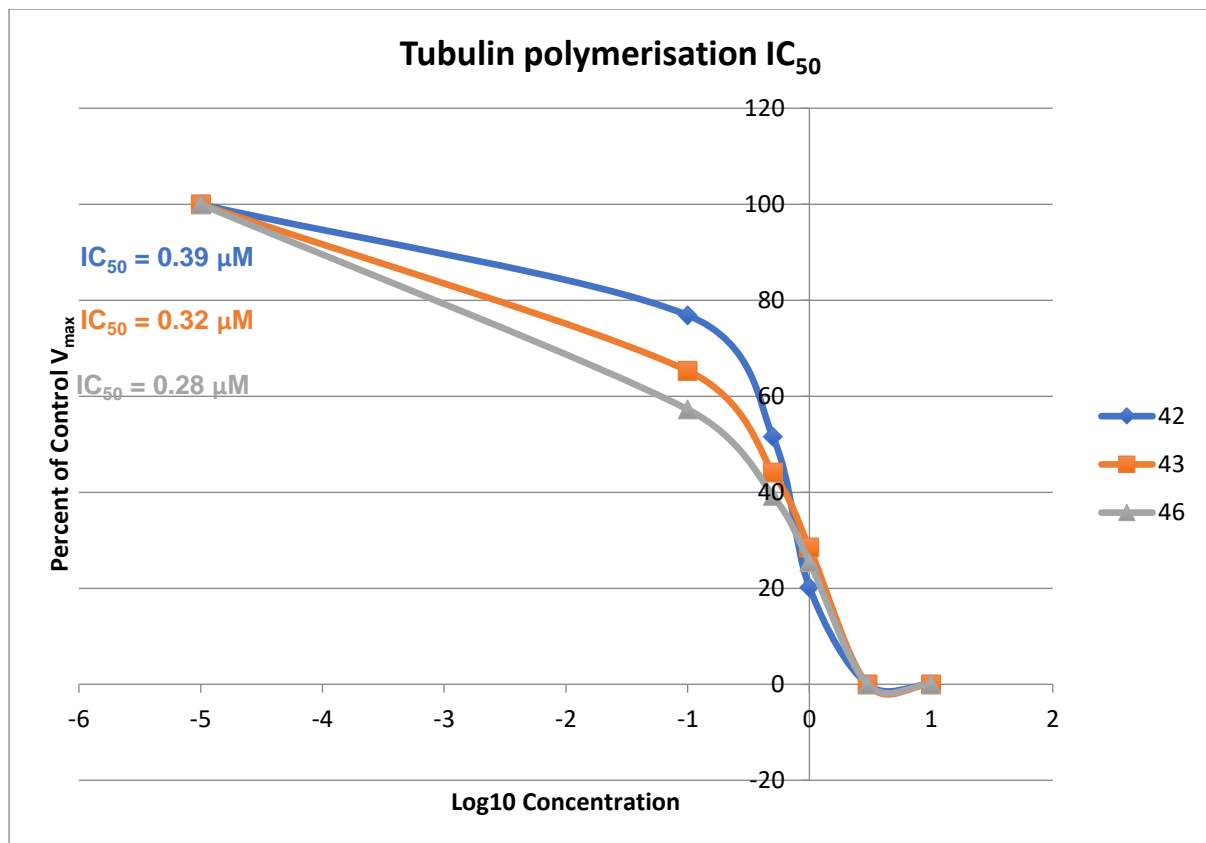


Figure 58 A plot of log concentration *versus* percentage tubulin inhibition to determine IC₅₀

4.3 Cell cycle analysis

The cell cycle is a series of events that occur in a cell leading to its DNA replication and consequent cell division into two new daughter cells. The cell cycle has two main phases; interphase and mitotic phase; the interphase is made up of G_1 , S and G_2 . The first stage of interphase is G_1 (growth) during which the cell accumulates genetic material such as proteins and organelles. From G_1 the cell may continue in the cell cycle to the S phase or enter the G_0 phase and become arrested. DNA duplication occurs during the S phase (synthesis); chromosomes are replicated forming two sister chromatids attached to the centromeric region. The centrosome is duplicated, giving rise to the mitotic spindle responsible for the movement of chromosomes during mitosis. In the next growth phase, G_2 , cells can replenish energy and proteins necessary for chromosome manipulation, preparing the cells for mitosis. The mitotic phase (M) is a multistep process during which the nucleus (karyokinesis) and cytoplasm (cytokinesis) divide forming two new identical daughter cells. These cells then continue in the cell cycle to G_1 in preparation for further cell division.

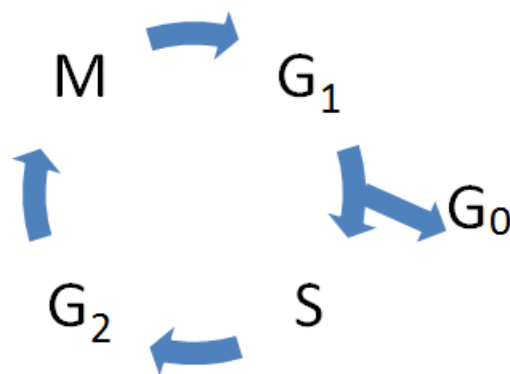


Figure 59 Schematic of the cell cycle

Flow cytometry is a powerful technique employed in cell sorting, cell counting and DNA quantification. Cell cycle analysis by quantification of DNA content was one of the first applications of flow cytometry. The DNA of cells can be stained by DNA binding dyes such as propidium iodide; the binding of these dyes is proportional to the amount of DNA present in cells. Cells in the S phase will have more DNA and thus be brighter than cells in G_1 . Similarly cells in G_2 will be approximately twice as bright as cells in G_1 . A plot of propidium iodide *versus* cell count gives a plot showing the number of cells in each phase of the cell cycle.

The effects of compounds of interest on the cell cycle was determined on HepG2 cells; cells were exposed to Z-combretastatins at indicated times and concentrations, fixed and stained with propidium iodide. The distribution of treated cells at different stages of the cell cycle could be analysed using flow cytometry. The HepG2 cell line is widely accepted as a standardized experimental model with biological properties of human liver carcinoma cells (Sassa *et al.*, 1987; Guillouzo *et al.*, 2007; Madan *et al.*, 2003), and so this cell line was used to gain an insight into cellular mechanisms.

During mitosis, the microtubule is critical for the separation of chromosomes. Exposure to microtubule targeting agents leads to damaged mitotic spindles resulting in mitotic arrest and subsequent apoptosis; it is widely accepted that the G₂/M cell cycle arrest is strongly associated with inhibition of tubulin polymerization (Kanthou *et al.*, 2004; Wang *et al.*, 1999; Zhu *et al.*, 2010). CA-4 and CA-4 phosphate induce mitotic arrest and cell death in human lung cancer cells (Vitale *et al.*, 2007), human gastric cancer cell lines (Lin *et al.*, 2007), human leukaemia (Petit *et al.*, 2008) and bladder cancer (Shen *et al.*, 2010).

The effect of combretastatin analogues on the cell cycle was examined by flow cytometric analysis of propidium iodide stained cells. The cell population represented the total number of cells (10,000-20,000); by making the cell population 100%, the percentage of cells in each stage of the cell cycle could be quantified relative to this (Greene *et al.*, 2010), quantification of sub-G1 cells allowed the determination of the number of apoptotic cells.

A plot of forwards scatter *versus* sideways scatter identified single cells from which the population of interest was gated in order to remove debris and identify the cell population of interest (Figure 60a); a gate is a boundary to define the characteristics of particles of interest (Adan *et al.*, 2017). The histogram plot of propidium iodide *versus* cell count (Figure 60b) showed the concentration of propidium iodide. Markers were applied in order to quantify the distribution of cells at different stages of the cell cycle. As expected, the plot showed an even distribution of cells throughout the cell cycle.

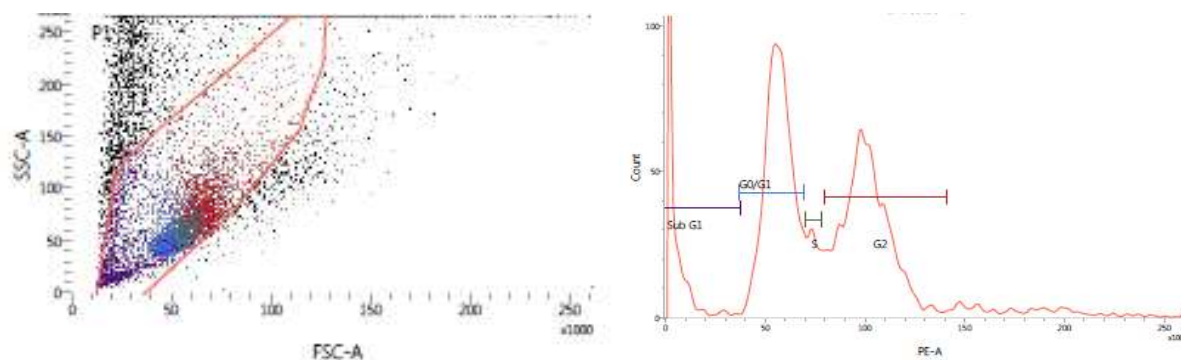


Figure 60 a) A dot plot of forward scatter versus side scatter with gate applied to identify cell population; b) propidium iodide histogram with markers to identify stages of the cell cycle

Treatment of cells with compound **42** at the IC_{50} identified in the cell viability assays (Table 14) showed a large increase of cells in the G_2M phase compared to that of the control cells; a mitotic block associated with tubulin polymerisation inhibition was identified by an increase in the number of cells arrested in the G_2M phase (91.6%) (Kanthou *et al.*, 2004; Kyprianou, 2012; Zhu *et al.*, 2010) compared to 28.4% in the control cultures. Further to this the increased population of cells in the G_2M phase correlated with a decrease of cells from G_0/G_1 - (3.5%) and S-phases (1.6%) compared to that of the control population (Zhu *et al.*, 2010). A divergence point, the point at which the percentage of apoptotic cells (sub G_1) increased (43.3%) as the percentage of G_2M arrested cells decreased (46.7%) was identified at 48 hours of treatment with compound **42**. The increased sub- G_1 population, suggested extensive DNA fragmentation indicating apoptosis as a direct result of mitotic arrest (Gerova *et al.*, 2016b). 72 h incubation with compound **42** resulted in a further increase in apoptotic cells (57.1%) as the number of cells arrested in G_2M further decreased (35.7%) again suggesting apoptosis as a direct result of mitotic arrest.

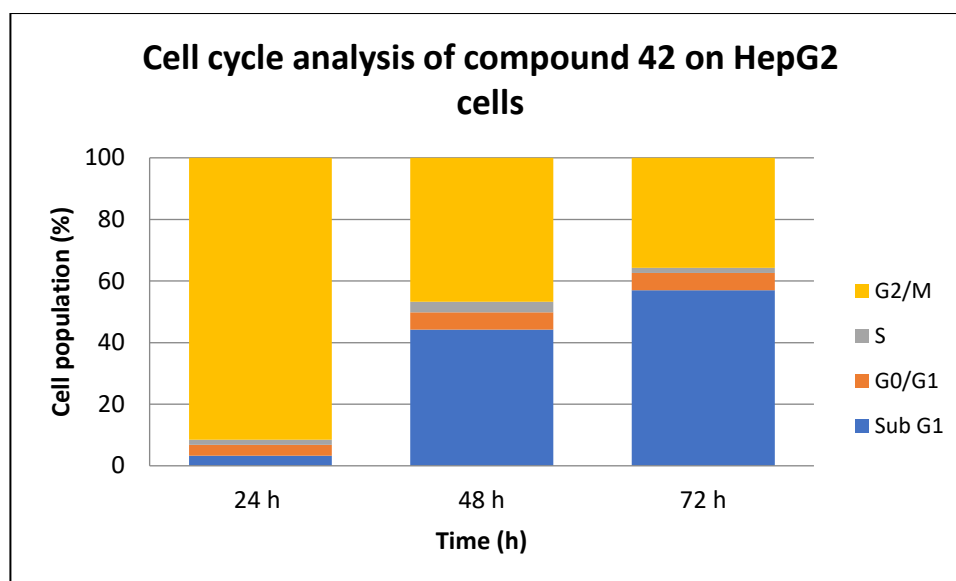


Figure 61 The effect of compound 42 on cell cycle progression of HepG2 cells determined by flow cytometry

Upon incubation of HepG2 cells with **43** at IC_{50} for 24 hours an increase in cells arrested in G₂M (94.6%) was also observed (Kanthou *et al.*, 2004; Kyprianou, 2012; Zhu *et al.*, 2010), again this can be linked to the inhibition of tubulin polymerisation that was identified in 4.3. When comparing the number of cells to that of the controls, an increase in G₂M cells was accompanied by a decrease in of cells from G₀/G₁- (2.8%) and S-phases (1.3%) (Kanthou *et al.*, 2004). At 48 h there was an increase in apoptotic cells (43.3%) and large decrease in G₂M cells (31.1%) suggesting the mitotic arrest had resulted in apoptosis. There was also an increase in G₀/G₁ cells (21.5%) suggesting some cells escaped mitotic arrest to the G₁ phase, overriding the mitotic block (Gerova *et al.*, 2016b). At 72 h there was further increase in apoptotic cells (64.12%) suggesting apoptosis occurred in both the interphase (9.2%) and due to mitotic arrest (24.7%).

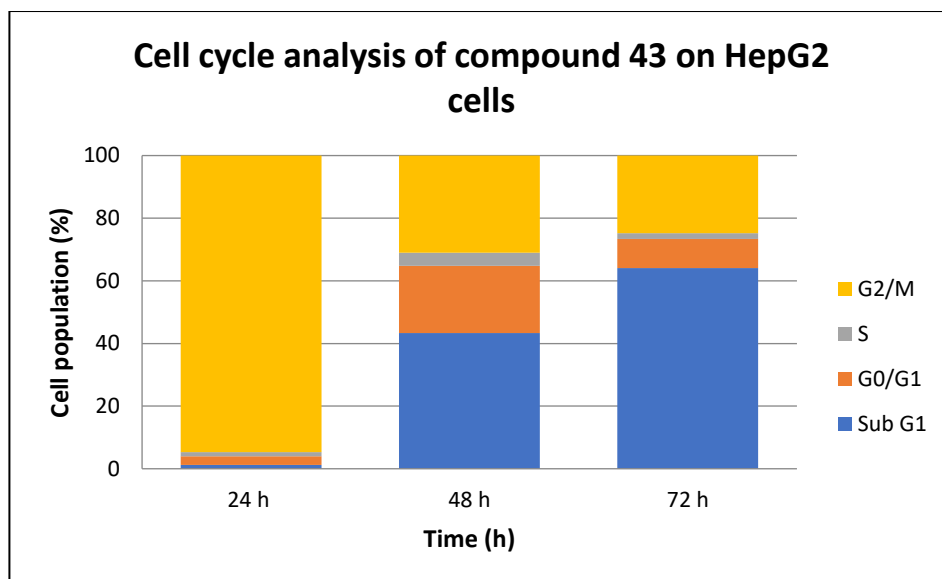


Figure 62 The effect of compound 43 on cell cycle progression of HepG2 cells determined by flow cytometry

FACS measurements in HepG2 cells showed that the percentage of cells in G₂M significantly increased within 24 h treatment with **46** (94% compared to 28% in the control cultures). At 48 h of treatment the HepG2 cells showed a decrease in the number of G₂M arrested cells and a significant increase in Sub G₁ cells suggesting the mitotic block directly caused apoptosis. After 72 h the number of apoptotic cells (sub-G₁) further increased as the number of cells in the G₂M phase decreased.

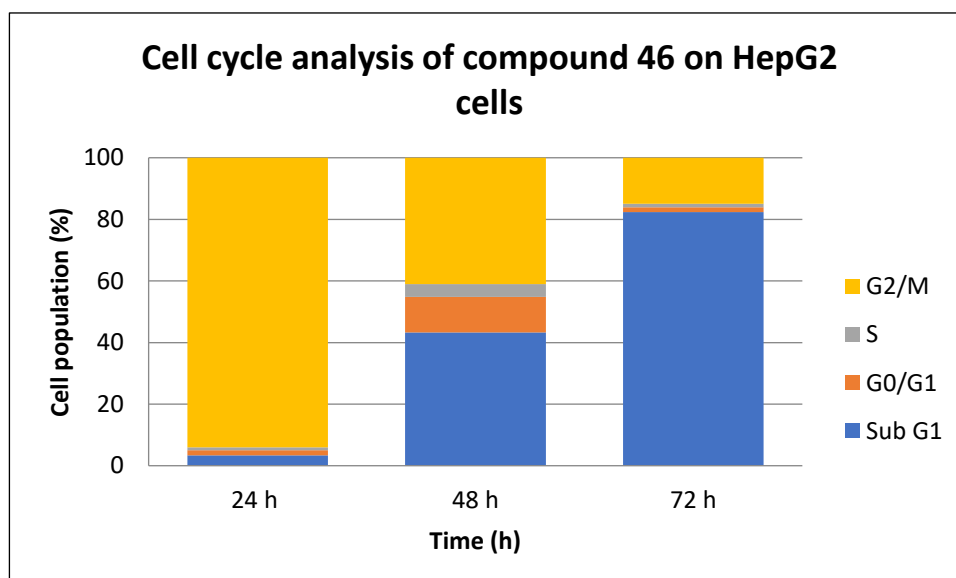


Figure 63 The effect of compound 46 on cell cycle progression of HepG2 cells determined by flow cytometry

5. Results & Discussion – Spectroscopic Properties of Combretastatins

In the following section, results for the one- and two-photon spectroscopic properties of *E*-combretastatin derivatives are discussed. Solvent dependent extinction coefficients, Stokes shifts, Lippert plots, fluorescent quantum yields, fluorescent lifetimes and two-photon absorption cross sections were determined. Spectrometric measurements were carried out in a range of non-polar, polar protic and polar aprotic solvents for which the properties are summarized in Table 16. It was important to determine the spectroscopic properties of compounds before imaging to aid in the design of experiments to be carried out at the Lasers for Science Facility at the Rutherford Appleton Laboratory.

Table 16 Polarities, dielectric constants (ϵ), refractive indices (η), viscosity (in centipoise (cP)) and the orientation polarizability (Δf) of the organic solvents used (Lide, 2002)

Solvent	Polarity	Dielectric constant (ϵ)	Refractive index (η)	Viscosity (cP)	Orientation polarizability (Δf)
Hexane	Non-polar	1.88	1.3749	0.31	-0.0014
MeOH	Polar protic	33	1.3284	0.59	0.3088
MeCN	Polar aprotic	37.5	1.3441	0.38	0.3054
DCM	Polar aprotic	9.1	1.4241	0.44	0.2185
EtOAc	Polar aprotic	6.02	1.3724	0.45	0.1996
DMSO	Polar aprotic	46.7	1.4793	2.24	0.2631

The spectroscopic properties obtained for these compounds in varying solvent systems was used in the following chapter to interpret observations of intracellular uptake and distribution and intracellular lifetimes of the different *E*-combretastatins in live mammalian monolayers (CHO and Hek 293 cells) and spheroids (Hek 293 cells).

5.1 Extinction coefficients, spectral shifts and Lippert plots of E-combretastatins

Solvent dependent spectral shifts (Stokes shift) were determined for the combretastatin derivatives that were cytotoxic and inhibited tubulin polymerisation *in vitro* in order to determine a Stokes shift. The Stokes shift is the difference in positions of the band maxima of the absorption and emission spectra of the same electronic transition; large Stokes shifts are indicative of a change in dipole moment. This increased dipole moment was indicative of charge transfer across the molecule upon excitation, a characteristic of molecules with a large two photon cross section. Combretastatins that exhibited large Stokes shifts, and thus the largest changes in dipole, were further assessed for their spectroscopic properties. A summary of Stokes shifts for *E*-combretastatins in a variety of solvents is shown in Table 17. A plot of ($\nu_A - \nu_F$) versus refractive index of solvent gave a slope that could be entered into the Lippert equation (Equation 5) to determine a change in dipole moment.

Table 17 Stokes shifts (cm⁻¹) of *E*-combretastatins in different solvents

Compound	Stokes shift (cm ⁻¹)					$(\mu^* - \mu)$ (Debye)
	Hexane	MeOH	MeCN	DCM	EtOAc	
42	6001	11571	9839	8613	7715	15.90 ± 2.09
43	4915	11351	9297	7981	7453	17.06 ± 2.24
44	4078	10758	9070	8038	7727	12.28 ± 1.62
46	5051	10311	9293	8131	7453	16.96 ± 2.24
47	4528	10552	9073	7834	6300	14.20 ± 1.87
48	4934	9941	10631	7880	7385	11.54 ± 1.52
52	4936	9357	9532	7016	6866	9.04 ± 1.19
53	5556	n.d.	10009	8571	7079	8.30 ± 1.09

Compounds **42**, **43** and **46** exhibited the largest spectral shifts and change in dipole upon excitation, these compounds were also amongst the most cytotoxic of combretastatins investigated and so were carried forward for further spectroscopic analysis.

Extinction coefficients were determined in a range of solvents and calculated from the spectra according to the Beer Lambert Law. The extinction coefficients have an estimated error of $\pm 5\%$ due to inaccuracies in sample preparation and instrumentation. Absorption and fluorescence maxima of combretastatins are also displayed to illustrate solvent dependent spectral shifts (Stokes shift in cm^{-1}). Absorption and fluorescence spectra of the different *E*-combretastatins in MeOH are shown in the following as examples. Spectra in all other solvents can be found in the appendix.

Molar extinction coefficient values for compound **42** ranged from around $\sim 20,000 \text{ dm}^3 \text{ mol}^{-1} \text{ cm}^{-1}$ in DMSO to $\sim 52,000 \text{ dm}^3 \text{ mol}^{-1} \text{ cm}^{-1}$ in DCM (Table 18). The highest values were measured in the less viscous solvents such as DCM and EtOAc which are also polar aprotic. The photo-physical behaviour of a solute depends on the nature of its environment and the solvent dielectric constant is often predicted to serve as a quantitative measure of solvent polarity (Pagni, 2005). The solvents with the largest dielectric constants were polar aprotic solvents and compound **42** had the highest molar extinction coefficient in these solvents. The lowest extinction coefficient was obtained in DMSO, which was suggested to be the result of the viscosity of DMSO (2.24 cP) compared with the other polar protic solvents (Bowen, 1959).

Table 18 Molar extinction coefficients (ϵ), absorption and emission peaks, and Stokes shifts of compound **42 (1 mM) in various solvents (estimated errors for $\epsilon(\lambda_{\text{max}})$ are $\pm 5\%$)**

Solvent	$\epsilon (\lambda_{\text{max}})$ ($\text{dm}^3 \text{ mol}^{-1} \text{ cm}^{-1}$)	$\lambda_{\text{max abs}}$ (nm)	$\lambda_{\text{max fl}}$ (nm)	Stokes shift (cm^{-1})
Hexane	30800	337	424	6001
MeOH	36300	349	577	11571
MeCN	33500	344	520	9839
DCM	52500	349	499	8613
EtOAc	41300	346	472	7715
DMSO	21700	349	527	9115

The molar extinction coefficients of compound **43** ranged from $\sim 20,000 \text{ dm}^3 \text{ mol}^{-1} \text{ cm}^{-1}$ in DMSO to $\sim 50,000 \text{ dm}^3 \text{ mol}^{-1} \text{ cm}^{-1}$ in DCM (Table 19). The range of extinction coefficients

was similar to that for compound **42**, and both compounds displayed the largest extinction coefficients in polar aprotic solvents with low viscosity and the lowest value was observed in the more viscous DMSO. Again this could be related to the solvent viscosity (Bowen, 1959).

Table 19 Molar extinction coefficients (ϵ), absorption and emission peaks, and Stokes shifts of compound **43** in various solvents (estimated errors for $\epsilon(\lambda_{\max})$ are $\pm 5\%$)

Solvent	$\epsilon (\lambda_{\max})$ ($\text{dm}^3 \text{mol}^{-1} \text{cm}^{-1}$)	λ_{\max} abs (nm)	λ_{\max} fl (nm)	Stokes shift [cm^{-1}]
Hexane	30300	344	414	4,915
MeOH	33900	342	559	11,351
MeCN	32100	339	495	9,297
DCM	48700	346	478	7,981
EtOAc	40500	342	459	7,453
DMSO	20900	n.d.	n.d.	n.d.

The molar extinction coefficients for compound **46** in a range from 17,300 $\text{dm}^3 \text{mol}^{-1} \text{cm}^{-1}$ in DMSO to around 50,000 $\text{dm}^3 \text{mol}^{-1} \text{cm}^{-1}$ in DCM were determined (Table 19). The extinction coefficients were similar to those measured in compounds **42** and **43**. Again the largest extinction coefficients were observed in polar aprotic solvents.

Table 20 Molar extinction coefficients (ϵ), absorption and emission peaks, and Stokes shifts of compound **46** in various solvents (estimated errors for $\epsilon(\lambda_{\max})$ are $\pm 5\%$)

Solvent	$\epsilon (\lambda_{\max})$ [$\text{dm}^3 \text{mol}^{-1} \text{cm}^{-1}$]	λ_{\max} abs (nm)	λ_{\max} fl (nm)	Stokes shift [cm^{-1}]
Hexane	30100	360	440	5,051
MeOH	33100	353	555	10,311
MeCN	34800	356	532	9,293
DCM	49300	363	515	8,131
EtOAc	45800	342	459	7,453
DMSO	17300	n.d.	n.d.	n.d.

For all compounds, the largest Stokes shifts were measured in MeOH (11571, 11351 and 10311 cm^{-1} respectively), indicating a relatively large loss of excitation energy on re-emission in polar solvents. Compound **43** showed a slightly larger Stokes shift in polar solvents; this compound has an OH group on the B-ring, increasing the solubility through increased hydrogen bonding. The smallest Stokes shifts of compound **42** (6001 cm^{-1} in hexane), **43** (4915 cm^{-1} in hexane) and **46** (5051 cm^{-1} in hexane) were observed in the non-polar solvents. This can be explained by a lack of dipole-dipole interactions between solute and solvent compared with *E*-combretastatins in polar solvents (Zakerhamidi, Ghanadzadeh & Moghadam, 2012). Another factor to consider is solvent viscosity; the more viscous the solvent the slower the reorientation of solvent molecules leading to a smaller Stokes shift (Herman *et al.*, 2012; Lakowicz, 2006) hence the Stokes shifts were largest in MeOH. Upon emission, the system can relax to a state of lower energy by the reorientation of the surrounding solvent molecules (solvent relaxation). Methanol is a polar protic solvent ($\epsilon = 33$) with low viscosity (0.59 cP). In a polar solvent, fluorophores will orientate to achieve a state of minimum energy. According to the Franck-Condon principle (Tellinghuisen, 1987), the redistribution of electron density upon excitation is faster than the reorientation of the nuclei causing the formation of an energetically unfavourable state. The system can relax to a state of lower energy by the reorientation of the surrounding solvent molecules (solvent relaxation) causing a red shift in the emission spectra. It is well known that a larger change in dipole moment upon excitation is observed in more polar solvents.

The determined Stokes shifts were much higher than those observed in previous experiments on *E*-combretastatins (Scherer *et al.*, 2014). This may be explained by the dynamics of fluorophores with a high dipole moment in polar solvents. From the Stokes shift in varying solvents, a Lippert plot was prepared to determine the change in dipole moment ($\Delta\mu = \mu_e - \mu_g$) between that of the ground state (μ_g) and excited state (μ_e) (in Debye) for each *E*-combretastatin. A plot of Stokes shift *versus* the orientation polarizability of solvents (Δf) in Figure 64 gave a slope that could be inserted into the Lippert-Mataga equation (Equation 5) to determine the values of $\Delta\mu$ for the different *E*-combretastatins. Compound **43** showed to have the largest dipole moment change ($\Delta\mu$) of the combretastatin derivatives studied (Figure 64).

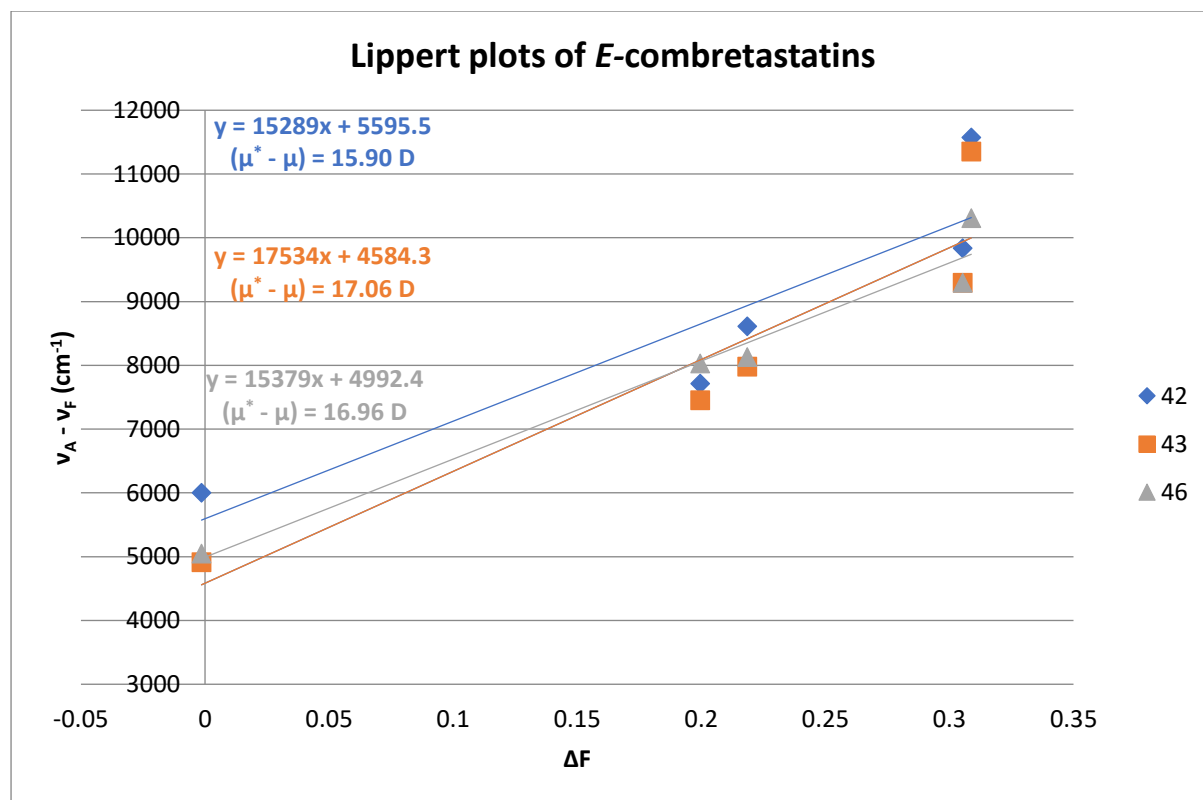


Figure 64 Lippert plot of *E*-combretastatins investigated. Inset: dipole moments of *E*-combretastatins

Absorption and emission spectra of combretastatin drug candidates in MeOH are shown in the following figures. Spectra in other solvents can be found in the appendix. Absorption spectra are characteristic stilbene spectra, with a structured absorption band indicative of vibrational states. The absorption and emission spectra of compounds **42**, **43** and **46** in MeOH are widely overlapping and display similar solvent characteristic shifts. The peak absorptions of all *trans*-combretastatin derivatives were slightly red shifted compared to the absorption spectra of *E*-CA4 (Figure 65). This effect was caused by the larger dipole moments of these new derivatives.

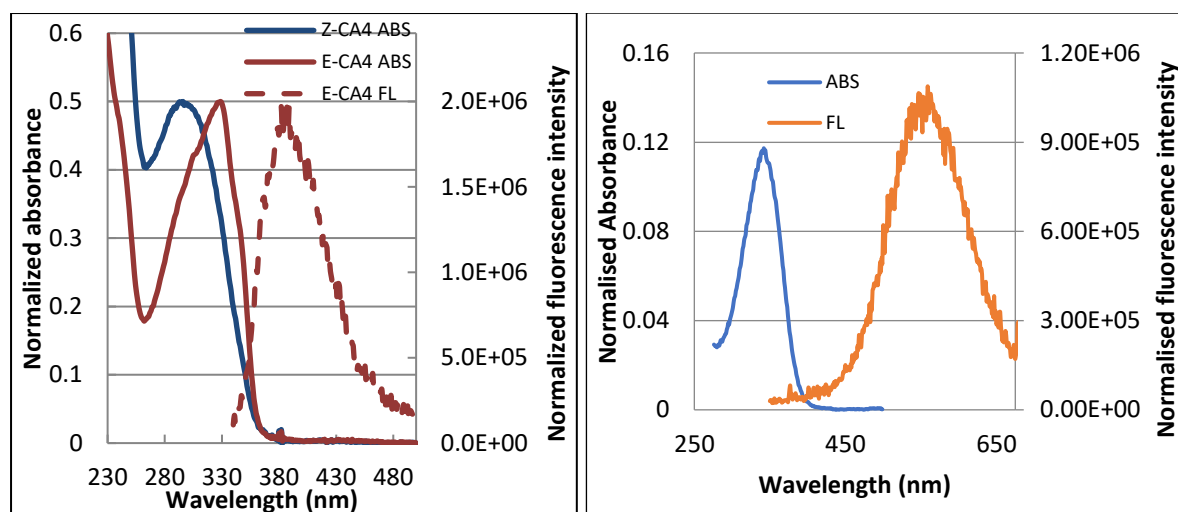


Figure 65 Normalised absorbance and emission spectra of *E*- and *Z*-CA4 (left) and compound **42** (right) in MeOH

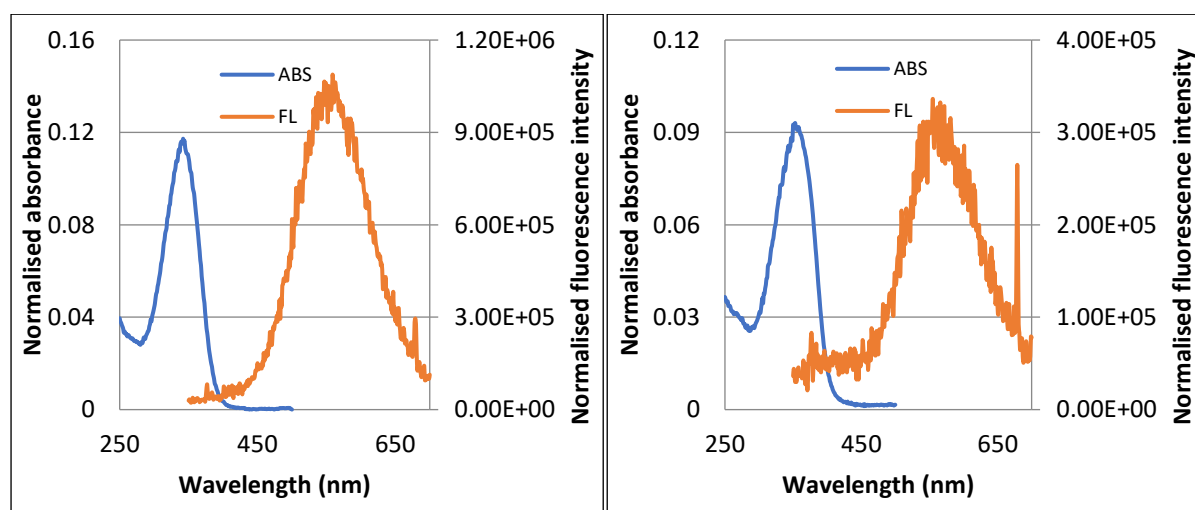


Figure 66 Normalised absorbance and emission spectra of compound **43** (left) and compound **46** (right) in MeOH

In summary the molar extinction coefficients and spectral shifts of *E*-combretastatins vary depending on solvent properties such as polarity, dielectric constant and viscosity (Pagni, 2005), and also on the fluorophore's own dipole moments (Lakowicz, 2006). The more polar compound **43** displayed larger Stokes shifts in polar solvents due to a larger energy loss during electronic transition from the excited to the ground state. The smallest Stokes shifts for all pro-drug candidates were found in a non-polar solvent (hexane). These red shifted absorption bands of the *E*-combretastatin derivatives compared to that of CA-4 made them more suited for two-photon excitation within the "tissue window".

5.2 Fluorescence quantum yields and lifetimes of *E*-combretastatins

The fluorescence quantum yields (Φ_F) and fluorescence lifetimes (τ_F) of *E*-combretastatins were determined in a range of solvents. An example of typical fluorescence decay obtained using Becker & Hickl SPCImage software is shown in Figure 67.

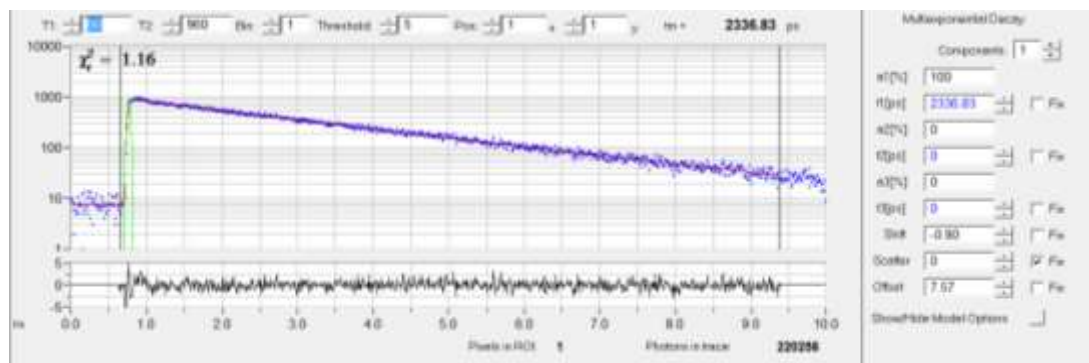


Figure 67 Single exponential decay of 42E in DMSO. Fluorescence was excited at 680 nm (0.2 mW)

Determination of Φ_{FS} and τ_{FS} in varying solvents allowed the observation of the *E*-combretastatins in environments with different properties such as polarity and viscosity. Φ_F 's determined the suitability of *E*-combretastatins for their use in fluorescence imaging.

5.2.1. Fluorescence quantum yield using the standard 9-chloroanthracene

The fluorescence quantum yields (Φ_F) were calculated using a comparative method with a fluorophore of known quantum yield (Jobin Yvon Ltd., 2004). A series of solutions with increasing concentrations (with an absorbance less than 0.1) were prepared and absorbances at the excitation wavelength were recorded together with the integrated area under the fluorescence spectra. A plot of fluorescence intensity *versus* fraction of light absorbed ($1-10^{-ABS}$), as shown in Figure 68, allowed the calculation of relative quantum yields from the ratio of the slope using Equation 6. For the example displayed below (Figure 68), a standard error of $\pm 3.1\%$ was obtained. For all other samples that will be discussed in this section good linear plots with standard errors $\leq \pm 5\%$ were obtained from which Φ_{FS} were calculated.

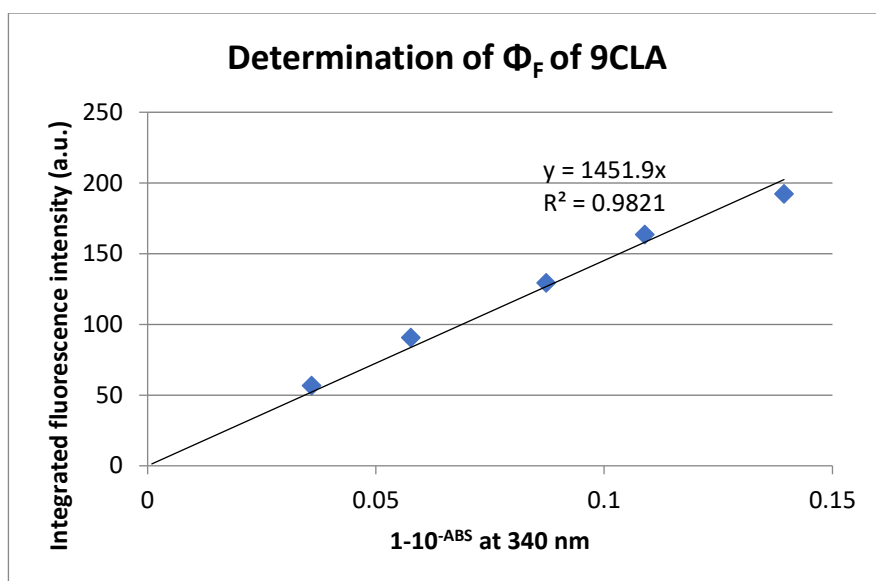


Figure 68 Plot of fraction of light absorbed *versus* integrated fluorescence to determine gradient (relative slope) for the calculation of Φ_F of the fluorescence standard 9CLA in DCM (excited at 340 nm)

The standard fluorophore used to calculate Φ_{FS} was 9-chloroanthracene (9CLA) in DCM. 9CLA showed good spectral overlap of both absorption and fluorescence spectra with those of the *E*-combretastatins. The absorption and emission spectra of 9CLA is quite red shifted with the main absorption band ranging from $\sim 295 - 420$ nm and the fluorescence emission covering a range from $\sim 375 - 530$ nm when excited at 350 nm.

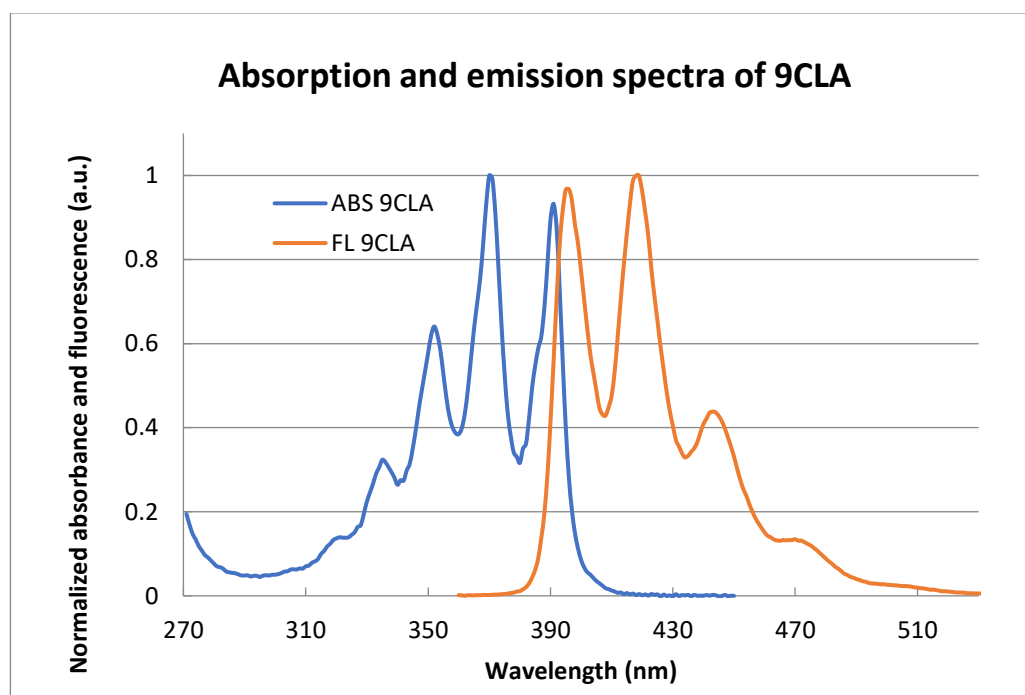


Figure 69 Normalized absorption and emission spectra of 9CLA in DCM (right)

5.2.2 Fluorescence lifetime and quantum yield of *E*-combretastatins

Fluorescence quantum yields (Φ_F) and fluorescence lifetimes (τ_F) exhibited a strong solvent-dependence (Table 21). Φ_{FS} of compound **42** ranged from ~ 0.092 in MeOH to 0.451 in hexane. In polar solvents the Φ_F s varied greatly with solvent viscosity. Low Φ_{FS} (0.092) were obtained in solvents with low viscosity such as MeOH (0.59 cP), whereas in more viscous solvents such as DMSO (2.24 cP) higher Φ_{FS} (~ 0.305). τ_F values were obtained as good single exponentials ($\chi^2 < 1.5$) and showed a dependence on solvent viscosity; the lowest τ_F was observed in methanol (0.290 ns). Methanol is a polar solvent with low viscosity. The highest τ_F value was observed in the most viscous solvent DMSO (1.203 ns). The effect of solvent viscosity on τ_F and Φ_F for stilbenes is well documented (Saltiel & Megarity, 1972; Saltiel & D'Agostino, 1972); the decrease in rate of isomerization with increasing solvent polarity occurs as a deactivating pathway in competition with fluorescence.

Table 21 Fluorescence quantum yields (Φ_F) (standard error $\pm 5\%$) and fluorescence lifetimes (τ_F) (error $\pm 10\%$, single exponentials) of compound **42**

Solvent	Φ_F	λ_{ex} (nm)	τ_F [ns]	λ_{ex} (nm)	χ^2
Hexane	0.451	340	#	#	#
MeOH	0.092	340	0.290	760	1.23
MeCN	0.251	340	0.375	760	1.43
DCM	0.280	340	0.684	760	1.30
EtOAc	0.294	340	0.734	760	1.17
DMSO	0.305	340	1.203	760	1.05

The plot of τ_{FS} versus Φ_{FS} in different solvents for compound **42** (Figure 70) illustrated the linear relationship between τ_{FS} and Φ_{FS} . Divergence from linearity increased at higher Φ_{FS} and longer τ_{FS} due to the poor solubility in non-polar and viscous solvents.

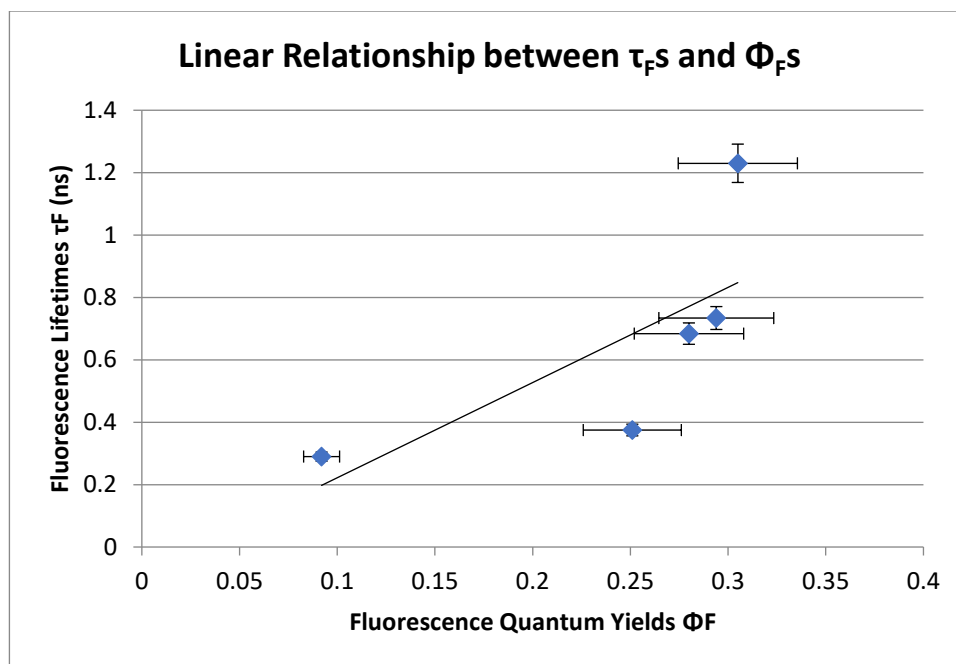


Figure 70 Linear relationship between τ_F s and Φ_F s of compound **42** in different solvents (error bars indicate $\pm 10\%$ error)

Φ_{FS} and τ_{FS} of compound **43** were determined in a range of different solvents and are displayed in Table 22. The lowest Φ_F s of compound **43** were found in the polar solvents methanol ($\Phi_F \sim 0.125$) whilst the highest Φ_F of compound **43** was obtained in the viscous polar solvent DMSO ($\Phi_F \sim 0.415$) as was observed in compound **42**. On average Φ_{FS} of compound **43** were slightly higher than for compound **42**; in polar protic solvents Φ_{FS} of compound **43** increased with solvent viscosity in a similar manner. Single exponential τ_{FS} of compound **43** in different solvents showed a similar trend to compound **42** displaying the shortest τ_{FS} in MeOH (~ 0.254 ns; and the longest in DMSO (~ 0.850 ns). This observation is related to the elongated solvent relaxation times in viscous solvents (Saltiel & Megarity, 1972; Saltiel & D'Agostino, 1972).

Table 22 Fluorescence quantum yields (Φ_F) (standard error $\pm 5\%$) and fluorescence lifetimes (τ_F) (error $\pm 10\%$, single exponentials) of compound **43**

Solvent	Φ_F	λ_{ex} (nm)	τ_F [ns]	λ_{ex} (nm)	χ^2
Hexane	#	#	#	#	#
MeOH	0.125	340	0.254	730	1.20
MeCN	0.365	340	0.314	730	1.35
DCM	0.253	340	0.439	730	1.19
EtOAc	0.255	340	0.294	730	1.25
DMSO	0.415	340	0.850	730	1.33

Φ_{FS} and τ_{FS} determined for compound **46** in a range of solvents are displayed in Table 23. Again a linear relationship between Φ_F and τ_F was observed with larger values obtained in more viscous solvents related to the longer solvent relaxation.

Table 23 Fluorescence quantum yields (Φ_F) (standard error $\pm 5\%$) and fluorescence lifetimes (τ_F) (error $\pm 10\%$, single exponentials) of compound **46**

Solvent	Φ_F	λ_{ex} (nm)	τ_F [ns]	λ_{ex} (nm)	χ^2
Hexane	#	#	#	#	#
MeOH	0.102	340	0.172	760	1.24
MeCN	0.356	340	0.283	760	1.48
DCM	0.343	340	0.361	760	1.12
EtOAc	0.411	340	0.242	760	1.30
DMSO	0.561	340	0.904	760	1.30

5.3 Nonlinear power dependence of *E*-combretastatins on two-photon excitation

It was crucial to show that the observed emission was a real two-photon process. Fluorescence spectra were acquired upon excitation at 680-900 nm in order to determine the optimal wavelength for excitation in the tissue window (Figure 71). Combretastatin **46** is the most red-shifted with an optimal excitation wavelength of 760 nm. **43** was the least red shifted with an optimal excitation wavelength of 720 nm but due to the tuning range of the laser system a wavelength of 730 nm was used for experiments. The optimal wavelength for **42** was around 740 nm but because good intensity was observed at 760 nm this wavelength was also used.

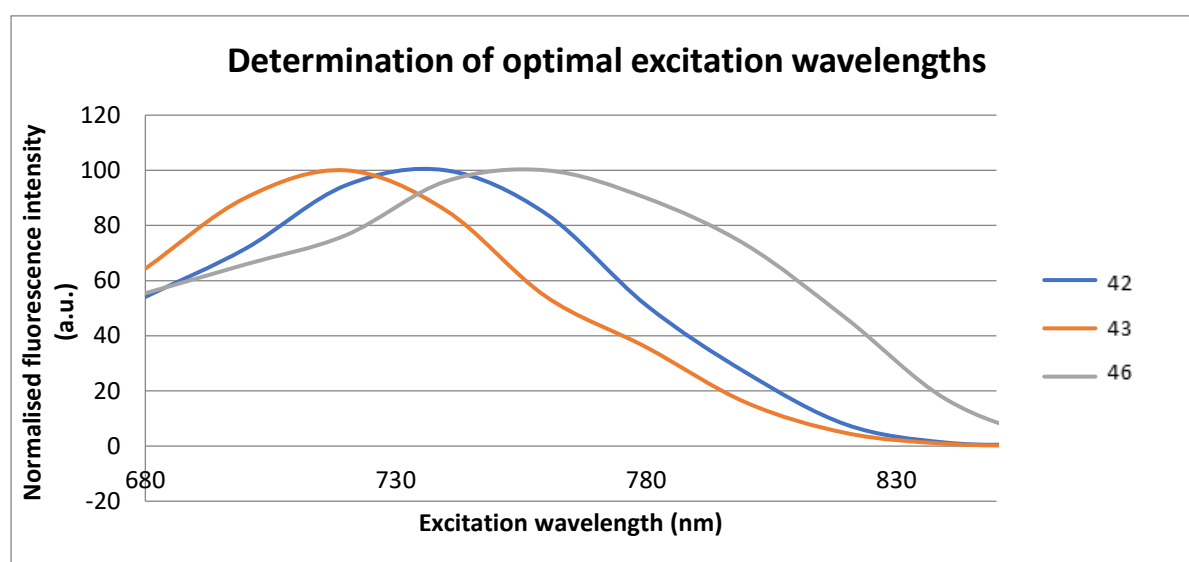


Figure 71 A plot of excitation wavelength (nm) versus maximum fluorescence intensity in order to determine optimal excitation wavelength

E-combretastatins were excited at 730 or 760 nm with increasing laser power (mW). A plot of fluorescence intensity versus laser power (mW) for each of the samples displayed a non-linear increase in fluorescence intensity with increasing laser power (Figure 72) following $I = kP^2$ or $I/P = kP$ (where k is a rate constant). Good quadratic dependences of fluorescence intensity for all *E*-combretastatin derivatives upon excitation at the wavelengths stated were observed suggesting that fluorescence the observed after excitation was a two photon process. This was further supported with a plot of fluorescence intensity/laser power versus laser power which displayed the anticipated linear correlation (Figure 73).

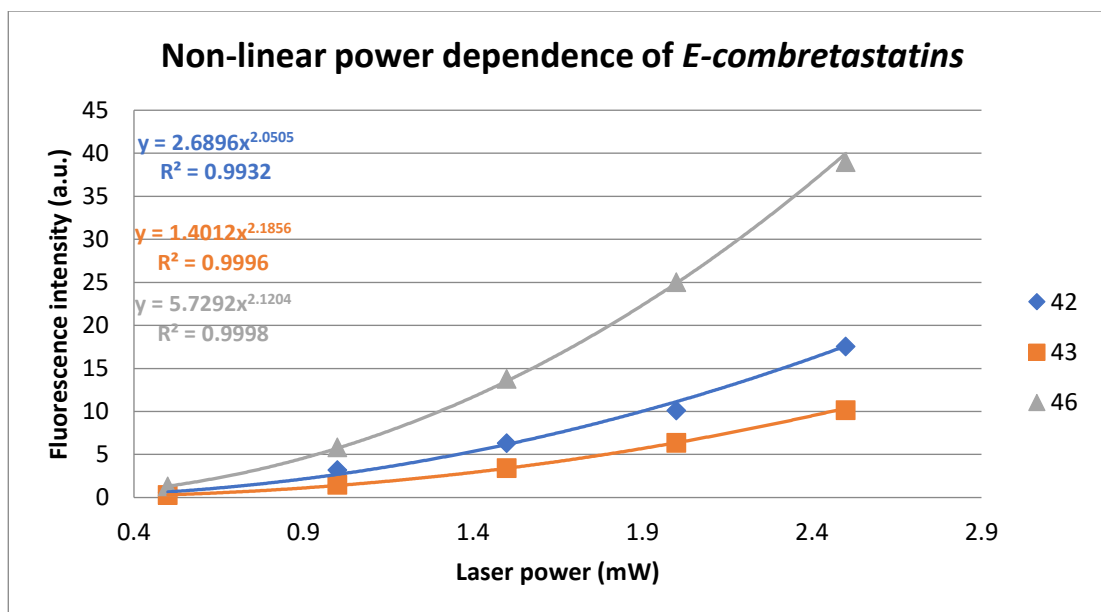


Figure 72 Non-linear power dependences of *E*-combretastatins (5 μ M) in DCM at room temperature (fluorescence was excited at 730 nm for 43 and 760 nm for 42 and 46).

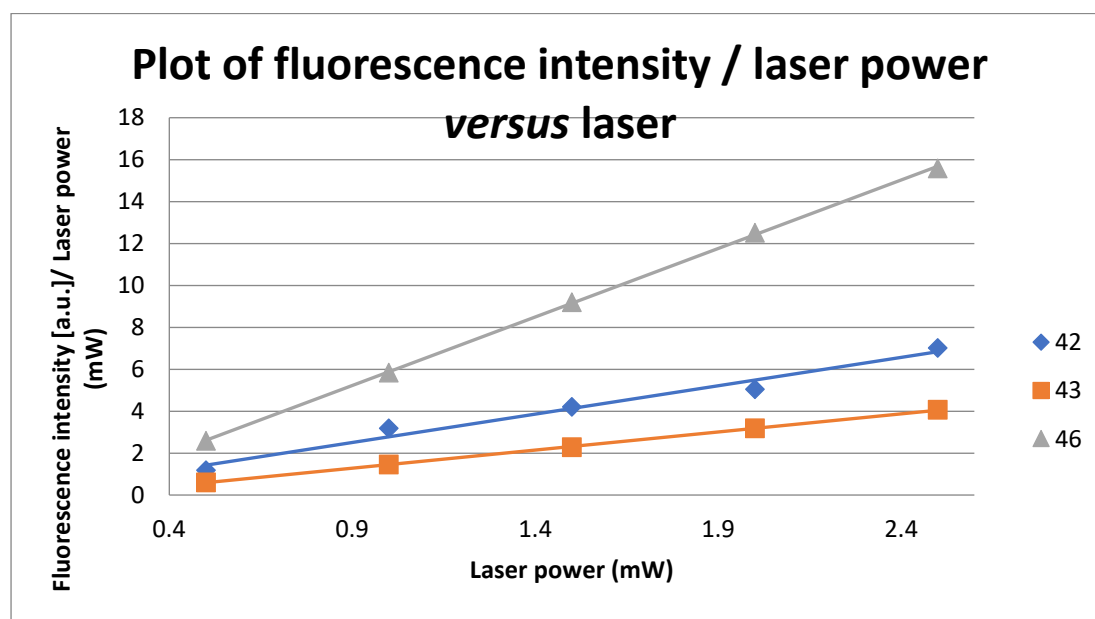


Figure 73 Plot of fluorescence intensity (a.u.)/laser power (mW) versus laser power (mW) for of *E*-combretastatins (5 μ M) in DCM (fluorescence was excited at 730 nm for 43 and 760 nm for 43 and 46).

5.4 Two-photon absorption (2PA) cross-sections of *E*-combretastatins

Drug candidates suited for application in two-photon phototherapy should ideally display high two-photon absorption cross-sections. Two-photon absorption (2PA) spectra were measured using a Leica TCS SP8 DLS light sheet fluorescent microscope. Two-photon absorption cross-sections (σ_2) were determined using the comparative fluorescence method of Makarov (Makarov *et al.*, 2008b) with 9CLA as the standard fluorophore and calculated from the raw data using the method by Mathai *et al.* (2007).

For all *E*-combretastatins significant changes of the 2PA cross-sections depending on the excitation wavelength were observed with the largest cross-section observed upon excitation at 700 nm. Calculated two-photon cross-sections at 700 nm were around three orders of magnitude larger than that of *E*-CA4 (<10 GM) (Scherer, 2012). Modifications were made to the stilbene structure to provide charge transfer across the molecule in order to increase their two-photon cross-section. Compounds 42 and 46 appeared to have a second absorption peak at 760 nm. This may be the result of TICT (twisted intramolecular charge transfer) state formation. Hence the two bands might correspond to a locally excited (LE) state and TICT state formed during 2PA absorption. High 2PA cross-sections within the tissue window, as observed with these *E*-combretastatin derivatives, are a highly desirable characteristic of pro-drug candidates for 2PA phototherapy.

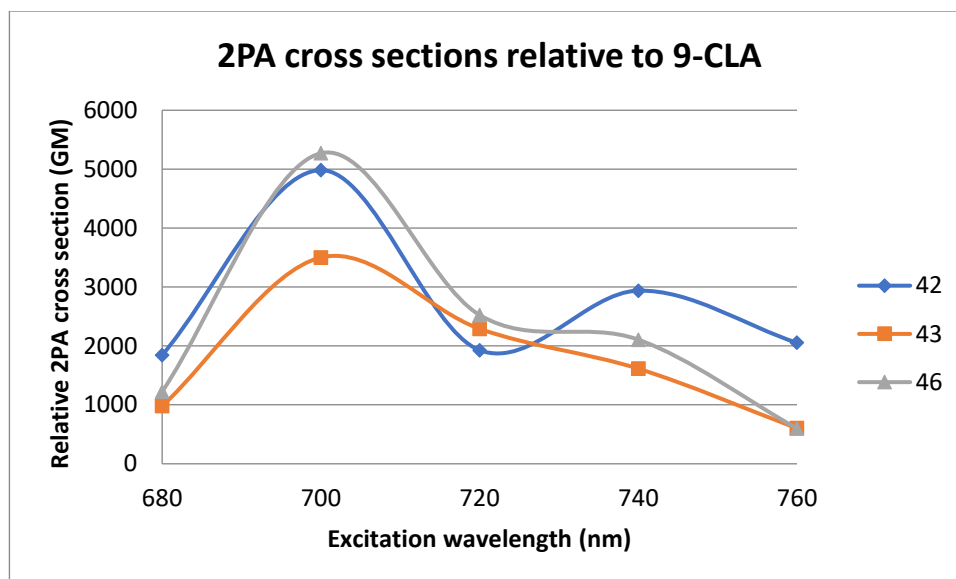


Figure 74 Two-photon absorption cross-sections (σ_2) of 42, 43 and 46 (1 μM) in DCM (in GM units) measured at room temperature.

6. Results & discussion – Imaging of Combretastatins in Live Mammalian Cells

Uptake and distribution of *E*-combretastatins was monitored using the light sheet, confocal and the multiphoton FLIM system at the Rutherford Appleton Laboratory.

6.1 Intracellular uptake and distribution of *E*-combretastatins in cell monolayers

E-combretastatins as pro-drugs for a novel form of two-photon phototherapy were evaluated to determine how rapidly the compounds were taken up by different live mammalian cells and where they accumulated within the cells. The *E*-combretastatins fluoresced with quantum yields high enough for fluorescence imaging, allowing confocal and multiphoton imaging to determine the behaviour of *E*-combretastatins within live cells.

6.1.1 Uptake of compound **42E** into cell monolayers

The intracellular uptake of combretastatin **42E** (1 μ M) in tissue culture medium (0.01% DMSO) by CHO cells in 35 mm Nunc glass bottom dish at room temperature was monitored by multiphoton FLIM and confocal microscopy over 4 min (Figure 75). A single image was recorded in a 1 s scan. Although accumulation for longer would have provided an improved image, the uptake was so rapid it required quick scans in order to observe the initial increase in fluorescent intensity and hence the initial uptake. Fluorescence was excited at 760 nm using laser power 1.2 mW. Following the addition of the combretastatin, images were recorded every 1 s. The first image in the series shows a control sample of cells in 1 mL medium before the addition of combretastatin in medium (1 mL) followed by images every 1 s. The increase in fluorescence intensity indicated the uptake of compound **42E** into the CHO cells. Intracellular distribution within the cells was observed just 60 s after addition. A plot of average counts/ pixel (fluorescence intensity) *versus* time (s) showed biphasic uptake with an initial rapid phase within the first 60 s and a slower phase lasting around 120 s where a plateau was observed indicating that drug uptake was complete. Combretastatin appeared to be distributed within the cytoplasm of the cell without any diffusion into the nucleus as expected of drugs that interact with tubulin which is found in the cytoplasm. The intensity images show the compound was located within the cell cytoplasm and intense

fluorescence was observed in localised regions which had previously been identified as lipid droplets (Bisby *et al.*, 2011a; Scherer *et al.*, 2015). Lipid droplets are relatively non-polar environments that form within cells over time during the process of maturation (Ju *et al.*, 2011).

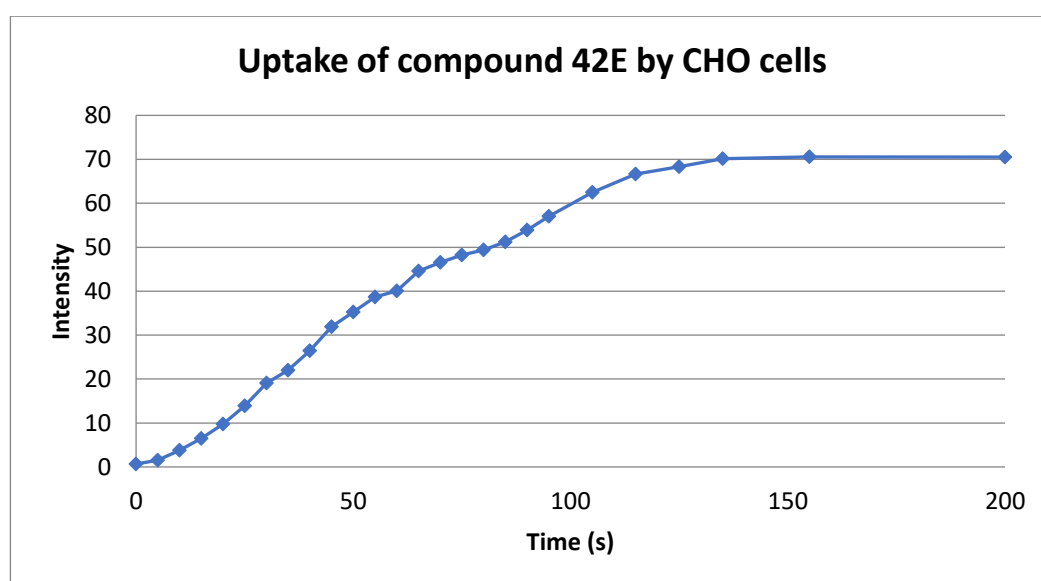
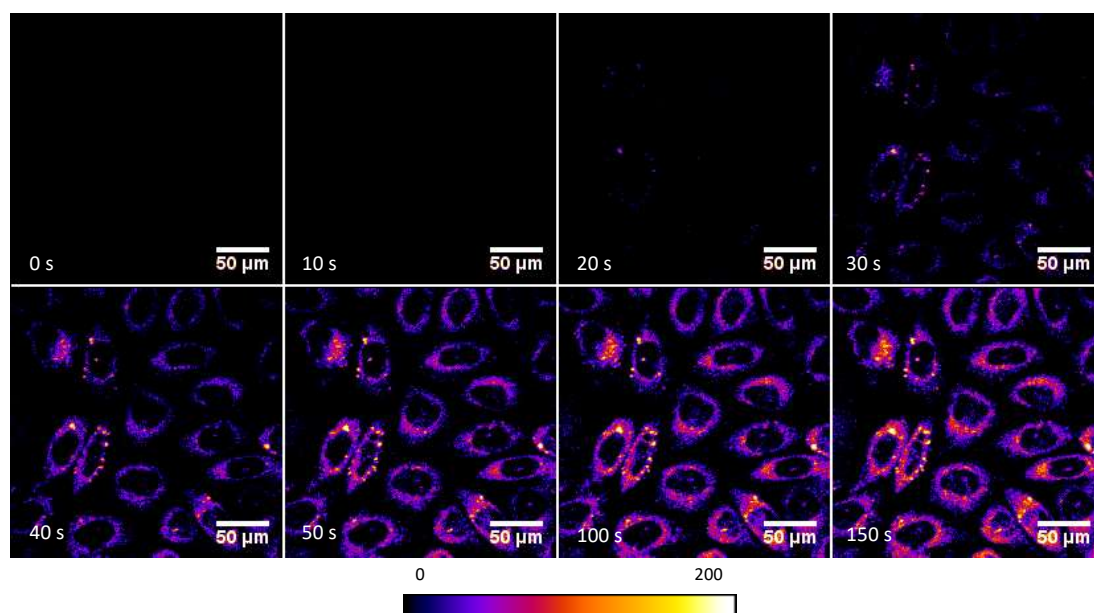


Figure 75 Fluorescence imaging of Chinese hamster ovary (CHO) cells before and after addition of compound 42E at 25 °C. Fluorescence at 400 nm was excited by two-photon absorption at 760 nm.

After 15 min of incubation of cells with compound 42E, the intensity (A) and FLIM (B) images in Figure 76 confirmed the distribution of combretastatin within the cytoplasm of live CHO cells with increased accumulation in localised regions which have previously been identified as lipid droplets (Bisby *et al.*, 2011a; Scherer *et al.*, 2015). The peak lifetime of intracellular

fluorescence at 1.05 ns ($\chi^2 = 1.16$) (C) suggested that the cytoplasmic environment was viscous as it is similar in value to that previously measured in the more viscous solvents.

The CHO cells were quite mature; in mature cells lipids could form clusters leading to the formation of lipid droplets, decreasing the cytoplasmic viscosity and hence shorter fluorescence lifetimes (Ju *et al.*, 2011).

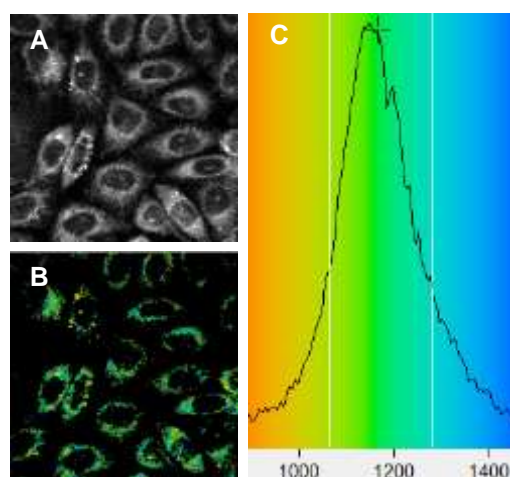


Figure 76 A) intensity image of compound **42E** in CHO cells; B) FLIM image of compound **42E** in CHO cells; C) fluorescence lifetime distribution in ps

The intracellular uptake by HEK293 cells of combretastatin **42E** (1 μ M) in tissue culture medium (0.01% DMSO) at room temperature was monitored by confocal microscopy over 5 min (Figure 77). A single image was recorded in a 0.7 s scan using the confocal 405 laser (1.3 mW). The confocal software allowed for an even faster scan as it was not required to sync the multiphoton laser to the software. Following the addition of compound **42E**, images were recorded every 0.7 s. The first image showed Hek293 cells before addition of compound **42E** and was used to subtract background fluorescence; the increased fluorescence could be directly correlated to the uptake of compound **42E**. The increase in fluorescence intensity indicated the uptake of compound **42E** into HEK293 cells was comparable to that in CHO cells. Intracellular distribution within the cells was observed just 60 s after addition. A plot of average counts/ pixel (fluorescence intensity) *versus* time (s) again showed biphasic uptake with an initial rapid phase within the first 60 s and a slower lasting around 120 s where a plateau was observed indicating uptake of compound **42E** was complete. Compound **42E** appeared to be distributed within the cytoplasm of HEK293 cells.

Compared to CHO cells, fewer lipid droplets were observed with compound 42 distributing evenly within the cytoplasmic region.

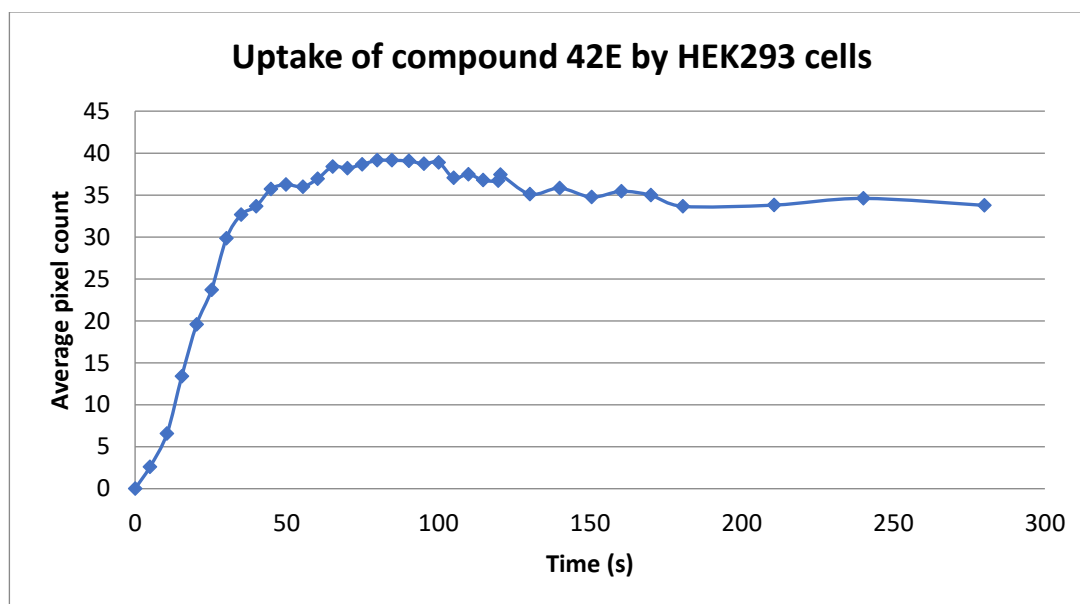


Figure 77 Uptake of compound 42E (1 μ M) by HEK293 cells over time at room temperature. 400 nm was excited by two-photon absorption at 760 nm

After 15 min of incubation of HEK293 cells with compound **42E** the intensity (Figure 76A) and FLIM (Figure 76B) images confirmed the distribution of combretastatin within the cytoplasm. The peak lifetime of intracellular fluorescence at 1.15 ns ($\chi^2 = 1.16$) (C) was longer than that observed in CHO cells suggesting a more viscous cytoplasmic environment in the HEK293 cells. The HEK293 cells were less confluent (~60%) than CHO cells (~80%). In less mature cells there are more free lipids in the cytoplasm leading to increased cytoplasmic viscosity and hence longer fluorescence lifetimes than those observed in the CHO cells (Ju *et al.*, 2011).

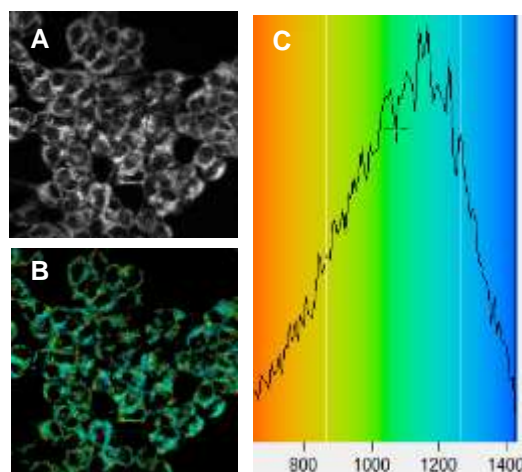


Figure 78 A) intensity image of compound 42E in HEK293 cells; B) FLIM image of compound 42E in HEK293 cells; C) fluorescence lifetime distribution in ps

6.1.2 Uptake of compound 43E into cell monolayers

The intracellular uptake of combretastatin **43E** (1 μM) in tissue culture medium (0.01% DMSO) by CHO cells in 35 mm Nunc glass bottom dish at room temperature was monitored by multiphoton FLIM and confocal microscopy over 4 min (Figure 79). Fluorescence was excited at 720 nm using laser power 1.2 mW. A single image was recorded before addition of compound **43E** to record any background fluorescence. Following the addition, images were recorded every 1 s. The increase in fluorescence intensity indicated the uptake of compound **43E** into the CHO cells; intracellular distribution within the cells was observed just 60 s after addition. A plot of average counts (fluorescence intensity) versus time (s) showed biphasic uptake with an initial rapid phase within the first 20 s and a slower phase lasting around 100 s where a plateau was observed indicating that drug uptake was complete. The uptake of compound **43E** into CHO cells was quicker than compound **42E**, Compound **43Z** showed to be more cytotoxic in cells with an IC_{50} value (0.23 μM , Table 13) and tubulin polymerisation IC_{50} (0.32 μM , Figure 58) compared to that of compound **42Z** (0.25 μM and 0.39 μM respectively). This may be due to the improved binding to tubulin observed with compound **43** due to the 3-OH group on the B-ring (Gaspari *et al.*, 2017). Compound **43** was distributed within the cytoplasm of the cell without any diffusion into the nucleus as expected of the drugs that interact with tubulin which is found in the cytoplasm. The intensity images show compound **43** accumulated within the cell cytoplasm with an intense fluorescence observed in lipid droplets (Bisby *et al.*, 2011a; Scherer *et al.*, 2015).

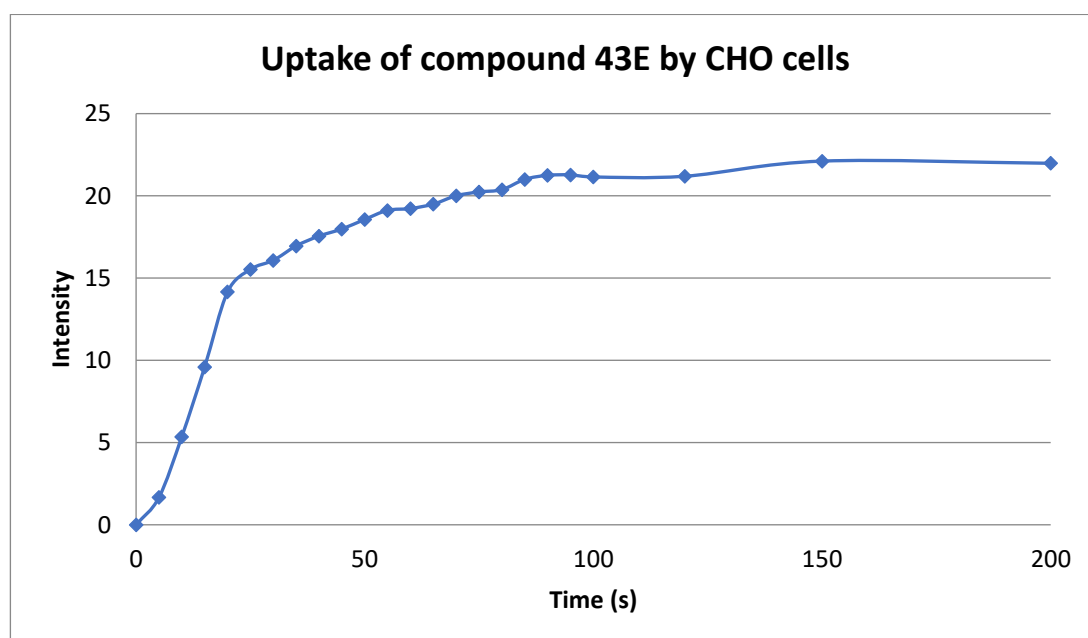
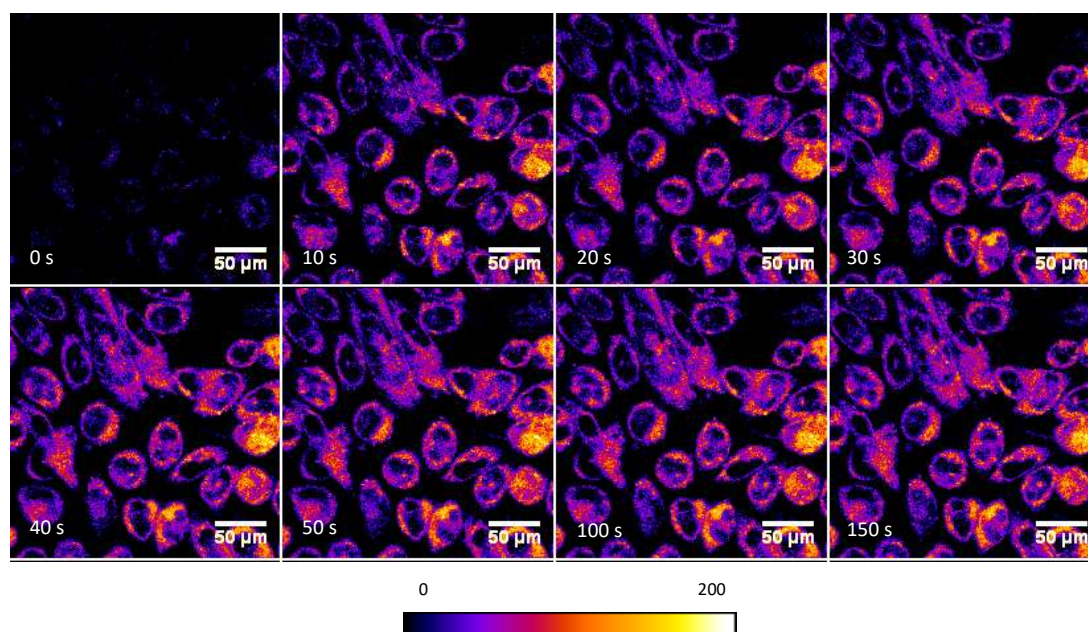


Figure 79 Uptake of 43E (1 μM) by CHO cells over time at room temperature. Fluorescence at 400 nm was excited by two-photon absorption at 720 nm

Intensity (Figure 80A) and FLIM (Figure 80B) images were recorded after 15 min of incubation of cells with compound **43E** and confirmed the distribution of combretastatin within the cytoplasm of live CHO cells with increased accumulation in lipid droplets (Bisby *et al.*, 2011a; Scherer *et al.*, 2015). The peak lifetime of intracellular fluorescence at 1.2 ns ($\chi^2 = 1.16$) (Figure 80C) again suggested that the cytoplasmic environment of the CHO cells was quite viscous.

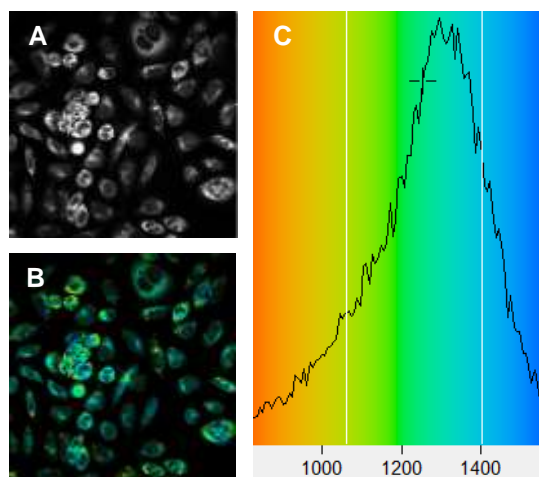


Figure 80 A) Intensity image of compound **43E** in CHO cells; B) FLIM image of compound **43E** in HEK293 cells; C) fluorescence lifetime distribution in ps

The intracellular uptake by HEK293 cells of combretastatin **43E** (1 μM) in tissue culture medium (0.01% DMSO) at room temperature was monitored by confocal microscopy over 5 min (Figure 81). A single image was recorded in a 0.7 s scan using the confocal 405 laser (1.3 mW); Following the addition of compound **43E**, images were recorded every 0.7 s; background fluorescence was recorded before the addition of compound **43E**. The increased fluorescence could be directly correlated to the uptake of compound **43E**. The increase in fluorescence intensity indicated the uptake of compound **43E** into HEK293 cells was comparable to that in CHO cells. Intracellular distribution within the cells was observed just 60 s after addition. A plot of average counts/ pixel (fluorescence intensity) *versus* time (s) showed initial rapid uptake within the first 60 s followed by a slight decrease before the fluorescence stabilised indicating uptake was complete. Compound **43E** appeared to be distributed within the cytoplasm of HEK293 cells after 60 s incubation.

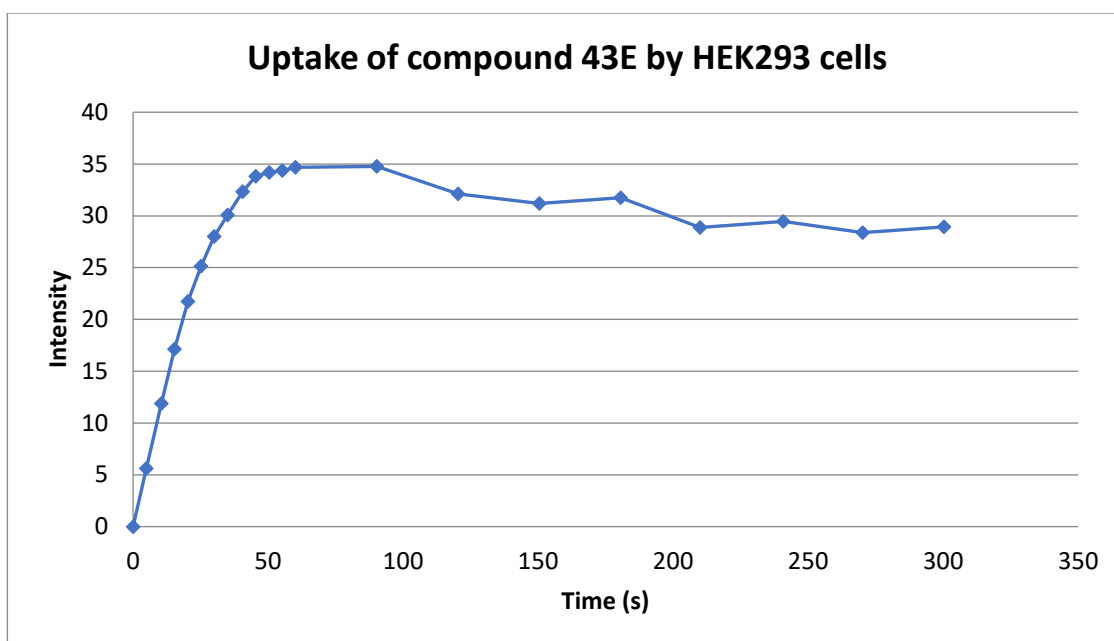


Figure 81 Uptake of 43E (1 μ M) by HEK293 cells over time at room temperature. Fluorescence at 400 nm was excited by two-photon absorption at 720 nm

HEK293 cells were incubated with compound **43E** for 15 min and intensity (Figure 82A) and FLIM (Figure 82B) images were recorded. Compound **43E** was distributed within the cell cytoplasm without any diffusion into the nucleus. The peak lifetime of intracellular fluorescence at 1.3 ns ($\chi^2 = 1.16$) (C) was again longer than that observed in the more mature CHO cells suggesting a viscous cytoplasmic environment due to the free lipids (Ju, Winterhalder & Zumbusch, 2011).

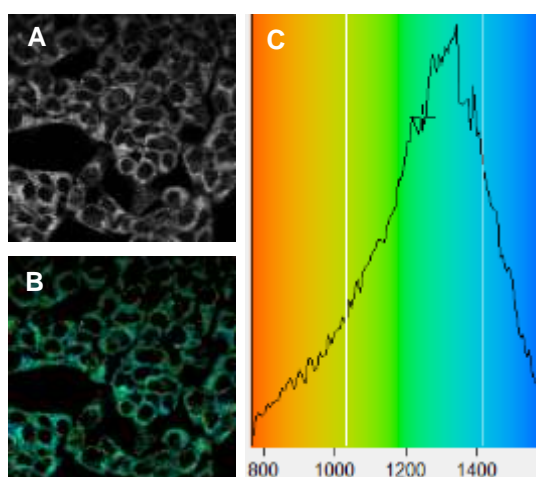


Figure 82 A) Intensity image of compound 43E in HEK293 cells; B) FLIM image of compound 43E in HEK293 cells; C) fluorescence lifetime distribution in ps

6.1.3 Uptake of compound **46E** into cell monolayers

The intracellular uptake of compound **46E** (1 μM) into CHO cells was monitored by multiphoton FLIM and confocal microscopy over 5 min (Figure 83). Fluorescence was excited at 760 nm using laser power 1.2 mW and a single image was recorded in a 1 s scan. Following the addition of the combretastatin, images were recorded every 1 s. The first image before addition of compound **46E** showed background fluorescence, any subsequent fluorescence could be related to the uptake. Intracellular distribution within the cells was observed just 50 s after addition. A plot of average counts/ pixel (fluorescence intensity) versus time (s) showed biphasic uptake with an initial rapid phase within the first 20 s and a slower lasting phase to around 50 s where a plateau was observed indicating that drug uptake was complete. The uptake of compound **46E** was quicker than with compounds **42E** and **43E** as expected due to the lower intracellular IC_{50} (0.06 μM) and tubulin polymerisation IC_{50} (0.28 μM). Compound **46E** distributed within the cytoplasm with intense fluorescence in localised regions which have previously been identified as lipid droplets (Bisby *et al.*, 2011a; Scherer *et al.*, 2015).

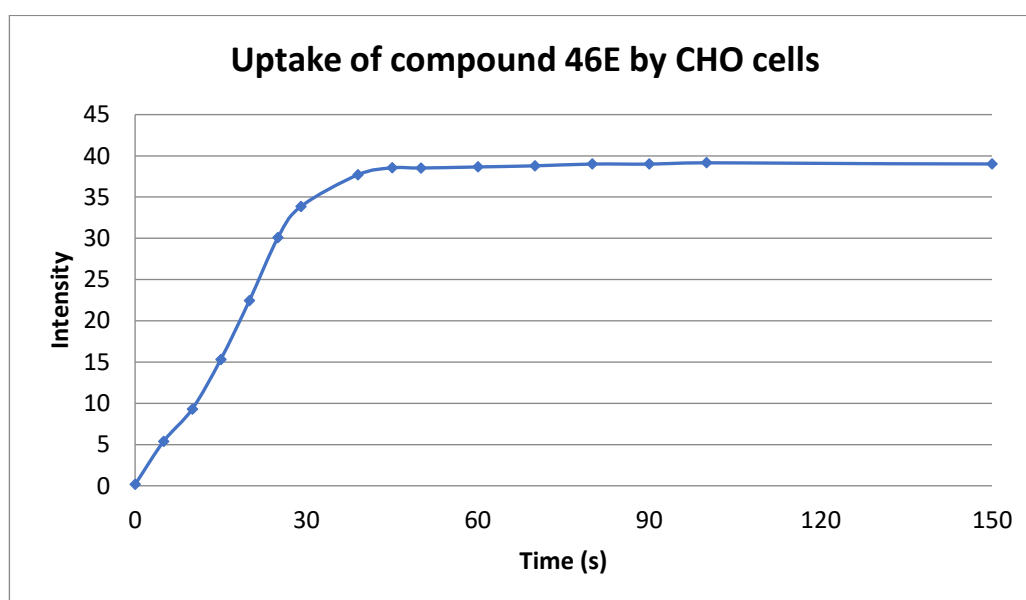
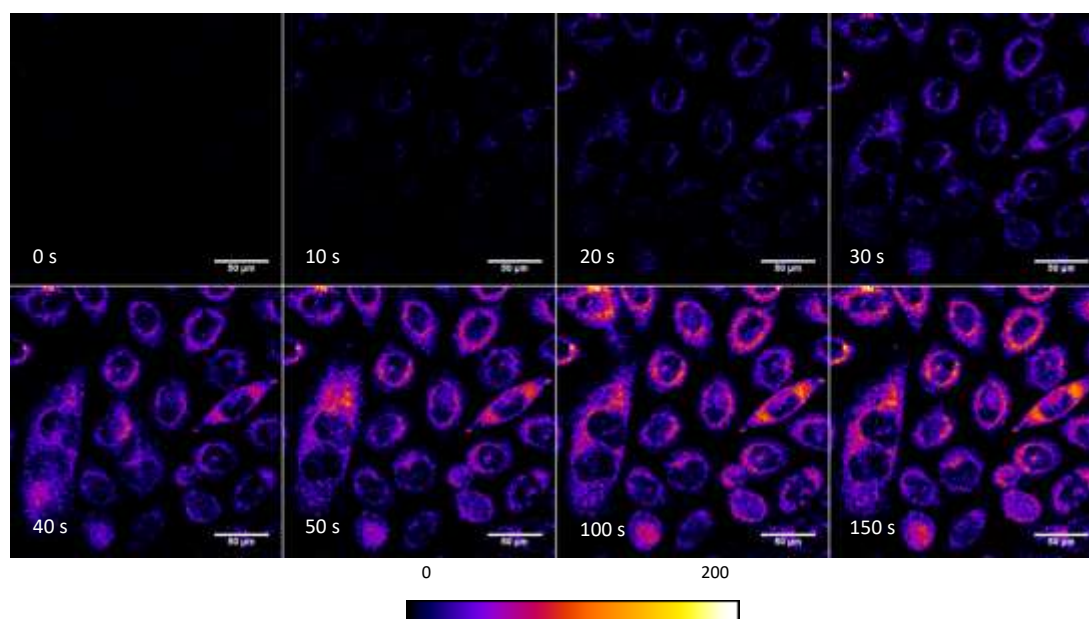


Figure 83 Uptake of 46E (1 μ M) by CHO cells over time at room temperature. Fluorescence at 400 nm was excited by two-photon absorption at 760 nm

Intensity (Figure 84A) and FLIM (Figure 84B) images were recorded after 15 min of incubation of CHO cells with compound **46E** and confirmed the distribution of combretastatin within the cytoplasm of live CHO cells with increased accumulation in localised regions which have previously been identified as lipid droplets (Bisby *et al.*, 2011a; Scherer *et al.*, 2015). The peak lifetime of intracellular fluorescence at 1.2 ns ($\chi^2 = 1.16$) (Figure 84C) suggested the cytoplasmic environment of the CHO cells was quite viscous.

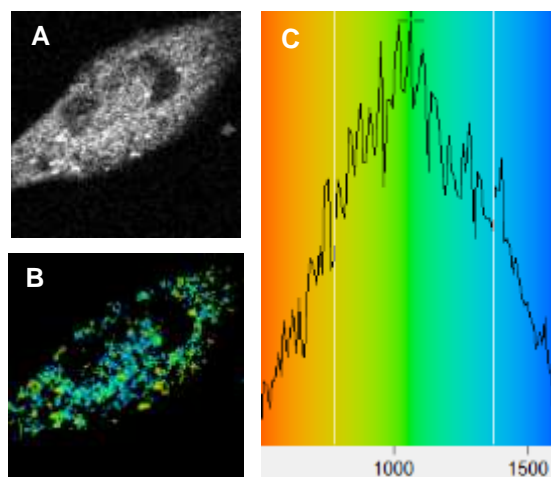


Figure 84 A) Intensity image of compound 46E in CHO cells; B) FLIM image of compound 46E in HEK293 cells; C) fluorescence lifetime distribution in ps

The intracellular uptake by HEK293 cells of combretastatin **46E** (1 μ M) appeared to be biphasic; an initial rapid phase within the first 30 s was observed followed by a slower phase lasting to around 120 s where a plateau was observed indicating that drug uptake was complete (Figure 85). The increase in fluorescence intensity indicated the uptake of compound 46 into HEK293 cells was comparable to that in CHO cells. Intracellular distribution within the cells was observed just 60 s after addition. A plot of average counts/pixel (fluorescence intensity) *versus* time (s) showed initial rapid uptake within the first 60 s followed by a slight decrease before the fluorescence stabilised indicating uptake was complete. Compound **46E** appeared to be distributed within the cytoplasm of HEK293 cells after 60 s incubation.

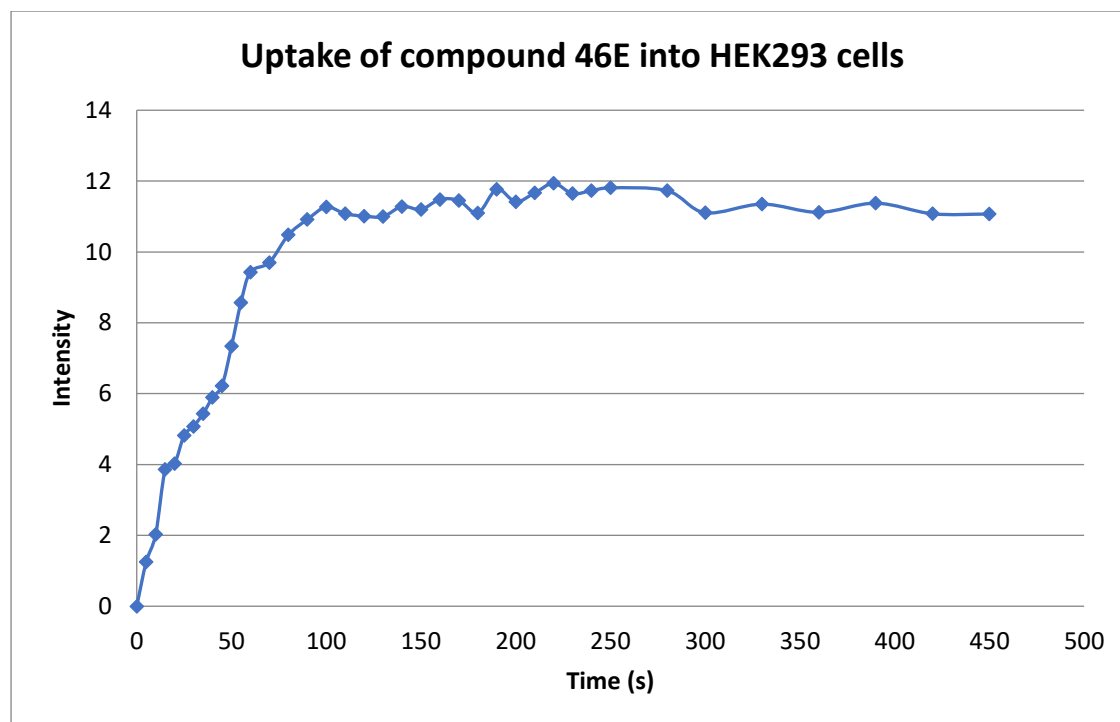


Figure 85 Uptake of 46E (1 μ M) by HEK293 cells over time at room temperature. Fluorescence at 400 nm was excited by two-photon absorption at 760 nm

Intensity (Figure 86A) and FLIM (Figure 86B) images were recorded after 15 min of incubation of HEK293 cells with compound **46E** confirming the distribution within the cytoplasm. The peak lifetime of intracellular fluorescence at 1.3 ns ($\chi^2 = 1.16$) (Figure 86C) suggested the cytoplasmic environment of HEK293 cells was more viscous than the more mature CHO cells. The HEK293 cells were less mature and so lipid droplets had not yet formed, the amount of free lipids in the cytoplasm increased viscosity (Ju *et al.*, 2011).

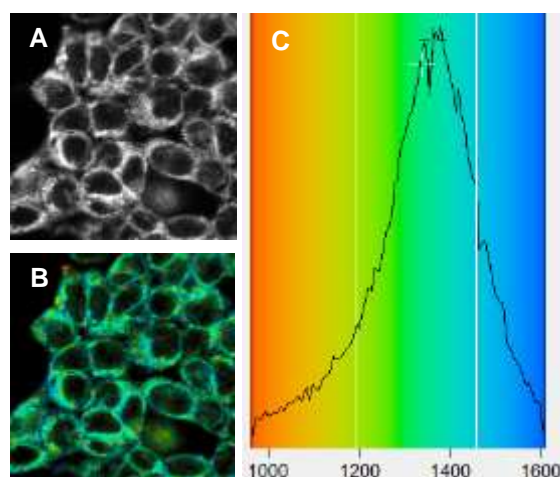


Figure 86 A) Intensity image of compound 46E in HEK293 cells; B) FLIM image of compound 46E in HEK293 cells; C) fluorescence lifetime distribution in ps

6.2 Intracellular uptake and distribution of *E*-combretastatins in cell spheroids

Once uptake of combretastatins was determined in monolayer cell cultures, the experiments were repeated in 3-D model systems to demonstrate uptake within a tissue model structure. A quantitative understanding of drug uptake and diffusion within tissues is an important aspect of drug development and cell spheroids are considered as a closer model to tumours than cell monolayers as these 3-D structures display some characteristics of solid tumours such as low central oxygen tension and a necrotic central core (Fennema *et al.*, 2013). Further to this, cells in tissues interact through chemical stimuli with adjacent cells along all three dimensions which is lost in cell monolayers (Pampaloni *et al.*, 2013). At the cellular and multicellular level, diffusion is the primary mechanism for drug movement into cells. The diffusion distance for a drug into a monolayer is relatively short compared to *in vivo* tissues, and biological barriers are not adequately replicated. Imaging of spheroids allowed for the quantification of the uptake and diffusion of combretastatin derivatives into 3-D structures that display some characteristics of solid tumours. Previously, it was reported that resolving the complete spheroid structure was difficult due to low light transmission and high scattering around the spheroid equator (Ma *et al.*, 2012). Light sheet fluorescence microscopy (LSFM) uses a plane of light to optically section and view tissues. It is well suited for imaging deep into tissues as there is only exposure to a thin plane of light and so

photobleaching and phototoxicity are reduced compared to confocal and multiphoton microscopy (Santi, 2011).

HEK spheroids were grown in phenol red-free MEM media then transferred to an agarose mount in a 35 mm Nunc glass bottom dish. A custom-made 3D printed mould was inserted into 35 mm Nunc glass bottom dish containing agarose (1%, 2 mL) and allowed to set. Excess agarose was cut away and medium (MEM, 2 mL) was added, spheroids were then mounted into the agarose wells (Figure 87).

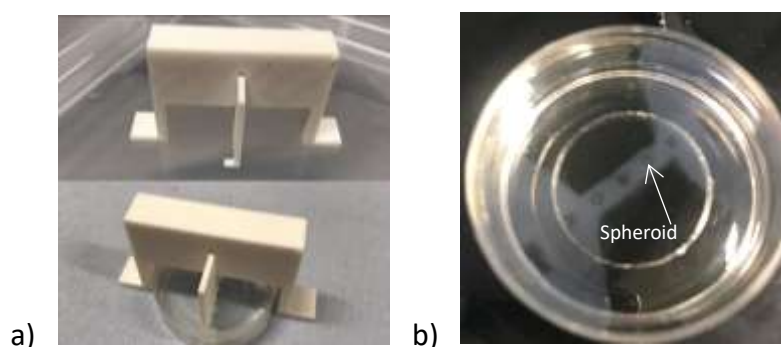


Figure 87 A - 3D printed moulds B – spheroids mounted into agarose wells in MEM media.

6.2.1 Uptake of compound 42E into HEK293 spheroids

The uptake of compound **42E** (1 μ M) in tissue culture medium (0.01% DMSO) by HEK spheroids in a 35 mm Nunc glass bottom dish at room temperature was monitored using the light sheet laser diode emitting at 405 nm over 20 min. A stack of 48 slices was collected in a 60 s scan and each slice represented a depth of 2.45 μ m in the z-plane. Using Fiji, the overall intensity was averaged from the z-stack to see how the drug interacted with the spheroid as a whole over time (Figure 88A-D). The first image at time 0 was used to determine background fluorescence which was subtracted from the subsequent images. A plot of the average pixel intensity of the stack *versus* time showed that the increase in intensity stabilised after 240 s indicating uptake throughout the spheroid was complete (Figure 88). Overall uptake into spheroids was slower than that observed in both CHO (Figure 75) and HEK293 (Figure 77) cell monolayers presumably due to the density of the cell cluster (Scherer *et al.*, 2015).

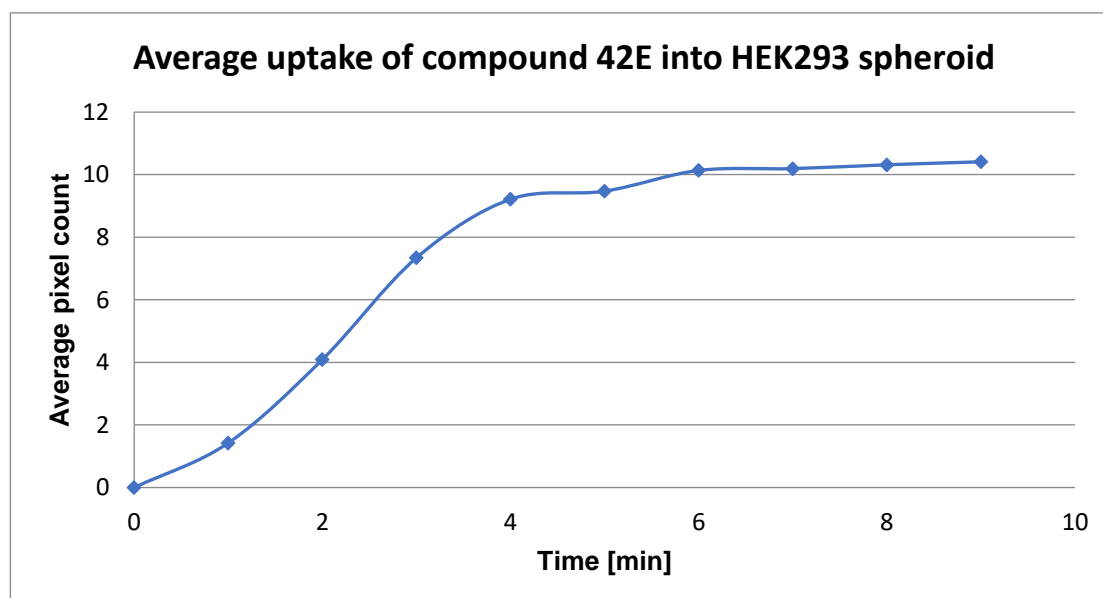
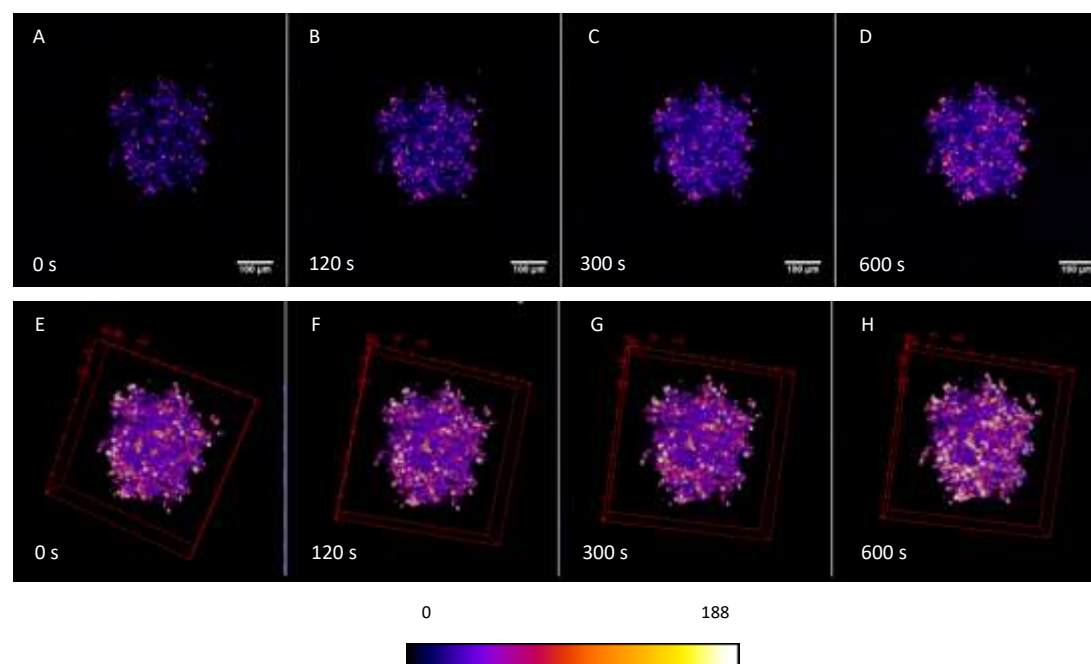


Figure 88 Uptake of 42E (1 μ M) by HEK293 spheroids over time at room temperature.

Light sheet fluorescence microscopy allowed the collection of a stack of images 2.45 μ m apart. Looking at individual slices allowed for the analysis of the uptake of compound 42 at various depths of the spheroid giving a better understanding of the kinetics of the compound with regards to a 3D tumour model. Unfortunately, the slices of images collected for compound **42E** were not of good quality due to the fact that the spheroid drifted during imaging. It should be noted that this is a new technique for imaging these spheroids and the process is not yet optimal. The first row of images (Figure 89 A) represented the medium surrounding the spheroid and was used to monitor any background fluorescence. The

uptake of compound **42E** into the spheroid was fastest at the surface of the spheroid and movement of compound **42E** into the z-plane (i.e. deeper into the spheroid) was observed over time and after around 300 s incubation, significant movement of compound **42E** into the centre spheroid image planes was observed (Figure 89 D). The uptake of compound **42E** was observed in the centre of the spheroid (Figure 89 D) after around 300 s, after which point the overall fluorescence appeared to become uniformly distributed throughout the whole spheroid. Further uptake at the surface of the spheroid from the medium and subsequent diffusion into the centre allowed for an even distribution of compound **42E** throughout the spheroid with time.

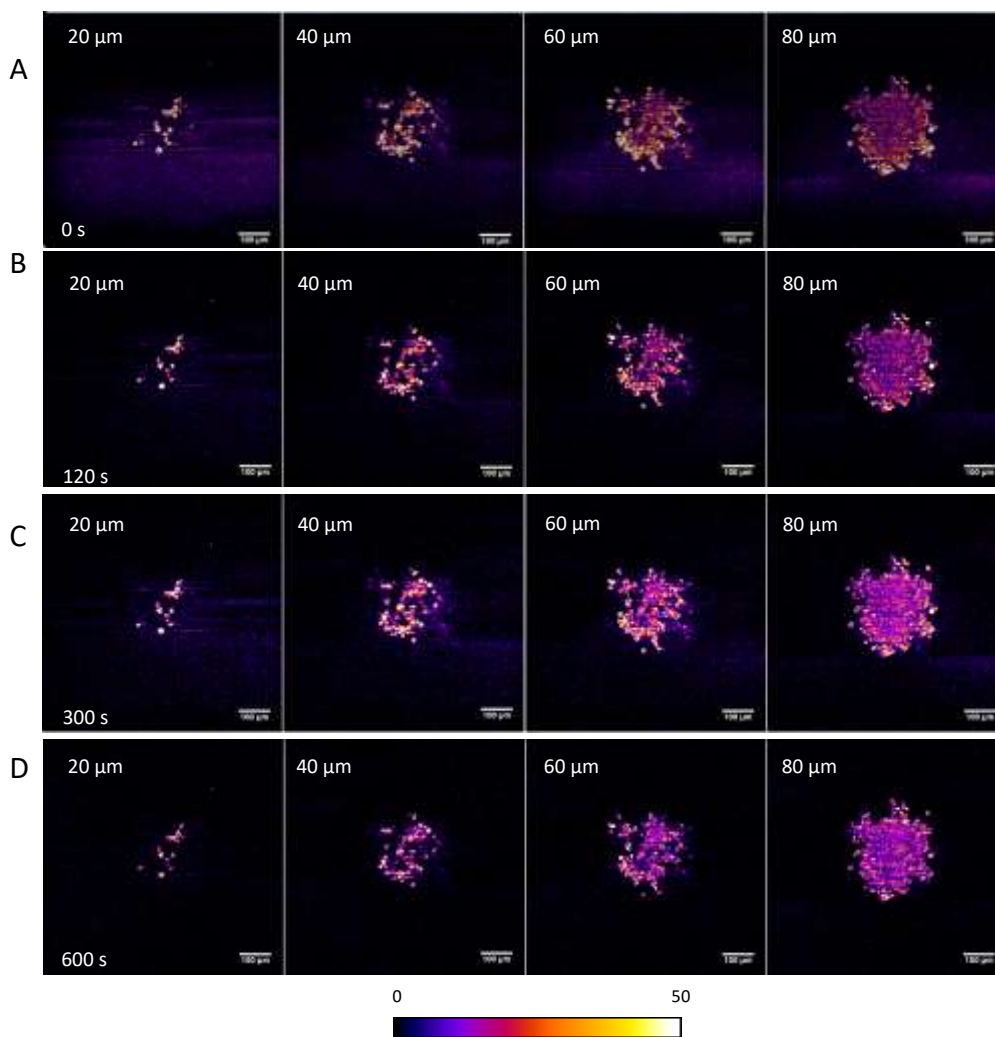


Figure 89 A) images showing different depths of the spheroid at time 0; B) images showing different depths of the spheroid at 120 s; C) images showing different depths of the spheroid at 300 s; D) images showing different depths of the spheroid at 600 s; E) plot of intensity versus time (s) of compound 42E at different depths of spheroid

The rate of uptake (k) and half-life ($t_{1/2}$) (Table 24) of compound **42E** at various depths into the spheroid was determined from the slope of the uptake graphs. The rate of uptake of compound **42E** into the spheroid decreased as the depth into the spheroid increased ($1.60 \times 10^{-2} \text{ s}^{-1}$ at $20 \mu\text{m}$ and $2.83 \times 10^{-3} \text{ s}^{-1}$ at $80 \mu\text{m}$). Further to this, the $t_{1/2}$ (i.e. the time for reach half the maximum uptake) increased closer to the core of the spheroid, demonstrating diffusion of compound **42E** into the spheroid.

Table 24 Rate of uptake (k) and half-life ($t_{1/2}$) of compound **42E** in HEK293 spheroid at varying depths

Depth (μm)	$k \text{ (s}^{-1}\text{)}$	$t_{1/2} \text{ (s)}$
20	1.60×10^{-2}	43
40	7.34×10^{-3}	94
60	7.25×10^{-3}	96
80	2.83×10^{-3}	245

6.2.2 Uptake of compound **43E** into HEK293 spheroid

The intracellular uptake of compound **43E** ($1 \mu\text{M}$) in tissue culture medium (0.01% DMSO) by HEK spheroids in 35 mm Nunc glass bottom dish at room temperature was monitored using the light sheet laser diode emitting at 405 nm over 20 min (Figure 90). A stack of 71 slices was collected in a 60 s scan and each slice represented a depth of $1.97 \mu\text{m}$ in the z-plane. Using Fiji, the overall intensity was averaged from the z-stack to see how the drug interacted with the spheroid as a whole over time (Figure 90A). A plot of the average pixel intensity of the stack *versus* time showed that the increase in intensity stabilised after 200 s indicating uptake throughout the spheroid was complete (Figure 90C). Again the uptake into spheroids was slower than that observed in both CHO (Figure 79) and HEK 293 (Figure 81) cell monolayers due to the density of the cell cluster. The uptake of compound **43E** into the spheroid was quicker than that of compound **42E**, as was observed in the cell monolayers. This faster uptake of compound **43E** can be related to the increased cytotoxicity within cells based on the intracellular IC_{50} value ($0.23 \mu\text{M}$, Table 13) and inhibition of tubulin

polymerisation IC_{50} ($0.32 \mu\text{M}$, Figure 58) compared to that of compound **42** ($0.25 \mu\text{M}$ and $0.39 \mu\text{M}$ respectively).

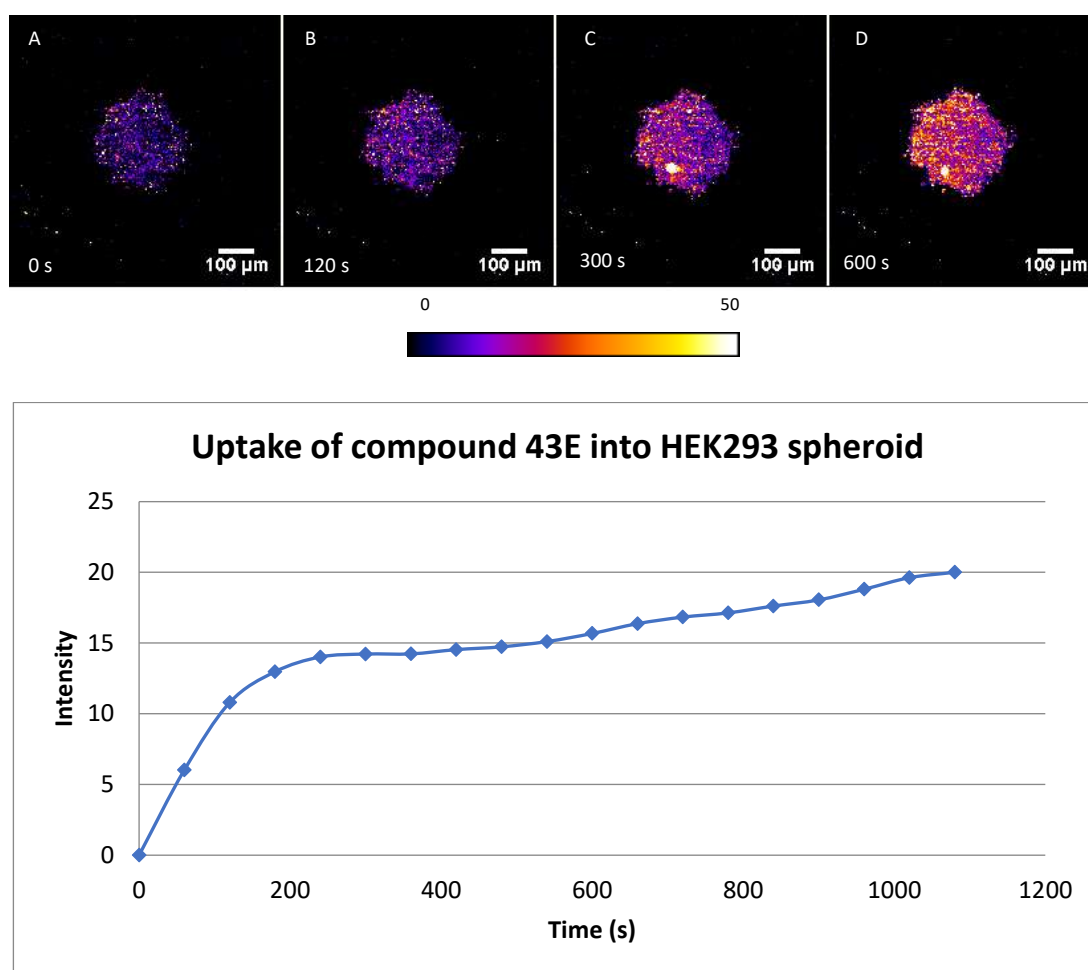


Figure 90 uptake of compound **43E** into HEK293 spheroid

The stack of images generated from the light sheet allowed for a closer look into specific slices of the spheroid, allowing for a better understanding of the kinetics of the compound with regards to a 3D tumour model. The following series of images show different slices of the spheroid over time. The background fluorescence was monitored in the first series of images (Figure 91 A). A plot of time *versus* intensity (Figure 91) at different slices of the spheroid showed the fastest uptake of compound **43E** into the spheroid was at the surface of the spheroid where the cells were the least dense. The rate of initial uptake into the peripheral cells was comparable to that of cell monolayers (Scherer *et al.*, 2015). After around 120 s incubation, a significant increase in fluorescence was observed further towards the core of the spheroid suggesting compound **43E** was diffusing into the spheroid (Achilli *et al.*, 2014).

A decrease in fluorescence at the surface of the spheroid occurred as the fluorescence increased towards the core of the spheroid; this can be explained by the diffusion of compound **43E** into the central planes. Compound **43E** had significantly accumulated in the centre of the spheroid after 200 s (Figure 91C); the images indicated that the highest concentration of compound **43E** was in the outer layer of the spheroid and concentration decreased toward the spheroid core as uptake and inward diffusion occurred. After this point, further uptake at the surface of the spheroid from the medium and subsequent diffusion into the centre allowed for an even distribution of compound **43E** throughout the spheroid with time (Figure 91D). The extent of accumulation of compound **43E** into cells was also observed in the cell monolayers. Similarly, the accumulation of *E*-CA-4 in spheroids was comparable to that observed in monolayers which was attributed to the lipophilicity of the compound (Bisby *et al.*, 2011a).

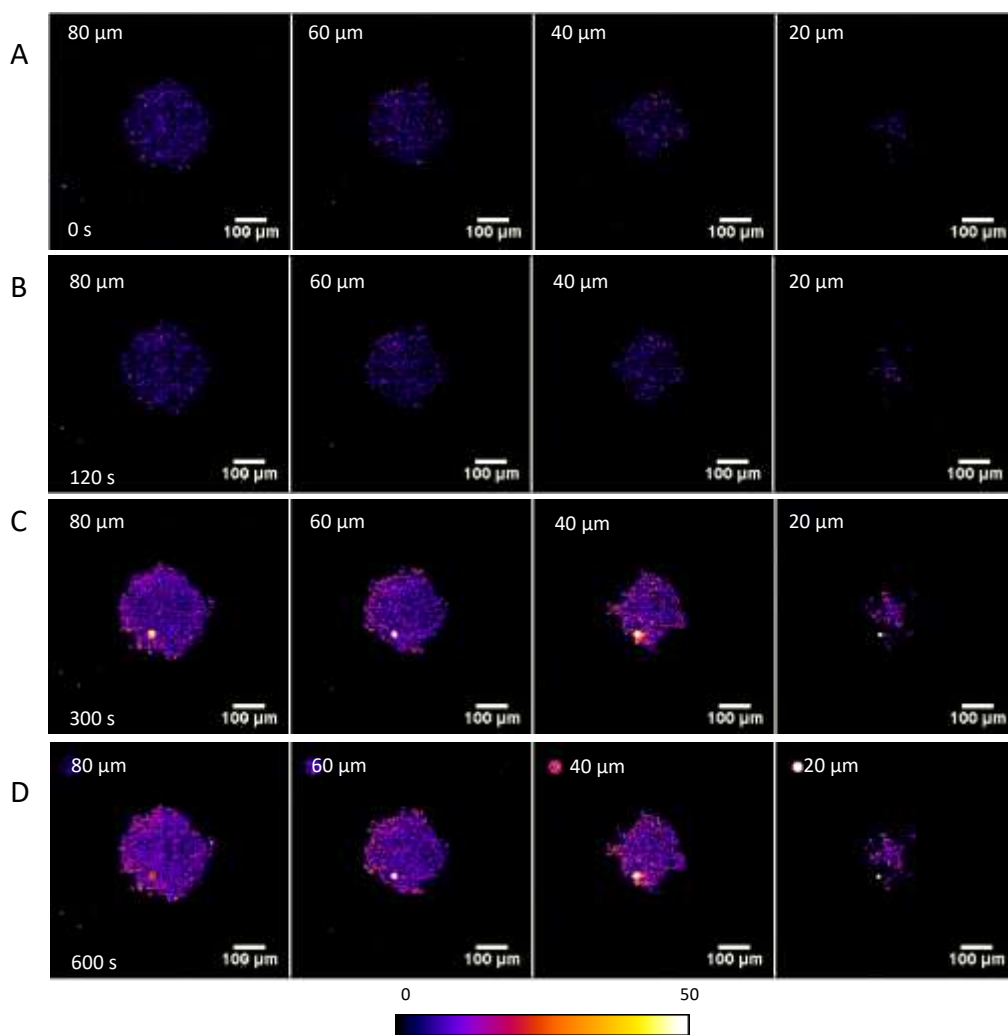


Figure 91 A) images showing different depths of the spheroid at time 0; B) images showing different depths of the spheroid at 120 s; C) images showing different depths of the spheroid at 300 s; D) images showing different depths of the spheroid at 600 s; E) plot of intensity versus time (s) of compound 43E at different depths of spheroid

The rate of uptake (k) and half-life ($t_{1/2}$) (Table 25) of compound **43E** at various depths into the spheroid could be determined from the data set as uptake represented a pseudo-first order association. The rate of uptake of compound **43E** into the spheroid decreased as the depth into the spheroid increased with a plateau at approximately the same point suggesting an even distribution throughout the spheroid after around 400 s. The difference in k closer to the surface was quite large ($2.22 \times 10^{-2} \text{ s}^{-1}$ at $20 \mu\text{m}$ and $1.02 \times 10^{-2} \text{ s}^{-1}$ at $30 \mu\text{m}$) whereas deeper into the spheroid the difference in rate of uptake was less (i.e. $4.54 \times 10^{-3} \text{ s}^{-1}$ at $70 \mu\text{m}$ and $2.65 \times 10^{-3} \text{ s}^{-1}$ at $80 \mu\text{m}$). This can be related to the density of cells at the surface compared to deeper within the spheroid. Further to this, the $t_{1/2}$ (i.e. the time for reach half the maximum uptake) appeared to increase in deeper slices of the spheroid, again suggesting a slower uptake was observed deeper into the spheroid.

Table 25 Rate of uptake (k) and half-life ($t_{1/2}$) of compound **43E** in HEK293 spheroid at varying depths

Depth (μm)	k (s^{-1})	$t_{1/2}$ (s)
20	2.22×10^{-2}	31
30	1.02×10^{-2}	68
40	8.19×10^{-3}	85
50	7.75×10^{-3}	110
60	6.29×10^{-3}	122
70	4.54×10^{-3}	153
80	2.65×10^{-3}	262

6.2.3 Uptake of compound **46E** into HEK293 spheroids

The intracellular uptake of compound **46E** ($1 \mu\text{M}$) in tissue culture medium (0.01% DMSO) by HEK spheroids in 35 mm Nunc glass bottom dish at room temperature was monitored using the light sheet laser diode emitting at 405 nm over 30 min (Figure 92). A stack of 48 slices was collected in a 60 s scan and each slice represented a depth of $2.5 \mu\text{m}$ in the z-plane. Using Fiji, the overall intensity was averaged from the z-stack to see how the drug interacted with the spheroid as a whole over time (Figure 92A-D); the first image at 0 s

represented background fluorescence and was subtracted from subsequent images. A plot of the average pixel intensity of the stack *versus* time showed that the increase in intensity began to stabilise after around 300 s indicating uptake throughout the spheroid was complete (Figure 92C). The cell density of the spheroid slowed the uptake of compound **46E** compared to CHO (Figure 83) and HEK 293 (Figure 85) cell monolayers due to the density of the cell cluster. The uptake of compound **46E** into the spheroid was comparable to that of compound **43E** and faster than compound **42E**, it was expected that the uptake of compound **46E** would be fastest as was observed in the cell monolayers which was related to the intracellular IC_{50} value ($0.06 \mu\text{M}$, Table 13) and inhibition of tubulin polymerisation IC_{50} ($0.28 \mu\text{M}$, Figure 58). The spheroid was quite a bit larger ($\sim 330 \mu\text{m}$ in diameter) than that which was treated with compound **43E** ($\sim 250 \mu\text{m}$) which may account for the slower uptake, there was also solubility issues with compound **46E** over time.

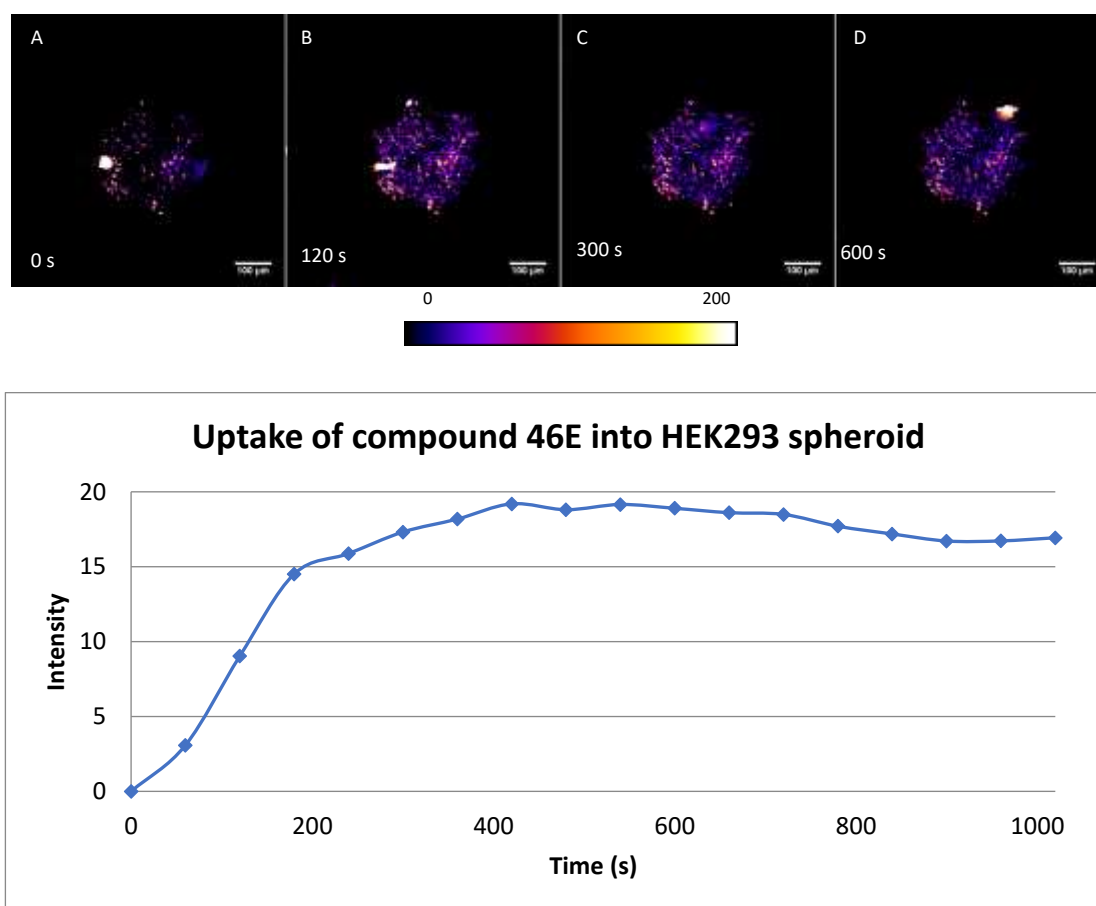


Figure 92 uptake of compound **46E** into HEK293 spheroid

The stack of images generated from the light sheet allowed for a closer look into specific slices of the spheroid, allowing for a better understanding of the kinetics of the compound

with regards to a 3D tumour model. The following series of images show different slices of the spheroid over time. The images at time 0 s were used to monitor any background fluorescence (Figure 93 A). A plot of time *versus* intensity (Figure 93) showed the fastest uptake of compound **46E** into the spheroid was observed at the surface of the spheroid; the rate of initial uptake into the peripheral cells was comparable to that of cell monolayers (Scherer *et al.*, 2015; Bisby *et al.*, 2011a). A significant increase in fluorescence was observed towards the core of the spheroid after around 200 s showed compound **46E** had diffused into the spheroid (Achilli *et al.*, 2014).

Again a slight decrease in fluorescence at the surface of the spheroid occurred as the fluorescence increased towards the core of the spheroid; this can be explained by the diffusion of compound **46E** into the central planes (Achilli *et al.*, 2014). After 300 s incubation, compound **46E** had diffused towards the centre of the spheroid (Figure 93 C); the images indicated that as uptake and inward diffusion occurred over time, the highest concentration of compound **46E** was in the outer layer of the spheroid and concentration decreased toward the spheroid core. After this point, further uptake at the surface of the spheroid from the medium and subsequent diffusion into the centre allowed for an even distribution of compound **46E** throughout the spheroid with time (Figure 93D).

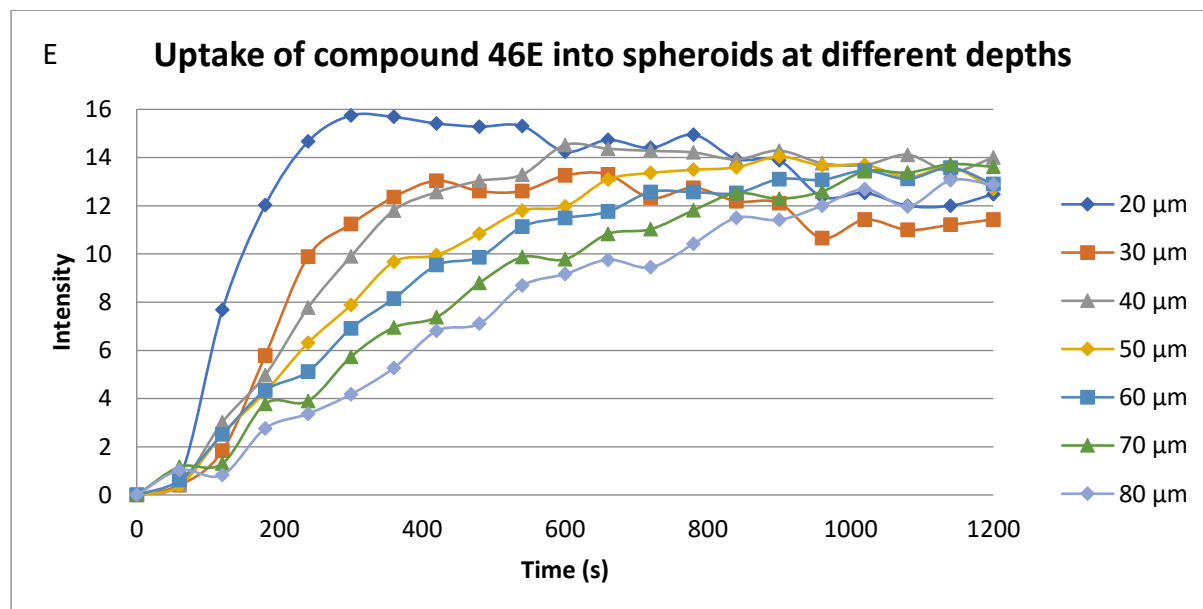
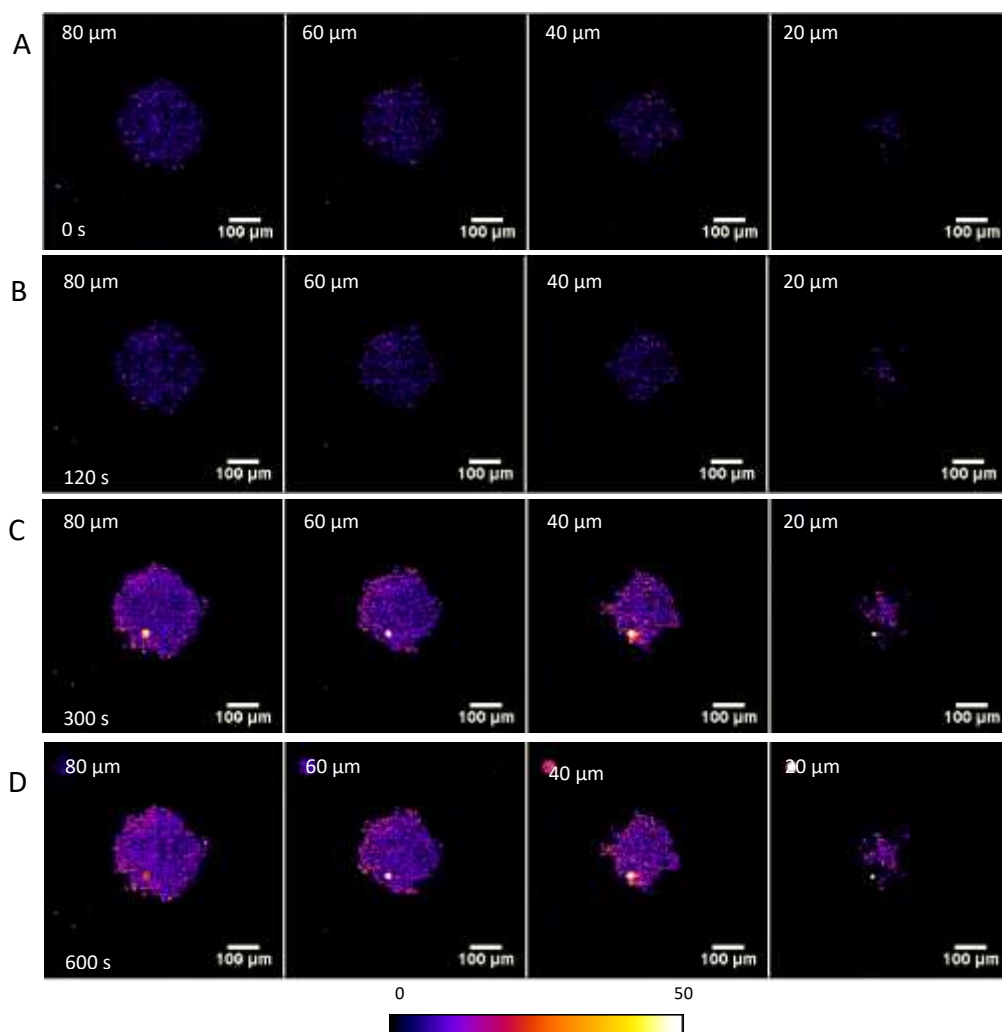


Figure 93 A) images showing different depths of the spheroid at time 0; B) images showing different depths of the spheroid at 120 s; C) images showing different depths of the spheroid at 300 s; D) images showing different depths of the spheroid at 600 s; E) plot of intensity *versus* time (s) of compound 46E at different depths of spheroid

The uptake curves represented a pseudo-first order association and so the rate of uptake (k) and half-life ($t_{1/2}$) (Table 26) of compound **46E** at different slices of the spheroid could be determined. Again, the rate of uptake of compound **46E** was much higher at the surface ($7.56 \times 10^{-3} \text{ s}^{-1}$) than the core ($5.28 \times 10^{-4} \text{ s}^{-1}$) of the spheroid. Towards the surface of the spheroid where there was a larger difference in the density of the cells the difference in the rate of uptake was quite large ($7.56 \times 10^{-3} \text{ s}^{-1}$ at $20 \mu\text{m}$ and $4.17 \times 10^{-3} \text{ s}^{-1}$ at $30 \mu\text{m}$) whilst towards the core of the spheroid where there was a similar density of cells, the difference in rate of uptake stabilised ($1.63 \times 10^{-3} \text{ s}^{-1}$ at $60 \mu\text{m}$ $1.04 \times 10^{-3} \text{ s}^{-1}$ at $70 \mu\text{m}$ and $5.28 \times 10^{-4} \text{ s}^{-1}$ at $80 \mu\text{m}$). The increase in $t_{1/2}$ towards the centre of the spheroid corresponded to the decrease in rate.

Table 26 Rate of uptake (k) and half-life ($t_{1/2}$) of compound **46E in HEK293 spheroid at varying depths**

Depth (μm)	k (s^{-1})	$t_{1/2}$ (s)
20	7.56×10^{-3}	92
30	4.17×10^{-3}	166
40	2.72×10^{-3}	255
50	1.96×10^{-3}	354
60	1.63×10^{-3}	426
70	1.04×10^{-3}	669
80	5.28×10^{-4}	n.d.

6.3 Intracellular power dependence of *E*-combretastatins

The non-linear power dependence of *E*-combretastatin dependence indicated a two-photon absorption process and a rapid uptake of the pro-drug candidates was observed in both living monolayers and spheroids. Next the power dependence of *E*-combretastatins was determined in the heterogeneous environment within live cells.

A series of multiphoton images of CHO cells were acquired for 30 s with increasing laser powers after 30 min incubation with compounds **42E**, **43E** and **46E** (5 μ M). Fluorescence was excited at 760 nm (compounds **42E** and **46E**) or 730 nm (compound **43E**). Images were analysed using Fiji. A plot of the pixel intensity *versus* laser power (mW) (Figure 94) demonstrated a quadratic dependence of *E*-combretastatin fluorescence intensity in live CHO cells providing strong evidence that the fluorescence in living cells could be generated by non-linear two-photon absorption.

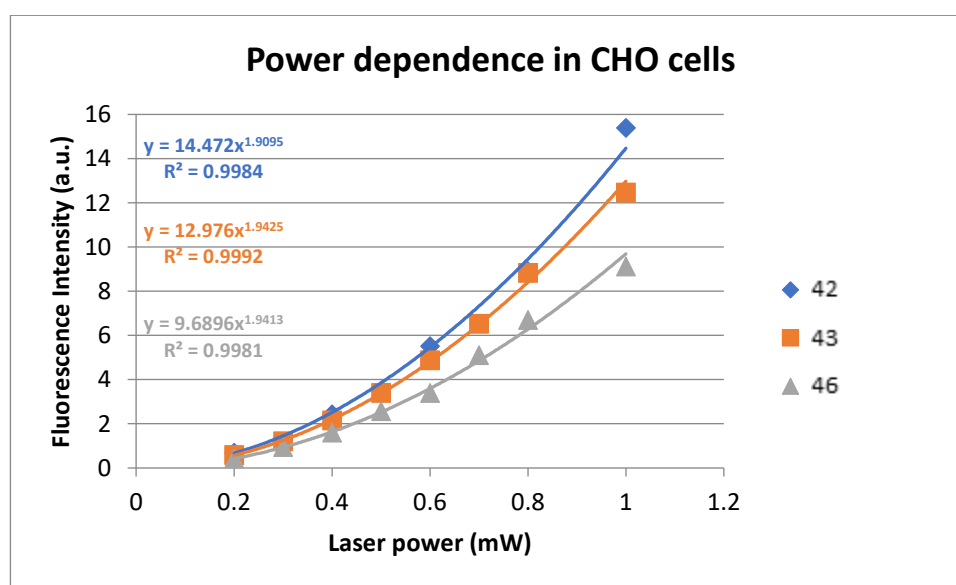


Figure 94 Power dependence of compounds **42**, **43** and **46** (5 μ M) fluorescence in CHO cells excited at 760 nm or 730 nm (cells were incubated for 30 min with compounds before fluorescence was excited).

The intracellular power dependence was also determined in HEK293 cells. Again cells were incubated for 30 min prior to imaging. A series of multiphoton images of HEK293 cells were acquired for 30 s with increasing laser powers after 30 min; fluorescence was excited at 760 nm (compounds **42E** and **46E**) or 730 nm (compound **43E**) and images were analysed using Fiji. A quadratic power dependence was observed upon plotting pixel intensity *versus* laser power (mW) (Figure 95) showing two-photon absorption was possible within cells.

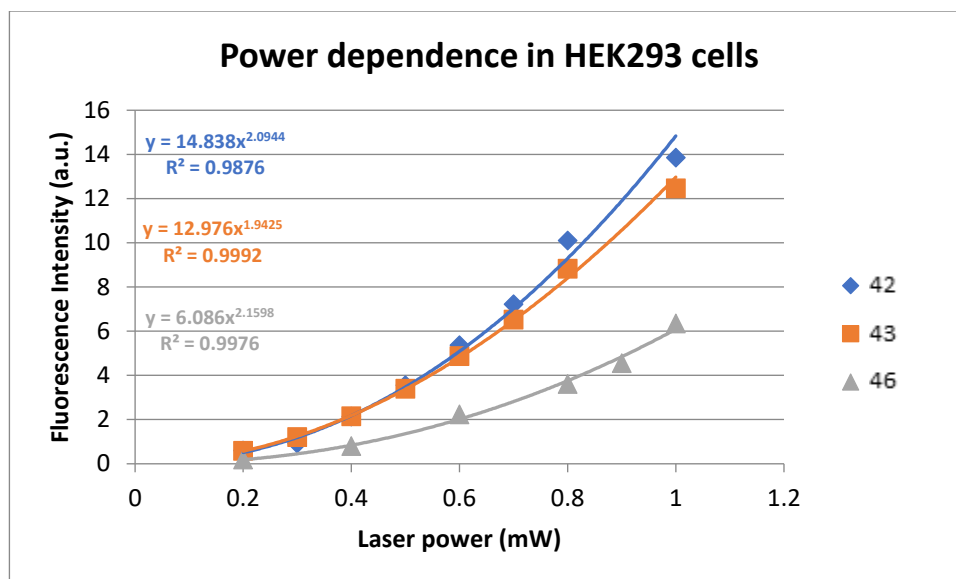


Figure 95 Power dependence of compounds 42, 43 and 46 (5 μ M) fluorescence in HEK293 cells excited at 760 nm or 730 nm (cells were incubated for 30 min with compounds before fluorescence was excited)

7. Conclusions & Future Outlook

In the course of this work a number of combretastatins were synthesised as drug candidates for type IV phototherapy. They were evaluated for their cytotoxicity against a number of cell lines and their ability to inhibit tubulin polymerisation. Further to this, cell cycle analysis was used to confirm the mode of action of these new combretastatins. The photochemical properties of compounds of interest were assessed to determine their suitability for this new form of phototherapy; high cytotoxicity and tubulin inhibition combined with good two-photon absorption cross sections are highly desirable features for the use of these compounds in phototherapy.

Most combretastatin derivatives were obtained in good yields using the Suzuki cross-coupling reaction. Combretastatins were first synthesised using the Wittig reaction but difficulty separating the *cis*- and *trans*-isomers was a major problem with this route. Further to this carbonyl and phenol functional groups required protection prior to synthesis. The Suzuki cross-coupling reaction appeared to overcome this with its mild reaction conditions and broad functional group toleration. A number of boronic acids are commercially available and boronic esters can be easily synthesised following the Miyaura borylation. This stereoselective synthesis allowed for a better yield of *cis*-combretastatins. A factor that needs to be considered in the future is drug delivery. One of the main issues with the combretastatins synthesised is their poor solubility in water; water soluble prodrugs of compounds **43** and **47** would be of interest. Their -OH functional group would allow for example a disodium phosphate salt prodrug with improved bioavailability (as with Z-CA4P).

The IC₅₀ values of the Z-combretastatins derivatives were determined *in vitro* on a number of cell lines (HepG2, HeLa and HCT116 cells) using the MTT assay. Low IC₅₀ values were obtained with IC₅₀ values <100 nM after 72 h for the compounds of interest. The cytotoxicity of combretastatins was highly dependent on the ring substitution pattern. The 3,4,5-trimethoxy pattern on the A ring was essential for activity (Gaukroger *et al.*, 2003). The requirement of a 4'-substitute for drug activity was evident. The IC₅₀ values were 2 orders of magnitudes higher when combretastatins did not have a substituent in the 4'-position. The 3'-OH was not essential for activity but increased activity slightly across all cell lines. Although these compounds were not as cytotoxic as CA-4 *in vivo* the combretastatin

derivatives completely inhibited tubulin polymerisation at only 1 μM with IC_{50} values comparable to CA-4. These new combretastatin derivatives possessed superior 2PA cross sections over CA-4 in the tissue window.

The spectroscopic evaluation of *E*-combretastatin pro-drug candidates provided valuable information on their behaviour in different environments. Generally high fluorescence quantum yields (Φ_{F}) and longer fluorescence lifetimes (τ_{F}) were observed in viscous solvents; the high Φ_{F} s of allowed multiphoton FLIM of *E*-combretastatin uptake in CHO and Hek293 cell monolayers and LSM of *E*-combretastatin uptake into Hek293 spheroids. It was determined that *E*-combretastatins accumulated within the cytoplasm and cytoplasmic lipid droplets. Moreover, a non-linear power dependence of fluorescence intensity upon two-photon excitation both in solution and within live cells was demonstrated. The techniques used to image the spheroids with LSM were quite new and involved some trial and error to optimise the imaging. Issues included slow accumulation of images due to the size of the stack, and the spheroid was not fixed and so could drift during imaging. Future work would include improving the technique used for imaging the spheroids, focusing on individual slices would allow for quicker accumulation of images to determine uptake at certain depths of the spheroids. Other work could include human melanoma skin tissue models (Sun *et al.*, 2006) to demonstrate trans-dermal *E*-combretastatin delivery since skin cancers would be an ideal target for light activated prodrugs. Further work would include developing an assay to show cell killing by Z-combretastatins upon two-photon excitation in 3D-tumour models. Previously cell killing in monolayers was determined using Annexin V AlexaFluor488 conjugate and propidium iodide as fluorescent markers for apoptosis (Bisby *et al.*, 2011b) however it was not possible to stain spheroids effectively with this method; Tang and co-workers reported live/dead cell staining of spheroids using Calcein AM and EthD-1 (Tang *et al.*, 2016).

8. References

- Abramowitz, M., Herman, B., Murphy, D.B. & Davidson, M.W. (2012) *Anatomy of the fluorescence microscope*. [Online]. 2012. Available from: <http://micro.magnet.fsu.edu/primer/techniques/fluorescence/anatomy/fluoromicroanatomy.html>.
- Achilli, T.-M., McCalla, S., Meyer, J., Tripathi, A., et al. (2014) Multilayer spheroids to quantify drug uptake and diffusion in 3D. *Molecular pharmaceuticals*. 11 (7), 2071–2081.
- Adams, M.W., Loftus, A.F., Dunn, S.E., Joens, M.S., et al. (2015) Light Sheet Fluorescence Microscopy (LSFM). *Current protocols in cytometry*. [Online] 71, 12.37.1-15. Available from: doi:10.1002/0471142956.cy1237s71.
- Adan, A., Alizada, G., Kiraz, Y., Baran, Y., et al. (2017) Flow cytometry: basic principles and applications. *Critical Reviews in Biotechnology*. [Online] 37 (2), 163–176. Available from: doi:10.3109/07388551.2015.1128876.
- Aden, D.P., Fogel, A., Plotkin, S., Damjanov, I., et al. (1979) Controlled synthesis of HBsAg in a differentiated human liver carcinoma-derived cell line. *Nature*. [Online] 282 (5739), 615–616. Available from: doi:10.1038/282615a0.
- Ahmed, B., Van Eijk, L.I., Bouma-ter Steege, J.C.A., Van Der Schaft, D.W.J., et al. (2003) Vascular targeting effect of combretastatin A-4 phosphate dominates the inherent angiogenesis inhibitory activity. *International Journal of Cancer*. [Online] 105 (1), 20–25. Available from: doi:10.1002/ijc.11010.
- Alberts (2008) Tumor Suppressor Genes and Oncogenes : Genes that Prevent and Cause Cancer. *Molecular Biology of the Cell; 5th Edition, Garland Science*. Chapter 20; Cancer, pp.1230–1256.
- Albota, M., Beljonne, D., Brédas, J.L., Ehrlich, J.E., et al. (1998) Design of organic molecules with large two-photon absorption cross sections. *Science (New York, N.Y.)*. [Online] 281 (5383), 1653–1656. Available from: doi:10.1126/science.281.5383.1653.
- Altshuler, G.B. & Yaroslavsky, I. (2004) Absorption characteristics of tissues as a basis for the

- optimal wavelength choice in photodermatology. *Palomar Medical Technologies, Burlington*.
- Do Amaral, D.N., Cavalcanti, B.C., Bezerra, D.P., Ferreira, P.M.P., et al. (2014) Docking, synthesis and antiproliferative activity of N-acylhydrazone derivatives designed as combretastatin A4 analogues Kamyar Afarinkia (ed.). *PLoS ONE*. [Online] 9 (3), e85380. Available from: doi:10.1371/journal.pone.0085380.
- Anderson, H.L., Yap, J.T., Milller, M.P., Robbins, A., et al. (2003) Assessment of pharmacodynamic vascular response in a phase I trial of combretastatin A4 phosphate. *Journal of Clinical Oncology*. 21 (15), 2823–2830.
- Ashraf, M., Shaik, T.B., Malik, M.S., Syed, R., et al. (2016) Design and synthesis of cis-restricted benzimidazole and benzothiazole mimics of combretastatin A-4 as antimitotic agents with apoptosis inducing ability. *Bioorganic & Medicinal Chemistry Letters*. [Online] 26 (18), 4527–4535. Available from: doi:10.1016/J.BMCL.2016.06.044.
- Atkins, J.H. & Gershell, L.J. (2002) From the analyst's couch: Selective anticancer drugs. *Nature Reviews Drug Discovery*. [Online] 1 (7), 491–492. Available from: doi:10.1038/nrd842.
- Attard, G.A., Bennett, J.A., Mikheenko, I., Jenkins, P., et al. (2013) Semi-hydrogenation of alkynes at single crystal, nanoparticle and biogenic nanoparticle surfaces: the role of defects in Lindlar-type catalysts and the origin of their selectivity. *Faraday Discussions*. [Online] 162 (0), 57. Available from: doi:10.1039/c3fd00007a.
- Aylett, C.H.S., Löwe, J. & Amos, L.A. (2011) *Chapter one - New Insights into the Mechanisms of Cytomotive Actin and Tubulin Filaments*. In: Kwang W Jeon B T - International Review of Cell Biology & Molecular (eds.). Academic Press. pp. 1–71.
- Baba, A.I. & Catoj, C. (2007) The Tumor Cell. In: *Comparative Oncology*. The Publishing House of the Romanian Academy. p.
- Bai, R., Covell, D.G., Pei, X.-F., Ewell, J.B., et al. (2000) Mapping the binding site of colchicinoids on beta -tubulin. 2-Chloroacetyl-2-demethylthiocolchicine covalently reacts predominantly with cysteine 239 and secondarily with cysteine 354. *J. Biol.*

- Chem.* 275 (51), 40443–40452.
- Balamuth, N.J. & Womer, R.B. (2010) Ewing's sarcoma. *The lancet oncology*. [Online] 11 (2), 184–192. Available from: doi:10.1016/S1470-2045(09)70286-4.
- Bassily, M.N., Wilson, R., Pompei, F. & Burmistrov, D. (2010) Cancer survival as a function of age at diagnosis: A study of the Surveillance, Epidemiology and End Results database. *Cancer Epidemiology*. [Online] 34 (6), 667–681. Available from: doi:10.1016/j.canep.2010.04.013.
- Beck, T.J., Burkanas, M., Bagdonas, S., Krivickiene, Z., et al. (2007) Two-photon photodynamic therapy of C6 cells by means of 5-aminolevulinic acid induced protoporphyrin IX. *Journal of photochemistry and photobiology. B, Biology*. [Online] 87 (3), 174–182. Available from: doi:10.1016/j.jphotobiol.2007.03.008.
- Becker, R.S. (1969) *Fundamentals of fluorescence spectroscopy - Theory and interpretation of fluorescence & phosphorescence*. USA, Wiley-Interscience.
- Becker, W. (2012) Fluorescence lifetime imaging - techniques and applications. *Journal of Microscopy*. [Online] 247 (2), 119–136. Available from: doi:10.1111/j.1365-2818.2012.03618.x.
- Becker, W., Begmann, A., Biscotti, G., Koenig, K., et al. (2004) High-speed FLIM data acquisition by time-correlated single photon counting. *Proceedings of SPIE*. 5323, 1–9.
- Bedford, S.B., Quarterman, C.P., Rathbone, D.L., Slack, J.A., et al. (1996) Synthesis of water-soluble prodrugs of the cytotoxic agent Combretastatin A4. *Bioorganic and Medicinal Chemistry Letters*. [Online] 6 (2), 157–160. Available from: doi:10.1016/0960-894X(95)00580-M.
- Bhattacharya, S., Das, A., Datta, S., Ganguli, A., et al. (2016) Colchicine induces autophagy and senescence in lung cancer cells at clinically admissible concentration: potential use of colchicine in combination with autophagy inhibitor in cancer therapy. *Tumor Biology*. [Online] 37 (8), 10653–10664. Available from: doi:10.1007/s13277-016-4972-7.
- Bilenker, J.H., Flaherty, K.T., Rosen, M., Davis, L., et al. (2005) Phase I Trial of Combretastatin

- A-4 Phosphate with Carboplatin. *Clinical Cancer Research*. [Online] 11 (4), 1527–1533. Available from: doi:10.1158/1078-0432.CCR-04-1434.
- Bisby, A., Bisby, R.H., Botchway, S.W., Hadfield, J.A., et al. (2011a) Fluorescence lifetime imaging of E- combretastatin uptake and distribution in live mammalian cells. *European Journal of Cancer*. [Online] 48 (12), 1896–1903. Available from: doi:10.1016/j.ejca.2011.11.025.
- Bisby, R.H., Botchway, S.W., Hadfield, J.A., MCGOWN, A.T., et al. (2011b) Fluorescence lifetime imaging of E-combretastatin uptake and distribution in live mammalian cells. *EUROPEAN JOURNAL OF CANCER*. [Online] 1–8. Available from: doi:10.1016/j.ejca.2011.11.025.
- Black, D.J. & Livingston, R.B. (1990) Antineoplastic drugs in 1990. A review (Part I). *Drugs*. 39 (4), 489–501.
- Böhle, A.S., Leuschner, I., Kalthoff, H. & Henne-Bruns, D. (2000) Combretastatin A-4 prodrug: A potent inhibitor of malignant hemangioendothelioma cell proliferation. *International Journal of Cancer*. [Online] 87 (6), 838–843. Available from: doi:10.1002/1097-0215(20000915)87:6<838::AID-IJC13>3.0.CO;2-7.
- Bonne, D., Heuséle, C., Simon, C. & Pantaloni, D. (1985) 4',6-Diamidino-2-phenylindole, a fluorescent probe for tubulin and microtubules. *The Journal of biological chemistry*. 260 (5), 2819–2825.
- Borowiak, M., Nahaboo, W., Reynders, M., Vollmar, A., et al. (2015) *Photoswitchable Inhibitors of Microtubule Dynamics Optically Control Mitosis and Cell Death*. [Online] Available from: doi:10.1016/j.cell.2015.06.049.
- Bowen, E.J. (1959) Viscosity and temperature effects in fluorescence. *Faraday Discussions*. [Online] 27, 40–42. Available from: doi:10.1039/DF9592700040.
- Brown, A.W., Fisher, M., Tozer, G.M., Kanthou, C., et al. (2016) Sydnone Cycloaddition Route to Pyrazole-Based Analogs of Combretastatin A4. *Journal of Medicinal Chemistry*. [Online] 59 (20), 9473–9488. Available from: doi:10.1021/acs.jmedchem.6b01128.
- Cai, S.X. (2007) Small molecule vascular disrupting agents: potential new drugs for cancer

- treatment. *Recent patents on anti-cancer drug discovery*. 2 (1), 79–101.
- Caley, A. & Jones, R. (2012) The principles of cancer treatment by chemotherapy. *Surgery*. [Online] 30 (4), 186–190. Available from: doi:10.1016/j.mpsur.2012.01.004.
- Cancer Research UK (2009a) *A trial looking at combretastatin and chemotherapy for advanced ovarian cancer, primary peritoneal cancer, and fallopian tube cancer (CA4P-UKCTC-207)*. 2009.
- Cancer Research UK (2009b) *A trial looking at combretastatin and chemotherapy for people with advanced solid tumours (CA4P - UKCTC-207)*. 2009.
- Cancer Research UK (2012a) *A trial looking at immunotherapy and combretastatin for advanced bowel and pancreatic cancer (A5B7-CA4P; PH1/092)*. 2012.
- Cancer Research UK (2016) *Breast cancer statistics for the UK*. [Online]. 2016. Cancer Research UK. Available from: <http://www.cancerresearchuk.org/health-professional/cancer-statistics>.
- Cancer Research UK (2014) *Cancer mortality statistics*. [Online]. 2014. Retrieved February 20, 2015 from, <http://www.cancerresearchuk.org/cancer-info/cancerstats/mortality/>. Available from: <http://www.cancerresearchuk.org/health-professional/cancer-statistics/mortality>.
- Cancer Research UK (2012b) *Combretastatin for advanced cancer*. 2012.
- Cardolaccia, T., Li, Y. & Schanze, K.S. (2008) Phosphorescent platinum acetylide organogelators. *Journal of the American Chemical Society*. [Online] 130 (8), 2535–2545. Available from: doi:10.1021/ja0765316.
- Chang, C., Sud, D. & Mycek, M. (2007) Fluorescence lifetime imaging microscopy. *Methods in cell biology*. [Online] 81 (06), 495–524. Available from: doi:10.1016/S0091-679X(06)81024-1.
- Chang, R. (2000a) *Physical Chemistry for the Chemical and Biological Sciences*. 3rd edition. Sausalito, California, University Science Books.
- Chang, R. (2000b) *Physical Chemistry for the Chemical and Biological Sciences*. University

Science Books.

- Chaplin, D.J. & Hill, S. a. (2002) The development of combretastatin A4 phosphate as a vascular targeting agent. *International Journal of Radiation Oncology Biology Physics*. [Online] 54 (5), 1491–1496. Available from: doi:10.1016/S0360-3016(02)03924-X.
- Charlton, J.L. & Saltiel, J. (1977) An analysis of trans-stilbene fluorescence quantum yields and lifetimes. *The Journal of Physical Chemistry*. [Online] 81, 1940–1944. Available from: doi:10.1021/j100535a011.
- Chinchilla, R. & Nájera, C. (2011) Recent advances in Sonogashira reactions. *Chemical Society Reviews*. [Online] 40 (10), 5084. Available from: doi:10.1039/c1cs15071e.
- Chrétien, D., Metoz, F., Verde, F., Karsenti, E., et al. (1992) Lattice defects in microtubules: protofilament numbers vary within individual microtubules. *Journal of Cell Biology*. 117 (5), 1031–1040.
- Christmann, U. & Vilar, R. (2005) Monoligated Palladium Species as Catalysts in Cross-Coupling Reactions. *Angewandte Chemie (International ed. in English)*. [Online] 44, 366–374. Available from: doi:10.1002/anie.200461189.
- Conde, C. & Caceres, A. (2009) Microtubule assembly, organization and dynamics in axons and dendrites. *Nat Rev Neurosci*. 10 (5), 319–332.
- Cooney, M.M., Radivoyevitch, T., Dowlati, A., Overmoyer, B., et al. (2004) Cardiovascular safety profile of combretastatin a4 phosphate in a single-dose phase I study in patients with advanced cancer. *Clinical Cancer Research*. 10, 96–100.
- Cox, G. (2002) Biological confocal microscopy. *Materialstoday*. 34–41.
- Cruet-Hennequart, S., Glynn, M.T., Murillo, L.S., Coyne, S., et al. (2008) Enhanced DNA-PK-mediated RPA2 hyperphosphorylation in DNA polymerase η -deficient human cells treated with cisplatin and oxaliplatin. *DNA Repair*. [Online] 7 (4), 582–596. Available from: doi:10.1016/j.dnarep.2007.12.012.
- Cushman, M., Nagarathnam, D., Gopal, D., Chakraborti, A.K., et al. (1991) Synthesis and evaluation of stilbene and dihydrostilbene derivatives as potential anticancer agents

- that inhibit tubulin polymerization. *Journal of Medicinal Chemistry*. 34 (8), 2579–2588.
- Davidson, M.W. & Abramowitz, M. (1999) *Optical microscopy*. 1–40.
- Demchenko, A.P. (2008) *Introduction to Fluorescence Sensing Introduction to Fluorescence Sensing*. [Online]. 2008. Available from: doi:10.1007/978-1-4020-9003-5.
- Denk, W., Strickler, J. & Webb, W. (1990) Two-photon laser scanning fluorescence microscopy. *Science*. 248, 73–76.
- Denk, W., Strickler, J.P. & Webb, W.W. (1991) *Two-photon laser scanning microscopy*. p.31.
- Denk, W. & Svoboda, K. (1997) Photon upmanship: why multiphoton imaging is more than a gimmick. *Neuron*. 18 (3), 351–357.
- Denney, R.C. & Sinclair, R. (1991) *Visible and ultraviolet spectroscopy*. Chichester, UK, John Wiley & Sons, Ltd.
- Dickinson, R.G. & Lotzkar, H. (1937) The Kinetics of the Thermal Isomerization of Cinnamic Acid Catalyzed by Iodine. *J. Am. Chem. Soc.* [Online] 59 (3), 472–475. Available from: doi:10.1021/ja01282a013.
- Dougherty, T.J., Kaufman, J.E., Goldfarb, A., Weishaupt, K.R., et al. (1978) Photoradiation therapy for the treatment of malignant tumors. *Cancer Research*. 38, 2628–2635.
- Dowlati, A., Robertson, K., Cooney, M., Petros, W.P., et al. (2002) A phase I pharmacokinetic and translational study of the novel vascular targeting agent combretastatin a-4 phosphate on a single-dose intravenous schedule in patients with advanced cancer. *Cancer research*. 62 (12), 3408–3416.
- Ehrlich, P.F., Hamilton, T.E., Grundy, P., Ritchey, M., et al. (2006) The value of surgery in directing therapy for patients with Wilms' tumor with pulmonary disease. A report from the National Wilms' Tumor Study Group (National Wilms' Tumor Study 5). *Journal of pediatric surgery*. [Online] 41 (1), 162–167. Available from: doi:10.1016/j.jpedsurg.2005.10.020.
- Engdahl, A.J., Torres, E. a., Lock, S.E., Engdahl, T.B., et al. (2015) Synthesis, Characterization, and Bioactivity of the Photoisomerizable Tubulin Polymerization Inhibitor azo-

- Combretastatin A4. *Organic Letters*. [Online] 17 (18), 4546–4549. Available from: doi:10.1021/acs.orglett.5b02262.
- Espinet, P. & Echavarren, A.M. (2004) The mechanisms of the Stille reaction. *Angewandte Chemie (International ed. in English)*. [Online] 43 (36), 4704–4734. Available from: doi:10.1002/anie.200300638.
- Evano, G., Blanchard, N. & Toumi, M. (2008) Copper-Mediated Coupling Reactions and Their Applications in Natural Products and Designed Biomolecules Synthesis. *Chemical Reviews*. [Online] 108 (8), 3054–3131. Available from: doi:10.1021/cr8002505.
- Fedorov, A., Liu, H.-J., Lo, H.-K. & Copéret, C. (2016) Silica-Supported Cu Nanoparticle Catalysts for Alkyne Semihydrogenation: Effect of Ligands on Rates and Selectivity. *Journal of the American Chemical Society*. [Online] 138 (50), 16502–16507. Available from: doi:10.1021/jacs.6b10817.
- Fellers, T.J. & Davidson, M.W. (2012) *Introduction to confocal microscopy*. 2012.
- Fennema, E., Rivron, N., Rouwkema, J., van Blitterswijk, C., et al. (2013) Spheroid culture as a tool for creating 3D complex tissues. *Trends in Biotechnology*. [Online] 31 (2), 108–115. Available from: doi:10.1016/j.tibtech.2012.12.003.
- Folkman, J. (1971) Tumour angiogenesis: Therapeutic implications. *The New England Journal of Medicine*. 285, 1182–1186.
- Foye, W.O., Lemke, T.L. & Williams, D.A. (1995) *Principles of Medicinal Chemistry*. Williams & Wilkins.
- Freres, P., Jerusalem, G. & Moonen, M. (2017) Categories of Anticancer Treatments. *Anti-Cancer Treatments and Cardiotoxicity*. [Online] 7–11. Available from: doi:10.1016/B978-0-12-802509-3.00002-9.
- Fuertes, M. a, Alonso, C. & Pérez, J.M. (2003) Biochemical modulation of Cisplatin mechanisms of action: enhancement of antitumor activity and circumvention of drug resistance. *Chemical reviews*. [Online] 103 (3), 645–662. Available from: doi:10.1021/cr020010d.

- Fürstner, A. & Nikolakis, K. (1996) Ethynylation of aryl halides by a modified Suzuki reaction. Application to the syntheses of combretastatin A-4, A-5, and lunularic acid. *Liebigs Annalen*. [Online] (12), 2107–2113. Available from: doi:10.1002/jlac.199619961224.
- Fürstner, A. & Seidel, G. (1995) Palladium-catalyzed arylation of polar organometallics mediated by 9-methoxy-9-borabicyclo[3.3.1]nonane: Suzuki reactions of extended scope. *Tetrahedron*. [Online] 51 (41), 11165–11176. Available from: doi:10.1016/0040-4020(95)00677-Z.
- Gao, D., Agayan, R.R., Xu, H., Philbert, M.A., et al. (2006) Nanoparticles for two-photon photodynamic therapy in living cells. *Nano Letters*. 6, 2383–2386.
- Gapud, E.J., Bai, R., Ghosh, A.K. & Hamel, E. (2004) Laulimalide and paclitaxel: a comparison of their effects on tubulin assembly and their synergistic action when present simultaneously. *Molecular pharmacology*. [Online] 66 (1), 113–121. Available from: doi:10.1124/mol.66.1.113.
- Gaspari, R., Prota, A.E., Bargsten, K., Cavalli, A., et al. (2017) Structural Basis of cis- and trans-Combretastatin Binding to Tubulin. *Cell*. [Online] 2, 102–113. Available from: doi:10.1016/j.chempr.2016.12.005.
- Gates, K.S. (2009) *An Overview of Chemical Processes That Damage Cellular DNA: Spontaneous Hydrolysis, Alkylation, and Reactions with Radicals*. [Online] 22 (11), 1747–1760. Available from: doi:10.1021/tx900242k.An.
- Gaukroger, K. (2001) *Structure Activity Study of Stilbenes Targeted at Tumour Vasculature*. University of Manchester Institute of Science and Technology (UMIST).
- Gaukroger, K., Hadfield, J. a., Hepworth, L. a., Lawrence, N.J., et al. (2001a) Novel syntheses of cis and trans isomers of combretastatin A-4. *Journal of Organic Chemistry*. [Online] 66 (24), 8135–8138. Available from: doi:10.1021/jo015959z.
- Gaukroger, K., Hadfield, J.A., Hepworth, L.A., Lawrence, N.J., et al. (2001b) Novel syntheses of cis and trans isomers of combretastatin A-4. *The Journal of Organic Chemistry*. 66, 8135–8138.
- Gaukroger, K., Hadfield, J.A., Lawrence, N.J., Nolan, S., et al. (2003) Structural requirements

- for the interaction of combretastatins with tubulin: how important is the trimethoxy unit? *Organic & biomolecular chemistry*. 1 (17), 3033–3037.
- Gee, M.S., Procopio, W.N., Makonnen, S., Feldman, M.D., et al. (2003) Tumor vessel development and maturation impose limits on the effectiveness of anti-vascular therapy. *The American journal of pathology*. [Online] 162 (1), 183–193. Available from: doi:10.1016/S0002-9440(10)63809-6.
- Gerova, M.S., Stateva, S.R., Radonova, E.M., Kalenderska, R.B., et al. (2016a) Combretastatin A-4 analogues with benzoxazolone scaffold: Synthesis, structure and biological activity. *European Journal of Medicinal Chemistry*. [Online] 120, 121–133. Available from: doi:10.1016/J.EJMECH.2016.05.012.
- Gerova, M.S., Stateva, S.R., Radonova, E.M., Kalenderska, R.B., et al. (2016b) Combretastatin A-4 analogues with benzoxazolone scaffold: Synthesis, structure and biological activity. *European Journal of Medicinal Chemistry*. [Online] 120, 121–133. Available from: doi:10.1016/j.ejmech.2016.05.012.
- Göppert-Mayer, M. (1931) Über Elementarakte mit zwei Quantensprüngen. *Annalen der Physik*. [Online] 401 (3), 273–294. Available from: doi:10.1002/andp.19314010303.
- Görner, H. & Kuhn, H.J. (1995) cis-trans Photoisomerization of stilbenes and stilbene-like molecules. *Advances in Photochemistry*. 19, 1–117.
- Gossiau, A., Pabbaraja, S., Knapp, S. & Yu Chen, K. (2008) *Author's personal copy Trans-and cis-stilbene polyphenols induced rapid perinuclear mitochondrial clustering and p53-independent apoptosis in cancer cells but not normal cells*.
- Gottlieb, H.E., Kotlyar, V. & Nudelman, A. (1997) *NMR Chemical Shifts of Common Laboratory Solvents as Trace Impurities In the course of the routine use of NMR as an aid for organic chemistry , a day-to-day problem is the identification of signals deriving from common contaminants literature , but the .* 3263 (3), 7512–7515.
- Gray, N. (2009) Milestone 3: Knowing the limit. *Nature Cell Biology*. [Online] 11. Available from: doi:10.1038/ncb1940.
- Greene, L.M., Nathwani, S.M., Bright, S.A., Fayne, D., et al. (2010) The Vascular Targeting

- Agent Combretastatin-A4 and a Novel cis-Restricted β -Lactam Analogue , CA-432 , Induce Apoptosis in Human Chronic Myeloid Leukemia Cells and Ex Vivo Patient Samples Including Those Displaying Multidrug Resistance. *Pharmacology*. [Online] 335 (2), 302–313. Available from: doi:10.1124/jpet.110.170415.potent.
- Griggs, J., Hesketh, R., Smith, G.A., Brindle, K.M., et al. (2001) Combretastatin-A4 disrupts neovascular development in non-neoplastic tissue. *British Journal of Cancer*. 84, 832–835.
- Griggs, J., Metcalfe, J.C. & Hesketh, R. (2001) Targeting tumour vasculature: the development of combretastatin A4. *The Lancet*. 2 (February), 0–5.
- Griggs, J., Skepper, J.N., Smith, G.A., Brindle, K.M., et al. (2002) Inhibition of proliferative retinopathy by the anti-vascular agent combretastatin-A4. *The American Journal of Pathology*. 160, 1097–1103.
- Grignard, V. (1900) Comptes rendus hebdomadaires des séances de l'Académie des sciences. *Compt. Rend.* 130, 1322–1325.
- Grosios, K., Holwell, S.E., McGown, A.T., Pettit, G.R., et al. (1999) In vivo and in vitro evaluation of combretastatin A-4 and its sodium phosphate prodrug. *British Journal of Cancer*. 81, 1318–1327.
- Grosios, K., Loadman, P.M., Swaine, D.J., Pettit, G.R., et al. Combination chemotherapy with combretastatin A-4 phosphate and 5-fluorouracil in an experimental murine colon adenocarcinoma. *Anticancer research*. 20 (1A), 229–233.
- Gu, B., Zhao, C., Baev, A., Yong, K.-T., et al. (2016) Molecular nonlinear optics: recent advances and applications. *Advances in Optics and Photonics*. [Online] 8 (2), 328. Available from: doi:10.1364/AOP.8.000328.
- Guan, Q., Yang, F., Guo, D., Xu, J., et al. (2014) Synthesis and biological evaluation of novel 3,4-diaryl-1,2,5-selenadiazol analogues of combretastatin A-4. *European Journal of Medicinal Chemistry*. [Online] 87, 1–9. Available from: doi:10.1016/j.ejmech.2014.09.046.

- Guillouzo, A., Corlu, A., Aninat, C., Glaise, D., et al. (2007) The human hepatoma HepaRG cells: A highly differentiated model for studies of liver metabolism and toxicity of xenobiotics. *Chemico-Biological Interactions*. [Online] 168 (1), 66–73. Available from: doi:10.1016/j.cbi.2006.12.003.
- Gunasekera, S.P., Gunasekera, M., Longley, R.E. & Schulte, G.K. (1990) Discodermolide: a new bioactive polyhydroxylated lactone from the marine sponge *Discodermia dissoluta*. *The Journal of Organic Chemistry*. [Online] 55 (16), 4912–4915. Available from: doi:10.1021/jo00303a029.
- Hadfield, J. a, Ducki, S., Hirst, N. & McGown, A.T. (2003a) Tubulin and microtubules as targets for anticancer drugs. *Progress in cell cycle research*. 5, 309–325.
- Hadfield, J.A., Ducki, S., Hirst, N. & McGown, A.T. (2003b) Tubulin and microtubules as targets for anticancer drugs. *Progress in Cell Cycle Research*. 5, 309–325.
- Hadfield, J.A., Gaukroger, K., Hirst, N., Weston, A.P., et al. (2005) Synthesis and evaluation of double bond substituted combretastatins. *European Journal of Medicinal Chemistry*. 47, 529–541.
- Hadfield, J.A. & McGown, A.T. (1998) Preparation and evaluation of diarylalkynes as antitumour agents. *Synthetic Communications*. 28 (8), 1421–1431.
- Hadfield, J.A., McGown, A.T., Gaukroger, K., Hepworth, L.A., et al. (2006) *Materials and methods for synthesizing stilbenes*.pp.1–16.
- Hadfield, J.A., McGown, A.T., Mayalarp, S.P., Land, E.J., et al. (2007) *Substituted stilbenes and their reactions*.pp.1–31.
- Hamel, E. & Lin, C.M. (1983) Interactions of combretastatin, a new plant-derived antimetabolic agent, with tubulin. *Biochemical Pharmacology*. [Online] 32 (24), 3864–3867. Available from: doi:10.1016/0006-2952(83)90163-6.
- He, X., Li, S., Huang, H., Li, Z., et al. (2011) A pharmacokinetic and safety study of single dose intravenous combretastatin A4 phosphate in Chinese patients with refractory solid tumours. *British Journal of Clinical Pharmacology*. [Online] 71 (6), 860–870. Available from: doi:10.1111/j.1365-2125.2011.03928.x.

- Heald, R. & Nogales, E. (2002) Microtubule Dynamics. *Journal of Cell Science*. 115 (1), 3–4.
- Hepworth, L.A. (2000) *New Procedures for the Photoactivation of Anticancer Prodrugs*. University of Manchester Institute of Science and Technology.
- Herman, B. (1998) *Microscopy handbooks 40 - Fluorescence microscopy*. 2nd edition. Bios Scientific Publishers Ltd.
- Herman, B., Lakowicz, J.R., Johnson, I.D. & Davidson, M.W. (2012) *Solvent effects on fluorescence emission*. 2012.
- Hirst, N. (2004) *Targeting the Colchicine Binding Site of Tubulin with Combretastatin Derivatives*. University of Manchester Institute of Science and Technology (UMIST).
- Hönigsmann, H. (2012) History of phototherapy in dermatology. *Photochemical & photobiological sciences : Official journal of the European Photochemistry Association and the European Society for Photobiology*. [Online] Available from: doi:10.1039/c2pp25120e.
- Horsman, M.R., Murata, R., Breidahl, T., Nielsen, F.U., et al. (2000) Combretastatins novel vascular targeting drugs for improving anti-cancer therapy. Combretastatins and conventional therapy. *Advances in experimental medicine and biology*. 476, 311–323.
- Ibrahim, M.A., Do, D. V, Sepah, Y.J., Shah, S.M., et al. (2013) Vascular disrupting agent for neovascular age related macular degeneration: a pilot study of the safety and efficacy of intravenous combretastatin a-4 phosphate. *BMC Pharmacology and Toxicology*. [Online] 14 (1), 7. Available from: doi:10.1186/2050-6511-14-7.
- Ishiyama, T., Murata, M. & Miyaura, N. (1995) Palladium (0)-catalyzed cross-coupling reaction of alkoxydiboron with haloarenes: a direct procedure for arylboronic esters. *J Org Chem*. [Online] 60 (23), 7508–7510. Available from: doi:10.1021/jo00128a024.
- Jain, R.K. & Carmeliet, P.F. (2001) Vessels of death or life. *Scientific American*. pp.38–45.
- Jobin Yvon Ltd. (2004) A guide to recording fluorescence quantum yields. *Constrained Coding and Soft Iterative Decoding*. pp.1–6.
- Ju, C., Winterhalder, M.J. & Zumbusch, A. (2011) *Fast and long term lipid droplet tracking*

- with CARS microscopy. [Online] 7, 1–7. Available from: doi:10.1002/jbio.201000120.
- Kaiser, W. & Garrett, C.G.B. (1961) Two-Photon Excitation in Ca F_2 : Eu^{2+} . *Physical Review Letters*. [Online] 7 (6), 229–231. Available from: doi:10.1103/PhysRevLett.7.229.
- Kamal, A., Shaik, A.B., Polepalli, S., Kumar, G.B., et al. (2015) Synthesis of arylpyrazole linked benzimidazole conjugates as potential microtubule disruptors. *Bioorganic & medicinal chemistry*. [Online] 23 (5), 1082–1095. Available from: doi:10.1016/j.bmc.2015.01.004.
- Kamal, A., Shaik, B., Nayak, V.L., Nagaraju, B., et al. (2014) Synthesis and biological evaluation of 1,2,3-triazole linked aminocombretastatin conjugates as mitochondrial mediated apoptosis inducers. *Bioorganic & medicinal chemistry*. [Online] 22 (19), 5155–5167. Available from: doi:10.1016/j.bmc.2014.08.008.
- Kampan, N.C., Madondo, M.T., McNally, O.M., Quinn, M., et al. (2015) Paclitaxel and Its Evolving Role in the Management of Ovarian Cancer. *BioMed research international*. [Online] 2015, 413076. Available from: doi:10.1155/2015/413076.
- Kanthou, C., Greco, O., Stratford, A., Cook, I., et al. (2004) The Tubulin-Binding Agent Combretastatin A-4-Phosphate Arrests Endothelial Cells in Mitosis and Induces Mitotic Cell Death. *The American Journal of Pathology*. [Online] 165 (4), 1401–1411. Available from: doi:10.1016/S0002-9440(10)63398-6.
- Knowles, M. & Selby, P. (2005) *Introduction to the cellular and molecular biology of cancer*. 4th edition. New York, USA, Oxford University Press.
- Koh, D.-M., Blackledge, M., Collins, D.J., Padhani, A.R., et al. (2009) Reproducibility and changes in the apparent diffusion coefficients of solid tumours treated with combretastatin A4 phosphate and bevacizumab in a two-centre phase I clinical trial. *European Radiology*. [Online] 19 (11), 2728–2738. Available from: doi:10.1007/s00330-009-1469-4.
- Konerding, M.A., Fait, E. & Gaumann, A. (2001) 3D microvascular architecture of pre-cancerous lesions and invasive carcinomas of the colon. *British journal of cancer*. [Online] 84 (10), 1354–1362. Available from: doi:10.1054/bjoc.2001.1809.

- König, K. (1999) Multiphoton microscopy in life sciences. *Journal of Microscopy*. 200, 83–104.
- Kovalenko, S. a., Dobryakov, a. L., Ioffe, I. & Ernsting, N.P. (2010) Evidence for the phantom state in photoinduced cis–trans isomerization of stilbene. *Chemical Physics Letters*. [Online] 493 (4–6), 255–258. Available from: doi:10.1016/j.cplett.2010.05.022.
- Kyprianou, N. (2012) *Molecular exploitation of apoptosis pathways in prostate cancer*. Imperial College Press.
- Lakowicz, J.R. (2006) *Principles of Fluorescence Spectroscopy*. Springer.
- Lane, N. (2003a) New light on medicine. *Scientific American*. [Online]. 288 (1) pp.38–45. Available from: doi:10.1038/scientificamerican0708-80sp.
- Lane, N. (2003b) New Light on Medicine. *Scientific American*. 288 (1), 26–33.
- Lennox, A.J.J. & Lloyd-Jones, G.C. (2014) Selection of boron reagents for Suzuki–Miyaura coupling. *Chem. Soc. Rev.* [Online] 43 (1), 412–443. Available from: doi:10.1039/C3CS60197H.
- Letcher, R.M. (1973) *STRUCTURE AND SYNTHESIS OF THE GROWTH INHIBITOR BATATASIN I FROM DIOSCOREA BATATAS*. 12.
- Ley, C.D., Horsman, M.R. & Kristjansen, P.E.G. (2007) Early Effects of Combretastatin-A4 Disodium Phosphate on Tumor Perfusion and Interstitial Fluid Pressure. *Neoplasia*. [Online] 9 (2), 108–112. Available from: doi:10.1593/NEO.06733.
- Li, J., Hua, R. & Liu, T. (2010) Highly chemo- and stereoselective palladium-catalyzed transfer semihydrogenation of internal alkynes affording cis-alkenes. *The Journal of organic chemistry*. [Online] 75 (9), 2966–2970. Available from: doi:10.1021/jo100247a.
- Lichtman, J.W. & Conchello, J. (2005) *Fluorescence microscopy*. [Online] 2 (12). Available from: doi:10.1038/NMETH817.
- Liebermann, C. (1890) Zur Kenntnis der Isozimmtsäure. *Berichte der deutschen chemischen Gesellschaft*. [Online] 23 (1), 512–516. Available from: doi:10.1002/cber.18900230186.

- Lin, C.M., Ho, H.H., Pettit, G.R. & Hamel, E. (1989) Antimitotic natural products combretastatin A-4 and combretastatin A-2: studies on the mechanism of their inhibition of the binding of colchicine to tubulin. *Biochemistry*. [Online] 28 (17), 6984–6991. Available from: doi:10.1021/bi00443a031.
- Lin, H.-L., Chiou, S.-H., Wu, C.-W., Lin, W.-B., et al. (2007) Combretastatin A4-Induced Differential Cytotoxicity and Reduced Metastatic Ability by Inhibition of AKT Function in Human Gastric Cancer Cells. *Journal of Pharmacology and Experimental Therapeutics*. [Online] 323 (1), 365–373. Available from: doi:10.1124/jpet.107.124966.
- Lindlar, H. (1952) Ein neuer Katalysator für selektive Hydrierungen. *Helvetica Chimica Acta*. 35, 446–450.
- Liu, P., Qin, Y., Wu, L., Yang, S., et al. (2014) A phase I clinical trial assessing the safety and tolerability of combretastatin A4 phosphate injections. *Anti-Cancer Drugs*. [Online] 25 (4), 462–471. Available from: doi:10.1097/CAD.0000000000000070.
- Loeb, L.A. (2001) *Perspectives in Cancer Research A Mutator Phenotype in Cancer 1*. (1), 3230–3239.
- Lorusso, G. & Rüegg, C. (2012) New insights into the mechanisms of organ-specific breast cancer metastasis. *Seminars in Cancer Biology*. [Online] 22 (3), 226–233. Available from: doi:10.1016/j.semcancer.2012.03.007.
- Lu, Y., Chen, J., Xiao, M., Li, W., et al. (2012) An Overview of Tubulin Inhibitors That Interact with the Colchicine Binding Site. *Pharmaceutical Research*. [Online] 29 (11), 2943–2971. Available from: doi:10.1007/s11095-012-0828-z.An.
- M. Scherer, K., H. Bisby, R., W. Botchway, S. & W. Parker, A. (2017) New Approaches to Photodynamic Therapy from Types I, II and III to Type IV Using One or More Photons. *Anti-Cancer Agents in Medicinal Chemistry*. [Online] 17 (2), 171–189. Available from: doi:10.2174/18715206166666160513131723.
- Ma, H., Jiang, Q., Han, S., Wu, Y., et al. (2012) Multicellular Tumor Spheroids as an in Vivo–Like Tumor Model for Three-Dimensional Imaging of Chemotherapeutic and Nano Material Cellular Penetration. *Molecular Imaging*. [Online] 11 (6), 7290.2012.00012.

Available from: doi:10.2310/7290.2012.00012.

Madadi, N.R., Penthala, N.R., Howk, K., Ketkar, A., et al. (2015) Synthesis and biological evaluation of novel 4,5-disubstituted 2H-1,2,3-triazoles as cis-constrained analogues of combretastatin A-4. *European journal of medicinal chemistry*. [Online] 103, 123–132. Available from: doi:10.1016/j.ejmech.2015.08.041.

Madan, A., Graham, R.A., Carroll, K.M., Mudra, D.R., et al. (2003) Effects of prototypical microsomal enzyme inducers on cytochrome P450 expression in cultured human hepatocytes. *Drug metabolism and disposition: the biological fate of chemicals*. 31 (4), 421–431.

Mader, R.M., Sieder, a E., Braun, J., Rizovski, B., et al. (1997) Transcription and activity of 5-fluorouracil converting enzymes in fluoropyrimidine resistance in colon cancer in vitro. *Biochemical pharmacology*. 54 (11), 1233–1242.

Mahal, K., Biersack, B., Schrufer, S., Resch, M., et al. (2016) Combretastatin A-4 derived 5-(1-methyl-4-phenyl-imidazol-5-yl)indoles with superior cytotoxic and anti-vascular effects on chemoresistant cancer cells and tumors. *European Journal of Medicinal Chemistry*. [Online] 118, 9–20. Available from: doi:10.1016/j.ejmech.2016.04.045.

Makarov, N.S., Drobizhev, M. & Rebane, A. (2008a) Two-photon absorption standards in the 550–1600 nm excitation wavelength range. *Optics Express*. 16 (6), 4029–4047.

Makarov, N.S., Drobizhev, M. & Rebane, A. (2008b) Two-photon absorption standards in the 550-1600 nm excitation wavelength range. *Optics express*. 16 (6), 4029–4047.

Malebari, A.M., Greene, L.M., Nathwani, S.M., Fayne, D., et al. (2017) β -Lactam analogues of combretastatin A-4 prevent metabolic inactivation by glucuronidation in chemoresistant HT-29 colon cancer cells. *European Journal of Medicinal Chemistry*. [Online] 130, 261–285. Available from: doi:10.1016/j.ejmech.2017.02.049.

Malkin, S. & Fischer, E. (1962) TEMPERATURE DEPENDENCE OF PHOTOISOMERIZATION. PART II.1 QUANTUM YIELDS OF cis \rightleftharpoons trans ISOMERIZATIONS IN AZO-COMPOUNDS. *Journal of Physical Chemistry*. [Online] 66 (12), 2482–2486. Available from: doi:10.1021/j100818a038.

- Mamiya, F., Ousaka, N. & Yashima, E. (2015a) Remote Control of the Planar Chirality in Peptide-Bound Metallomacrocycles and Dynamic-to-Static Planar Chirality Control Triggered by Solvent-Induced 3_{10} -to- α -Helix Transitions. *Angewandte Chemie International Edition*. [Online] 54 (48), 14442–14446. Available from: doi:10.1002/anie.201507918.
- Mamiya, F., Ousaka, N. & Yashima, E. (2015b) Remote Control of the Planar Chirality in Peptide-Bound Metallomacrocycles and Dynamic-to-Static Planar Chirality Control Triggered by Solvent-Induced 3_{10} -to- α -Helix Transitions. *Angewandte Chemie - International Edition*. [Online] 54 (48), 14442–14446. Available from: doi:10.1002/anie.201507918.
- Mangiatordi, G.F., Trisciuzzi, D., Alberga, D., Denora, N., et al. (2017) Novel chemotypes targeting tubulin at the colchicine binding site and unbiassing P-glycoprotein. *European Journal of Medicinal Chemistry*. [Online] 139, 792–803. Available from: doi:10.1016/j.ejmech.2017.07.037.
- Marvin, M. (1961) *Microscopy apparatus*.
- Mathai, S., Bird, D.K., Stylli, S.S., Smith, T.A., et al. (2007) Two-photon absorption cross-sections and time-resolved fluorescence imaging using porphyrin photosensitisers. *Photochemical & Photobiological Sciences*. 6 (9), 1019–1026.
- Mehta, D.R., Foon, K. a, Redner, R.L., Raptis, A., et al. (2011) Fludarabine and cytarabine in patients with acute myeloid leukemia refractory to two different courses of front-line chemotherapy. *Leukemia research*. [Online] 35 (7), 885–888. Available from: doi:10.1016/j.leukres.2010.12.030.
- Meyer, S.D. & Schreiber, S.L. (1994) Acceleration of the Dess-Martin Oxidation by Water. *The Journal of Organic Chemistry*. [Online] 59 (24), 7549–7552. Available from: doi:10.1021/jo00103a067.
- Mikstacka, R., Stefański, T. & Rózański, J. (2013) Tubulin-interactive stilbene derivatives as anticancer agents. *Cellular and Molecular Biology Letters*. [Online] 18 (3), 368–397. Available from: doi:10.2478/s11658-013-0094-z.

- Minsky, M. (1957) Microscopy Apparatus. *US Patent 3013467*. [Online]. 3013467 (3013467) p.5. Available from: doi:US3013467A.
- Mitton, D. & Ackroyd, R. (2008) A brief overview of photodynamic therapy in Europe. *Photodiagnosis and Photodynamic Therapy*. [Online] 5, 103–111. Available from: doi:10.1016/j.pdpdt.2008.04.004.
- Miyaura, N. & Suzuki, A. (1995) Palladium-Catalyzed Cross-Coupling Reactions of Organoboron Compounds. *Chemical Reviews*. [Online] 95 (7), 2457–2483. Available from: doi:10.1021/cr00039a007.
- Miyaura, N. & Suzuki, A. (1979) Stereoselective synthesis of arylated (E)-alkenes by the reaction of alk-1-enylboranes with aryl halides in the presence of palladium catalyst. *Journal of the Chemical Society, Chemical Communications*. [Online] 0 (19), 866. Available from: doi:10.1039/c39790000866.
- Miyaura, N., Yamada, K., Suginome, H. & Suzuki, A. (1985) Novel and convenient method for the stereo- and regiospecific synthesis of conjugated alkadienes and alkenynes via the palladium-catalyzed cross-coupling reaction of 1-alkenylboranes with bromoalkenes and bromoalkynes. *Journal of the American Chemical Society*. [Online] 107 (4), 972–980. Available from: doi:10.1021/ja00290a037.
- Miyaura, N., Yamada, K. & Suzuki, A. (1979) A new stereospecific cross-coupling by the palladium-catalyzed reaction of 1-alkenylboranes with 1-alkenyl or 1-alkynyl halides. *Tetrahedron Letters*. [Online] 20 (36), 3437–3440. Available from: doi:10.1016/S0040-4039(01)95429-2.
- Molloy, J.J., Metternich, J.B., Daniliuc, C.G., Watson, A.J.B., et al. (2018) Contra-Thermodynamic, Photocatalytic *E* → *Z* Isomerization of Styrenyl Boron Species: Vectors to Facilitate Exploration of Two-Dimensional Chemical Space. *Angewandte Chemie International Edition*. [Online] 57 (12), 3168–3172. Available from: doi:10.1002/anie.201800286.
- Mooney, C.J., Nagaiah, G., Fu, P., Wasman, J.K., et al. (2009) A phase II trial of fosbretabulin in advanced anaplastic thyroid carcinoma and correlation of baseline serum-soluble

- intracellular adhesion molecule-1 with outcome. *Thyroid: official journal of the American Thyroid Association*. [Online] 19 (3), 233–240. Available from: doi:10.1089/thy.2008.0321.
- Morinaga, Y., Suga, Y., Ehara, S., Harada, K., et al. (2003) Combination effect of AC-7700, a novel combretastatin A-4 derivative, and cisplatin against murine and human tumors in vivo. *Cancer Science*. [Online] 94 (2), 200–204. Available from: doi:10.1111/j.1349-7006.2003.tb01419.x.
- Muizebelt, W.J. & Nivard, R.J.F. (1968) Iodine atom-catalysed isomerisation of symmetrically substituted cis-stilbenes. *Journal of the Chemical Society B: Physical Organic*. [Online] 0 (0), 913. Available from: doi:10.1039/j29680000913.
- Murata, M., Watanabe, S. & Masuda, Y. (1997) Novel Palladium(0)-Catalyzed Coupling Reaction of Dialkoxyborane with Aryl Halides: Convenient Synthetic Route to Arylboronates. *The Journal of Organic Chemistry*. [Online] 62 (19), 6458–6459. Available from: doi:10.1021/jo970963p.
- Mustafa, M., Abdelhamid, D., Abdelhafez, E.S.M.N., Ibrahim, M.A.A., et al. (2017) Synthesis, antiproliferative, anti-tubulin activity, and docking study of new 1,2,4-triazoles as potential combretastatin analogues. *European Journal of Medicinal Chemistry*. [Online] 141 (October), 293–305. Available from: doi:10.1016/j.ejmech.2017.09.063.
- Nabha, S.M., Mohammad, R.M., Wall, N.R., Dutcher, J.A., et al. (2001) Evaluation of combretastatin A-4 prodrug in a non-Hodgkin's lymphoma xenograft model: preclinical efficacy. *Anti-cancer drugs*. 12 (1), 57–63.
- Nam, N.-H. (2003) Combretastatin A-4 analogues as antimitotic antitumor agents. *Current medicinal chemistry*. 10 (17), 1697–1722.
- Nasir, S., Bukhari, A., Kumar, G.B., Revankar, H.M., et al. (2017) *Development of combretastatins as potent tubulin polymerization inhibitors*. [Online] Available from: doi:10.1016/j.bioorg.2017.04.007.
- Nathan, P., Zweifel, M., Padhani, A.R., Koh, D.-M., et al. (2012) Phase I Trial of Combretastatin A4 Phosphate (CA4P) in Combination with Bevacizumab in Patients

- with Advanced Cancer. *Clinical Cancer Research*. [Online] 18 (12), 3428–3439. Available from: doi:10.1158/1078-0432.CCR-11-3376.
- Ng, Q.-S., Mandeville, H., Goh, V., Alonzi, R., et al. (2012) Phase Ib trial of radiotherapy in combination with combretastatin-A4-phosphate in patients with non-small-cell lung cancer, prostate adenocarcinoma, and squamous cell carcinoma of the head and neck. *Annals of Oncology*. [Online] 23 (1), 231–237. Available from: doi:10.1093/annonc/mdr332.
- Noble, R.L., Beer, C.T. & Cutts, J.H. (1958) Role of chance observations in chemotherapy: Vinca rosea. *Annals of the New York Academy of Sciences*. 76 (3), 882–894.
- Obasaju, C.K., Cowan, R.A. & Wilkinson, P.M. (1993) *Oncology Original Article*. 203–206.
- Oliner, J.D., Kinzler, K.W., Meltzer, P.S., George, D.L., et al. (1992) Amplification of a gene encoding a p53-associated protein in human sarcomas. *Nature*. [Online] 358 (6381), 80–83. Available from: doi:10.1038/358080a0.
- Olson, A.R. (1931) The study of chemical reactions from potential energy diagrams. *Transactions of the Faraday Society*. [Online] 27, 69. Available from: doi:10.1039/tf9312700069.
- Osterod, F., Peters, L., Kraft, A., Sano, T., et al. (2001) Luminescent supramolecular assemblies based on hydrogen-bonded complexes of stilbenecarboxylic acids and dithieno[3,2-b:2',3'-d]thiophene-2-carboxylic acids with a tris(imidazoline) base. *Journal of Materials Chemistry*. [Online] 11 (6), 1625–1633. Available from: doi:10.1039/b009406o.
- Padera, T.P., Kadambi, A., di Tomaso, E., Carreira, C.M., et al. (2002) Lymphatic metastasis in the absence of functional intratumor lymphatics. *Science (New York, N.Y.)*. [Online] 296 (5574), 1883–1886. Available from: doi:10.1126/science.1071420.
- Pagni, R. (2005) Solvents and Solvent Effects in Organic Chemistry, Third Edition (Christian Reichardt). *Journal of Chemical Education*. [Online] 82 (3), 382. Available from: doi:10.1021/ed082p382.2.
- Pampaloni, F., Ansari, N. & Stelzer, E.H.K. (2013) High-resolution deep imaging of live

- cellular spheroids with light-sheet-based fluorescence microscopy. *Cell and Tissue Research*. [Online] 352 (1), 161–177. Available from: doi:10.1007/s00441-013-1589-7.
- Pantel, K., Brakenhoff, R.H. & Brandt, B. (2008) Detection, clinical relevance and specific biological properties of disseminating tumour cells. *Nature Reviews Cancer*. [Online] 8 (5), 329–340. Available from: doi:10.1038/nrc2375.
- Parson, W.W. (2007) *Modern optical spectroscopy with examples from biophysics and biochemistry*. Heidelberg, Germany, Springer.
- Patrick, G.L. (2009a) *An Introduction to Medicinal Chemistry*. 4th edition. New York, United States, Oxford University Press.
- Patrick, G.L. (2009b) *An Introduction to Medicinal Chemistry*. [Online]. Oxford University Press, USA. Available from: doi:10.1017/CBO9781107415324.004.
- Patterson, D.M. & Rustin, G.J.S. (2007a) Vascular damaging agents. *Clinical oncology (Royal College of Radiologists (Great Britain))*. [Online] 19 (6), 443–456. Available from: doi:10.1016/j.clon.2007.03.014.
- Patterson, D.M. & Rustin, G.J.S. (2007b) Vascular Damaging Agents. *Clinical Oncology*. [Online] Available from: doi:10.1016/j.clon.2007.03.014.
- Pawlicki, M., Collins, H.A., Denning, R.G. & Anderson, H.L. (2009) Two-photon absorption and the design of two-photon dyes. *Angewandte Chemie - International Edition*. [Online] 48 (18), 3244–3266. Available from: doi:10.1002/anie.200805257.
- Pelletier, P. & Caventou, J.B. (1820) Chemical examination of several plants of the meadow saffron family, and of the active principle that they contain. *Annales de Chimie et de Physique*. 14, 69–81.
- Petit, G.R., Singh, S.B., Boyd, M.R., Hamel, E., et al. (1995) Antineoplastic Agents. 291. Isolation and Synthesis of Combretastatins A-4, A-5, and A-6. *Journal of medicinal chemistry*. 38, 1666–1672.
- Petit, I., Karajannis, M.A., Vincent, L., Young, L., et al. (2008) The microtubule-targeting agent CA4P regresses leukemic xenografts by disrupting interaction with vascular cells

- and mitochondrial-dependent cell death. *Blood*. [Online] 111 (4), 1951–1961. Available from: doi:10.1182/blood-2007-05-089219.
- Pettit, G.R., Cragg, G.M., Herald, D.L., Schmidt, J.M., et al. (1982) Isolation and structure of combretastatin. *Canadian Journal of Chemistry*. [Online] 60 (11), 1374–1376. Available from: doi:10.1139/v82-202.
- Pettit, G.R. & Singh, S.B. (1987) Isolation, structure, and synthesis of combretastatin A-2, A-3, and B-2. *Canadian Journal of Chemistry*. [Online] 65 (10), 2390–2396. Available from: doi:10.1139/v87-399.
- Pettit, G.R., Singh, S.B., Boyd, M.R., Hamel, E., et al. (1995a) Antineoplastic agents. 291. Isolation and synthesis of combretastatins A-4, A-5, and A-6. *Journal of Medicinal Chemistry*. 38, 1666–1672.
- Pettit, G.R., Singh, S.B., Hamel, E., Lin, C.M., et al. (1989) Isolation and structure of the strong cell growth and tubulin inhibitor combretastatin A-4. *Experientia*. 45 (2), 209–211.
- Pettit, G.R., Singh, S.B., Niven, M.L., Hamel, E., et al. (1987) Isolation, structure, and synthesis of combretastatins A-1 and B-1, potent new inhibitors of microtubule assembly, derived from *Combretum caffrum*. *Journal of natural products*. [Online] 50 (1), 119–131. Available from: doi:10.1021/np50049a016.
- Pettit, G.R., Temple, C., Narayanan, V.L., Varma, R., et al. (1995b) Antineoplastic agents 322. synthesis of combretastatin A-4 prodrugs. *Anti-cancer drug design*. 10 (4), 299–309.
- Phua, P.-H., Lefort, L., Boogers, J.A.F., Tristany, M., et al. (2009) Soluble iron nanoparticles as cheap and environmentally benign alkene and alkyne hydrogenation catalysts. *Chemical Communications*. [Online] 0 (25), 3747. Available from: doi:10.1039/b820048c.
- Pinney, K.G., Mejia, M.P., Villalobos, V.M., Rosenquist, B.E., et al. (2000) Synthesis and biological evaluation of aryl azide derivatives of combretastatin A-4 as molecular probes for tubulin. *Bioorganic & Medicinal Chemistry*. 8, 2417–2425.
- Potter, S.M. (1996) *Vital imaging : Two photons are better than one*. 1595–1598.

- Pratt, W.B. (1994) *The Anticancer Drugs*. Oxford University Press.
- PSA-Rising (2001) *Combretastatin update 1: in Ohio phase I trial, some tumors respond, patients experience vascular stress*. 2001. Prostate Cancer News.
- Puck, T.T., Cieciura, S.J. & Robinson, A. (1958) Genetics of somatic mammalian cells. III. Long-term cultivation of euploid cells from human and animal subjects. *The Journal of experimental medicine*. 108 (6), 945–956.
- Quaresma, M., Coleman, M.P. & Rachet, B. (2015) 40-year trends in an index of survival for all cancers combined and survival adjusted for age and sex for each cancer in England and Wales, 1971–2011: a population-based study. *The Lancet*. [Online] 385 (9974), 1206–1218. Available from: doi:10.1016/S0140-6736(14)61396-9.
- Rajaram, J., Narula, A.P.S., Chawla, H.P.S. & Dev, S. (1983) Semihydrogenation of acetylenes: Modified lindlar catalyst. *Tetrahedron*. [Online] 39 (13), 2315–2322. Available from: doi:10.1016/S0040-4020(01)91960-X.
- Rang, H.P., Dale, M.M., Ritter, J.M. & Moore, P.K. (2003) *Pharmacology*. 5th edition. Bath, UK, Churchill Livingstone.
- Ravelli, R.B.G., Gigant, B., Curmi, P.A., Jourdain, I., et al. (2004) Insight into tubulin regulation from a complex with colchicine and a stathmin-like domain. *Nature*. [Online] 428 (6979), 198–202. Available from: doi:10.1038/nature02393.
- Reddy, N., Burra, V.R., Ravindranath, L.K., Sreenivasulu, R., et al. (2016) Synthesis and biological evaluation of benzoxazole fused combretastatin derivatives as anticancer agents. *Monatshefte für Chemie - Chemical Monthly*. [Online] 147 (3), 593–598. Available from: doi:10.1007/s00706-016-1685-y.
- Rendell, D. (1987) *Fluorescence and phosphorescence*. London, UK, John Wiley & Sons.
- Richmond, E. & Moran, J. (2015) Ligand Control of *E* / *Z* Selectivity in Nickel-Catalyzed Transfer Hydrogenative Alkyne Semireduction. *The Journal of Organic Chemistry*. [Online] 80 (13), 6922–6929. Available from: doi:10.1021/acs.joc.5b01047.
- Romagnoli, R., Baraldi, P.G., Prencipe, F., Oliva, P., et al. (2016) Design and Synthesis of

- Potent in Vitro and in Vivo Anticancer Agents Based on 1-(3',4',5'-Trimethoxyphenyl)-2-Aryl-1H-Imidazole. *Scientific Reports*. [Online] 6 (1), 26602. Available from: doi:10.1038/srep26602.
- Romano, P., Manniello, A., Aresu, O., Armento, M., et al. (2009) Cell Line Data Base: structure and recent improvements towards molecular authentication of human cell lines. *Nucleic acids research*. [Online] 37 (Database issue), D925-32. Available from: doi:10.1093/nar/gkn730.
- Rustin, G.J., Shreeves, G., Nathan, P.D., Gaya, A., et al. (2010) A Phase Ib trial of CA4P (combretastatin A-4 phosphate), carboplatin, and paclitaxel in patients with advanced cancer. *British Journal of Cancer, Published online: 13 April 2010; | doi:10.1038/sj.bjc.6605650*. [Online] 102 (9), 1355. Available from: doi:10.1038/sj.bjc.6605650.
- Rustin, G.J.S., Galbraith, S.M., Anderson, H., Stratford, M., et al. (2003) Phase I clinical trial of weekly combretastatin A4 phosphate: clinical and pharmacokinetic results. *Journal of clinical oncology : official journal of the American Society of Clinical Oncology*. [Online] 21 (15), 2815–2822. Available from: doi:10.1200/JCO.2003.05.185.
- Saltiel, J. (1968) Perdeuteriostilbene. The triplet and singlet paths for stilbene photoisomerization. *Journal of the American Chemical Society*. [Online] 90, 6394–6400. Available from: doi:10.1021/ja01025a026.
- Saltiel, J. & D'Agostino, J.T. (1972) Separation of viscosity and temperature effects on the singlet pathway to stilbene photoisomerization. *Journal of the American Chemical Society*. [Online] 94 (18), 6445–6456. Available from: doi:10.1021/ja00773a031.
- Saltiel, J. & Megarity, E.D. (1972) Mechanism of direct cis-trans photoisomerization of the stilbenes. Solvent viscosity and the azulene effect. *Journal of the American Chemical Society*. [Online] 94, 2742–2749. Available from: doi:10.1021/ja00763a035.
- Saltiel, J., Zafiriou, O.C., Megarity, E.D. & Lamola, A.A. (1968) Tests of the singlet mechanism for cis-trans photoisomerization of the stilbenes. *Journal of the American Chemical Society*. [Online] 90, 4759–4760. Available from: doi:10.1021/ja01019a063.

- Santi, P.A. (2011) Light Sheet Fluorescence Microscopy. *Journal of Histochemistry & Cytochemistry*. [Online] 59 (2), 129–138. Available from: doi:10.1369/0022155410394857.
- Sassa, S., Sugita, O., Galbraith, R.A. & Kappas, A. (1987) Drug metabolism by the human hepatoma cell, Hep G2. *Biochemical and biophysical research communications*. 143 (1), 52–57.
- Scherer, K.M. (2012) *Two-Photon Microscopy of E-Combretastatin Uptake and Activation in Live Mammalian Cells*. PhD thesis, University of Salford.
- Scherer, K.M., Bisby, R.H., Botchway, S.W., Greetham, G.M., Hadfield, J.A., et al. (2014) Spectroscopy and fluorescence lifetime imaging in live cells of a cyano-substituted combretastatin. *Spectroscopy & Imaging*.
- Scherer, K.M., Bisby, R.H., Botchway, S.W., Hadfield, J.A., et al. (2015) Three-dimensional imaging and uptake of the anticancer drug combretastatin in cell spheroids and photoisomerization in gels with multiphoton excitation. *Journal of Biomedical Optics*. [Online] 20 (7), 078003. Available from: doi:10.1117/1.JBO.20.7.078003.
- Scherer, K.M., Bisby, R.H., Botchway, S.W. & Parker, A.W. (2017) New Approaches to Photodynamic Therapy from Types I, II and III to Type IV Using One or More Photons. *Anti-Cancer Agents in Medicinal Chemistry*. [Online] 17 (2), 171–189. Available from: doi:10.2174/1871520616666160513131723.
- Scherer, W.F. & Syverton, J.T. (1952) Studies on the propagation in vitro of poliomyelitis viruses. III. The propagation of poliomyelitis viruses in tissue cultures devoid of nerve cells. *The Journal of experimental medicine*. 96 (4), 389–400.
- Schindelin, J., Arganda-Carreras, I., Frise, E., Kaynig, V., et al. (2012) Fiji: an open-source platform for biological-image analysis. *Nature Methods*. [Online] 9 (7), 676–682. Available from: doi:10.1038/nmeth.2019.
- Schulte-Frohlinde, D., Blume, H. & Güsten, H. (1962) PHOTOCHEMICAL cis-trans-ISOMERIZATION OF SUBSTITUTED STILBENES. *The Journal of Physical Chemistry*. [Online] 66 (12), 2486–2491. Available from: doi:10.1021/j100818a039.

- Semba, K., Fujihara, T., Xu, T., Terao, J., et al. (2012) Copper-Catalyzed Highly Selective Semihydrogenation of Non-Polar Carbon-Carbon Multiple Bonds using a Silane and an Alcohol. *Advanced Synthesis & Catalysis*. [Online] 354 (8), 1542–1550. Available from: doi:10.1002/adsc.201200200.
- Shen, C.-H., Shee, J.-J., Wu, J.-Y., Lin, Y.-W., et al. (2010) Combretastatin A-4 inhibits cell growth and metastasis in bladder cancer cells and retards tumour growth in a murine orthotopic bladder tumour model. *British journal of pharmacology*. [Online] 160 (8), 2008–2027. Available from: doi:10.1111/j.1476-5381.2010.00861.x.
- Sheppard, C.J.R. & Shotton, D.M. (1997) *Microscopy handbooks 38 - Confocal laser scanning microscopy*. Oxford, UK, Bios Scientific Publishers Ltd.
- Siedentopf, H. & Zsigmondy, R. (1902) Über Sichtbarmachung und Größenbestimmung ultramikroskopischer Teilchen, mit besonderer Anwendung auf Goldrubingläser. *Annalen der Physik*. [Online] 315 (1), 1–39. Available from: doi:10.1002/andp.19023150102.
- Siemann, D.W. (2006) Tumor vasculature: a target for anticancer therapies. In: D. W. Siemann (ed.). *Vascular-Targeted Therapies in Oncology*. Chichester, UK, John Wiley & Sons, Ltd. pp. 1–8.
- Siemann, D.W., Mercer, E., Lepler, S. & Rojiani, A.M. (2002) Vascular targeting agents enhance chemotherapeutic agent activities in solid tumor therapy. *International journal of cancer*. 99 (1), 1–6.
- Sigmond, J., Kamphuis, J. a E., Laan, a C., Hoebe, E.K., et al. (2007) The synergistic interaction of gemcitabine and cytosine arabinoside with the ribonucleotide reductase inhibitor triapine is schedule dependent. *Biochemical pharmacology*. [Online] 73 (10), 1548–1557. Available from: doi:10.1016/j.bcp.2007.01.025.
- Silverstein 1916-, R.M. (Robert M. (1998) *Spectrometric identification of organic compounds*. Francis X Webster (ed.).
- Simoni, D., Romagnoli, R., Baruchello, R., Rondanin, R., et al. (2008) Novel A-ring and B-ring modified combretastatin A-4 (CA-4) analogues endowed with interesting cytotoxic

- activity. *Journal of Medicinal Chemistry*. [Online] 51 (19), 6211–6215. Available from: doi:10.1021/jm8005004.
- Simoni, D., Romagnoli, R., Baruchello, R., Rondanin, R., et al. (2006) Novel combretastatin analogues endowed with antitumor activity. *Journal of Medicinal Chemistry*. [Online] 49 (11), 3143–3152. Available from: doi:10.1021/jm0510732.
- Skoufias, D.A. & Wilson, L. (1992) Mechanism of inhibition of microtubule polymerization by colchicine: inhibitory potencies of unliganded colchicine and tubulin-colchicine complexes. *Biochemistry*. [Online] 31 (3), 738–746. Available from: doi:10.1021/bi00118a015.
- So, P.T.C. (2002) *Two-photon Fluorescence Light Microscopy*. 1–5.
- So, P.T.C., Dong, C.Y., Masters, B.R. & Berland, K.M. (2000) Two-photon excitation fluorescence microscopy. *Annual Review of Biomedical Engineering*. 2, 399–429.
- Sonogashira, K., Tohda, Y. & Hagihara, N. (1975) A convenient synthesis of acetylenes: catalytic substitutions of acetylenic hydrogen with bromoalkenes, iodoarenes and bromopyridines. *Tetrahedron Letters*. [Online] 16 (50), 4467–4470. Available from: doi:10.1016/S0040-4039(00)91094-3.
- Sosa, J.A., Balkissoon, J., Lu, S., Langecker, P., et al. (2012) Thyroidectomy followed by fosbretabulin (CA4P) combination regimen appears to suggest improvement in patient survival in anaplastic thyroid cancer. *Surgery*. [Online] 152 (6), 1078–1087. Available from: doi:10.1016/j.surg.2012.08.036.
- Splettstoesser, T. (2015) *No Title*. [Online]. 2015. Available from: www.scistyle.com.
- Spring, K.R. & Davidson, M.W. (2012) *Introduction to fluorescence microscopy*. 2012.
- Sriram, M., Hall, J.J., Grohmann, N.C., Strecker, T.E., et al. (2008) Design, synthesis and biological evaluation of dihydronaphthalene and benzosuberene analogs of the combretastatins as inhibitors of tubulin polymerization in cancer chemotherapy. *Bioorganic & Medicinal Chemistry*. [Online] 16 (17), 8161–8171. Available from: doi:10.1016/j.bmc.2008.07.050.

- Stefański, T., Mikstacka, R., Kurczab, R., Dutkiewicz, Z., et al. (2018) Design, synthesis, and biological evaluation of novel combretastatin A-4 thio derivatives as microtubule targeting agents. *European Journal of Medicinal Chemistry*. [Online] 144, 797–816. Available from: doi:10.1016/j.ejmech.2017.11.050.
- Stevenson, J.P., Rosen, M., Sun, W., Gallagher, M., et al. (2003) Phase I trial of the antivasular agent combretastatin A4 phosphate on a 5-day schedule to patients with cancer: magnetic resonance imaging evidence for altered tumor blood flow. *Journal of Clinical Oncology*. [Online] 21, 4428–4438. Available from: doi:10.1200/JCO.2003.12.986.
- Stevenson, P.J., Treacy, A.B. & Nieuwenhuyzen, M. (1997) Preparation of Dess–Martin periodinane—the role of the morphology of 1-hydroxy-1,2-benziodoxol-3(1H)-one 1-oxide precursor. *Journal of the Chemical Society, Perkin Transactions 2*. [Online] 0 (3), 589–592. Available from: doi:10.1039/a605253c.
- Stockert, J.C., Blázquez-Castro, A., Cañete, M., Horobin, R.W., et al. (2012) MTT assay for cell viability: Intracellular localization of the formazan product is in lipid droplets. *Acta Histochemica*. [Online] 114 (8), 785–796. Available from: doi:10.1016/j.acthis.2012.01.006.
- Strachan, J., Sharp, J.T. & Parsons, S. (1998) *via nitrile ylide cyclisations and their rearrangement to*. 807–812.
- Suppan, P. (1994) *Chemistry and light*. 1st edition. Cambridge, Royal Society of Chemistry.
- Suzuki, A. (1999) Recent advances in the cross-coupling reactions of organoboron derivatives with organic electrophiles. *Journal of Organometallic Chemistry*. 576, 147–168.
- Takagi, J., Takahashi, K., Ishiyama, T. & Miyaura, N. (2002) Palladium-Catalyzed Cross-Coupling Reaction of Bis(pinacolato)diboron with 1-Alkenyl Halides or Triflates: Convenient Synthesis of Unsymmetrical 1,3-Dienes via the Borylation-Coupling Sequence. *Journal of the American Chemical Society*. [Online] 124 (27), 8001–8006. Available from: doi:10.1021/ja0202255.

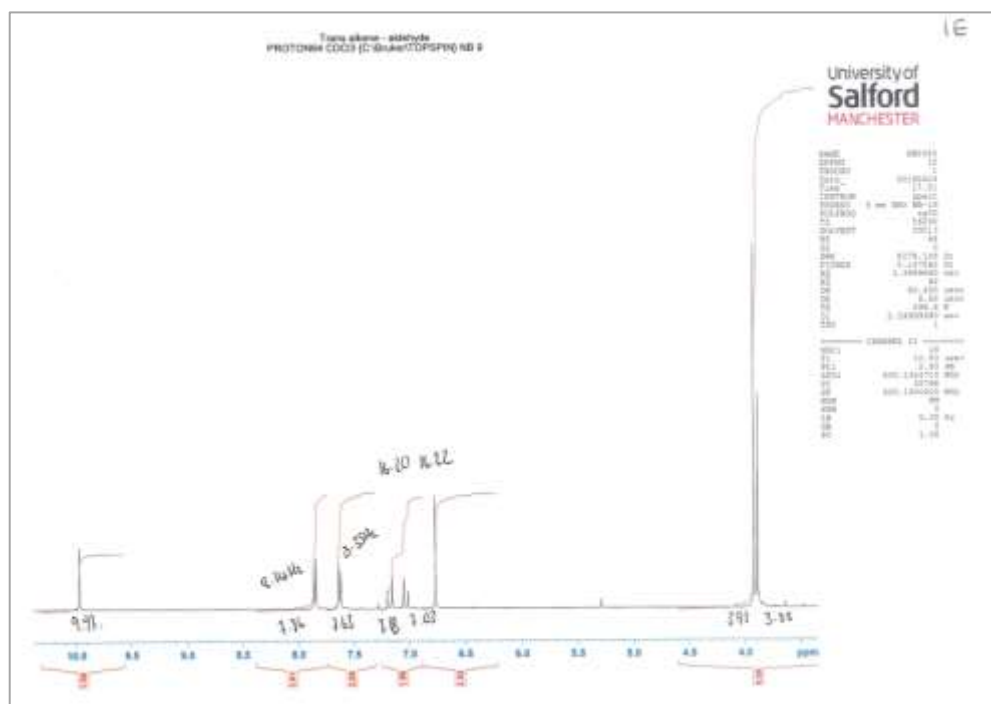
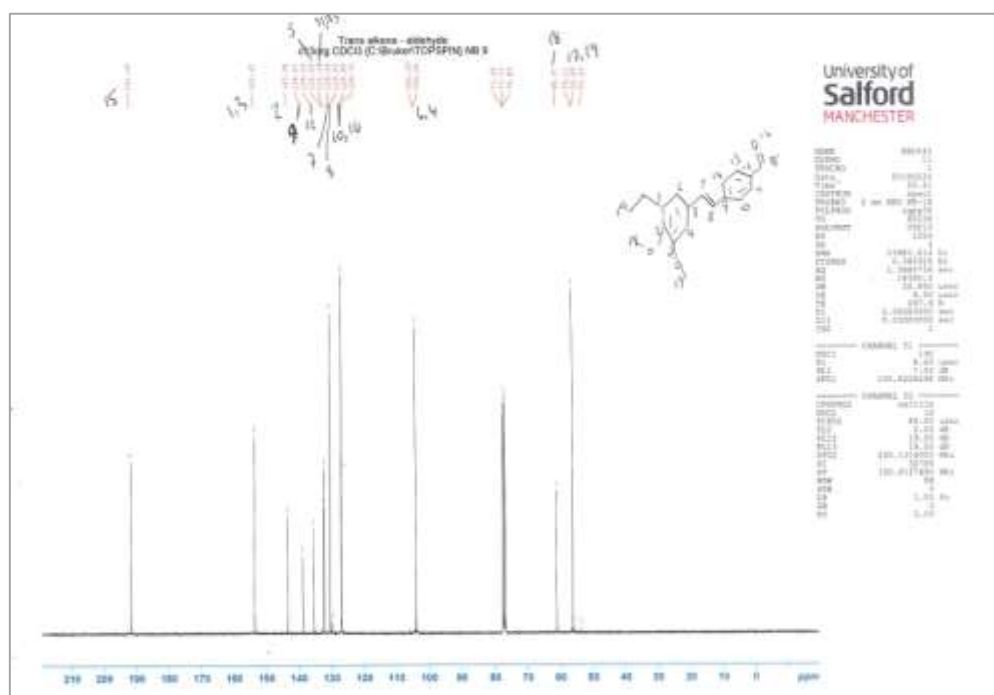
- Takimoto, B.C.H. & Calvo, E. (2008) Principles of oncologic pharmacotherapy. In: R Pazdur, LD Wagman, KA Camphausen, & WJ Hoskins (eds.). *Cancer*. London, UK, UBM Medica. pp. 23–42.
- Tang, Y., Liu, J. & Chen, Y. (2016) Agarose multi-wells for tumour spheroid formation and anti-cancer drug test. *Microelectronic Engineering*. [Online] 158 (C), 41–45. Available from: doi:10.1016/j.mee.2016.03.009.
- Tani, K., Ono, N., Okamoto, S. & Sato, F. (1993) Palladium(0)-catalysed transfer hydrogenation of alkynes to cis-alkenes with HCO₂H–NEt₃. *J. Chem. Soc., Chem. Commun.* [Online] 0 (4), 386–387. Available from: doi:10.1039/C39930000386.
- Tarade, D., Ma, D., Pignanelli, C., Mansour, F., et al. (2017) Structurally simplified biphenyl combretastatin A4 derivatives retain in vitro anti-cancer activity dependent on mitotic arrest Chryso Kanthou (ed.). *PLOS ONE*. [Online] 12 (3), e0171806. Available from: doi:10.1371/journal.pone.0171806.
- Techne (2008) *Memetic algorithms, convergence and pre-existing fitness landscapes*. 2008. Teleomechanist Blog.
- Tellinghuisen, J. (1987) *The Franck-Condon Principle*. In: [Online]. Springer, Berlin, Heidelberg. pp. 149–156. Available from: doi:10.1007/978-3-642-71778-9_21.
- Thurston, D.E. (2007a) *Chemistry and pharmacology of anticancer drugs*. 1st edition. Boca Raton, CRC Press, Taylor & Francis Group.
- Thurston, D.E. (2007b) *Chemistry and pharmacology of anticancer drugs*. 1st edition. Boca Raton, CRC Press, Taylor & Francis Group.
- Tjio, J.H. & Puck, T.T. (1958) Genetics of somatic mammalian cells. II. Chromosomal constitution of cells in tissue culture. *The Journal of experimental medicine*. 108 (2), 259–268.
- Tozer, G.M., Kanthou, C., Lewis, G., Prise, V.E., et al. (2008) Tumour vascular disrupting agents: combating treatment resistance. *The British Journal of Radiology*. [Online] 81 (special_issue_1), S12–S20. Available from: doi:10.1259/bjr/36205483.

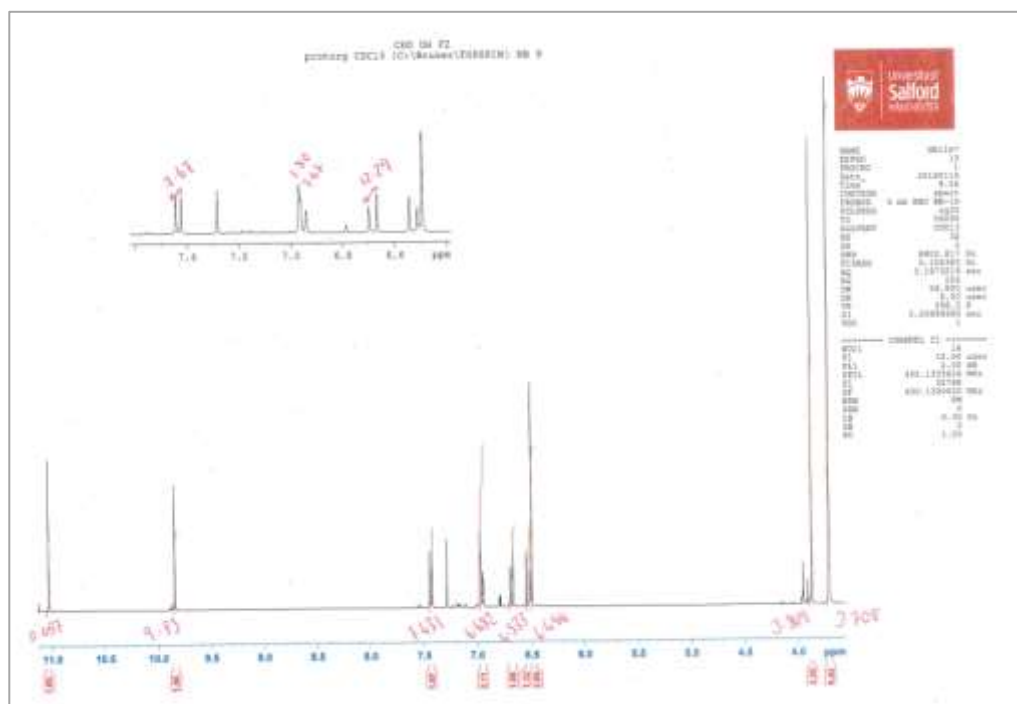
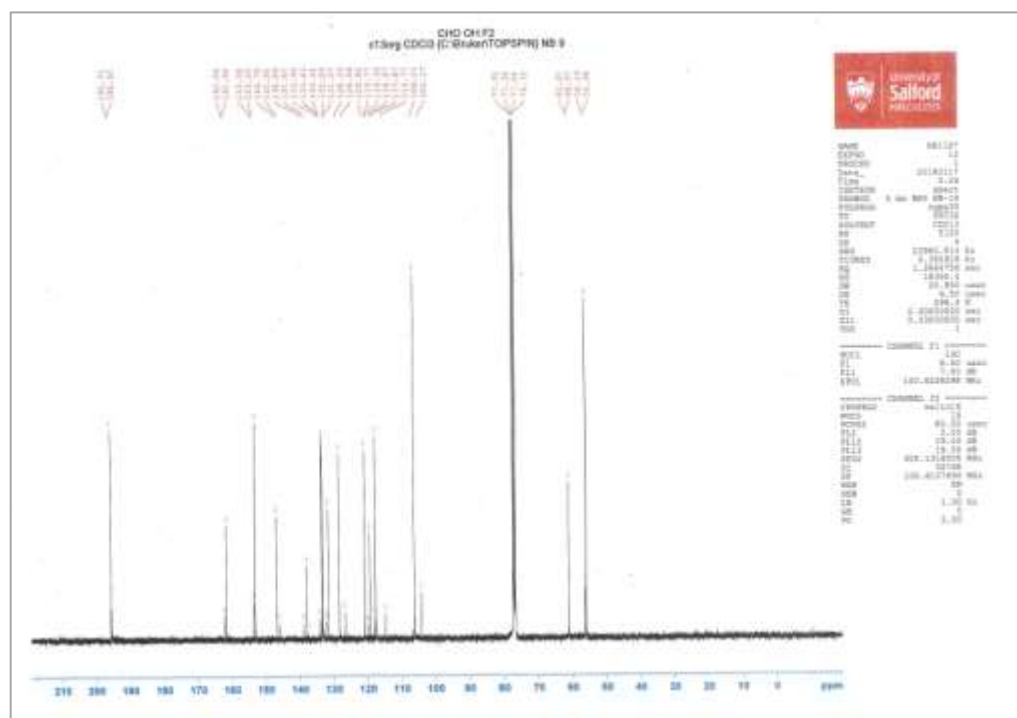
- Tozer, G.M., Kanthou, C., Parkins, C.S. & Hill, S.A. (2002) The biology of the combretastatins as tumour vascular targeting agents. *International Journal*.
- Tozer, G.M., Prise, V.E., Wilson, J., Locke, R.J., et al. (1999) Combretastatin A-4 phosphate as a tumor vascular-targeting agent: Early effects in tumors and normal tissues. *Cancer Research*. 59, 1626–1634.
- Trost, B.M. & Braslau, R. (1989) A convenient chemoselective semihydrogenation of acetylenes using homogeneous catalysis. *Tetrahedron Letters*. [Online] 30 (35), 4657–4660. Available from: doi:10.1016/S0040-4039(01)80767-X.
- Tulpule, A., Rarick, M.U., Kolitz, J., Bernstein, J., et al. (2001) *Original article Liposomal daunorubicin in the treatment of relapsed or refractory non-Hodgkin ' s lymphoma **. 457–462.
- Uphoff, C.C. & Drexler, H.G. (2011) Cancer Cell Culture. *Methods in molecular biology (Clifton, N.J.)*. [Online] 731, 105–114. Available from: doi:10.1007/978-1-61779-080-5.
- Uppalapati, M., Huang, Y., Aravamuthan, V., Jackson, T.N., et al. (2011) *Integrative Biology ““ Artificial mitotic spindle ”” generated by dielectrophoresis and protein micropatterning supports bidirectional transport of kinesin-coated beads*. [Online] 57–64. Available from: doi:10.1039/c0ib00065e.
- Vaupel, P., Fortmeyer, H.P., Runkel, S. & Kallinowski, F. (1987) Blood flow, oxygen consumption, and tissue oxygenation of human breast cancer xenografts in nude rats. *Cancer research*. 47 (13), 3496–3503.
- Vedejs, E. & Peterson, M.J. (1994) *Topics in stereochemistry. Volume 21*. John Wiley.
- Vitale, I., Antocchia, A., Cenciarelli, C., Crateri, P., et al. (2007) Combretastatin CA-4 and combretastatin derivative induce mitotic catastrophe dependent on spindle checkpoint and caspase-3 activation in non-small cell lung cancer cells. *Apoptosis*. [Online] 12 (1), 155–166. Available from: doi:10.1007/s10495-006-0491-0.
- Vogelstein, B. & Kinzler, K.W. (2004) Cancer genes and the pathways they control. *Nature Medicine*. [Online] 10 (8), 789–799. Available from: doi:10.1038/nm1087.

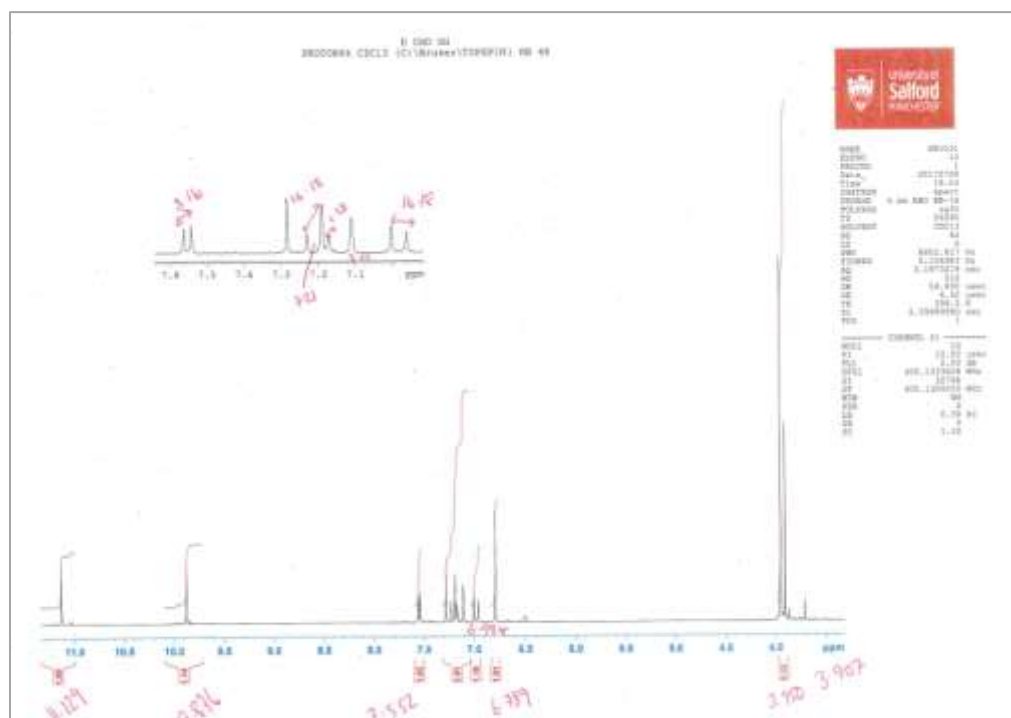
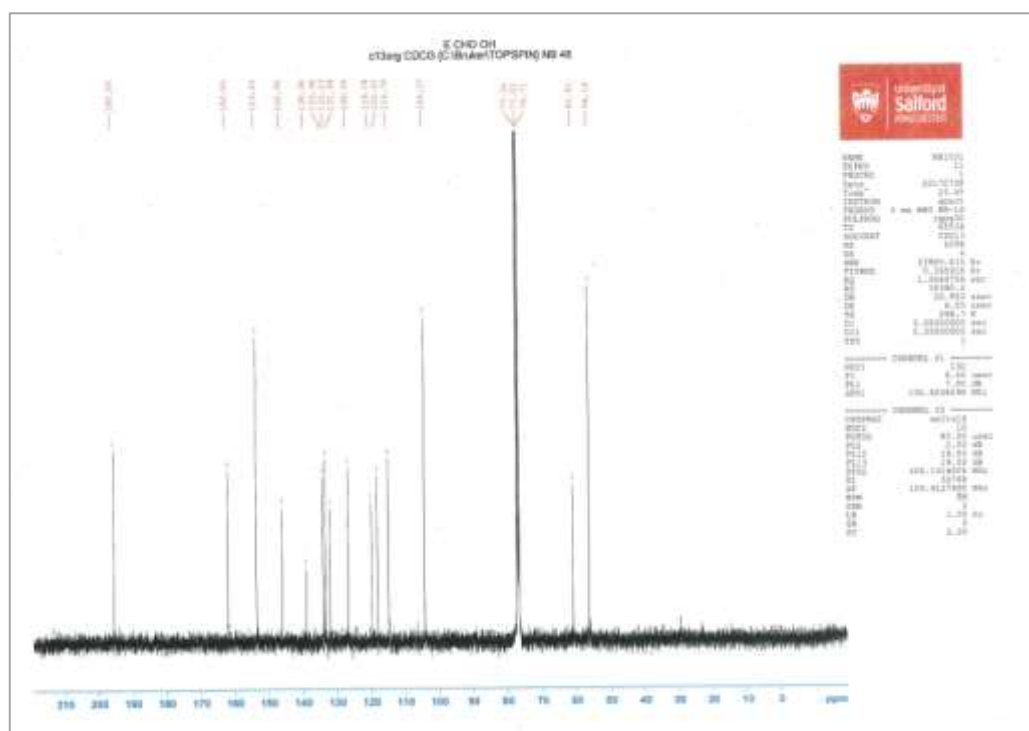
- Voie, A.H., Burns, D.H. & Spelman, F.A. (1993) Orthogonal-plane fluorescence optical sectioning: three-dimensional imaging of macroscopic biological specimens. *Journal of microscopy*. 170 (Pt 3), 229–236.
- Wagh, Y.S. & Asao, N. (2015) Selective Transfer Semihydrogenation of Alkynes with Nanoporous Gold Catalysts. *The Journal of Organic Chemistry*. [Online] 80 (2), 847–851. Available from: doi:10.1021/jo502313d.
- Waldeck, D.H. (1991) Photoisomerization dynamics of stilbenes. *Chem. Rev.* 91, 415–436.
- Walker, R., O'Brien, E., Pryer, N., Soboeiro, M., et al. (1988) Dynamic instability of individual microtubules analysed by video light microscopy: rate constants and transition frequencies. *Journal of Cell Biology*. 107, 1437–1448.
- Wang, L.G., Liu, X.M., Kreis, W. & Budman, D.R. (1999) The effect of antimicrotubule agents on signal transduction pathways of apoptosis: a review. *Cancer Chemotherapy and Pharmacology*. [Online] 44 (5), 355–361. Available from: doi:10.1007/s002800050989.
- Wang, T.C., Cheng, L.P., Huang, X.Y., Zhao, L., et al. (2017) Identification of potential tubulin polymerization inhibitors by 3D-QSAR, molecular docking and molecular dynamics. *RSC Advances*. [Online] 7 (61), 38479–38489. Available from: doi:10.1039/C7RA04314G.
- Wang, Z., Yang, Q., Bai, Z., Sun, J., et al. (2015) Synthesis and biological evaluation of 2,3-diarylthiophene analogues of combretastatin A-4. *MedChemComm*. [Online] 6 (5), 971–976. Available from: doi:10.1039/C5MD00028A.
- Wani, M.C., Taylor, H.L., Wall, M.E., Coggon, P., et al. (1971) Plant antitumor agents. VI. Isolation and structure of taxol, a novel antileukemic and antitumor agent from *Taxus brevifolia*. *Journal of the American Chemical Society*. [Online] 93 (9), 2325–2327. Available from: doi:10.1021/ja00738a045.
- Weaver, B.A. (2014) How Taxol/paclitaxel kills cancer cells. *Molecular biology of the cell*. [Online] 25 (18), 2677–2681. Available from: doi:10.1091/mbc.E14-04-0916.
- Webb, R.H. (1996) Confocal optical microscopy. *Reports on Progress in Physics*. [Online] 59 (3), 427–471. Available from: doi:10.1088/0034-4885/59/3/003.

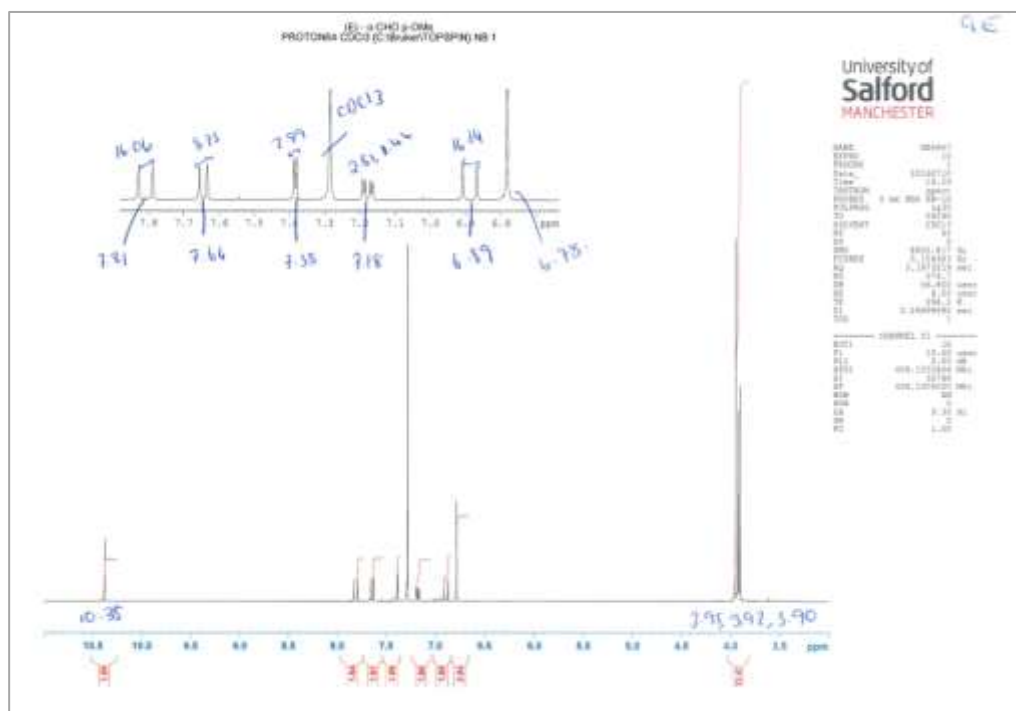
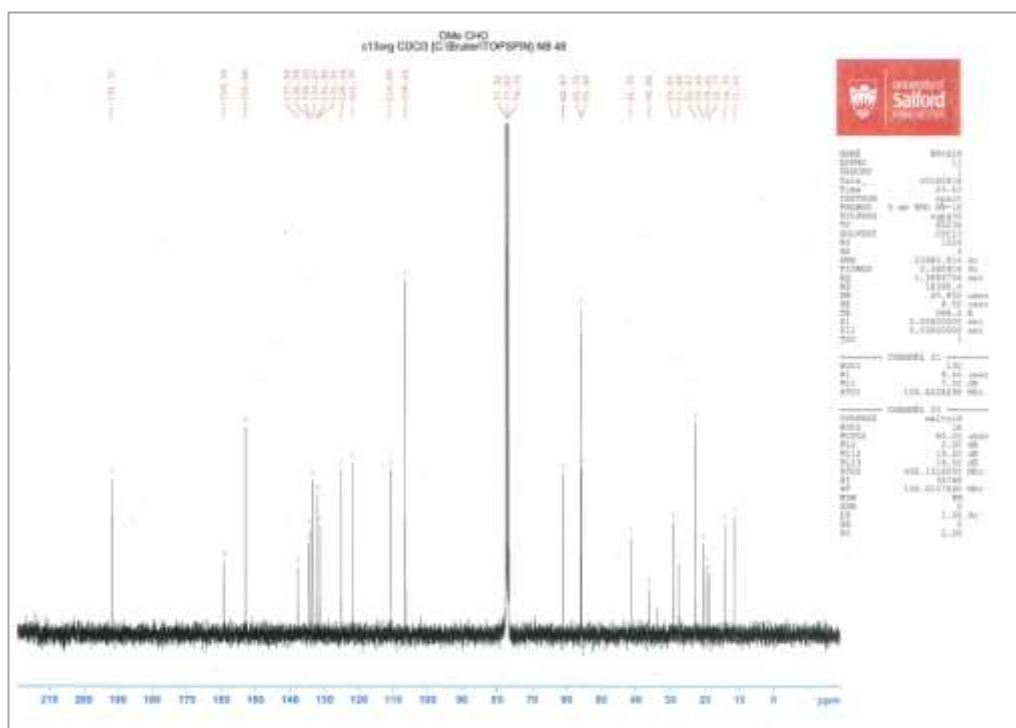
- Weigel, a & Ernsting, N.P. (2010) Excited stilbene: intramolecular vibrational redistribution and solvation studied by femtosecond stimulated Raman spectroscopy. *The journal of physical chemistry. B.* [Online] 114 (23), 7879–7893. Available from: doi:10.1021/jp100181z.
- Weisenberg, R.C., Broisy, G.G. & Taylor, E.W. (1968) Colchicine-binding protein of mammalian brain and its relation to microtubules. *Biochemistry.* [Online] 7 (12), 4466–4479. Available from: doi:10.1021/bi00852a043.
- Wilson, B. & Patterson, M. (2008a) The physics, biophysics and technology of photodynamic therapy. *Physics in medicine and biology.* [Online] 61. Available from: doi:10.1088/0031-9155/53/9/R01.
- Wilson, B.C. & Patterson, M.S. (2008b) The physics, biophysics and technology of photodynamic therapy. *Physics in Medicine and Biology.* 53, 61–109.
- Wittig, G. & Schöllkopf, U. (1954a) Über Triphenyl-phosphin-methylene als olefinbildende Reagenzien (I. Mitteil. *Chemische Berichte.* [Online] 87 (9), 1318–1330. Available from: doi:10.1002/cber.19540870919.
- Wittig, G. & Schöllkopf, U. (1954b) Über Triphenyl-phosphin-methylene als olefinbildende Reagenzien I. *Chemische Berichte.* 87 (9), 1318.
- Wu, M., Sun, Q., Yang, C., Chen, D., et al. (2007) Synthesis and activity of Combretastatin A-4 analogues: 1,2,3-thiadiazoles as potent antitumor agents. *Bioorganic & Medicinal Chemistry Letters.* [Online] 17 (4), 869–873. Available from: doi:10.1016/j.bmcl.2006.11.060.
- Yano, S., Hirohara, S., Obata, M., Hagiya, Y., et al. (2011) Current states and future views in photodynamic therapy. *Journal of Photochemistry and Photobiology C: Photochemistry Reviews.* [Online] 12, 46–67. Available from: doi:10.1016/j.jphotochemrev.2011.06.001.
- Yeung, S.-C.J., She, M., Yang, H., Pan, J., et al. (2007) Combination Chemotherapy Including Combretastatin A4 Phosphate and Paclitaxel Is Effective against Anaplastic Thyroid Cancer in a Nude Mouse Xenograft Model. *The Journal of Clinical Endocrinology &*

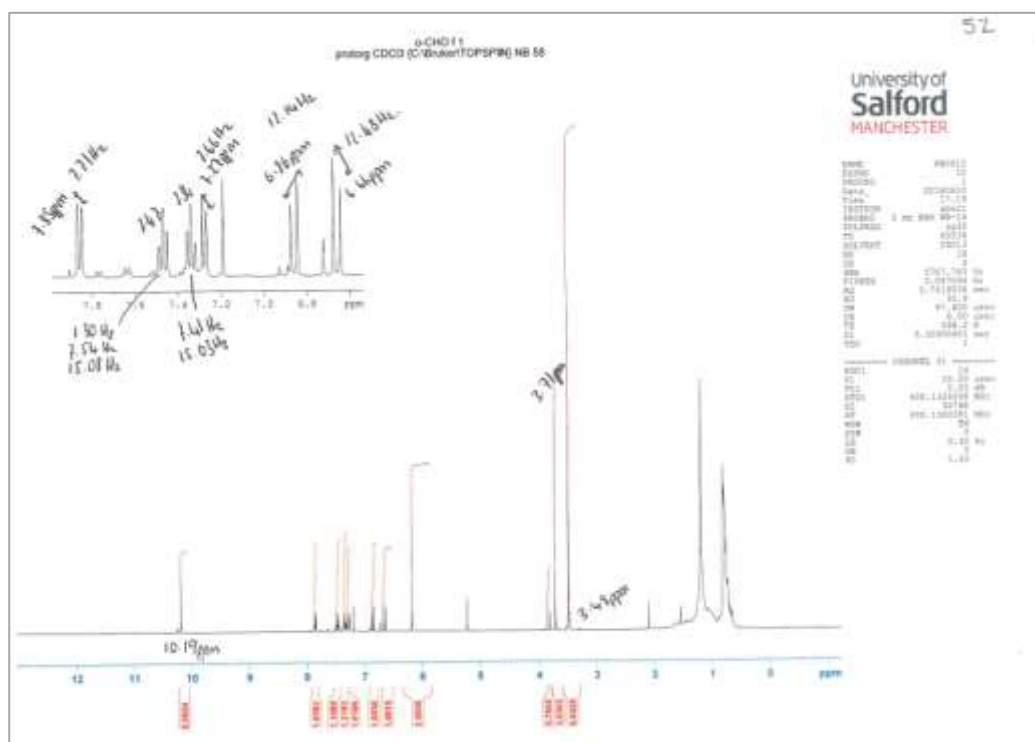
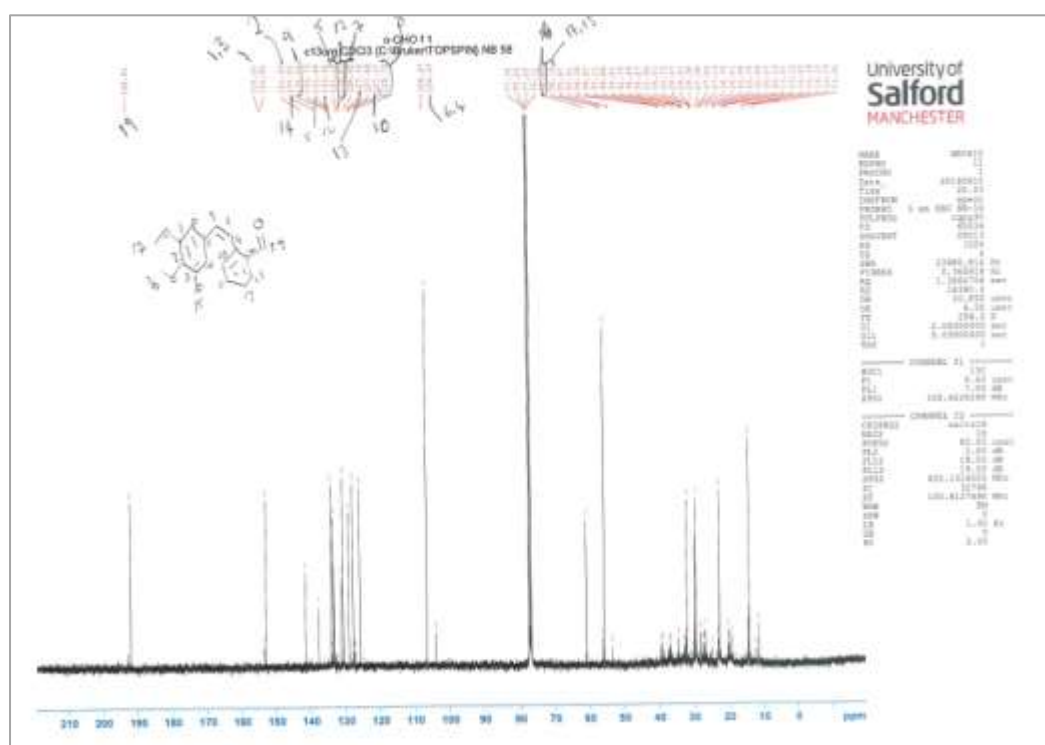
- Metabolism*. [Online] 92 (8), 2902–2909. Available from: doi:10.1210/jc.2007-0027.
- Zakerhamidi, M.S., Ghanadzadeh, A. & Moghadam, M. (2012) Solvent Effects on the UV/Visible Absorption Spectra of Some Aminoazobenzene Dyes. *Chem Sci Trans*. [Online] 1 (1), 1–8. Available from: doi:10.7598/cst2012.118.
- Zheng, S., Zhong, Q., Mottamal, M., Zhang, Q., et al. (2014) Design, Synthesis, and Biological Evaluation of Novel Pyridine- Bridged Analogues of Combretastatin-A4 as Anticancer Agents. *Journal of medicinal chemistry*. [Online] 57, 3369–3381. Available from: doi:10.1021/jm500002k.
- Zhu, M.-L., Horbinski, C.M., Garzotto, M., Qian, D.Z., et al. (2010) Tubulin-targeting chemotherapy impairs androgen receptor activity in prostate cancer. *Cancer research*. [Online] 70 (20), 7992–8002. Available from: doi:10.1158/0008-5472.CAN-10-0585.
- Zweifel, M., Jayson, G.C., Reed, N.S., Osborne, R., et al. (2011) Phase II trial of combretastatin A4 phosphate, carboplatin, and paclitaxel in patients with platinum-resistant ovarian cancer. *Annals of Oncology*. [Online] 22 (9), 2036–2041. Available from: doi:10.1093/annonc/mdq708.

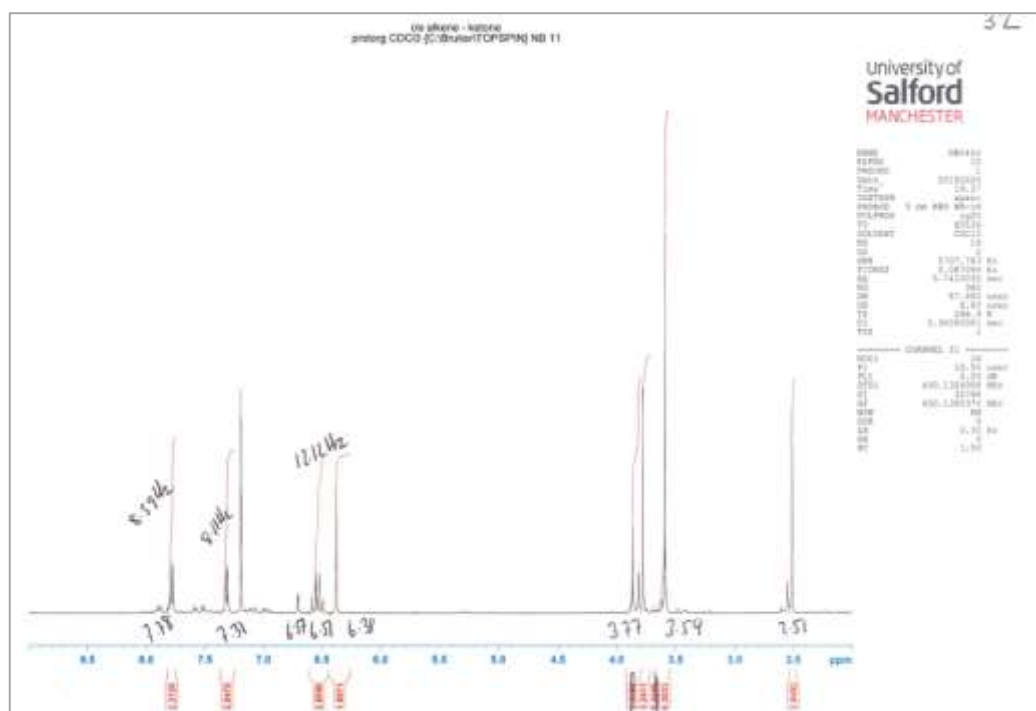
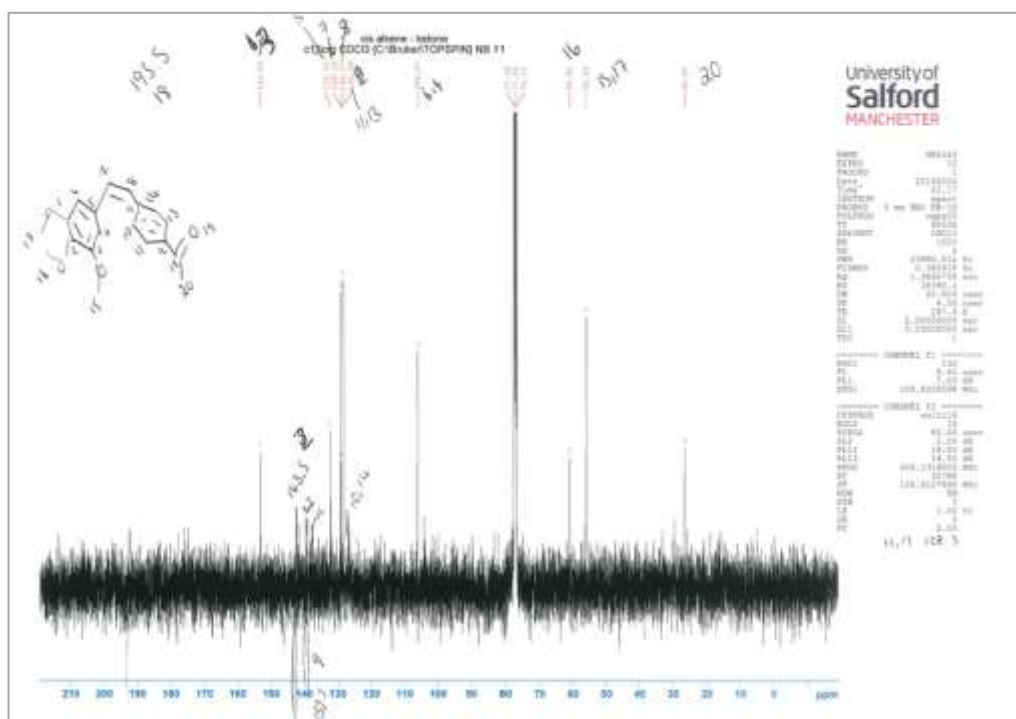
Figure 98 $^1\text{H-NMR}$ of (*E*)-4-(3',4',5'-trimethoxystyryl)benzaldehyde 42EFigure 99 $^{13}\text{C-NMR}$ of (*E*)-4-(3',4',5'-trimethoxystyryl)benzaldehyde 42E

Figure 100 $^1\text{H-NMR}$ of (Z)-2-hydroxy-4-(3',4',5'-trimethoxystyryl)benzaldehyde 43ZFigure 101 $^{13}\text{C-NMR}$ of (Z)-2-hydroxy-4-(3',4',5'-trimethoxystyryl)benzaldehyde 43Z

Figure 102 ¹H-NMR spectra of (E)-2-hydroxy-4-(3',4',5'-trimethoxystyryl)benzaldehyde 43EFigure 103 ¹³C-NMR of spectra (E)-2-hydroxy-4-(3',4',5'-trimethoxystyryl)benzaldehyde 43E

Figure 106 ¹H-NMR spectra of (E)-5-methoxy-2-(3',4',5'-trimethoxystyryl)benzaldehyde 44EFigure 107 ¹³C-NMR spectra of (E)-5-methoxy-2-(3',4',5'-trimethoxystyryl)benzaldehyde 44E

Figure 108 $^1\text{H-NMR}$ spectra of (Z)-2-(3',4',5'-Trimethoxystyryl)benzaldehyde 45ZFigure 109 $^{13}\text{C-NMR}$ spectra of (Z)-2-(3',4',5'-Trimethoxystyryl)benzaldehyde 45Z

Figure 110 $^1\text{H-NMR}$ spectra of (Z)-4-(3',4',5'-trimethoxystyryl)acetophenone 46ZFigure 111 $^{13}\text{C-NMR}$ spectra of (Z)-4-(3',4',5'-trimethoxystyryl)acetophenone 46Z

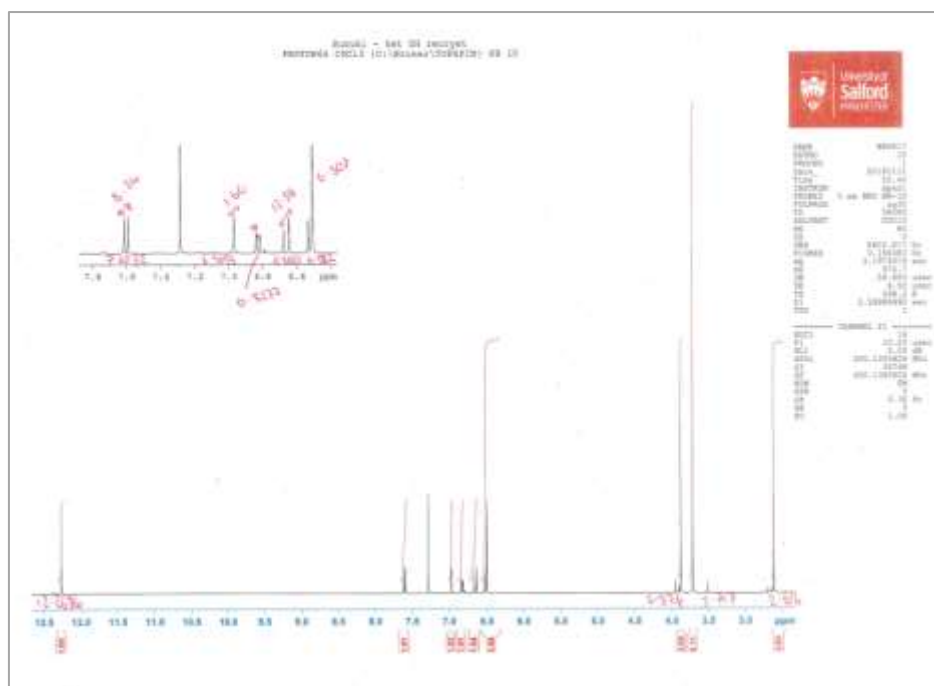


Figure 114 $^1\text{H-NMR}$ spectra of (Z)-2-hydroxy-4-(3',4',5'-trimethoxystyryl)phenyl)acetophenone 47Z

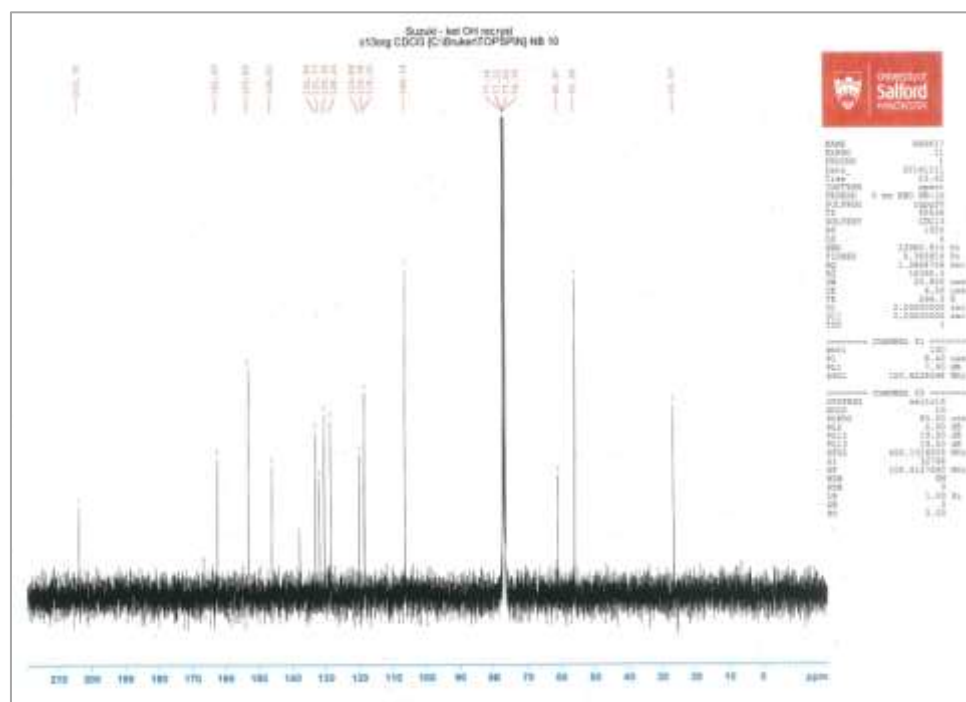
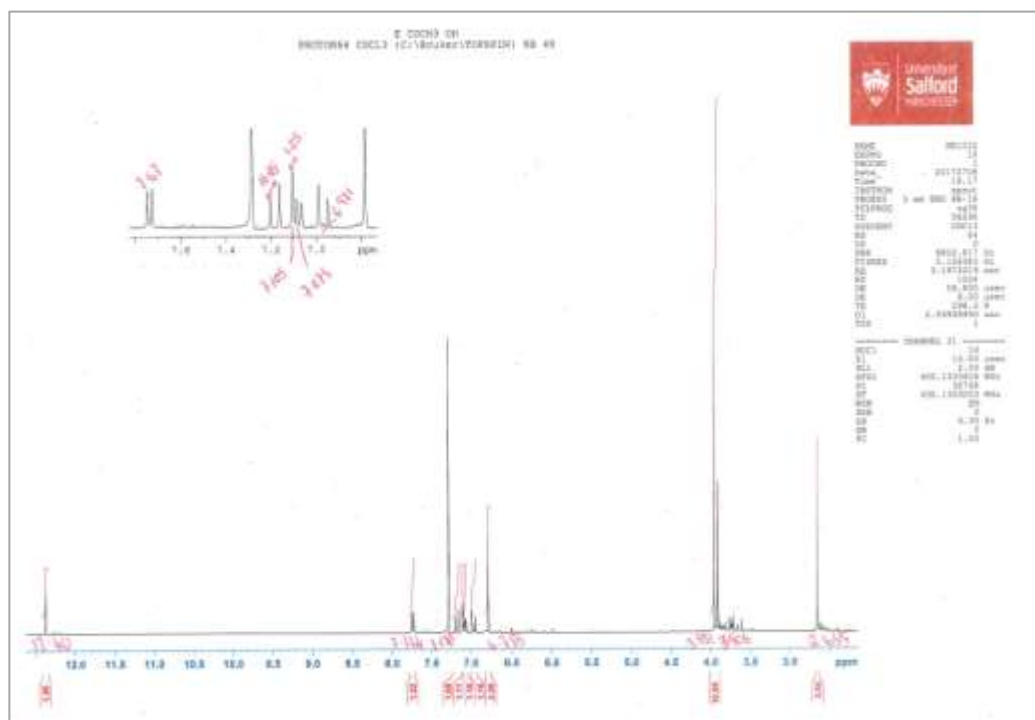
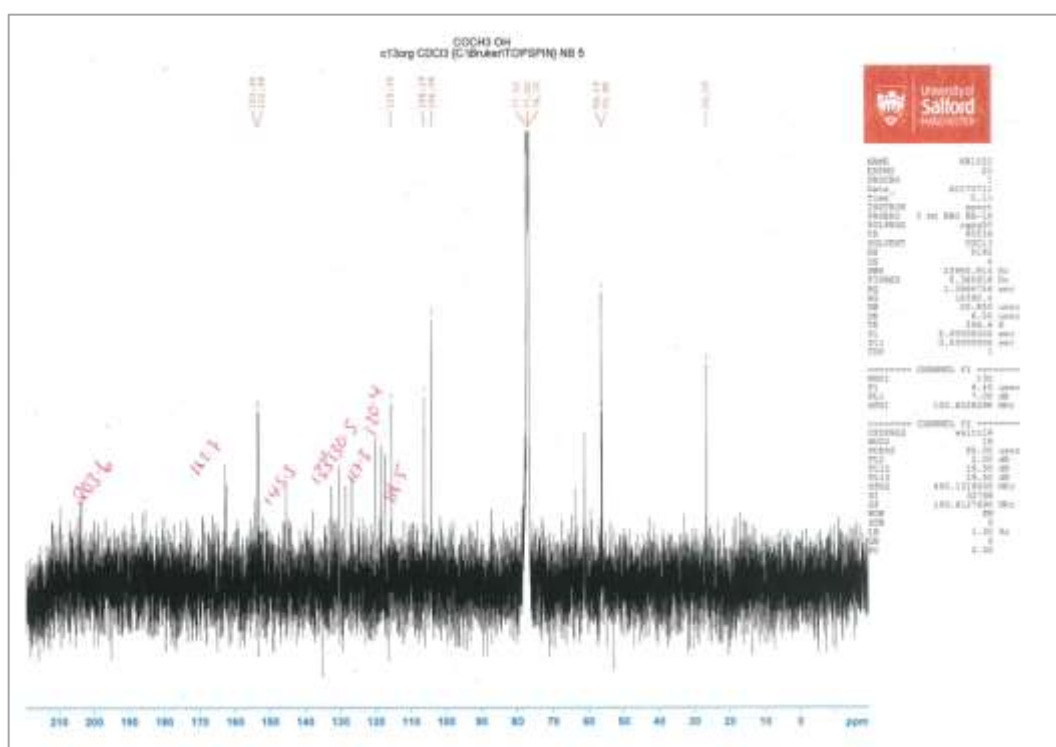
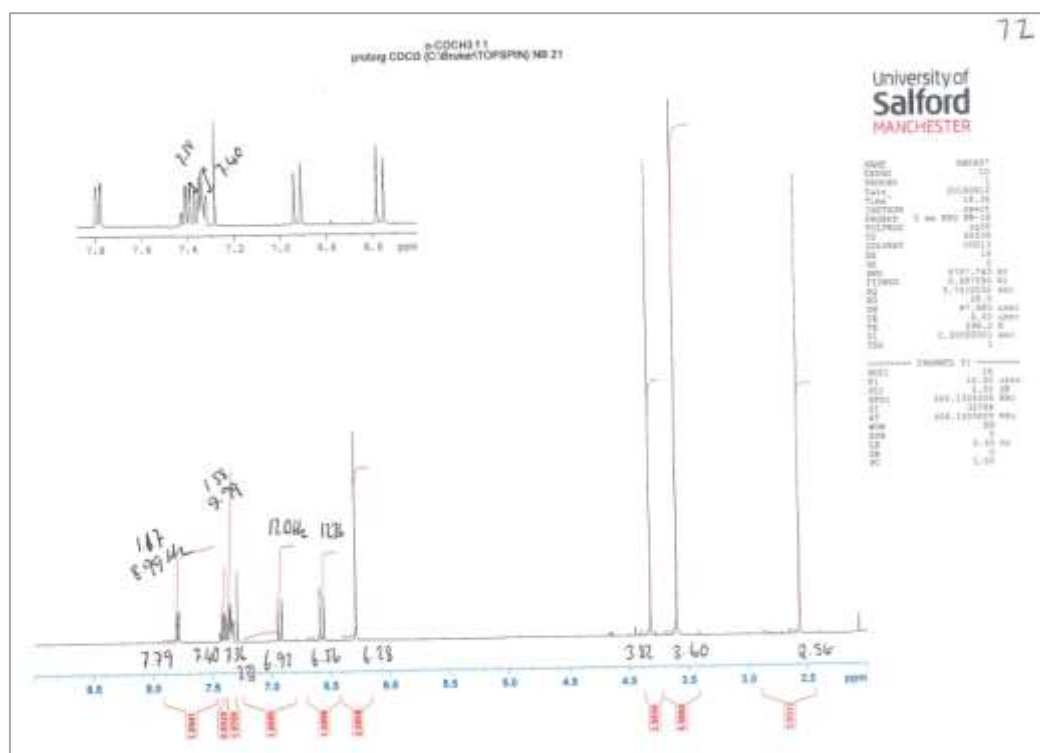
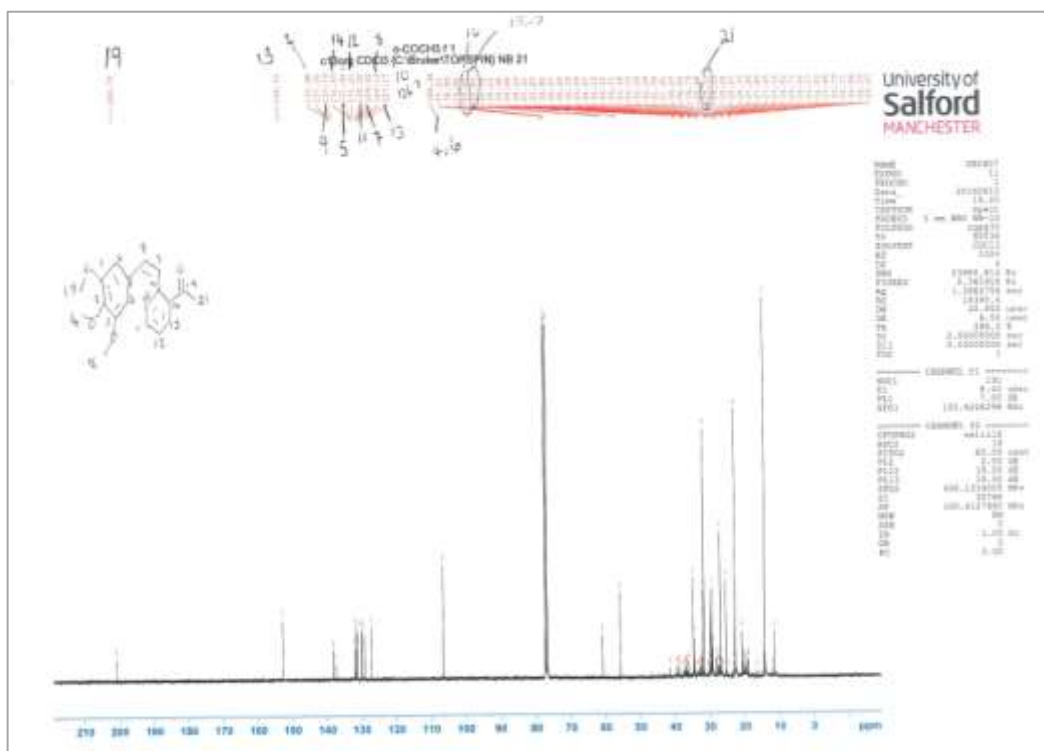
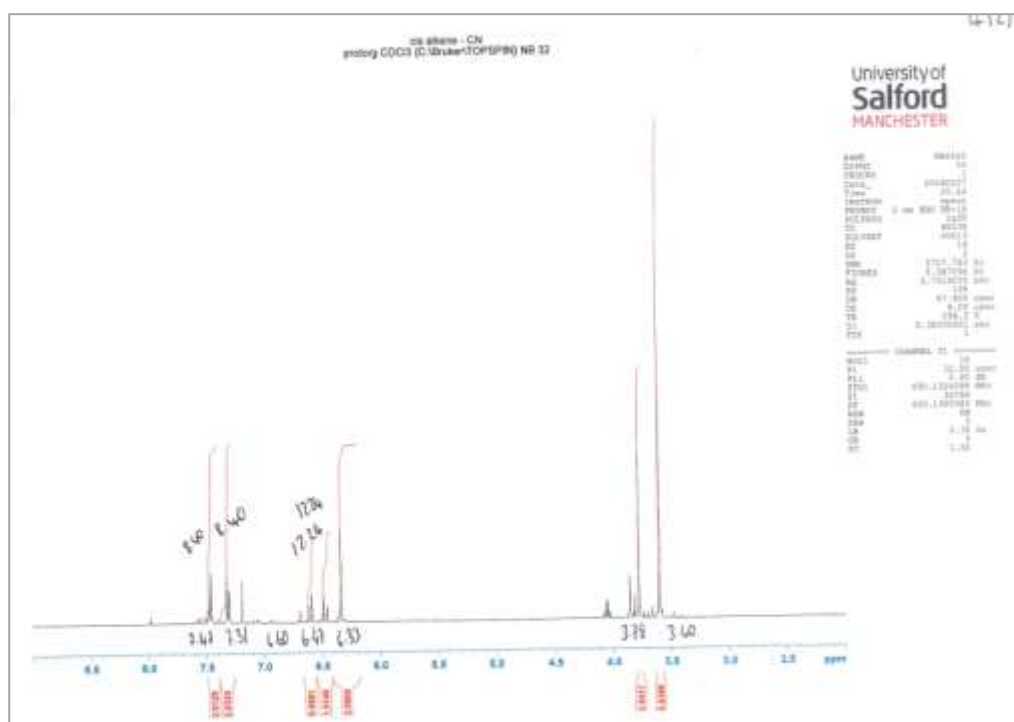
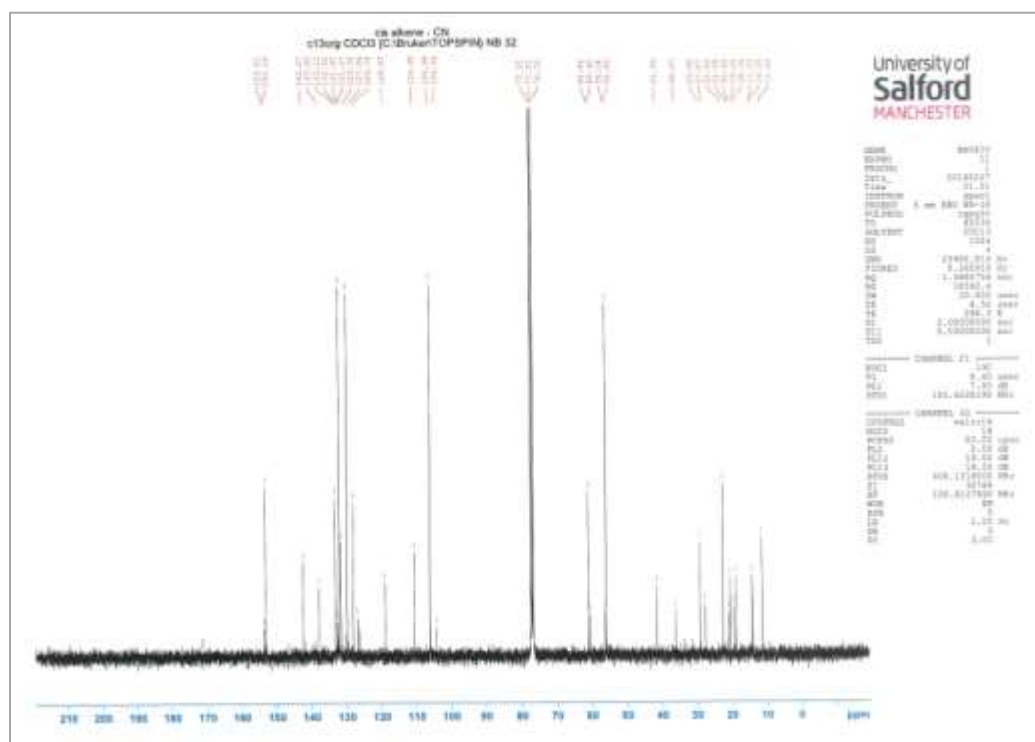
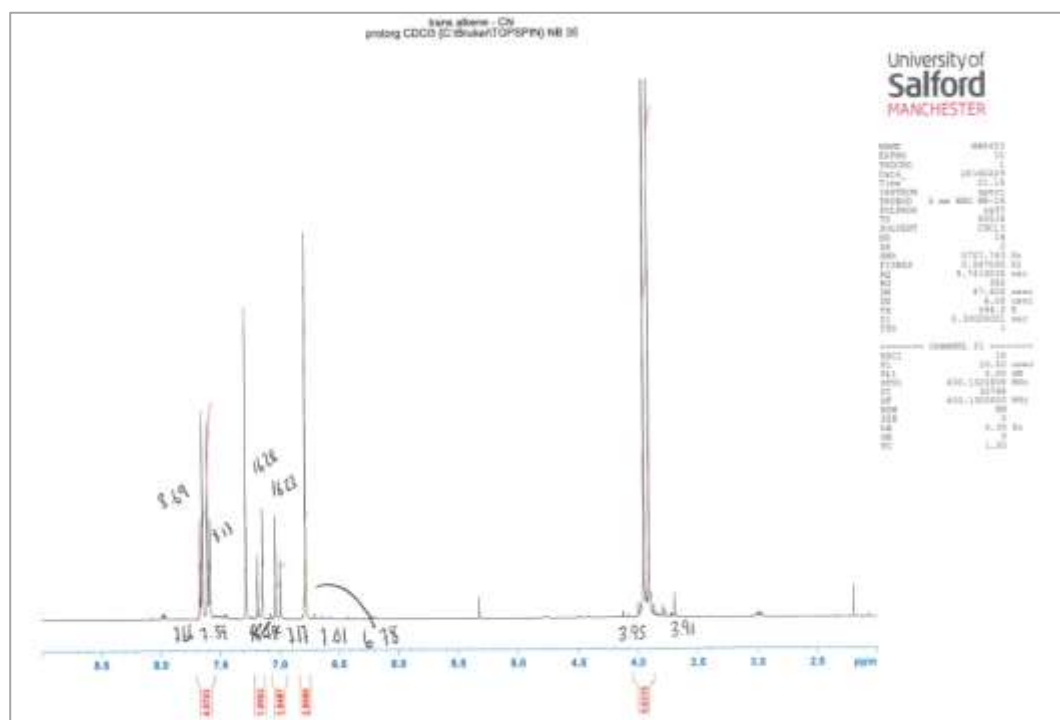
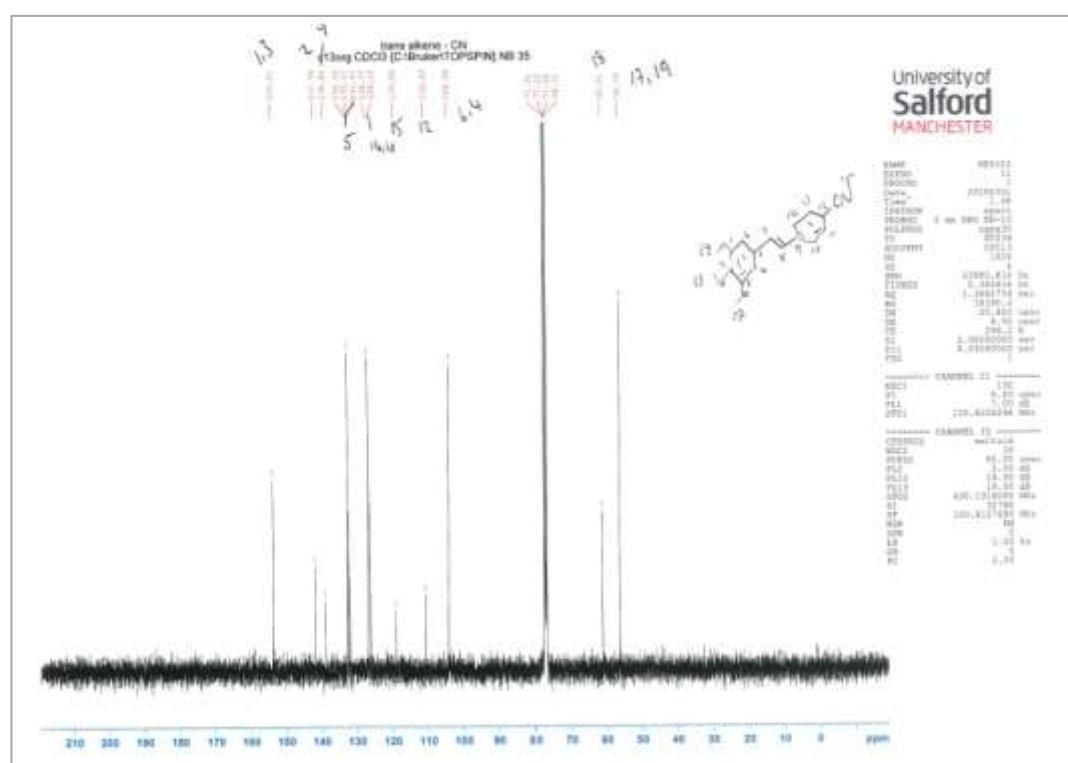


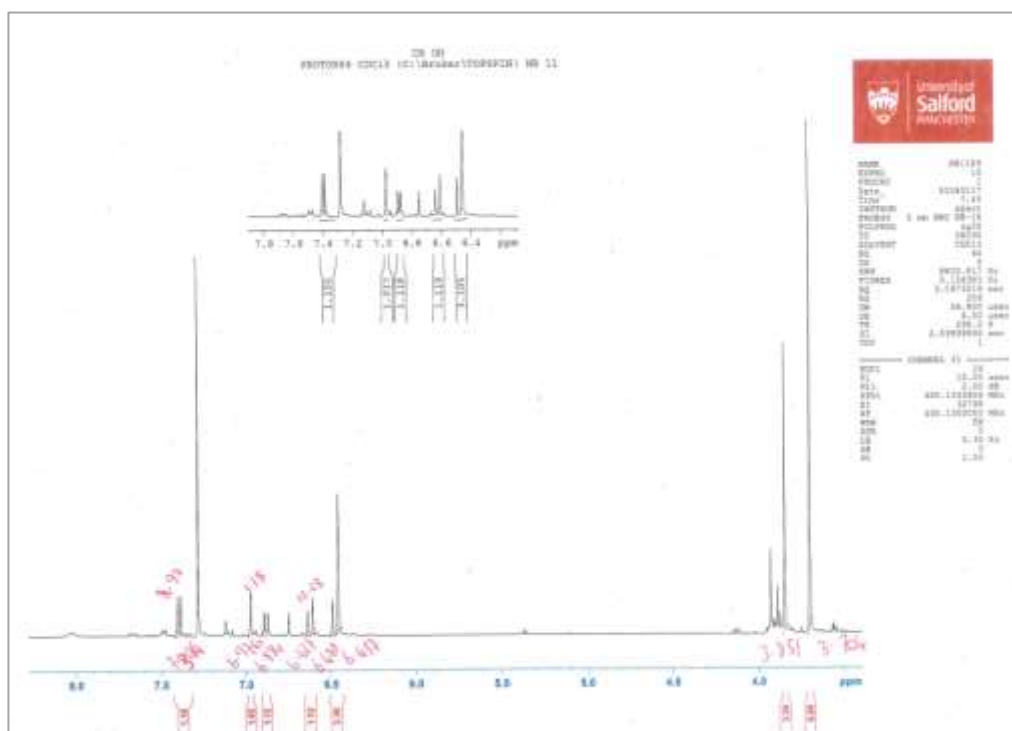
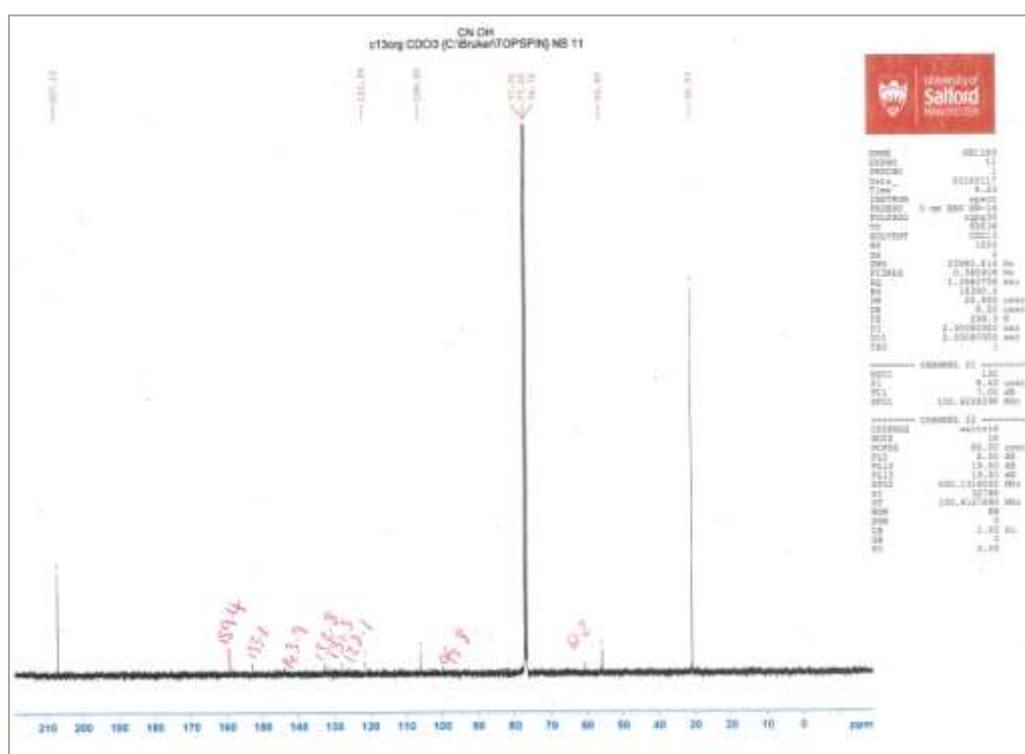
Figure 115 $^{13}\text{C-NMR}$ spectra of (Z)-2-hydroxy-4-(3',4',5'-trimethoxystyryl)phenyl)acetophenone 47Z

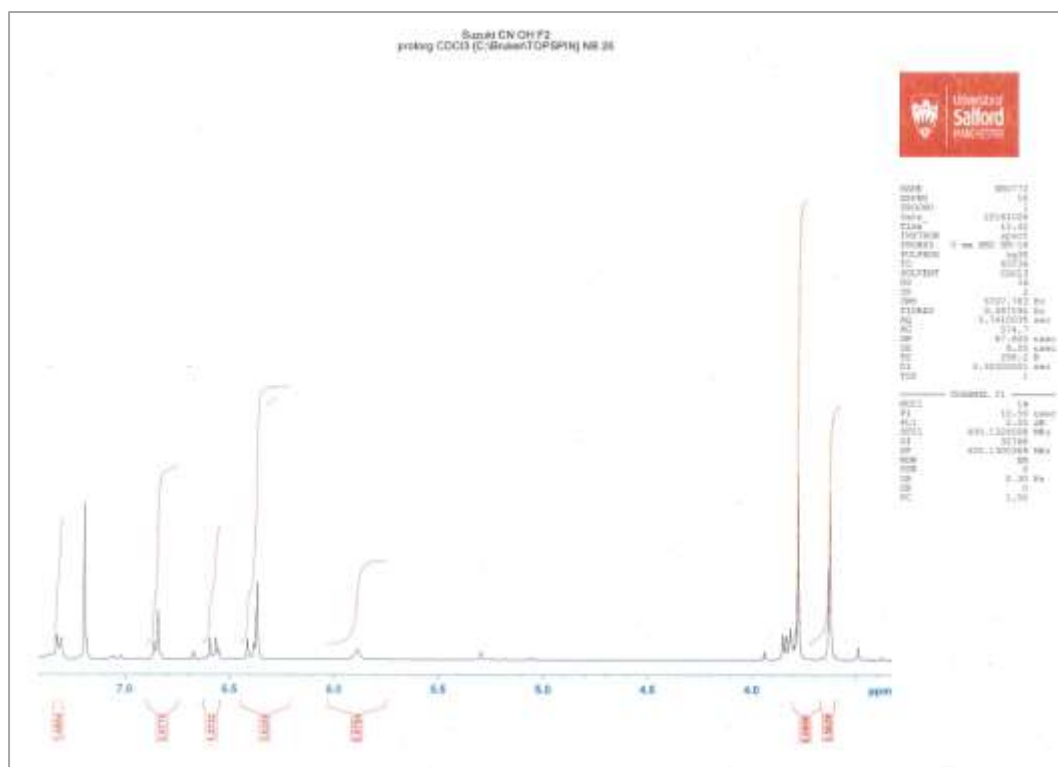
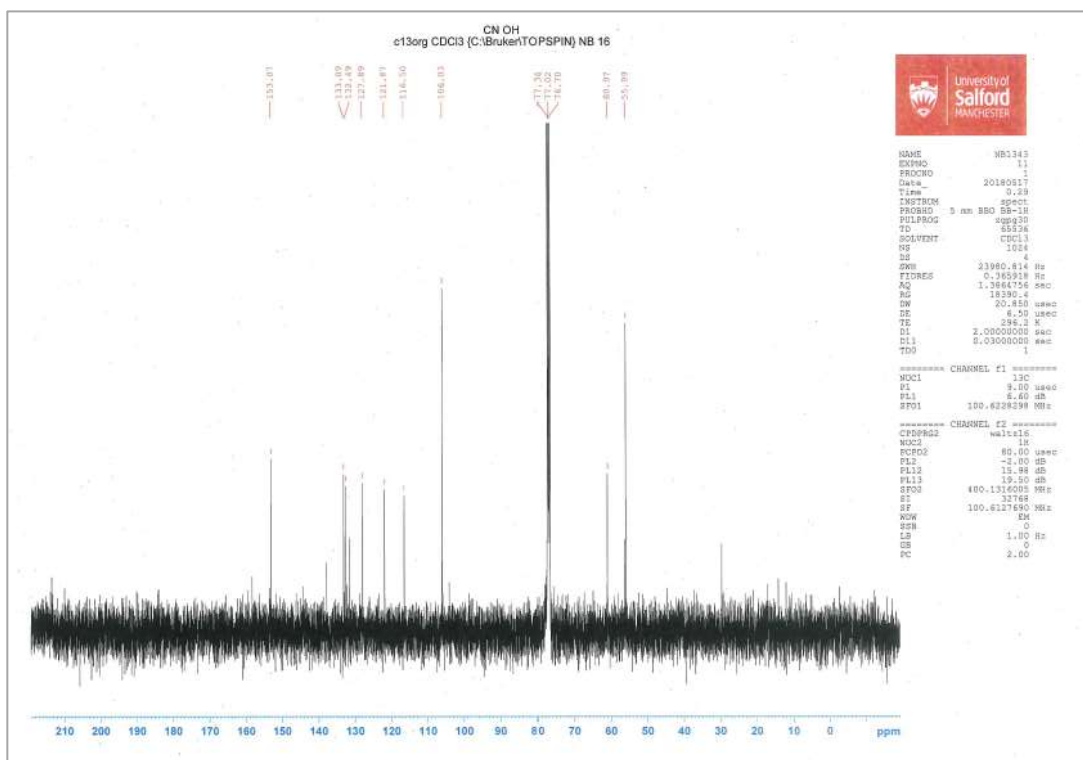
Figure 116 $^1\text{H-NMR}$ spectra of (E)-2-hydroxy-4-(3',4',5'-trimethoxystyryl)phenyl)acetophenone 47EFigure 117 $^{13}\text{C-NMR}$ spectra of (E)-2-hydroxy-4-(3',4',5'-trimethoxystyryl)phenyl)acetophenone 47E

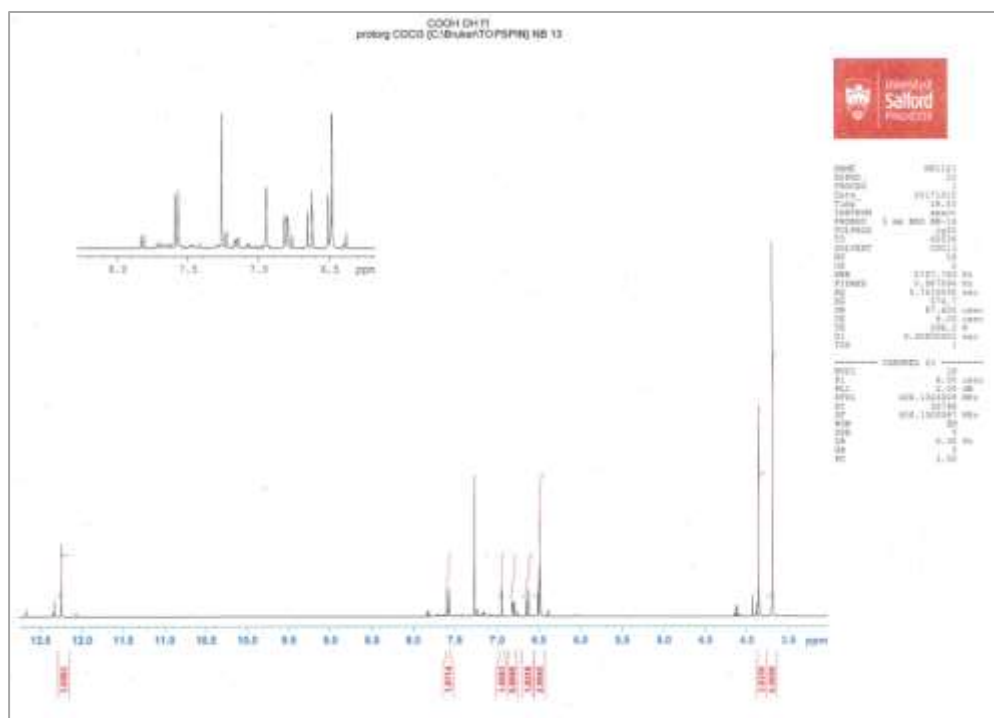
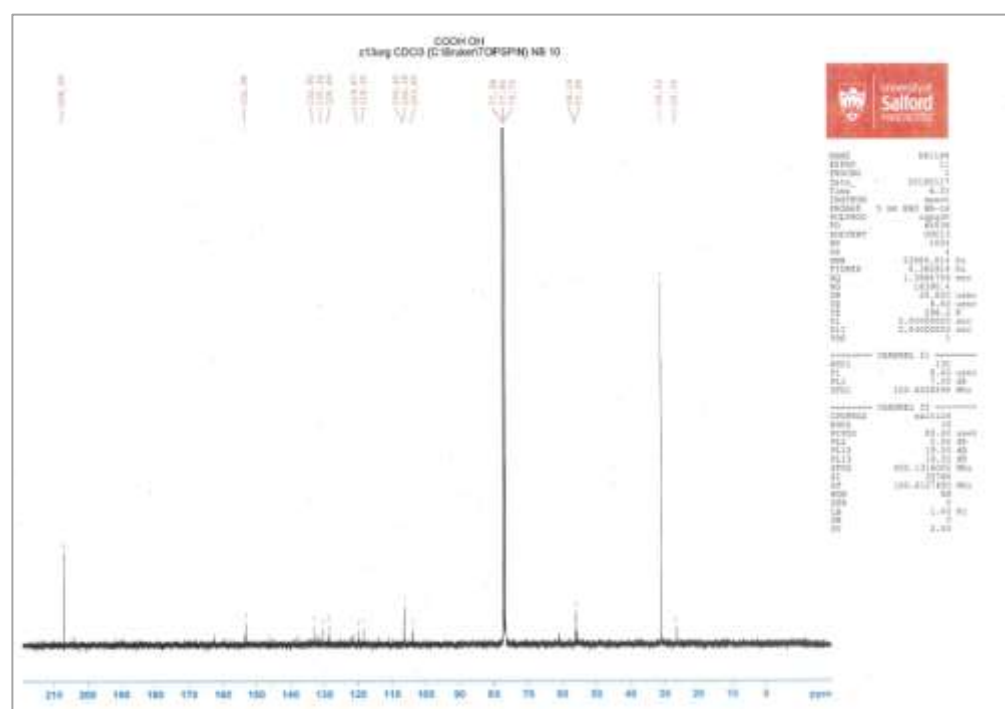
Figure 118 ^1H -NMR spectra of (Z)-2-(3',4',5'-trimethoxystyryl)acetophenone 48ZFigure 119 ^{13}C -NMR spectra of (Z)-2-(3',4',5'-trimethoxystyryl)acetophenone 48Z

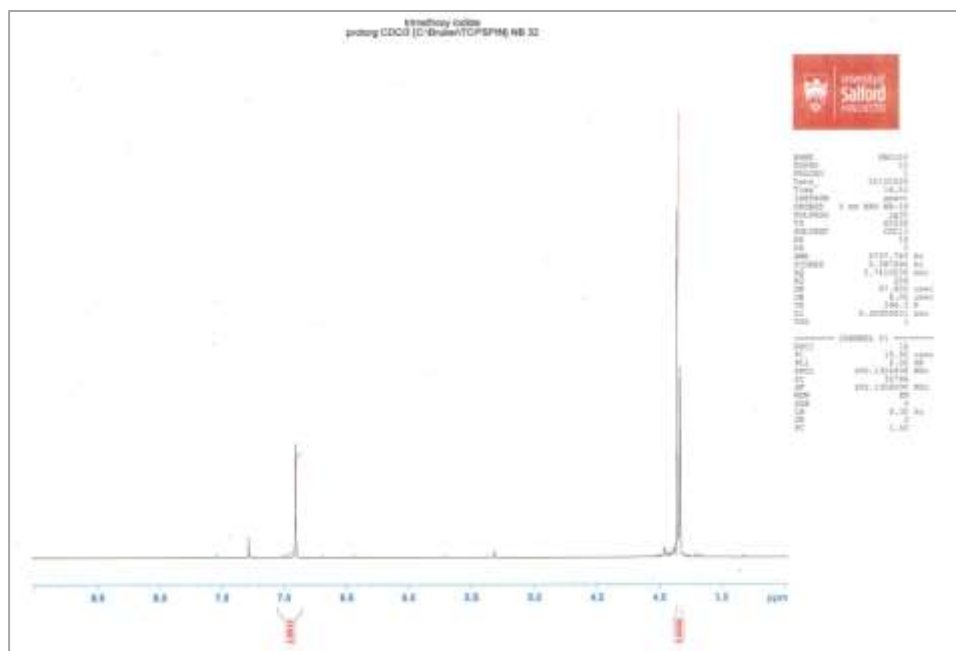
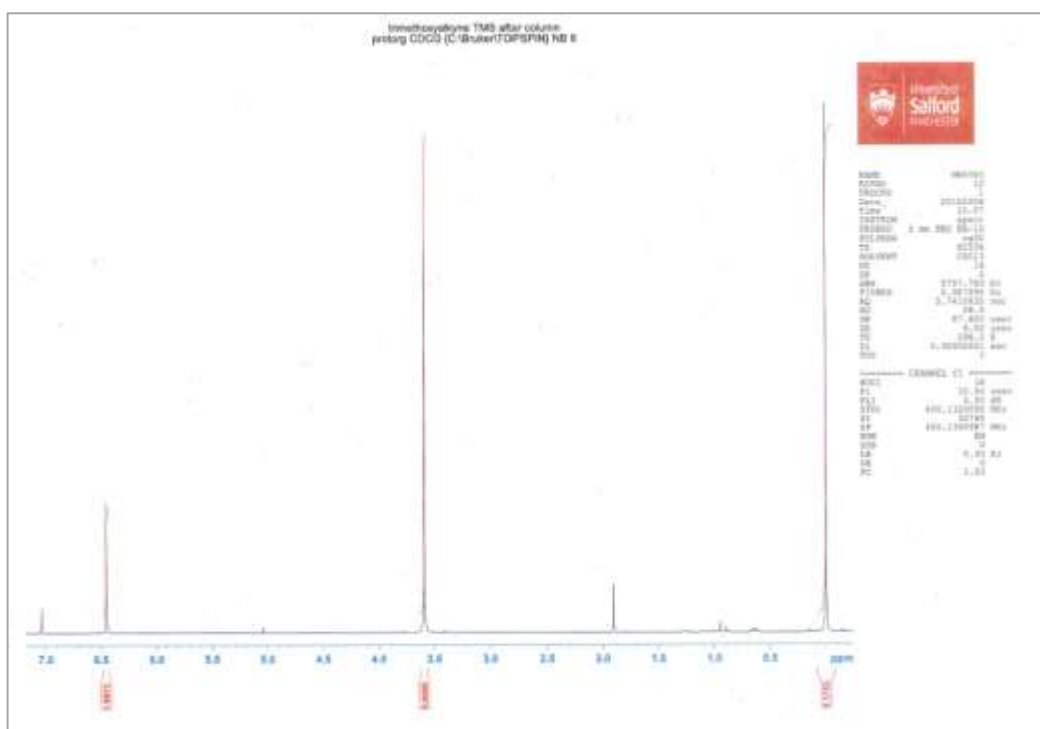
Figure 120 ^1H -NMR spectra of (Z)-4-(3',4',5'-trimethoxystyryl)benzotrile 50ZFigure 121 ^{13}C -NMR spectra of (Z)-4-(3',4',5'-trimethoxystyryl)benzotrile 50Z

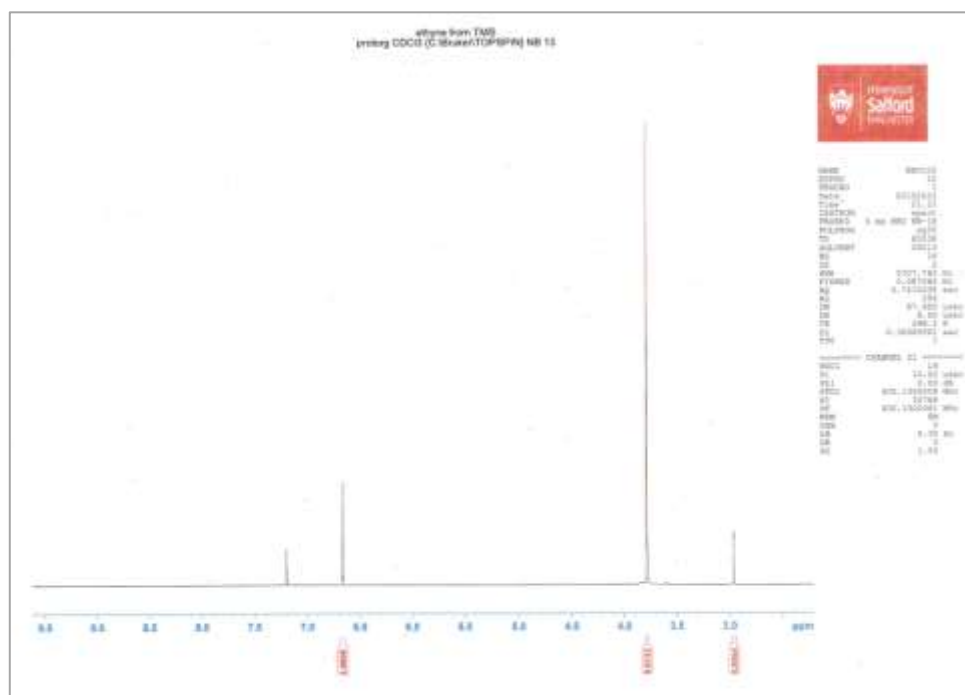
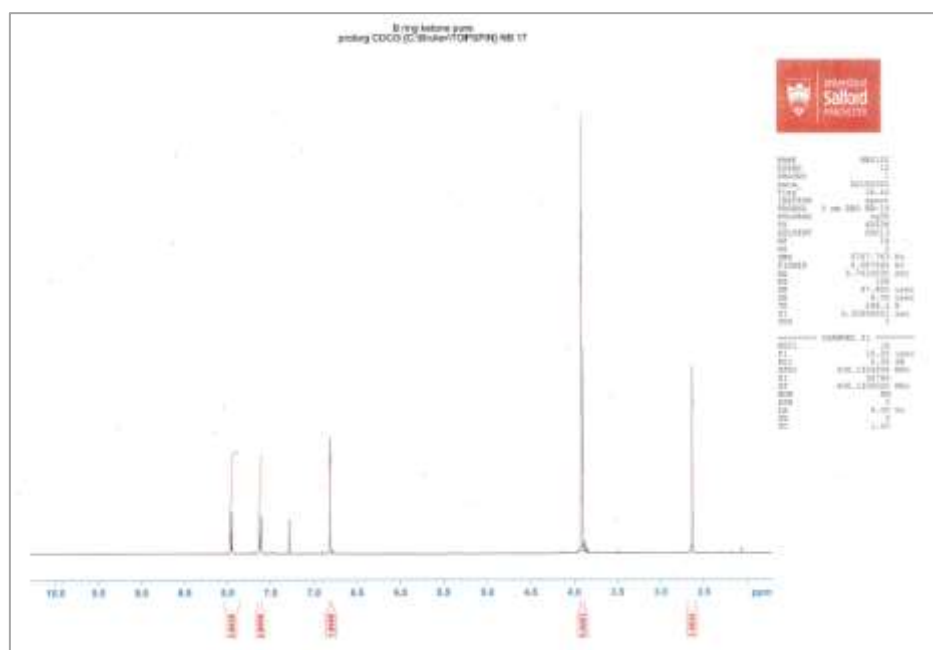
Figure 122 $^1\text{H-NMR}$ spectra of (E)-4-(3',4',5'-trimethoxystyryl)benzotrile 50EFigure 123 $^{13}\text{C-NMR}$ spectra of (E)-4-(3',4',5'-trimethoxystyryl)benzotrile 50E

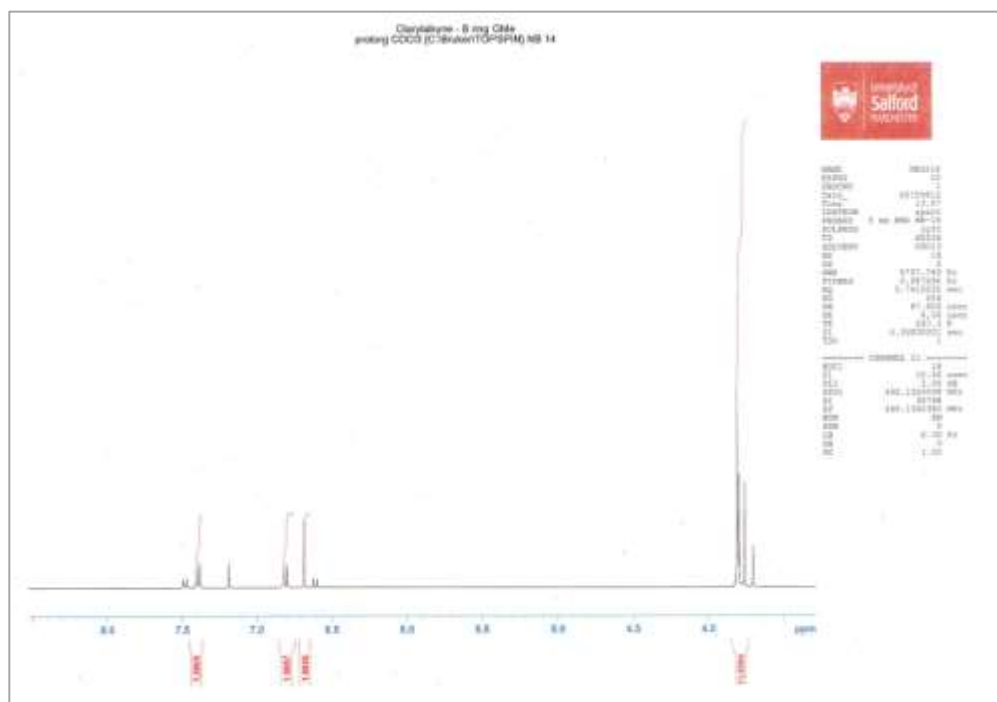
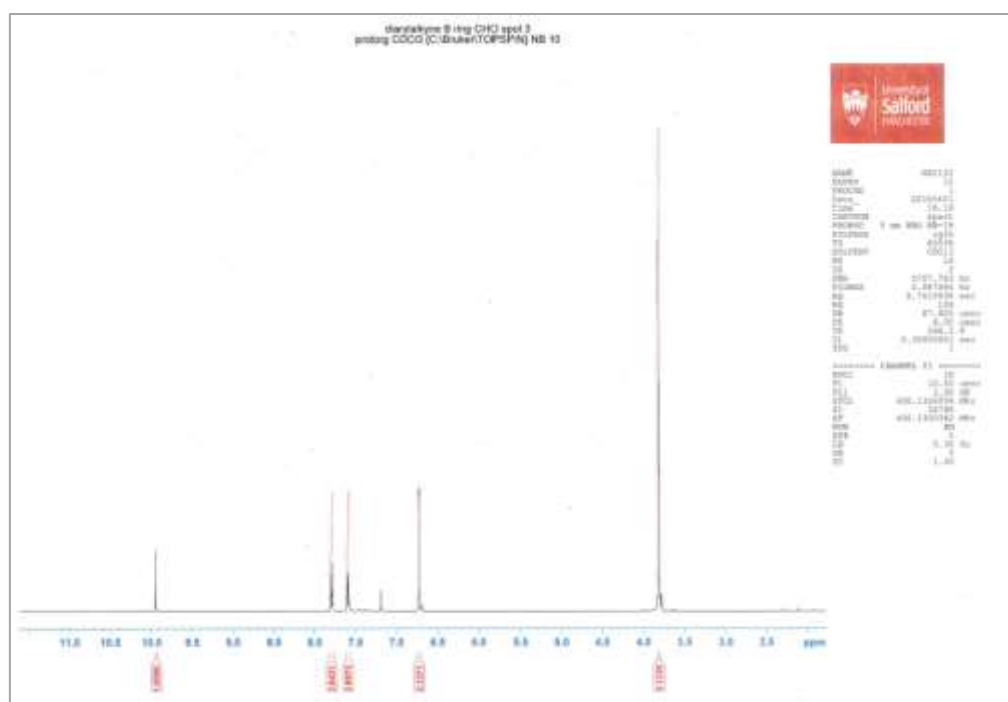
Figure 124 $^1\text{H-NMR}$ spectra of (Z)-2-hydroxy-4-(3',4',5'-trimethoxystyryl)benzotrile 512Figure 125 $^{13}\text{C-NMR}$ spectra of (Z)-2-hydroxy-4-(3',4',5'-trimethoxystyryl)benzotrile 512

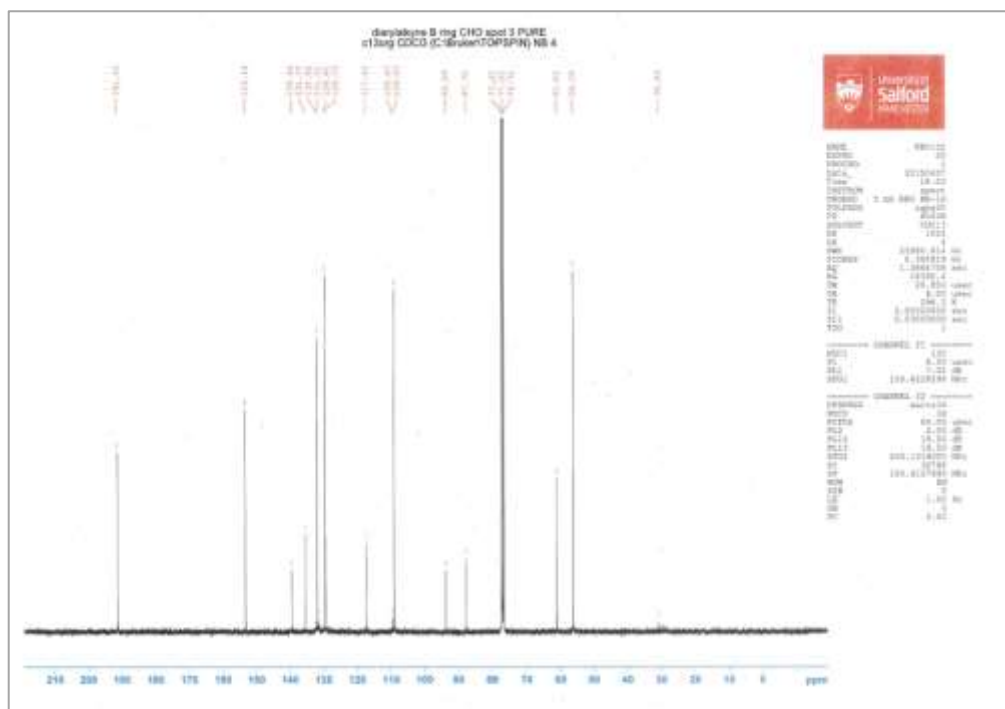
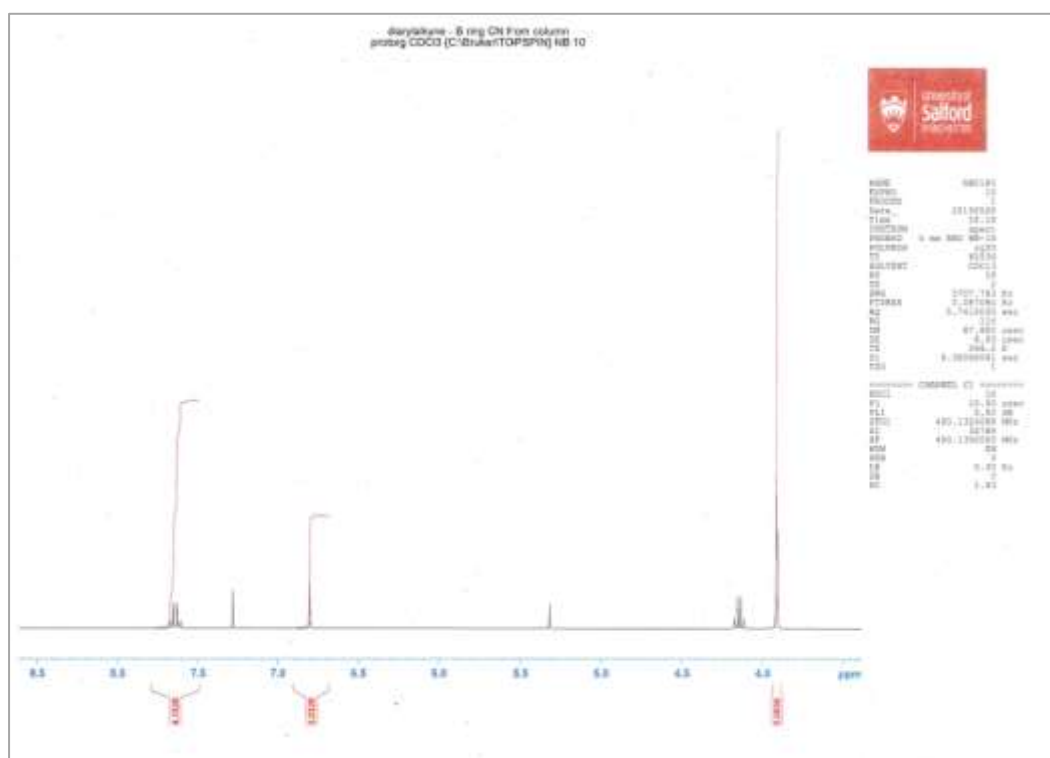
Figure 126 $^1\text{H-NMR}$ spectra of (E)-2-hydroxy-4-(3',4',5'-trimethoxystyryl)benzointrile 51EFigure 127 $^{13}\text{C-NMR}$ spectra of (E)-2-Hydroxy-4-(3',4',5'-trimethoxystyryl)benzointrile 51E

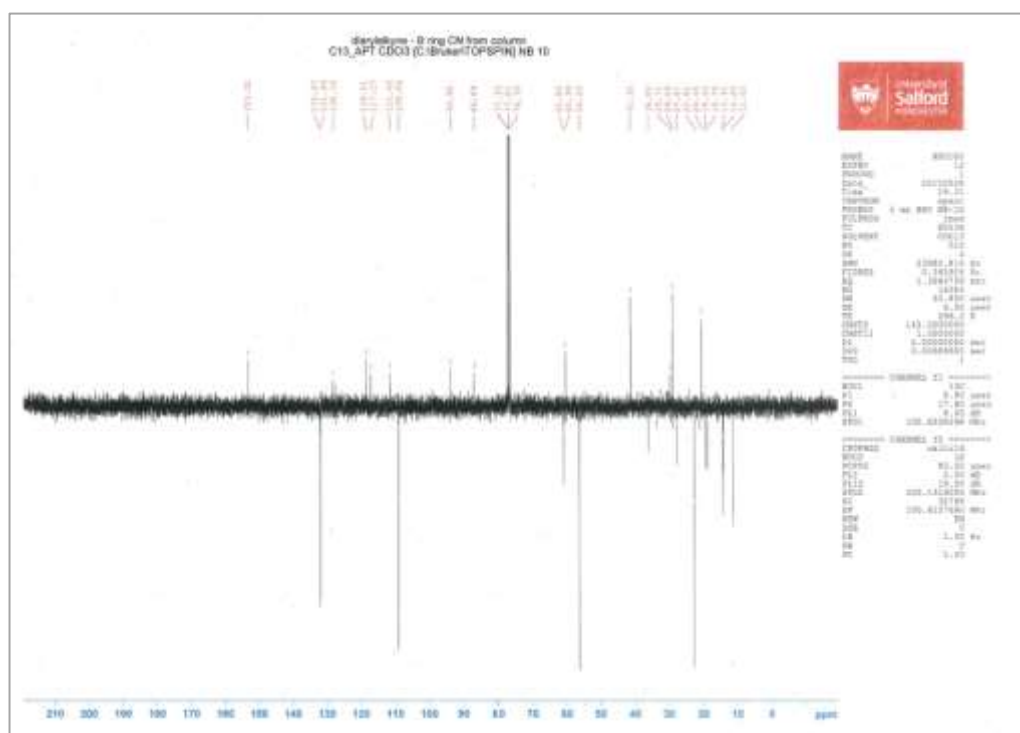
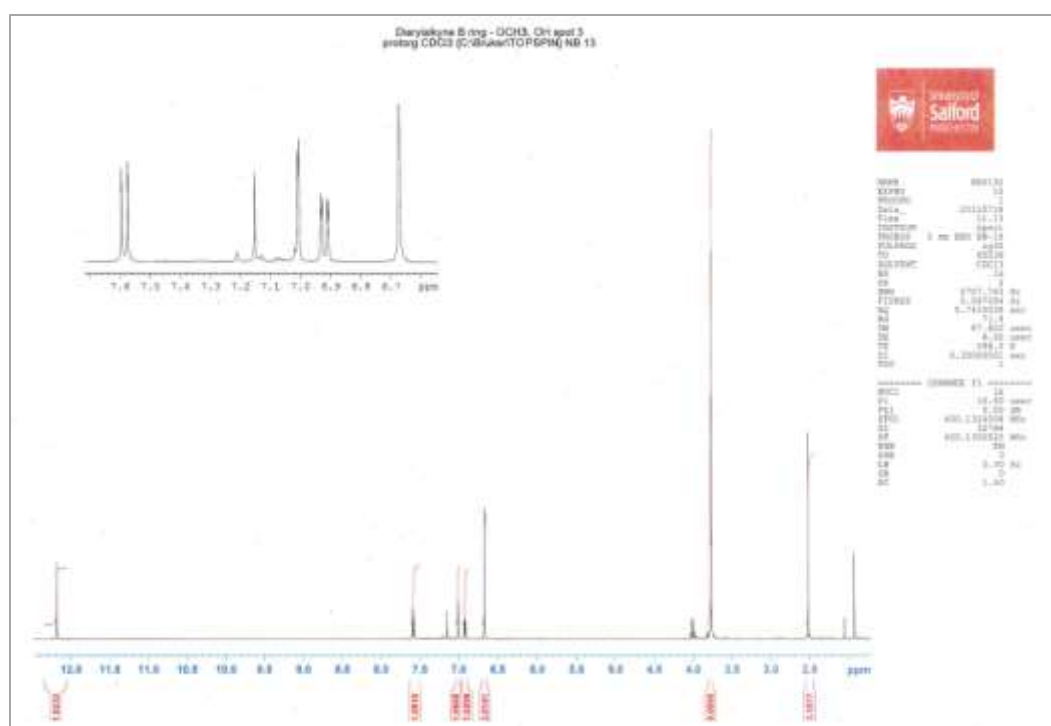
Figure 132 ¹H-NMR spectra of (Z)-2-hydroxy-4-(3',4',5'-trimethoxystyryl)benzoic acid 53ZFigure 133 ¹³C-NMR spectra of (Z)-2-hydroxy-4-(3',4',5'-trimethoxystyryl)benzoic acid 53Z

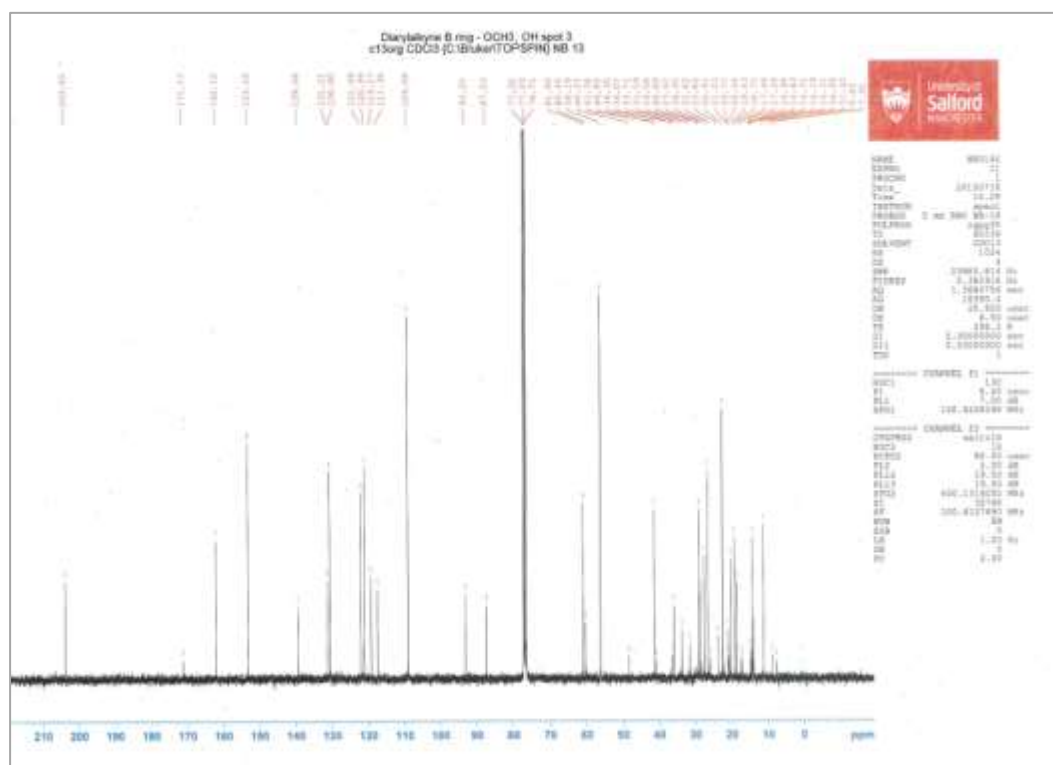
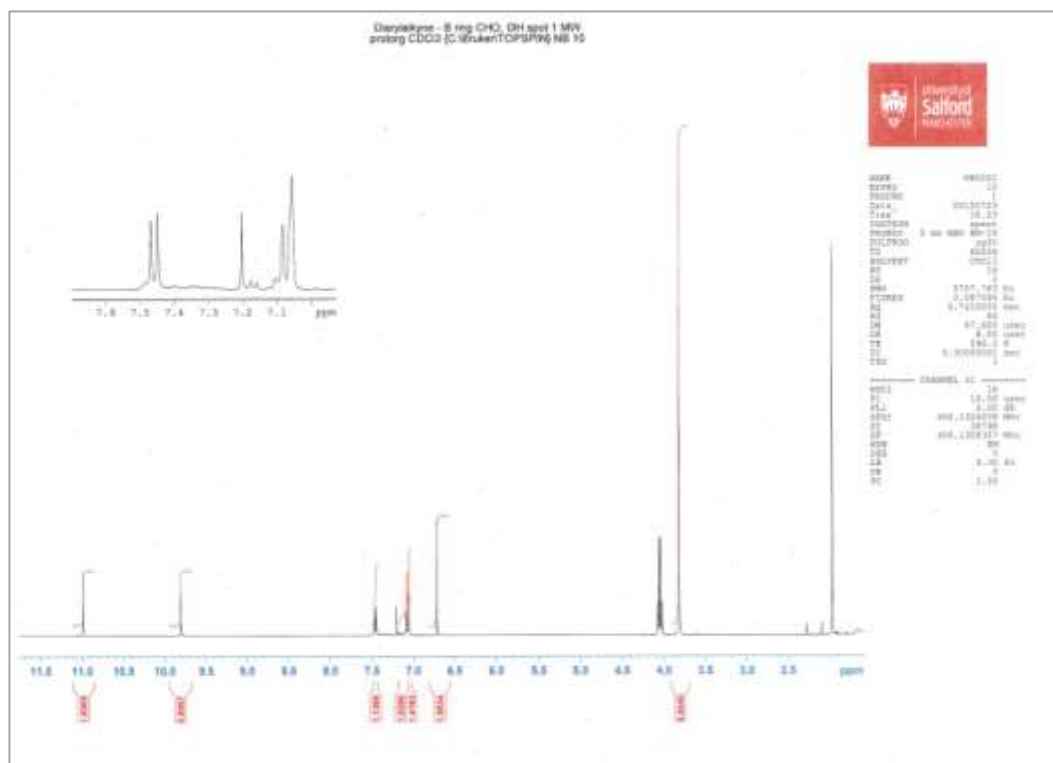
Figure 134 ¹H-NMR spectra of 5-iodo-1,2,3-trimethoxybenzene 55Figure 135 ¹H-NMR spectra of trimethyl((3,4,5-trimethoxyphenyl)ethynyl)silane 56

Figure 136 $^1\text{H-NMR}$ spectra of 3,4,5-trimethoxyacetylene 57Figure 137 $^1\text{H-NMR}$ spectra of 1-(4'-acetylphenyl)-2-(3',4',5'-trimethoxyphenyl)ethyne 58

Figure 138 ¹H-NMR spectra of 1-(4''-methoxyphenyl)-2-(3',4',5'-trimethoxyphenyl)ethyne 59Figure 139 ¹H-NMR spectra of 1-(4''-formylphenyl)-2-(3',4',5'-trimethoxyphenyl)ethyne 60

Figure 140 ¹³C-NMR spectra of 1-(4''-formylphenyl)-2-(3',4',5'-trimethoxyphenyl)ethyne 60Figure 141 ¹H-NMR spectra of 1-(4''-cyanophenyl)-2-(3',4',5'-trimethoxyphenyl)ethyne 61

Figure 142 ¹³C-NMR spectra of 1-(4''-cyanophenyl)-2-(3',4',5'-trimethoxyphenyl)ethyne 61Figure 143 ¹H-NMR spectra of 1-(4''-acetyl-3''-hydroxyphenyl)-2-(3',4',5'-trimethoxyphenyl)ethyne 62

Figure 144 ¹³C-NMR spectra of 1-(4''-acetyl-3''-hydroxyphenyl)-2-(3',4',5'-trimethoxyphenyl)ethyne 62Figure 145 ¹H-NMR spectra of 1-(4''-formyl-3''-hydroxyphenyl)-2-(3',4',5'-trimethoxyphenyl)ethyne 63

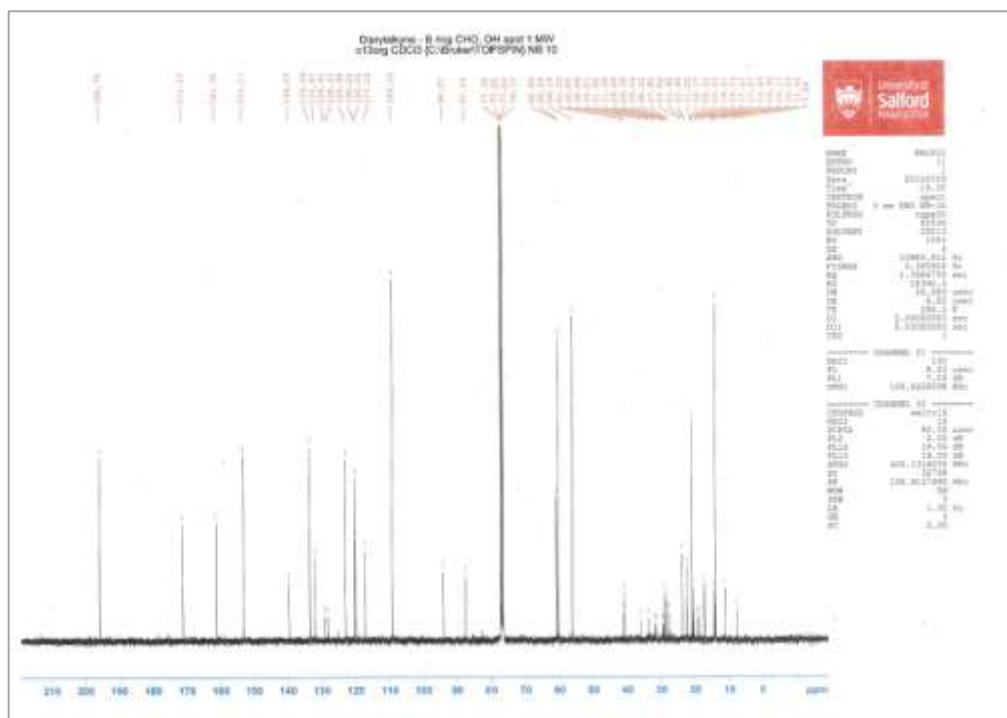


Figure 146 ¹³C-NMR spectra of 1-(4''-formyl-3''-hydroxyphenyl)-2-(3',4',5'-trimethoxyphenyl)ethyne 63

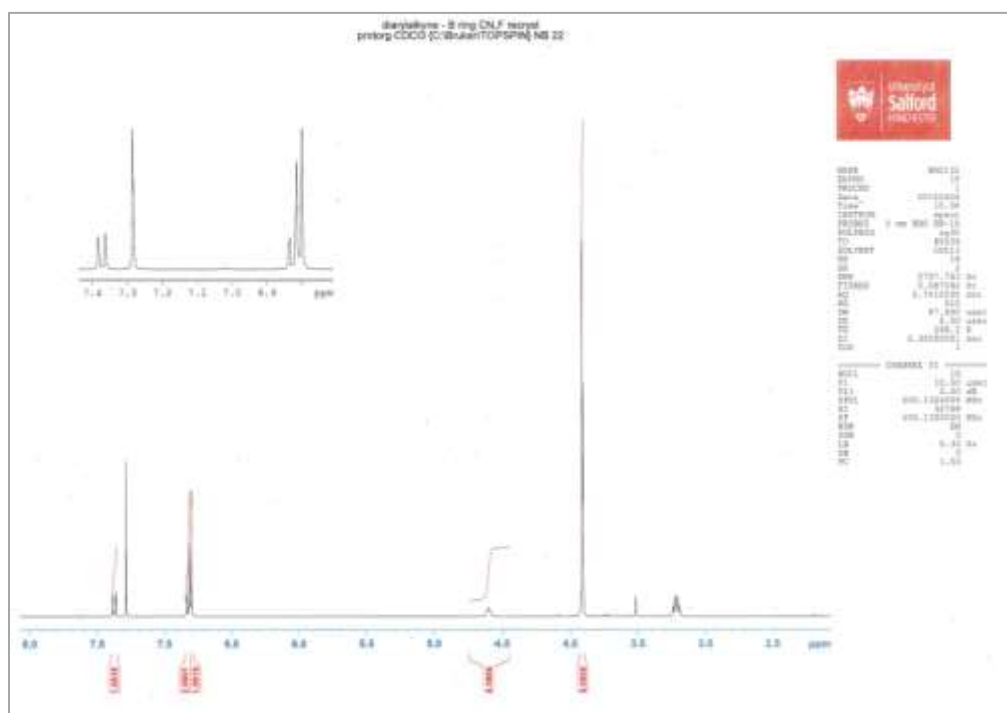
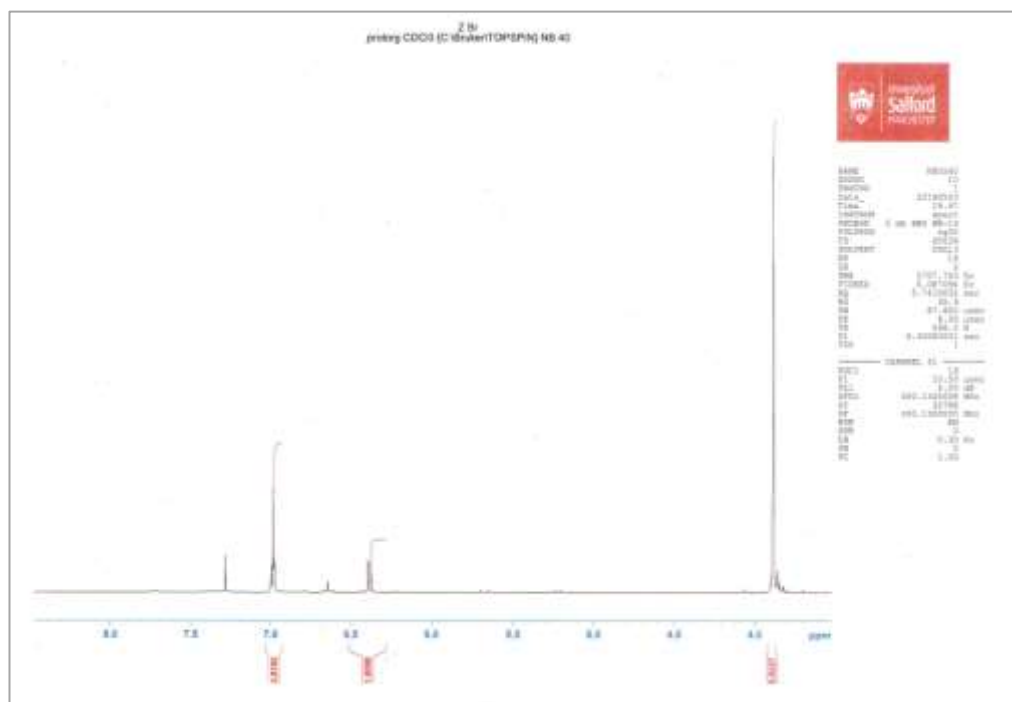
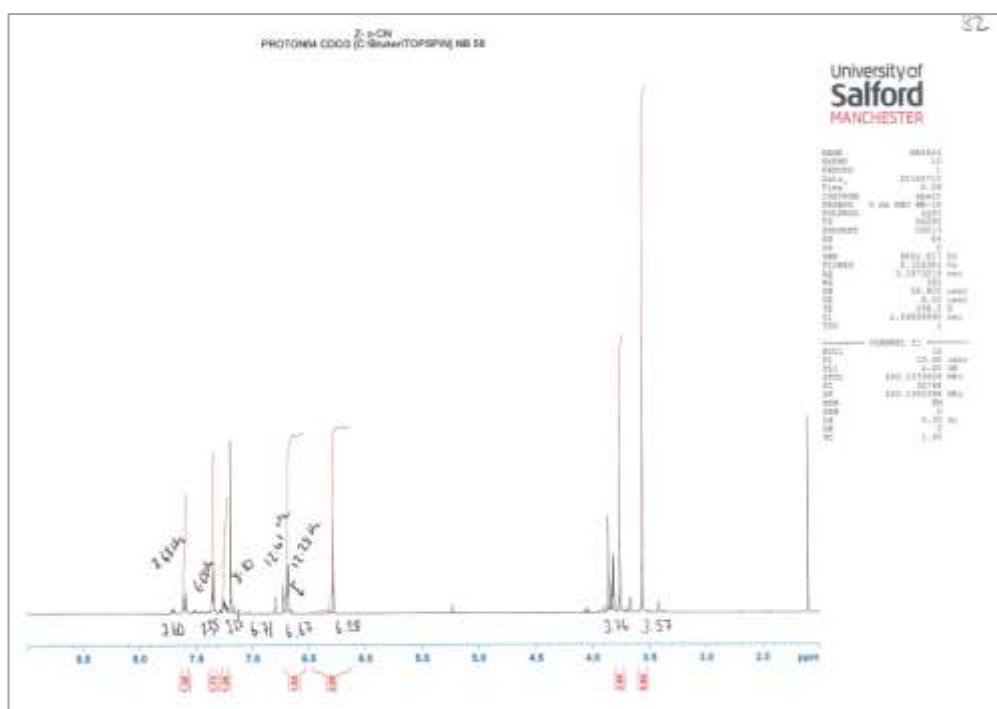
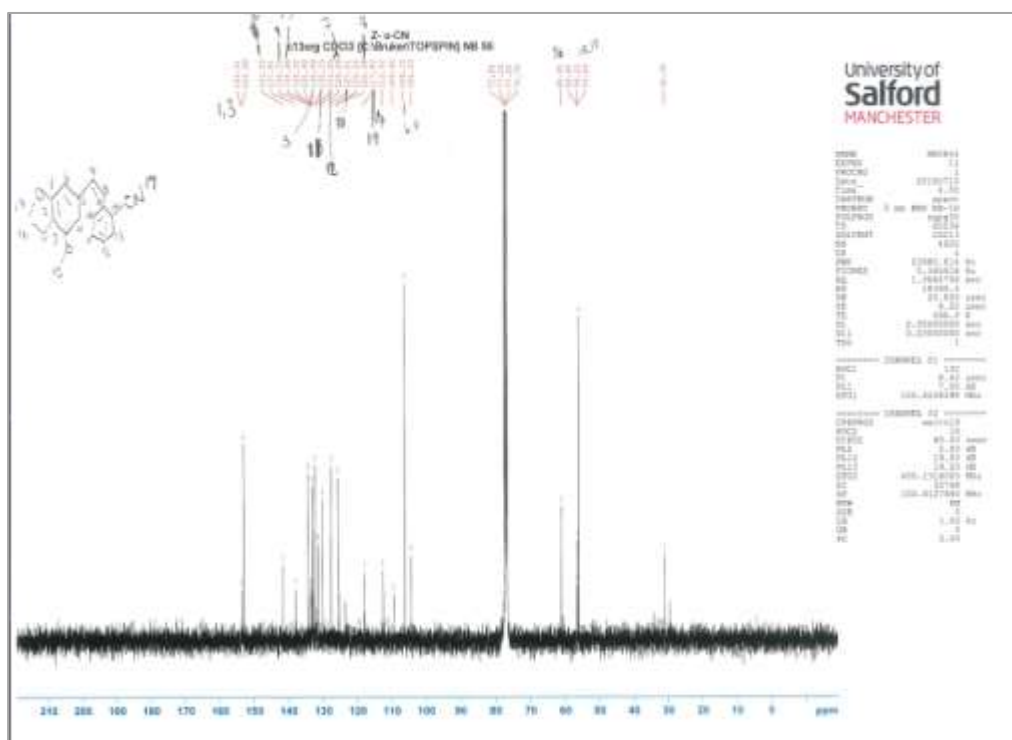
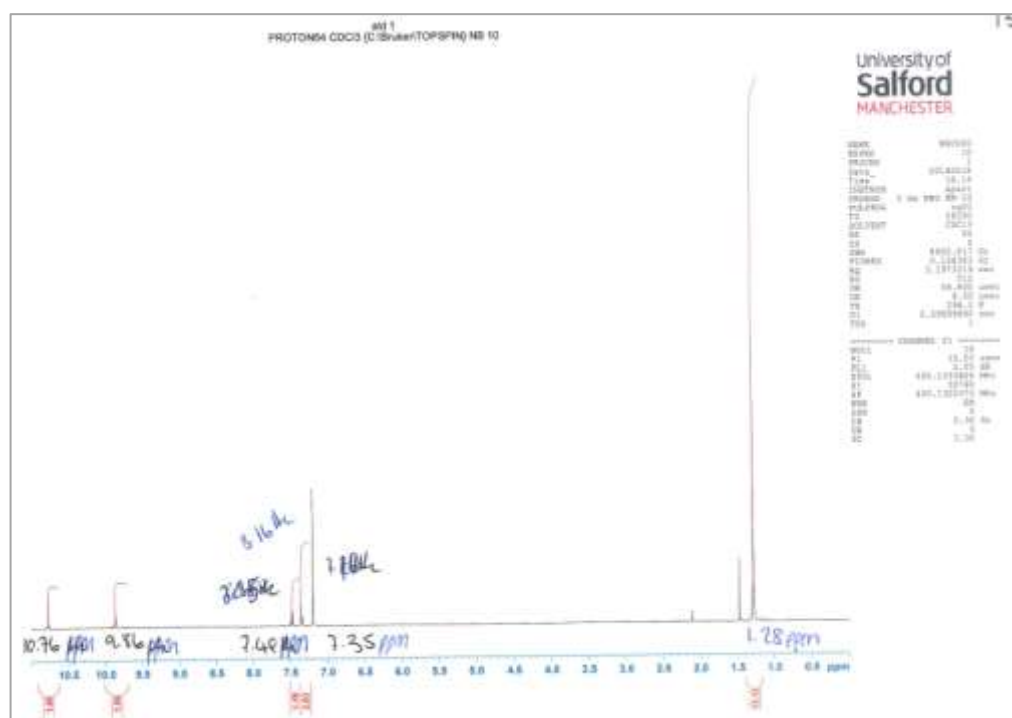


Figure 147 ¹H-NMR spectra of 1-(4''-cyano-3''-fluorophenyl)-2-(3',4',5'-trimethoxyphenyl)ethyne 64

Figure 152 ¹H-NMR spectra of 5-[(Z)-2-bromovinyl]-1,2,3-trimethoxybenzene 70Figure 153 ¹H-NMR spectra of (Z)-2-(3',4',5'-trimethoxystyryl)benzotrile 71

Figure 154 ^{13}C -NMR spectra of (Z)-2-(3',4',5'-trimethoxystyryl)benzonitrile 71Figure 155 ^1H -NMR spectra of 2-hydroxy-4-(4,4,5,5-tetramethyl-1,3,2-dioxaborolan-2-yl)benzaldehyde 73

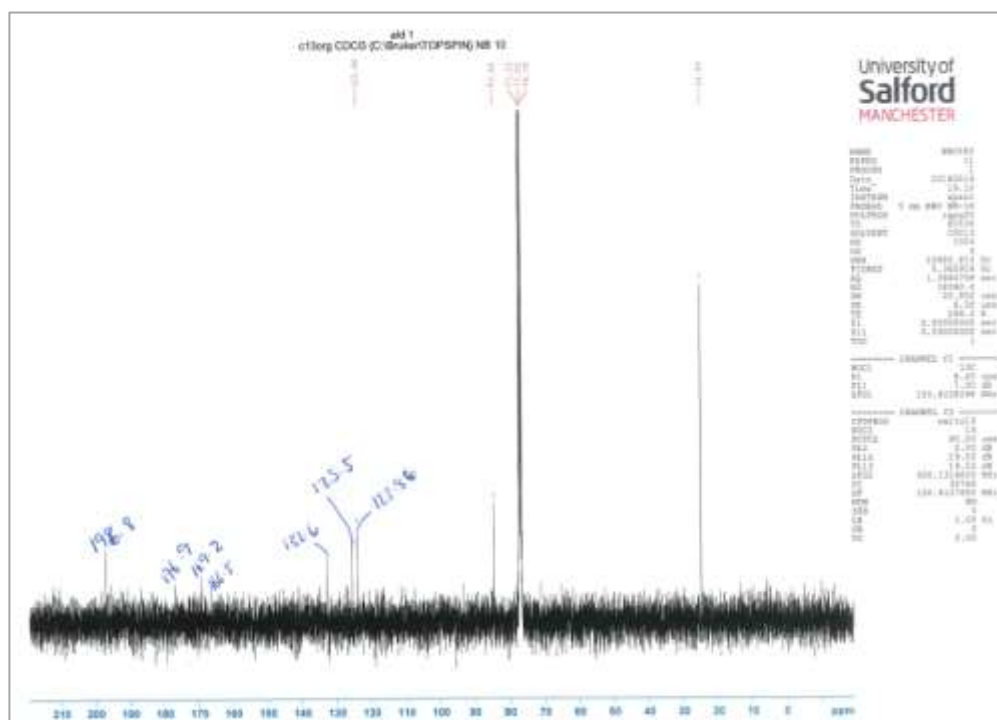


Figure 156 ¹³C-NMR spectra of 2-hydroxy-4-(4,4,5,5-tetramethyl-1,3,2-dioxaborolan-2-yl)benzaldehyde 73

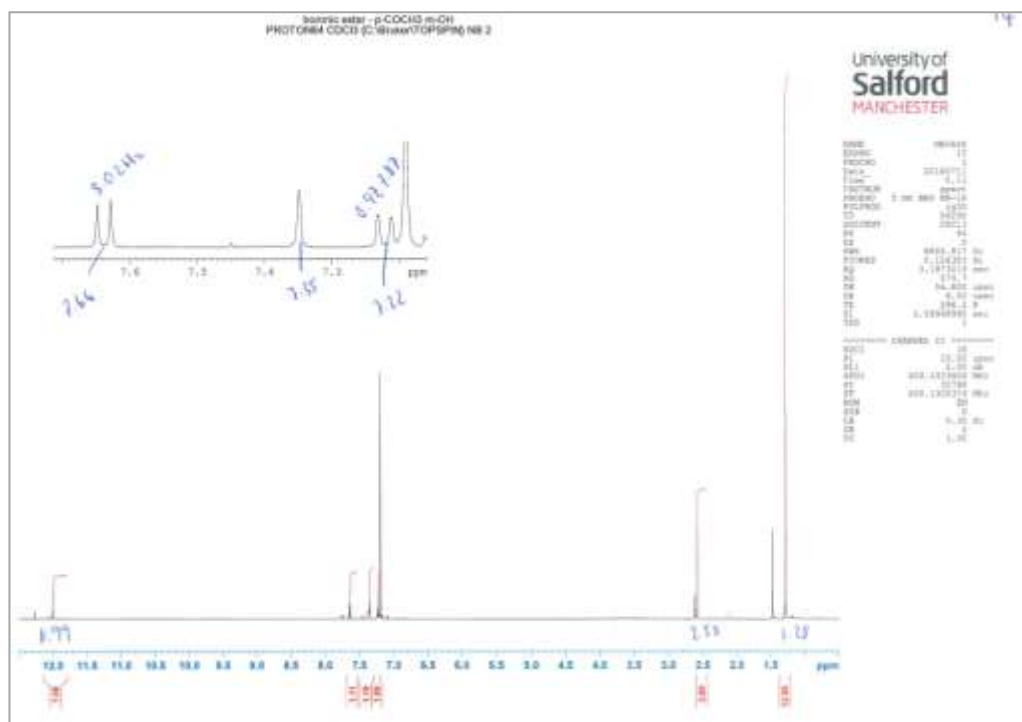


Figure 157 ¹H-NMR spectra of 2-hydroxy-4-(4,4,5,5-tetramethyl-1,3,2-dioxaborolan-2-yl)acetophenone 75

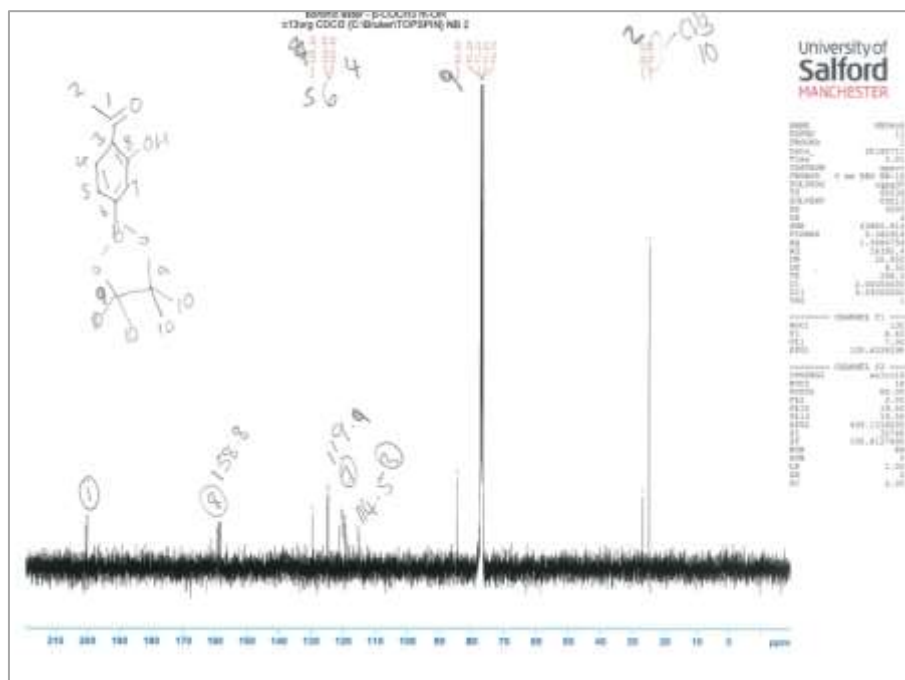


Figure 158 ¹³C-NMR spectra of 2-hydroxy-4-(4,4,5,5-tetramethyl-1,3,2-dioxaborolan-2-yl)acetophenone 75

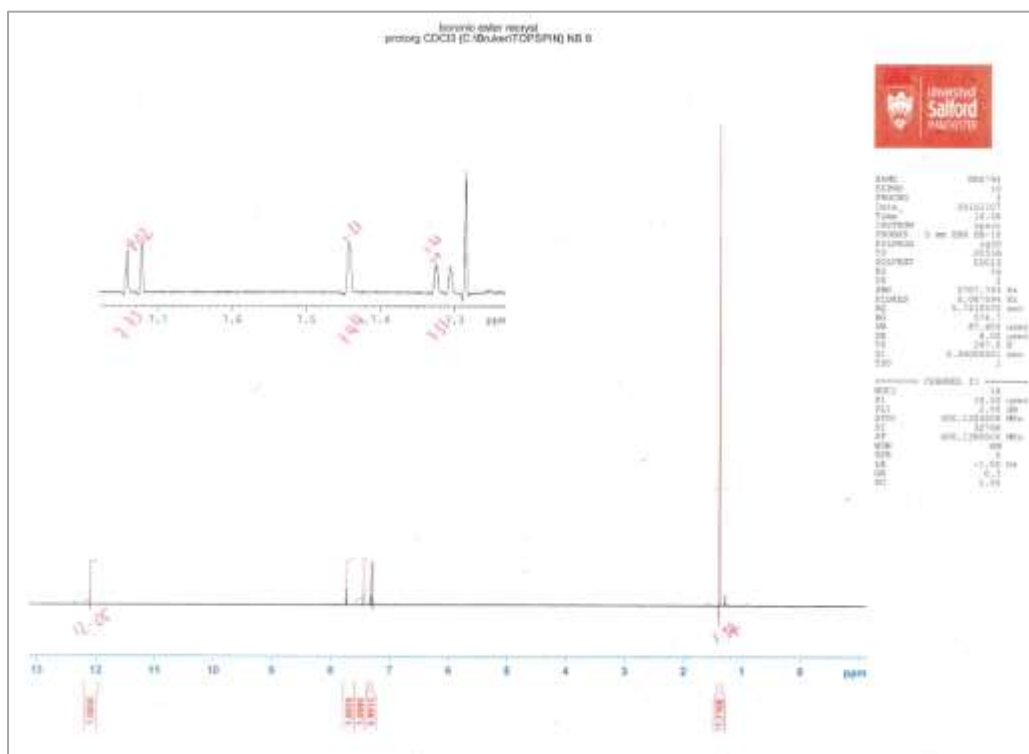
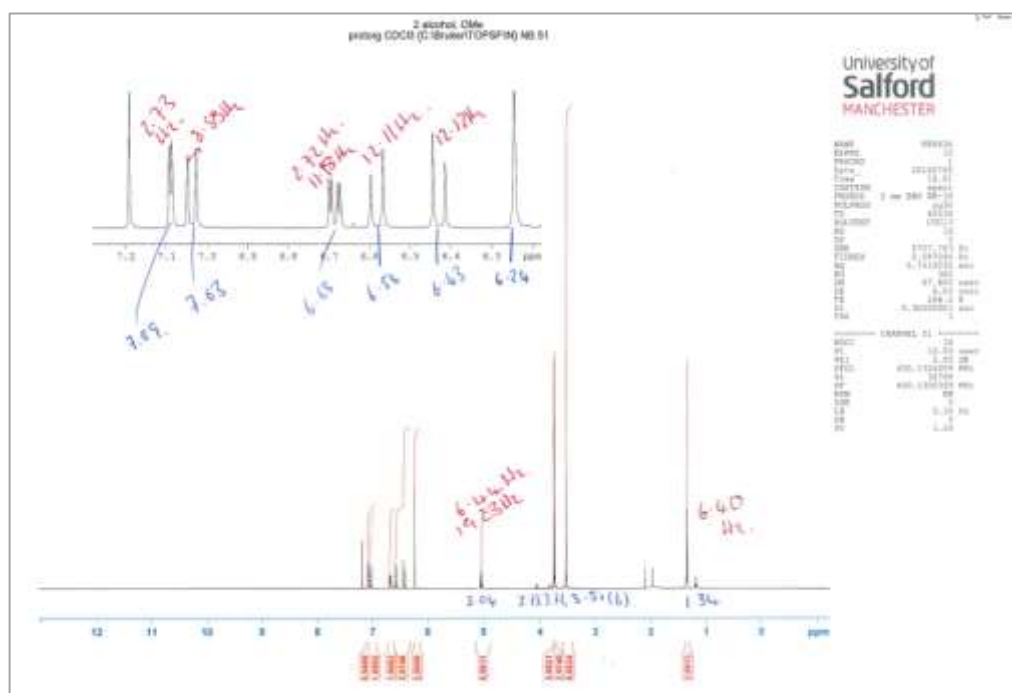
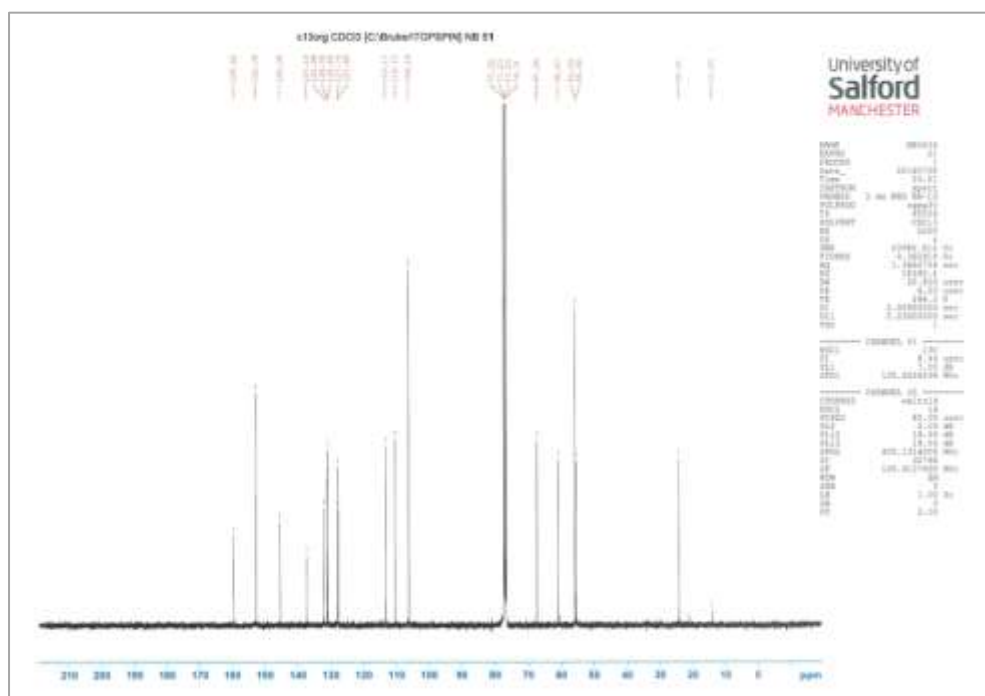


Figure 159 ¹H-NMR spectra of 2-Hydroxy-4-(4,4,5,5-tetramethyl-1,3,2-dioxaborolan-2-yl)benzoic acid 69

Figure 160 ¹H-NMR spectra of (Z)-1-(5-methoxy-2-(3',4',5'-trimethoxystyryl)phenyl)ethanol 80Figure 161 ¹³C-NMR spectra of (Z)-1-(5-methoxy-2-(3',4',5'-trimethoxystyryl)phenyl)ethanol 80

9.2 FTIR spectra

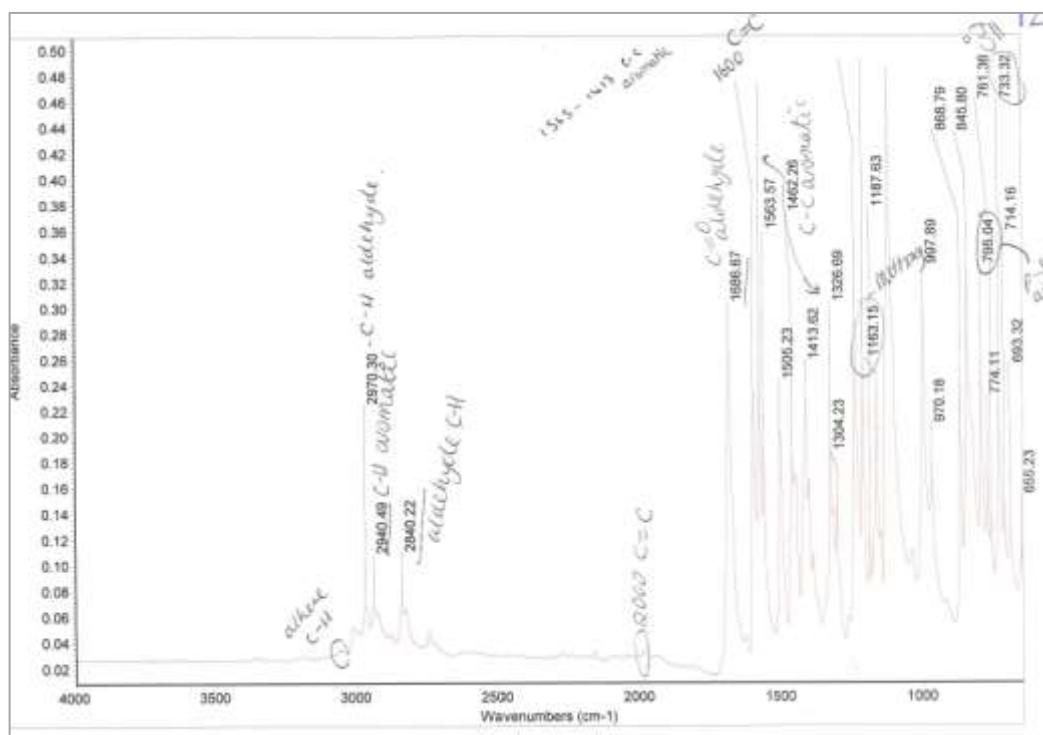


Figure 164 FTIR spectra of (Z)-4-(3',4',5'-trimethoxystyryl)benzaldehyde 42Z

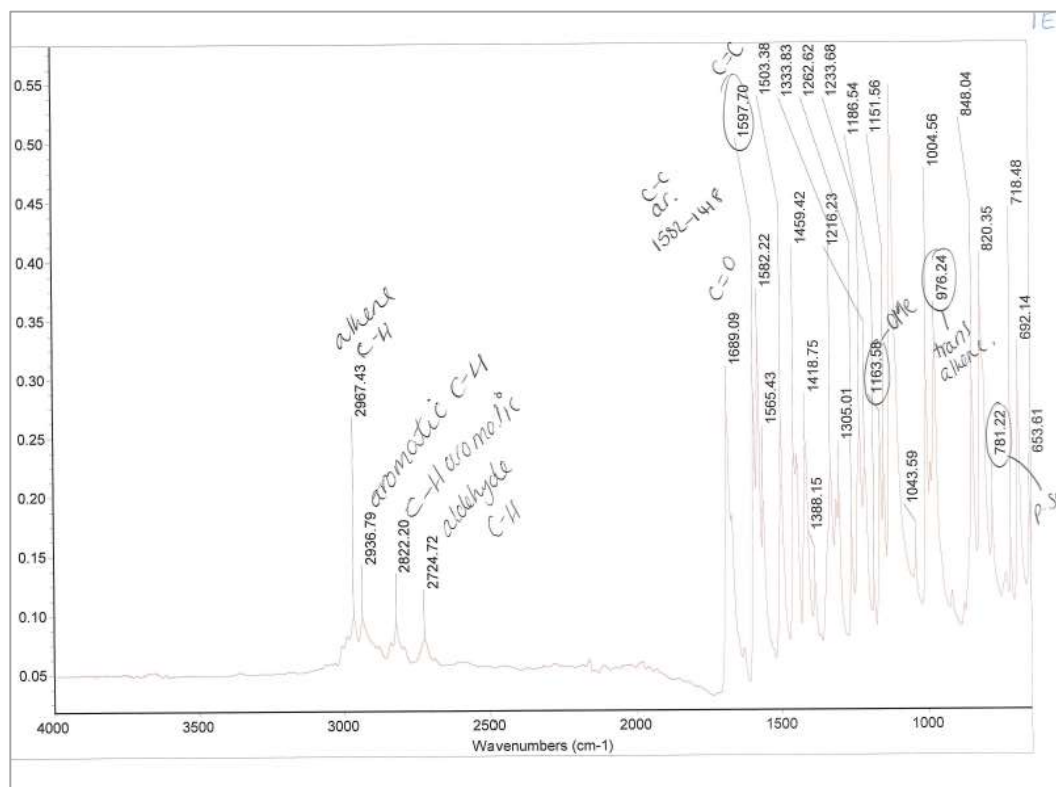


Figure 165 FTIR spectra of (E)-4-(3',4',5'-trimethoxystyryl)benzaldehyde 42E

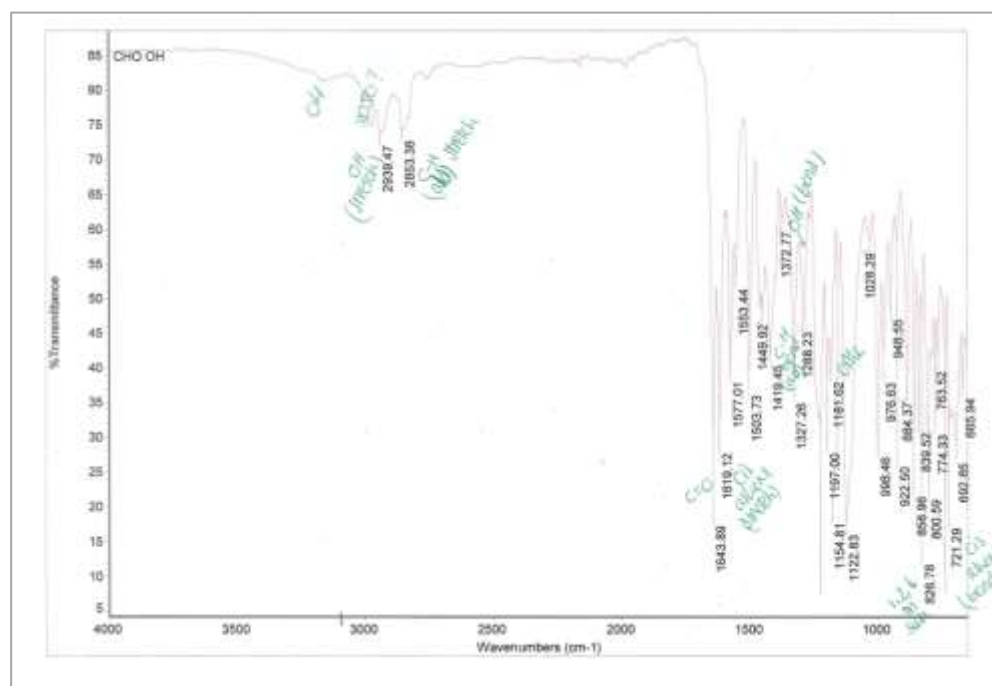


Figure 166 FTIR spectra of (Z)-2-hydroxy-4-(3',4',5'-trimethoxystyryl)benzaldehyde 43Z

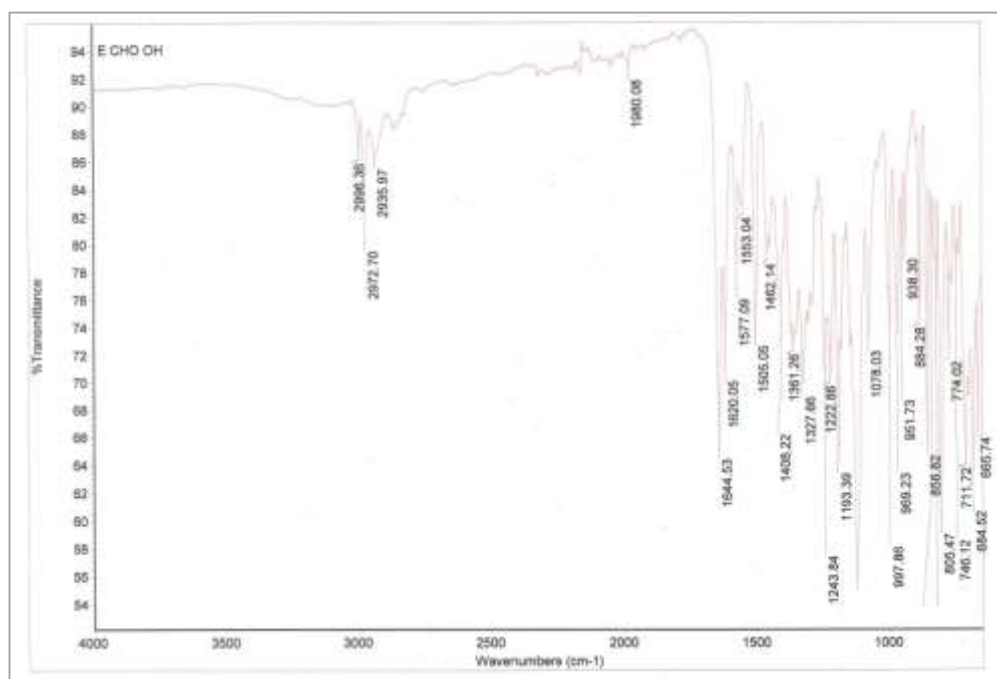


Figure 167 FTIR spectra of (E)-2-hydroxy-4-(3',4',5'-trimethoxystyryl)benzaldehyde 43E

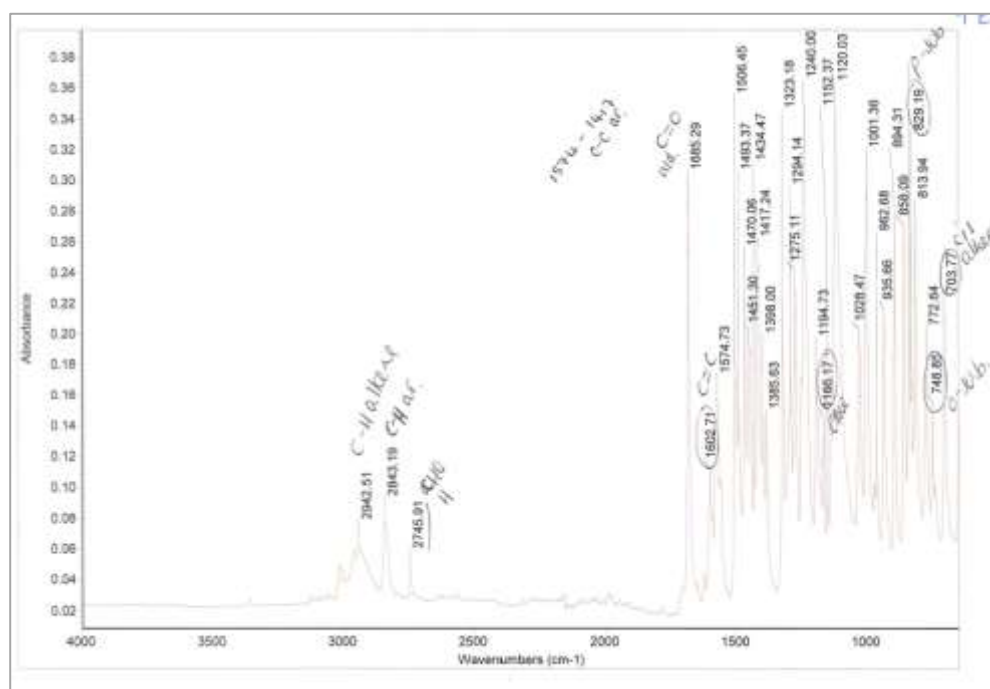


Figure 168 FTIR spectra of (Z)-5-methoxy-2-(3',4',5'-trimethoxystyryl)benzaldehyde 44Z

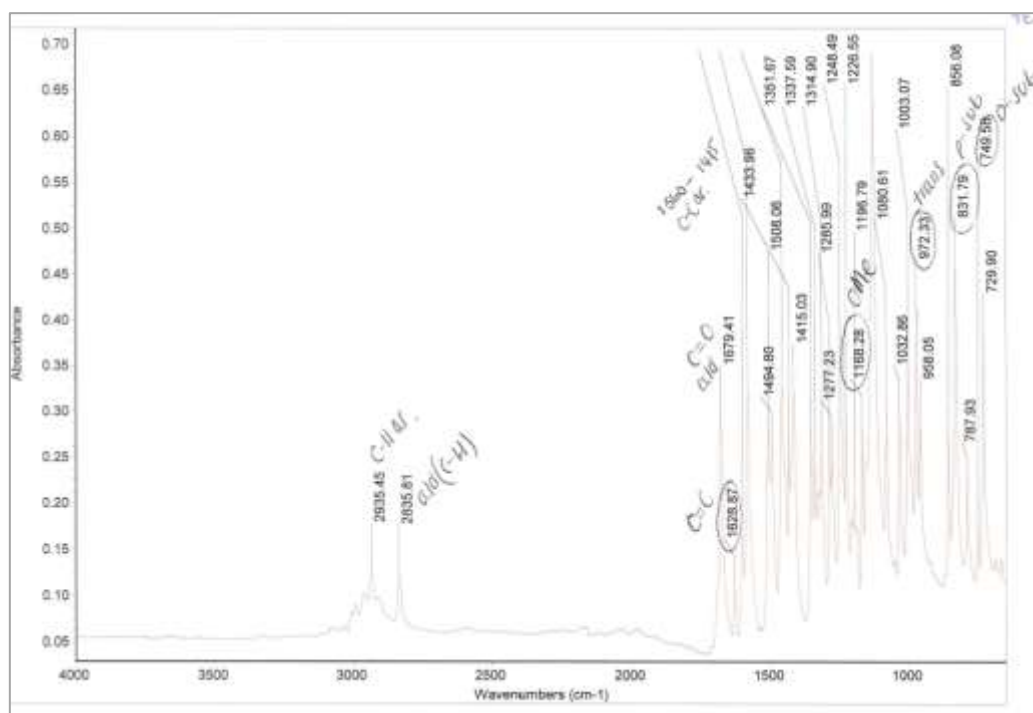


Figure 169 FTIR spectra of (E)-5-methoxy-2-(3',4',5'-trimethoxystyryl)benzaldehyde 44E

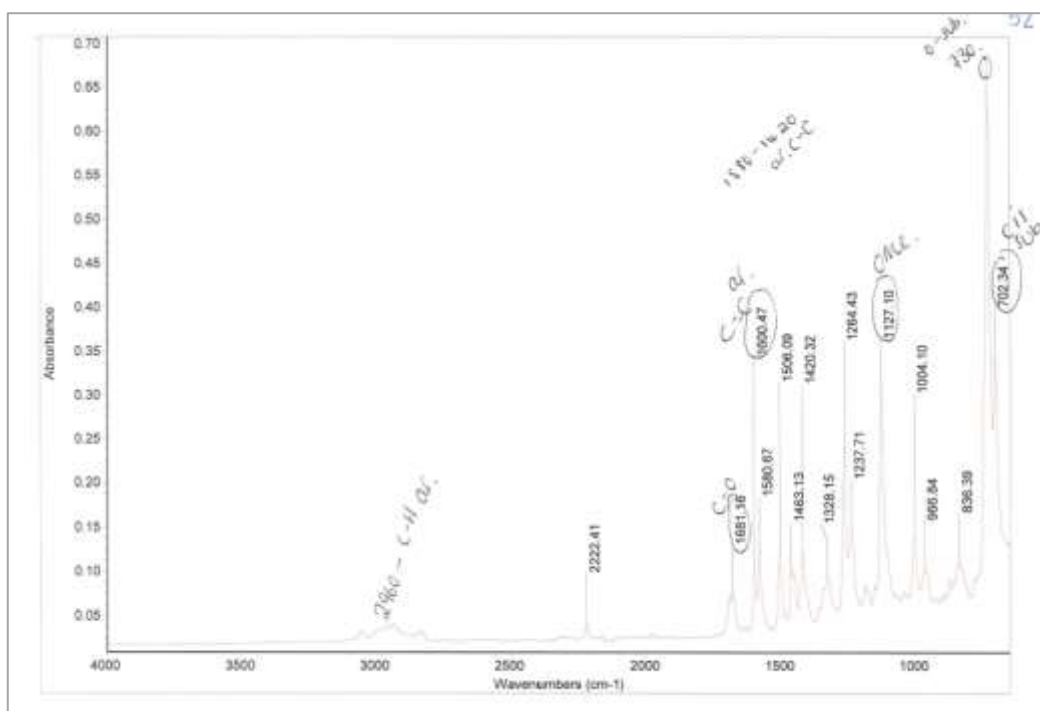


Figure 170 FTIR spectra of (Z)-2-(3',4',5'-trimethoxystyryl)benzaldehyde 45Z

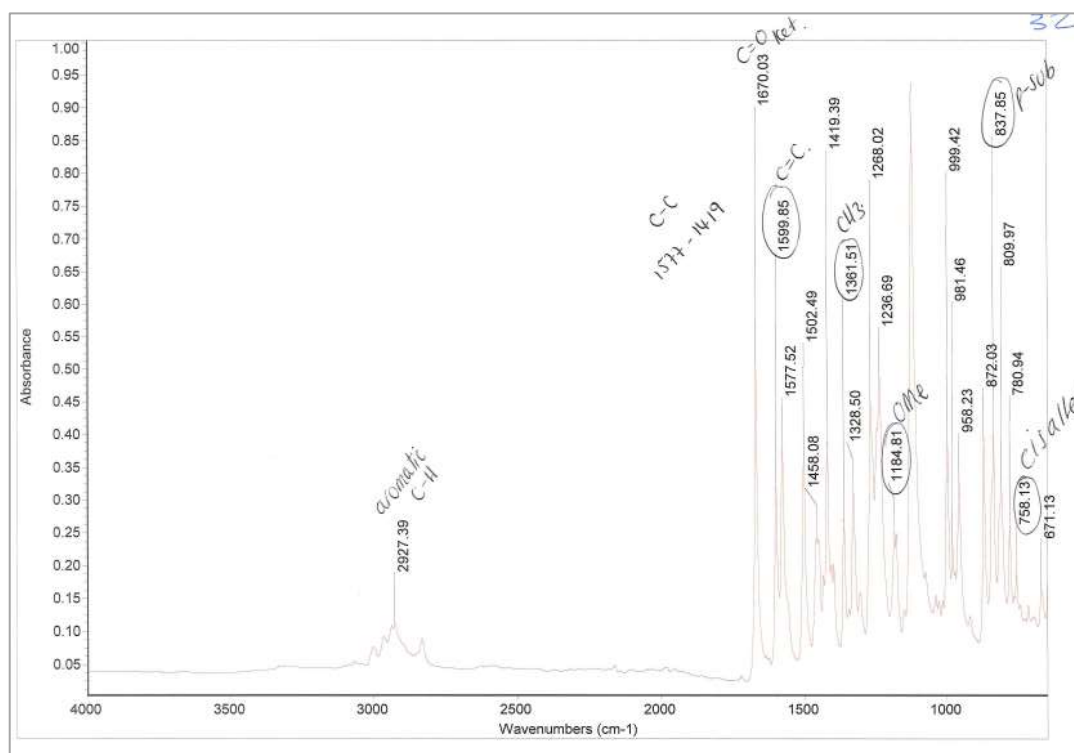


Figure 171 FTIR spectra of (Z)-4-(3',4',5'-trimethoxystyryl)acetophenone 46Z

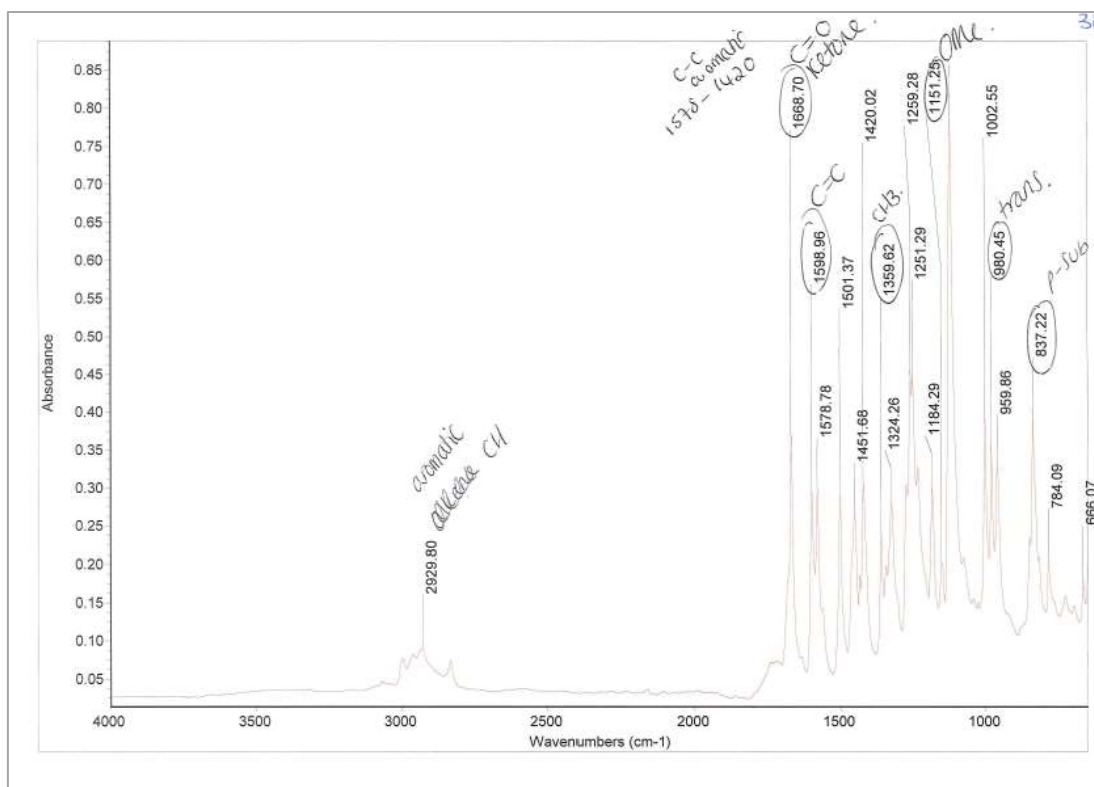


Figure 172 FTIR spectra of (E)-4-(3',4',5'-trimethoxystyryl)acetophenone 46E

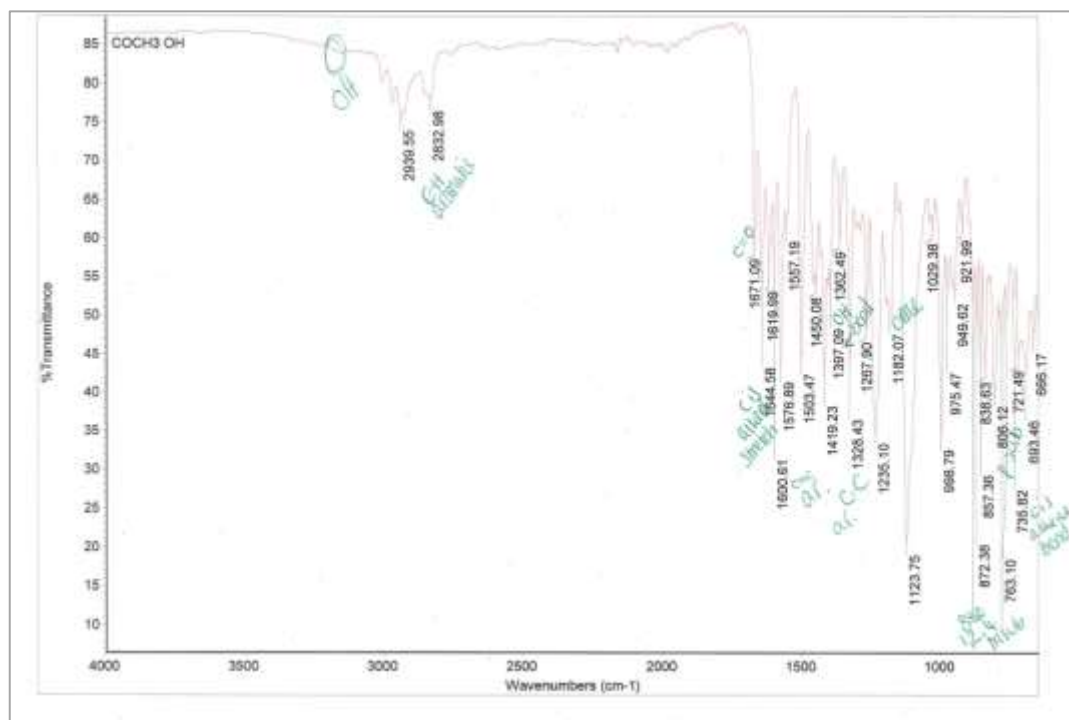


Figure 173 FTIR spectra of (Z)-2-hydroxy-4-(3',4',5'-trimethoxystyryl)phenyl)acetophenone 47Z

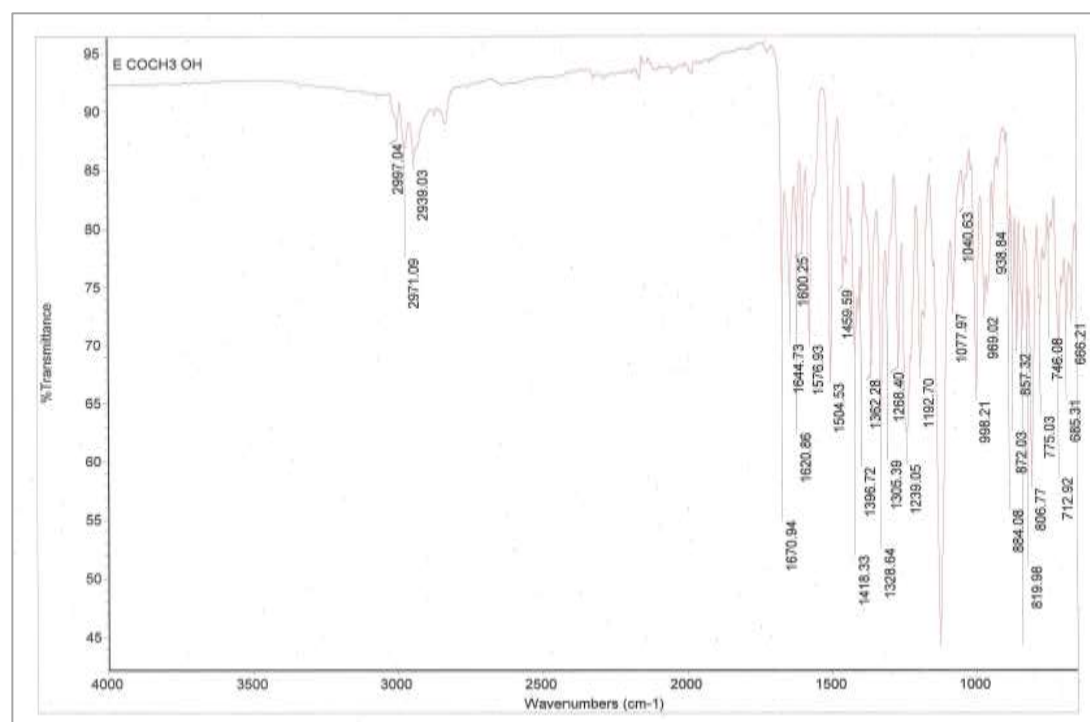


Figure 174 FTIR spectra of (E)-2-hydroxy-4-(3',4',5'-trimethoxystyryl)phenyl)acetophenone 47E

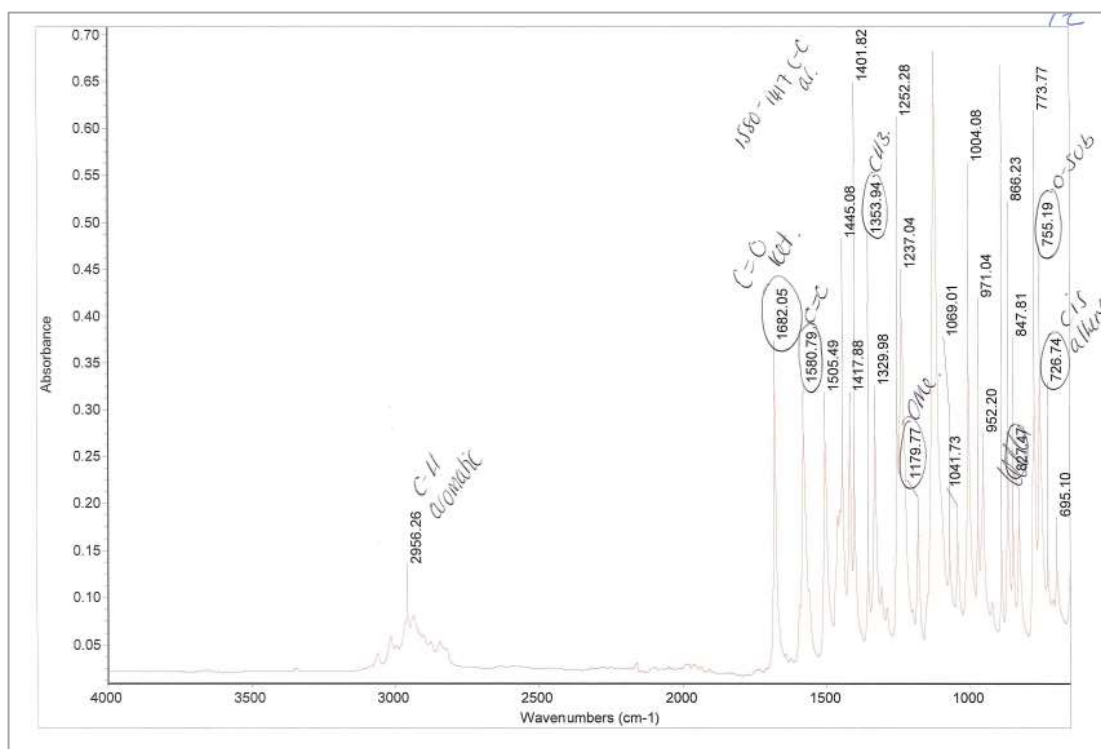


Figure 175 FTIR spectra of (Z)-2-(3',4',5'-trimethoxystyryl)acetophenone 48Z

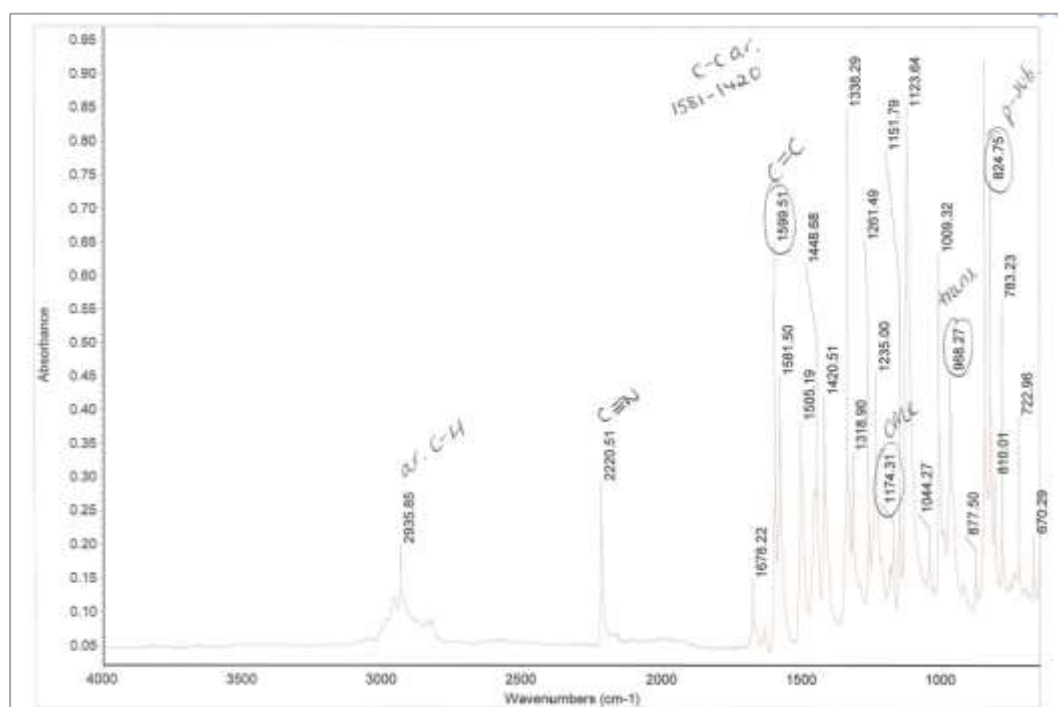


Figure 176 FTIR spectra of (E)-4-(3',4',5'-trimethoxystyryl)benzotrile 48E

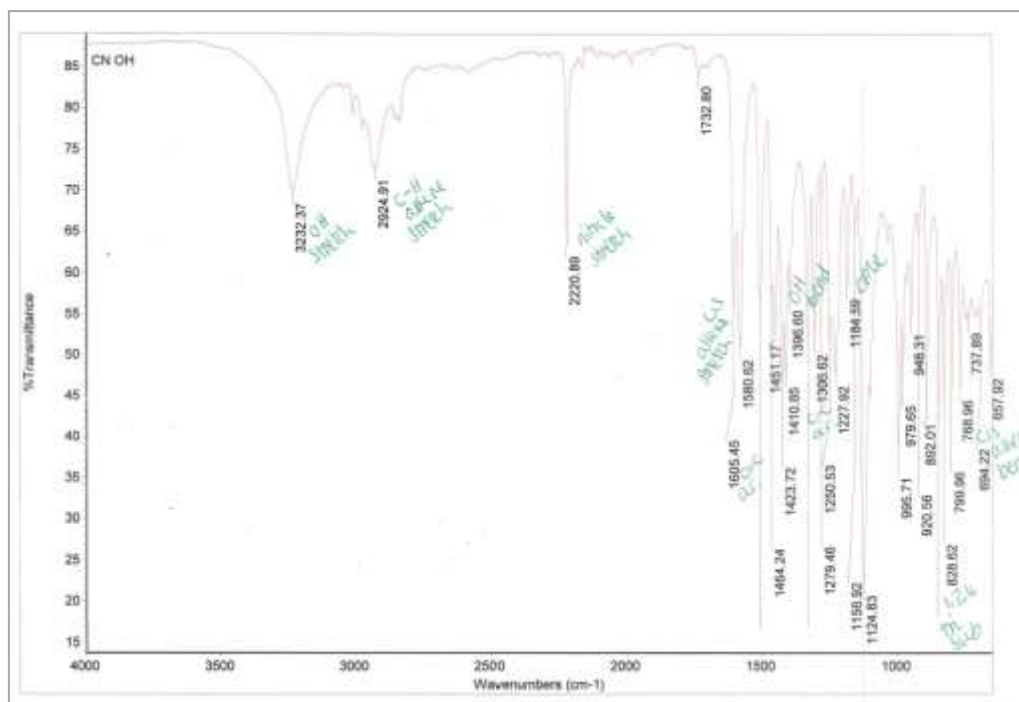


Figure 177 FTIR spectra of (Z)-2-hydroxy-4-(3',4',5'-trimethoxystyryl)benzointrile 51Z

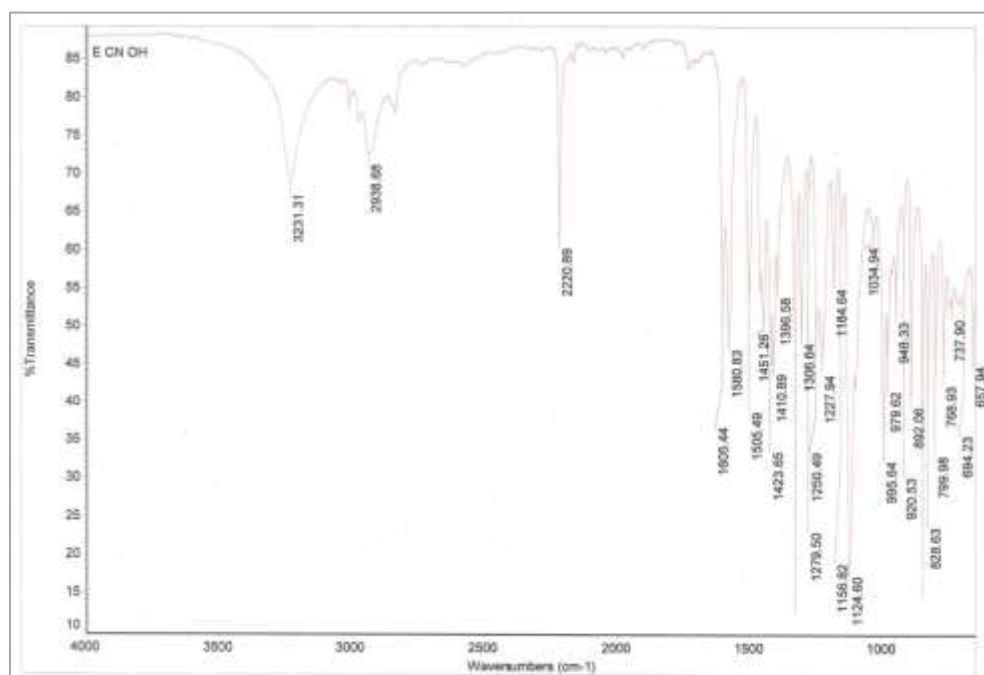


Figure 178 FTIR spectra of (E)-2-hydroxy-4-(3',4',5'-trimethoxystyryl)benzointrile 51E

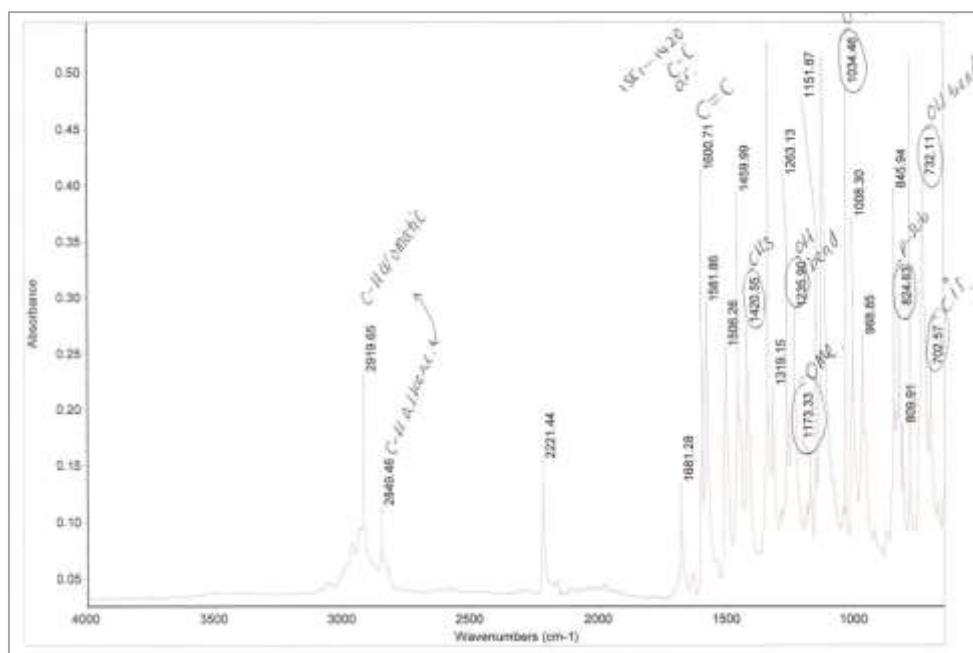


Figure 179 FTIR spectra of (Z)-1-(4-(3',4',5'-trimethoxystyryl)phenyl)ethanol 52Z

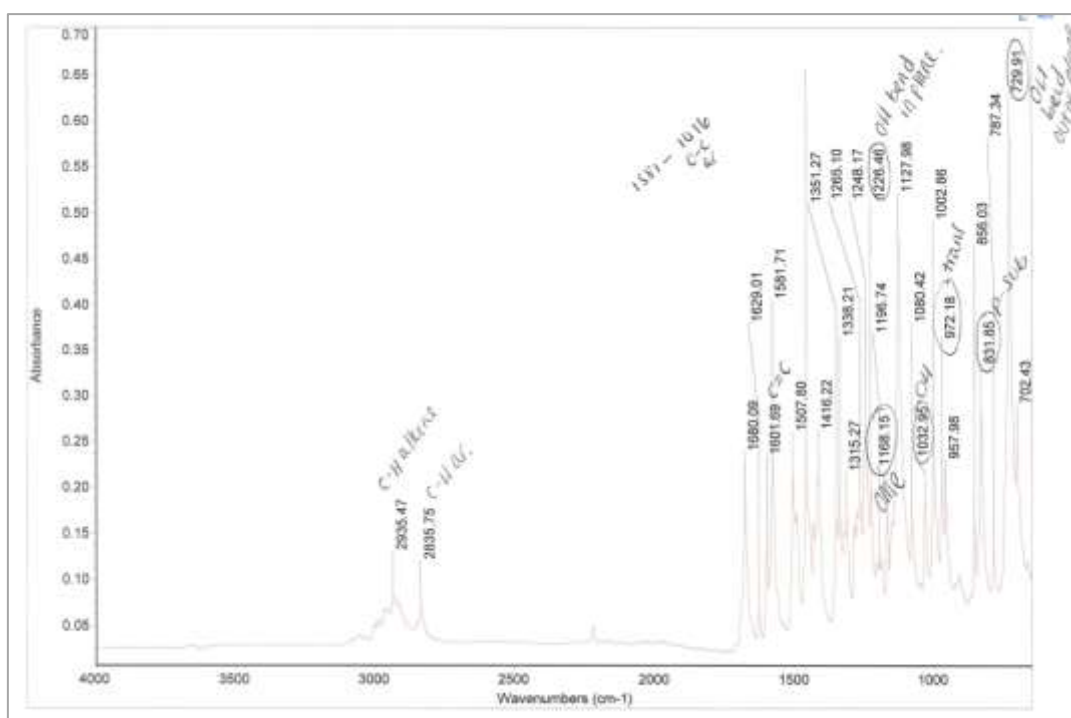


Figure 180 FTIR spectra of (E)-1-(4-(3',4',5'-trimethoxystyryl)phenyl)ethanol 52E

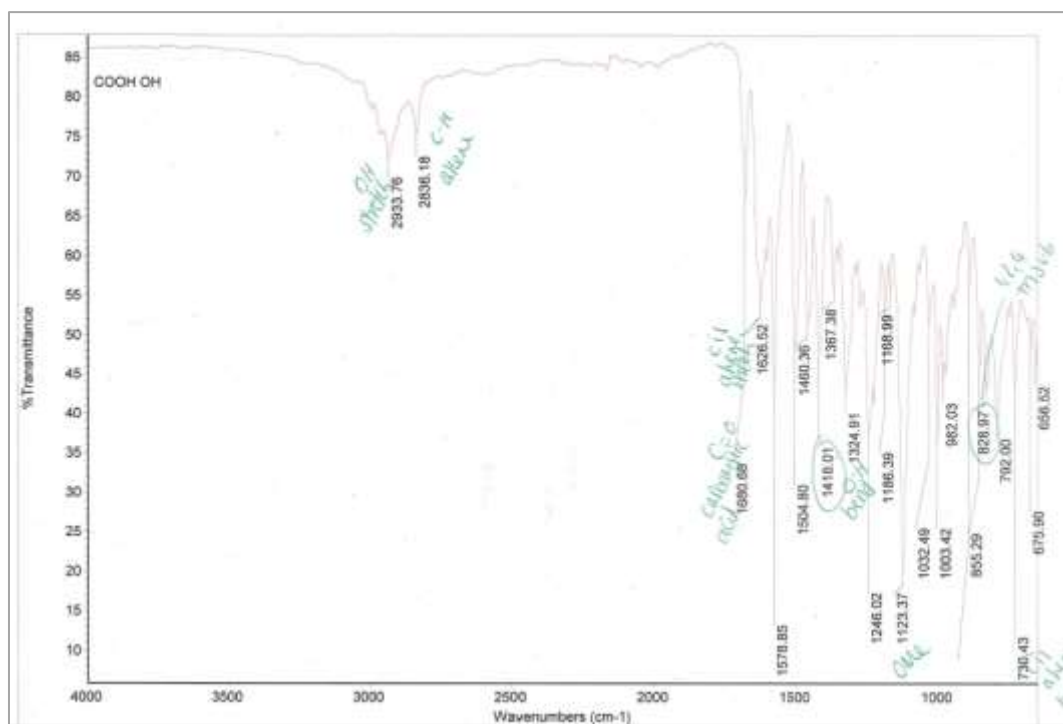


Figure 181 FTIR spectra of (Z)-2-hydroxy-4-(3',4',5'-trimethoxystyryl)benzoic acid 53Z

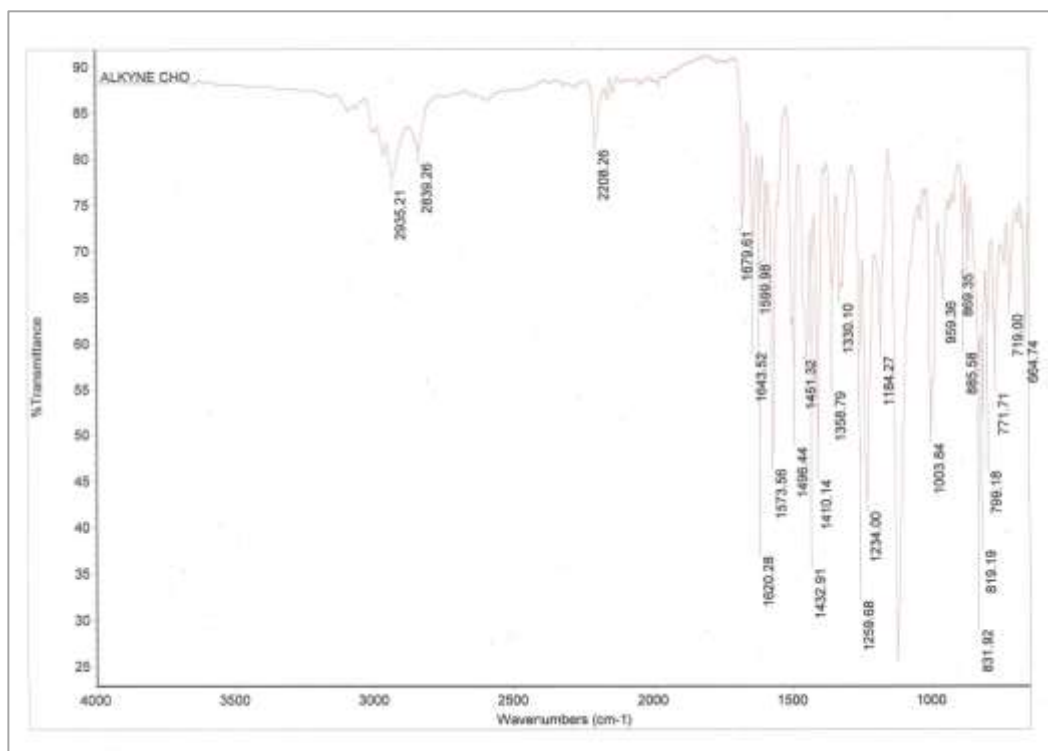


Figure 182 FTIR spectra of 1-(4''-formylphenyl)-2-(3',4',5'-trimethoxyphenyl)ethyne 60

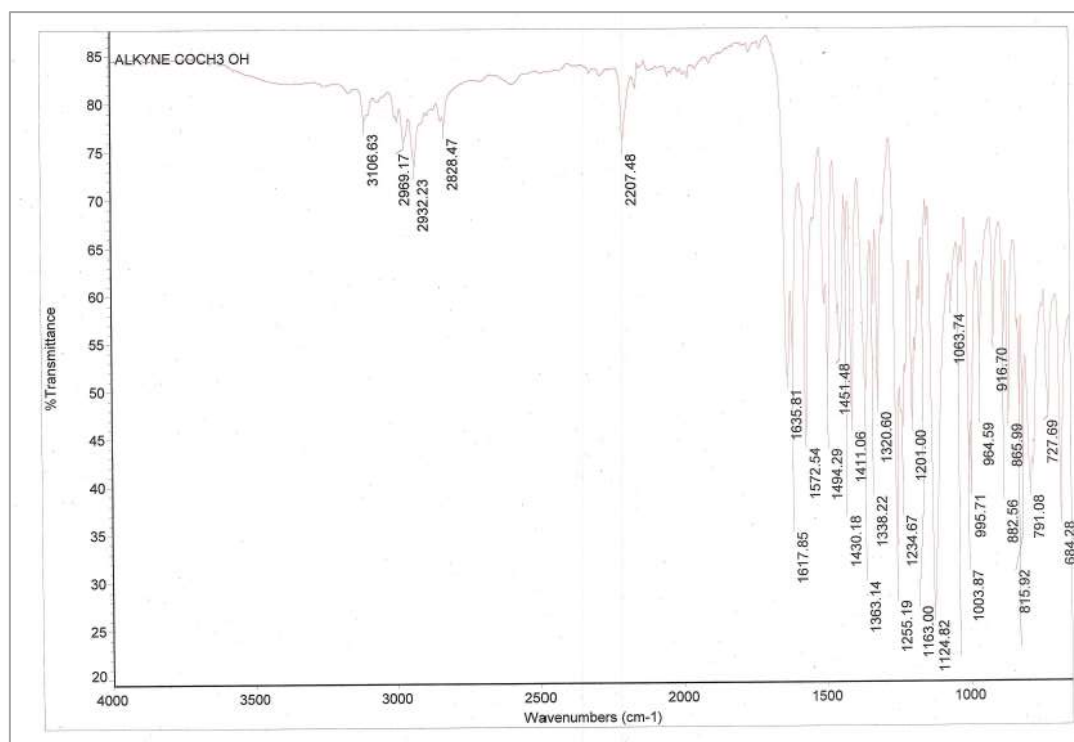


Figure 183 FTIR spectra of 1-(4''-acetyl-3''-hydroxyphenyl)-2-(3',4',5'-trimethoxyphenyl)ethyne 62

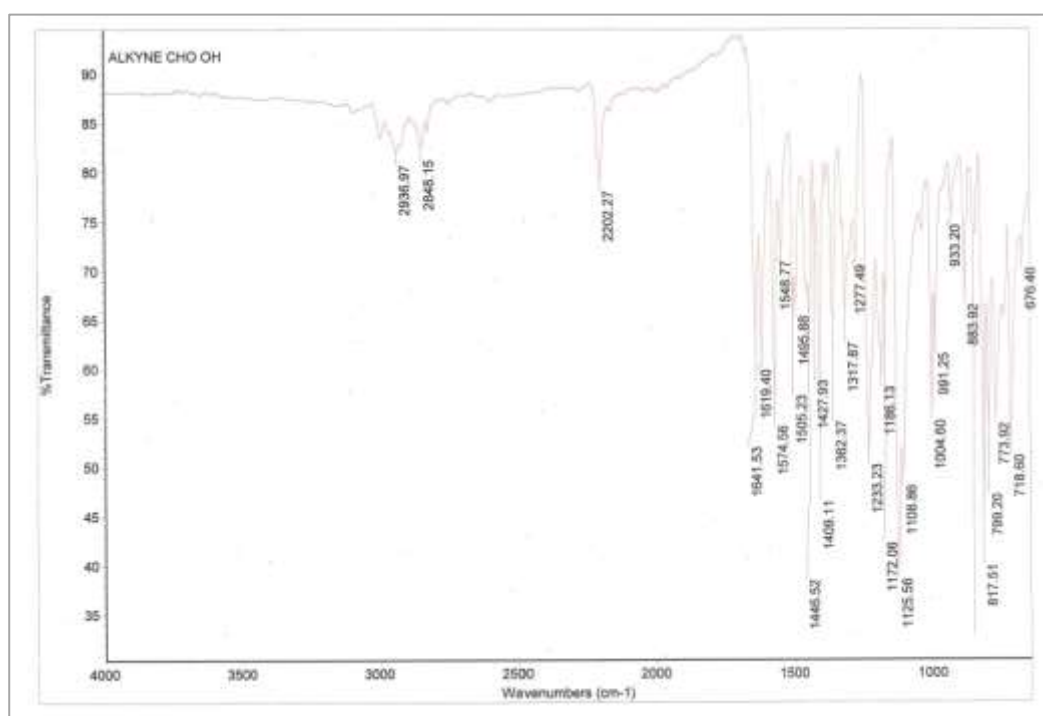


Figure 184 FTIR spectra of 1-(4''-formyl-3''-hydroxyphenyl)-2-(3',4',5'-trimethoxyphenyl)ethyne 63

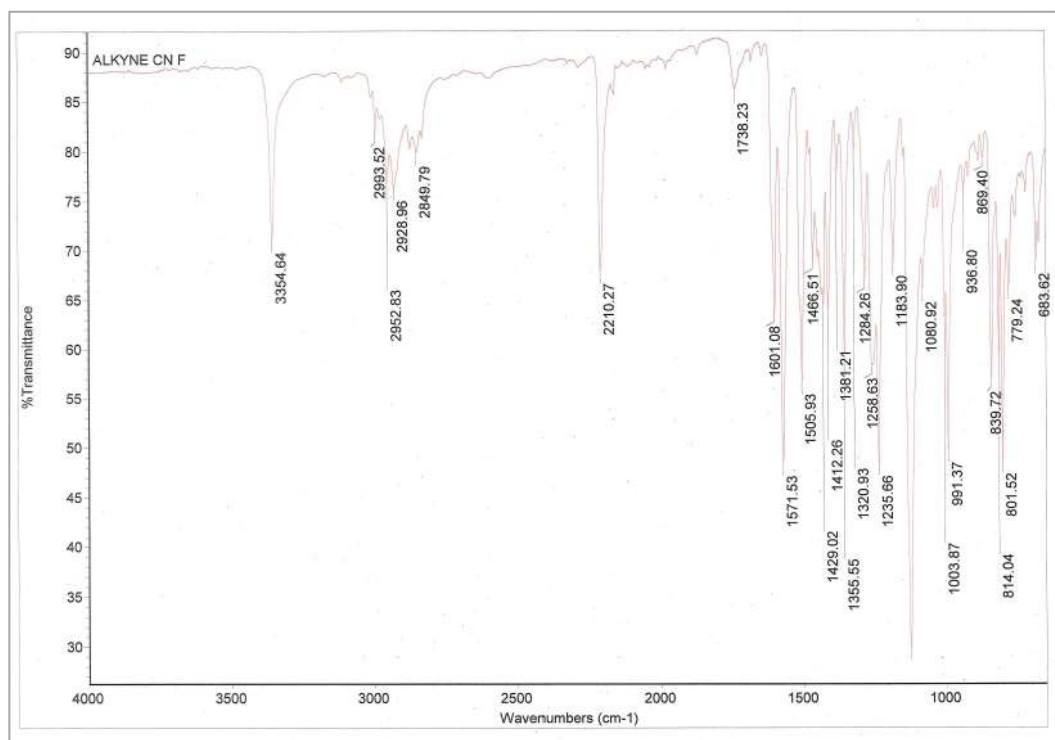


Figure 185 FTIR spectra of 1-(4''-Cyano-3''-fluorophenyl)-2-(3',4',5'-trimethoxyphenyl)ethyne 64

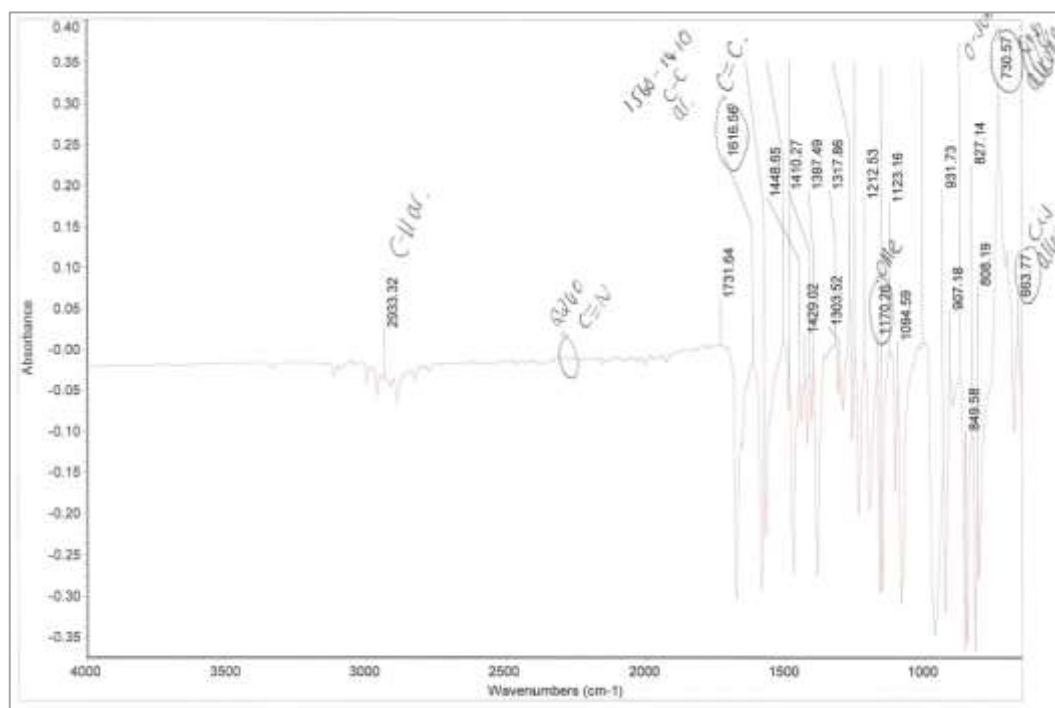


Figure 186 FTIR spectra of (Z)-2-(3',4',5'-trimethoxystyryl)benzonitrile 71

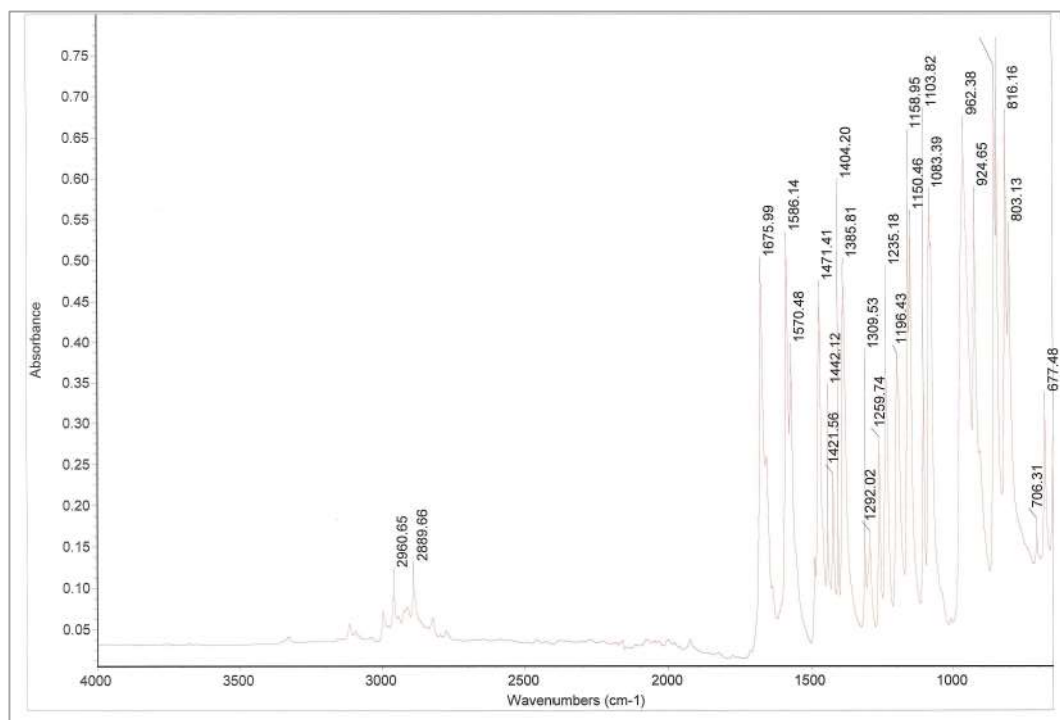


Figure 187 FTIR spectra of 2-hydroxy-4-(4,4,5,5-tetramethyl-1,3,2-dioxaborolan-2-yl)acetophenone 75

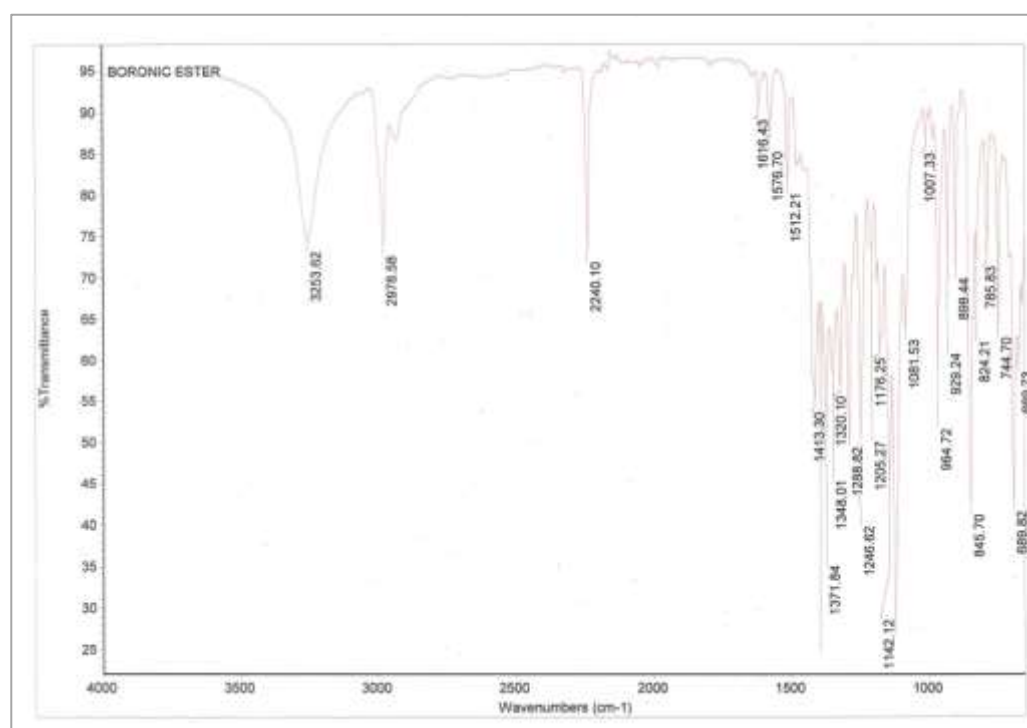


Figure 188 FTIR spectra of 2-hydroxy-4-(4,4,5,5-tetramethyl-1,3,2-dioxaborolan-2-yl)benzonitrile 77

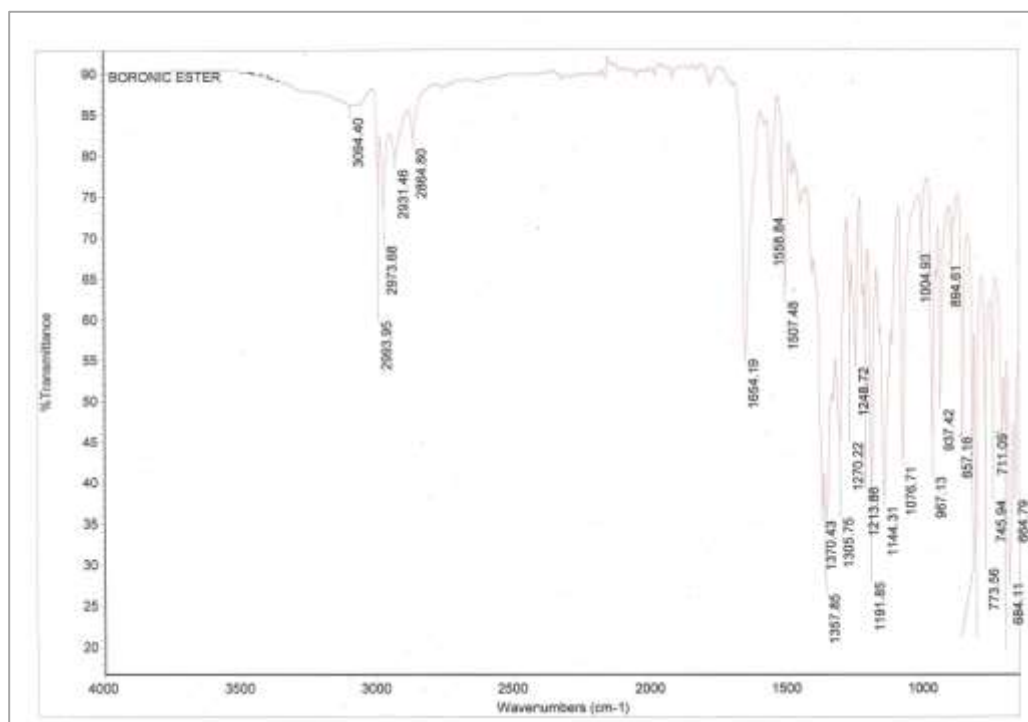


Figure 189 FTIR spectra of 2-Hydroxy-4-(4,4,5,5-tetramethyl-1,3,2-dioxaborolan-2-yl)benzoic acid 79

9.3 Mass spectra

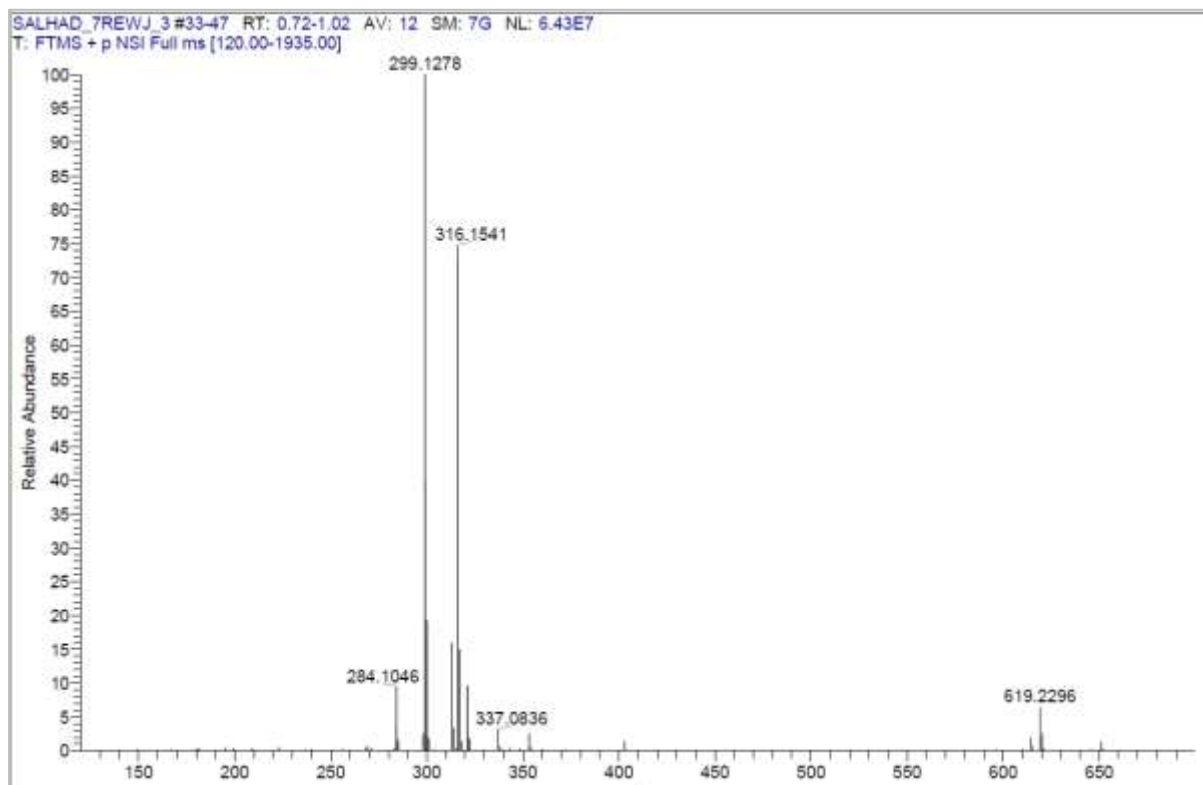
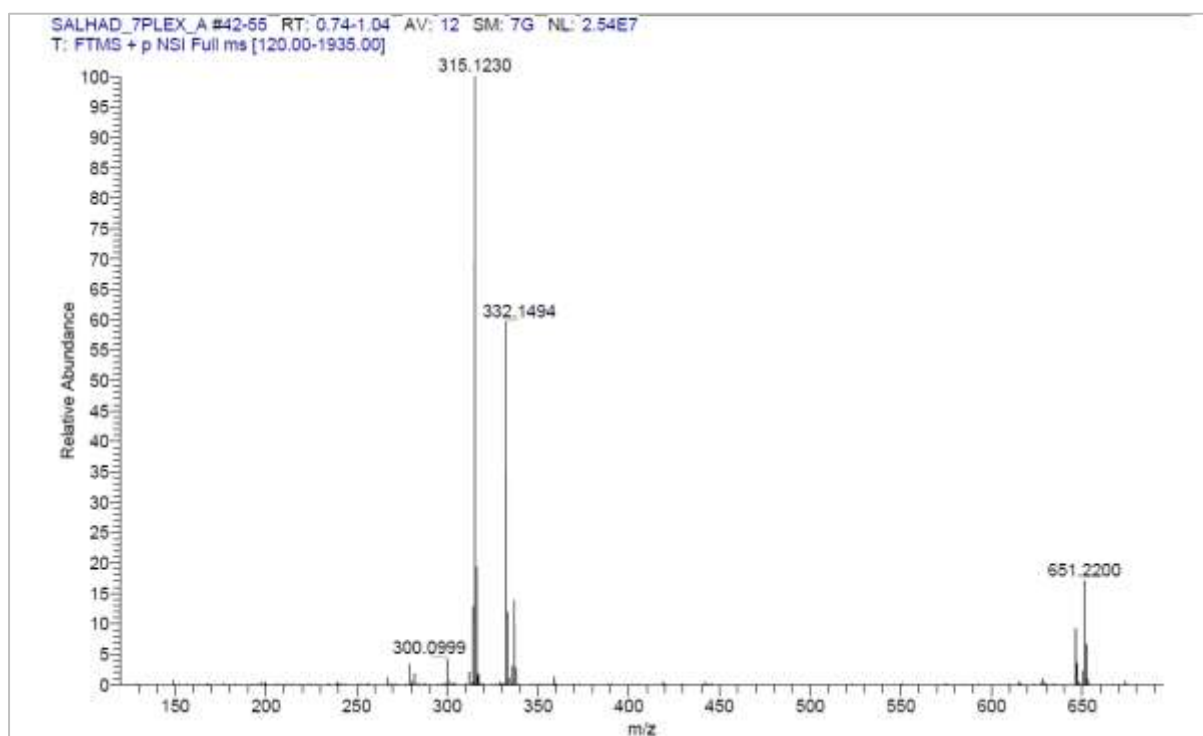
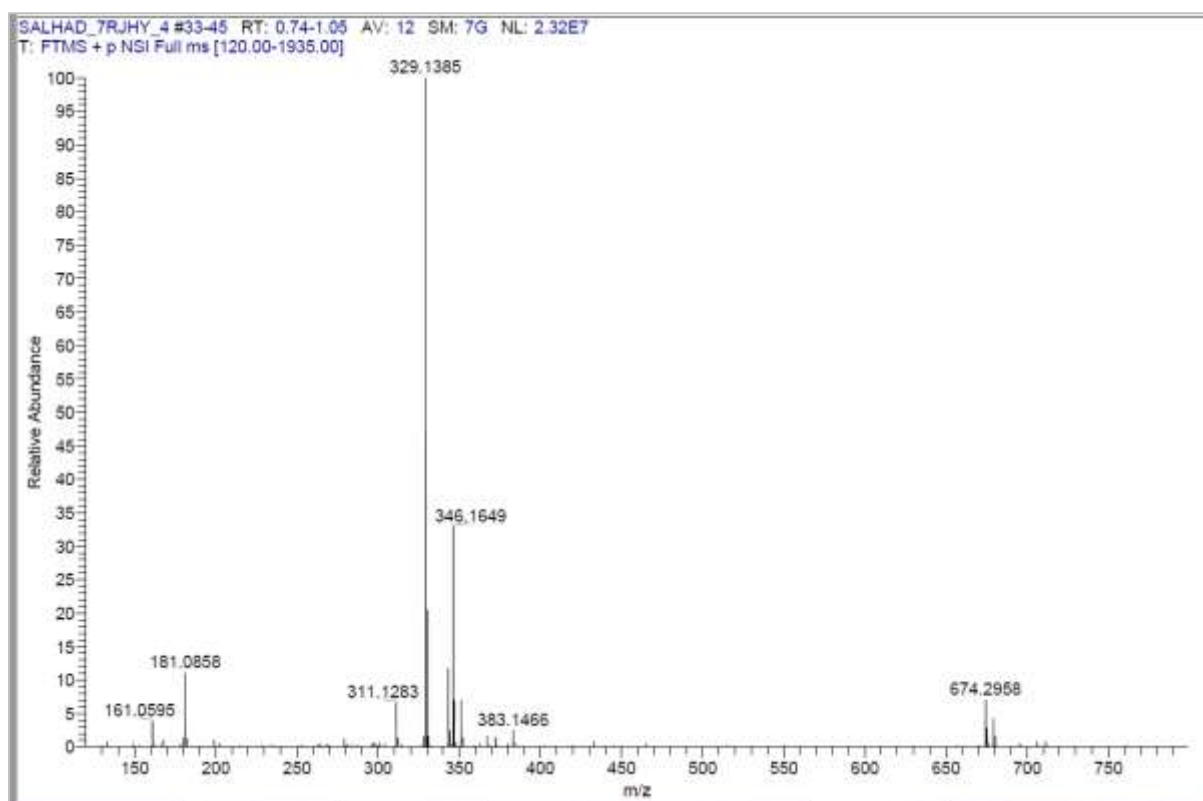
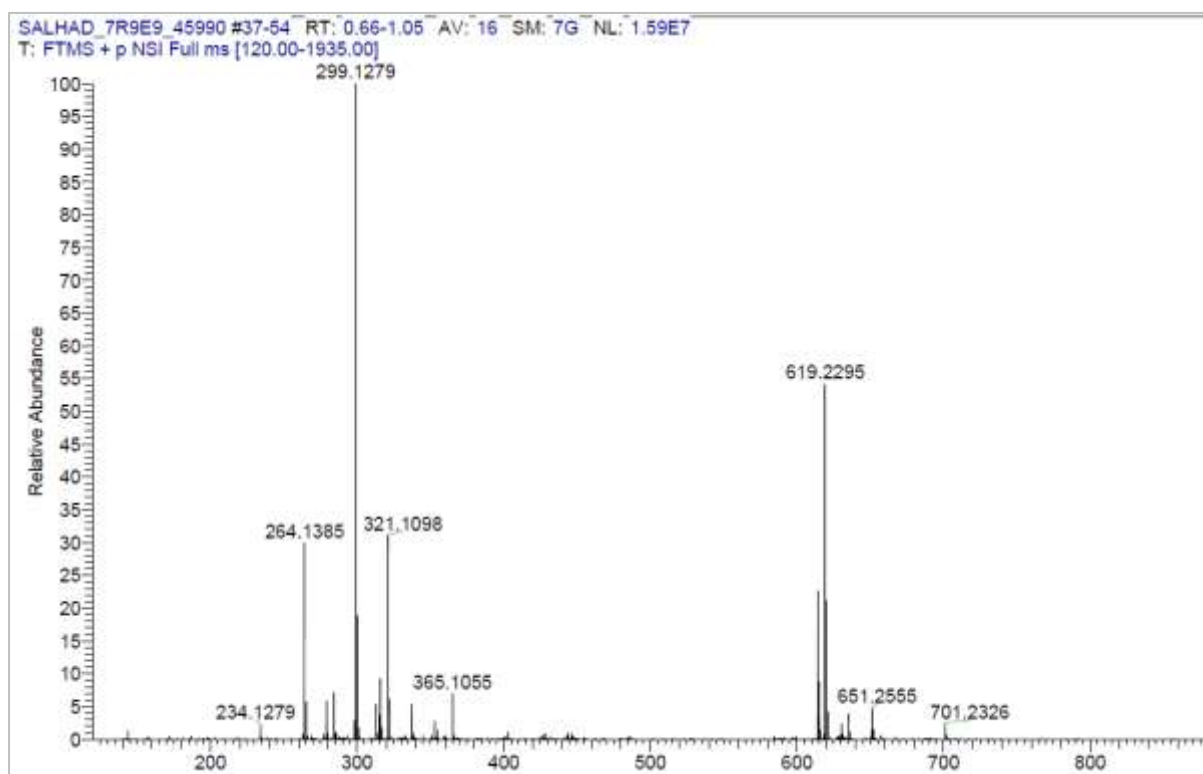
Figure 190 Mass spectra of (*E/Z*)-4-(3',4',5'-trimethoxystyryl)benzaldehyde (C₁₈H₁₉O₄) 42

Figure 191 Mass spectra of (*E/Z*)-2-hydroxy-4-(3',4',5'-trimethoxystyryl)benzaldehyde 43Figure 192 Mass spectra of (*E/Z*)-5-methoxy-2-(3',4',5'-trimethoxystyryl)benzaldehyde (C₁₉H₂₁O₅) 44Figure 193 Mass spectra of (*Z*)-2-(3',4',5'-trimethoxystyryl)benzaldehyde (C₁₈H₁₈O₄Na) 45

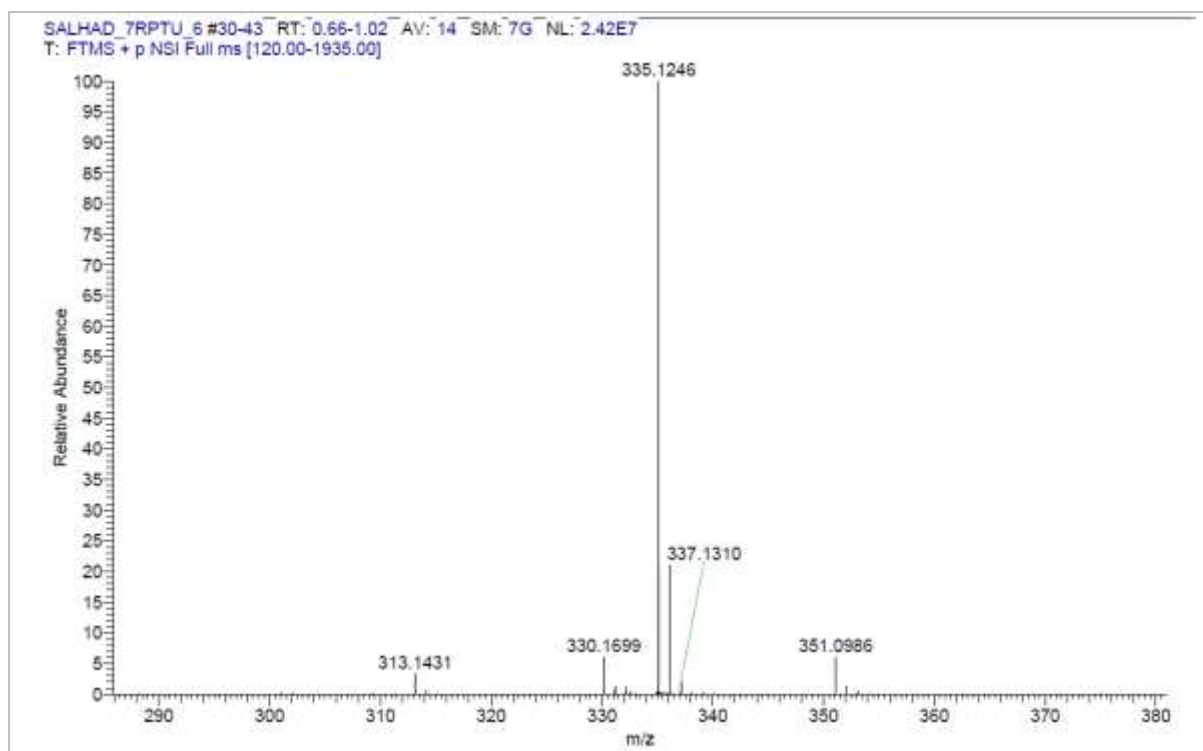


Figure 194 Mass spectra of (*E/Z*)-4-(3',4',5'-trimethoxystyryl)acetophenone ($C_{19}H_{21}O_4$) 46

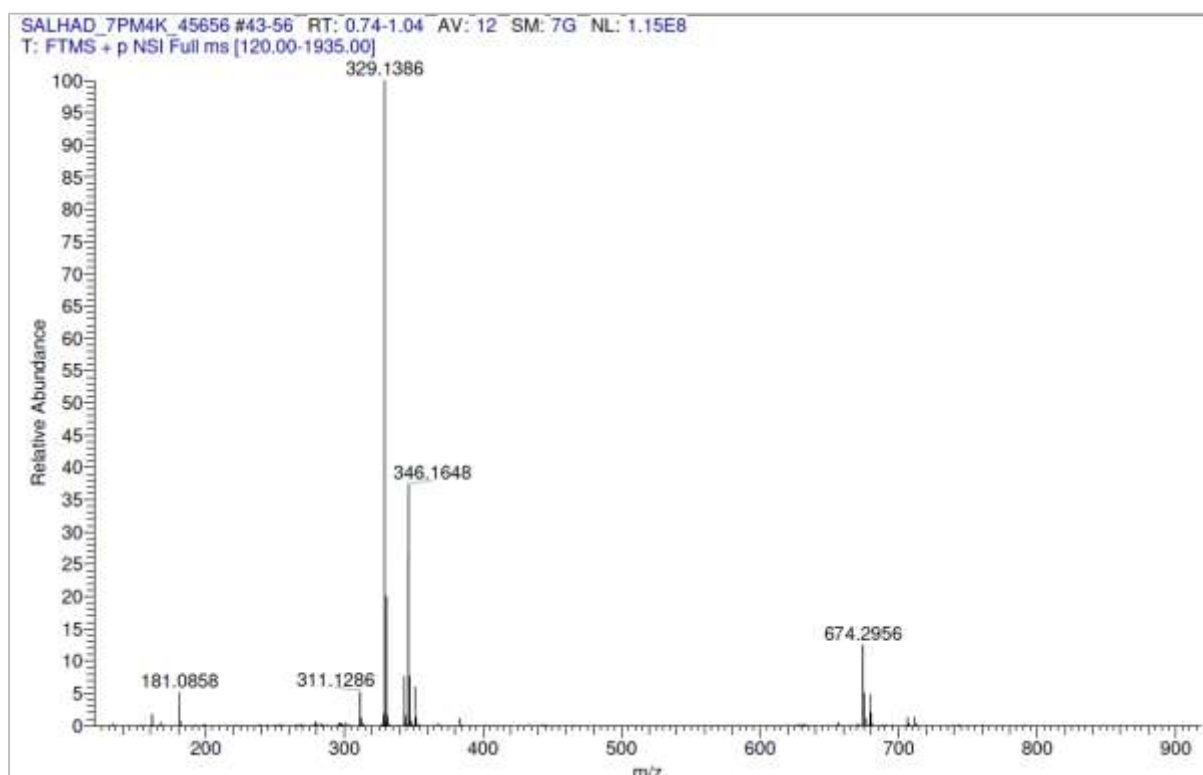


Figure 195 Mass spectra of (*E/Z*)-2-Hydroxy-4-(3',4',5'-trimethoxystyryl)phenyl)acetophenone ($C_{19}H_{20}O_5Na$) 47

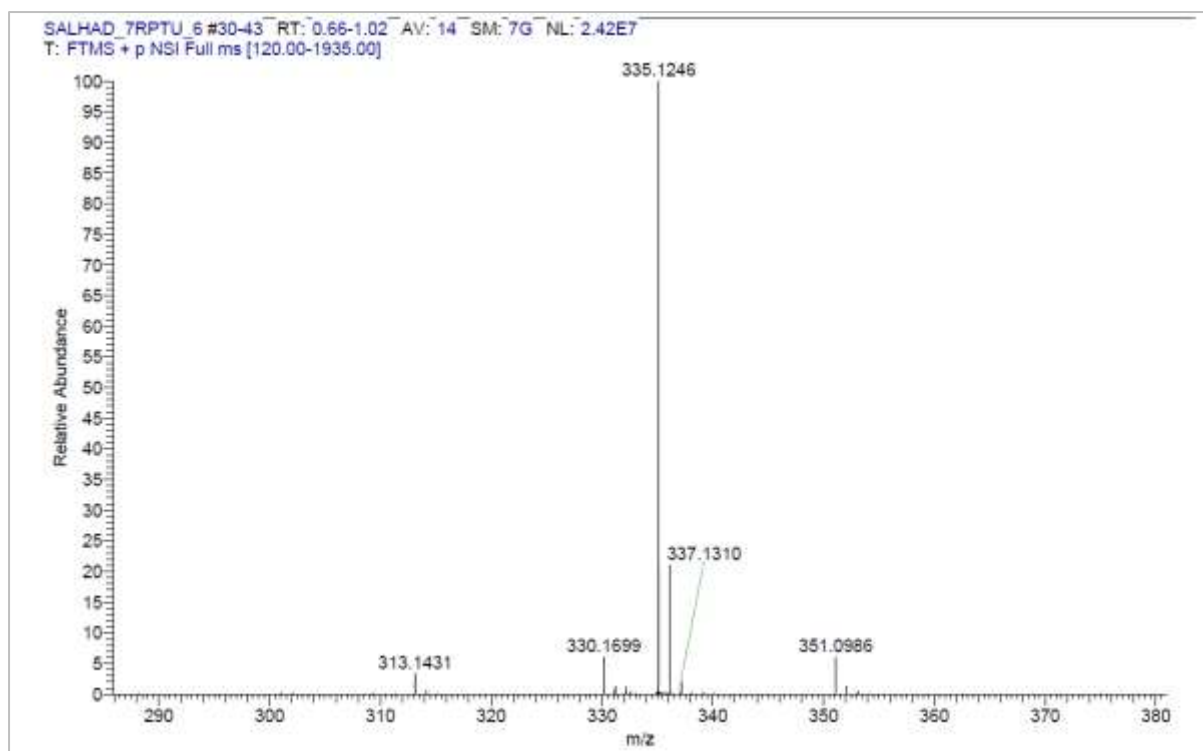


Figure 196 Mass spectra of (*Z*)-2-(3',4',5'-trimethoxystyryl)acetophenone (C₁₉H₁₉O₄) 48

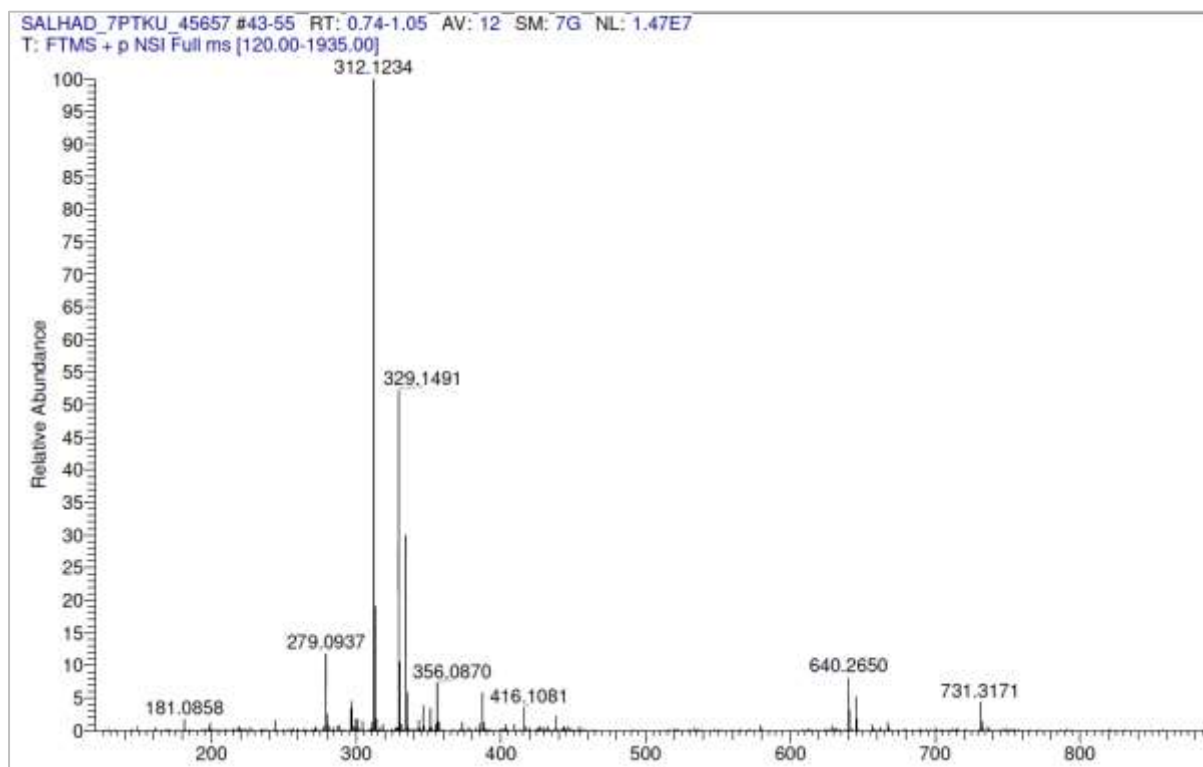


Figure 197 Mass spectra of (*E/Z*)-2-hydroxy-4-(3',4',5'-trimethoxystyryl)benzointrile (C₁₈H₁₈NO₄) 51

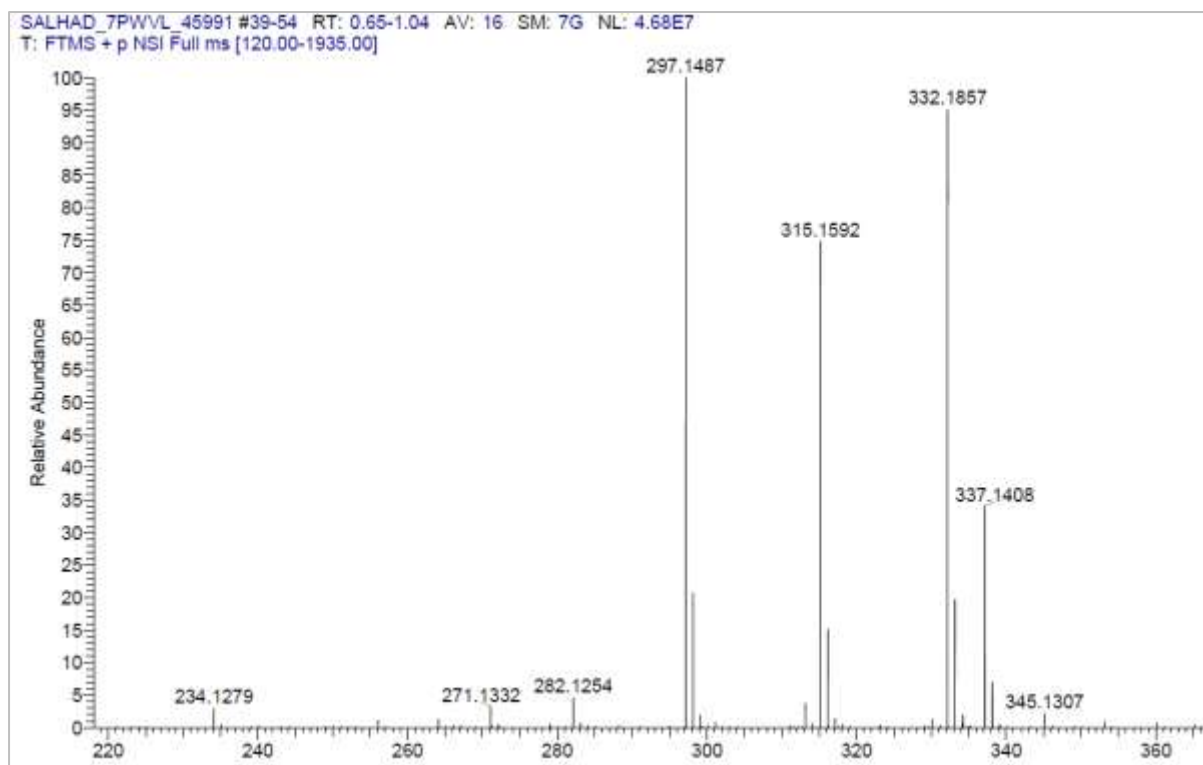


Figure 198 Mass spectra of (*E/Z*)-1-(4-(3',4',5'-trimethoxystyryl)phenyl)ethanol (C₁₉H₂₃O₄) 52

9.4 Absorbance and fluorescence spectra

9.4.1 (E)-4-(3',4',5'-Trimethoxystyryl)benzaldehyde (42)

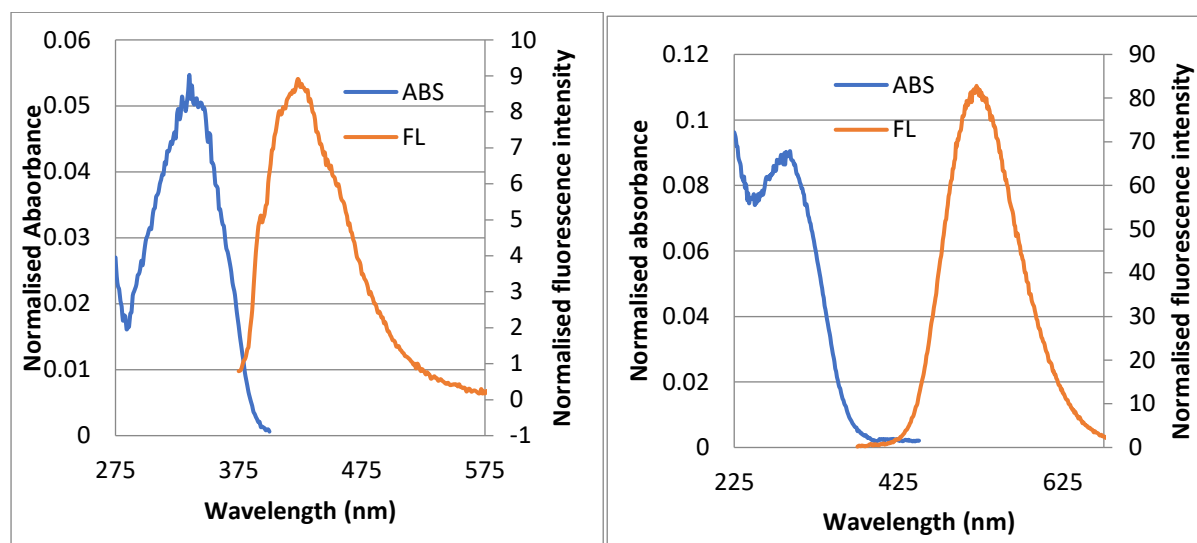


Figure 199 Absorbance and fluorescence spectra of 42 in hexane (left) and MeCN (right)

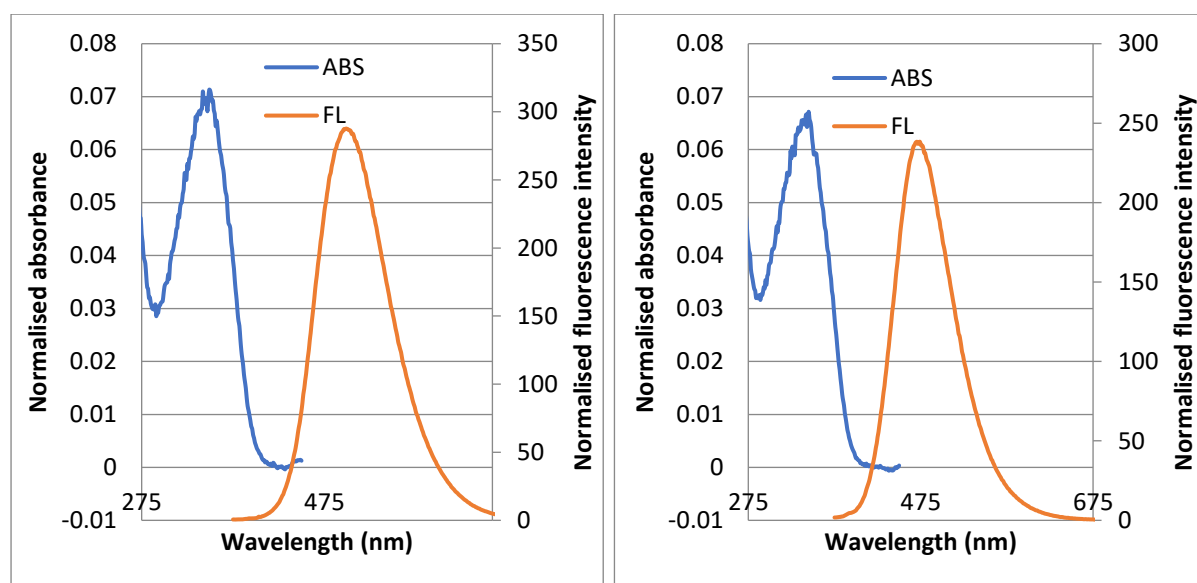


Figure 200 Absorbance and fluorescence spectra of 42 in DCM (left) and EtOAc (right)

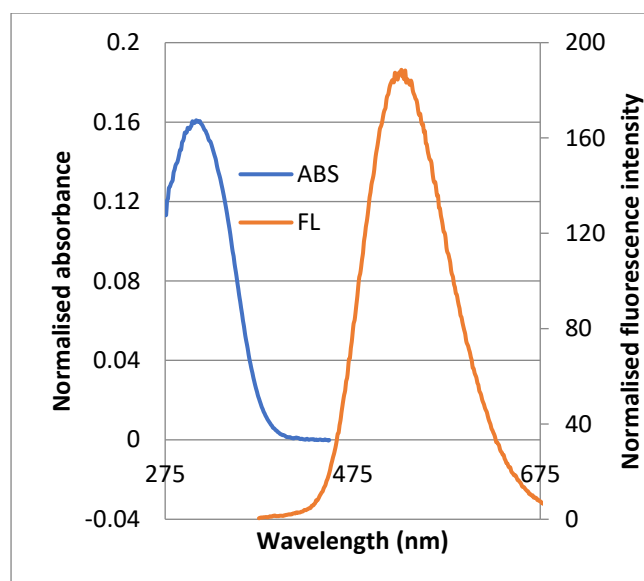


Figure 201 Absorbance and fluorescence spectra of 42 in DMSO

9.4.2 (E)-2-Hydroxy-4-(3',4',5'-trimethoxystyryl)benzaldehyde (43)

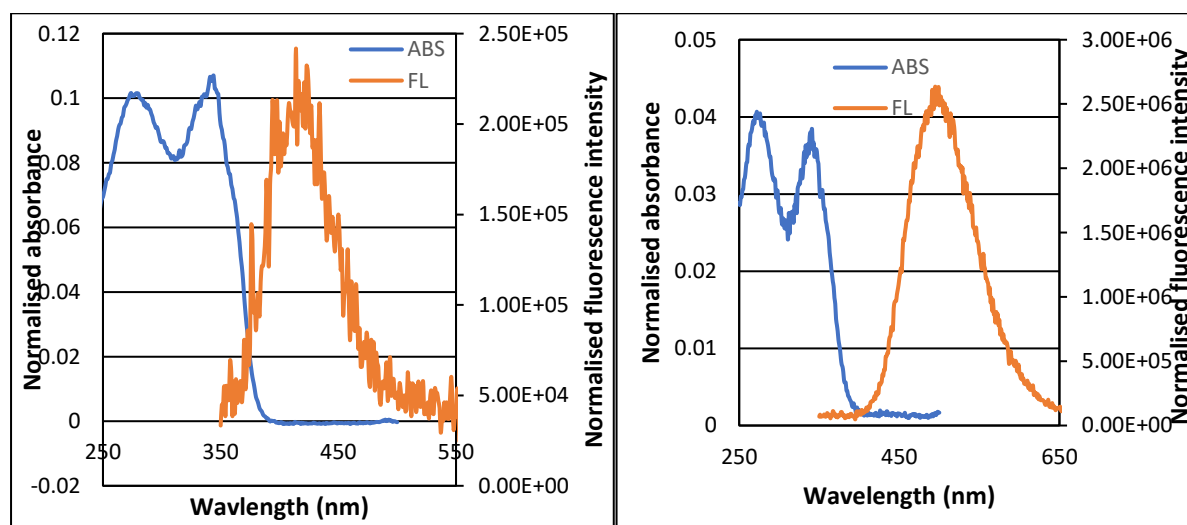


Figure 202 Absorbance and fluorescence spectra of 43 in hexane (left) and MeCN (right)

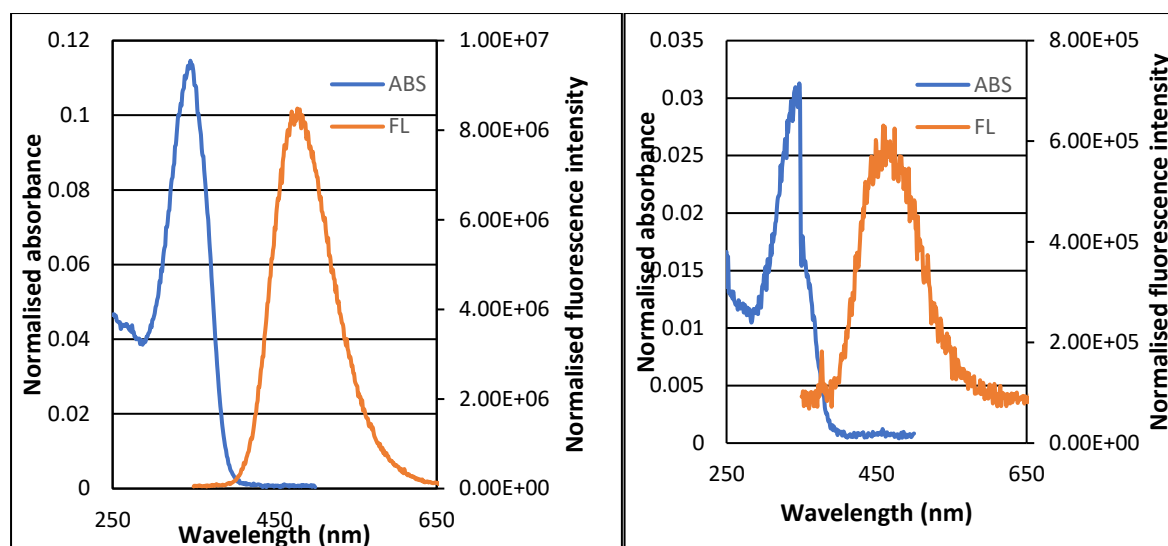


Figure 203 Absorbance and fluorescence spectra of 43 in DCM (left) and EtOAc (right)

9.4.3 (E)-4-(3',4',5'-Trimethoxystyryl)acetophenone (46)

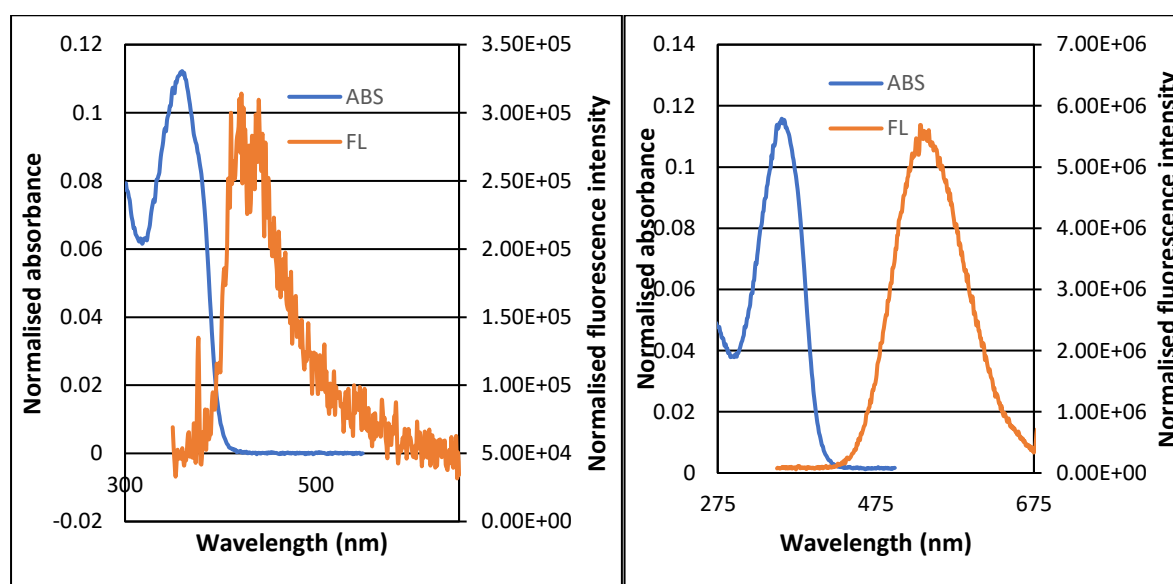


Figure 204 Absorbance and fluorescence spectra of 46 in hexane (left) and MeCN (right)

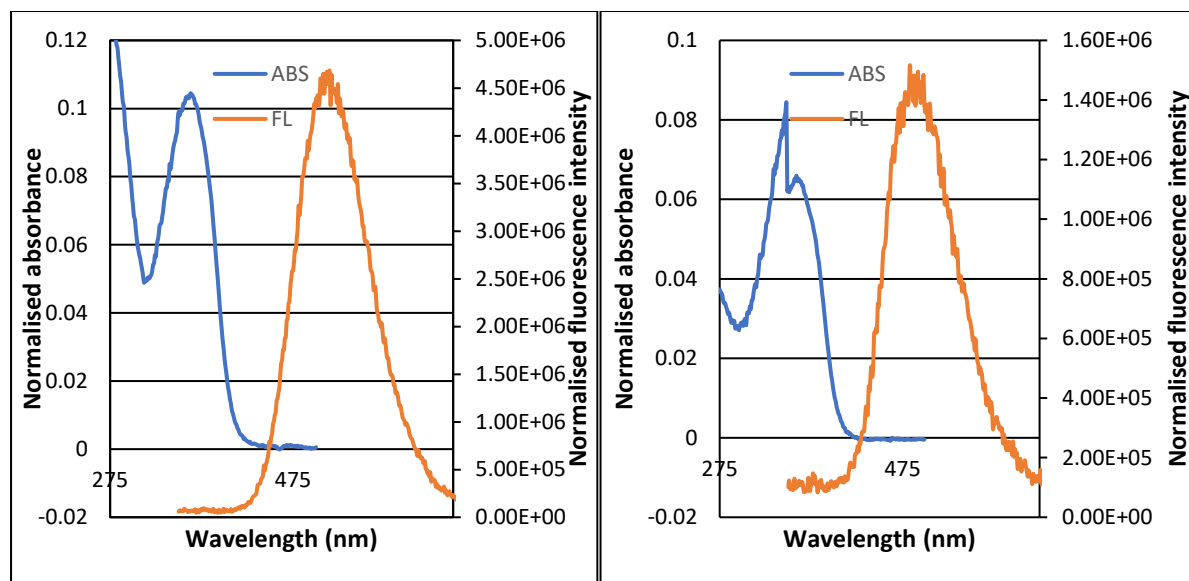


Figure 205 Absorbance and fluorescence spectra of 46 in DCM (left) and EtOAc (right)